Computer aided engineering methodology for the durability assurance of welded automotive components.

Ollier, Jenny-Louise

Computer Aided Engineering Methodology for the Durability Assurance of Welded Automotive Components

Jenny-Louise Ollier

Submitted to the Swansea University in fulfilment of the requirements for the Degree of Doctor of Engineering (EngD)

at

Swansea University,
August 2008

EngD in Steel Technology,
Materials Research Centre

DECLARATION

This work has not previously been accepted in substance for any degree and is not being concurrently submitted in candidature for any degree.

Signed .....(candidate)

Date 28/8/08

STATEMENT 1

This thesis is the result of my own investigations, except where otherwise stated. Where correction services have been used, the extent and nature of the correction is clearly marked in a footnote(s).

Other sources are acknowledged by footnotes giving explicit references. A bibliography is appended.

Signed ... .(candidate)

Date 28/8/08

STATEMENT 2

I hereby give consent for my thesis, if accepted, to be available for photocopying and for inter-library loan, and for the title and summary to be made available to outside organisations.

Signed . .....(candidate)

Date 3/9/08

ABSTRACT

Accurate durability analysis of MIG/MAG seam welds in automotive structures is a complex procedure. Evaluating stress accurately around the weld would require detailed finite element (FE) meshes. Since there are over 10 meters of such welds within a car structure, detailed FE modelling for weld durability assessment becomes impractical.

For effective weld Computer Aided Engineering (CAE) durability assessments, a balance is required between FE model details (mesh density) to achieve accuracy and the need to follow common modelling practices required by other CAE evaluations of a vehicle structure.

Therefore, new durability assessment approaches for welds are needed. In particular, suitable fatigue damage parameters, under the general term of "structural stress", are to be selected for improved weld fatigue life predictions.

This EngD research is concerned with computer aided fatigue life analysis of seam welds in automotive structures, especially in chassis assemblies. This has been achieved through:

- Weld Fatigue Data Generation
- Prediction
    - Damage accumulation in welds
    - Weld fatigue analysis

This research does not cover:

- Improving weld fatigue performance
- Fatigue mechanisms in welded structures

Among the main conclusions drawn as a result of my EngD research are:

Analysis of variable amplitude coupon and Front Upper Control Arm (FUCA) component testing shows that mean stress does affect fatigue lives.

There were three modes of fatigue failure recorded – toe, throat and interface failure. Overall, for both Volvo and Battelle approaches, structural stress-life (S-N) curves for welds are dependent on failure modes. For each failure mode, however, a master S-N curve does exist and is relatively independent of joint geometry.

One of the main achievements of the current EngD research is the extension of the existing Volvo and Battelle methods to allow life prediction of fatigue failure from weld throat and interface.

CONTENTS

LIST OF FIGURES

LIST OF TABLES

LIST OF ABBREVIATIONS

Chapter 1:

kg	Kilogram
ABS	Anti-Locking Braking System
ULSAB	Ultra-Light Steel Auto Body
ULSAS	Ultra Light Steel Auto Suspension
HSS	High Strength Steel
CAE	Computer Aided Engineering
FE/FEM	Finite Element/ Finite Element Modelling
FUCA	Front Upper Control Arm

Chapter 2:

Stage I	Crack Initiation and Growth of Short Fatigue cracks
Stage II	Propagation of "Long" Cracks
R	Fatigue stress or load ratio
S-N	Stress-Life Data
E-N	Strain-Life Data
LEFM	Linear Elastic Fracture Mechanics

MPa	Mega Pascal (1MPa = 10^6Pa)
LCF	Low Cycle Fatigue
HCF	High Cycle Fatigue
σ_{max}	Maximum Stress
σ_{min}	Minimum Stress
$\Delta\sigma$	Stress Range
σ_a	Stress Amplitude
σ_m	Mean Stress
Nf	Number of Cycles to Failure
'A' or 'a'	y-axis intercept value
'b'	Basquin Exponent
'm'	Inverse of slope
S_e	Endurance Limit
Su or σ_u	Ultimate Tensile Stress
σ_f	True Fracture Stress
σ_y	Yield Stress
$\Delta\varepsilon$	Strain Range
$\Delta\varepsilon_p$	Plastic Strain Range
$\Delta\varepsilon_e$	Elastic Strain Range
$\frac{\Delta\varepsilon}{2}$	Strain Amplitude
σ'_f	Fatigue Strength Coefficient (MPa)
E	Young's Modulus (MPa)
$2N_f$	Number of Reversals to Failure (1 reversal = ½ cycle)
b	Fatigue Strength Exponent
ε'_f	Fatigue Ductility Coefficient
c	Fatigue Ductility Exponent
K	Stress Intensity Factor (MPa$\sqrt{}$mm)
K_c	Stress Intensity Factor Critical Value
ΔK	Range of Stress Intensity Factor
$\frac{da}{dN}$	Crack Propagation Rate
σ	Applied Stress to the Component (MPa)
a	Crack Length (mm)
Y	Correction Factor Related to Specimen and Crack Geometry.
C and m	Material Constants
ΔK_{th}	Threshold Value

Chapter 3:

MIG	Metal Inert Gas Welding
MAG	Metal Active Gas Welding
HAZ	Heat Affected Zone
TIG	Tungsten Inert Gas Welding

Chapter 5:

CO_2	Carbon Dioxide
AHSS	Advanced High Strength Steel
BIW	Body-in-White

SUVs	Sport Utility Vehicles
CAD	Computer Aided Design
UHSS	Ultra High Strength Steel
HSLA	High Strength Low Alloy Steel
LCF	Low Cycle Fatigue
C-Mn	Carbon- Manganese Steel
TRIP	Transformation-induced Plasticity Steel

Chapter 6:

σ_{geo}	Structural Geometric Stress
$P_k(t)$	Force Time History
$P_{k,fea}$	Magnitude of the Force, Applied to FE Model
$\sigma_{ij,k}$	Static Stress Component for Load Case k
D	Damage Constant for Miner's Rule
n_i/N_i	Cycle Ratio
n_i,	Number of Cycles observed at the Stress Level
N_i	Number of Cycles to Failure at the Same Stress Level.
FLOW	Fatigue Life of Welds (in-house Land Rover Software)
FEMFAT	Finite Element Method/Fatigue
R1MS	Radius 1mm with Mean Stress and Scatter
R03MS	Radius 0.3mm with Mean Stress and Scatter
JIP	Joint Industry Partnership

Chapter 7:

GF	Gauge Factor
R	Resistance of the Undeformed Gauge
ΔR	Change in Resistance Caused by Strain
ε	Strain
GFP	Grey Field Polariscope

Chapter 10:

Hz	Hertz, Frequency Unit
FF	Final Failure
SD	Stiffness Drop
$\Delta\sigma$	Fatigue Stress Range
ΔF	Fatigue Load Range
$\Delta\delta$	Displacement Range
Quad4	4-Noded Quadrilateral FE Elements
2D	2-Dimensional
f_y	The Line Force Vectors
m_x	Moment Vectors
$F_1, \ldots, F_n$	The Element Nodal Force
$f_1, \ldots, f_n$	The Line Force
$l_1, \ldots, l_{n-1}$	The Element Length
f_y	Line forces with respect to y'
m_x	Line Moments with respect to x'
t	Thickness
s_s	Structural Stress
S_s	Equivalent Structural Stress
r	Loading Mode Ratio

I(r)	Loading Mode Correction for Load-Controlled Loading
F_1	First Load Level (Block Loading)
F_2	Second Load Level (Block Loading)
k	Scaling Factor
δ	Offset Factor
F_{max}	Maximum Load
F_{min}	Minimum Load
S_{max}	Maximum Signal Level
S_{min}	Minimum Signal Level
M_1	Slope between R=-1 and R=0.1 on Goodman Diagram
M_2	Slope between R=0.1 and R=0.5 on Goodman Diagram
$\sigma_a^{R=-1}$	Stress Amplitude at R=-1
f	Force per unit weld length
GKN	Coupon Manufacturer
TKA	(TKA-Tallent) Coupon Manufacturer
GM1	Partially Welded Lap-Shear Coupon Fabricated by GKN
GM2	Fully Welded Lap-Shear Coupon Fabricated by GKN
GM3	Partially Welded Peel Coupon Fabricated by GKN
GM4	Fully Welded Peel Coupon Fabricated by GKN
GM5, 6, 8	T-Shaped Coupon Fabricated by GKN
GM11A	Partially Welded Lap-Shear Coupon Fabricated by GKN
GM11B	Fully Welded Double Lap-Shear Coupon Fabricated by GKN
TM1	Partially Welded Lap-Shear Coupon Fabricated by TKA
TM2	Fully Welded Lap-Shear Coupon Fabricated by TKA
TM11A	Partially Welded Lap-Shear Coupon Fabricated by TKA
TM11B	Fully Welded Double Lap-Shear Coupon Fabricated by TKA
M1	Partially Welded Lap-Shear Coupon used in Photoelasticity
M2	Fully Welded Lap-Shear Coupon used in Photoelasticity
M11A	Partially Welded Lap-Shear Coupon used in Photoelasticity
Z1	Lower Surface of a Shell Element
Z2	Upper Surface of a Shell Element

ACKNOWLEDGEMENTS

I would like to acknowledge the help and support from my colleagues at Corus ASU in particular my industrial supervisor Dr. Yi Gao for his patience and guidance, Ray Long for his help in modelling, Dave Norman for his help in cross product vectors from global to local coordinate systems. Not to mention Martin Whitwood in Corus STC for helping me use the SEM, and my EngD theme leader Vicky Cuddy.

I would like to express my gratitude to Mr Andrew Vass of Corus RD&T IJmuiden, whose secondment in 2004 to Jaguar and Land Rover helped initiate the welded coupon fatigue tests and laid the ground for my subsequent testing for weld fatigue data generation.

At Jaguar and Land Rover I would also like to thank the Strength and Durability team for their continuous support throughout the project. In particular my industrial supervisor Dr. Lu for his knowledge of fatigue testing, and Peter Randle in chassis who produced the baseline FUCA model and helped me understand how to use FLOW and Verity.

At Swansea University I would like to acknowledge the help and support from my academic supervisor Professor John Evans, and also Dr. Mark Whittaker for their support throughout this project.

1. INTRODUCTION

Since the development of the monocoque autobody in 1922 by Vincenzo Lancia, sheet steel has become the most important material in the automotive industry. Sheet steels give strength, recyclability, relative ease of manufacture and weldability. Unfortunately, the industry is under continuing demands to meet tougher legislation requiring significant improvement in performance, weight reduction, enhanced safety, increased fuel efficiency, reduced fuel emissions with increased recyclability and climate protection. Consequently, as consumers in Europe become more environmentally aware, the successful vehicle manufacturers will be the ones with the best fuel economy and therefore lower polluting emissions. Thus reducing the weight of the steel body structure and components will aid weight saving, which subsequently has great financial implications as light vehicles will not only be cheaper to manufacture, but also be more attractive to customers. (Clough 2003)

Since the drastic rise of fuel prices in the seventies, the reduction of vehicle weight has become a basic requirement for the development of new cars, trucks and busses. Nevertheless there is the general tendency in the opposite direction. The reasons for this contradiction are, on the one hand additional features for more comfort and safety in modern vehicles, as well as increased motor torque. On the other hand, the potential for mass savings in the basic structure is not enormous. For example, the benefit of a magnesium transmission housing for a passenger car compared to an equivalent one made of aluminium is a weight saving of about 5 kg.

The arrival of options such as air conditioning, passenger airbags, ABS, satellite navigation etc, which are standard fitments on the majority of cars, and aid to customer ride and drive satisfaction, has resulted in overall weight increases of vehicles. This is constantly working against the overall objective of weight reduction.

The increase in weight from customer safety and comfort systems has coincided with an overall decrease in the proportion of steel used in a car compared to other more lightweight materials, which are finding their ways into automotive structures. To maintain a competitive edge in the automotive market over materials such as composites and aluminium, the steel industry has developed and is continuing to

develop stronger, thinner steels for lightweight automotive body-in-white structures, chassis members and suspension components.

Projects such as ULSAB (Ultra Light Steel AutoBody) and ULSAS (Ultra Light Steel AutoSuspension) co-ordinated by an international steel producers consortium have been developed to identify approaches to vehicle weight reduction. They have already shown that use of high strength steels (HSS), tailor welded blanks, tube hydroforming and continuous joining techniques allow a weight saving of greater than 20% to be achieved for steel autobody and suspension construction, compared to current vehicles in service. (Hughes 1995)

During design of a welded component, materials are selected with properties which allow a margin of safety against the material yielding at service loads, where typically designers try to ensure that peak stresses are below $^{2}/_{3}$ of the yield stress. However, under cyclic loading, fatigue failure can occur at loads well below this value. Fatigue is important for designers, as it is the single largest cause of component failure, estimated at approximately 90% of all failures. Fatigue crack initiation is usually attributed to the presence of some inherent stress concentration in the structure associated with the fabrication or design. (Ellwood and Lewis 1999)

Many failures can be attributed to poor component design. Designers commonly allowed large safety factors to reduce the likelihood of fatigue failure but in today's market this is becoming increasingly unacceptable. For example, automotive designers aim to improve structural performance, crashworthiness, reduce weight and improve reliability at the same time.

Welding is still a predominant assembly technique for automotive components such as suspension arms and chassis members. Therefore automotive designers must appreciate the stress concentrations that fusion seam welds introduce into automotive components, if component validation test programmes are to be significantly reduced and virtual prototyping is to be introduced.

High strength steel structures are still required to satisfy specific performance criteria of the automotive manufactures particularly with respect to impact and durability.

Lighter vehicles require better understanding of fatigue properties under service conditions. To increase understanding and prediction accuracy then full size components must be tested in their in-service environment with a representative load regime.

Vehicle components are exposed to loading conditions that vary in magnitude and frequency. The steel thickness, type of joining mechanism and in-service loading conditions are the main influences in the durability of seam-welded structures. Data for determining the fatigue strength of seam-welded structures is usually available in the form of simple welded joint load versus life, encompassing uniaxial constant amplitude loading of simple components through to testing of a component with multiaxial, in-service loading.

With the drive to have more environmentally friendly cars, vehicle manufacturers are reducing vehicle weight by using high strength steels, so it is important that designers have reliable techniques to evaluate the life of seam welds throughout the various stages of vehicle development.

In the automotive industry there is a drive to decrease the development lead-times and costs for new car models. To achieve this, automotive manufacturers have increased their usage of computer aided engineering (CAE) tools at all stages of vehicle development. There is a need to conduct CAE durability analysis in the early stages of design to ensure that fatigue related problems are reduced or removed before any costly prototypes are made.

Accurate durability analysis of seam welds in automotive structures is a complex procedure. Evaluating stress around such welds would require a detailed finite element (FE) mesh. Within each car structure, especially chassis and suspension structure, there may be well over 10 meters of welds, which inevitably result in too large a model to be practical if such detailed FE weld representation is adopted.

Therefore, effective weld CAE durability analyses require a balance between accuracy of the FE model and the common practices involved in CAE evaluation of

automotive structures. Current CAE fatigue analysis methods have a lack of correlation and validation with physical testing.

Weld fatigue life prediction in the current EngD research is based on a "structural stress" that is derived from FE analyses. The outcome of this research is to enable complex components and structures to be represented simply in the early FE stage of analysis but to gain accurate FE assessment of the components.

The EngD research to be described and summarised in this thesis is a 4-year evaluation and development of new CAE weld durability assessment techniques of seam welds in automotive structures, especially in chassis assemblies. This has been accomplished through:

- Experimental Testing
    - Data Generation using simple coupon lap-shear, peel and t-shaped joints. S-N curves will be produced from the "structural stress" arising from the FE models of the coupon joints.
    - Front Upper Control Arm (FUCA) component testing – to gain lives of an automotive chassis component, for comparisons with weld fatigue life predictions.
- "Structural Stress" Analysis
    - Using a coarse FE mesh for all coupon geometries due to the impracticality of a very fine mesh.
    - With simple weld representation to aid the accurate FE assessment.
- Prediction
    - Damage Accumulation in welds – validating Miner's Rule for variable amplitude loading.
    - Weld Fatigue Analysis – FUCA component estimation of life with comparison to actual test data.

This research does not cover:

- Improving weld fatigue performance.
- How fatigue mechanisms occur in welded structures – in-depth observations of the weld fracture surfaces and microstructures.

2. FATIGUE

2.1 Introduction – A Brief History

The term 'fatigue' was first used over 150 years ago by early investigators who noticed that, when cyclic stresses were applied, they caused gradual but no noticeable change in the materials ability to resist stress, although the materials were thought to be tired or fatigued. On removing the stresses, the tired material did not recover, as the damage was cumulative. This damage accumulation was termed 'fatigue'. (Dowling 1993)

Since the realisation that fatigue affects metals, it has been an important area of research especially when bridge and railroad components in Europe were noticed to be cracking under repeated loads in service in the mid 1800s.

The first fatigue investigation was thought to be done by a German mining engineer W.A.S. Albert in 1828 who applied cyclic loads to iron mine hoist chains. The earliest recorded fatigue failure occurred in stagecoach axles and subsequently in railroad axles as they developed. August Wöhler, a German railroad engineer in 1850s, conducted fatigue tests on full-scale railway axles and on small laboratory specimens using different materials to establish stress levels at which fatigue does not occur. Wöhler started the development of design strategies, which became the basis of the modern-day fatigue analysis.

Since the 1850s, extensive research has been carried out into all aspects of fatigue such as the fatigue lives of different materials, further understanding of fatigue and producing methodologies to allow designers and engineers to estimate the fatigue lives of components. Even with all this research and understanding however, fatigue failure in components and structures is still a major problem, with approximately 80-90% of all failures in service being attributed to it. Fatigue is also important in the automotive industry, which is driven to reduce component weight while improving design stress levels.

2.2 Fatigue and Fatigue Failure Processes

Fatigue is a failure process where accumulative damage or premature failure can occur in machine components, vehicles and structures, which are subjected to

dynamic, fluctuating stress from repetitive loading. Fatigue therefore is a major design criterion in establishing the structural integrity of components in many engineering applications.

There are many definitions describing fatigue, but a formal description may be considered to be:
"The process of progressive localised permanent structural change occurring in a material that is subjected to conditions that produce fluctuating stresses and strains at some point or points and that may culminate in crack or complete fracture after sufficient number of fluctuations". (ASTME 1995)

Fatigue damage is caused by the simultaneous actions of three basic factors: 1) cyclic stress, 2) tensile stress and 3) plastic strain. If one of these factors is not present then fatigue failure becomes more difficult. The plastic strain initiates the crack, tensile stress promotes the crack growth, and failure often occurs at stress levels, which are much lower than that required under static loading. Therefore if the structure undergoes a steady (static) load, then fatigue failure will not occur, although in reality it is generally very rare to find a structure not undergoing any dynamic loading. Other factors such as variations in pressure, temperature, corrosion, overload, microstructure, vibrations, wind, etc, can all introduce a fluctuating load into a structure. In today's society, many structures can be affected such as automobiles, ships, aircraft, bridges, and pressure vessels etc.

Fatigue is a localised phenomenon, which occurs in structures under elastic engineering conditions; this is the reason why fatigue damage is insidious. Under static loading plastic deformation occurs, but with fatigue failure there is no obvious deformation as local plasticity initiates a crack or defect, but more of a brittle type of structural appearance.

Generally the process of fatigue crack development involves a number of well-defined stages, and the formation of small cracks occurs on a localised scale with non-uniform deformation. Manufacturing processes such as turning, grinding etc. cause surface roughness flaws from which microcrack formation can occur.

The defined stages of fatigue crack development are:

- Stage I - Crack initiation
- Stage II - Crack propagation
- Accelerated crack growth to failure (overload – fracture toughness has been exceeded)

Each stage of the process can be classified as a separate issue and is influenced by many factors. The overall process is shown in figure 2.1a.

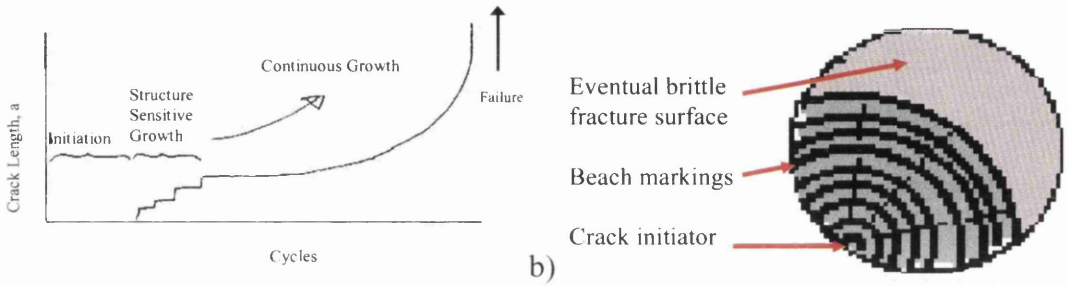

Figure 2.1: a) Fatigue Crack Growth Process, b) Typical Microstructural Fracture Surface of Fatigue Failure (Ritchie 1999)

Fatigue cracks usually initiate at free surfaces, which have the highest stress concentration, in surface grains where environmental interaction encourages crack formation. Crack propagation tends to show beach markings, which appear perpendicular to the crack direction. During the final stage of growth, the fracture surface shows an increasing proportion of features associated with static failure as shown in figure 2.1b. (Ritchie 1999)

2.3 Factors Affecting Fatigue

Many factors can have a significant influence on fatigue of structures. These factors are related to material characteristics, manufacturing process as well as service conditions. Fatigue crack initiation and propagation are determined to a large extent by such factors as surface conditions, component shape and geometry and the type of material used.

Material factors influencing fatigue properties may include the material type or family (e.g. mild steel, high-strength steels, or aluminium alloys etc.), mechanical properties (i.e. yield and tensile strengths, elongation to failure, and fracture

toughness etc.), microstructures (e.g. grain sizes, phases and inclusions), and surface conditions (e.g. surface roughness, scratches or notches, and hardness).

Manufacturing factors relates to the component fabrication details, such as work hardening from metal forming operations, welding processes and residual stresses resulting from machining and tooling operations, as well as surface treatments, .

Structural components under in-service load and experimental test conditions can experience a number of different stress/strain-time histories. Service life factors affecting fatigue are (1) the nature of the loads, i.e. whether the components are undergoing tensile or compressive stresses; and (2) stress state, i.e. whether a component is subjected to uniaxial loading or multi-axial loading during service.

2.3.1 Surface Finish Effects

Fatigue properties are very sensitive to surface conditions, as they will strongly influence the initiation of a crack. Surface scratches, notches and residual stresses remaining from machining and tooling operations, all act as stress raisers, which magnify the stress level locally and therefore shorten the period required for cracks to initiate.

2.3.2 Surface Treatments

Surface treatments can introduce compressive stress at the surface and improve the fatigue performance by changing the residual stress state. There are three different methods of treatments: mechanical, thermal and plating. (Dieter 2001)

- **Mechanical** processes such as cold rolling or shot/needle peening are the most common ways of introducing compressive residual stresses; the material strength increases through work hardening. This form of treatment only influences long lives.
- **Thermal** treatments such as carburising and nitriding rely on diffusion of carbon or nitrogen into the steel surface, improving the material strength and producing the required compressive surface residual stresses.
- **Plating** processes using nickel or chrome create tensile residuals thus reducing the fatigue limit of the steel significantly, although annealing after the plating treatment will relieve the stresses.

2.3.3 Stress Concentration Effects

In general engineering, many fatigue design methods often use an average or nominal stress value that will depend on the service load and the cross sectional area. During normal service loads, it is very important that material yielding never occurs and that nominal stress levels are kept below the limit of proportionality (elasticity) over the bulk of the component. Otherwise, areas of excessively high local stress concentration may exist, usually coinciding with such features as holes, sharp corners etc.

K_t, the stress concentration factor, is the ratio of maximum stress to average stress and is based on geometrical effects and elastic conditions. If many discontinuities are present in a component, they can interfere with each other if they are close together. Widely spaced holes do not interfere with each other and therefore affect the stress field, whereas holes in close proximity to each other will cause the stress fields to interact and behave as a single stress field.

2.3.4 Temperature

As the temperature is lowered the endurance limit tends to increase. At high temperatures between 370-540°C, steel's distinct endurance limit is removed, as the dislocations are mobile. Temperatures over 50% of the melting point cause creep phenomena to become a critical factor. Furthermore, high temperatures can remove the beneficial residual stresses.

2.3.5 Environment

The service environment which the component is subjected to can affect the fatigue life. A corrosive environment is the most critical as it attacks the metal surface and produces an oxide layer promoting further corrosive attack. This corrosion causes the formation of pits on the surface, which act as stress concentrations, thus accelerating fatigue failure. (Fine and Chung; Cui 2002)

2.4 Fatigue Loading Regimes

The most common loading sequences for test purposes are constant and variable amplitude.

2.4.1 Constant Amplitude Loading

Constant amplitude loading is represented by a simple stress history, which has a constant maximum and minimum stress. This is also the quickest and cheapest method for gathering data. The majority of tests completed are simple constant amplitude tests and the tests are usually carried out at fixed min/max stress ratios, R, of R=0 (zero to full tensile load), R=-1 (fully reversed loading) or $0<R<1$ stress about a positive mean, described in section 2.5.1.

Metal fatigue has been recognised as a random or stochastic process and, as a result, produces scatter in results even under carefully controlled experiments, this ultimately complicates the analysis of test data and application of it into design. Fatigue considerations are of major importance when designing for durability of components and structures particularly for motor vehicles. Since the work of August Wöhler, constant amplitude testing of materials and structures has been adopted as the method to characterise basic fatigue properties and the effect of design variations. The information gathered from these experiments is however not adequate when adopted for fatigue assessment of components and structures under variable amplitude loading.

2.4.2 Variable Amplitude Loading

Automobile components rarely undergo constant amplitude loading during their lifetime. Instead these components experience in-service load histories, which have variable amplitude and therefore can be quite complex. Therefore, the automotive industry is mainly interested in estimating the lives of vehicle components in terms of how many miles the vehicle can travel before the occurrence of fatigue crack initiation. All components in the vehicle are designed with a life well above the target vehicle design life.

Since in-service components experience more complex loadings/waveforms, which have a small probability of repetition over the component life, they are classified as enduring variable amplitude loading (figure 2.2 shows a typical history).

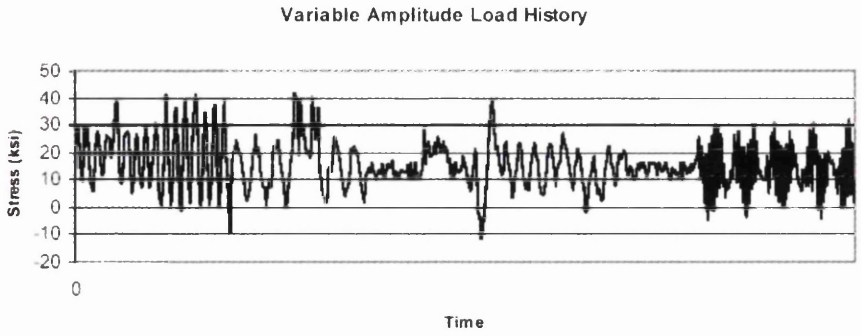

Figure 2.2: Typical Variable Amplitude History

The amount of fatigue damage occurring during initiation is very difficult to observe, as during this phase the damage mechanisms happen on a microstructural level, and unlike crack propagation, the damage cannot be measured. Fatigue data for materials under constant amplitude loading are usually expressed as the number of cycles to failure against the level of load applied. Sequence effects also influence crack propagation under complex loading - the order in which cycles are applied affects the rate of crack growth. Randomly varying load patterns cause life to be expressed as time (in cycles) whereas the service load history correlates to a distance travelled (e.g. miles). In addition, the random nature of the loading patterns cause problems with counting the number of applied "effective" load cycles.

The Linear Damage Rule is a method where the amount of cumulative damage can be determined, Palgrem in 1924 first proposed the rule, which Miner subsequently developed further in 1945, and is commonly referred to as either the Miner Rule or Palgrem-Miner Rule. For variable amplitude load history, the complex cycle is broken down into a series of individual effective load cycles, and the fatigue damage for each of these cycles can be determined based on constant amplitude test results at the same load or stress amplitude.

There are several different methods to categorise variable amplitude loading, the earliest methods being: Level-Crossing Counting, Peak Counting and Range Counting. (Dowling 1987) However these methods all have drawbacks and the most common and reliable method is the Rainflow Cycle Counting. (Power 1978)

2.5 Characterising Fatigue Performance of Materials

There are three primary methods to analyse fatigue, these are: stress–life (S-N) approach, strain–life (E-N) approach, and fracture mechanics approach.

The S-N method is the oldest nominal stress approach and is used where the applied stress is within the elastic range of the material and is applicable for long life, or high-cycle fatigue (HCF) applications. With short lives or low-cycle fatigue (LCF) the S-N approach does not work well as the applied strains have a significant plastic component due to high load levels. This approach does not account for the local behaviour of the material. Unfortunately this method does not distinguish between crack initiation and propagation but deals with the whole life of a component.

The E-N method accounts for local behaviour and is more applicable for short life applications where the strain is no longer elastic but plastic. It is also often considered as a crack initiation approach.

The crack propagation or fracture mechanics approach is based on the linear elastic fracture mechanics (LEFM) principles adapted for cyclic loading. This method is used to predict the propagation life from an initial crack or defect. For predicting the total fatigue life, it is used in conjunction with the E-N approach.

2.5.1 Stress-Life (S-N) Data

Wöhler first utilised the stress life or S-N method for understanding the concept of fatigue, and it stood as the main method for obtaining fatigue data for nearly a century. Therefore, it is often called the Wöhler curve. The S-N method involves applying a sinusoidal cyclic load to a specimen. The nominal stress resulting from the applied load is plotted against the number of cycles to failure, and this test is then repeated for a range of loads to give the S-N curve for smooth or unnotched specimens. Stress is always plotted on the y-axis with number of cycles on the x-axis. The curves are then plotted using a logarithm (log) scale to obtain results in a straight line, but it is also common to find S-N curves being plotted on semi log scales. Figure 2.3 shows such examples of S–N curves.

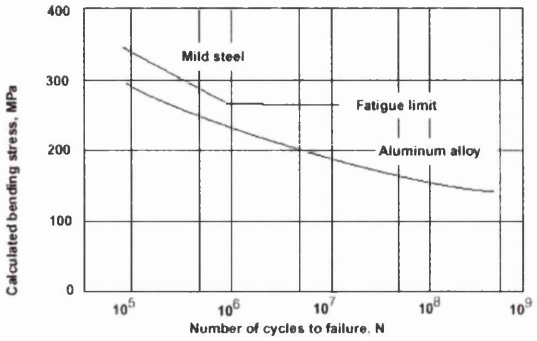

Figure 2.3: Typical S-N Curves for Ferrous and Non-Ferrous Metals

The S-N method has a major disadvantage in that it still assumes that the stresses in a component, even the local ones (but not at grain level) are below the elastic limit at all times. As a result, this method can only be considered for components with fatigue lives, which are expected to be long, and the stresses are normally within the elastic limit i.e. during High Cycle Fatigue (HCF) where fatigue lives are normally above 10^5 cycles. The specimens used to generate fatigue data must have a smooth and polished surface area and be free of any geometric stress concentrations. Variables commonly used for fatigue tests are defined as follows:

Maximum stress $= \sigma_{max}$

Minimum stress $= \sigma_{min}$

Stress Range, $\Delta\sigma = \sigma_{max} - \sigma_{min}$

Stress Amplitude, $\sigma_a = \Delta\sigma/2$

Mean Stress, $\sigma_m = (\sigma_{max} + \sigma_{min})/2$

Stress Ratio, R $= \sigma_{min} / \sigma_{max}$

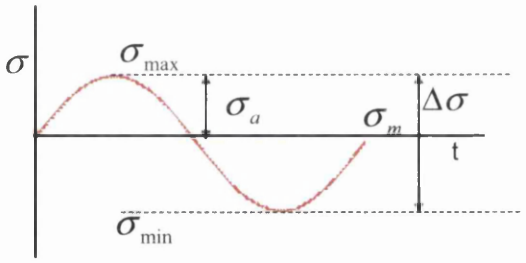

The applied cyclic load must be defined in terms of stress amplitude, σ_a, and mean load, σ_m, as the S-N curve is normally plotted in terms of cyclic stress range versus the number of cycles to failure. Typically sinusoidal stress waves are selected for fatigue tests, and the mean value is also required. These tests can be done under conditions which are fully reversed so that the mean stress value is zero ($\sigma_m = 0$ or R= -1), although tests at non-zero mean stress are also possible.

From the plotted data, the resulting straight line S-N curve produces the convenient relationship shown in Eq.1, shown also in the illustration.

$$\Delta\sigma = A \cdot N_f^b \quad \text{or} \quad Nf = a \cdot \Delta\sigma^{-m} \qquad \text{Eq.1}$$

With: $a = A^{-\frac{1}{b}}$, $m = -\frac{1}{b}$

Where: -

'N_f' = the number of cycles,

'A' or 'a' = the y-axis intercept value

'$\Delta\sigma$' = the stress range (MPa)

'b' = the Basquin exponent.

'm' = the inverse gradient of the line

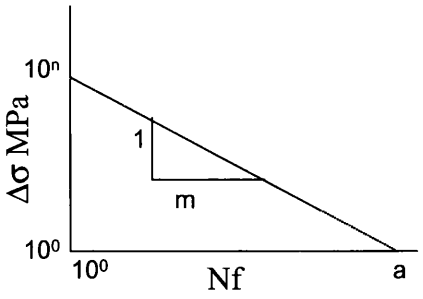

From S-N curves an important parameter can be determined - the fatigue or endurance limit where failure does not occur under normal conditions and is a stress level below which the material is classed as having 'infinite life'. This can be identified from an S-N curve where it flattens off at high lives e.g. 10^7 cycles, if the specimen does not fail after the 'cut-off' life, then it is classified as a 'run-out'. HCF tests have to be limited to a specific number of cycles; the stress at which the limit is reached is considered to be the fatigue limit of the material.

For steels, there is a fatigue limit (as shown in figure 2.3) due to the pinning of dislocations by the interstitial elements e.g. carbon, nitrogen atoms. Pinning prevents slip and so initiation is said not to occur. However, problems can arise when using the fatigue limit in design, as it is very sensitive to such factors as the mean stress, defects, corrosive environment, high temperatures (which mobilise dislocations) and periodic overloading (which unpins dislocations). They can cause stresses to exceed the limit and can even remove the limit altogether so that the stress cycles become damaging in terms of fatigue.

Non-ferrous materials, on the other hand, tend not to have a fatigue limit and the S-N curve shows a continuous slope. Instead, fatigue strength is calculated for these materials as the stress value corresponding to a life value of $5x10^8$ cycles. Welded joints also do not tend to show this limit so all cycles applied are damaging, instead they show a change in gradient.

2.5.1.1 Effect of Mean Stress

Many engineering components do experience non-zero mean stresses during their service life, such as in the case of residual stresses. The fatigue strength of materials is influenced by the mean stress, and a positive mean tensile stress will result in a shorter fatigue life than a zero mean stress. A Haigh diagram (shown in figure 2.4) is often used to take account of the effects of mean tensile stress during fatigue life analysis.

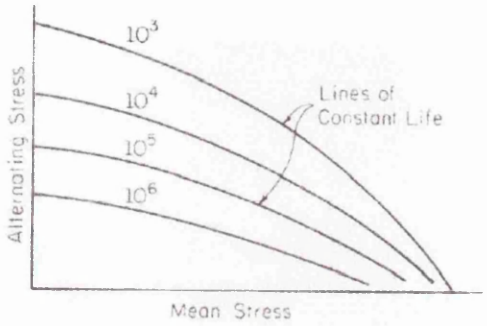

Figure 2.4: A Haigh Diagram (Bannantine, Comer et al. 1990)

Figure 2.4 indicates that as the mean stress increases, the stress range needs to decrease, in order for a material to survive for the same fatigue life. A Haigh diagram shows a series of constant lifelines, each of which represents all possible combinations of mean stress and stress amplitude that will give certain constant safe life for a material. Goodman, Gerber, and Söderburg developed empirical formulas to estimate lines of infinite life or a prescribed design life (e.g. 10^7 cycles). These formulas link the endurance limit (the stress level below which a specimen will withstand cyclic stress indefinitely without exhibiting fatigue failure), S_e, on the stress amplitude axis to the ultimate tensile strength, S_u, or true fracture stress, σ_f, on the mean stress axis. This avoids the large number of tests required to produce a Haigh diagram.

Goodman assumed that the decrease in σ_a follows a linear relationship as σ_m increases. Gerber, on the other hand, discovered that constant life curves results were more closely related to a parabolic relationship. This is known as Gerber's parabola, which is used for tensile mean stress only. Söderburg's relationship uses the yield stress, σ_y, instead of the ultimate tensile stress, σ_u; this also gives a straight line. These expressions can be shown below. (Bannantine, Comer et al. 1990; Kihl and Sarkani 1999)

Gerber (1874): $$\frac{\sigma_a}{S_e}+\left(\frac{\sigma_m}{S_u}\right)^2=1$$

Goodman (1899): $$\frac{\sigma_a}{S_e}+\frac{\sigma_m}{S_u}=1$$

Söderburg (1930): $$\frac{\sigma_a}{S_e}+\frac{\sigma_m}{\sigma_y}=1$$

Morrow (1960): $$\frac{\sigma_a}{S_e}+\frac{\sigma_m}{\sigma_f}=1$$

The stress corrections developed by Gerber and Goodman are widely used with S-N curves but are usually plotted with nominal stress, which assumes that there are no local stress concentrations. It has been noticed that actual test data mainly falls between the Gerber and Goodman curves. Söderburg's expression is very conservative and is therefore seldom used. The Morrow formula is another modification, which uses the true fracture stress, σ_f instead of the ultimate tensile stress, which is more applicable to ductile steels. This formula predicts less sensitivity to the mean stress. A comparison of all above mentioned mean stress correction equations is shown in figure 2.5.

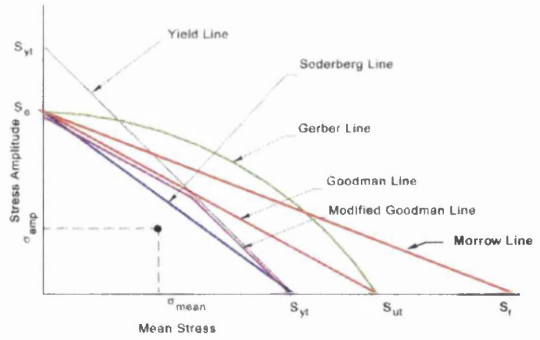

Figure 2.5: Comparison of the Mean Stress Equations (Bannantine, Comer et al. 1990)

2.5.2 Strain–Life (E-N) Data

The strain–life method was developed during the 1950s – 1960s, and is based on the observation that the material response in fatigue critical locations of many components is strain or deformation dependent. Results from the early research into fatigue shows that damage is dependent on the plastic deformation or strain. Therefore, the strain life data considers the plastic deformation that may occur in localised regions around crack initiation sites, and directly makes use of this

deformation in fatigue analysis. At long lives, both the stress-life and strain-life data are basically the same, as plastic strain is negligible, as shown in figure 2.6.

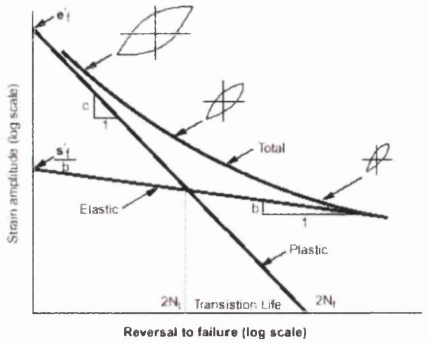

Figure 2.6: Elastic, Plastic & Total Strain Resistance to Fatigue Loading

The majority of engineering components and structures are designed so that the nominal loads remain elastic, although stress concentrations often cause plastic strain to develop locally, especially in the vicinity of notches. There is an elastic stress field surrounding such a localised plastic zone. Any fatigue damage at the notch root is believed to be controlled by the level of strain in the plastic zone.

As shown in figure 2.7a, the E-N method assumes that during testing of smooth specimens under strain control, fatigue damage can be caused at the notch root and similarly in engineering components. Failure of the component is assumed to occur when an equally stressed volume of material fails. Strain values in specimens are determined by measuring specimen extension with an extensometer, through which the applied strains can in turn be controlled during fatigue tests. Fatigue lives can subsequently be recorded and plotted in a similar manner to the S-N curves, but with the vertical axis being strain amplitude instead. However this method does allow components of short fatigue lives to be analysed.

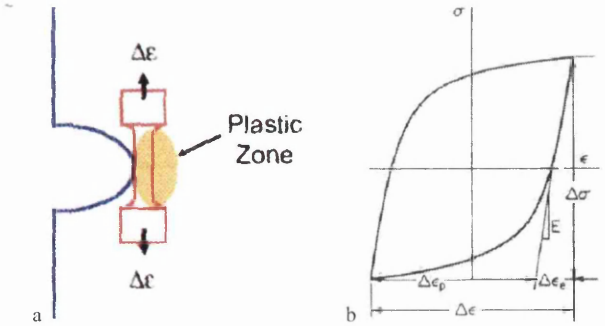

Figure 2.7: a) A Smooth Test Specimen, b) A Hysteresis Loop (Dowling 1987; Bannantine, Comer et al. 1990)

High levels of cyclic loads applied to a material, produces a series of stress - strain hysteresis loops from the data recorded. Although under a tension – compression load cycle, it takes several hundred of reversals for a stable hysteresis loop to form, as shown in figure 2.7b. The applied strain range, $\Delta\varepsilon$, and the applied stress range, $\Delta\sigma$, are denoted by the width and height of the hysteresis loop, respectively. The strain range, $\Delta\varepsilon$, is composed of $\Delta\varepsilon_p$ the plastic strain range and $\Delta\varepsilon_e$ the elastic strain range.

The strain-life curve can be separated into the individual contributions from the elastic and plastic material deformations. The total strain life to failure is the combination of both the elastic and plastic regions. Coffin and Manson through individual work found that a straight line could represent the plastic strain portion when plotted on a graph of logarithmic scale.(Manson 1953)

The equation for the line is represented in Eq.2:

$$\frac{\Delta\varepsilon}{2} = \frac{\sigma'_f}{E}(2N_f)^b + \varepsilon'_f(2N_f)^c \qquad \text{Eq.2}$$

Elastic Plastic

Where: -

$\frac{\Delta\varepsilon}{2}$	=	Strain Amplitude
σ'_f	=	Fatigue Strength Coefficient (MPa)
E	=	Young's Modulus (MPa)
$2N_f$	=	Reversals to Failure (1 reversal = ½ cycle)
b	=	Fatigue Strength Exponent
ε'_f	=	Fatigue Ductility Coefficient
c	=	Fatigue Ductility Exponent

The above equation consists of two terms: - one accounts for the effect of the elastic strain and the other the plastic strain. The sum of these strain effects, will give that of the total strain.

2.5.3 S-N vs. E-N

Strain-life testing offers the best representation of cyclic behaviour at the notch root. Whether to use the S-N or E-N data often depends on the duration of life. For short lives, which have high levels of fatigue loads, strain-life testing is more appropriate as it is better placed to account for plasticity, whereas at lives longer than 10^5, stress-life testing is more appropriate as stresses are low and linear in relation to strain.

Unfortunately strain controlled testing is not suitable for welded components, however, as welded components have complex stress and strain distributions at the failure site. This can cause difficulties in presenting the data in stress/strain cycles. Instead, the data is often presented in a load-cycle format.

2.5.4 Crack Propagation Performance Data

The fatigue life of components is made up of two stages: crack initiation and propagation. Fracture mechanics or damage tolerant design deals with solely the stage of crack propagation. This method is best used for components with inherent defects.

At the crack tip, stress and strain values become extremely large with material plastically deforming locally as the yield stress is exceeded. A parameter known as the stress intensity factor at the crack tip is used to define the magnitude and distribution of local stresses around the crack tip. It depends on the applied stress, material properties and shape and size of the crack, with general form given in Eq.3:

$$K = Y\sigma\sqrt{(\pi a)} \quad \text{Eq.3}$$

Where: -

K = Stress Intensity Factor (MPa$\sqrt{}$mm)

σ = the applied stress to the component (MPa)

a = the crack length (mm)

Y = the correction factor related to specimen and crack geometry.

Fatigue crack propagation or fracture mechanics data is obtained using the above equation. Propagation of fatigue cracks is caused by the fluctuation or change in the applied stress. Therefore, it is the range of stress intensity factor ΔK at the crack tip,

which corresponds to the applied stress range $\Delta\sigma$, which drives crack growth. The stress intensity factor range is defined in Eq.4:

$$\Delta K = K_{max} - K_{min} = Y\Delta\sigma\sqrt{(\pi a)} \qquad \text{Eq.4}$$

In fatigue, therefore, the stress intensity factor range ΔK provides the driving force for crack growth, and governs the rate of crack growth, which is expressed as da/dN. The two are related by a crack growth "law", the best-known being the Paris Law derived by P. C. Paris in 1960, shown in Eq.5:

$$\left(\frac{da}{dN}\right) = C(\Delta K)^m \qquad \text{Eq.5}$$

Where: -

C and m	=material constants
a	=crack length (mm)
da/dN (mm/cycle)	=crack propagation rate, or change in crack length per cycle

Data is usually collected as crack size, a, versus number of cycles, and converted into da/dN and then plotted against ΔK on a log scale. The subsequent sigmoidal curve is shown in figure 2.8, which may be divided into three distinct regions according to the curve shape, the mechanisms of crack extension and the other various influences on the curve.

- Region I: Threshold value, ΔK_{th}, defined as the stress intensity factor range below which fatigue cracks do not propagate under cyclic loading. Above ΔK_{th} cracks grow increasing both the crack growth rate and the ΔK value.
- Region II: shows a simple log–linear relationship between ΔK and da/dN shown in Eq.5.
- Region III: represents the rapid and unstable crack growth to fracture as K_{max} becomes equal to K_c.

This method is usually used for assessing the rate of crack extension in relation to changes in stress intensity factor range ΔK. (Ewalds and Wanhill 1996)

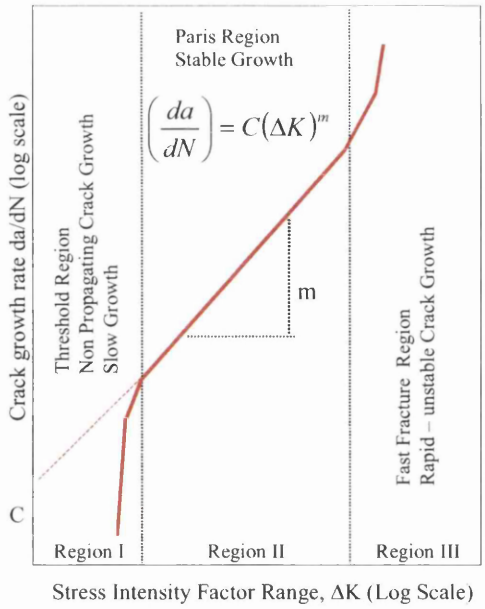

Figure 2.8: Schematic Representation of Fatigue Crack Growth Behaviour (Dieter 2001)

3. WELDING AND WELD FATIGUE PERFORMANCE

Welding refers to a wide variety of processes in which metals are joined by fusion. The metal at the interface of two or more parts is melted or fused by application of intense, localised heat. A filler metal, supplied by an electrode, is commonly used. A metallurgical bond is formed as the joint solidifies and with proper selection of consumables, the weld should have strength at least equivalent to the base materials.

Welded joint assemblies can carry loads, which are very similar to those the component carries without requiring any extra mass or volume to be added to the component assembly. Welded joints have a high strength to weight ratio, which ultimately compensates for the high processing temperatures and the environmental hazards, which are associated with it. (Brandon and Kaplan 1997)

In the automotive industry the commonly used welding techniques include resistance spot welding, MIG welding, laser welding and adhesive bonding. The focus of my EngD research is on MIG/MAG welds, and therefore will described in more detail.

3.1 Metal Inert/Active Gas (MIG/MAG) Welding

MIG or MAG welding are arc welding processes, which incorporate the automatic feeding of a continuous, consumable electrode that is shielded by an externally supplied gas. MIG or MAG welding involves similar processes the only differences are with the shielding gas. This type of welding is the most commonly used arc-welding technique for sheet metal. The MAG process is suitable both for steel and unalloyed, low-alloy and high-alloy based materials. The MIG process, on the other hand, is used for welding aluminium and copper materials. The technique is easy to use and there is no need for slag cleaning. Another advantage is the extremely high productivity that MIG/MAG welding makes possible. (Suban and Tušek 2001)

The principle of MIG/MAG welding is that a metallic wire is fed through the welding gun and melted in an arc as shown in figure 3.1. The wire serves the dual purpose of acting as the current-carrying electrode and the weld metal filler wire. Electrical energy is supplied by a welding power source. A shielding gas that flows through the gas nozzle protects the arc and the pool of molten material.

The shielding gas is either inert (MIG) or active (MAG). In this context, an inert gas is one that does not react with the molten material, e.g. argon and helium. Active gases, on the other hand, participate in the process between the arc and the molten material e.g. Argon containing a small proportion of carbon dioxide or oxygen.

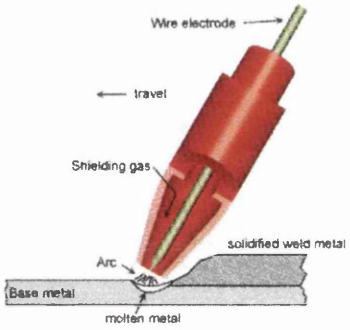

Figure 3.1: The MIG/MAG Welding Process

3.2 Weld Defects

Weld defects are primarily geometrical imperfections in the material in the weld joint caused by the manufacturing process. Imperfections can be classified into those produced on fabrication of the component, or those that form during service. Welding imperfections are attributed to the welder or the process technique and can lead to premature failure of the component in service. The British Standard EN25817:1992 governs these imperfections for guidance on the levels of imperfections in arc-welded joints in steel.

3.2.1 Geometry Discontinuities

These are problems associated with imperfect shape or unacceptable weld contour, and some typical discontinuities are shown in figure 3.2.

- **Undercut** is a gap located at the toe or root of a weld that occurs when the weld metal does not completely fill the gap at the surface of the groove to form a smooth junction at the weld toe.
- **Poor Shape** is a defect of the weld and includes excessive reinforcement on the face of the weld.
- **Underfill** is defined as a depression on the face of a weld or root surface extending below the surface of the adjacent base metal.

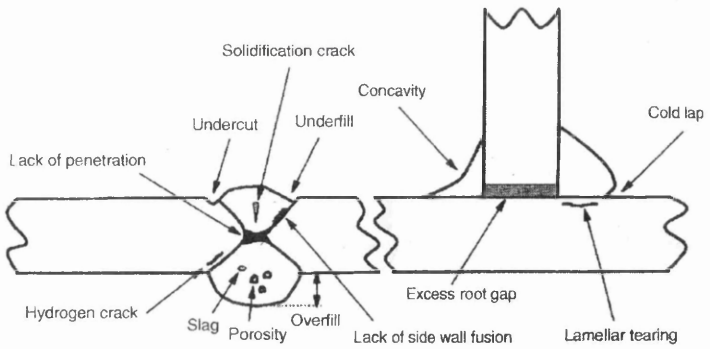

Figure 3.2: Typical Discontinuities in Welded Joints (Becker and Shipley 2002)

- **Lack of Fusion**
  - **Incomplete Fusion**: is a weld discontinuity caused by incomplete coalescence between the weld metal and fusion faces or adjoining weld beads.
  - **Incomplete joint penetration**: is a discontinuity in a groove weld in which the weld metal has not penetrated through the joint thickness due to the filler metal or base metal not filling the root of the weld completely.
- **Porosity** consists of cavities or pores that form in the weld metal as a result of entrapment of gases evolved or air enclosed during the welding process. Metals susceptible to porosity are those, which can dissolve large quantities of gas in the molten pool and then reject this gas during solidification.
- **Inclusions** are unmelted surface oxides or slag inclusions, which are formed during flux-shielded welding.
- **Cracking** is caused by stress concentration near discontinuities in welds and base metal and near mechanical notches in the weldment design. There are two types of cracks formation – cold and hot.
  - **Cold Cracking** – is where cracks develop after solidification of the weld, as a result of stresses.
  - **Hot Cracking** – is where cracks form while a weld is solidifying or when a weldment is reheated.
- **Lamellar Tearing** – is a type of cracking found to occur in the base metal or Heat Affected Zone (HAZ) of restrained welded joints, and results from inadequate ductility in the through-thickness direction of the steel parent plate. (TWI 1999; Kou 2003)

3.3 Fatigue of Welds

3.3.1 Current Design Approaches

Joining components by welding is the most widespread manufacturing method for metal structures; therefore fatigue strength of welds is very important as most structures contain welds or joints of some kind. Much work in fatigue of welds has been done so far and there are set guidelines available, such as British standards BS7608 and BS5400, as to the design of welds and/or welded components. They assume that any complex weld geometry can be described by one of the standard classifications of weld configurations.(BSI BS 5400:Part 10:1980)

Welds give a greater degree of complexity as the effects of component geometry, loading history and the material properties are less well defined. For the purpose of evaluating fatigue, weld joints are divided into several classes. The classification of a weld joint depends on:

a) The macroscopic geometry of the pieces welded,

b) The direction of the cyclic loads/stresses, and

c) The location of the crack that leads to failure.

Unwelded and welded steels are classified into groups ranging from A, B, C, D, E, F, F_2, G, and W. Type A is the unwelded material, the others represent different fusion welded joints such as butt, lap, and fillet, under various loading types. Two fillet welds are shown below in figure 3.3. Class D refers to a weld, which is loaded parallel to the weld toe. Class F2 refers to a partial penetration butt or fillet weld loaded perpendicular to the weld toe.

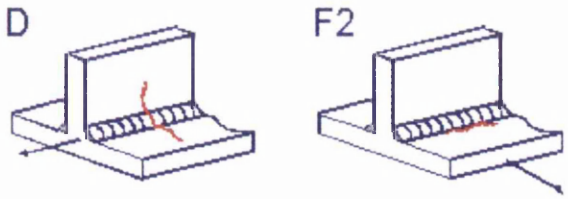

Figure 3.3: Fillet Welds Classes D and F2

The heat from the welding process alters the material properties, creates residual stresses and introduces distortions, which results in increased bending stresses. All of these are difficult to quantify. As a result, baseline data for welded joints is

usually obtained from full-scale tests of various weld joint details. These results are then summarized in typical S-N curves, as shown in figure 3.4.

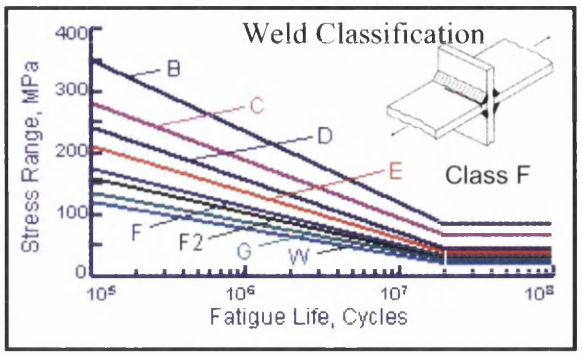

Figure 3.4: Influences of Joint Design on Fatigue Life

However these categories are only for fusion welded steel and were created from constant amplitude testing of thick plate material i.e. thickness >10mm. (BSI BS 7608:1993)

The design stress is limited by fatigue failure if components and structures are subjected to fluctuating loads. This is particularly true with welded components as their fatigue strengths are much lower than unwelded components, and this is shown in figure 3.5. Fatigue failure in welded components can occur under both tensile and compressive forces and welded joints can fail at nominal stress ranges below 30MPa.

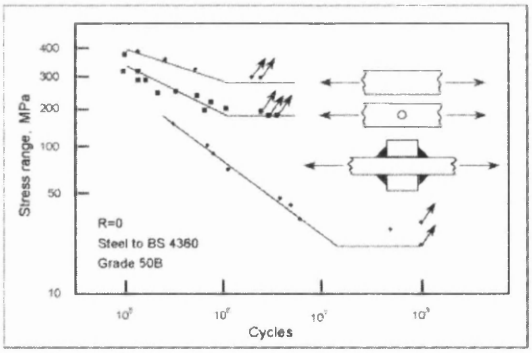

Figure 3.5: Comparison of Unnotched, Notched and Fusion Welded C-Mn Steel (Maddox 1991)

Fatigue crack initiation in welded components occupies a relatively small proportion of the total fatigue life unlike unwelded components where crack initiation involves the majority of the life. Therefore Stage II or crack propagation appears to be relevant for welded components. This is due to the joining process being effectively

the initiation stage. There are several features of welded joints that affect the fatigue strength and are discussed below.

Welding two sheets together produces a weld bead, thus creating a shape change within the structure and hence a stress concentration. The stress concentration occurs at the weld toes; the junction of the sheet surface and weld metal, and the magnitude of the stress, depends on the type of weld and the transition between the weld and the base material:

- Smooth transition – the stress level will be low
- Abrupt transition – due to a change in geometry the stress level will be high (shown in figure 3.6).

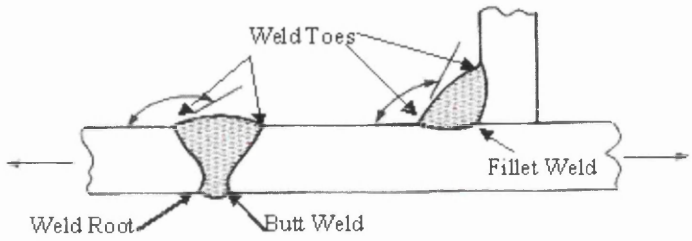

Figure 3.6: Comparison of Butt and Fillet Weld Shapes

For some welds, e.g. an attachment weld, the weld itself does not carry or transmit load. The weld forms an integral member of a component, onto which it is deposited. When stressed, the attachment weld or a bracket can still cause stress concentration due to the sudden change of section.

Fatigue cracks will therefore propagate at these areas of high stress concentration when the component is under fluctuating loading. The direction of loading also has an effect. Loading transverse to the toe, the weld toe itself is the most probable site for crack initiation, whereas loading parallel to the weld, the discontinuities of the surface such as surface ripples, or stop/start irregularities can cause stress concentrations but are less severe than the toe. Loading parallel to the weld has better fatigue strength than loading transverse to the weld.

Weld toe geometry is more complex than the general profile shows and this is due to the existence of weld discontinuities such as undercutting, intrusions with pre-existing cracks at the weld toe. These discontinuities compound the stress concentrations at the weld toes thus reducing the fatigue strength even more.

Unfortunately, most fusion welding processes will introduce at the weld toe these small crack-like discontinuities. Watkinson and Graville showed that on inspection of the failure site that the cracks initiated from slag inclusions remaining from the welding process.

Imperfections such as porosity, inclusions, and lack of fusion also influence the fatigue life as they produce stress concentrations, which if more severe than weld geometry sites, provide alternative crack initiation sites. Misalignment of the welded joint produces a secondary localised bending stress, which under loading increases the severity of the stress on the joint.

Welded joints with partial penetration cause stress concentrations to be localised at the root and lack of penetration area is crack-like so crack propagation is the main failure mode. The stresses localised at the root can be more severe than the toe and consequently cause crack initiation depends on the joint geometry and the depth of penetration.

With unwelded materials the fatigue strength increases with increasing material tensile strengths, whereas with welded materials this is not the case as in welded joints failure is through crack propagation of crack-like flaws. Propagation of cracks is influenced more by local weld geometries than the complex microstructures formed during the welding cycle, as crack growth less sensitive to microstructure.

Extensive testing has been completed on HSS fusion welded fatigue performance to determine if the parent material strength has any influence on performance life. The results show that material strength has no effect on the fatigue performance.

Overall the fatigue behaviour of welded joints will vary depending on:

- Joint type
- Loading direction
- Any combination of weld features – inclusions etc.

The presence of crack-like discontinuities within welded joints produces a limited fatigue crack initiation period, and the factors which influence initiation of cracks

have different effects on the propagation of the crack which takes up the remainder of the joints life. So it has been stated that, at welds, which have inclusions, the crack has already initiated so propagation of cracks is of concern.

The fatigue performance of steel, as mentioned previously, increases with increasing tensile strength. In spite of the complexity of the steels microstructure, the propagation rate of a crack does not vary significantly between steels. (Pope 1959; Maddox 1991) This indicates that improved fatigue performance can be attributed to a longer initiation period as the strength increases. However if inclusions are considered as the start of a crack then only the propagation period is considered, and as such steel strength would appear to influence on the fatigue performance of welded joints. This statement is illustrated clearly by figure 3.7.

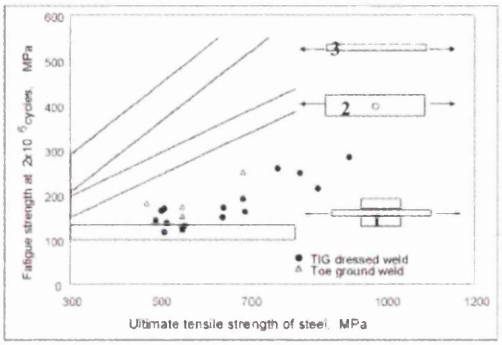

Figure 3.7: Effect of Steel Tensile Strength on Fatigue Performance of Fusion MAG Welded Joints (1) Compared to Unwelded (2 & 3) (Maddox 1991)

3.3.2 Methods of Improving the Fatigue Performance of Fusion Welded Joints

Overcoming the problems mentioned in the previous section would aid in improving the fatigue performance of the joint. There are two main ways to improve weld life:

1. Increase the weld performance through:
    a. Toe dressing
    b. Needle/shot peening
    c. Reduce the defects
2. Reduce loads/stress on welds through
    a. Joint design change
    b. Gauge increase
    c. Dynamic loading reduction

Removing the intrusions and the high stress concentrations at the weld toe would benefit the joint by improving the fatigue life. Machining or grinding the weld toe to such a depth where the intrusions are eliminated can accomplish this as shown in figure 3.8. Also machining reduces the geometric stress concentration on the joint.

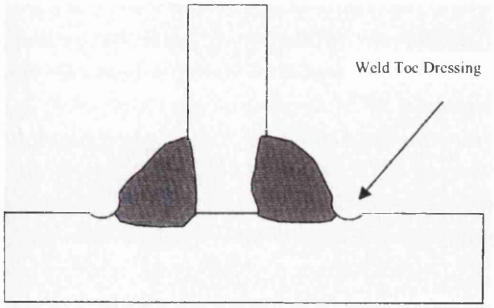

Figure 3.8: Weld Toe Dressing to Remove Geometric Stress Concentrations and Intrusions

Other postwelding operations such as weld toe grinding or Tungsten Inert Gas (TIG) dressing and plasma dressing are useful methods for significant improvements of fatigue life by remelting the weld toe and washing the weld into the parent metal to achieve a smoother weld profile. (Millington 1973)

These dressing methods make the slope of the S-N curve shallower thus increasing the stress endurance limit. Crack initiation along with other defects, now plays a significant role instead of the predominating factor only being the crack propagation so the welded joint behaves like unwelded parent material.

Manufacturing operations prior to welding often produce residual stresses, which remain within the material, and these are completely independent of loading conditions.

During the welding cycle, additional thermal residual stresses can arise primarily due to the non-uniform solidification and cooling process, and thus uneven or restricted contraction of metal within the weld and its surrounding region. The magnitude of residuals introduced from welding will depend on the strengths of the parent material and the weld. High levels of tensile residual stress can exacerbate fatigue failure of welded joints since it can increase the level of mean stress for the same applied cyclic stress range.

A low tensile residual stress, or better, compressive residual stress field in the weld region will be beneficial for weld fatigue. Not only does the compressive residual stress minimise the chance of fatigue crack initiation, but also it hinders the propagation of a crack even if it did manage to initiate.

Therefore, the most effective method for improving fatigue strengths of welds which fail at weld toes is through the introduction of compressive stresses. Compressive stresses can be produced through cold working of the welded joint and the most common method is by shot or needle peening the weld toe. Residual stress-based treatment methods, such as needle peening, work by reducing the effective stress intensity factor range, K_{eff}, at the surface, and thus slowing early crack growth.

4. AUTOMOBILE STRUCTURES

Modern cars are made of a combination of steel, aluminium and plastics (un-reinforced and composites). Steel is by far the most widely used material due to its high strength, durability and formability. However there is considerable external pressure from environmental groups and government legislation in two areas: 1) Reduce Carbon Dioxide (CO_2) levels to help slow down the effects of global warming; 2) Reduce fuel consumption by reducing the vehicle weight (this is important as the cost of fuel will continue to rise at twice the rate of inflation due to the diminishing supplies and the difficulty in recovering fuel from tar and other compounds as oil becomes scarce). This weight reduction may be accomplished by either the use of the latest developments in advanced steels, or through material substitution. Currently there are many investigations on the potential use of high strength steels (HSS) and advanced high strength steels (AHSS) for auto bodies e.g. the Ultra Lightweight Steel Auto Body (ULSAB) project, or into suspension and chassis structures in the Ultra Lightweight Steel Auto Suspension (ULSAS).

The primary structure of mainstream automobiles consists of the unpainted body structure which is also referred to as a body-in-white (BIW), and chassis components such as subframes, suspension systems etc.

4.1 Importance of the Chassis

The chassis connects the car body with the road surface via the suspension. Its functions are multifaceted and range from providing support and suspension for the vehicle mass to supporting, steering and braking the wheels, to transmitting the drive torque. These functions demand on the developers not only for the highest level of technical expertise concerning the entire process chain, but also for great innovative potential.

The chassis consists of the frame, suspension system, steering system, tyres and wheels.

- The **frame** is the structural load-carrying member that supports a car's engine and body, which are in turn supported by the suspension and wheels.

- The **suspension system** is an assembly used to support weight, absorb and dampen road shock, and help maintain tyre contact as well as proper wheel to chassis relationship.
- The **steering system** is the entire mechanism that allows the driver to guide and direct a vehicle.

4.2 Land Rover Chassis and Suspension System

Land Rover's Defender, Range Rover and Discovery models are vehicles of body-on-frame construction each having a separate "ladder" chassis frame, whilst the FreeLander is of "body frame integral" or monocoque construction.

4.2.1 Ladder Frame Chassis

This type was widely used in cars until the late 1940s although the current-day Sport Utility Vehicles (SUVs) still use this structure. The Ladder frame is a twin – longitudinal rail chassis that is interconnected by several laterals and cross braces. The longitudinal rails are the main stress members as they take the load and the accelerating and braking forces, whilst the cross members provide resistance to lateral forces and increase torsional rigidity, as shown in figure 4.1 the AC Cobra. (Clough 2003)

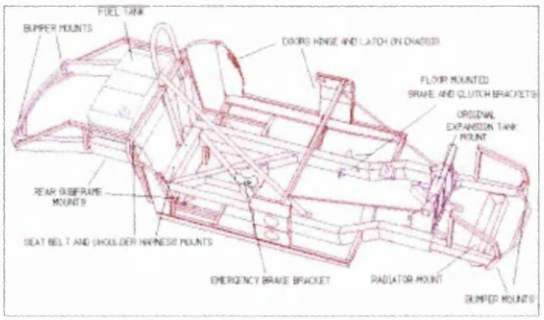

Figure 4.1: Ladder Chassis

Land Rover Discovery suspension is by double-wishbone front (as shown in figure 4.2) and rear, and is independent. Base models have coil-sprung suspension, whilst higher-specification models get air springs. The air springs will be combined with novel active suspension.

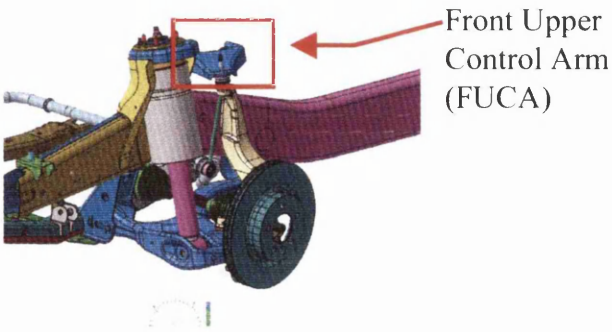

Figure 4.2: Double Wishbone (Control Arm) Front Suspension

Suspension components must be able to withstand the forces from daily use, and these are complex. The complex loading in the suspension system arises from the fundamental forces that are generated at the tyre contact patch. These forces act in the three primary directions as shown in figure 4.3 and there is an additional torque loading from the brake reaction.

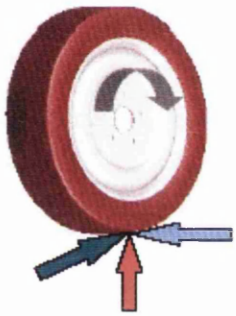

The 3 primary forces at tyre contact patch are:

- Longitudinal
- Lateral
- Vertical

Additional Torque Loading

- From Braking (Combined with Longitudinal Force)

Figure 4.3: Basic Forces Acting on the Suspension

The effects from these forces will be distributed in the suspension system causing the components to move in various ways so that the car ride and handling are maintained as smoothly as possible. How these forces are controlled by the complex suspension structure is shown in table 4.1.

Table 4.1: Forces and Movements Acting on Suspension

Movements	**Forces**
Longitudinal	Longitudinal
Lateral	Lateral
Ride	Vertical
Steer	
Camber Rolling	Braking/ Acceleration

4.3 Major Design Issues, Philosophies and Challenges

Cars are designed nowadays using Computer Aided Design (CAD) or Engineering (CAE) software tools, and are then analysed and tested through complex rig testing before full vehicle proving ground testing. With costs of testing procedures increasing and the time for development decreasing, virtual testing through complex multibody simulations in FE packages is needed.

4.3.1 Durability Analysis in the Automotive Industry

Traditionally durability of vehicle component and subsystems has been established, optimised and verified by testing physical prototypes. Today, increasingly higher demands for lighter and more cost-effective structures, together with shorter time to market, have been changing design philosophies within the automotive industries. It is generally recognised that getting products to market quickly cannot be achieved by developing the design mainly through the testing and modification of a series of mechanical prototypes.

Designing new automotive models in shorter periods is a challenge, which requires the use of Computer Aided Engineering (CAE) analysis. This reduces the reliance on physical verification tests at the intermediate design stages, and rig tests are carried out for final confirmation of CAE analysis therefore minimising the number of prototype vehicles built.

For these reasons, fatigue life predictions are becoming an essential part of the development process for many vehicle manufacturers. There are two main categories of fatigue life computations: 1) Based on measured stresses and strains, 2) Based on stresses and strains computed analytically using Finite Element Modelling and Analysis.

4.3.1.1 Vehicle Durability

In the past, the customers were the final inspectors and testers of vehicle design due to limited knowledge of customer usage. In today's automotive industry, durability and reliability are key areas and using analytical methods for sheet metal structures can enhance product quality over more traditional methods.

- Durability is defined as "the capacity of a component or assembly-of-parts to endure service duty without premature failures."
- Reliability is defined as "the probability of a component or assembly-of-parts enduring service duty for a specific life and meeting or exceeding its specifications."
- Quality is defined as "products, which meet or exceed customer needs and expectations throughout their service life at a cost, which represents value."

Engineers are faced with many decisions during the product development process. In the last decade, development times between conceptual design and the finished production item have been reduced from approximately five years to around two years. The challenge for the testing community is to meet these timing targets while retaining quality and durability. This is combined with the need to save weight, select optimum materials and economise on production processes whilst satisfying operational demands placed on the product. Accurate measurement, data acquisition and analysis, and testing are key factors in the process of calculating product performance. Figure 4.4 shows the effect of using CAE durability methods over traditional methods with development time.

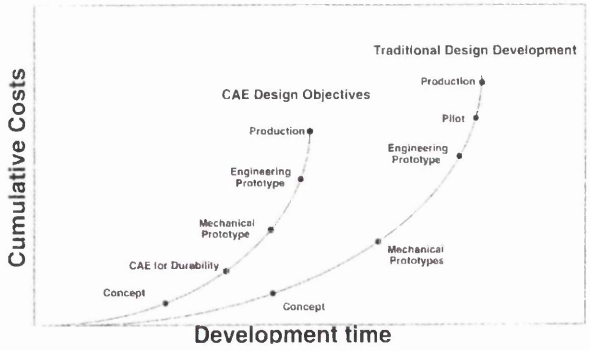

Figure 4.4: Product Development Life Cycle Costs (The MSC Institute of Technology 1995)

The reduction in prototype vehicle testing is exerting further pressure on the analysis community to more accurately predict potential fatigue areas during the design development phases. With less time available for building and testing prototypes before manufacturing, it has become vital to simulate structures on computers and accurately predict potential functional issues. However, there are still many variables that analytical methods cannot adequately consider, such as manufacturing processes,

assembly, material non-homogeneity and residual stresses, although improvements are being made in these areas. Laboratory durability testing and vehicle proving grounds will still be necessary for both design verification and system or full vehicle sign-off. (Berger, Eulitz et al. 2002)

Laboratory-based durability testing is intended to reproduce failure modes and locations similar to those observed on the proving ground, but in shorter time and a more controlled and reproducible environment. The complexity and configuration of the tests required depend on the complexity of the components under investigation. Therefore, they can range from single to multiple channels of synchronous actuation.

Product performance is dictated by the loads experienced in service, the distribution of stresses and strains in the product due to these loads, and the behaviour of the product materials under these conditions. Combining this information in computer models enables rapid evaluation of component durability, as shown in the fatigue life model figure 4.5. Hence, expensive prototype, laboratory and service trials can be minimized.

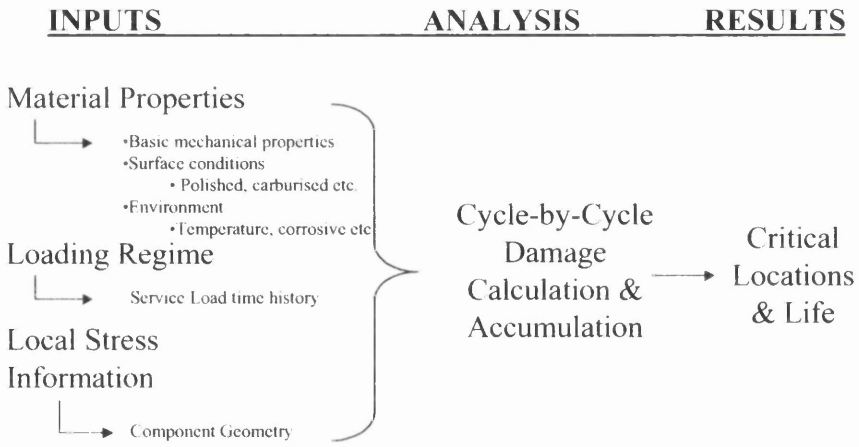

Figure 4.5: Fatigue Life Model (Five Box Trick) (Plaskitt and Musiol 2002)

4.3.1.2 Material Properties

The material properties required for fatigue prediction are how the base material or a weld behaves under cyclic loading conditions. Also information on fatigue improvement techniques, surface finish and environment are also required. Material properties under cyclic loading are used to calculate elastic-plastic stress-strain response and the rate at which fatigue damage accrues due to each fatigue cycle.

4.3.1.3 Loading Regime

Accurate load time history is required for the component being modelled. Determining the load time history is a complex task and can be obtained by a number of different methods such as strain gauges and load cells. Care must be taken when recording the data to ensure that there is sufficient data to represent the typical conditions.

Only rarely can all forces acting on a component built into a subsystem or vehicle be measured. In these cases, computer multibody simulations (MBS) can help. Most mechanical systems with moving components such as automobiles can be modelled as multibody systems. A multibody system, in general, consists of flexible or rigid bodies, kinematic joints, springs, dampers, and actuators, which is used to build a virtual vehicle model. Computers have aided this by providing the required link between applied loads and the stress response at regular intervals across the structure.

4.3.1.4 Local Stress Information

For fatigue life prediction, calculated stress is needed for hot spots or nominal stresses. This can be achieved by using finite element analysis. The accuracy of the stress information produced is dependent on the geometry of the specimen, as the actual stress state in the weld is difficult to determine. In this context, the geometry is used to describe how loads are transformed into stresses and strains at a particular point on the specimen, and this can be difficult to model.

4.3.1.5 Cycle-by-Cycle Damage Accumulation

With the accumulated data from the three inputs, a stress time history is generated and then broken down into the individual cycles, usually by a "rainflow cycle counting" method. From this the fatigue life can be determined. (Fermér and Svensson 2001; Plaskitt and Musiol 2002)

4.4 Drive for Lightweight Vehicles

Cars are part of our culture and will continue to be in the foreseeable future and over the last 10 years and especially in the United States, more people are buying less fuel-efficient sport utility vehicles (SUVs), mini-vans and trucks instead of the lighter weight saloon cars.

Modern trends regarding the environmental impact of motor vehicles are forcing automotive manufacturers to produce lighter and more fuel-efficient vehicles. Vehicle structure offers an appropriate scope for potential weight saving, with the BIW providing the largest contribution through the use of new technologies or new lightweight materials. Recent developments have revealed that up to 30% reduction of the total weight of the car can be achieved by substituting steel with aluminium-alloy. However, the substitution of one material by another may give rise to various problems, and one of them is the method of joining.

The critical issue is the transportation sector's impact on global warming, and the best way to reduce carbon dioxide is to reduce fuel usage or increase fuel efficiency. Concerns over environmental impact of fossil fuels has galvanised the international community to reduce emissions. The stringent safety measures and comfort systems, required in cars are making them much heavier. New lightweight materials are thus required to reduce the weight.

A Frost and Sullivan research report shows that 75% of fuel consumption relates directly to the vehicle weight and, therefore, potential reductions resulting in price-performance ratio would drive lightweight materials usage in automobiles. Combined with increasing fuel efficiency demands, the automotive industry is looking for lightweight materials to achieve this. A 10% vehicle weight reduction would give a 6-8% improvement in fuel efficiency, which results in approximately 20kg reduction in carbon dioxide per kilogram of weight reduction over the vehicle's lifetime. (Wallentowitz, Leyers et al. 2003; Neard 2004) Alongside these tougher legislative environmental demands there are market and business pressures, which require reduction in product development and manufacturing costs and lead-time for new products to enter the market. This has a negative impact on the new technological innovations, which usually occur for new models. (Pekkari; Evans, Crawford et al. 1997)

Steel dominated the automotive market from the first commercial development of automobiles, but with current trends the usage of steel has steadily declined throughout the last decade. In 1990, 75% of the car weight was steel whereas currently steel comprises nearly 70%. This is due to alternative materials like

aluminium, magnesium, plastics, composites and glass. (Johnson and Mascarin 2002) Automobiles are roughly composed of 70% steel (55% plain carbon steels, 15% special steel), 6% aluminium and 7% plastics (average in 1992). Figure 4.6 shows the weight of the materials used to produce a typical family car.

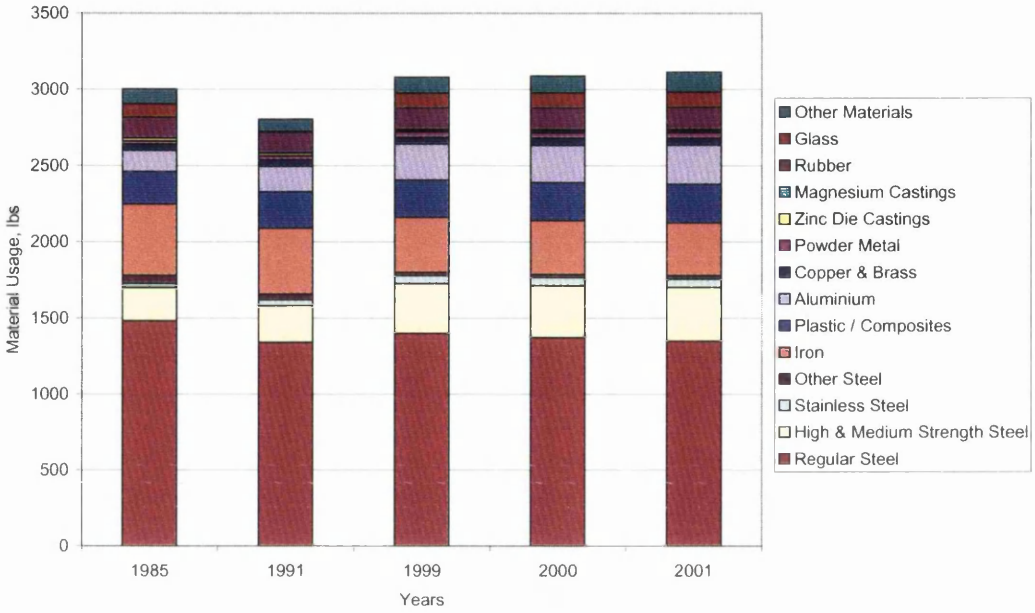

Figure 4.6: Material Usage of Typical Family Cars between 1977 & 2001 (Haight 2003)

New materials are considered for incorporation into vehicle to satisfy fuel efficiency regulations, only if they provide benefits at an affordable cost. However new materials have many properties, which are required, including the effects on vehicle dynamics, durability (warranty), damageability, repair, and crash worthiness. All these are related to the effect of metallurgical characteristics and the impact of manufacturing practice on material and product performance. (Cole and Sherman 1994)

Different lightweight materials are currently available including high strength and ultra high strength steels, aluminium, magnesium and various composites. High strength and ultra high strength steels have already proved to be a cost effective solution in lightweight vehicle bodies. In the well-publicised ULSAB project, it was shown that a reduction in body-in-white mass of 25% is possible for a medium-sized car and also that a potential for cost reduction exists in parallel to weight reduction when using these materials.

5. SHEET STEELS FOR AUTOMOTIVE APPLICATIONS

Sheet or strip steel has been used over the last 20 years in automobiles and comprises around 70% of a typical car's weight and with current international recycling directives coming in, steel is one of the most recyclable material available. (Wards) This has been achieved through improvements in the modern steelmaking process, which aided the development of High Strength Steels (HSS) while maintaining the desired properties of them.

Sheet steels are available in either hot rolled or cold rolled or coated conditions. Hot rolled sheet steels are produced from the rolling of steel slabs at temperatures over 850°C, and have a thickness of 1.6mm or greater whilst cold rolled steels have thicknesses less than 1.6mm due to the further reduction of the hot rolled product at room temperature. Automotive applications use cold rolled steel with a thickness of about 0.6mm for body panels, but up to about 4mm thick for structural components.

High strength steels are produced in both the hot and cold rolled conditions and are becoming increasingly part of the modern vehicles and are also being highly researched with the aim to reduce the automotive weight.

5.1 High Strength Steels

For automotive applications, the steel industry can provide automotive designers with an extensive range of high strength sheet steels, which are being aggressively explored for cost-effective solutions for vehicle light-weighting and thus improved fuel economy. These steels combine good formability with higher strength and are considered for many safety-critical structural applications. With these unique properties, they can be closely matched to a required performance. The use of high strength steel grades has increased by 162% since 1977 and has replaced the older carbon steel grades according to the American Metal Market. (Hartmann, Heidtnamm et al. 1997; Newsletter 1999; Abdalla, Neto et al. 2001)

Strengthening of sheet steels can occur through the following methods:

- Grain refinement,
- Solid solution strengthening,
- Transformation hardening

- Precipitation of second phase particles i.e. pearlite, bainite, martensite.

Finer grains and precipitations within structures hinder dislocation movement and consequently enhance the mechanical properties. Figure 5.1 shows the relationship between total elongation and tensile strength of several classes of sheet steels available to the automotive industry.

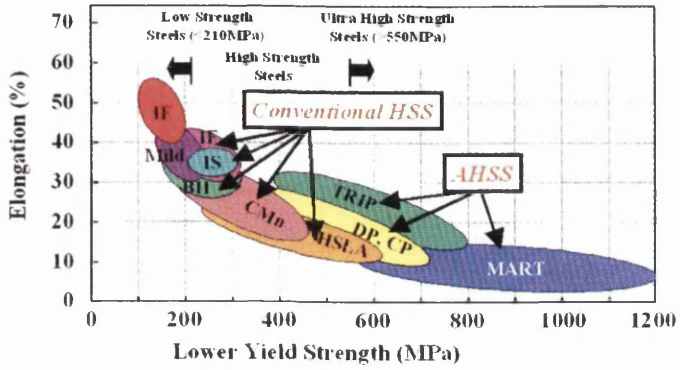

Classification of steel types:
Conventional Steel Types:
Mild = Mild Steel
IF = Interstitial-Free
IS = Isotropic
BH = Bake Hardenable
C-Mn = Carbon- Manganese
HSLA = High strength, low alloy
Advanced High Strength Steel (AHSS) Types:
DP = Dual phase
CP = Complex phase
TRIP = Transformation -induced plasticity
Mart = Martensitic

Figure 5.1: Strength–Formability Relationships for Mild Steel, Conventional HSS and AHSS. (Shaw and Zuidema 2001)

The main difference between HSS and AHSS is their microstructure; AHSS are multiphase steels containing sufficient quantities of martensite, bainite and/or retained austenite to produce the desired mechanical properties. AHSS also have superior strength in combination to good formability due to strain hardening arising from their low yield strength to ultimate tensile strength ratio. (ULSAB-AVC 2001)

Micro-alloyed Steels – Also commonly known as High Strength Low Alloyed (HSLA) steel, where small quantities of niobium, titanium and/or vanadium used individually or in combination are added to low carbon aluminium-killed steels (aluminium-killed steel is steel deoxidised with aluminium in order to reduce the oxygen content to a minimum so that no reaction occurs between carbon and oxygen during solidification). The higher strengths occur from the precipitation hardening of the ferrite, and thermo-mechanical treatment during the hot rolling leading to a finer grain size. These steels have yield strengths in the range of 300 – 550MPa.

5.2 Fatigue of High Strength Steels (HSS)

Steels are still among the most important engineering materials, and therefore their fatigue properties still remain of great interest to engineers. Also there are a wide

variety of steels, which exhibit a comparable range of different microstructures, improving the understanding in their fatigue properties therefore remains a challenge. Fatigue damage of steel undergoes the same three stages as all other materials – crack initiation, crack propagation and fracture. These stages are influenced by several factors such as microstructure, chemical composition and tensile strength. Significant improvements in fatigue performance have come from the understanding of complex chemistries and the extensive use of thermo-mechanical processing. Thermo-mechanical treatment of steels exploits the effect of plastic deformation on the austenitic microstructure to produce the required microstructure properties.

5.2.1 Effect of Microstructure and Composition

Various mechanisms of strengthening exist including solid solution, grain refinement, and precipitation mechanisms. Through various investigations it is noticeable that mechanisms, which suppress the dislocation movement, like solid solutioning and precipitation, have a beneficial effect on the increase in fatigue limit as the tensile strength increases.

During the initial stages of fatigue in metals, mechanical properties change as the distribution and density of lattice defects changes throughout the material. Localised plastic deformation is responsible for initiation and propagation of the crack and the materials microstructure influences both of these stages by inhibiting or modifying the deformation process. The microstructure also determines whether the cracking process is changed from ductile to brittle, plastic deformation to cleavage. (Klesnil and Lukáš 1967)

Some attributes, which affect fatigue, are:

Grain Size: For most metals, smaller grain size results in higher yield strength and, as a result, longer fatigue lives. However, the presence of surface defects or scratches will have a greater negative influence on fatigue lives than that from coarser grains. Researches have suggested that the greatest effect that grain size has on fatigue is in the low-stress high-cycle fatigue (HCF) regime.

Alloys of identical chemical composition can have significantly different fatigue limits depending on the sizes of their grains. The fatigue limit is proportional to the square root of grain diameter, which is also the relationship that exists between the

yield strength and grain size. Cazaud observed that with mild steel increasing the grain size has a declining effect on the endurance limit. (Cazaud 1953)

- Alloying: The influence of chemical composition on fatigue is approximately proportional to its influence on tensile strength. So additions of carbon, and other alloying elements will increase the fatigue limit.
- Second phases: These affect crack propagation due to the strain caused by the presence of the second phase, the stress concentration of the second phase (shape, distribution) and the nature of the bond.

In alloys, where a second phase is used for strengthening, spherical dispersion of the second phase provides superior fatigue properties at the same strength level.

- Work hardening: Work-hardened alloys show lower crack propagation rates and small deformation increases during fatigue. Cold working can increase fatigue strength.
- Heat Treatment: Fatigue strength is generally increased by any heat treatment that increases tensile strength.

In welded structures all the material benefits from the heat treatment occurring from the welding sequence, unfortunately as the microstructures change the benefits vanish due the heat affected zone.

5.2.2 Effect of Yield and Tensile Strength

In metallic materials, there is a direct correlation between the tensile and fatigue strengths. Fatigue strength of high strength steels increases with the simultaneous increase in tensile strengths due to an increased crack initiation period. For many years, it has been known that the fatigue performance of unnotched specimens is approximately proportional to the tensile strength.

There have been a number of reports relating to fatigue strength with respect to tensile strength. Lewis studied the effects of fatigue performance on unwelded and fusion welded Carbon Manganese (C-Mn) HSS and compared to TRIP (Transformation-induced Plasticity) steels of similar tensile strength. In the unwelded condition fatigue life increases simultaneously with material strength, whereas in the welded condition, at lives of 10^5 cycles TRIP steels have better fatigue performance than C-Mn steels. (Lewis 1996)

Due to their high strength, the TRIP grades have significantly better fatigue properties than conventional steels. Furthermore, they are improved by the paint baking treatment. Fatigue strength is generally expressed as an endurance limit, corresponding to the maximum stress for a given number of cycles to failure.

Sperle and Trogen showed that with increasing tensile strength the fatigue strength also increased, and from their studies of the influence of yield ratio on fatigue strength, fatigue strength to tensile strength ratio increased with increasing yield ratio. The results concluded that yield strength must strongly influence fatigue strength of unnotched base metal. (Sperle 1989)

Tomita et al investigated the effect on fatigue strength of sheet steels with respect to surface roughness and subsequently found that fatigue life is influenced strongly by the surface roughness condition and can often be treated as being similar to a notch effect. (Tomita 2000)

6. FE-BASED FATIGUE LIFE PREDICTION FOR WELDED STRUCTURES

6.1 Finite Element Analysis

Finite Element Modelling (FEM) is based on the idea of building a complicated object with simple blocks or dividing it into small pieces known as "elements". FEM consists of a computer model of a material or design that is stressed and analysed for specific results and is used in new product design and existing product refinement.

FEM uses a complex system of grid-points called nodes, which make a grid called a mesh. This mesh is programmed to contain the material and structural properties, which define how the structure will react to certain loading conditions. Nodes are assigned at a certain density throughout the material depending on the anticipated stress levels of a particular area. Regions which may experience a high level of stress usually have a higher node or mesh density. Points of interest may consist of: fracture point of previously tested material, fillets, corners, complex geometry, and high stress areas. The mesh acts like a spider web in that from each node, there extends a mesh element to each of the adjacent nodes. This web of vectors is what carries the material properties to the object, creating many elements. Specific loading conditions are applied to a system then analysed, and subsequently reprocessed for the required data.

FEM has become one of the most widely used analytical techniques for the task of predicting failure due to unknown stresses by showing potential problematic areas in a component/structure and allowing designers to visualise all of the theoretical stresses within. This method of product design and virtual testing is far superior to other methods, especially in helping reduce development and manufacturing costs, which would be accrued if each design option for a component was actually built and tested.

FE modelling is a three-stage process: 'pre-processing', 'analysis' and 'post-processing'.

6.1.1 Pre-Processing

This stage involves many steps such as building Geometry, creating FE Mesh, applying Boundary and Load Conditions, inputting Material Properties, and conducting Pre Analysis checks.

- Geometry: - The first step is to generate the computer model representing a real life component or coupon. This forms the basis onto which loading conditions are applied.
- FE Mesh: - This step involves taking the geometry model and dividing it up into a mesh of nodal points, which forms the basis of the elements, i.e. each element is defined by four nodes. Figure 6.1 shows a diagram of how the welds are modelled in the current study.

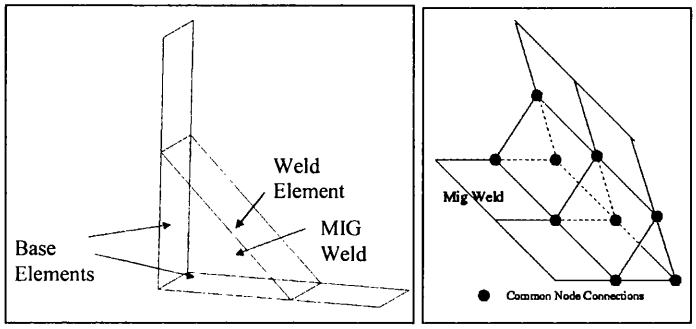

Figure 6.1: Diagram Showing How a Weld in MSC Patran is Constructed and a Typical MIG Weld

- Boundary Conditions: - Application of boundary and load conditions is applied to the FE model to represent the loading and how the component is constrained in the physical tests.
- Material Properties: - Specific material properties are applied to the FE Model and are generic so each model contains the same information therefore comparisons can be made directly between models.

For a linear-elastic FE analysis, the required material properties include Modulus of elasticity (Young's Modulus) and Poisson's Ratio.

6.1.2 Analysis

This stage involves selecting the correct outputs i.e. the required analysis, resulting stresses (Maximum Principal, Von Mises, Tresca) and strains which get compiled before being processed. This is the most computer intensive part of the process. In essence, it involves solving simultaneous equilibrium equations. Each equation

represents the balance of a component's internal forces (e.g. due to elastic deformation) with externally applied forces at each node and in one particular direction, known as a degree of freedom.

6.1.3 Post Processing

This stage involves representing the results by displaying illustrative animations of the deformation behaviour, the resulting stresses in the time range, damage distribution of the FEM model, and detailed analysis of stress-time series etc.

6.2 Computer Aided (Fe-Based) Fatigue Analysis

Finite Element Modelling (FEM) is a long established CAE analysis tool, which is widely used, in all-engineering industries. Fatigue analysis is becoming increasingly easier, faster and more cost effective due to the vast improvements in computer power, speed and software packages. FEM is on the increase as an effective tool in tackling durability problems. Modern software enables the design engineer to have an input into the final component from the concept stage through to the final 'sign – off' test.

In the automotive industry there is a drive to decrease the development lead-times and costs for new car models. To achieve this automotive manufactures have increased their usage in CAE tools at all stages of vehicle development. There is a need to conduct CAE durability analysis in the early stages of design to ensure that fatigue related problems are reduced or removed before any costly prototypes are made.

Most early design phase assessments using CAE analysis include crashworthiness, stiffness and modal analysis. Current processes at the early design stage include CAE assessments to identify and prevent durability related failures. Early fatigue and durability assessments using CAE tools should aid in preventing new model developments failing at later stages i.e. track testing or laboratory durability testing, which would cause longer new model lead times and elevate the development costs. So for automotive manufacturers, having accurate and efficient CAE durability analysis tools for vehicle structure manufacture is essential.

In weld fatigue, joints in components are stress raisers and fatigue cracks are more likely to propagate from the highest stressed region in a component.(MSC 1999; Gao, Chucas et al. 2001; BSI BS 7608:1993) Therefore to prevent over–design in fatigue critical components whilst maintaining the safety margins, placement of welds is important. FE models must be constructed carefully and compared with specimen testing and full sized component testing. FEM is used to calculate a stress distribution for an entire component or structure and so provides an ideal precursor to fatigue analysis. All analytical components require correlation with something physical to validate the analytical model so that the results generated are realistic. This is the reason simple geometry tests and full sized component test programmes are combined with FEM. Finite element analysis therefore offers an effective tool for evaluating fatigue durability problems.

It is essential to be able to identify fatigue hotspots and predict time to failure in a given real-life loading environment. Predicting fatigue life is a critical aspect of the design cycle because virtually every product manufactured will wear out or break down. The critical issues are whether the product/component/assembly will reach its expected life, and if damaged, whether the product/component/assembly will remain safely in service until the damage can be discovered and repaired. As with most simulation analysis, the earlier the fatigue analysis is deployed in the product development process, the more benefits will be realized, including safety and economy.

6.2.1 Metal Fatigue CAE: Stress-Life Approach

Metal FE fatigue analysis for stress-life (S-N) method uses linear - elastic analysis methods. The S-N method is used in a variety of situations including long life fatigue problems where there is little plasticity, and for components where crack initiation or crack growth modelling is not appropriate, such as non-ferrous materials, composites, welds, and plastics. The S-N method may be summarized as follows:

1. Linear static FEM derives the local stress time history from the load time histories, including superpositioning of multiple FEM/load time history load cases. Many structural fatigue analysis problems can be treated as linear static problems, scaled by load time histories. Linear Superposition is accomplished using the following Eq.6.

$$\sigma_{ij}(t) = \sum_k P_k(t)\left(\frac{\sigma_{ij,k}}{P_{k,fea}}\right) \qquad \text{Eq.6}$$

Where $P_k(t)$ is the force time history, $P_{k,fea}$ is the magnitude of the force used to produce the static load case and $\sigma_{ij,k}$ is the static stress component for load case k.

2. However, it is important to ensure that the S-N data applies to the situation being modelled; most S-N curves are for nominal stress, not local stress.
3. Extract the fatigue cycles in the local stress time history by means of a rainflow algorithm.

Rainflow Counting

Matsuishi and Endo developed Rainflow cycle counting in 1968, with the name deriving itself from an analogy they used. (Matsuishi and Endo 1968) Plotting a stress/strain time history and orientating it vertically, a series of 'pagoda roofs' are created, and the cycles are defined by the way rain would fall off the roofs as shown in figure 6.2. This method of counting requires a set of rules to be followed correctly:
The load sequence must start and finish at the same stress or strain value
Flow begins at each reversal and continues until:

- It encounters an earlier Rainflow
- It began as a local maximum and falls to the opposite local maximum which has a greater value than at the beginning

It began at a local minimum and falls opposite a local minimum with a greater value than at the beginning.

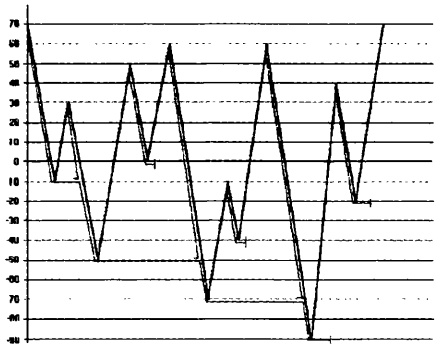

Figure 6.2: Rainflow Cycle Counting Method

Rainflow counting is easily done for simple load histories yet with more complex histories a computer program is better used for implementing this method. (Bannantine, Comer et al. 1990; Dowling 1993; Dieter 2001)

4. Assess the damage contribution of each cycle by referring to the selected damage curve. Linearly sum the damage associated with each cycle by using Miner's rule.

Miner's Rule

The Linear damage rule is based on the concept of fatigue damage. A damage fraction, D, is defined as the fraction of life used up by an event or a series of events. The damage criterion for failure is assumed to be equal to 1.0.

The linear damage rule states that damage fraction, D_i, at stress level σ_i, is equal to the cycle ratio n_i/N_i, where n_i, is the number of cycles observed at the stress level and N_i is the number of cycles to failure at the same stress level.

The failure criterion can now be identified as the sum of the damage where the life to failure can be estimated by summing the percentage of life used at each stress level as shown in Eq.7.

$$\Sigma \frac{n_i}{N_i} \geq 1 \qquad \text{Eq.7}$$

6.2.3 Metal Fatigue CAE: Strain – Life Approach

Strain Life (E-N) analysis uses cyclic stress-strain modelling and Neuber's elastic-plastic correction (or modifications of Neuber's method such as Seeger-Beste or Merten-Dittman). Typically, the E-N method is used for components or metallic structures that are mostly defect-free and for locating where a crack could begin. The strain-life method may be summarised as follows:

- By means of linear elastic FEM derive the local stress-strain time history from the load-time histories, including superpositioning of multiple FEM Load–time history load cases (or use stress-strain time history directly from linear transient or forced vibration FE analysis).
- Extract the fatigue cycles in the local stress time history by means of a rainflow algorithm (as in section 7.4.2.1).
- Make the elastic-plastic correction using the Neuber's rule.
- Model the fatigue crack initiation process using hysteresis loop simulation based on the cyclic stress-strain curve.

- Assess the damage contribution of each closed hysteresis loop by referring to the selected damage curve. The damage curve selected is based on the mean stress correction model used—Smith-Watson-Topper or Morrow.
- Linearly sum the damage associated with each cycle by using Miner's rule (as in section 7.4.2.1).

Neuber's Rule for Plasticity Correction

This rule allows for the fact that the material may yield. The local stresses and strains around a notch can be determined using the elastic stress concentration factor K_t. Figure 6.3 shows where the nominal and local maximum stress concentrations are.

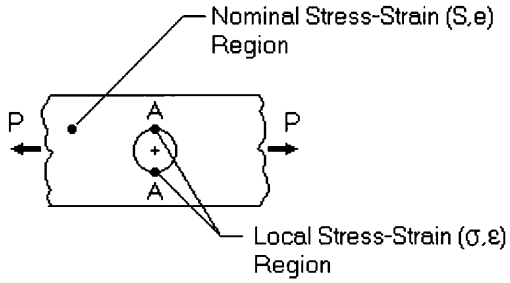

Figure 6.3: Nominal and Local Stress Regions (Bannantine, Comer et al. 1990)

As the nominal stress increases K_t remains constant until yielding begins. Upon yielding the local stresses and strains are no longer linearly related so K_t can no longer be used to relate local values to nominal values. For plastic deformation, Neuber proposed that K_t is equal to the local stress and strain concentration factors where:

$$K_\sigma = \frac{\sigma_{max}}{\sigma_{nom}} \quad K_\varepsilon = \frac{\varepsilon_{max}}{\varepsilon_{nom}} \qquad \text{Eq.8}$$

Neuber's Rule is shown in Eq.9 (Bannantine, Comer et al. 1990)

$$K_t = \sqrt{K_\sigma K_\varepsilon} \text{ or } K_t^2 \Delta\sigma_{nom}\Delta\varepsilon_{nom} = \Delta\sigma\Delta\varepsilon \qquad \text{Eq.9}$$

6.2.3 FE – Based Fatigue Analysis

Welds inherently represent a geometric discontinuity, which poses problems for the FE analysis. Local geometry around welds in welded components dominates the fatigue performance and high levels of stress concentration therefore arise at the welds. FE cannot accurately assess the real stress at the fatigue critical locations so an indirect approach is required. Notches and corners in components are difficult to

be assessed for their stress and strain levels therefore correct fatigue damage parameters are required.

For predicting fatigue life of welded components, four methods are used in industry:

- Nominal Stress
- Hot Spot or Structural Stress
- Effective Notch Stress
- Linear Elastic Fracture Mechanics (LEFM)

Of these methods, only nominal and structural stress are described in this thesis, as they are particularly relevant to durability assessment of automotive structures.

6.2.4 Nominal Stress Approach

The nominal stress approach is the simplest out of all the approaches. Fatigue assessment according to the nominal stress approach uses standard S-N curves and detailed classes of the basic joints. These can be found in many standards and guidelines. The nominal stress is defined as the stress calculated across the sectional area and disregards the local stress effects of the welded joint whilst including the effect of the component shape in the area of the joint. The nominal stress is the maximum stress due to sectional forces or moments or the combination of the two at the location of possible cracking. In this approach, neither the weld toe nor the properties of the material constitutive relations are taken into consideration. The S-N curve resulting from this analysis is unique to the structural detail for which it is established. Fatigue lives for components containing a notch can be calculated using the S-N curve with a factor that corresponds to the component's geometry or type of notch. Nominal stresses can vary over a section and can often be calculated using basic theories of structural mechanics, although for more complex cases Finite Element Modelling (FEM) may be used. (Dowling 1987; Moan and Berge 1997; Fricke 2003)

Determining the nominal stress of the component for which the fatigue prediction is required is generally carried out with Finite Element Analysis (FEM). However, care must be taken to ensure that all stress raising effects of the structural detail of the welded joint are excluded when calculating the nominal stress.

Having obtained the component nominal stress and the relevant S-N curve, these are put into the five-box process as described in section 4.3.1., and the analysis completed.

Weld Classification Method

This is the more traditional method of weld fatigue analysis requiring the use of the BS7608 and BS5400 standards and is often used in several of the different approaches mentioned below. This method requires experience of engineering and the ability to understand the standard and classify welds. The engineers using this technique need a level of subjectivity, which comes with experience. Loading of the welds needs to be simplified into major levels and directions, which is difficult to apply for multidirectional and variable loading for complex structures such as chassis systems. Therefore the more complex FE techniques attempt to address this problem.

6.2.5 Hot Spot or Structural Stress Approach

The hot spot or structural stress approach takes the nominal stress method one stage further and considers the stress increase due to the structural configuration, i.e. the macro–geometry. This approach is especially suited for situations in which a simple nominal stress for welded joints is difficult or impossible to compute due to complex geometrical effects in the weld or the surrounding structure, or where there is no classification of the joint. However, this method is limited to determining the fatigue performance at the weld toe. (Mansour, Wirsching et al. 1995)

For a welded joint submitted to cyclic loading, the critical points where cracks initiate are usually located at the weld toes. These highly stressed zones can locally heat up, due to high levels of repeated plasticity, when subjected to high cyclic loads, hence termed 'Hot Spot'. The actual stresses responsible for fatigue damage at hot spots are extremely difficult to determine, due to the complex local stress distribution around the weld toe. (Radaj 1987)

The stress used in this approach is commonly called the hot spot or geometric stress and includes all stress raising effects of the structural detail at the toe, such as the membrane and the shell bending stress, while excluding all non-linear stress concentrations due to the weld profile. Structural geometric stress, σ_{geo}, is usually

encountered in plate, shell, and tubular structures. This method is recommended for welded geometries that have no clearly defined nominal stress because of complicated geometries. Therefore the stress value is determined by global dimensions and loading parameters of the component in the vicinity of the joint. Geometric stresses can be divided into the membrane stress and the shell bending stress components.

The geometric stress has to be determined in the critical location of the welded joint, i.e. at the weld toe, where crack initiation is expected. Figure 6.4 shows the determination of the hot spot stress.

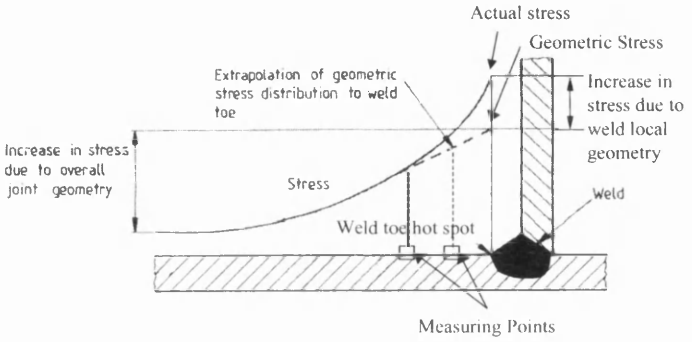

Figure 6.4: Determination of the Hot Spot or Structural Stress Concept

For both the nominal and hot spot concepts, the structural stress is determined in the critical location of the welded joint where crack initiation is expected to occur by measurement or calculation as shown in figure 6.4. Analysis of a structural discontinuity to obtain geometric stresses by using analytical methods is not possible. Therefore FEM analysis is applied, and the principal stresses are calculated.

The geometric stress can be measured through strain gauges placed at particular distances from the weld toe and then extrapolating the stresses from the gauges. Placement of the gauges must lead to reasonable extrapolation to the weld (critical) point, so distances are proposed by Nieme of $0.4t$ and $1.0t$ from the toe, where 't' is the sheet thickness. For much coarser meshes, gauges are placed at distances $0.5t$ and $1.5t$ from the weld toe. If the sheet is thin the gauge should be situated $0.3t$ away from the weld toe. The distances proposed by Nieme were selected to be as close as possible to the weld toe but outside the region affected by the weld toe singularity. (Nieme 2001)

To define the fatigue performance of the component an S-N curve is generated and the curve is then applied with the damage summation theory at the hot spot to determine an appropriate life. (Poutianinen, Tanskanen et al. 2004)

There are several methods available for FE analysis of weld fatigue such as MSC.Fatigue & FE-Fatigue, FLOW (Ford's in-house "Fatigue Life Of Welds" program or the Battelle Technique), LMS – FALANCS, FEMFAT (finite element modelling / fatigue), FE-Safe Verity.

MSC.Fatigue (MSC Software) and FE-Fatigue (nCode)

FE-Fatigue and MSC.Fatigue have similar capabilities and use the same well-proven nCode technology in different operating environments. MSC.Fatigue is integrated into MSC.Patran software so accesses a wide range of FE analysis. FE-Fatigue is a separate product, which directly accesses result files from a variety of industry-standard FE codes.

MSC.Fatigue is a structural stress based technique whereby welds are represented by thick shell elements as shown in figure 6.5a. These elements are relatively stiff when compared to the neighbouring shell elements representing vehicle parts. Weld failure is predicted currently at weld toes as shown in figure 6.5b. The damage parameter used in this technique is the "structural stress". Structural stress is the principal stress value at weld toes (top surface), originally determined from weld toe forces and moments. Currently the stress is calculated using the Nastran "cubic" option for nodal stress extrapolation. Weld toe bending (flex) ratio is also calculated to determine whether the weld toe is predominantly in bending or tension. Results from this analysis produce two curves, one for bending (flexible) and one for tension this is shown in figure 6.5c. These curves were produced with the understanding of the assumption that certain weld quality was of an acceptable standard.

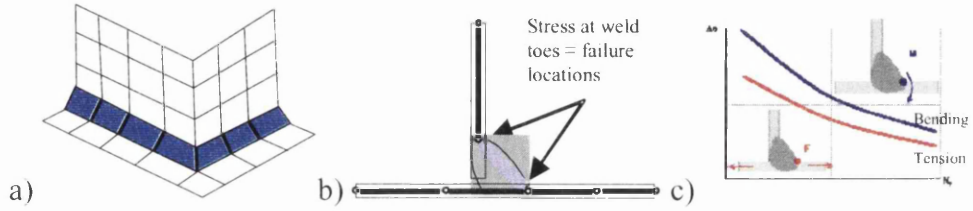

Figure 6.5: a) Element Size, b) Weld Representation, c) Bending & Tension Curves

This process uses simple and coarse elements for the welds and doesn't require the weld classification input. Although the cubic stress value may be dependent on element size so a valid range of element sizes will be used. At present, in fatigue life assessment, either the "bending" or "tension" S-N curve is used, rather than one that is based on the weld toe-bending ratio.

FLOW (Battelle Method)

The Battelle technique inside FLOW (**F**atigue **L**ife **O**f **W**elds) is a user-friendly CAE technology developed by Ford Motor Company in conjunction with Battelle providing fatigue characteristics for continuous and discrete connections between sheet metal. It is compatible with other software systems such as MSC.Nastran, HyperMesh and IDEAS. With weld fatigue life, maximum equivalent stresses are the current results from the FE analysis. (Kyuba and Dong 1993; Dong, Hong et al. 2003)

This is a nodal force method and a "structural stress" technique in which welds are represented by thick shell elements. Although depending on the weld penetration level there is a difference in the way parts are connected. For full penetration welds are formed as triangles as shown in figure 6.6a, whereas partial penetration only the inclined elements are connected as shown in figure 6.6b. Failure locations predicted by the technique are at the weld toe and across the weld throat.

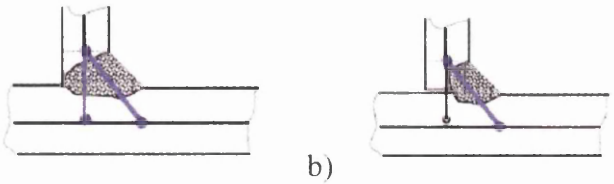

Figure 6.6: a) Full Penetration Weld, b) Partial Penetration Weld

Damage is calculated using the total stress equation:

Total stress = Structural Stress + Notch Stress.

Structural stress balances the applied loads and is determined from FE nodal forces followed by post processing using elastic shell theory shown in figure 6.7a. Whilst notch stress is self-equilibrating, S-N data captures notch and residual stress effects as shown in figure 6.7b.

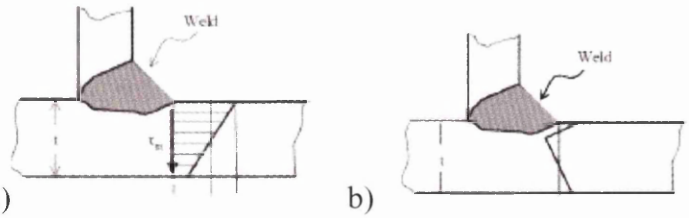

Figure 6.7: a) Structural Stress Approach, b) Notch Effect

A single master S-N curve for each welded material or one master curve for all steels based on the received wisdom that parent metal grades make little difference in weld fatigue with the certain acceptable weld quality is assumed. The welds consist of simple and coarse elements, with no weld classification required whilst the stress values at the weld are claimed to be insensitive to the FE element mesh size. Unfortunately this technique is unavailable in commercial codes.

Fe-Safe Verity™ (Battelle Method)

This is the new Battelle methodology known as the Verity™, which has been developed in collaboration with over a dozen leading engineering companies, members of Battelle's Joint Industry Project (JIP). Verity™ is a mesh-insensitive structural stress methodology so that detailed FEA models are not required. The method can be applied equally well to structural welds in thick plate, seam welds in thin sheets, and spot-welds. It is compatible with other software such as HyperMesh where a tool exists to support Verity, Nastran, ABAQUS and ANSYS for post processing.

The Verity method is a major departure in that it uses nodal forces to determine a 'structural stress' at the weld toe so that the user does not need to determine nominal stresses at some distance from the weld toe. A single S-N curve can then be applied to all types of welded joint to a good level of accuracy. This avoids the 'weld classification' problem, because the stress refers to the weld toe there is no 'distance' problem, and the method is insensitive to mesh density and element type. It can also be applied to a much wider range of welds - structural welds, spot welds, etc, all with a single S-N curve.

Verity is a module within the fatigue analysis software Fe-Safe, which computes equivalent structural stresses, based on the Battelle "structural stress" method and

uses these stresses to calculate the fatigue lives. The method is described in detail in chapter 10.6.

LMS–FALANCS

LMS International developed this software. (LMS 1999-2000)

This is a stress concentration factor technique, which is based on a German research consortium's research. R1MS (**R**adius **1**mm with **M**ean stress and **S**catter) with notch radius of 1mm is shown in figure 6.8, whilst R03MS has a radius of 0.3mm used for thin sheets. LMS has two approaches for R1MS – Detailed or Coarse. Weld failure can be predicted at both weld toes and roots.

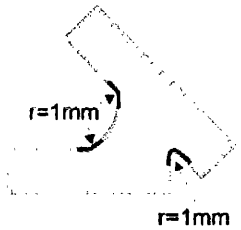

Figure 6.8: Showing the Location of Radii

The detailed method involves the stress being obtained from the FE model directly, which provides more accurate results. For the coarse method the stress is determined by multiplying nominal stresses from the coarse FE model with notch factors stored in a database which is more consistent with current FE practice for vehicle modelling i.e. shell representation of vehicle structures. The curves produced are one S-N curve for steels and for aluminium alloys. This is based on experimental evidence that weld performance of parent material is dominated strongly by the welds local geometry.

Unfortunately this is essentially a weld classification method, which relies on analyst's experience, and for thin walled parts – plate thickness t<2mm verification is required. The types of welds available in the weld notch factor database will limit the coarse method.

FEMFAT

Magna / Steyr-Daimler-Puch developed FEMFAT (**F**inite **E**lement **M**ethod / **Fat**igue) software for fatigue simulation of dynamically loaded components. The calculation methods for the influencing parameters considered in this software are

fixed by German guidelines such as FKM or TGL. (Brenner, Unger et al. 1998; Unger, Dannbauer et al. 2003)

This technique uses no special weld elements only straightforward connections between parts. Weld configurations and seams are determined by assigning proper material types e.g. MAT105 to parts being welded as shown below in the butt welds and t-joint in figure 6.9a and b.

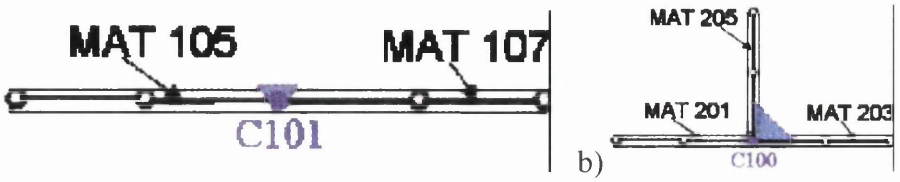

Figure 6.9: Example of a) Butt Weld, b) T – Joint

Weld locations are either the weld end or within the weld line by specifying the weld node colour e.g. C100. Failure locations predicted by this technique are at the weld toe or root if weld notch factors exist. The damage parameter is the stress normal to the weld line at weld toes and or weld root. This is a stress concentration factor or a notch factor method like LMS-FALANCS. The database of weld notch factors and weld material data is predetermined and coded into the software. The weld stress value is calculated by multiplying the nominal stress by the relevant concentration factors. Notch factors are determined by FEM or welds and based on the LMS-FALANCS RMS method. For the parameters such as sheet thickness and loading modes they have connection methods. The predicted results are produced in one S-N curve for all welded steels and one for aluminium alloys.

This technique has simple meshing as no weld elements are present, and that the weld stress connection reduces sensitivity to weld element size. Unfortunately this technique is very similar to the LMS–FALANCS and is a type of weld classification approach, which in turn complicates the method. Fatigue analysis preparation can be potentially very time consuming.

Any of these five methods are valid for FE modelling and subsequent analysis of fatigue critical locations in components. For this project however the current focus will be on the comparison of Volvo MSC.Fatigue and the Ford FLOW methods for analysing welding fatigue of simple geometry coupons and components.

7. MEASURING STRESS & STRAIN BY EXPERIMENTAL METHODS

Alternative methods for determining stresses and strains in FE are through strain gauging and photoelasticity.

7.1 Strain Gauge

Strain (ε) is the amount of deformation of a body due to an applied force and is defined as the fractional change in length from L to L+ΔL. The ratio ΔL/L is called strain and is shown in Eq.10.

$$\varepsilon = \frac{\Delta l}{l} \qquad \text{Eq.10}$$

As the ratio of deformation is often very small, it is often represented in units of μstrain or 10^{-6}. The most common method of measuring strain is with a strain gauge, a device whose electrical resistance varies in proportion to the amount of strain in the device. The metallic strain gauge consists of a very fine wire or a metallic foil arranged in a grid pattern. The grid pattern maximises the amount of metallic wire or foil subject to strain in the parallel direction shown in figure 7.1. The cross sectional area of the grid is minimized to reduce the effect of shear strain and Poisson strain. The grid is bonded to a thin backing, which is attached directly to the test coupon. Therefore, the strain experienced by the test coupon is transferred directly to the strain gauge, which responds with a linear change in electrical resistance.

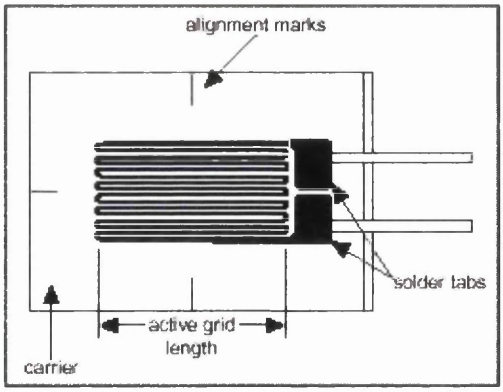

Figure 7.1: A Strain Gauge

The gauge factor of a strain gauge relates strain to change in electrical resistance. The gauge factor (GF) is defined as the ratio of fractional change in electrical resistance to the change in strain, which is shown in equation 11.

$$GF = \frac{\Delta R/R}{\varepsilon} \qquad \text{Eq.11}$$

Where R is the resistance of the undeformed gauge, ΔR is the change in resistance caused by strain, and ε is strain. (Wikipedia 2006)

7.2 Photoelasticity

Photoelasticity is a whole-field technique for measuring and visualising stresses and strains in structures. The method involves applying a given stress state to a model and utilising the induced birefringence of the material to examine the stress distribution within the model. In response to an applied stress a substance may change its dielectric constant and consequently, in transparent materials, change its refractive index. The optical anisotropy is known as either photoelasticity or the piezo-optical effect. The magnitude and direction of stresses at any point can be determined by examination of the fringe pattern, and related to the studied structure.

Birefringence is the ability of the material to split incident light into two component rays. This property only exists when the material is being stressed. The direction and speed of the propagating light are always coincident with and proportional to the direction and magnitude of the principal stresses, respectively.

It is a technique, consisting of a number of polarising plates surrounding a model. A polarizer is a collection of parallel slits only emitting light components in the direction of the slits. The emerging light is termed polarised light. This polarised light is then incident on the object being analysed either reflecting or transmitting through the material, depending on the opacity of the material. The light out of phase as it emerges from the material, passes through an analyser, where only the components parallel to the axis of the analyser are transmitted, and creates interference patterns. The amount of interference is proportional to the phase difference of the propagating light and is therefore directly proportional to both the difference in principal stresses and the maximum shear stress.

The interference patterns, which appear as colourful fringes unique to a specific stress distribution provide an immediate representation of the shear stress distribution throughout the model.

The layout of the Grey Field Polariscope (GFP) is shown in figure 7.2a and consists of a projector unit delivering circularly polarised light and a CCD camera with a constantly rotating analyser. For each revolution of the analyser a number of images are captured which allow the intensity of the reflected light to be measured. The returning polarised light if there is a stress causing birefringence present is elliptical, and from this intensity data it is possible to calculate the axes of the ellipse and its angle of retardation. From this the captured image can be expressed as defined by a Mohr's circle solution representing the shear stresses in vertical and horizontal planes together with the maximum shear stress.

The fringe pattern is based on a contrast between the colours blue and red as shown in figure 7.2b. Areas that are blue represent areas in compression, and areas that are red represent tension. The variation of intensity and shades of the two primary colours represents the difference and strength of the stress magnitude.

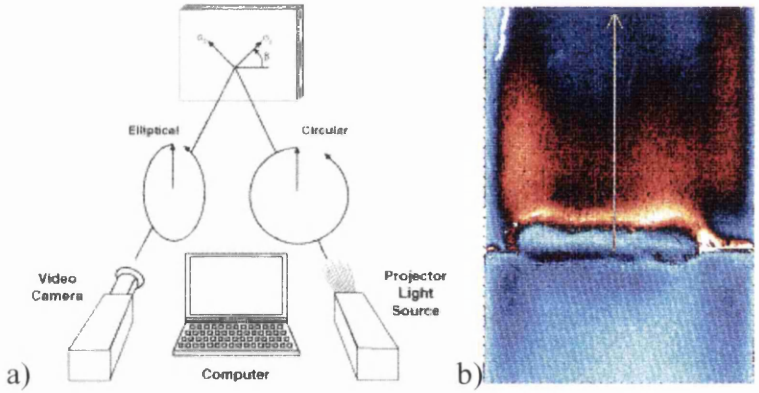

Figure 7.2: a) GFP 1200 Polariscope Setup Diagram, b) M11A Maximum Shear Stress Distribution

The GFP allows for photoelasticity of opaque, non-birefringent objects through use of a thin, birefringent epoxy coating applied to the outer surface of the model. The coating thickness does not need to be completely uniform, as the GFP automatically measures and accounts for slight thickness variation. The object itself must have a reflective covering, so that the light can be reflected through the epoxy coating. The strain distribution on the surface of the model is then transmitted to the coating, which in turn is the strain distribution pattern that is visible during analysis. This strain distribution is directly proportional to the stress distribution, so an immediate qualitative stress analysis is available. A quantitative stress analysis is available through the use of Hooke's relations of principal stresses and strains. In order to

make this conversion, the Young's Modulus and Poisson's Ratio for the specific birefringent material must be known. (Higdon, Ohlsen et al. 1985; Boyce, Calvert et al. 2003)

8. SUMMARY OF LITERATURE REVIEW

Fatigue has been a much-researched phenomenon for nearly 200 years and will remain an area of extreme importance for many industries, especially in the automotive industry. Testing methods are extensive and varied, and the best methods for analysis will depend on the type and application of the final component. Most of the research to date has been dealing with constant amplitude testing of simple components.

The automotive industry designs and manufactures numerous complex components, many of which are welded. They experience complex fatigue loading conditions in service. These conditions are hard to reproduce in laboratories and, therefore, there is a lack of confidence in the current predictive methods for fatigue analysis.

With the automotive industry under significant legislative pressure to reduce weight and improve vehicle emissions, lighter materials by substituting conventional mild steels with thinner high strength steels , which have improved fatigue properties, are now being investigated. Fatigue properties of high strength steels can influence the level of weight reduction achievable and are related to the steels UTS. These properties are also affected when notches are introduced and the extent to which performance is affected by the notch depends on its severity. Welds, which act as severe notches and other joining mechanisms drastically reduce the fatigue strength. Welds mainly change the microstructure and by doing so remove the benefit of the high strength of the parent material.

Moreover, many studies have shown that, gauge for gauge, welded high strength steels do not have improved fatigue performance over welded conventional mild steels.

Therefore the effects of welding fatigue are very important for the durability assessment of components. The automotive industry is currently in the process of reducing the number of prototype vehicles produced and tested which is exerting pressure on the analysis community to more accurately predict potential fatigue areas during the design and development phases. With less time available for building and

testing prototypes before manufacturing, it has become vital to simulate structures on computers and accurately predict potential functional issues.

On this basis, the fatigue properties of seam welded high strength sheet steel will be investigated. Work will be carried out on a variety of test specimens, ranging from simple geometry seam welded lap-shear and tension-peel coupon specimens through to full scale automotive components. A variety of loading regimes will be used to test the specimens including simple constant amplitude sinusoidal signals of varying loads and ratios to variable amplitude signals.

Two weld fatigue CAE techniques, proposed by Volvo and Battelle are being incorporated into MSC.Fatigue, FLOW and FE-Safe Verity finite element fatigue analysis software packages, and will therefore be reviewed in this project. These CAE techniques will form the analysis for both the coupon tests to produce S-N curves and the subsequent life predictions of the automotive component.

Experimental verification of the FE models in the form of strain gauges and photoelasticity will be employed to compare the stress distribution away from the weld. Using these techniques will also allow confidence to be gained in the method of FE modelling the coupon joints.

9. PROJECT OBJECTIVE OVERVIEW

This research project aims to develop the ability of using CAE methodology for the durability assessment of welded steel automotive components to reduce the amount of physical testing required for verification purposes.

9.1 Objectives

More specifically, the objectives of this project include:

- Review CAE seam weld durability assessment techniques
- Generate seam-weld fatigue data (coupon joints)
- Conduct component and coupon durability tests
- Perform FE stress and fatigue analyses
- Correlate physical tests with FE modelling
- Propose new or improved techniques

9.2 Project Scope

Figure 9.1 shows how the objectives of this project were achieved through three main areas of activities:

Data generation involved using the different coupon geometries under constant and variable amplitude, and a block loading sequence of constant amplitude loading. This data was analysed from load-life curves to "structural stress vs. life" curves.

For the CAE durability assessments of the front upper control arm, the generated structural stress-life curves were used. These S-N curves were generated from the coupon data analysis, and used as the material curves for the analysis. From this predicted lives for the front upper control arm were obtained.

Component Rig-Tests will generate the actual lives of the Front Upper Control Arm (FUCA) under constant amplitude, block loading and variable amplitude loading conditions. These lives will be used to check the CAE predicted lives.

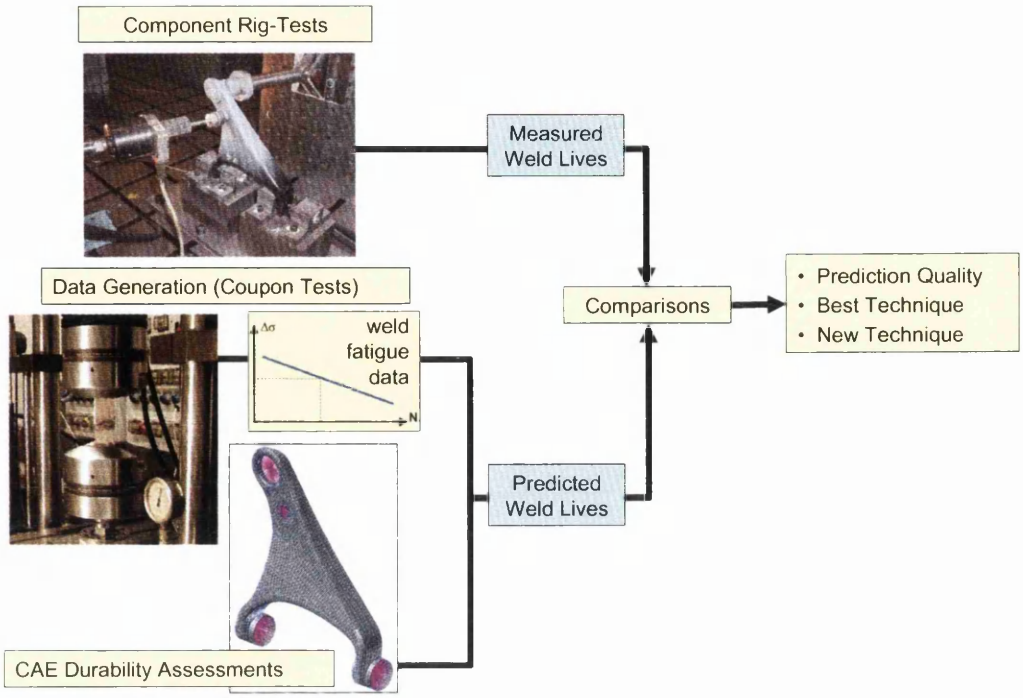

Figure 9.1: Outline of Project Scope

10. EXPERIMENTAL AND ANALYTICAL PROCEDURES

The test programme objectives are as follows:

1. Data generation for input into fatigue analysis
2. Component test comparison with fatigue life predictions

The coupons were designed based on the Jaguar & Land Rover previous fatigue work on CAE weld based fatigue life predictions. Most chassis or suspension components were either made at GKN Autostructures or TKA-Tallent. It was deemed appropriate for both suppliers to prepare the coupon joints, so as to ensure consistency in the welding conditions between coupon joints and the welded FUCA components. The welding conditions were not supplied but assurances were given that the coupons met the same welding standard as the welded components.

The FUCA component was chosen on the recommendation of Jaguar & Land Rover. It was deemed a fatigue critical component during vehicle development as fatigue cracks had been identified on this component during the development stage. Some investigations were completed and potential issues discussed, the FUCA component was deemed a suitable component for more detailed investigations.

10.1 Material Selection and Composition

The coupon specimens are made of a typical high strength low alloyed (HSLA) automotive grade steel – Corus XF350 (S355MC EN 10149-2:1996). It is a hot rolled, micro alloyed steel strengthened through the process of precipitation hardening and grain refinement. The composition of the steel, and typical mechanical properties are shown in Table 10.1.

Table 10.1: XF350 Steel Composition and Mechanical Properties

Chemical Composition								Tensile Properties		
Grade	C	Mn	Si	P	S	Al	Nb	Yield strength MPa	Tensile strength MPa	% El.
XF350	≤0.1	≤1.2	≤0.04	≤0.025	≤0.01	≤0.02	≤0.3	≥350	≥430	≥23
XF350 (2-3mm thick) Typical								393	469	27
Coupon	0.082	0.414	0.019	0.0147	0.0062	0.049	0.019			
FUCA	0.104	0.515	0.027	0.0332	0.0054	0.045	0.0261			

Values of composition are in weight percentages

The chemical compositions of both the FUCA component and the coupons were checked and found to be consistent with that of XF350 grade of steel, also shown in

the table 10.1. The composition of both the coupons and the FUCA is well within the bounds of XF350, and therefore the same material.

For component testing, a right hand side Front Upper Control Arm (FUCA) from Land Rover Discovery 3 was selected as shown in figure 10.1. It is made of 3mm XF350 steel with MIG welds, and supplied with bushes and ball joints fitted.

Figure 10.1: Front Upper Control Arm (FUCA)

The typical microstructure for a HSLA grade of steel used for both coupon suppliers and the FUCA component is shown below in figures 10.2 – 10.4. The typical parent material microstructure is a mixture of ferrite and pearlite phases, whilst the weld material shows typical columnar grains with large ferrite grains produced from the welding consumable.

At the diffusion line the columnar grains of the weld material change into a coarse grained HAZ. 1mm from the diffusion line the HAZ has a much finer grained structure.

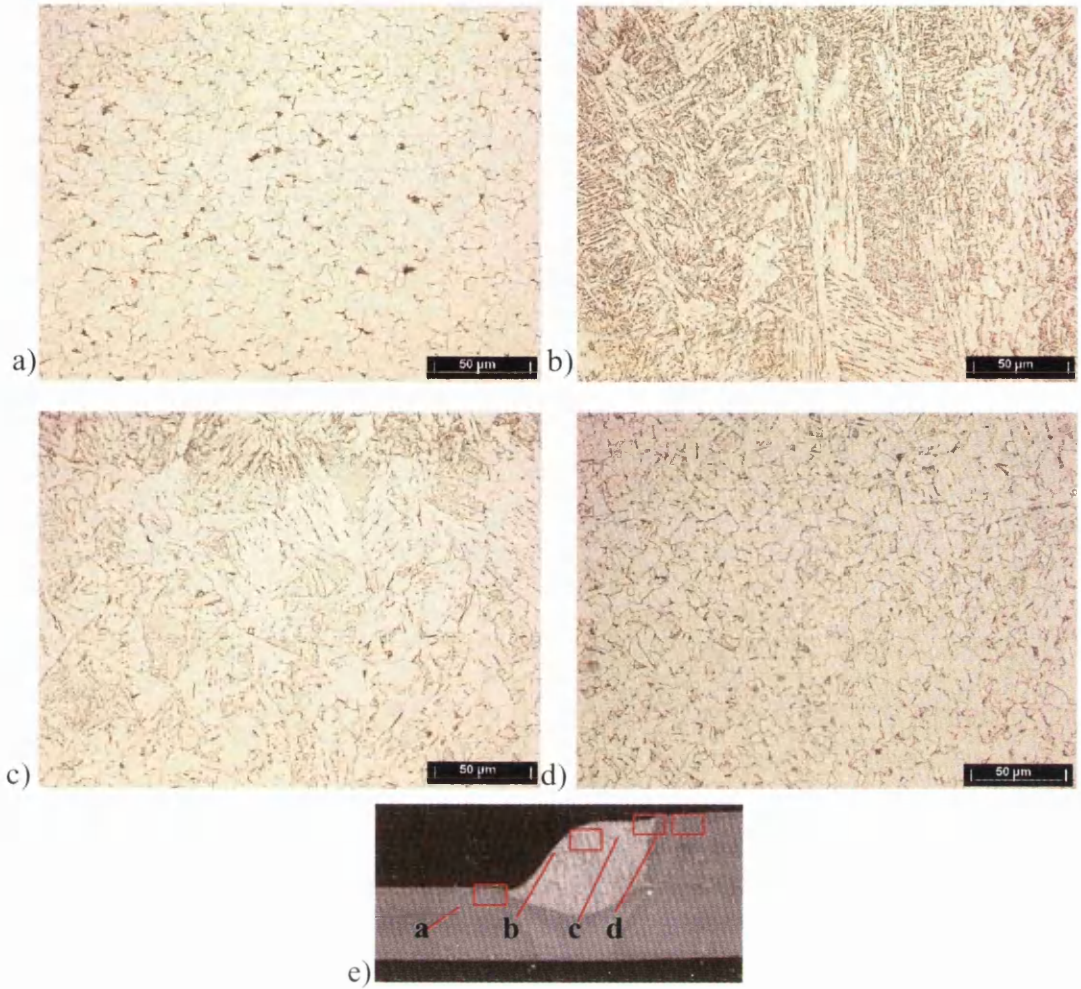

Figure 10.2: Typical Micrographs for GKN Coupons, a) Parent Material, b) Weld Material, c) Diffusion Line and HAZ, d) HAZ Distance 1mm from Diffusion Line, e) Illustration of Weld Micrograph Positions

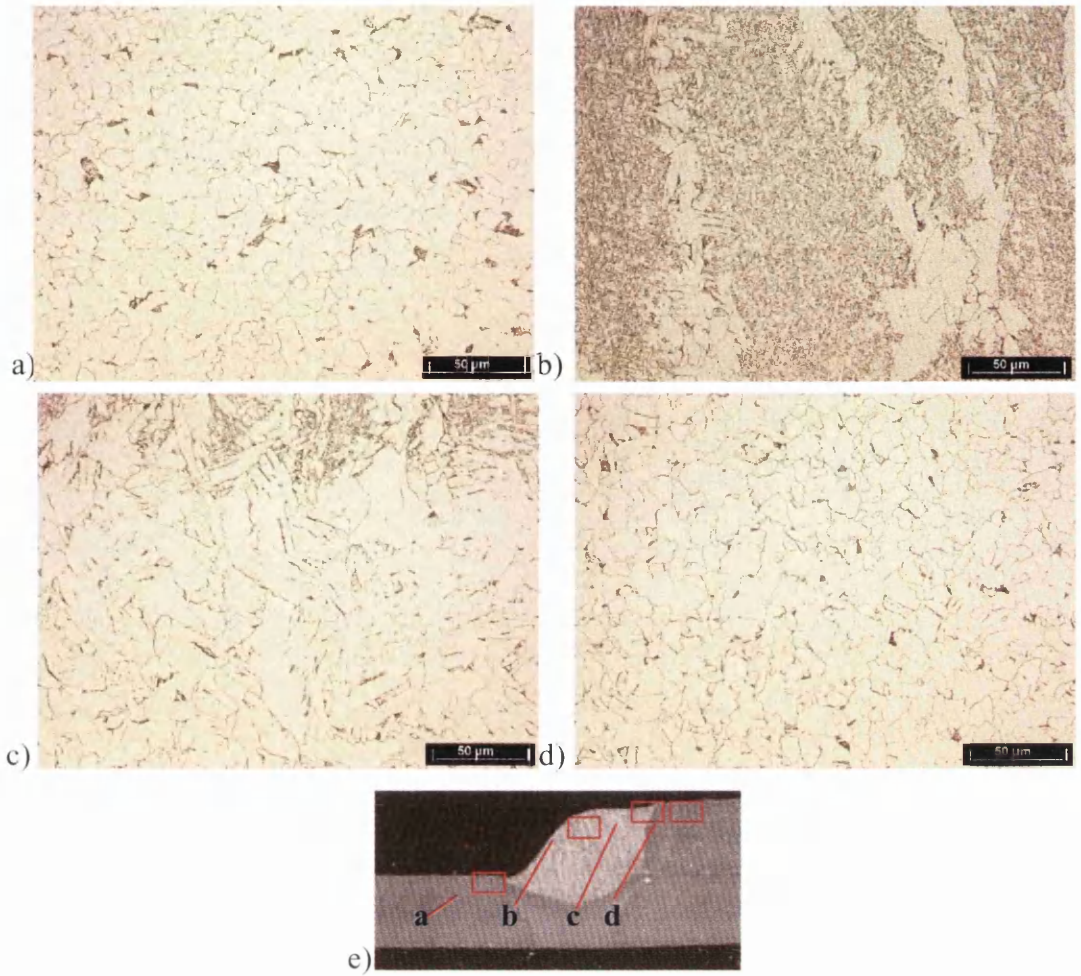

Figure 10.3: Typical Micrographs for TKA Coupons, a) Parent Material, b) Weld Material, c) Diffusion Line and HAZ, d) HAZ Distance 1mm from Diffusion Line, e) Illustration of Weld Micrograph Positions

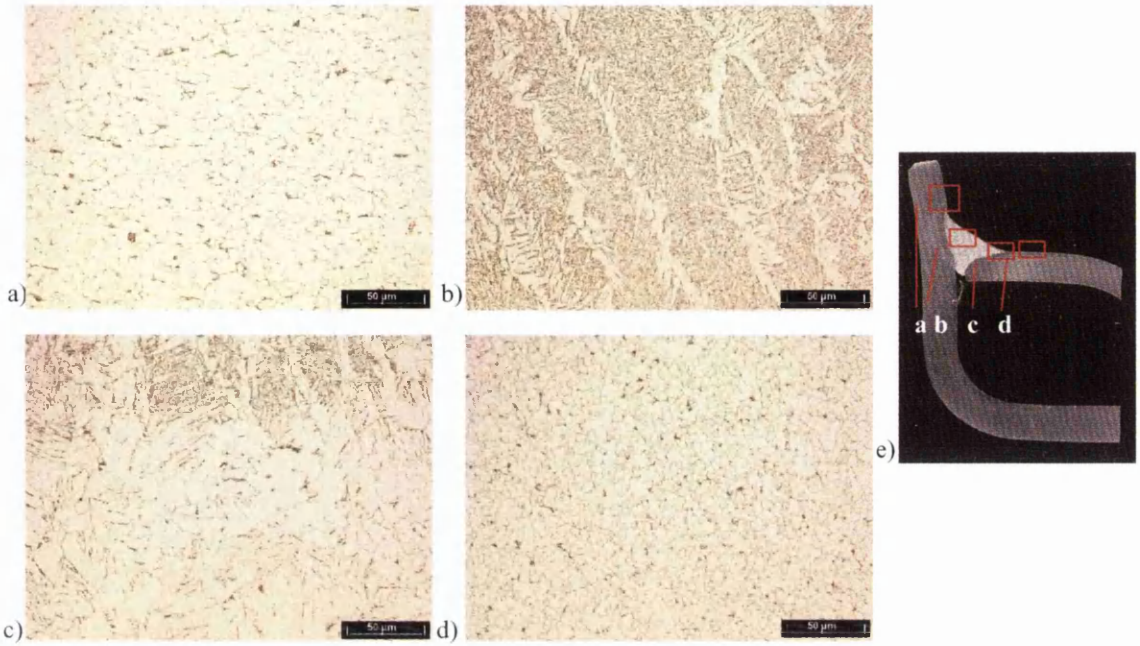

Figure 10.4: Typical Micrographs for FUCA Components, a) Parent Material, b) Weld Material, c) Diffusion Line and HAZ, d) HAZ Distance 1mm from Diffusion Line, e) Illustration of Weld Micrograph Positions

From examining the FUCA component microstructure at lower magnifications, the appearance of weld porosity defects near the edge of the weld material were noted and shown in figure 10.5a, and b shows the location of the porosity in the weld.

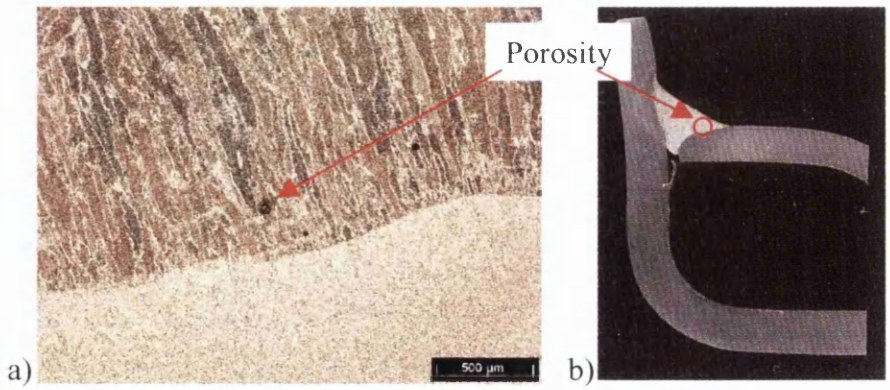

Figure 10.5: a) Weld Porosity in the FUCA Components, b) Location of Porosity

10.2 Coupon Testing for Data Generation

10.2.1 Coupon Joint Configurations

Two suppliers of Land Rover - GKN and TKA-Tallent provided simple geometry specimens to generate data for input into subsequent fatigue analysis. Figures 10.6 – 10.9 show the 4 different geometries, each with either a full stitch weld or partial weld.

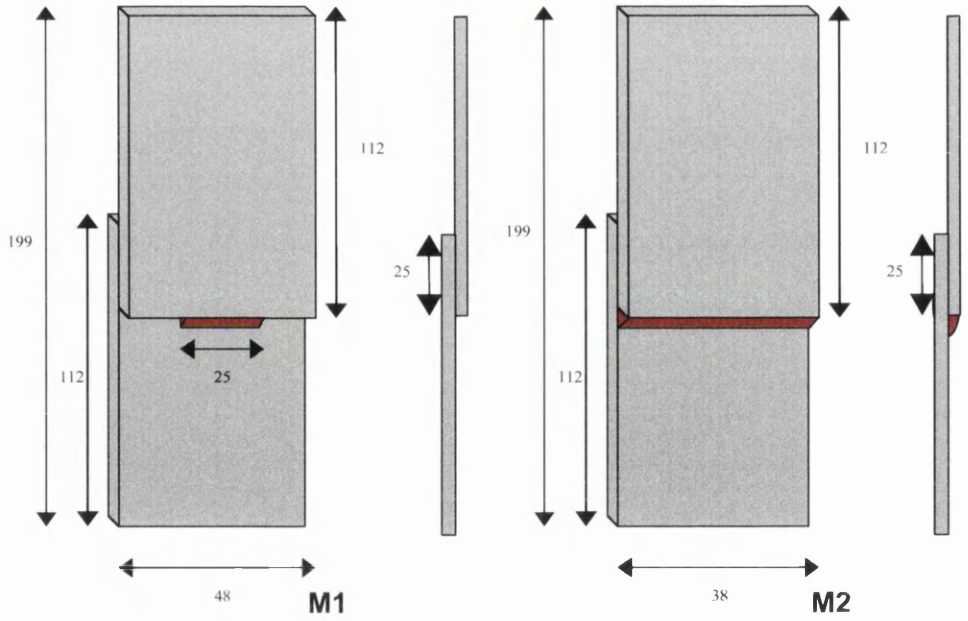

Figure 10.6: M1 and M2 Lap-Shear Geometry

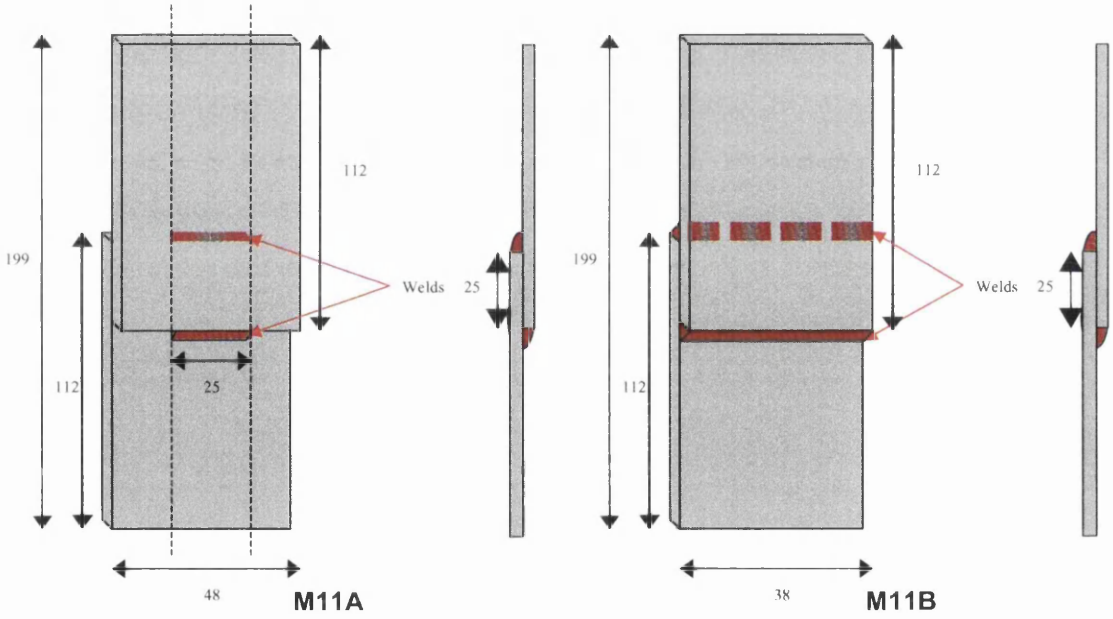

Figure 10.7: M11 Short and Full Double Lap-Shear Geometry

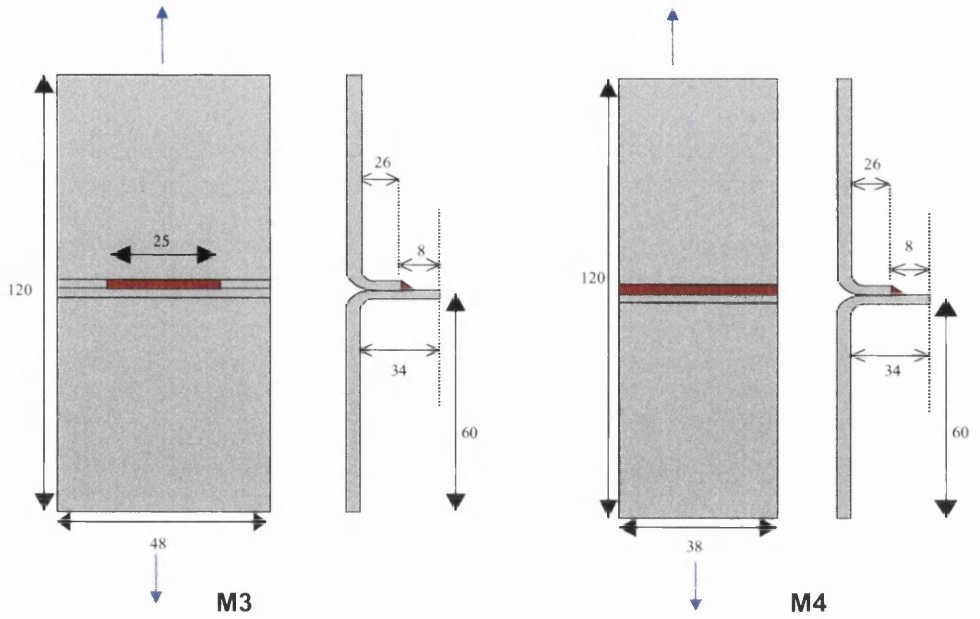

Figure 10.8: M3 and M4 Peel Geometries

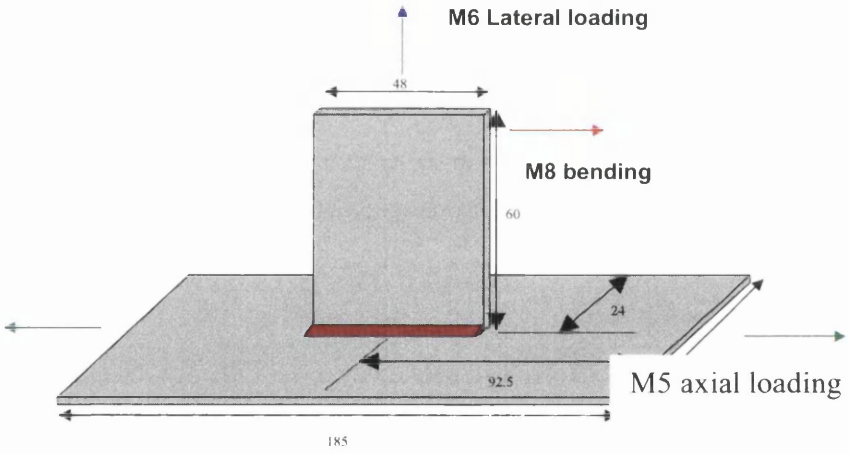

Figure 10.9: M5, M6, M8 T-Shaped Geometry with 3 Different Loading Directions

10.2.2 Test Machines and Rig

To compare basic weld fatigue properties, constant amplitude stress-life tests were carried out using a servo-hydraulic Dartec fatigue machine fitted with a 25kN – 50kN actuator load cell, MTS 647 Hydraulic wedge grips and a Dartec controller, as shown in figure 10.10a.

The test setup for the T-shaped joints is a servo-hydraulic test arrangement consisting of an MTS 458 controller and a 10kN actuator mounted on a bedplate as shown in figure 10.10b. Data collection uses a high cycle fatigue rig controlled by Land Rover in-house software.

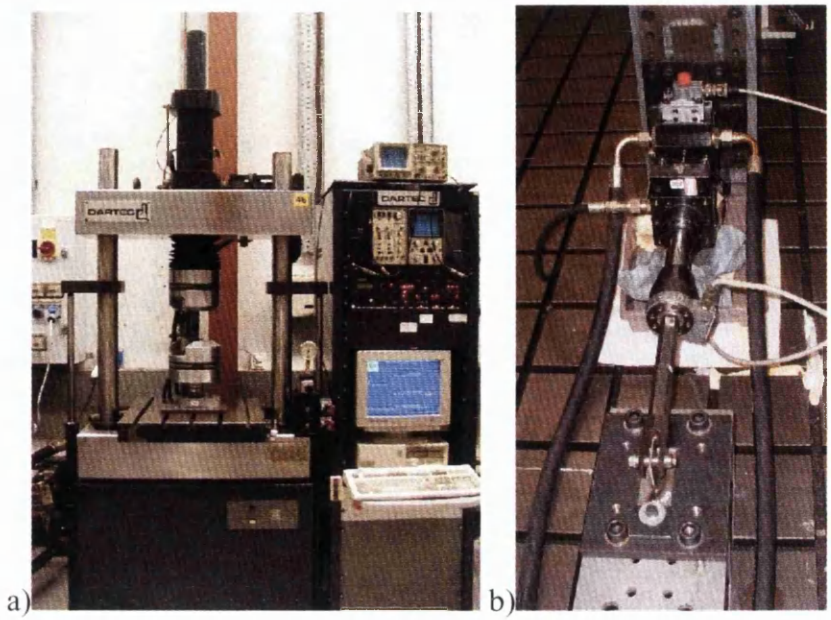

Figure 10.10: a) Coupon Test Machine, b) T-shaped Coupon Rig

10.2.3 Fatigue Loads

10.2.3.1 Constant Amplitude Loading

For all the coupon geometries shown in figures 10.6 – 10.9 were tested at an R-ratio R=0.1.

From the remaining coupon specimens the geometries with enough specimens for a valid test were used to conduct further investigations into changing R-values. TM11B was selected for testing at R-ratios of R=0.5 and R=-1. GM2 was selected for testing at R=0.5.

10.2.3.2 Variable Amplitude Loading

Two methods of variable amplitude loading was considered 1) 2-level block loading, 2) Random loading using the SAE Bracket Load-Time history.

2-Level Block Loading

A block-loading load time history programme was created to enable an easier method of evaluation of the cumulative damage rule for welds, such as Miner's Rule. Two load levels which cycled around the mean were chosen for the programme, under R=0.1 conditions as shown in figure 10.11 (20kN and 10kN) and figure 10.12 (15kN and 7.5kN).

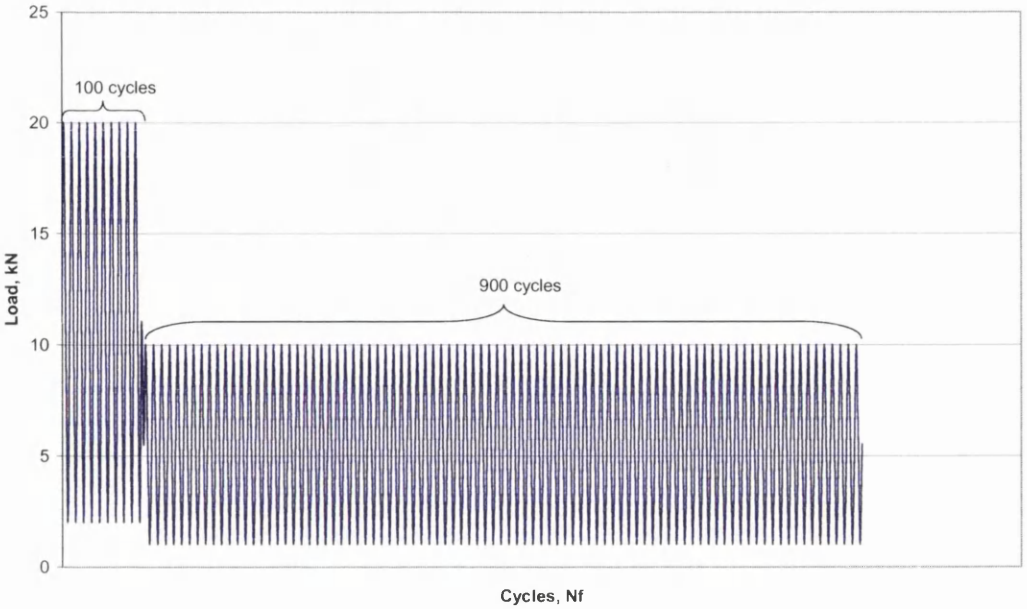

Figure 10.11: 1st Load Level Sequence

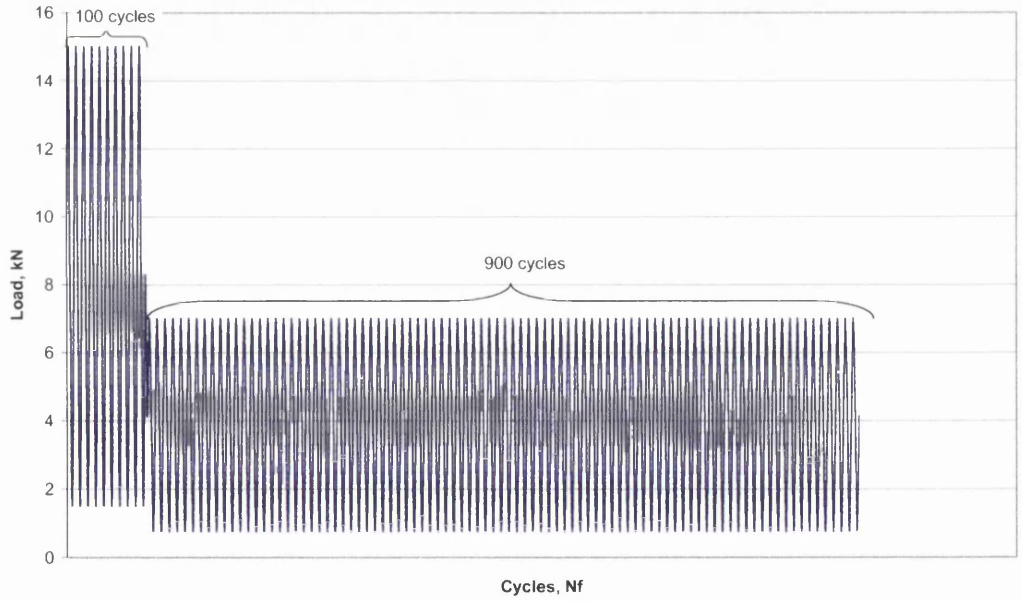

Figure 10.12: 2nd Load Level Sequence

Double–weld line lap-shear coupon GM11A was selected for the block loading sequence due to having enough specimens available for testing, and was tested using the same servo-hydraulic Dartec machine used for constant amplitude testing.

"Random" SAE Bracket Loading

The SAE Bracket load-time history was chosen on the recommendation of Jaguar & Land Rover. This load-time history is a "random" variable amplitude loading which is relevant for chassis components.

Variable amplitude loading followed constant amplitude testing. Double lap–shear, single lap–shear, and T–Shaped coupons geometries were selected: TM11A, GM1 and GM8.

SAE Bracket Load–Time history was used and scaled so that the peak load levels of the history corresponded to the levels used during the constant amplitude tests as shown in figure 10.13. The test was controlled using a Jaguar and Land Rover in-house variable-amplitude fatigue test control software program, which scales the load levels using volts.

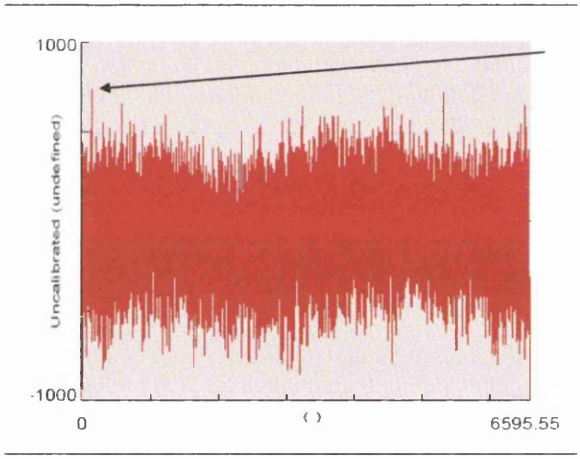

Figure 10.13: SAE Bracket Load – Time History

Rainflow cycle counting was performed using the MSC.Patran software MSLF tool with a counting bin number of 128. The results from analysing the SAE Bracket load-time history are shown in figures 10.14 – 10.16. Figure 10.14 shows the number of cycles in the load-time history for the given load range of 18kN to 0kN and shows that the majority of the cycles are not at the peak load level.

Figure 10.15 show the number of cycles either side of the mean, whilst figure 10.16 shows the effect of the number of cycles for the range. The rainflow counting, mean and range effect on number of cycles remains the same for the other load levels used

for TM11A, GM1 and GM8 with just the axis scaling changing. Therefore these graphs are not shown.

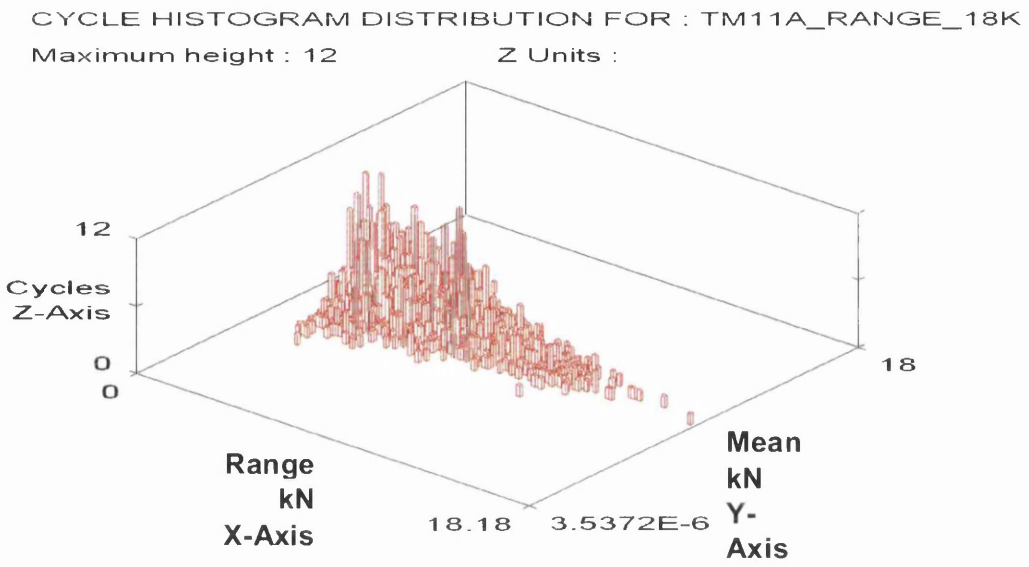

Figure 10.14: Number of Cycles for a given Load Range and Mean

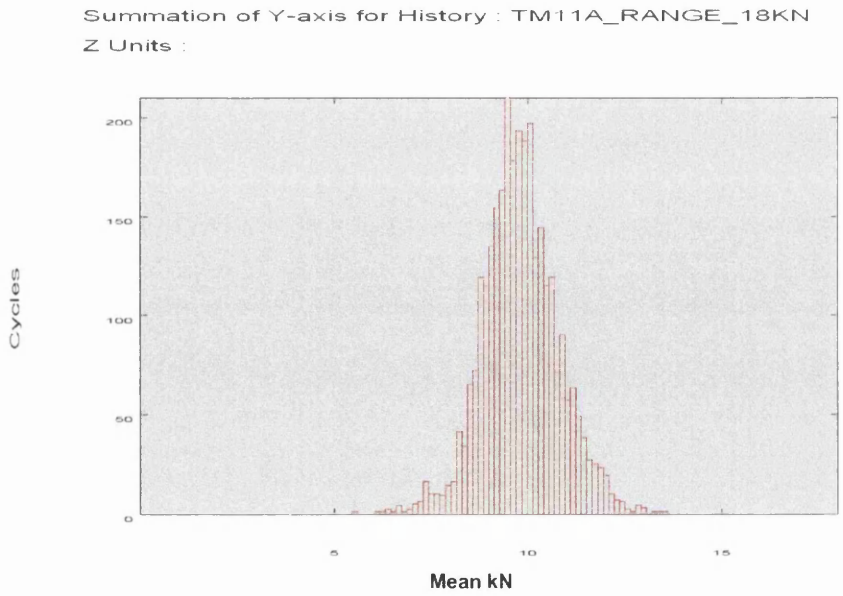

Figure 10.15: Number of Cycles for the Y-Axis of the SAE Bracket Load-Time History

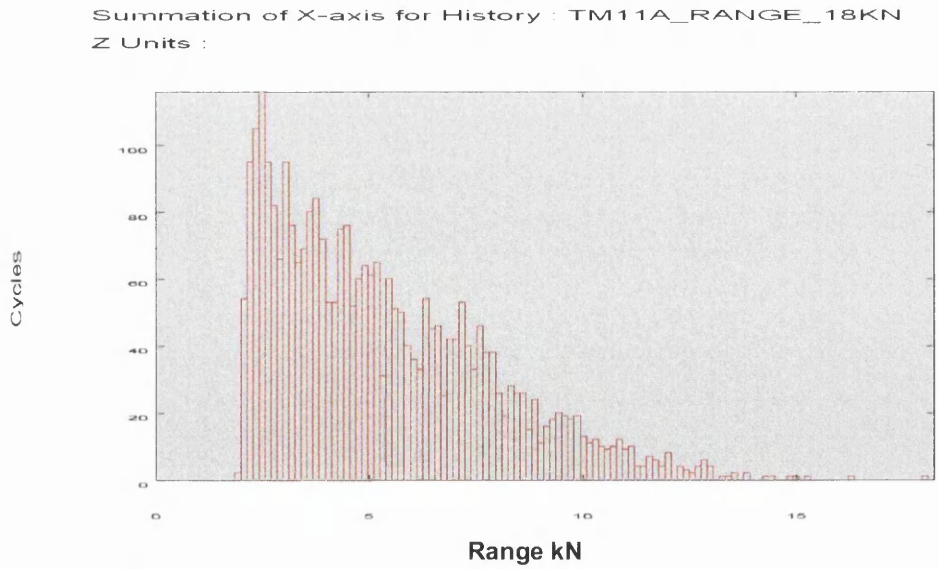

Figure 10.16: Number of Cycles for the X-Axis of the SAE Bracket Load-Time History

10.2.4 Test Procedure

For all the coupon testing completed, the testing conditions are detailed in Table A10.2.1 in Appendix 1.

10.2.4.1 Constant Amplitude Fatigue Tests

The Dartec or MTS 458 controller allows all the parameters such as load levels, waveform, frequency, and test limits required in the test to be controlled. For all R ratios, the uniaxial tests were carried out on the selected geometries with a frequency of 5 – 15Hz. Tests were performed over a range of applied constant amplitude loads to target fatigue lives of 10^4-10^6 cycles. The data generated from the machine is then collected by a Land Rover in-house high cycle fatigue test control program, which records the load, displacement, and number of load reversals (which is double the number of cycles).

For the lap-shear and peel geometries (figures 10.6 – 10.8), loading was applied by means of a servo-hydraulic Dartec fatigue machine fitted with a 50kN actuator load cell, MTS 647 Hydraulic wedge grips and a Dartec controller. Spacer plates were fitted to ensure true alignment of the coupon in an attempt to avoid loading misalignment. For the T-Shaped geometry (figure 10.9), loading was applied using a servo-hydraulic test system consisting of a MTS 458 controller and a 10kN actuator mounted on a bedplate as shown in figure 10.10b.

Tests were then performed over a range of constant amplitude loads to gain data points with lives of 10^4-10^6 cycles.

1. Applied load range from 8 – 20kN for lap-shear geometries
2. Applied load range from 0.5 – 1.2kN for peel geometries
3. Applied load range from 2 – 36kN for T-shaped geometries

The termination criterion for the tests is the coupon breaking from complete crack propagation through the weld. The life to failure is then recorded. From this the 10% stiffness drop was calculated from the recorded load and displacement data.

Stiffness = Load range / Displacement range

Tests were deemed a runout if they achieved 2,000,000 cycles without reaching the termination criterion.

10.3 Component Testing

The front upper control arm (FUCA) supplied by TKA-Tallent formed the basis of the component testing.

The uniaxial test rig is a servo-hydraulic test system consisting of an MTS 458 controller and a 25kN actuator mounted on a bedplate, as shown in figure 10.17a. The location of the FUCA in the car suspension is shown in figure 10.17b. The actuator loads the component to represent the vertical loads (in the vehicle Z-direction) experienced in service. The load is applied through the anti roll bar (stabi) link through the stabiliser mount.

The FUCA component has all the joints tightened to the required torque levels – ball joint 60Nm, Stabi link 98Nm and chassis/wishbone 149Nm. A close-up of how the load is applied to the FUCA is shown in figure 10.18.

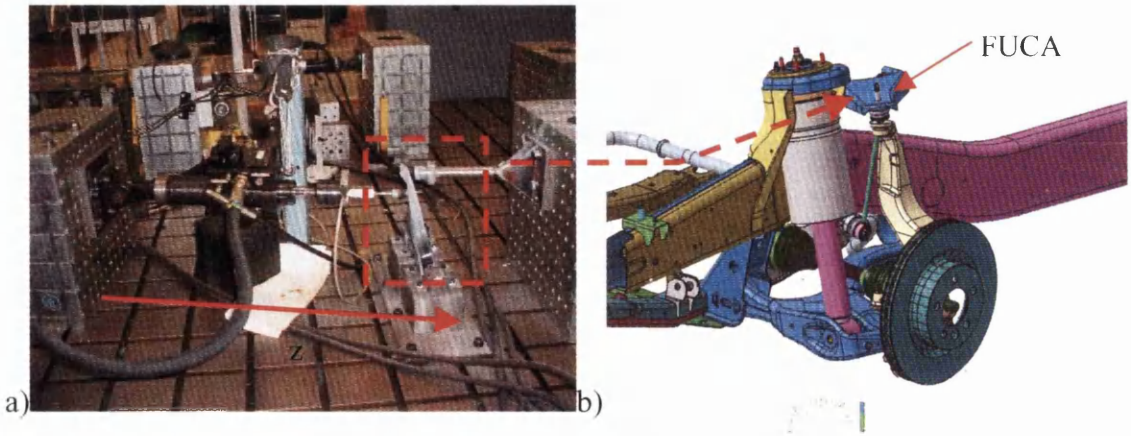

Figure 10.17: Uniaxial Z-axis Rig with a FUCA Component on Test, b: Location of FUCA in the Car Subframe

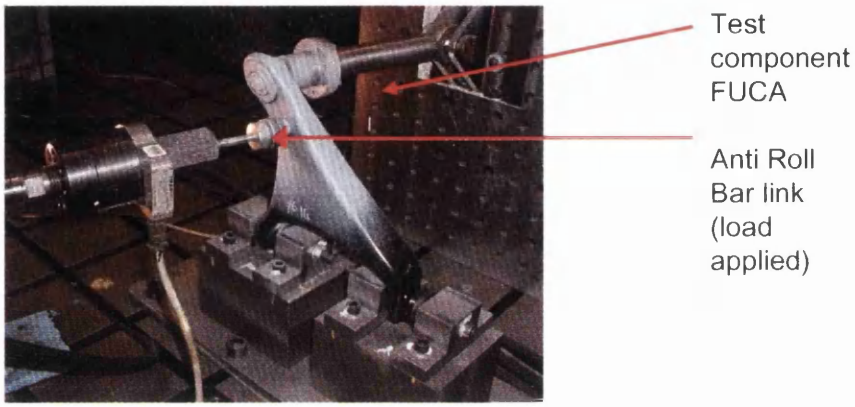

Figure 10.18: Load Applied through the Anti Roll Bar Link

To gain a thorough comparison with the initial tests carried out by the TKA–Tallent, the rig setup had to replicate, as far as possible, the one used at Tallent. Nevertheless, slight alterations to the Tallent setup were made for ease of keeping the FUCA component straight and applying the load into the stabiliser link hole at a 9° angle from an axis 'Normal' to the anti roll bar link hole instead of having the component at a 9° angle.

10.3.1 Test Procedure

It is important to ensure that required torque levels are applied to the fitted component. The MTS 458 controller allows all the parameters such as load, waveform, frequency, cycle counter, and test limits required in the test to be controlled.

Crack initiation is monitored by visual inspection. A crack size of approximately 10mm, the smallest size crack visible by eye from the rig setup was the defined as the crack initiation point. The termination criterion for component failure was defined as a crack size of between 40 – 50mm for which a life to failure is recorded.

10.3.1.1 Constant Amplitude Fatigue Tests

Uniaxial tests were carried out on the FUCA under R = -1 conditions. Tests were performed over a range of applied constant amplitude loads from 2 – 7kN to gain data points with lives of 10^4-10^6 cycles. The weld of the component under test is shown in figure 10.19 with the notch and possible crack propagation path being indicated.

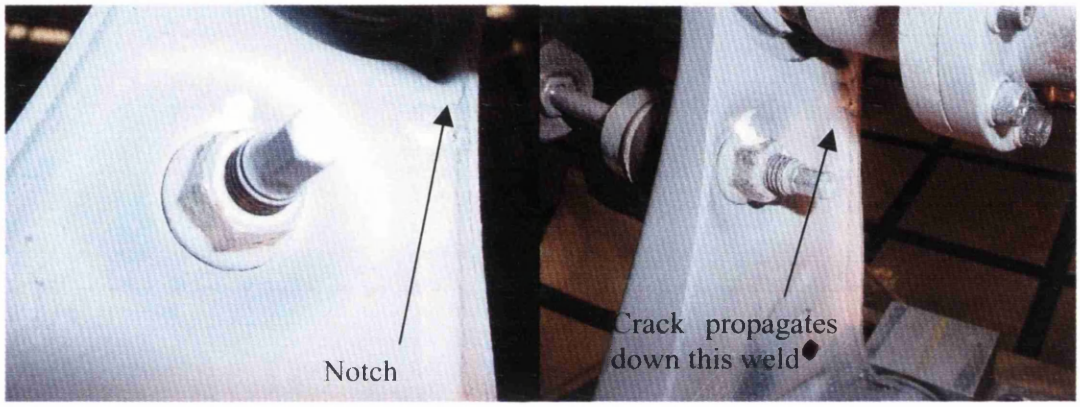

Figure 10.19: Location of Crack Initiation on the FUCA Component

10.3.1.2 Variable Amplitude Fatigue Tests – Block Loading

A block load-time history programme was created based on the loads used during constant amplitude testing, which are shown in figures 10.20 and 10.21. The sequence was created as one block and then repeated until failure of the component. Each block was counted as one repeat. Block loading signal 1 (figure 10.20) shows load levels of 7kN and 3.5kN were chosen and cycled around the mean under R=-1 conditions. Block loading signal 2 (figure 10.21) shows load levels of 4kN and 2kN were chosen and cycled around the mean under R=-1 conditions.

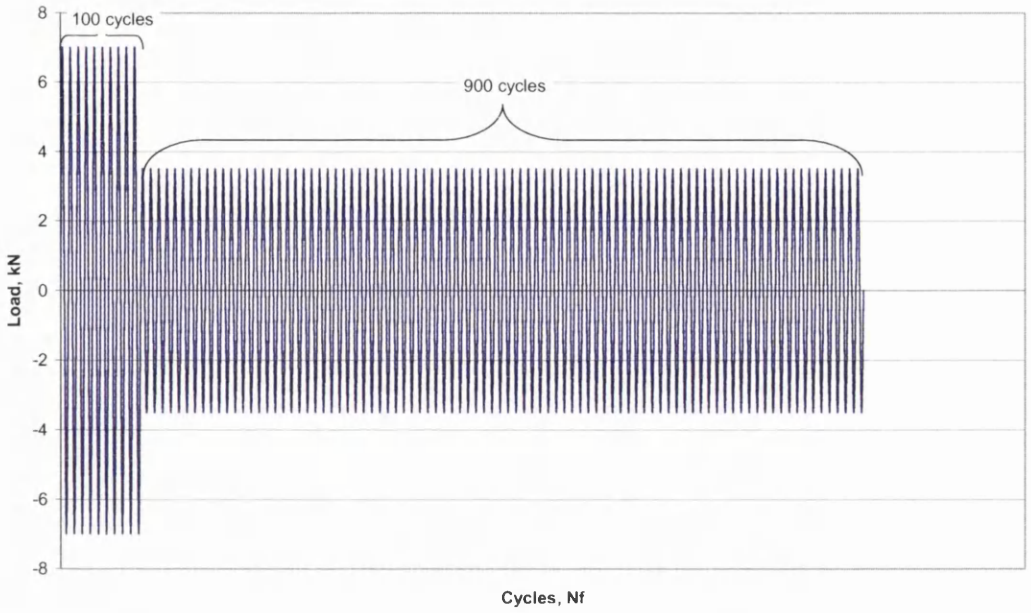

Figure 10.20: R=-1 Block Loading Signal for the 1st Load Level

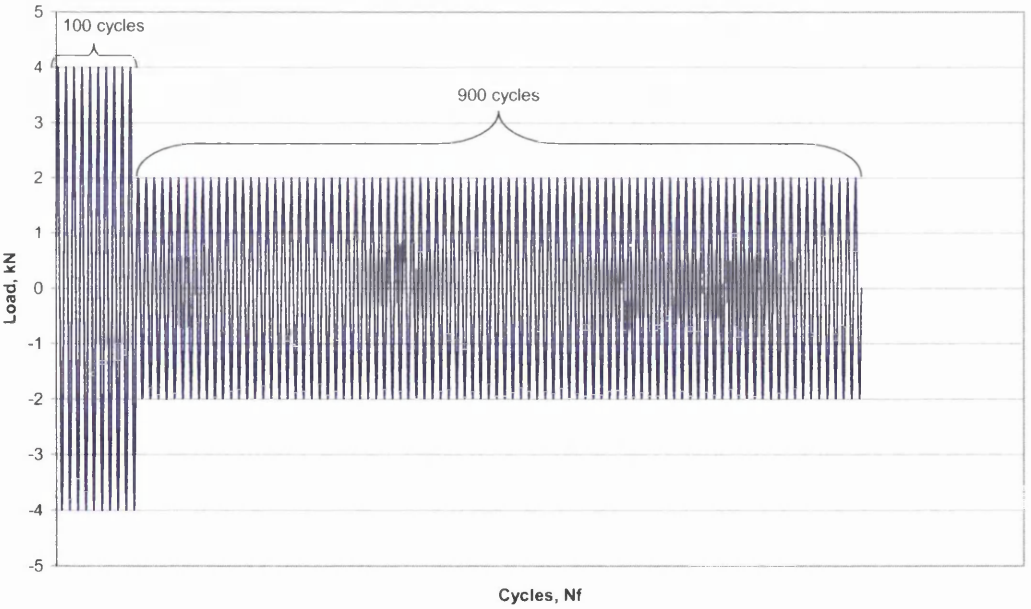

Figure 10.21: R=-1 Block Loading Signal for the 2nd Load Level

Figure 10.22 shows the block loading sequence use for a single test using a different loading condition of R=0.1 using similar load levels of 7kN and 3.5kN. This test will determine if there is an effect of mean stress on the fatigue lives of weld components, which currently most welding and design engineers are advised not to consider.

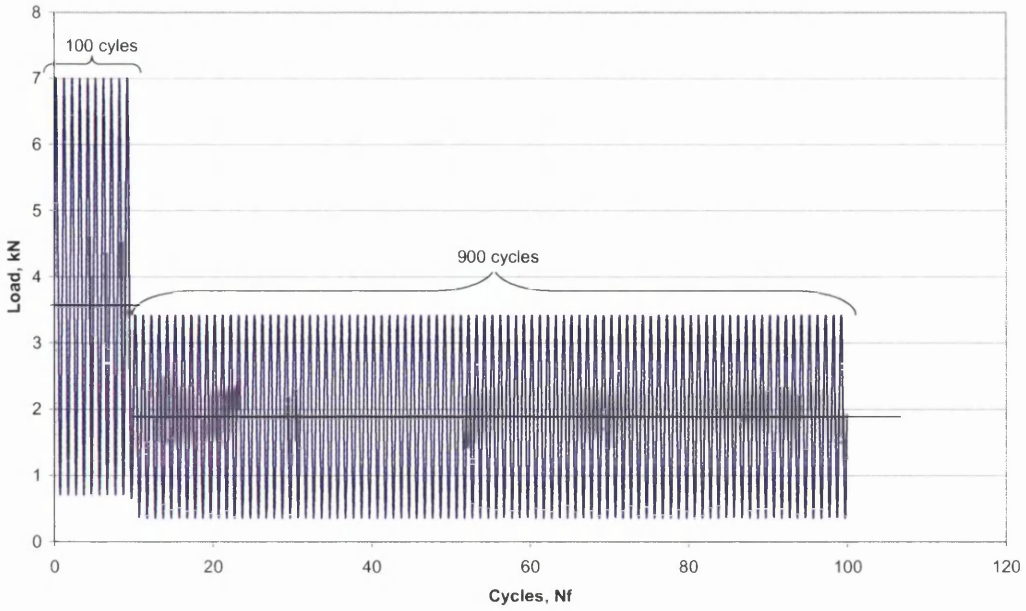

Figure 10.22: R=0.1 Block Loading Signal

10.3.1.3 Variable Amplitude Fatigue Tests – SAE Bracket Load-Time History

Variable amplitude loading followed constant amplitude testing. Initially an internal Land Rover test load-time history, known as the Handling and Cornering course, was used but this failed to crack the FUCA during a reasonable period of time and scaling the handling course did not reduce the testing period so an alternative programme was used.

SAE Bracket Load – Time history was used instead and scaled so that the maximum peak of the history ranged between ±7kN as shown in figure 10.23.

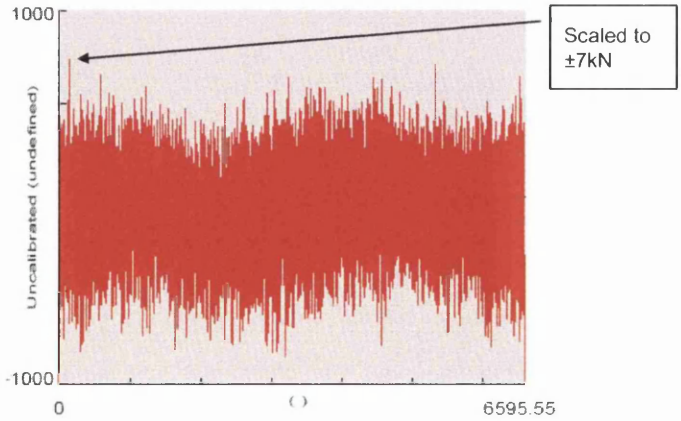

Figure 10.23: SAE Bracket Load – Time History

Rainflow cycle counting was again conducted using MSC.Patran software with the counting using a bin number of 128. The results from analysing the SAE Bracket load-time history are shown in figures 10.24 – 10.26. Figure 10.24 shows the number of cycles in the load-time history for the given load range of 7kN to -7kN and shows that the majority of the cycles are not at the peak load level. Figure 10.25 show the number of cycles either side of the mean, whilst figure 10.26 shows the effect of the number of cycles for the range.

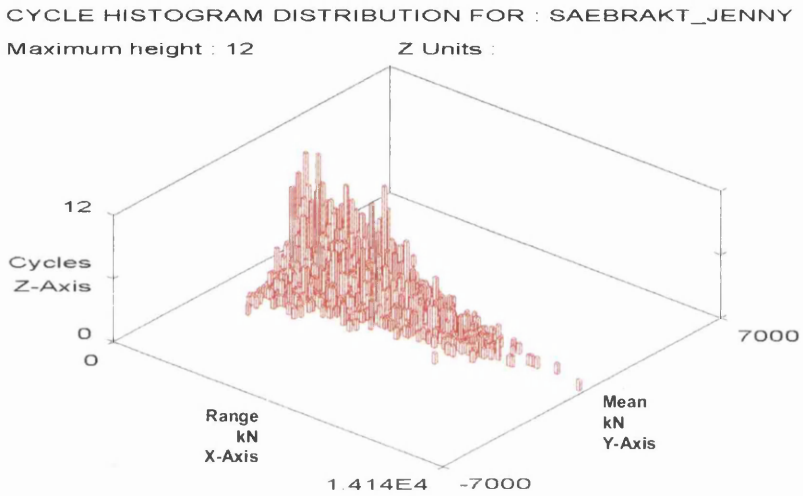

Figure 10.24: Number of Cycles for a given Load Range and Mean

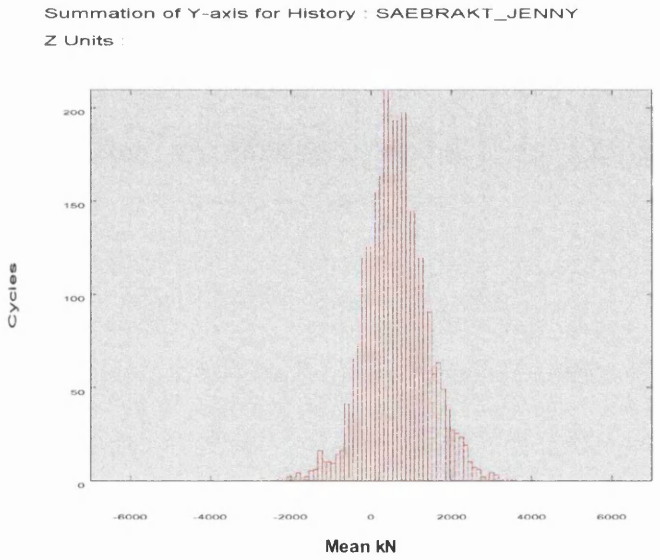

Figure 10.25: Number of Cycles for the Y-Axis of the SAE Bracket Load-Time History

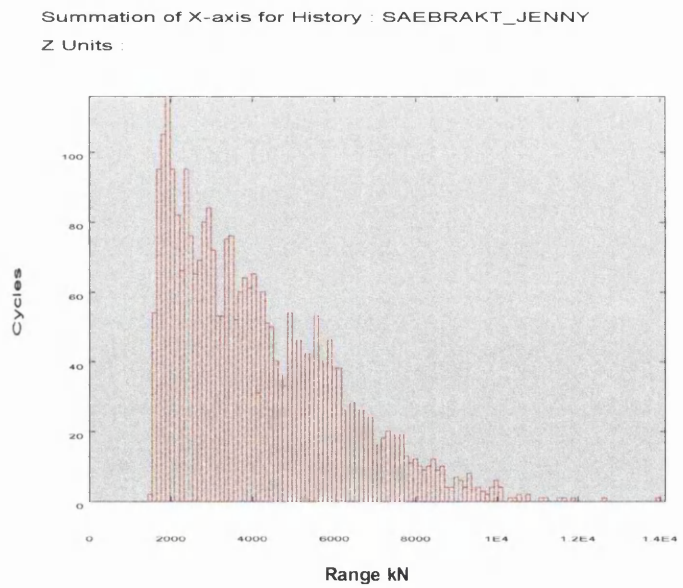

Figure 10.26: Number of Cycles for the X-Axis of the SAE Bracket Load-Time History

All FUCA component-testing conditions are detailed in Table A10.3.1 in Appendix 1.

10.4 Fracture Surface and Microstructural Examination

10.4.1 Scanning Electron Microscopy (SEM)

For both the coupons and the FUCA components fracture surface analysis, scanning electron microscopy (SEM) was conducted using a Philips XL 40 Microscope. This was used to investigate the crack initiation sites on the specimen fracture surfaces.

10.4.2 Optical Microscopy

In order to obtain an overview of the weld fracture surface for both the coupons and the FUCA components, an Olympus Photo/Binocular Microscope with a JVC TK-C1381EG model Colour Video Camera was used. The image software used to obtain the microscope image was Aquinto Software A4i Docu.

10.4.3 Optical Microscopy for Microstructural Analysis

Traditional metallographic preparation techniques were used to prepare the specimens for the microscopic investigation. Weld Specimens were sectioned longitudinally through the weld and parent material and subsequently mounted in Bakelite resin, ground, polished and then etched in 2% Nital. To reveal the

microstructure, an etching time of 30 seconds was used. Images were obtained using a Nikon Epiphot 200 Microscope with a 3CCD digital camera model JVC KYF75U. The image software used to obtain the microscope image was Adobe Photoshop Limited Edition.

10.5 Stress Measurements of Coupon Specimens for FE Comparison

Photoelastic coating was applied to the three different geometry seam weld tensile specimens in order to obtain a stress/strain distribution over the front face of each specimen. Particular interest was focused on the weld root and its effect on the strain distribution and intensity.

10.5.1 Strain Gauging Test Procedure

Strain gauges used were the type CEA-06-125UW-350, from Micro-Measurements. Strain gauges were applied to the front and rear faces on each of the three coupons as shown in figure 10.27, using the standard Micro-Measurements cement M-Bond 200 with a room temperature cure.

Initial testing was carried out with just two strain gauges per coupon face. Loading was applied by means of servo-hydraulic Dartec fatigue machine fitted with a 50kN load cell, MTS 647 Hydraulic wedge grips and a Dartec controller. Spacer plates were fitted, to ensure true alignment of the coupon in the grips, and in an attempt to avoid loading misalignment stresses.

Strain gauges were zeroed with the coupon fixed in the top grip only and when it was hydraulically clamped in the lower grip further gauge reading were taken. The gauges were then re-zeroed and incremental loading applied at 1kN intervals up to a maximum of 7kN with strain gauge results recorded at each increment. This was repeated 3 times for each coupon then final strain gauge readings were recorded after the specimen was released from the grips.

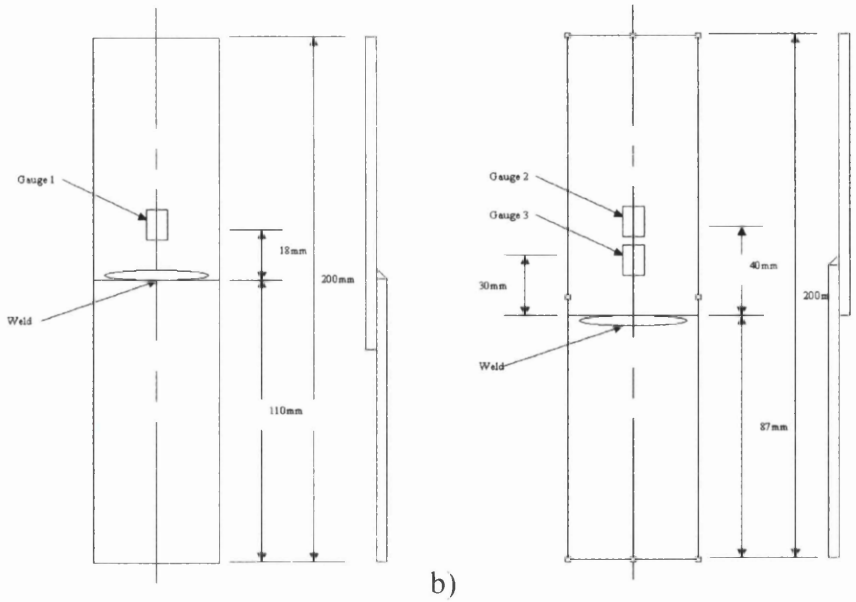

a) b)

Figure 10.27: a) Front Face, b) Rear Face

There were 3 types of specimen geometry as shown below in figure 10.28 they are: 1) M1 – Single partial weld, 2) M2 – Single full weld and 3) M11A – Double partial weld.

Figure 10.28: Coupons used in both Strain Gauging and Photoelasticity

10.5.2 Photoelasticity Test Procedure

The coupons were firstly sprayed with a reflective silver paint (Krylon Dull Aluminium) and then coated with a 0.5mm layer of epoxy resin (Devcon 2Ton), to provide the photo-reflective coating. Loading was applied by means of an servo-hydraulic Dartec fatigue machine. The grips used were standard wedge grips and

spacer plates were fitted in an attempt to avoid loading misalignment stresses and keep the coupon straight.

Strain gauges were attached as shown in figure 10.27 on the coupons shown in figure 10.28 so that absolute values of stress could be calculated at those points. Readings from the strain gauges and the photoelastic coating were taken after assembly to record stresses due to possible misalignment. The gauges were zeroed to enable stresses only due to loading to be recorded. The photoelastic results were recorded and subsequently subtracted from the incremental loading results for the same reason.

Results from both strain gauges and photoelastic coatings were taken at 1kN loading increments up to 7.0kN and repeated 3 times to allow for any "settling" of the loading fixtures. The Stress Photonics GFP1200 automated polariscope was used to obtain the photoelastic fringe patterns. This polariscope has the ability of measuring fractions of a fringe order, which enables the use of thin photoelastic coatings to avoid stiffening the specimen.

The photoelastic results were analysed using the GFP 1200's DeltaVision software and line plots were taken down the centre line onto the weld and 10mm either side of the centre line. This was carried out to highlight the stress concentration factor generated by the weld and also to clearly demonstrate the uneven distribution due to the weld and specimen geometry, plus any misalignment effects due to the testing machine.

10.6 FE Modelling

In the current EngD study, welded coupon joints and the FUCA component were modelled using the FE-package MSC.Nastran version 2005.1. The FE models of the coupon joints were created using the FE pre-processor package MSC.Patran Version 2005r2 on a PC workstation. The geometry was modelled as a 2-dimensional (2D) surface, i.e. shell elements in the finite element (FE) analysis.

An FE mesh was produced to represent the sheet metal by using four-noded quadrilateral shell (Quad4) elements with an element size of approximately 3mm.

Material properties of the steel coupons used in the FE models include a Young's Modulus of 200,000MPa, and a Poisson's ratio of 0.3. Thickness of the steel was measured using vernier callipers.

Load and boundary conditions simulate the fatigue loading and fixing of the specimens in the fatigue–testing machine. There are 6 degrees of freedom in the model, 3 degrees of freedom for translation and 3 degrees of rotation. For the fixed end of the coupon model, all 6 degrees of freedom were fixed i.e. fully constrained. At the loading end it was constrained in all the rotations, and x, and z translations, while the translation in y or longitudinal direction was left free to apply the load. A unit load of 1kN was applied to all models. The servo–hydraulic test machine applied the load by imposing a displacement. This is simulated in MSC.Nastran by using a multi-point constraint RBE2 or rigid beam elements, which simulate the applied load as shown in figure 10.29. The RBE2 element ensured that all nodes along the loading end (the dependent or slave nodes) have the same displacement as the centre node (independent or master node), to which the unit load was applied.

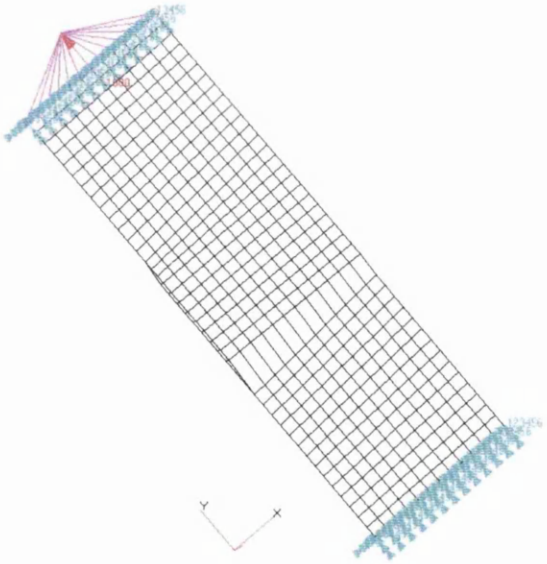

Figure 10.29: Applied Load and Boundary Conditions

All MSC.Nastran FE analyses of the coupons were linear elastic.

Volvo Method Weld Representation

Welds were represented by thick four-noded shell elements, whose thickness was derived by adding together the thickness of the two plates of sheet metal. The weld single shell elements are inclined at an angle of approximately 45° to the base steel

sheet, as shown in figure 10.30a. Figure 10.30b illustrates the weld and weld toes, used in modelling the coupon joints.

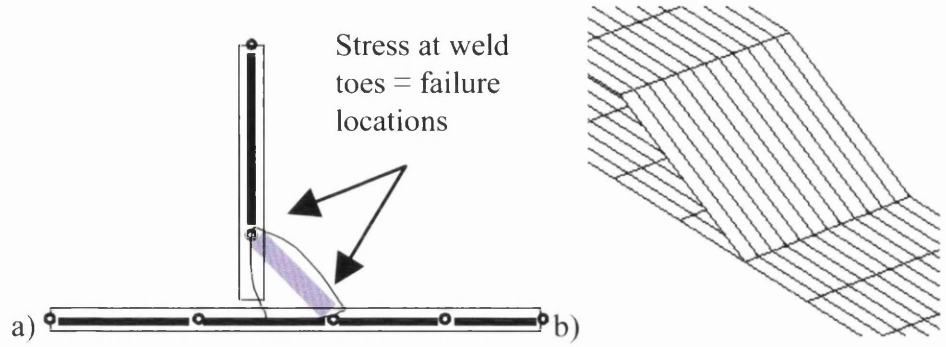

Figure 10.30: Weld Representation a) Diagram (MSC, 1999) b) Weld FE Model

The Battelle Method of Weld Representation

Welds were represented by thick four-noded shell elements, whose thickness was derived by adding together the thickness of the two plates of sheet metal. The weld shell elements are inclined at an angle of approximately 45° to the base steel sheet. The inclined weld shell elements are joined to the two plates at the weld toe with a back-panel to form a triangular weld. The weld element nodal positions coincide with those of the weld toes as shown in figure 10.31.

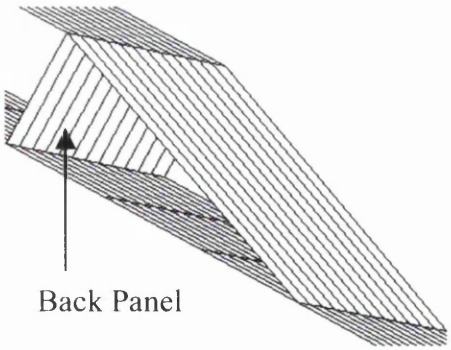

Figure 10.31: Weld Representation

10.6.1 FE Modelling of Coupon used in Photoelasticity

FE Stress analysis was carried out by using MSC.Nastran, and the results were imported back into MSC.Patran, from which stress contour maps were produced and the stresses used to compare with the photoelastic results. Figure 10.32 show the undeformed basic model of the coupons used in the photoelasticity and strain gauging.

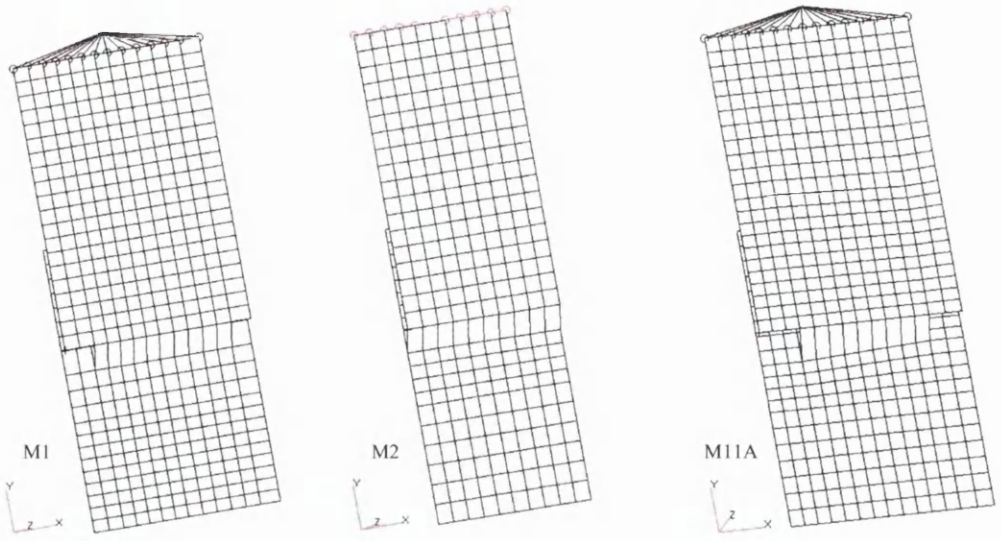

Figure 10.32: FE Models of M1, M2 and M11A

10.6.2 FE Modelling of Coupons for Structural Stress Calculations

Coupon joints were modelled in the CAE packages to establish the σ_s/F ratio. All the coupon models were carried out on PC workstations using several different software packages as summarised below:

- Stress Analysis using MSC.Nastran Version 2005.1, Vendure FLOW, FE-Safe
- Fatigue Analysis using MSC.Fatigue within Patran 2005r2, FE-Safe Verity version, Vendure FLOW
- Post Processing occurred in MSC.Patran, HyperView Version 7.0

Each tested coupon was measured to get all accurate dimensions for modelling using vernier callipers and a travelling microscope to get the weld dimensions.

FE Stress analysis was performed by MSC.Nastran and the results were imported back into MSC.Patran from which stress contour maps were produced. The MSC.Fatigue module inside MSC.Patran was used to calculate the fatigue damage and lives at the weld toe, from which fatigue damage on life contour maps was produced.

Basic FE models

Figures 10.33 – 10.34 show the undeformed basic model of the TKA–Tallent and GKN coupons for both the Volvo and Battelle Structural Stress calculations respectively and used in the analysis of the constant amplitude test work.

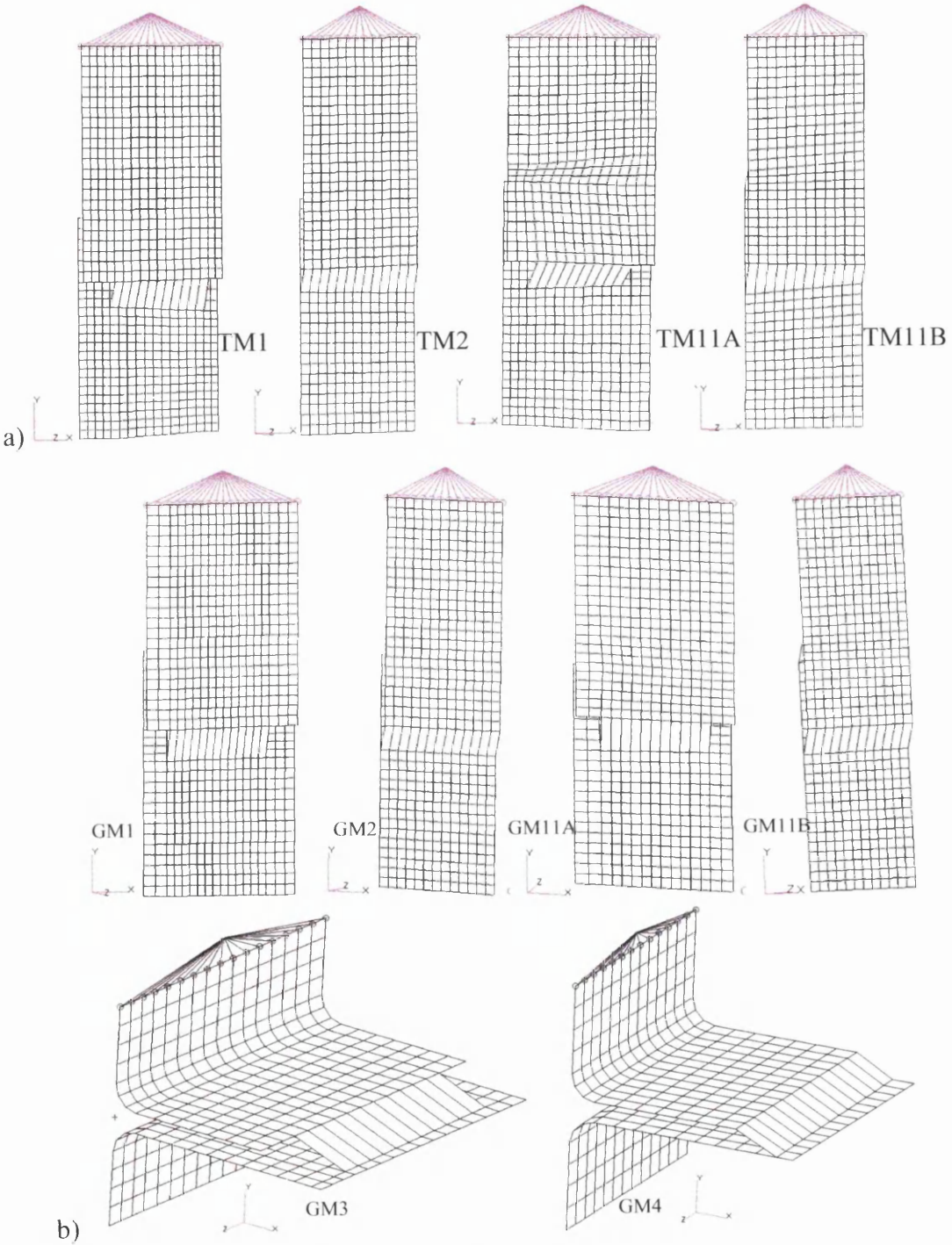

Figure 10.33: The Undeformed Models for Volvo Structural Stress Calculations a) TKA–Tallent Coupons, b) GKN Coupons Predicted

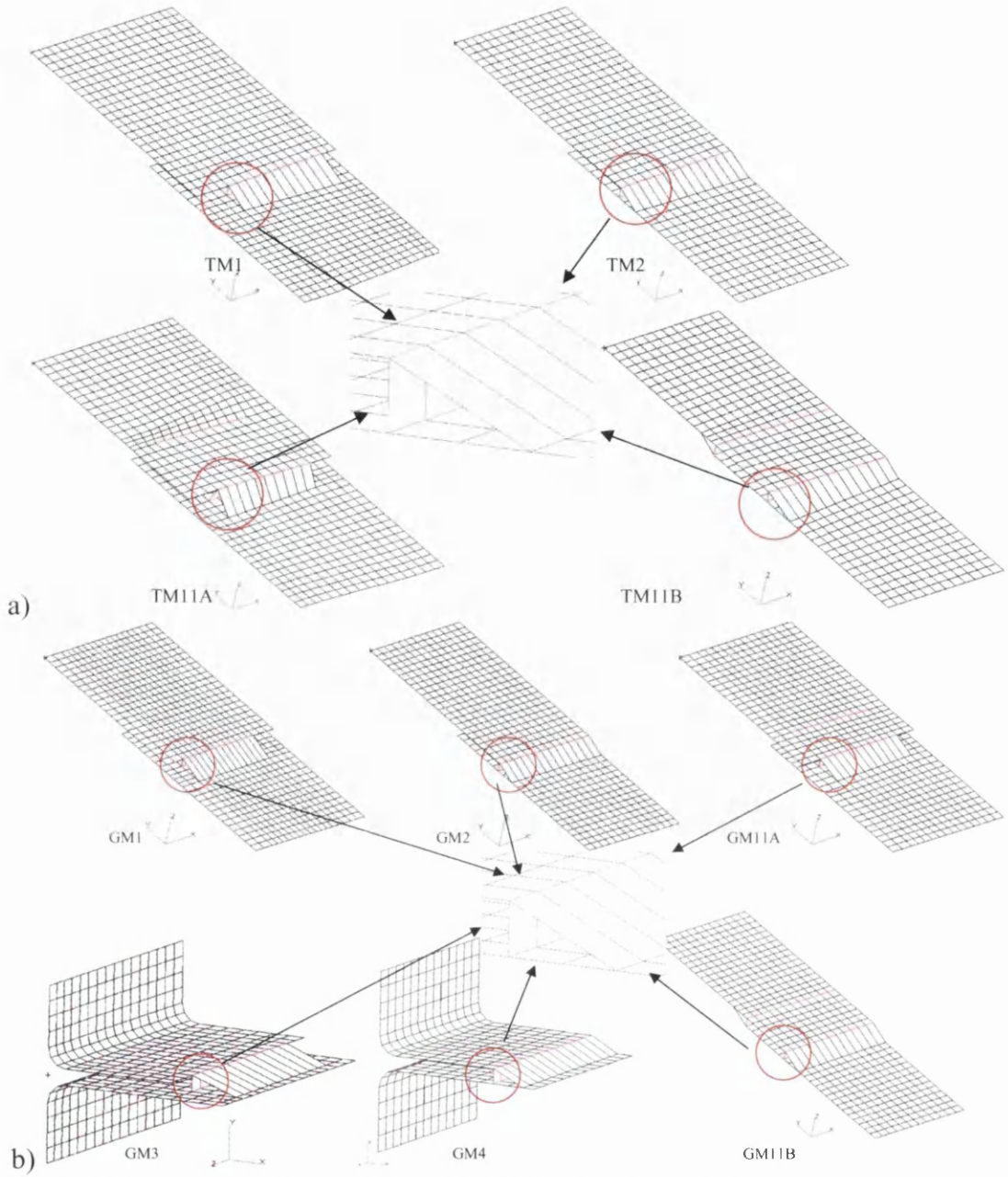

Figure 10.34: The Undeformed Models for Battelle Structural Stress Calculations a) TKA–Tallent Coupons b) GKN Coupons

10.6.3 FE Modelling of FUCA Component

The basic component model was constructed at Corus using CATIA to modify the original CAD model of the FUCA component, which came from TKA-Tallent. This model was orientated in the car line as shown in figure 10.35a. The "car-line" is a standard reference co-ordinate system for car structures, which is used by automotive manufacturers. The model, required re-orientation into the rig set up as on the bedplates as shown in figure 10.35b.

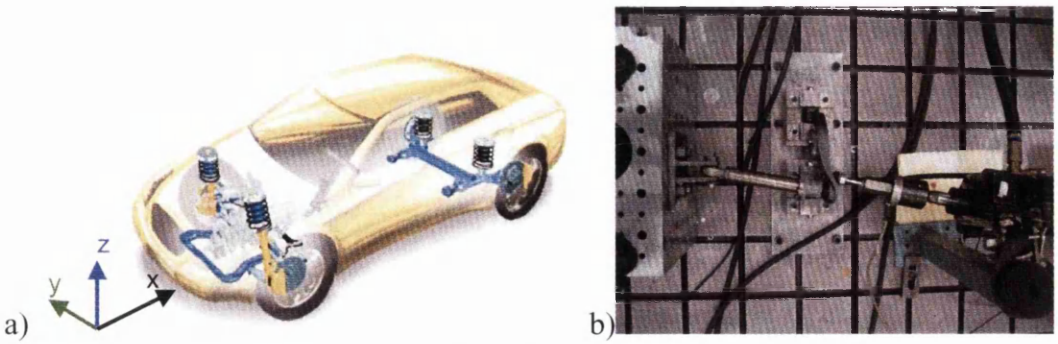

Figure 10.35: a) Car Line Description, b) FUCA Rig Set Up

To create the actuator bar and the ball joint support as shown in figure 10.35b, beam elements were used with the pin connections controlling the 6 degrees of freedom. The FUCA FE model includes two solid elements, which are the ball joint and the anti roll bar link ball joint. Rigid beam elements or RBE3 elements were used in the bushes and both the FUCA ball joint and the anti roll bar ball joint. RBE3 elements have no stiffness but average all the displacements of the nodes connected to it to the centre node. Bush modelling involved using coincident nodes with 6 degrees of freedom, shell elements to represent the bush outer structure and the non-linear bush rates from TKA-Tallent.

The FE mesh was created on the mid-surface of the sheet metal. The elements used were mainly the 4-noded quadrilateral shell (Quad4) elements with the occasional 3-noded triangular (Tri3) elements, with an element size of 3mm.

The weld shell elements are inclined at an angle of approximately 45° to the base sheet, and incorporate back elements so that the weld forms a triangular shape, which is required for various CAE techniques.

The load and boundary conditions applied to the FUCA FE model simulate the fatigue loading and fixing on the rig. There are 6 degrees of freedom for each FE node in the model, 3 degrees of freedom for translation and 3 degrees of rotation. For the bushes the boundary conditions involve all 6 degrees of freedom being fully fixed. The anti roll bar ball joint which applies the 7kN load is fixed in the x and y translation and in the z rotational direction. The FUCA ball joint is fully fixed in all 3 translational directions and also in the z rotational direction, this is shown in figure 10.36.

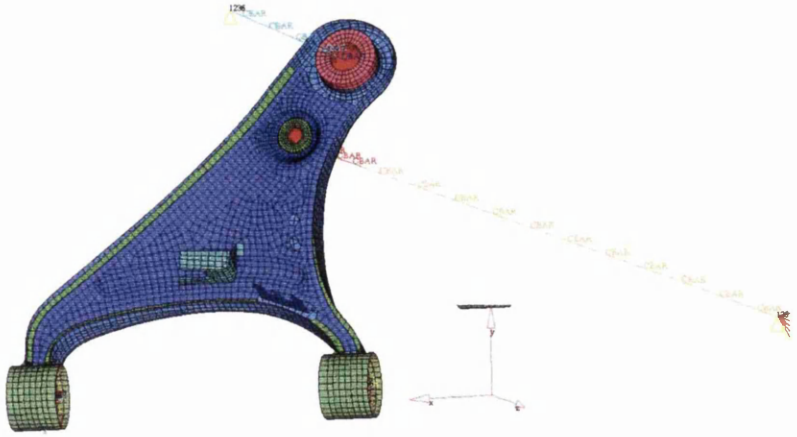

Figure 10.36: Load and Boundary Conditions Applied to the FUCA FE Model

The FE Modelling was carried out on PC or UNIX workstations using several different software packages as summarised below:

- The FUCA component was modelled in Hypermesh version 7.0
- The Bushes were analysed in both Abaqus version and Nastran version 2001
- Welds were created using CATIA and imported back to Hypermesh version 7.0
- Stress Analysis using MSC.Nastran Version 2001
- Post Processing occurred using Hyperview version 7.0

10.6.3.1 CAE Model Verification

Modal Analysis was used to determine the resonant frequency of the FUCA component. The control arm was supported in free mode using soft bungees and artificially excited using a hammer at point 1 in figure 10.37. An extensometer transducer will measure the tri-axial acceleration from the FUCA after it has been excited. The FUCA still had the rubber bushes in when tested. The results were processed using LMS Modal Software on a UNIX workstation.

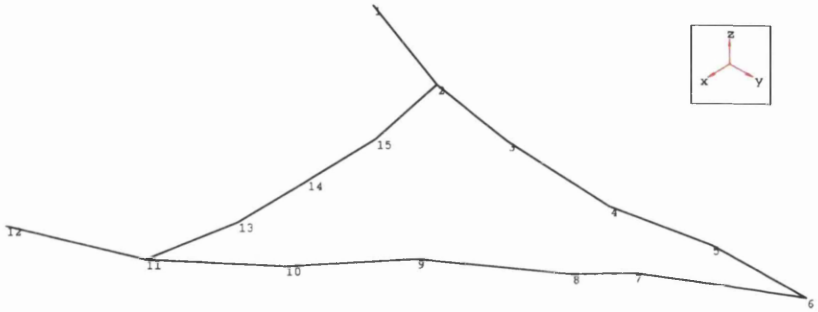

Figure 10.37: Location of the Frequency Recorded

The results of the Modal Analysis are shown in table 10.2. Mode I is associated with the bending and twisting of the bushes, Mode II is the bending of the arm, Mode III is the bending of the ball joint.

Table 10.2: Frequency from Modal Analysis

Modes	Frequency	Damping
Mode 1	517.65 Hz	5.74%
Mode 2	614.04 Hz	1.84%
Mode 3	725.58 Hz	2.74%

The damping shown in table 10.2 arises from the damping mainly in the bushes in Mode 1, to damping in the steel in modes 2 and 3. Figure 10.38 shows the typical frequency plot with the corresponding amplitude range produced at the various modes.

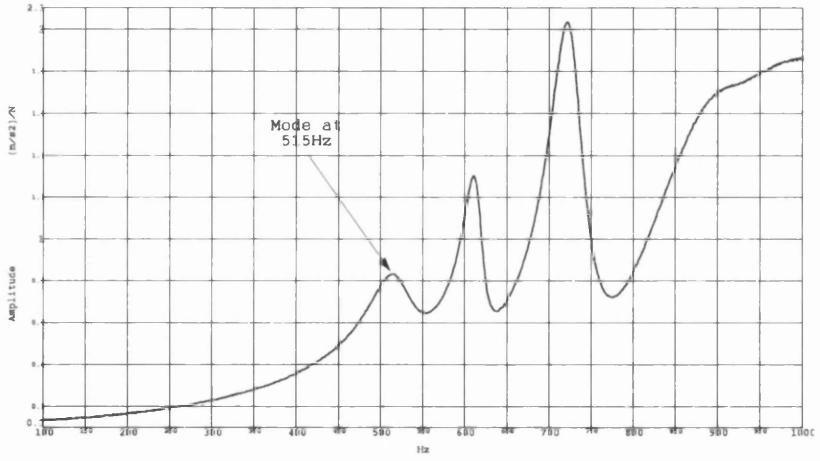

Figure 10.38: Typical Frequency Graph

This information is used to check the FUCA FE model, which will be used in finite element analysis.

In ensuring that the FUCA model was aligned and correct a Faro arm was used to measure tall parts of the rig to a global co-ordinate system based on the bedplates. This enables modification of the FUCA CAE model to ensure that the loading direction and deflection is correct.

The modal results generated were used to compare the modal testing of the FUCA FE model and to therefore ensure that the FE model responded the same way when excited using the FE packages.

10.6.3.2 FUCA Weld Modelling

From the baseline model created, the welds in the model required modification for use in the Battelle Method i.e. the welds required a back element as shown in figure 10.31. Figure 10.39 shows a schematic diagram of the differences between the triangular back panel weld and the standard Volvo weld representation.

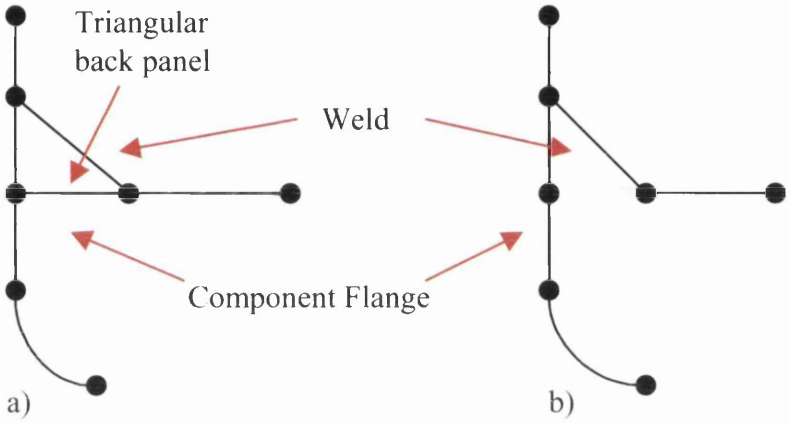

Figure 10.39: Weld FE Representation a) Triangular Weld, b) Standard Volvo Weld Representation

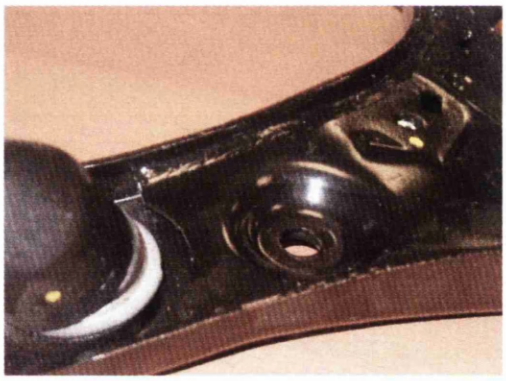

Figure 10.40: Actual FUCA Component

Observation and measurement of the actual FUCA component as shown in figure 10.40, indicates that there are variations in the weld starting positions. To take this into account, a further modification to the weld line was the removal of the first element from the weld under investigation to represent the FUCA tested components, which had variable weld locations. Four models were generated: Full-Length, Full-Length Tri shown in figure 10.41, Cut-Length and Cut-Length Tri as shown in figure 10.42.

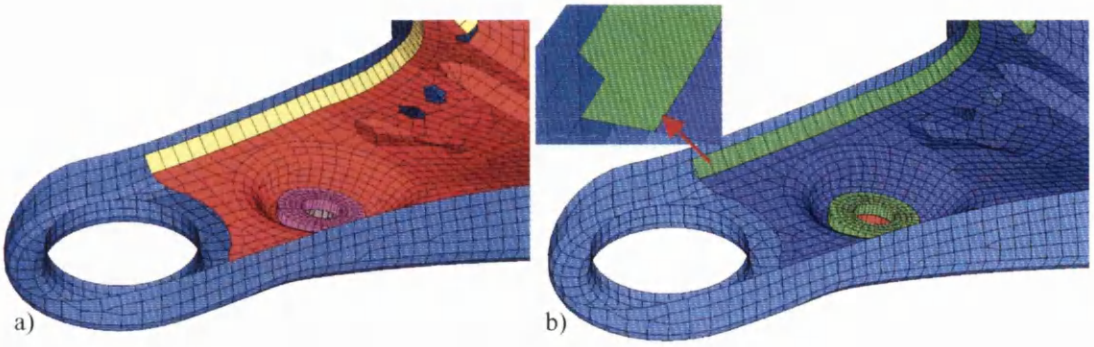

Figure 10.41: Weld line a) Full-Length b) Full-Length Tri (with the back panel)

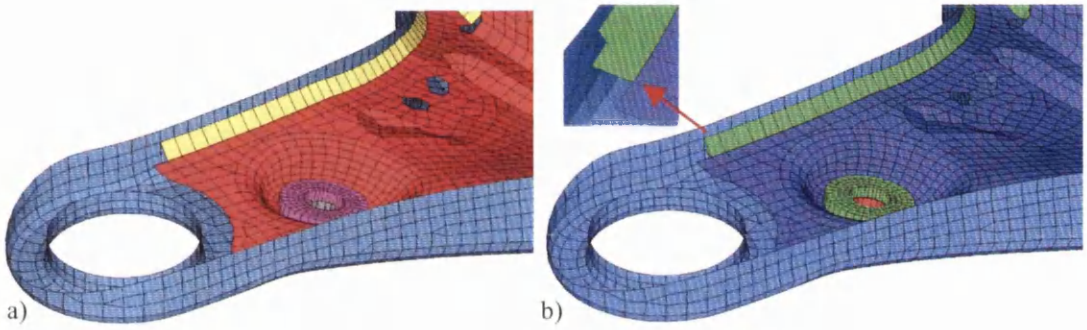

Figure 10.42: Weld line a) Cut-Length b) Cut-Length Tri (with the back panel)

10.7 Manual Calculation for the Battelle Method

The 'Battelle Structural Stress' approach is a method which is available as a commercial FE-package. However the format can be completed by manual calculation.

For the manual calculation a completed FE-stress analysis of the welded structure under analysis is required with the relevant unit load and boundary constraints applied which are as seen in the fatigue test conditions. The balanced nodal forces and moments of each element along the weld toe are then extracted from the FE results and used in an Excel spreadsheet, with respect to their fixed global coordinate system (as shown in figure 10.43a and b). Forces and moments in the global coordinate system for structural stress calculations must be resolved into a local coordinate system aligned with the weld-line to obtain the relevant line forces and moments.

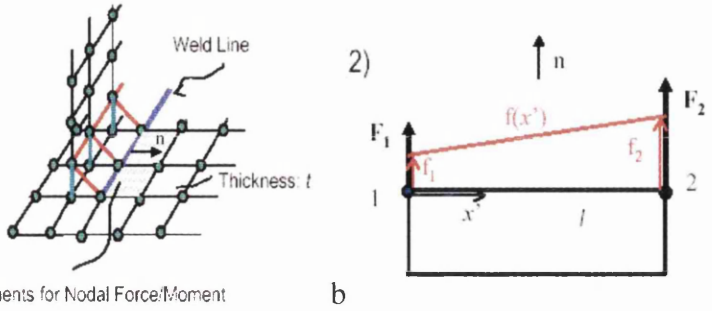

Figure 10.43: a) Location of Elements for Nodal Force and Moment, b) Transforming Elemental Forces (Dong 2005)

The line force and moment vectors f_y and m_x are obtained by transforming the elemental nodal forces as shown in figure 10.42b, by using the following equations 12 – 13. Manual calculation the line forces and moments using Excel requires the use of a matrix as shown in figure 10.44.(Dong 2001; Potukutchi, Agrawal et al. 2004)

$$f_1 = \frac{2}{l}(2F_1 - F_2) \qquad m_1 = \frac{2}{l}(2M_1 - M_2) \quad \text{Eq.12}$$

$$f_2 = \frac{2}{l}(2F_2 - F_1) \qquad m_1 = \frac{2}{l}(2M_2 - M_1) \quad \text{Eq.13}$$

$$\begin{Bmatrix} F_1 \\ F_2 \\ F_3 \\ \vdots \\ F_n \end{Bmatrix} = \begin{bmatrix} \frac{l_1}{3} & \frac{l_1}{6} & 0 & 0 & \cdots & 0 \\ \frac{l_1}{6} & \frac{(l_1+l_2)}{3} & \frac{l_2}{6} & 0 & \cdots & 0 \\ 0 & \frac{l_2}{6} & \frac{(l_2+l_3)}{3} & \frac{l_3}{6} & 0 & 0 \\ 0 & 0 & \ddots & \ddots & \ddots & 0 \\ \vdots & \ddots & \ddots & \ddots & \frac{(l_{n-2}+l_{n-1})}{3} & \frac{l_{n-1}}{6} \\ 0 & \cdots & \cdots & 0 & \frac{l_{n-1}}{6} & \frac{l_{n-1}}{3} \end{bmatrix} \begin{Bmatrix} f_1 \\ f_2 \\ f_3 \\ \vdots \\ f_n \end{Bmatrix}$$

Figure 10.44: Matrix Used to Generate the Structural Stress

Where:

$F_1, \ldots, F_n$ = the element nodal force

$f_1, \ldots, f_n$ = the line force

$l_1, \ldots, l_{n-1}$ = the element edge length

The Structural stress is then calculated by using the following equation 14.

$$\sigma_s = \sigma_m + \sigma_b = \frac{f_y}{t} + \frac{6m_x}{t^2} \quad \text{Eq.14}$$

Where:

f_y = Line forces with respect to y'

m_x = Line Moments with respect to x'

t = Thickness

The Structural Stress (σ_s), is only a surface stress and therefore other stress factors could influence the fatigue life. These other factors are incorporated into the Equivalent Structural Stress, S_s, through modifying the structural stress equation (Eq.14) to consider the effects of the stress concentrations ($\Delta\sigma_s$), thickness (t) and loading mode (r), that are detrimental on the fatigue performance (as shown in Eqs.15 – 17) (Kyuba, H and Dong, P.,2003)

$$\Delta S_s = \frac{\Delta\sigma_s}{t^{\frac{2-m}{2m}} \cdot I(r)^{\frac{1}{m}}} \qquad \text{Eq.15}$$

$$I(r) = 0.294r^2 + 0.846r + 24.815 \qquad \text{Eq.16}$$

$$r = \frac{\sigma_b}{(\sigma_m + \sigma_b)} \qquad \text{Eq.17}$$

Where:

S_s = Equivalent Structural Stress

t = Plate Thickness

m = Slope of the crack growth curve

I(r) = Loading Mode correction for Load-Controlled Loading

r = Loading Ratio

The Battelle process and the ability to calculate the structural stress manually is advantageous as its mesh insensitivity and representation of welds uses simple coarse elements. This method only requires the use of one S-N curve so eliminates the need of weld classification.

A step-by-step guide is shown in Appendix 2.

10.8 Statistical Analysis of S-N Data

Fatigue performance data for any structural material is usually shown as Stress–Life (S–N) data. Frequently this S–N data requires some regression analysis results supplied in the form of curves fitting certainties of survival, which are used in FE – based fatigue life predictions.

10.8.1 Regression Analysis Based on Structural Stress

This regression is used to predict life by minimising the error in life through linear regression as shown in figure 10.45. The calculations for this statistical analysis involve using linear regression analysis: "The Least Squares Method". Fatigue performance data is plotted on a standard S-N graph with fatigue life on x-axis and Stress on y-axis. This method requires the log(life) to be the dependent variable "y" with the log(stress) being the independent variable. The regression data then uses Standard Error and the coefficients of the curve (equation of the line) for use in the Basquin S–N equation. Also the inverse of the standard normal cumulative distribution, which has a mean of zero and a standard deviation of one, is used. 3σ or 99.87% certainty of survival is used. (Arnold 2001)

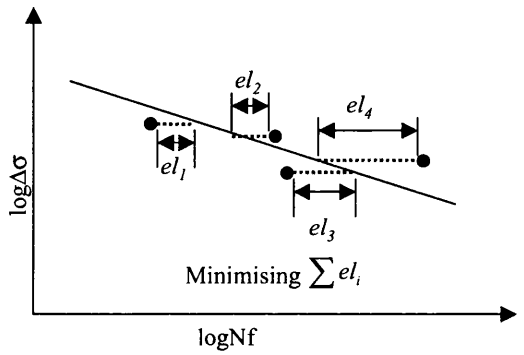

Figure 10.45: Least Squares Method to Minimise Life Error

10.8.2 Regression Analysis Based on Life

This regression is used to predict stress for a given life used mainly by vehicle designers. This is achieved by minimising the error in stress through linear regression as shown in figure 10.46. This method also uses the linear regression method "Least Squares" with log(Life) as x-variable and log(stress) as y-variable. The calculation uses Standard Deviation of log(Range) and R^2 (which is the coefficient of determination and compares the estimated and actual y-values, and ranges in value from 0 to 1) to calculate the Standard Error. The mean and constant comes from the equation of the line, with the mean being used to calculate ±3 standard deviations or 99.87% certainty of survival.

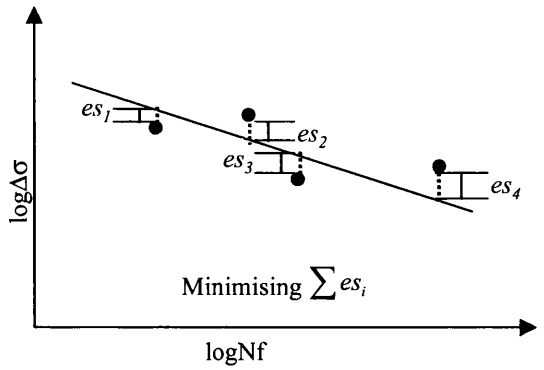

Figure 10.46: Least Squares Method to Minimise Stress Error

10.9 Cumulative Damage Rule – Miner's Rule Calculation

In actual service, parts are seldom stressed repeatedly at only one stress level and, hence, the problem arises as to the cumulative damage effect of operations at various levels of stress reversal. Consequently, Miner's rule is used. As mentioned in the literature review section 6.2.5, Miner's Rule is used to calculate the fatigue damage. A damage fraction, D, is defined as the fraction of life used up by an event or a series of events. The damage criterion for failure is assumed to be equal to 1.0.

The linear damage rule states that damage fraction, D_i, at stress level σ_i, is equal to the cycle ratio n_i/N_i, where n_i, is the number of cycles observed at the stress level and N_i is the number of cycles to failure at the same stress level, as shown in Eq.18

$$\Sigma \frac{n_i}{N_i} \geq 1 \qquad \text{Eq.18}$$

10.9.1 Variable Amplitude Fatigue Tests – Block Loading

With the various block loading load-time histories being tested on both the coupons and FUCA components, the fatigue damage requires calculating. This is done through analysing the load-time history and calculating the percentage of life consumed (i.e. damage) at each loading level as shown in figure 10.47.

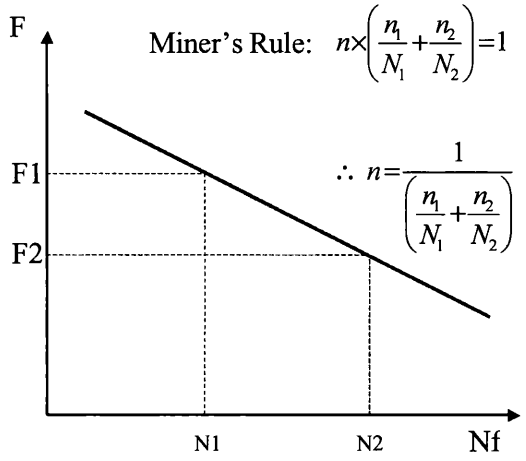

Figure 10.47: Miner's Rule for the 2-Level Block Fatigue Loading

The variable amplitude block-loading signal used in the tests has two load levels so the fatigue damage is calculated at both levels. The damage at the first load level, F_1: $D_1 = \frac{n_1}{N_1}$ and the corresponding damage for the second load level, F_2: $D_2 = \frac{n_2}{N_2}$.

The total damage at failure is therefore sum of the damage at both load levels F1 and F2: $D = \frac{n_1}{N_1} + \frac{n_2}{N_2}$. The estimated life, n, of the component is shown in equation 19.

$$n = \frac{1}{\frac{n_1}{N_1} + \frac{n_2}{N_2}} \qquad \text{Eq. 19}$$

10.9.2 Variable Amplitude Fatigue Tests – SAE Bracket Load-Time History

The SAE Bracket load-time history as shown in figure 10.23, shows a signal with many different load range and mean levels. To calculate the number of cycles at each of these load levels would first require Rainflow Counting of the complex signal. This was done using the MSC.Fatigue tool MSLF within MSC.Patran. MSLF is a single-location fatigue analysis module. Damage accumulation was then calculated both manually in a spreadsheet and from this tool. Both manual and calculated damage constants were shown to be the same.

10.9.2.1 Calculating Damage Using Miner's Rule

The Range, Mean and Damage data generated from the Rainflow Counting program are required and input in an Excel spreadsheet. This range and mean data will require subsequent scaling to the applied load as shown in figure 10.48.

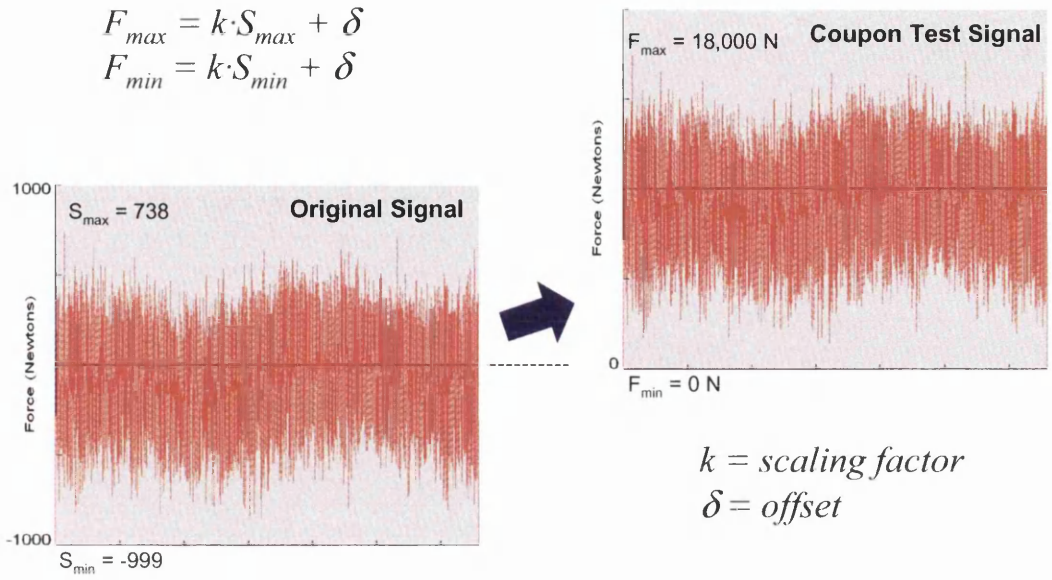

Figure 10.48: SAE Bracket Load-Time History Scaling and Offset Factors

Solving the F_{max} and F_{min} equations shown in figure 10.48 for the scaling factor, k is shown below in equations 20 – 21 and the offset factor, δ is shown in equation 22.

$$F_{max} - F_{min} = k \cdot (S_{max} - S_{min}) \qquad \text{Eq.20}$$

$$k = \frac{F_{max} - F_{min}}{S_{max} - S_{min}} = \frac{\Delta F}{\Delta S} \qquad \text{Eq.21}$$

$$\delta = F_{max} - kS_{max} \text{ or } \delta = F_{min} - kS_{min} \qquad \text{Eq.22}$$

These factors are input into a spreadsheet and used to adjust the range and the mean. Damage is calculated using the scaled range data and the constant amplitude loading data curve fitting equation. Summing up the total damage, the estimated block repeats of the signal is calculated as $\frac{1}{\sum D}$.

10.9.2.2 Calculating the Effects of Mean Stress using Miner's Rule

When using a variable amplitude signal such as SAE Bracket, it is important to understand the effect that different mean stresses from the load-time history will have on the Damage, the damage will have to be recalculated. From the scaled and offset rainflow counting data of the load-time history, the R-Ratio is calculated from equation 23.

$$R = \frac{(Mean - \frac{Range}{2})}{(Mean + \frac{Range}{2})} \qquad \text{Eq.23}$$

Sorting the data by the R-Ratio will show the proportion of the data which is above R=0.5 and therefore affected by mean stress. For all the data ≤0.5 (block 1) use the curve fitting equation for the constant amplitude data R=0.1. For all the data ≥0.5 (block 2) use the curve fitting equation for the constant amplitude data R=0.5. Sum the damage for each block. The total damage, D is the sum of the damage from both blocks and the estimated block repeats will be $\frac{1}{\sum D}$.

10.9.3 Miner's Rule using Volvo Mean Stress Correction

For variable amplitude load-time histories, which have variable mean stresses, a correction factor for mean stress is required. To estimate variable amplitude loading fatigue lives (the block repeats) using the weld S-N data generated at constant amplitude and R=0.1, the variable signal must be converted back to the constant amplitude R=0.1 data. This is shown in figure 10.49.

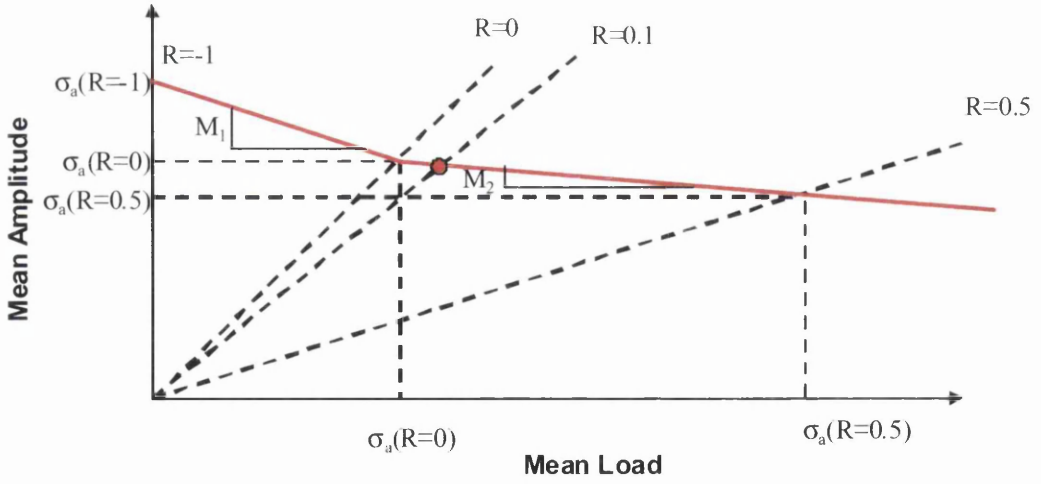

Figure 10.49: Goodman Diagram for Back Calculating the Mean Stress Values

To correct for mean stress the Goodman diagram (described in section 2.5.1.1) is used, from which the following equations are derived depending on whether R<0 or R≥0.

For R≥0, then the following equations 24 – 28 explain the mean stress correction.

$$\sigma_{a\_-1} = (1+M_1)\cdot\frac{\sigma_{a\_-0.1}+M_2\cdot\sigma_{a\_-0.1}}{1+M_2} = (1+M_1)\frac{\sigma_{a-R}+M_2\cdot\sigma_{a\_R}}{1+M_2} \qquad \text{Eq.24}$$

Rearranged to Eq.25.

$$\sigma_{a\_-0.1}+M_2\cdot\sigma_{a\_-0.1} = \sigma_{a\_R}+M_2\cdot\sigma_{a\_R} \qquad \text{Eq.25}$$

$$\Delta\sigma_{0.1} = \frac{1+M_2\cdot\frac{1+R}{1-R}}{1+M_2\cdot\frac{11}{9}}\Delta\sigma_R \qquad \text{Eq.26}$$

For $M_2 = 0.1$, the damage calculation is shown in equations 27 – 28:

$$\Delta\sigma_{0.1} = 0.8910891\cdot(1+0.1\frac{1+R}{1-R})\Delta\sigma_R \qquad \text{Eq.27}$$

Or based on load:

$$\Delta F_{0.1} = 0.8910891\cdot(1+0.1\frac{1+R}{1-R})\Delta F_R \qquad \text{Eq.28}$$

For R<0, to convert to R=0.1, then the following equations are required:

$$\sigma_a^{-1} = \sigma_a(1+M_1\cdot\frac{1+R}{1-R}) = \sigma_a^{0.1}\frac{1+M_1}{1+M_2}\cdot(1+M_1\cdot\frac{1+0.1}{1.-0.1}) \qquad \text{Eq.29}$$

Rearranged to equation 30.

$$\sigma_a^{0.1} = \frac{1+M_1\cdot\frac{1+R}{1-R}}{\frac{1+M_1}{1+M_2}\cdot(1+\frac{11}{9}\cdot M_2)}\cdot\sigma_a \qquad \text{Eq.30}$$

Using either of equations 27 – 28 and 30, along with the scaled Range of load-time history and its respective R-Ratio, the equivalent range can be calculated. The subsequent corrected damage calculation for mean stress occurs using the constant amplitude R=0.1 curve fitting equation. Summing up the total corrected damage, then calculating the estimated block repeats of the signal is done using $\frac{1}{\sum D}$.

10.9.3.1 Estimating TM11A R=0.5 Load-Life Curve

The TM11A R=0.5 curve was generated from calculating the ratio between TM11B R=0.1 and TM11B R=0.5 curves and using this ratio to estimate the TM11A R=0.5 curve and equation of the curve. The ratio is shown in figure 10.50 and equation 30.

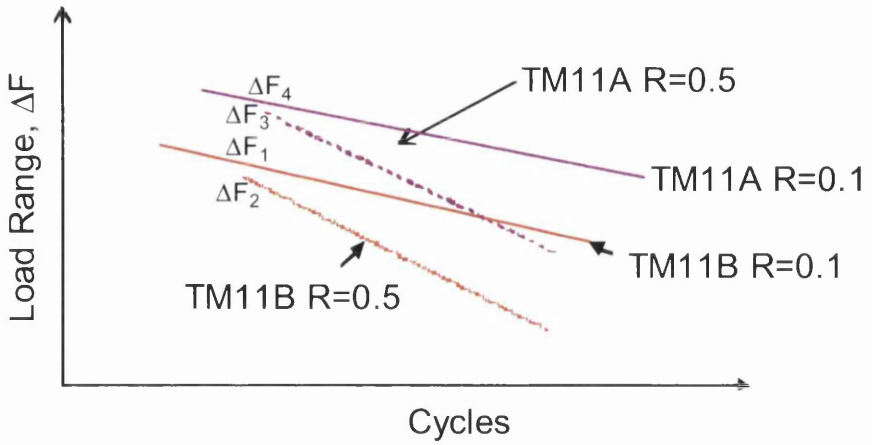

Figure 10.50: Calculating TM11A R=0.5

$$\Delta F_4 = \frac{\Delta F_3 \cdot \Delta F_2}{\Delta F_1} \qquad \text{Eq.30}$$

Where:-

ΔF_1 = Test load range for welded coupon TM11B at fatigue load ratio R=0.1

ΔF_2 = Test load range for welded coupon TM11B at fatigue load ratio R=0.5

ΔF_3 = Test load range for welded coupon TM11A at fatigue load ratio R=0.1

ΔF_4 = Estimated load range for welded coupon TM11A at fatigue load ratio R=0.5

10.9.3.2 Calculating M_2 Values

As shown in figure 10.49 M_2 is the slope between R=0.1 and R=0.5 lines, therefore to calculate M_2 both the load amplitude and the mean load for both R=0.1 and R=0.5 is required. Equations 31 – 32 show how the amplitude and mean is calculated.

$$\sigma_a = \frac{\sigma_{max} - \sigma_{min}}{2} = \frac{1-R}{2} \cdot \sigma_{max} \qquad \text{Eq.31}$$

$$\sigma_m = \frac{\sigma_{max} + \sigma_{min}}{2} = \frac{1+R}{2} \cdot \sigma_{max} \qquad \text{Eq.32}$$

Therefore load amplitude is shown in Eq.33 and the mean load is shown in Eq.34

$$\frac{\sigma_a}{\sigma_m} = \frac{1-R}{1+R} \text{ so } \sigma_a = \frac{1-R}{1+R} \cdot \sigma_m \qquad \text{Eq.33}$$

$$\sigma_m = \frac{1-R}{1+R} \cdot \sigma_a \qquad \text{Eq.34}$$

Calculating M_2 from Equations 33 and 34 is shown in Eq.35

$$M_2 = \frac{\sigma_{a^{0.1}} - \sigma_{a^{0.5}}}{\sigma_{m^{0.1}} - \sigma_{m^{0.5}}} \qquad \text{Eq.35}$$

10.9.4 Converting R=0.1 to R=-1

Converting the R=0.1 using the Goodman diagram in figure 10.49, this is done through converting both the load amplitude of the block loading sequence from R=0.1 to R=-1. This conversion is shown in Eq.36 and uses the initial Volvo M_1=0.25, M_2=0.1 values.

$$\sigma_a^{R=-1} = (1+M_1)\cdot\frac{1+M_2\dfrac{1+R}{1-R}}{1+M_2}\cdot\sigma_a \qquad \text{Eq.36}$$

Using the R=-1 corrected amplitude values, life is then calculated using the constant amplitude fitted curve equation.

11. RESULTS

11.1 Determination of Test Termination Criterion

Fatigue lives to a small visible crack length are required in for automotive components. Unfortunately, detecting small visible cracks is incredibly difficult until they become a certain length. To overcome this dilemma, monitoring the change in load and displacement during a test will enable the coupon stiffness to be calculated. Using 10% stiffness drop is the common method of determining a small crack.

When testing the coupons in the servo-hydraulic Dartec machine, load and displacement data were recorded to complete failure of the coupon. This is the termination criterion for the test. As a fatigue crack initiates and subsequently propagates, the stiffness of the coupon joint reduces. By analysing the recorded load and displacement data, it is possible to identify the life at which the coupon stiffness has reduced by 10% from its original value. Incidentally, the coupon stiffness is defined as recommended by Ford/Volvo as Load range / Displacement range.

However, after analysing all the constant amplitude tests from both suppliers the final failure (FF) 1mm extension and 10% stiffness drop (SD) were found to be very close, showing that the test termination criterion had little effect on test results. This is shown in figures 11.1 and 11.2.

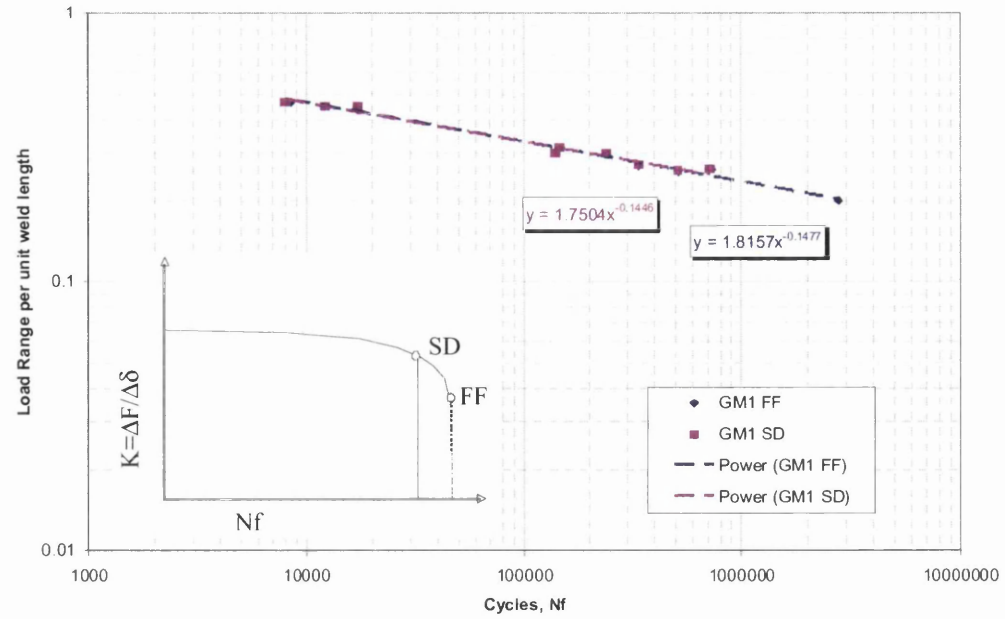

Figure 11.1: GKN Fabricated M1 (GM1) Coupon Joint Final Failure and 10% Stiffness Drop (R=0.1)

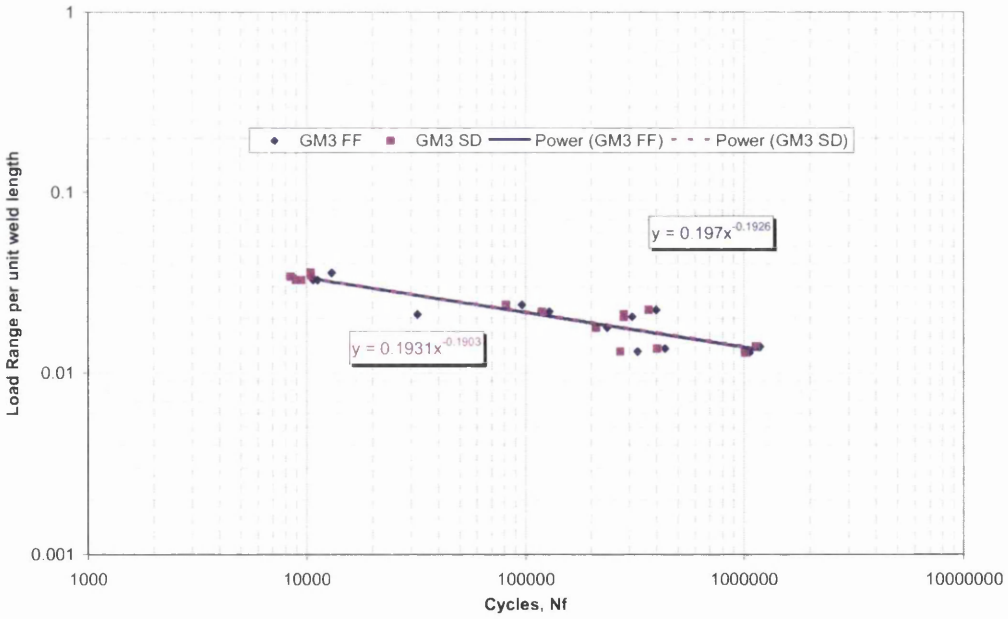

Figure 11.2: GKN Fabricated M3 (GM3) Coupon Joint Final Failure and 10% Stiffness Drop (R=0.1)

From both figures 11.1 and 11.2 little difference was found between final failure and 10% stiffness drop regardless of the difference in the test coupon geometry. So the test termination criterion became complete failure (1mm extension) of the coupon

and is a representative criterion also for "fatigue life". The results for other geometries can be found in Appendix 3.

11.2 Constant Amplitude Coupon Testing for Data Generation

Load-life data for various coupon joint configurations, which are shown in the following sections, are used to obtain the "structural stress vs. life" curves (S-N curves). From these S-N curves, an ideal outcome is that all the coupon fatigue life curves condense together to produce one "master" S-N curve regardless of geometry and failure mode.

An important aspect of the current EngD study is to examine to what extent, such master curves exist for the welded joints investigated.

The S-N curves are used as one of the inputs for CAE weld fatigue life analysis of automotive chassis structures.

11.2.1 Comparison of Full and Partial Welds of Coupon Lap-shear and Peel Geometries Test Results

The level of load applied to the weld within a coupon depends on the coupon widths and, more importantly, the length of the weld line. Therefore, a more appropriate weld loading parameter should be the load (force) per unit weld length as defined in figure 11.3.

To analyse the coupon test data, the load range is based on the actual weld length of each coupon as indicated in figure 11.3. Figure 11.4 describes the weld length and width dimensions. Figures 11.5 – 11.10 show the effect of differences between full and partial welded geometries for the same manufacturer against the original test data.

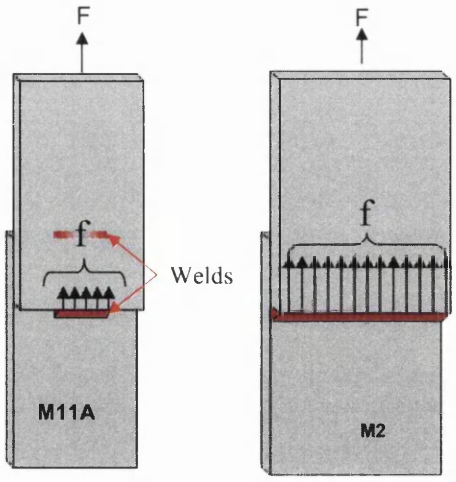

$$f = \frac{Force(F)}{WeldLength}$$

f ~ Load per Unit of Weld Length

Figure 11.3: Load (Force) per Unit Weld Length Definition

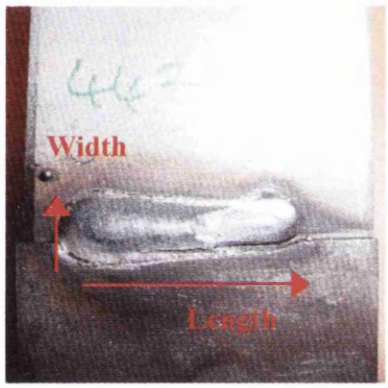

Figure 11.4: Diagram Showing Weld Length and Width

On the basis of total load on a coupon, figure 11.5a suggests that in the original test data GM2 appears to have better fatigue performance than GM1. Whilst in figure 11.5b, the partially welded GM1 coupons have very similar fatigue performance to the fully welded GM2, on a per actual unit weld length basis.

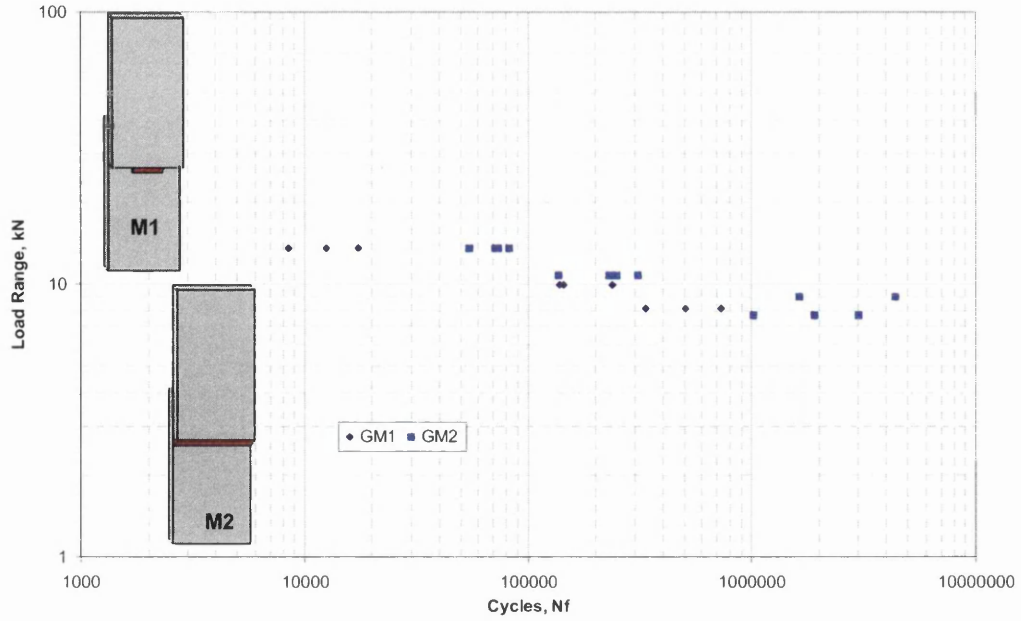

a)

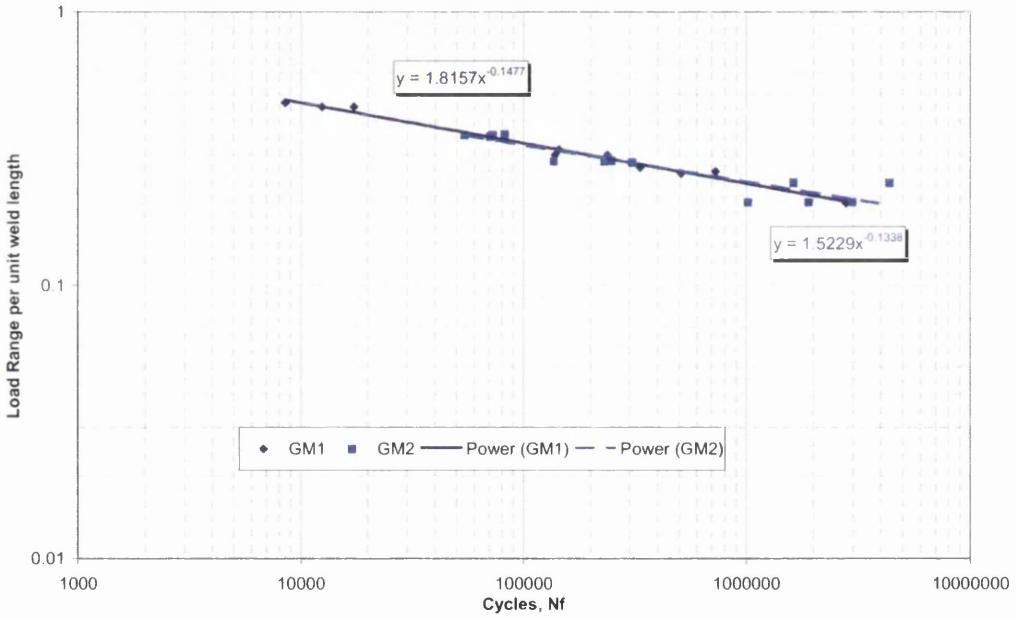

b)

Figure 11.5: R=0.1 Load-Life Data for GM1 and GM2 Joints (Throat Failure) – Final Failure a) Original, b) Normalised

As the original test data does not account for the effect of the weld on the fatigue life, these results will now be found in Appendix 4. The results subsequently shown will be the normalised results of per unit weld length.

With TM1 and TM2 coupons the difference between fully and partially welded geometries is shown in figures 11.6. The test data is normalised to the weld length, showing that TM1 has an increased fatigue performance over TM2.

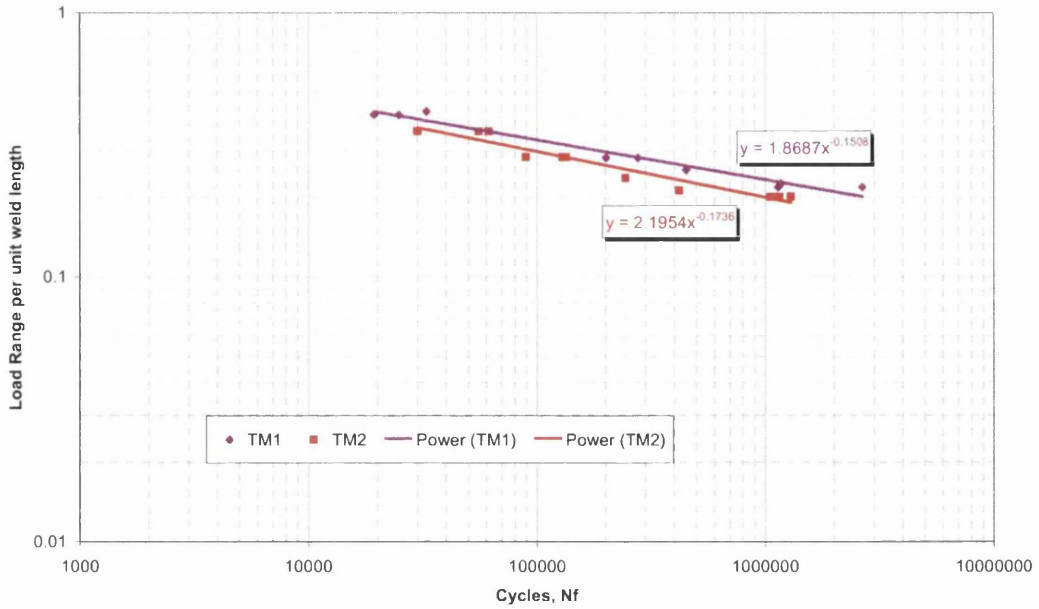

Figure 11.6: R=0.1 Load-Life Data for TM1 and TM2 Joints (Mostly Throat and Toe Failure Respectively) – Final Failure

Similarly, normalised fatigue results for double lap-shear geometries GM11A and GM11B are presented in figure 11.7. The partially welded GM11A displays better fatigue lives than the fully welded GM11B on a per actual weld length basis. GM11A survives 200,000 cycles more at 0.29 load range per unit weld length basis than GM11B.

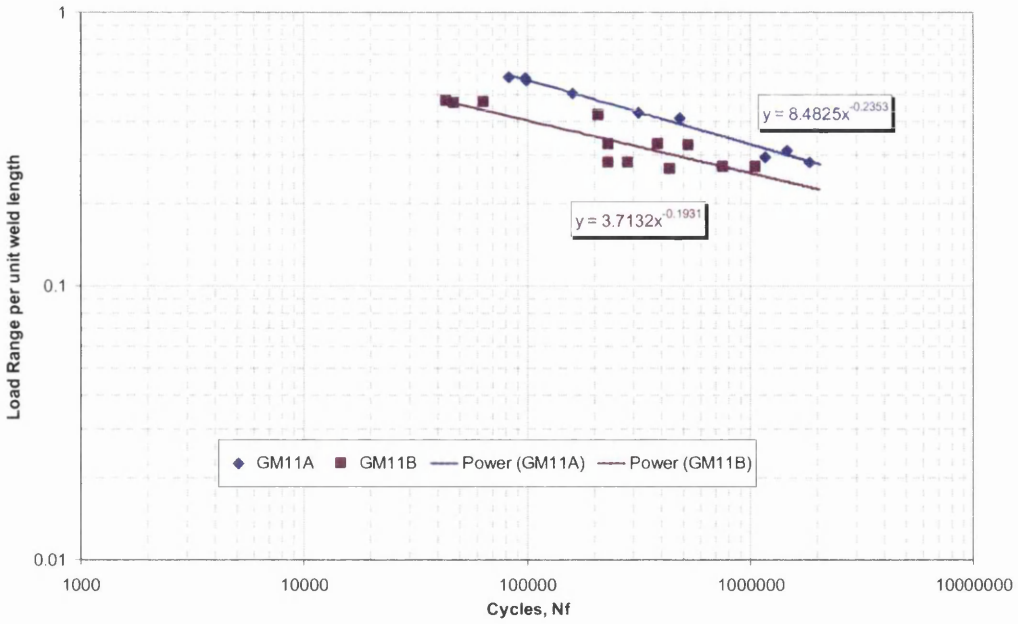

Figure 11.7: R=0.1 Load-Life Data for GM11A and GM11B Joints (Toe Failure) – Final Failure

TM11A has better fatigue performance on an actual per unit weld length basis when compared to the fully welded TM11B as illustrated in figure 11.8.

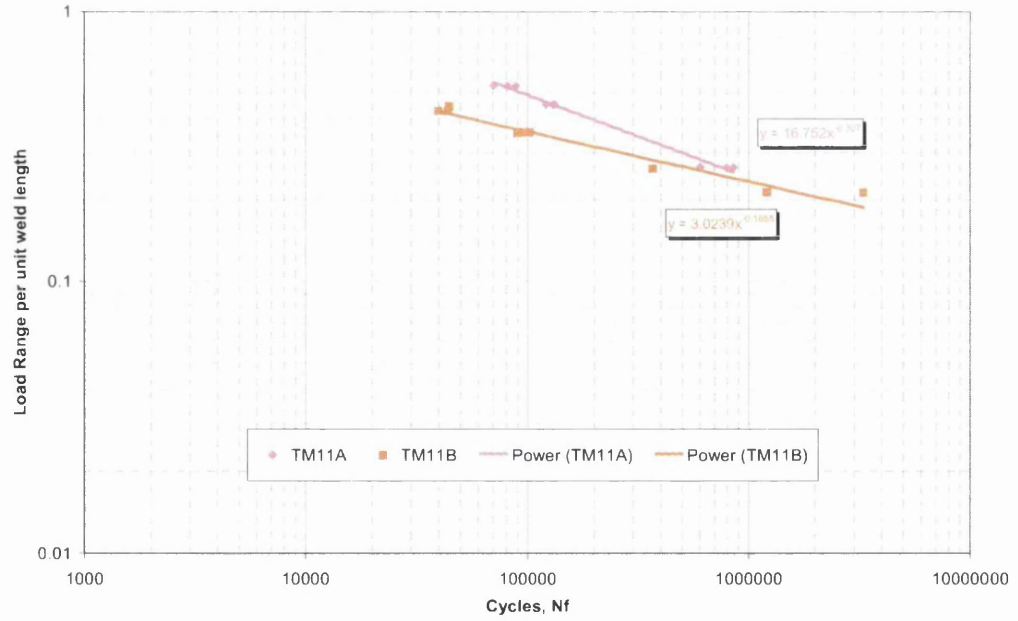

Figure 11.8: R=0.1 Load-Life Data for TM11A and TM11B Joints (Toe Failure) – Final Failure

For peel joints, GM3 and GM4 have very similar fatigue performance as shown in figure 11.9.

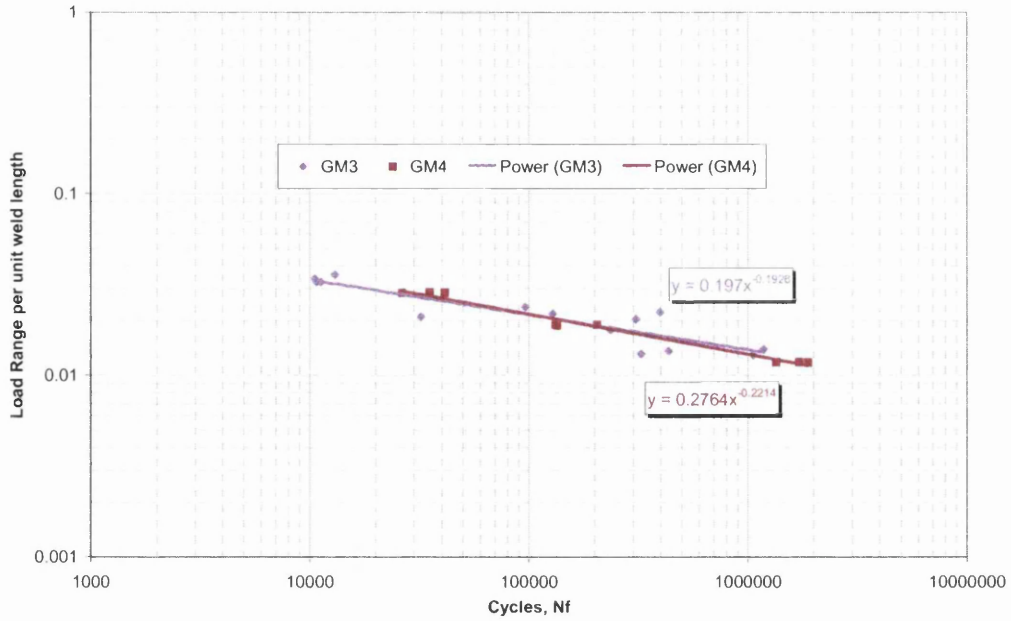

Figure 11.9: R=0.1 Load-Life Data for GM3 and GM4 Joints (Throat Failure)– Final Failure

11.2.2 T- Shaped Coupon Geometries Test Results

T-shaped coupons have been tested using all three loading types as indicated in figure 10.9. Figure 11.10 shows the T-shaped tensile M5, lateral M6 and bending M8 fatigue results. Load range levels giving lives of 100,000 cycles and 1,000,000 cycles are 32.54kN and 18.85kN for GM5 respectively. GM6 has load range levels giving lives of 100,000 cycles and 1,000,000 cycles of 3.5kN and 2.02kN respectively. On the other hand, for GM8, the load range levels giving lives of 100,000 cycles and 1,000,000 cycles are 3.02kN and 1.95kN respectively.

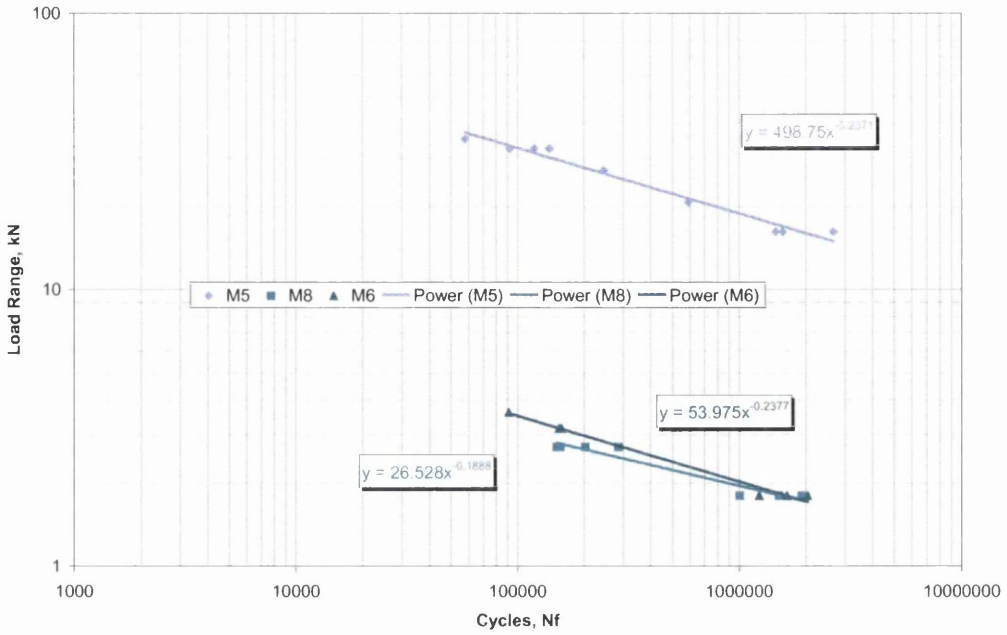

Figure 11.10: R=0.1 Load-Life Data for GM5, GM6 and GM8 Final Failure (Throat Failure)

11.2.3 Effects of Mean Stress (R-Ratios)

Investigating the effects of mean stress on the fatigue life for GM2 and TM11B coupon joints by altering the R-Ratios are shown in figure 11.11 and 11.12 respectively.

In figure 11.11, it shows that at high loads (short fatigue lives) the effect of altering the mean stress is less significant, whereas at high fatigue lives (low loads) mean stress has a greater effect. Load range levels giving life of 50,000 cycles for GM2 R=0.1 and R=0.5 are 13.61kN and 11.16kN respectively, a strength ratio of ≈1.22:1. On the other hand load range levels giving life of 4,000,000 cycles for GM2 R=0.1 and R=0.5 are 7.23kN and 5.25kN respectively, a strength ratio of ≈1.38:1.

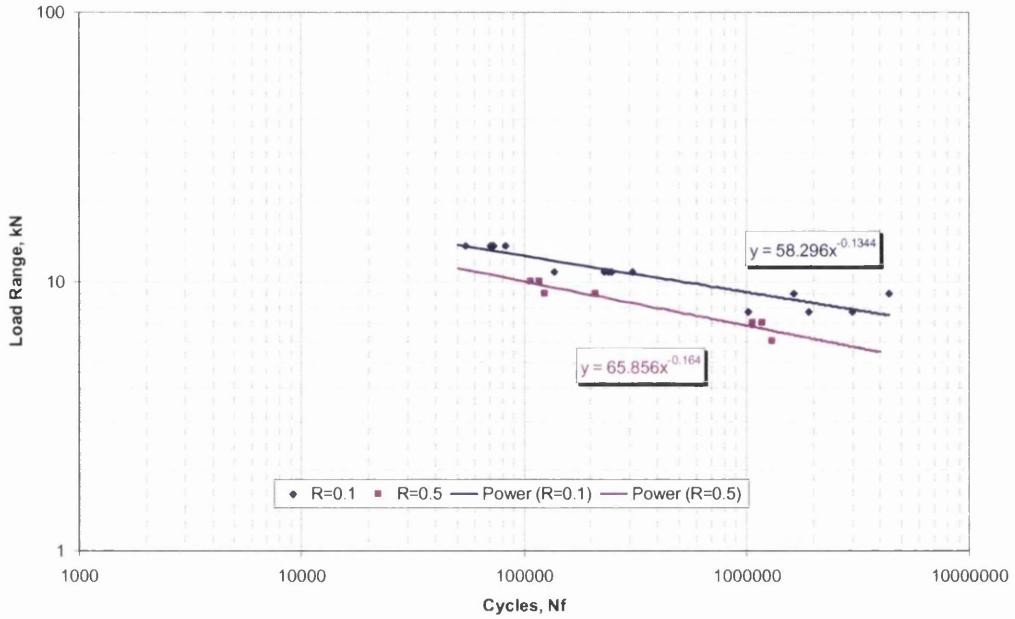

Figure 11.11: Load-Life Data for the Different R-Ratios for GM2

In figure 11.12, the effect on short fatigue lives seems to be negligible, whilst at long lives mean stress does have an effect. Load range levels giving life of 40,000 cycles for TM11B R=0.1 and R=0.5 are 15.33kN and 16.74kN respectively, a strength ratio of ≈0.92:1. Whilst load range levels giving life of 5,000,000 cycles for TM11B R=0.1 and R=0.5 are 6.62kN and 4.47kN respectively, a strength ratio of ≈1.48:1.

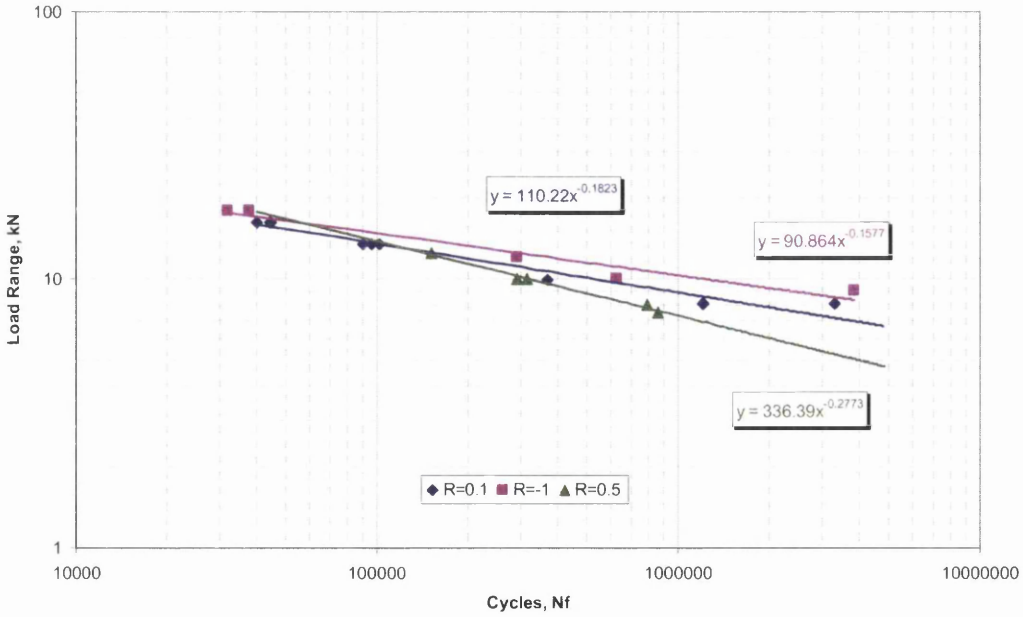

Figure 11.12: Load-Life Data for the Different R-Ratios for TM11B

11.3 Variable Amplitude Loading

The major reason for carrying out variable-amplitude loading tests is that a prediction of fatigue life under complex loading can be made. By calculating the cumulative effect of damage from random load-time histories, the concept developed by Palgrem-Miner – Miner's Rule can be checked. Miner first presented the Palgrem linear damage concept as a measure of fatigue damage, with the basic assumption of a constant work absorption per cycle leading to a linear summation of cycle ratio or damage.

11.3.1 Block Loading Coupon Test Results

Figure 11.13 shows the results of the two block load levels tested. The graph is plotted to show the effect of the life against the range of both load levels applied in each of the block loading signals. This shows that the first load range of each level has the most damaging cycles.

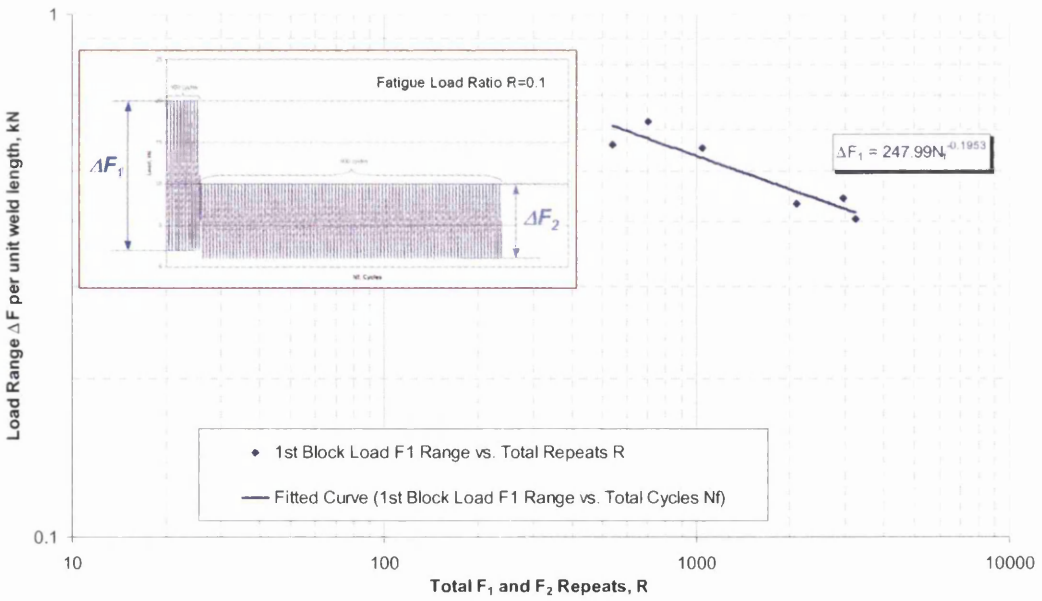

Figure 11.13: Block Loading Results, R=0.1

The suitability of Miner's rule for cumulative damage evaluation will be discussed in Section 12.2.1, using the test results presented in this section.

11.3.2 Variable Amplitude SAE Bracket Coupon Test Results

Figure 11.14 shows the results of using the SAE Bracket load–time history. TM11A has better fatigue performance than GM1 due to the fact that TM11A has twice the

weld line lengths. However, TM11A does not offer twice the strength due to more weld line. GM8 load range lives are a magnitude lower than either of the lap-shear geometries.

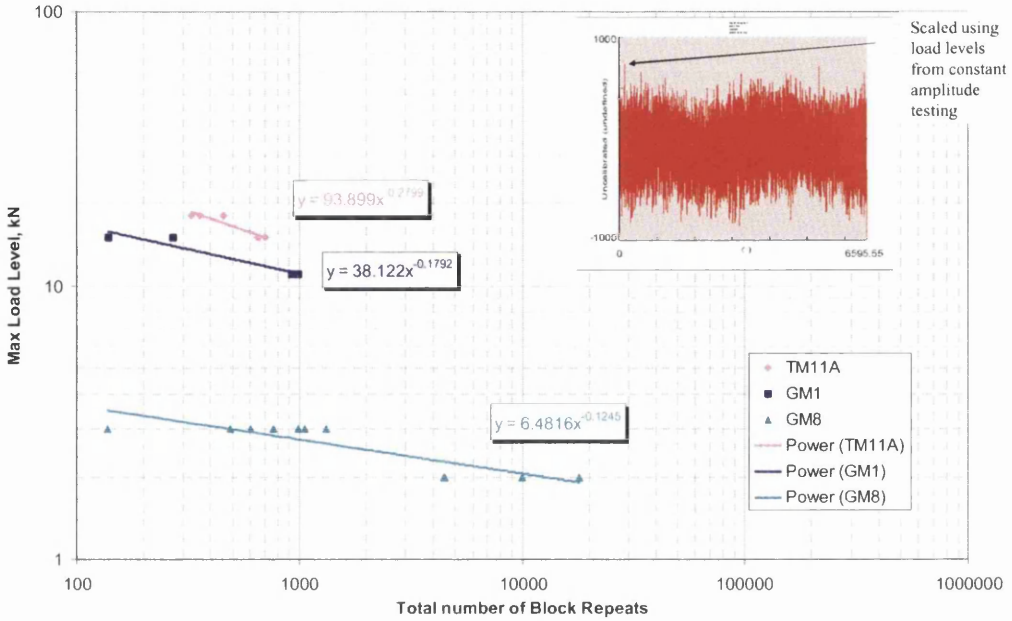

Figure 11.14: Variable Amplitude Fatigue Loading Results for GM1, GM8, TM11A Final Failure

The suitability of Miner's rule for cumulative damage evaluation will be discussed in Section 12.2.2, using the test results presented in this section.

11.4 Coupon Testing Failure Modes and Locations

On close examination of the crack initiation sites on failed specimens, there are the two traditional types of failure locations: the weld throat and weld toe as shown in figure 11.15. The typical failure location for each geometry and supplier is shown in Table 11.1.

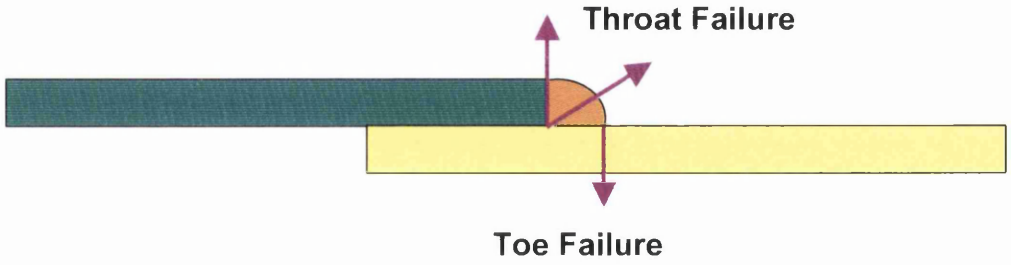

Figure 11.15: Traditional Failure Locations in Welded Structures

Table 11.1: Typical Failure Location for all Coupon Geometries.

Geometry	Failure Locations	Loading
GM1	Throat	Constant
GM2	Throat and Toe	Constant
GM2_R=0.5	Throat	Constant
GM11A	Toe	Constant
GM11B	Toe	Constant
TM1	Throat and Toe	Constant
TM2	Toe	Constant
TM11A	Toe	Constant
TM11B	Toe	Constant
GM3	Throat	Constant
GM4	Throat	Constant
GM5	Toe	Constant
GM6	Toe	Constant
GM8	Throat	Constant
TM11B_R=-1	Toe	Constant
TM11B_R=0.5	Toe	Constant
GM11A	Toe	Block Loading
TM11A	Toe	Variable
GM1	Throat	Variable
GM8	Toe	Variable

The partially welded M1 specimens display only throat failures, whilst the fully welded M2 specimens provide a mixture of throat and toe failures. Figures 11.16 – 11.17 show the general structure of the failures for both M1 and M2 specimens.

Figure 11.16: Typical Throat Failure of M1 Specimens

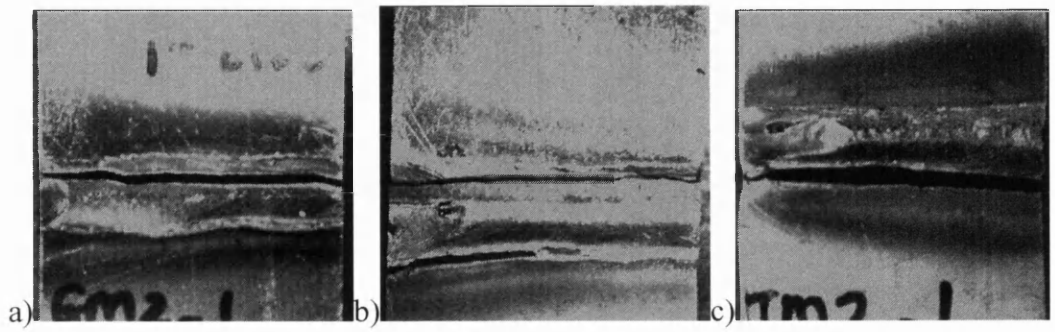

Figure 11.17: Typical Failures of M2 Specimens a) Throat Failure, b) Throat and Toe Failure, c) Toe Failure

For GKN and TKA M11A and M11B, the typical toe failures are shown in figure 11.18, whilst typical peel failures for GM3 and GM4 are shown in figure 11.19.

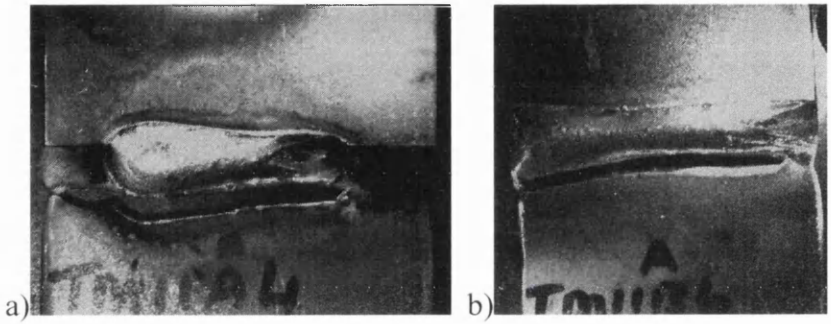

Figure 11.18: Typical Toe Failure for a) M11A, b) M11B

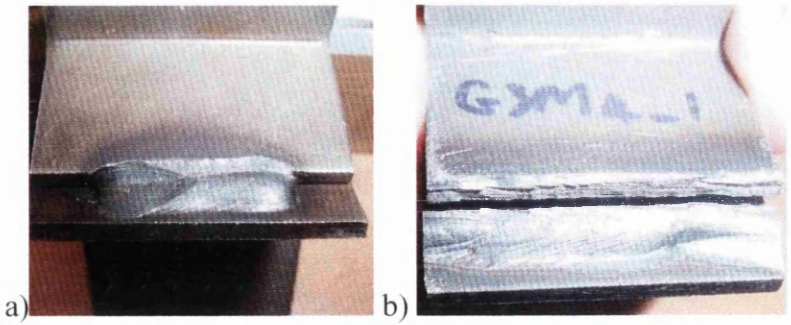

Figure 11.19: Typical Throat Failures for a) M3 b) M4

Figure 11.20 shows the typical failures for GM5, GM6 and GM8 coupons.

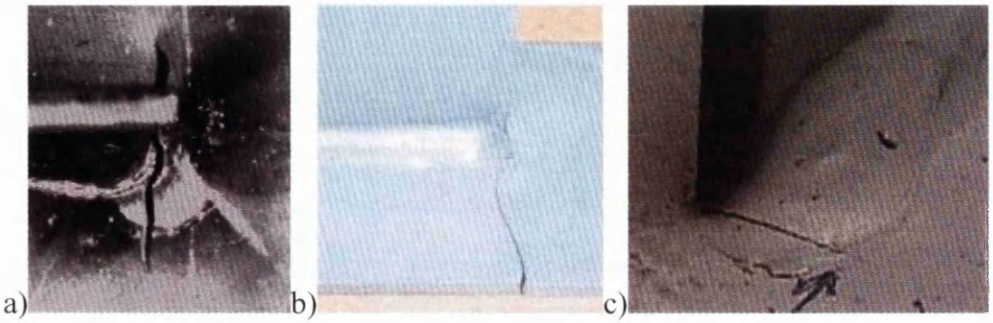

Figure 11.20: Typical Failure of a) M5 Toe, b) M6 Toe, c) M8 Throat

Investigating the effects of mean stress on TM11B and GM2 is shown in figures 11.21 – 11.22 respectively.

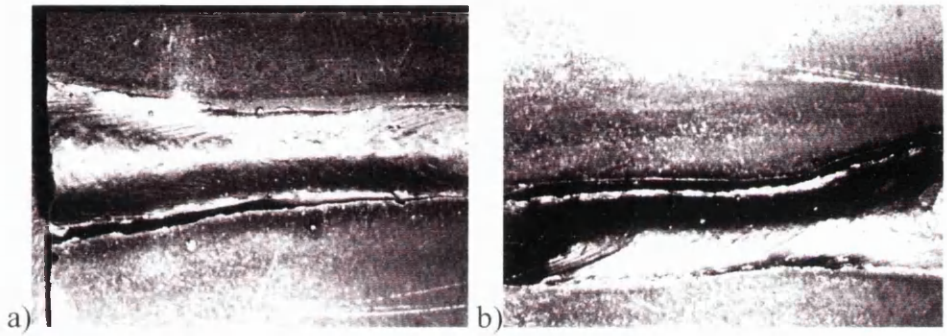

Figure 11.21: Typical Weld Toe Failure of TM11B under R-Ratios of a) R=0.5, b) R=-1

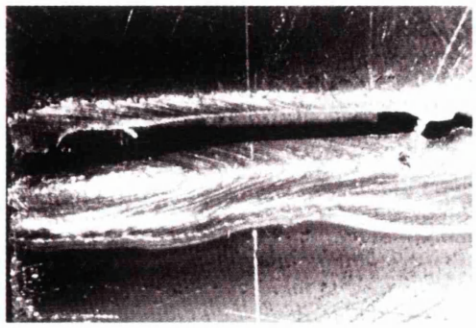

Figure 11.22: Typical Weld Toe Failure of GM2 under R-Ratios of R=0.5

Figure 11.23 shows the general structure of failure for GM11A under block loading conditions.

Figure 11.23: Typical Failure Location of Variable Amplitude Block Loading GM11A

Figure 11.24 shows the general structure of the failures for the variable amplitude loading of GM1, TM11A and GM8.

Figure 11.24: Typical Failure Locations for Variable Amplitude SAE Bracket Loading of a) GM1, b) TM11A, c) GM8

11.4.1 Fracture Surface Examination

From observing the main modes of failure shown in figures 11.15 – 11.24, figure 11.25 shows how the following fracture surfaces were examined using the traditional methodology of failure modes. The typical fracture surfaces for weld toe failures and weld throat failures are shown below in figures 11.26 – 11.28.

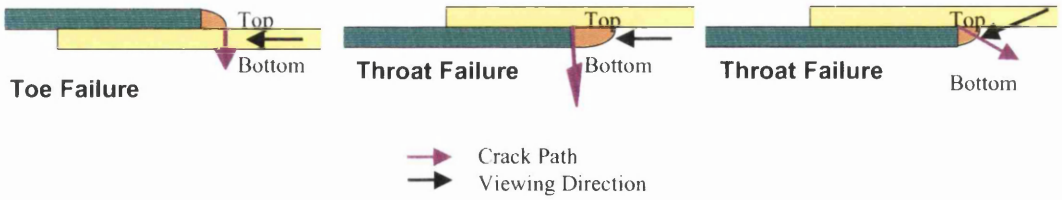

Figure 11.25: Viewing Angles for the Fracture Surface Examination

Figure 11.26 shows the typical fracture surface for all the coupon weld toe failures. The surface shows that the cracks initiated from multiple areas mainly in the centre of the weld. At the start/stop areas of the weld, more latter stage crack propagation than initiation occurred.

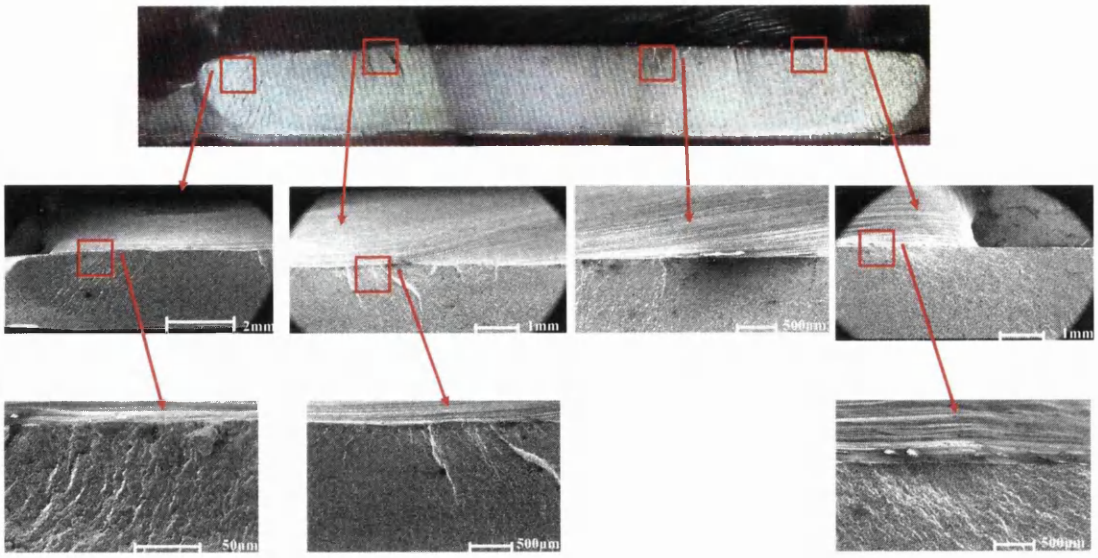

Figure 11.26: Typical Weld Toe Failure – GM11A

For typical weld throat failures, figures 11.27 – 11.28 show the fracture surfaces. From figure 11.27 again the crack initiation sites are more in the centre of the weld than at either the start/stop. This is shown quite clearly as at the edges, crack propagation occurs. Figure 11.28 shows the weld view of the throat failure, and this to shows similar results.

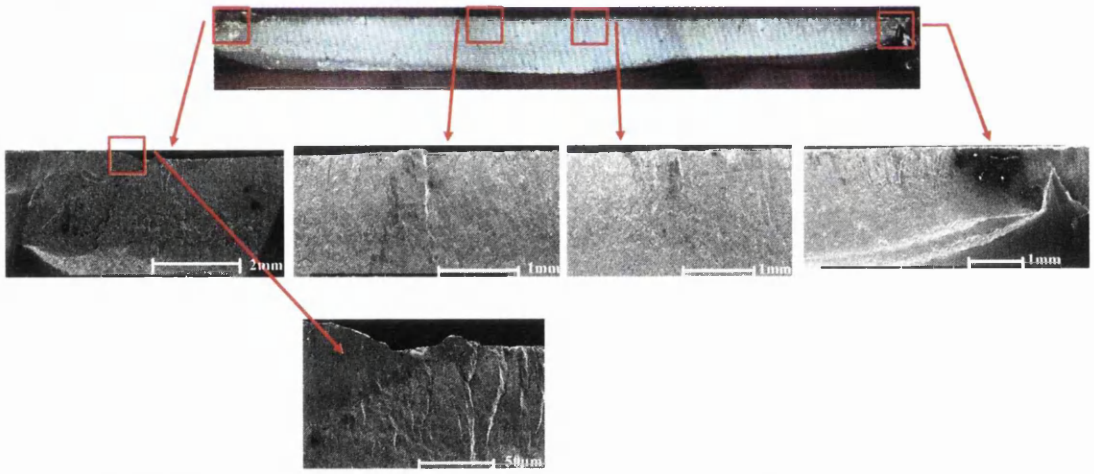

Figure 11.27: Typical Weld Throat Failure – Sheet View, GM1

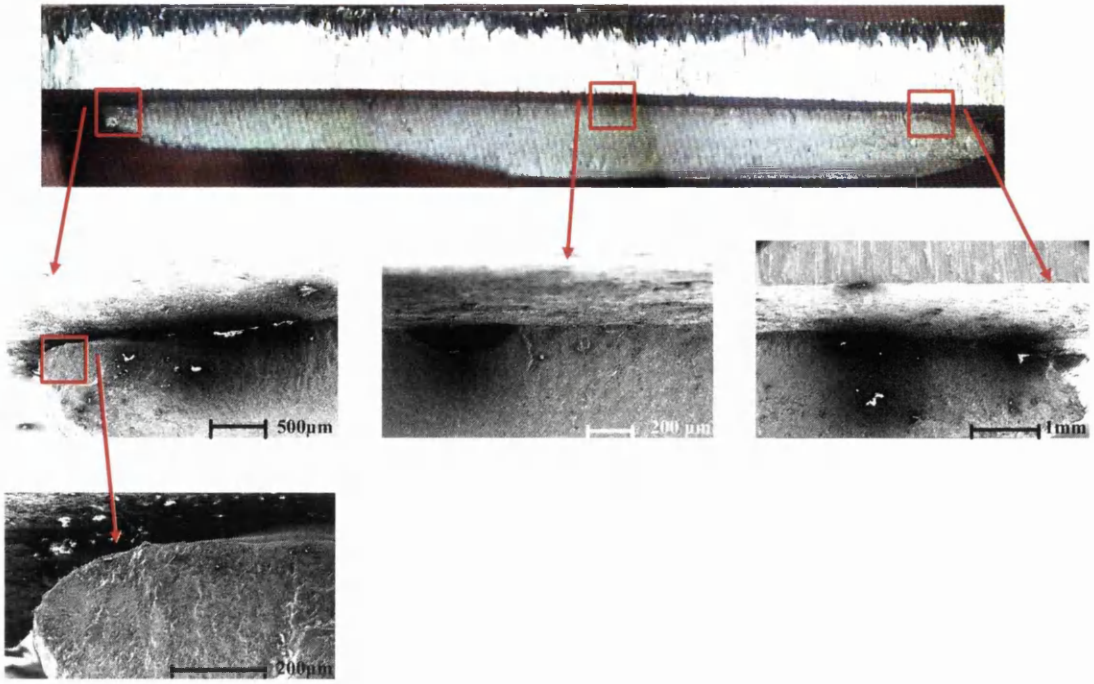

Figure 11.28: Typical Weld Throat Failure – Weld View, GM1

Figures 11.29 – 11.30 show the typical throat failures for the peel specimens GM3 and GM4. Figure 11.29 shows the sheet view of the fracture surface with the fatigue initiation occurring from the root. Damage is noticeable nearer the weld surface due to the bending motion during the fatigue testing.

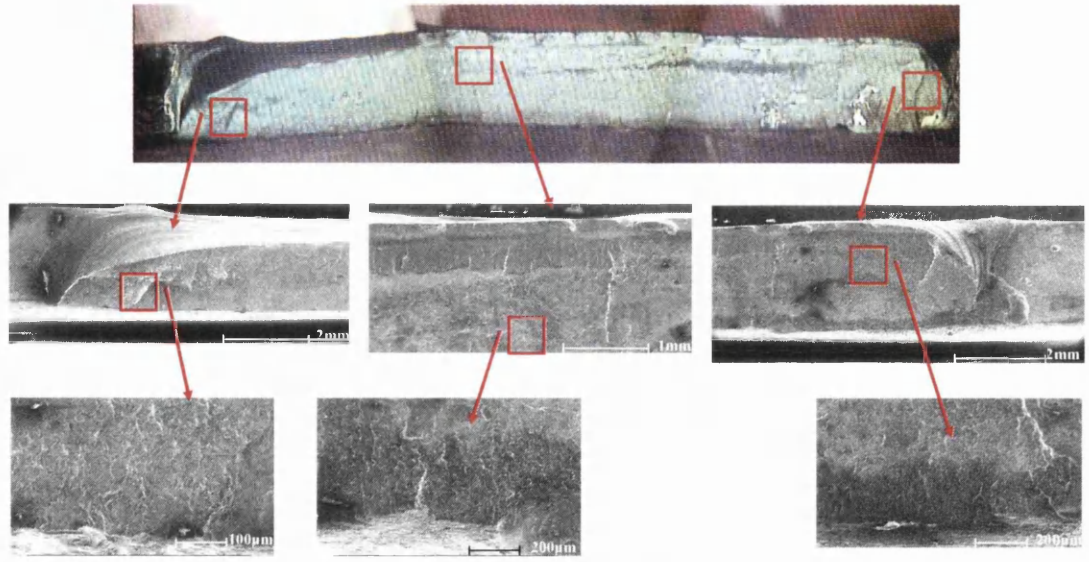

Figure 11.29: Typical Weld Throat Failure – Sheet View, GM3

Figure 11.30 shows the weld view of the fracture surface, showing also that in parts there are some weld defects such as porosity in the weld material.

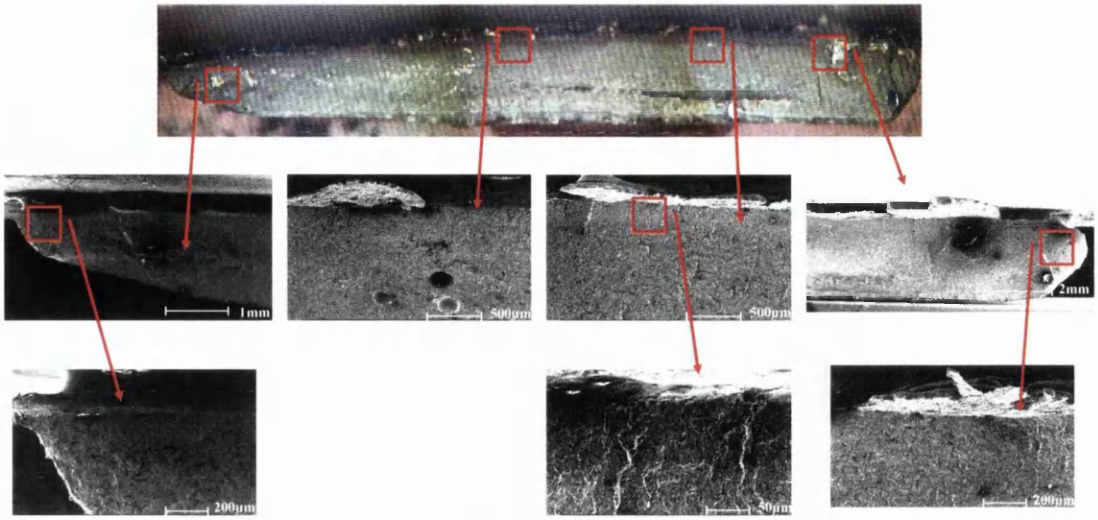

Figure 11.30: Typical Weld Throat Failure – Weld View, GM3

Figure 11.31 shows a typical T-Shaped geometry fracture surface. Fatigue initiation occurs from the root of the weld and then the crack propagates through the weld start and into the parent material.

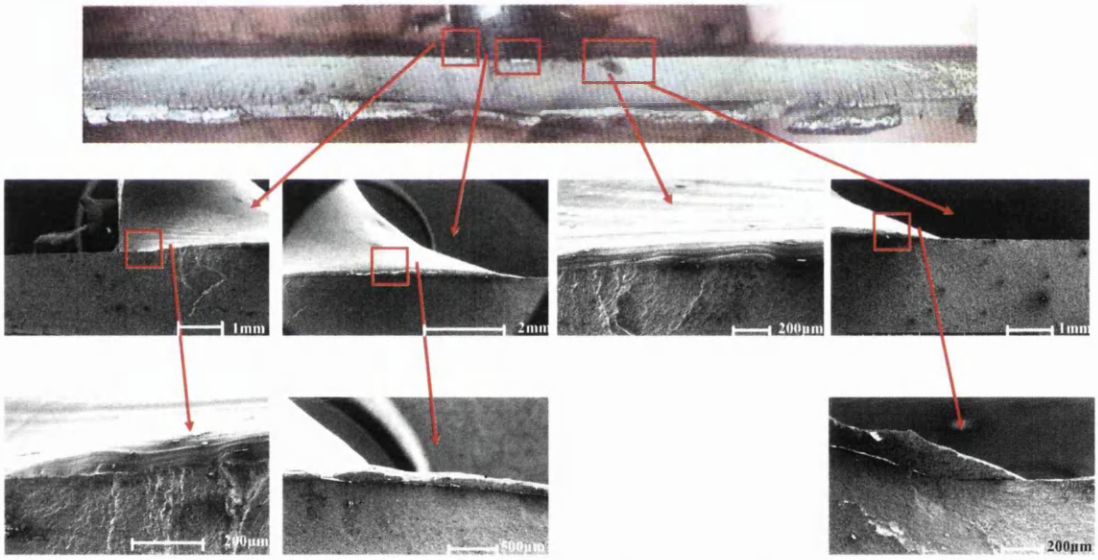

Figure 11.31: Typical Weld Throat Failure – Weld View, GM8

As all the fracture surfaces show similar trends to figures 11.26 – 11.31, the fracture surfaces for the remaining coupon geometries are shown within Appendix 5.

Noticeable from both Table 11.1 and the fracture surfaces in Appendix 5, TM1 has two modes of failure which also show that the main initiation sites occur from the centre of the weld and propagate out to the weld start/stop. The throat failures of

TM1 could occur from the areas at the root of the weld where the weld metal has not filled the gap – i.e. weld undercut.

GM2 also has two failure modes, which also have the main initiation sites occurring from the centre of the weld. For weld toe failure the cracks initiated from the toe of the weld even though there is a large crack, which could have formed during the welding cycle, which also has secondary fatigue cracks surrounding it. Wherever there are welding defects on the weld more fatigue cracks initiate.

For the majority of GM2 coupons the failure mode was through the weld throat. From the sheet fracture surface, it is noticeable that the weld did not penetrate the parent material completely. From this many fatigue crack initiation sites were located. Also present within the fracture surface are some porosity cavities. The weld fracture surface shows areas in the weld root with poor penetration. Porosity holes are also noticed within the weld. Fatigue cracks are initiating from the weld root due to the welding defects present.

Peel geometries GM3 and GM4, which show, throat failures initiating from the root and propagating into the weld. Within the fracture surfaces, noticeable are weld defects such as porosity holes. Fatigue initiation occurred from the weld root.

For T-shaped coupons under all three loading conditions, failure was from the weld throat. Fatigue cracks have initiated from the weld root and propagated around the weld toe. In areas of weld metal overlap fatigue initiation sites are more frequent.

From all the fracture surface analysis the traditional definitions of the weld throat failures and weld toe failures (as shown in figure 11.15) require redefining due to the clear distinction between the two types of throat failure and this will be discussed in section 12.3.

11.5 Coupon FE Modelling Results

The purpose of FE modelling of coupons is to produce the "Structural Stress" and use this stress to convert the load life data into stress life data. FE analysis was done

using the models shown above in figures 10.33 – 10.34, and the actual test data shown in section 11.1. The method is summarised below in figure 11.32.

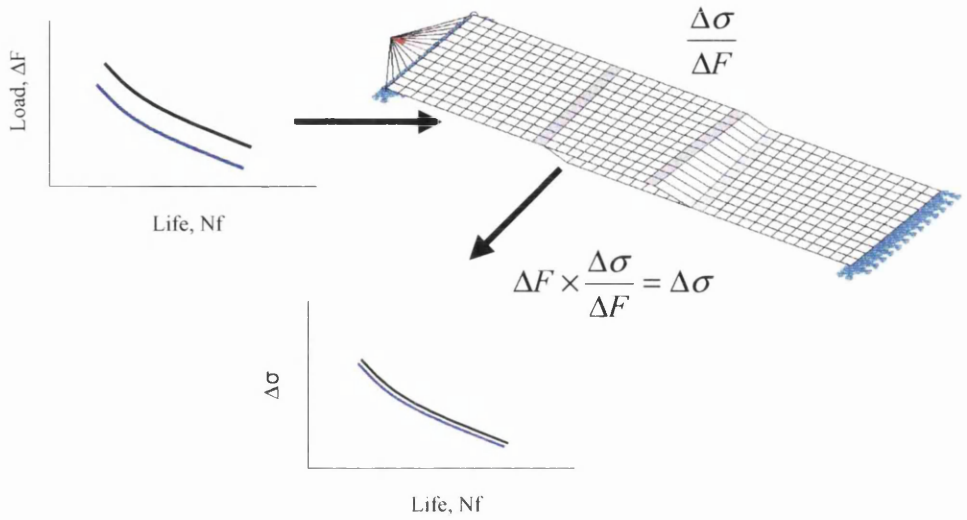

Figure 11.32: Analysis Process from Load- Life Curves to S-N Curves

For analysis purposes when using MSC.Fatigue, elements either side of the weld (the weld toe elements) were grouped as Weld Toe elements as this is where the stress would be taken from, as shown in figure 11.33.

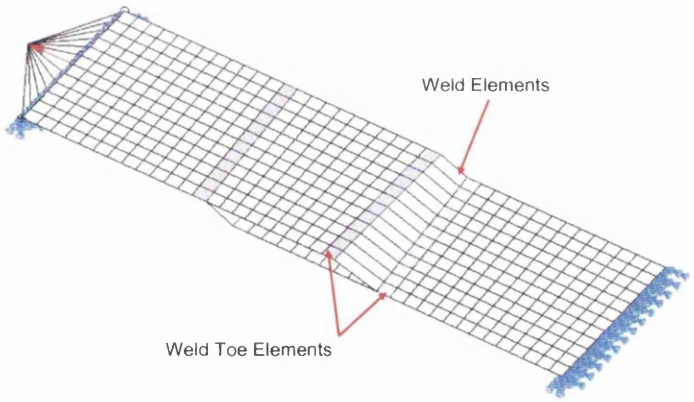

Figure 11.33: FE Model Showing Weld and Weld Toe Element Location

From all the constant amplitude testing, there were three methods of failure by the weld toe or the weld throat –two types. For analysis purposes, the weld toe is the only failure location at which all the current FE packages predict the stress. For the weld throat failures, the FE stress locations must be researched and the two possible locations are shown below in figure 11.34. The correct surface of the element must also be chosen, as shown in figure 11.35.

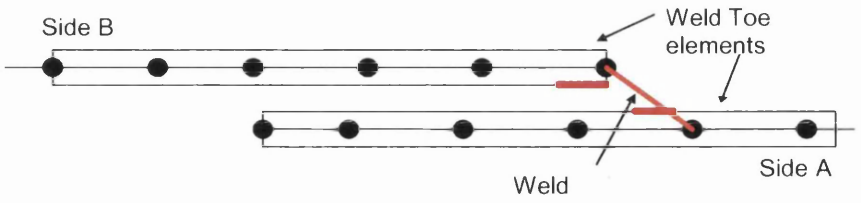

Figure 11.34: Possible Locations for Extracting the Predicted Stress for Throat Failures

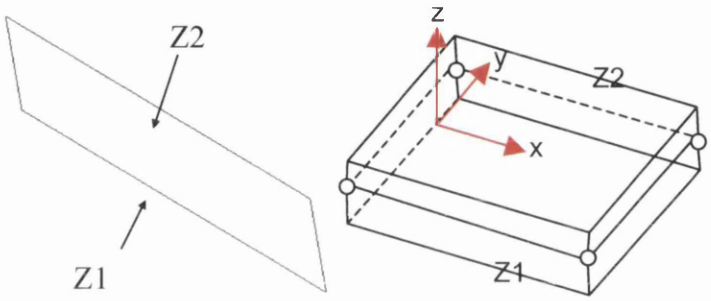

Figure 11.35: Surfaces of an Element

11.5.1 FE Modelling With Experimental Verification

Experimental verification of the FE models in the form of strain gauges and photoelasticity was required to compare the stress distribution away from the weld. Also to gain FE confidence of the method of modelling the coupon joints.

Coupon geometries were modelled and meshed using the MSC.Patran software based in Corus Automotive. The structures were then analysed by another FE package MSC.Nastran to obtain the structural deformation, stress and strain. The deformation models of the three coupons used for photoelasticity are shown below in figure 11.36.

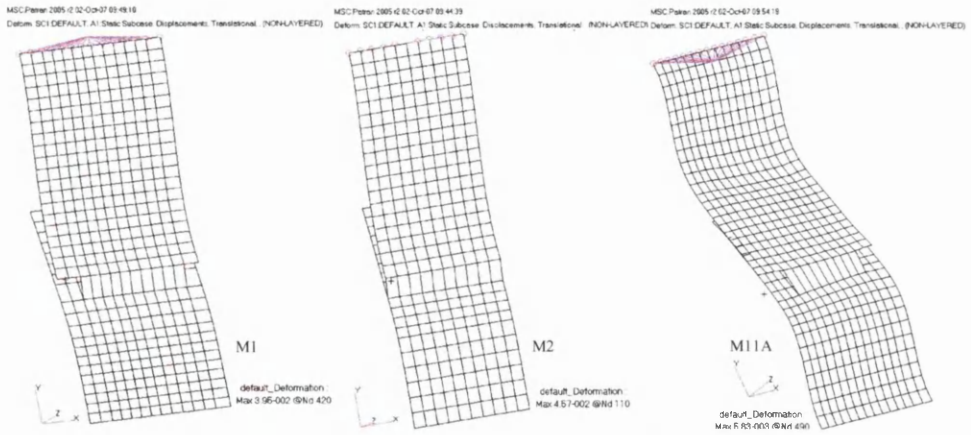

Figure 11.36: Deformation Models of Coupons used in Photoelasticity

11.5.1.1 Effects of Weld Representation in FE Model

For M2 three different methods of modelling the weld line were considered and shown in figure 11.37: 1) normal Quad4 mesh, 2) strengthening the weld with elements forming a triangle at the weld, referred to as Tri, 3) doubling the thickness of the weld, referred to as "Thick" weld representation.

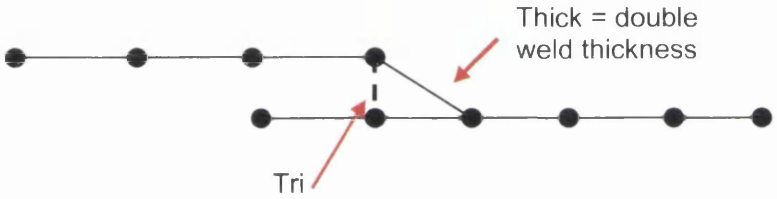

Figure 11.37: Alternative Methods of Modelling the Weld

The stress distribution along the coupon centre line obtained for each variation of the FE analysis of the M2 coupon is shown in figure 11.38a and b. For each variation, the maximum principal stress and the stress in the "y" direction (σ_y stress), i.e. the longitudinal stress, were extracted and plotted against the distances from the weld line in figure 11.38a and b. Noticeable from the graph, the further away from the weld the less the weld stress raising effect has on the σ_y stress distribution for the "Thick" FE variation.

The results in figure 11.38 suggests that using the different methods of representing the weld in an FE model has little effect on the predicted values of stress at any distance greater than 11mm away from the weld.

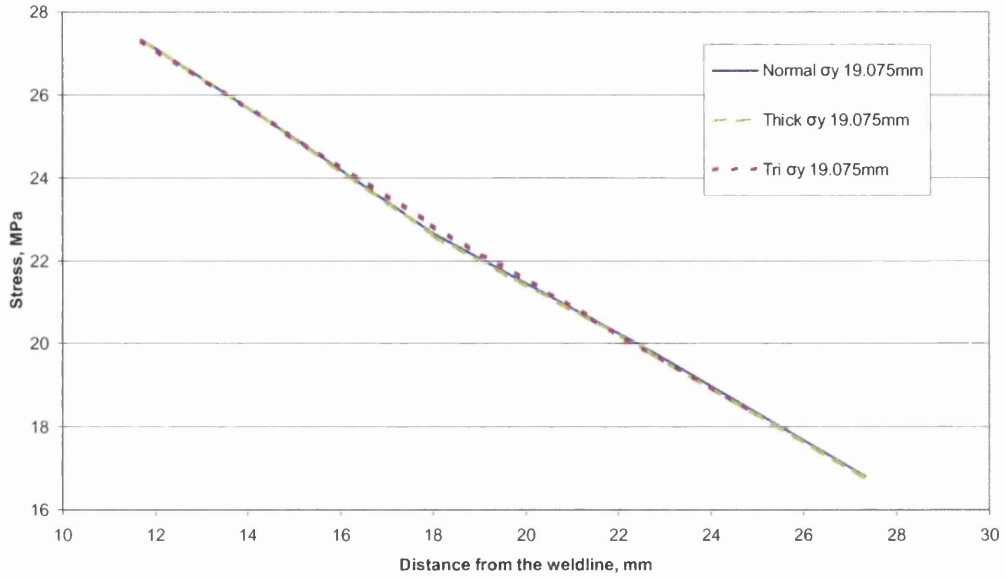

a)

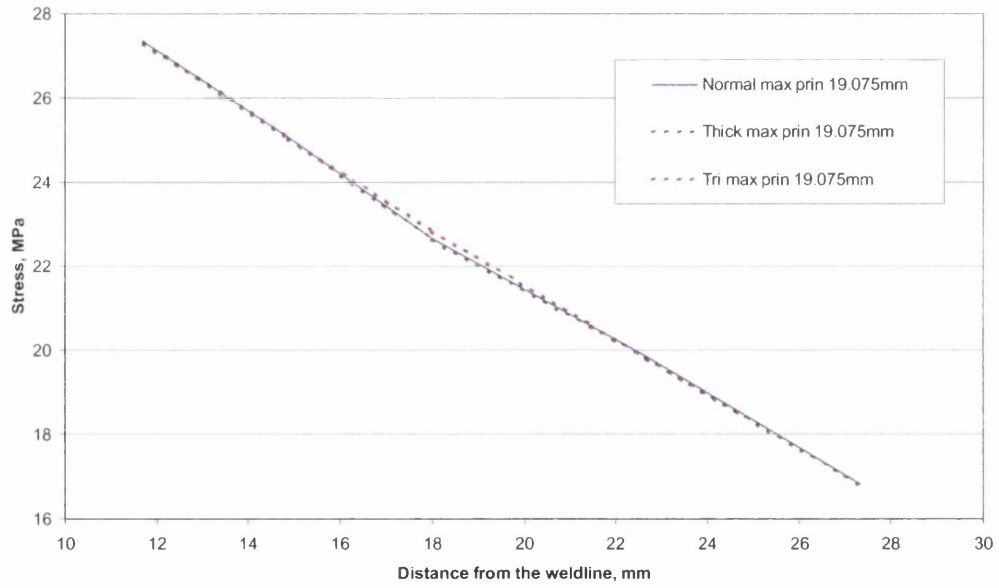

b)

Figure 11.38: Various Ways of Modelling the M2 Weld a) σ_y Stress, b) Max Principal Stress (Applied Load 1kN)

The weld was also represented by a 8-noded solid/brick FE elements, whose stress results were compared with those from the shell-element model. The comparison of stress distribution between the solid and shell models is shown in figure 11.39. The figure indicates that solid-element stress values obtained were only very marginally lower than, if not almost identical to, their shell-element equivalents.

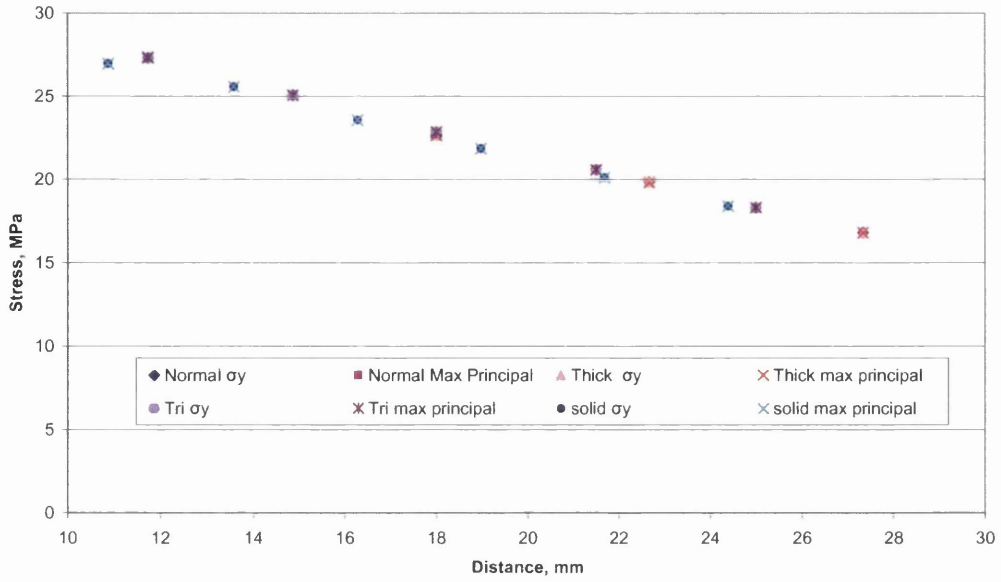

Figure 11.39: Difference between Solid and Shell M2 Models (Applied Load 1kN)

Overall, it appears that little difference exists among stress results from various FE weld representations. In addition, figures 11.38 – 11.39 also indicate no significant difference between the maximum principal stress and the stress in "y" direction σ_y stress. Consequently, for the rest of the Results section, only σ_y stress results from FE models using the shell-element weld representation are presented.

The stress was collected from three distributions:

1) The centre line of the weld
2) 10mm left of the centre line
3) 10mm right of the centre line

The stress along the longitudinal "y" direction "σ_y" was chosen, as this is the stress that is aligned with the loading direction i.e. the longitudinal stress. Figures 11.40 – 11.42 show the longitudinal stress distribution across the coupon width at distances from the weld. Figure 11.40 shows that further away from the weld in the M1 coupon, the three stress distributions are very close.

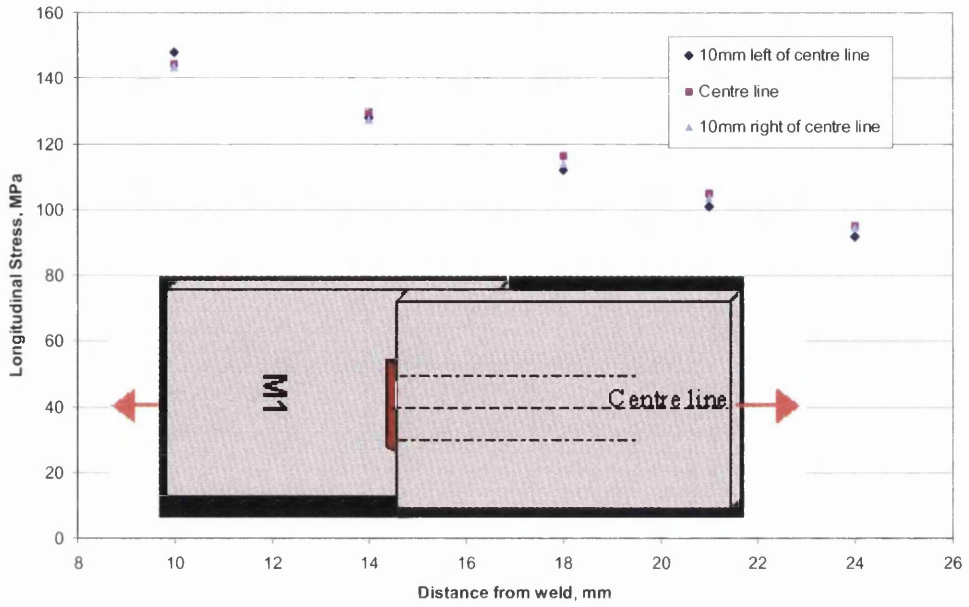

Figure 11.40: Longitudinal FE Stress Results for M1 Joint at 6kN

The same three stress results taken from the FE model of the M2 coupon are shown in figure 11.41. Again, further away from the weld, the stress values seem to virtually converge.

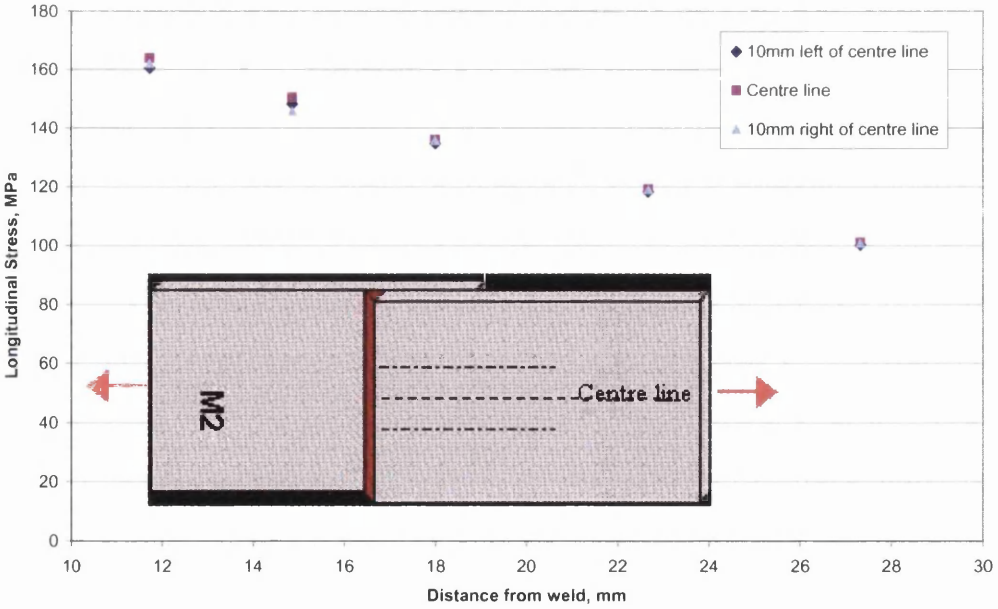

Figure 11.41: Longitudinal FE Stress Results for M2 Joint at 6kN

The stress distributions along the same three lines on the M11A coupon are shown in figure 11.42 and, as one can see, 11mm from the weld, the stress values along the three chosen lines start to slowly converge, and become very close as the distance increases, in a similar fashion to those of M1 and M2 coupons.

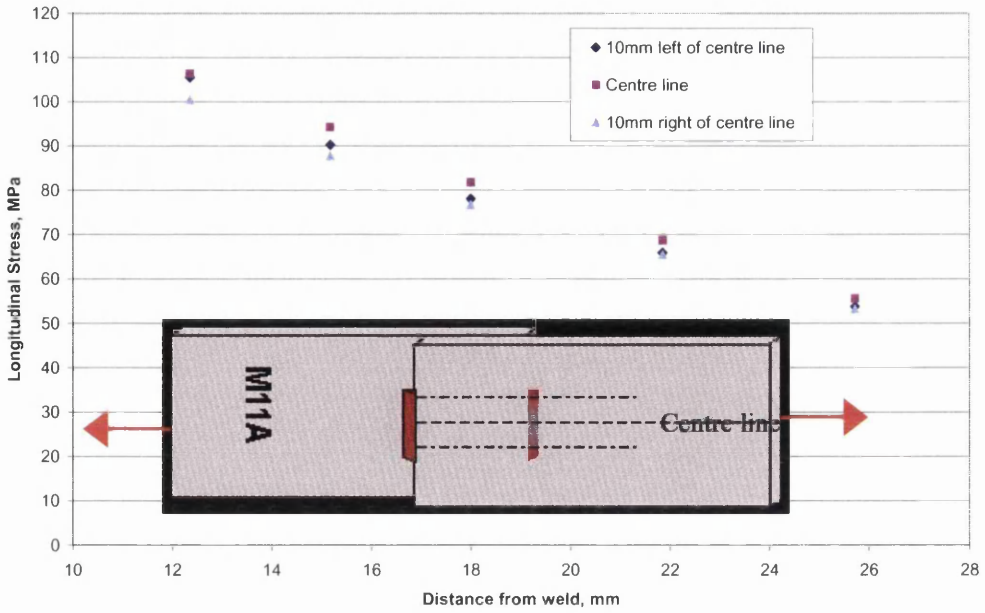

Figure 11.42 Longitudinal FE Stress Results for M11A Joint at 6kN

11.5.1.2 FE vs. Strain Gauge Results

Figures 11.43 – 11.45 compare results of the longitudinal stress converted strain gauge measurements against those of the predicted FE stress. At low loads, all the graphs show that the predicted and measured stress is very close, whilst at higher loads the FE stress values become lower than the strain gauge results.

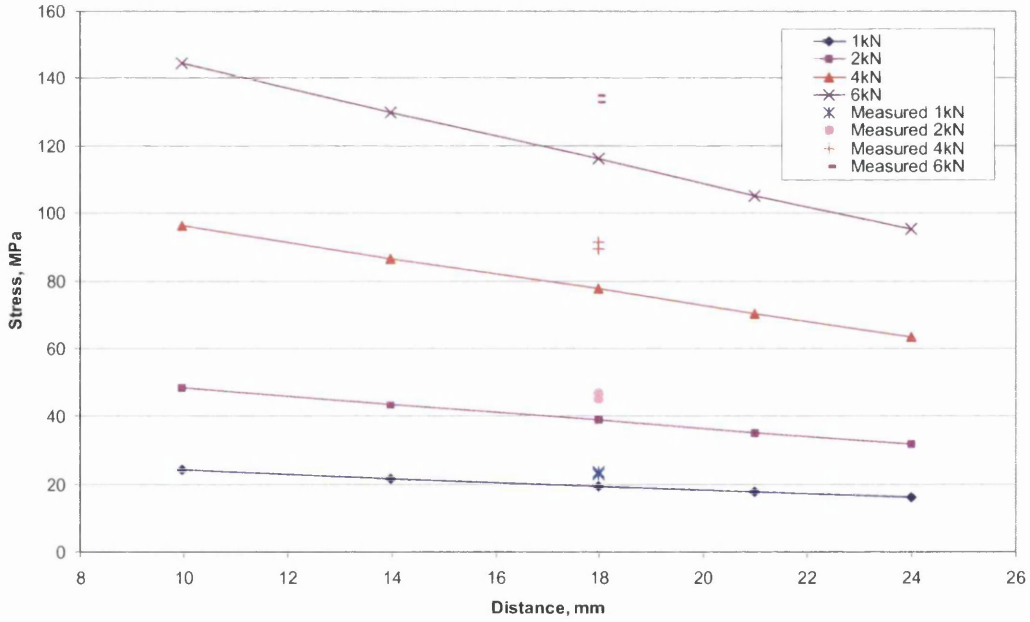

Figure 11.43: Strain Gauge vs. FE Stress in Longitudinal Direction for M1

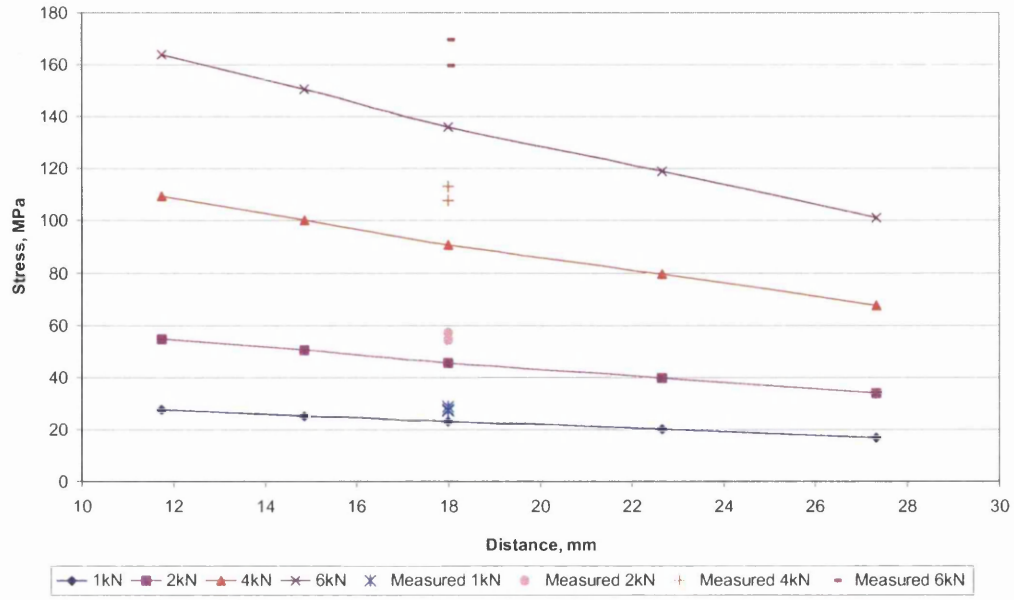

Figure 11.44: Strain Gauge vs. FE Stress in Longitudinal Direction for M2

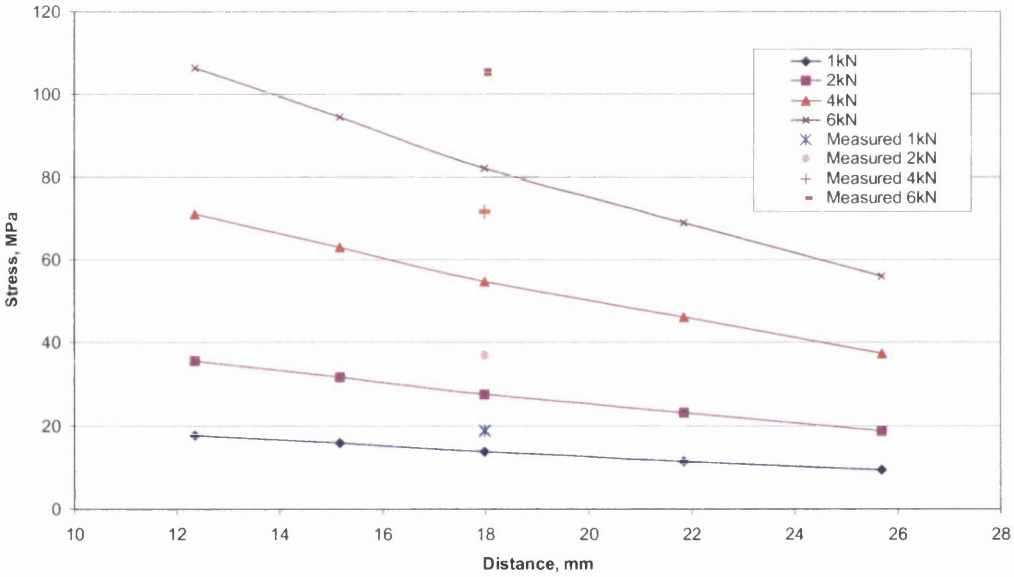

Figure 11.45: Strain Gauge vs. FE Stress in Longitudinal Direction for M11A

11.5.1.3 FE vs. Photoelasticity and Strain Gauging

The longitudinal stress distribution results for all three methods of stress evaluations for M1 coupon are presented in figure 11.46, which shows that the FE prediction of longitudinal stress is slightly lower than the stress values obtained from the other two methods: photoelasticity and strain-gauge measurements.

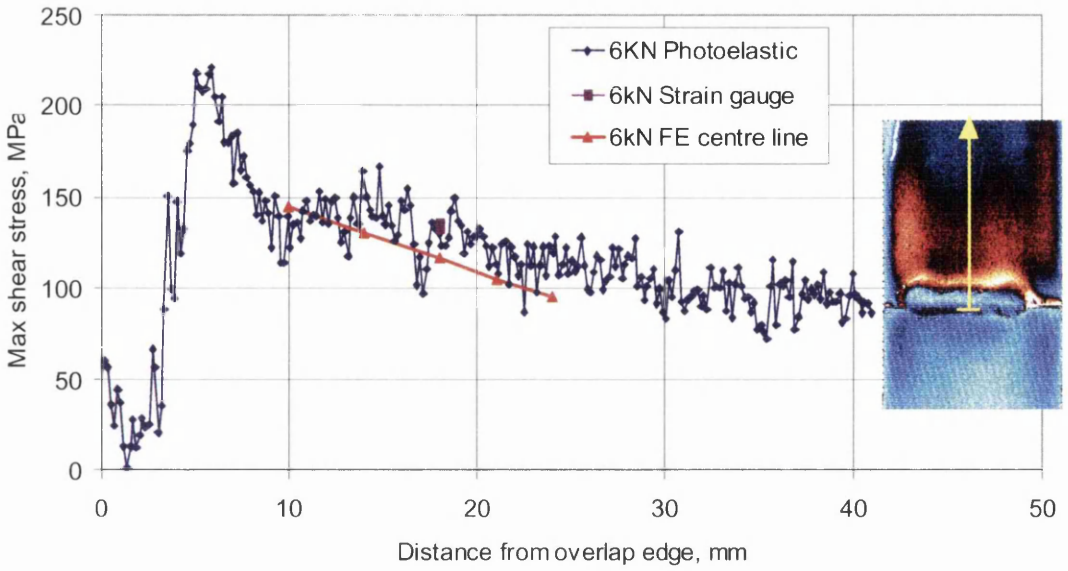

Figure 11.46: M1 6kN Comparison between FE, Photoelastic and Strain Gauging

The results from comparing the three methods of evaluating stress in M2 are shown in figure 11.47 The FE results are again under-predicting the stress measured by the strain gauge in the coupon, but they fall within the photoelastic stress scatter.

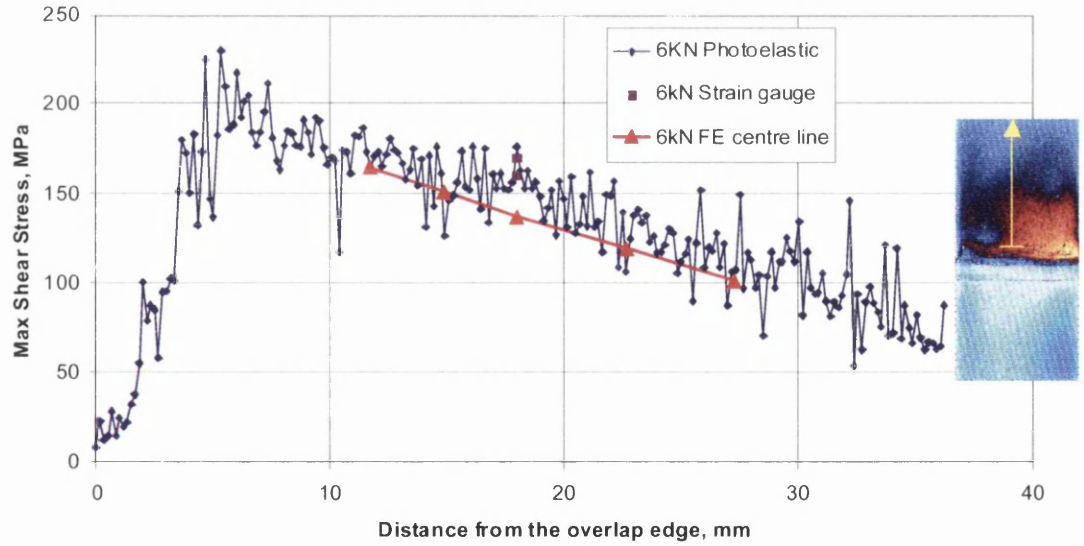

Figure 11.47: M2 6kN Comparison between FE, Photoelastic and Strain Gauging

The FE results for M11A produced a significant under-prediction of the coupon longitudinal stress when compared to both the photoelastic and strain gauging results, as shown in figure 11.48. This under-prediction could also be due to how the FE coupon was modelled, which is discussed in section 12.4.1.

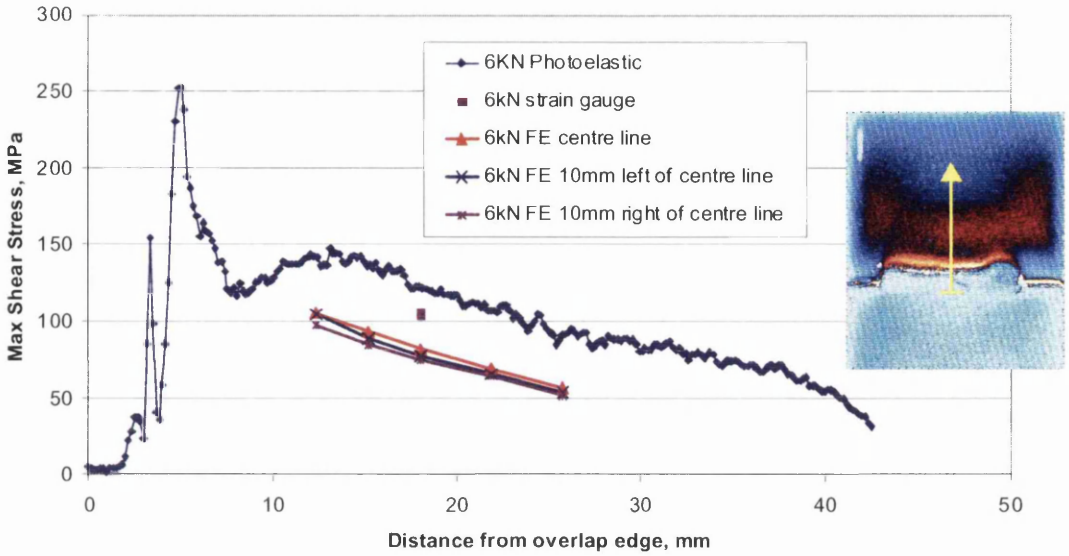

Figure 11.48: M11A 6kN Comparison between FE, Photoelastic and Strain Gauging

11.5.2 Coupon Models used for Volvo Structural Stress Calculations

Coupon geometries were modelled and meshed using the MSC.Patran software based in Corus Automotive. The structures were then analysed by another FE package (MSC Nastran) to obtain the structural deformation stress and strain. Figures 11.49a and 11.49b show the deformation models for GKN and TKA coupon geometries.

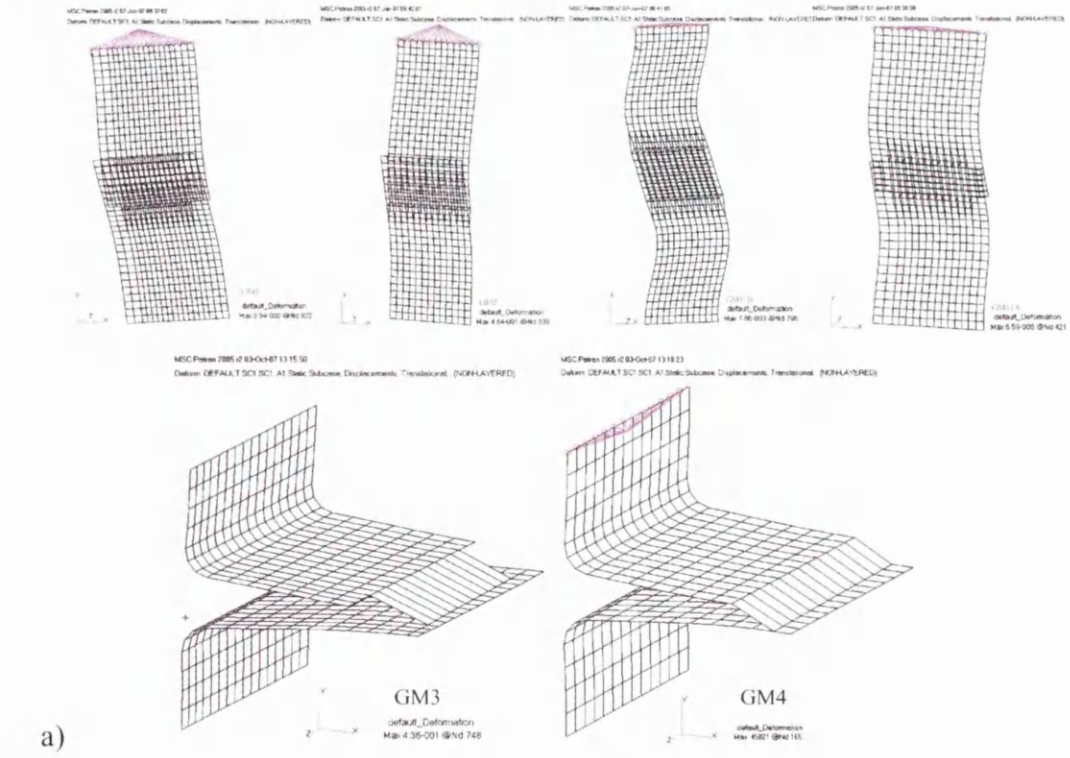

a)

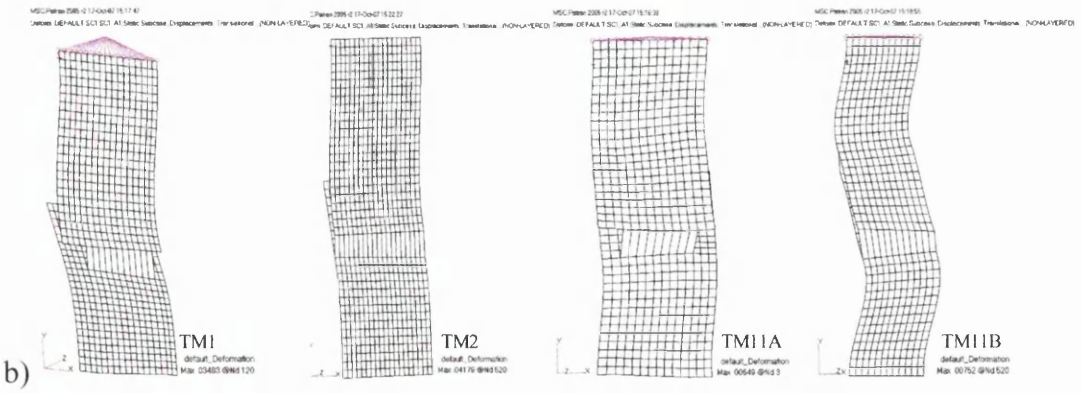

Figure 11.49: The Deformation Models for a) GKN Coupons, b) TKA–Tallent Coupons

11.5.2.1 Volvo Structural Stress for Weld Toe Failure

Figures 11.50 – 11.52 show the stress contour map at the weld toe with a 1kN load applied for TM11A, TM11B and TM2 with the corresponding illustration of failure in the coupons. Table 11.2 shows the structural stresses used to convert load-life to stress-life curves.

Table 11.2: Structural Stress for Toe Failures for a 1kN Applied Load

Coupon	Failure Location	Structural Stress MPa
GM11A	Weld Toe	27.525
GM11B	Weld Toe	25.842
TM11A	Weld Toe	27.421
TM11B	Weld Toe	26.630
TM2	Weld Toe	30.954

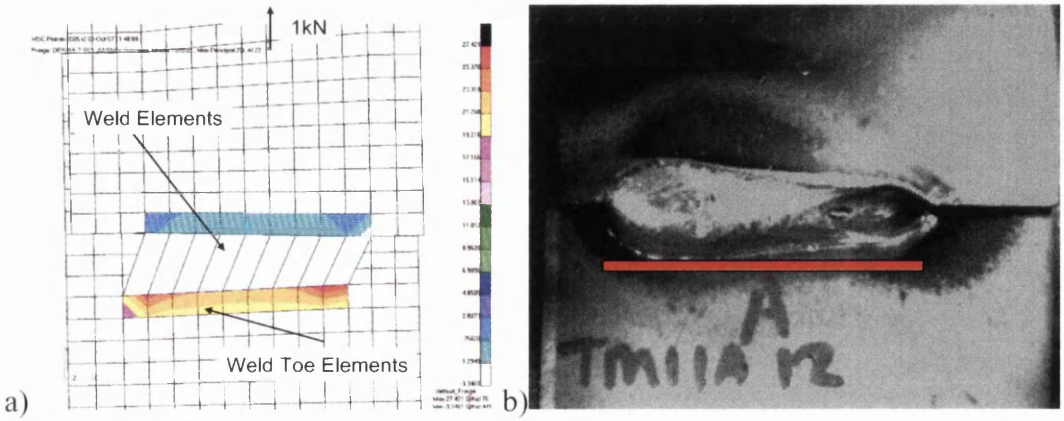

Figure 11.50: a) TM11A FE-Fatigue Stress Contour Map at Weld Toe, b) Location of TM11A Failure

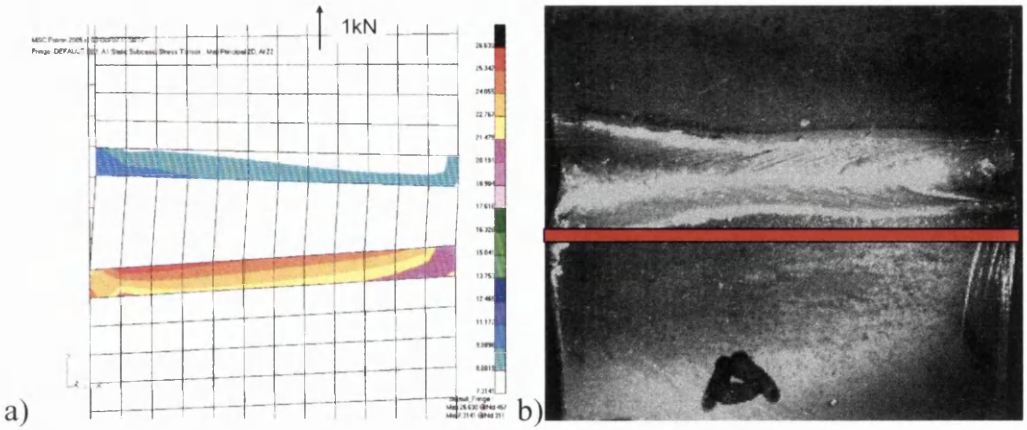

Figure 11.51: a) TM11B FE-Fatigue Stress Contour Map at Weld Toe, b) Location of TM11B Failure

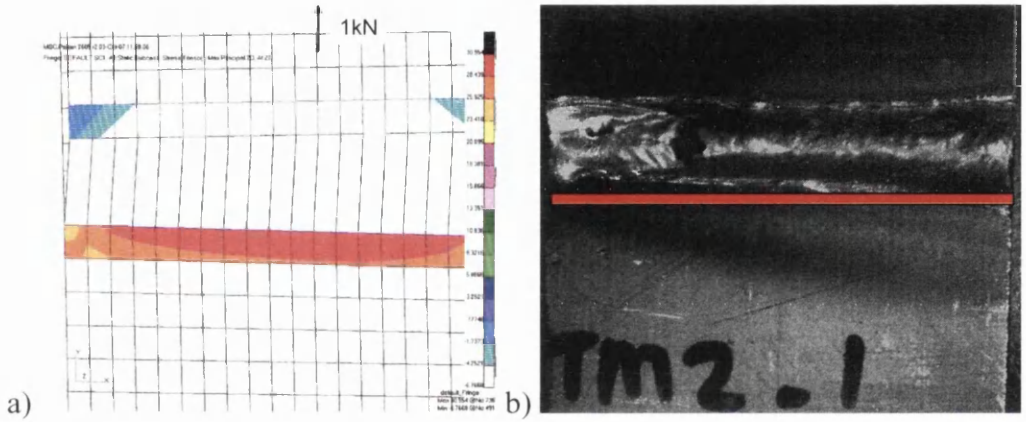

Figure 11.52: a) TM2 FE-Fatigue Stress Contour Map at Weld Toe, b) Location of TM2 Failure

GM11A and GM11B also fail at the weld toe and the MSC.Fatigue stress contour maps and illustration of failure in the coupons are shown in figures 11.53 – 11.54.

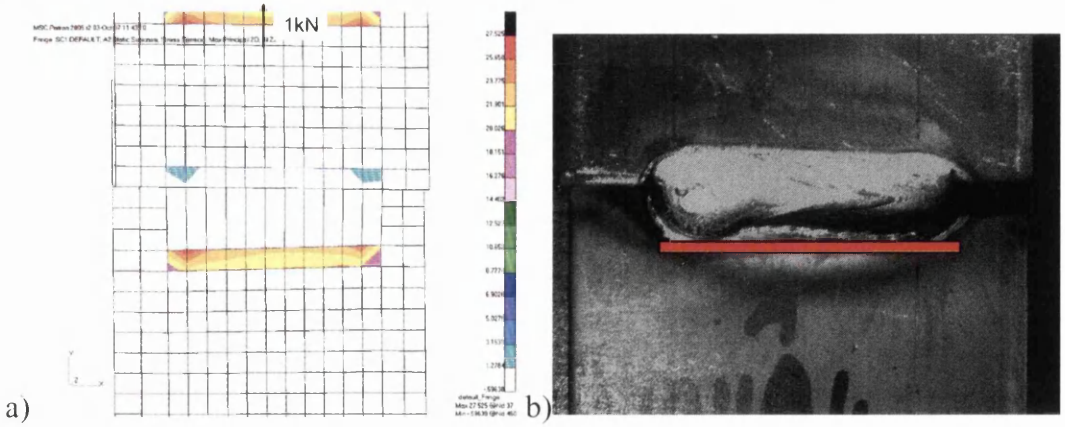

Figure 11.53: a) GM11A FE-Fatigue Stress Contour Map at Weld Toe, b) Location of GM11A Failure

a) 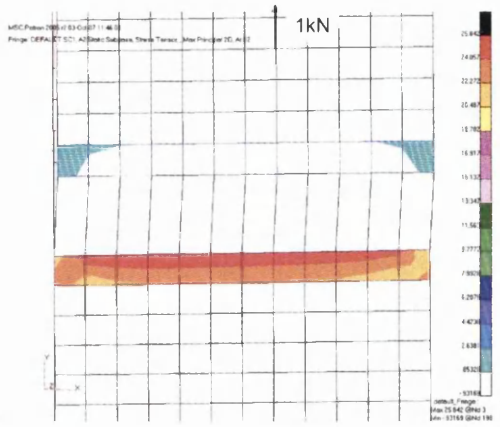

b) 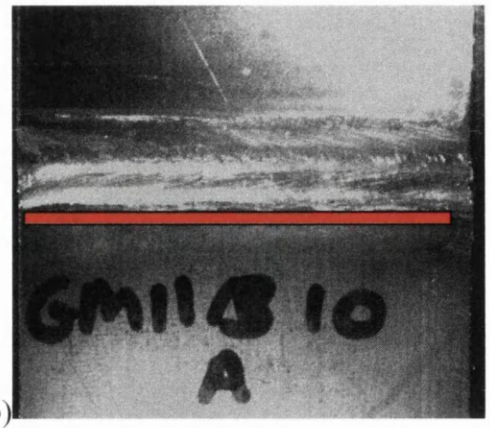

Figure 11.54: a) GM11B FE-Fatigue Stress Contour Map at Weld Toe, b) Location of GM11B Failure

11.5.2.2 Volvo Structural Stress for Weld Throat Failures

All current FE packages have a limitation, which is the inability to predict stress for throat failures. So to use the FE packages, the predicted stress used to calculate fatigue life was researched. From investigating the possible stress locations, shown in figure 11.34, fatigue lives must be calculated from either of these locations. This is done through using the relevant stress from the elements and remembering that each element has two sides (shown in figure 11.35).

Both extraction locations have been investigated and the stresses for throat failure are shown in Table 11.3. Table 11.3 shows that Side B stresses are the highest for the majority of the welds and so therefore the most likely side for fatigue failure to occur.

Table 11.3: Structural Stress at Each Surface of the Element for Throat Failures for a 1kN Applied Load

Coupon	Failure Location	Structural Stress MPa	
		Side A	Side B
TM1	Weld Throat	0.009	**51.867**
GM1	Weld Throat	-0.849	**48.942**
GM2	Weld Throat	0.903	**39.129**
GM3	Weld Throat	488.240	**330.820**
GM4	Weld Throat	426.050	**302.150**

Figures 11.55 – 11.57 show the results from the MSC.Fatigue stress contour maps for GM1, GM2 and TM1 with the corresponding illustration of failure in the coupons.

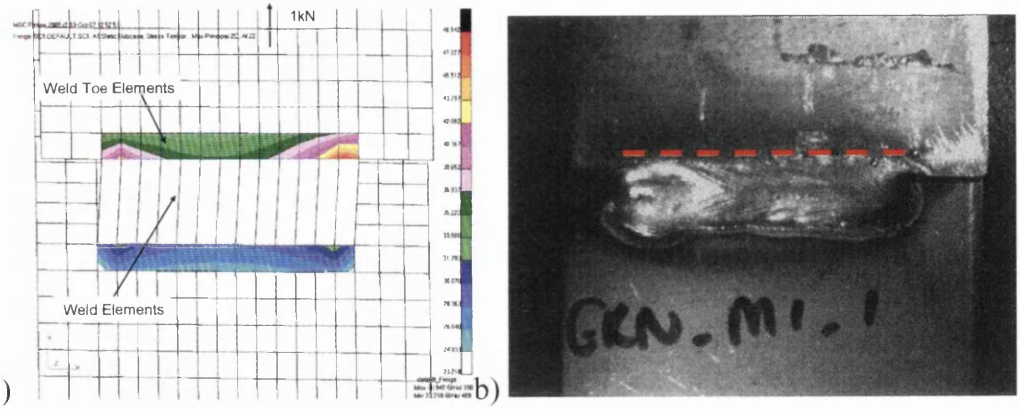

Figure 11.55: a) GM1 FE-Fatigue Stress Contour Map at Weld Throat, b) Location of GM1 Failure

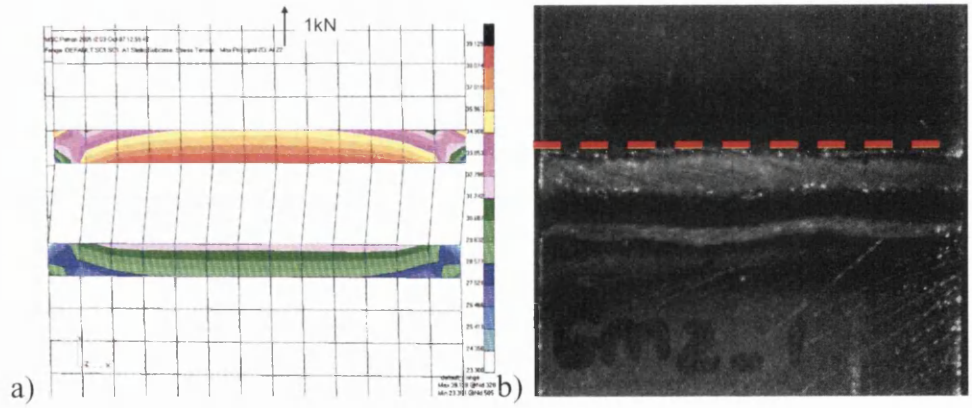

Figure 11.56: a) GM2 FE-Fatigue Stress Contour Map at Weld Throat, b) Location of GM2 Failure

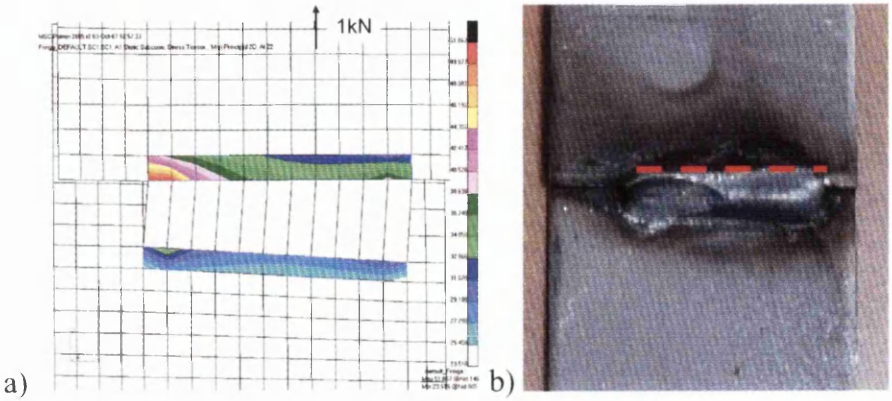

Figure 11.57: a) TM1 FE-Fatigue Stress Contour Map at Weld Throat, b) Location of TM1 Failure

Both GM3 and GM4 (peel geometries) failed at the weld throat and therefore the FE stress was also located behind the weld, the results are shown in figures 11.58 – 11.59.

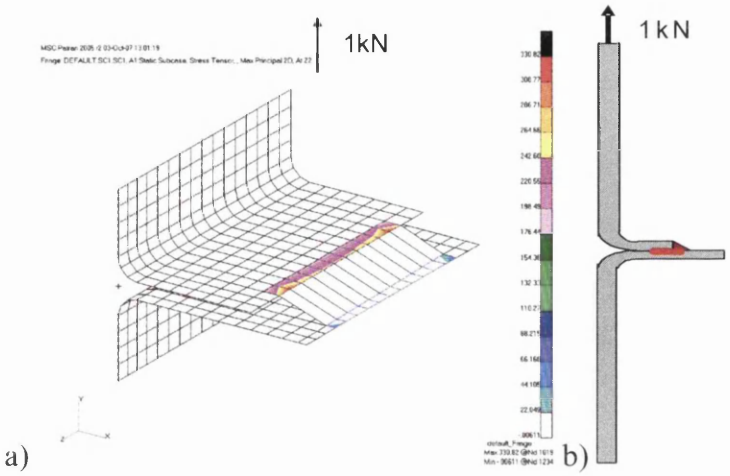

Figure 11.58: a) GM3 FE-Fatigue Stress Contour Map at Weld Throat, b) Location of GM3 Failure

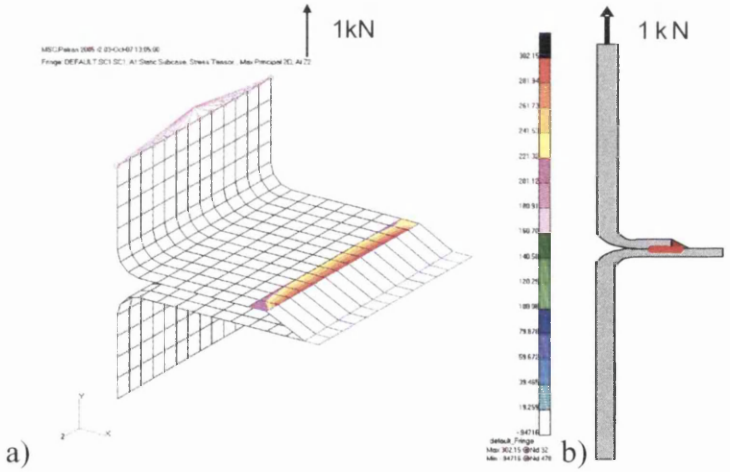

Figure 11.59: a) GM4 FE-Fatigue Stress Contour Map at Weld Throat, b) Location of GM4 Failure

With the coupon geometries modelled and the stress locations found, the $\Delta\sigma/\Delta F$ must be calculated. The results from analysing all the coupon geometries are shown in Table 11.4, which will be used to convert the load–life test data to the S–N master curves.

Table 11.4: MSC.Fatigue (Volvo) Structural Stress for a 1kN Applied Load

Coupon	Failure Location	Structural Stress MPa	Bending Ratio	
			Curve	Value
GM11A	Weld Toe	27.525	Flexible	0.639
GM11B	Weld Toe	25.842	Flexible	0.632
TM11A	Weld Toe	27.421	Flexible	0.660
TM11B	Weld Toe	26.630	Flexible	0.633
TM2	Weld Toe	30.954	Flexible	0.704
		Side B		
TM1	Weld Throat	51.867	Flexible	0.749
GM1	Weld Throat	48.942	Flexible	0.734
GM2	Weld Throat	39.129	Flexible	0.756
GM3	Weld Throat	330.820	Flexible	0.990
GM4	Weld Throat	302.150	Flexible	0.993

11.5.3 Coupon Models used for Battelle Structural Stress Manual Calculations

The Battelle Structural Stress was calculated from these three methods for all the coupon joints:

1) Manual Calculation
2) FLOW software
3) Fe-Safe Verity®

The results shown are the Manual Calculation, with the FLOW and Verity results in the Appendix 6.

All techniques using the Battelle method require the "Structural stress" to be converted into the Equivalent Structural Stress as described in section 10.7. Equivalent Structural stress is calculated from the structural stress using Eq.15

$$\Delta S_s = \frac{\Delta \sigma_s}{t^{\frac{2-m}{2m}} . I(r)_m^{\frac{1}{m}}} \qquad \text{Eq.15}$$

This correction factors in the denominator of Eq.15 are based on the unit 'mm', but this unit is not used in the formula so as a result the equivalent structural stress still uses the unit Nmm^{-2} or MPa.

Coupon geometries were modelled and meshed using the MSC.Patran software based in Corus Automotive. The structures were then analysed by another FE package (MSC Nastran) to obtain the structural deformation stress and strain. Figures 11.60a

and 11.60b show the deformation models for GKN and TKA-Tallent coupon geometries.

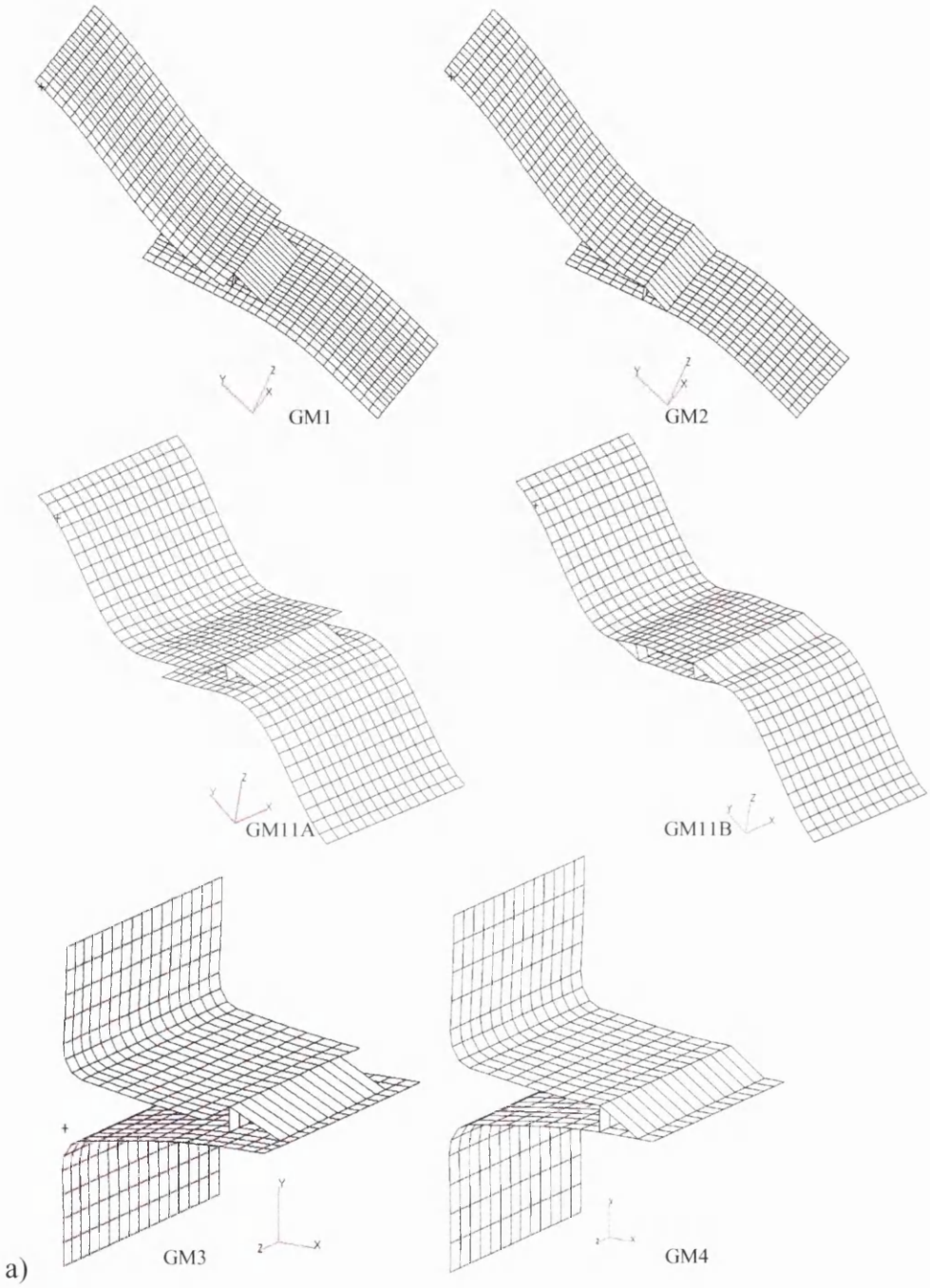

a)

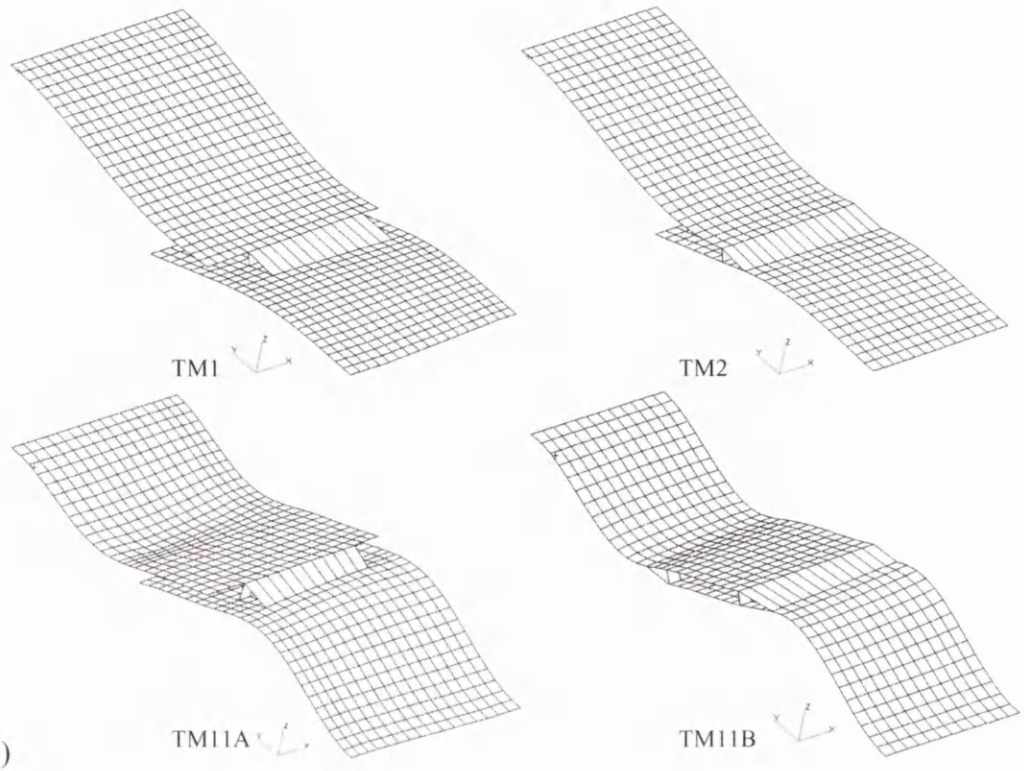

Figure 11.60: The Deformation Models for a) GKN Coupons, b) TKA–Tallent Coupons

11.5.3.1 Battelle Structural Stress for Weld Toe Failures

Using the method explained in section 10.7 the results of the Battelle Manual Calculation is shown below in Figures 11.61 – 11.65. Alongside all the figures is the typical picture of each of the weld geometries, which were tested. The manual calculation involved calculating the structural stress and the equivalent structural stress. For all geometries the equivalent structural stress is higher than the structural stress.

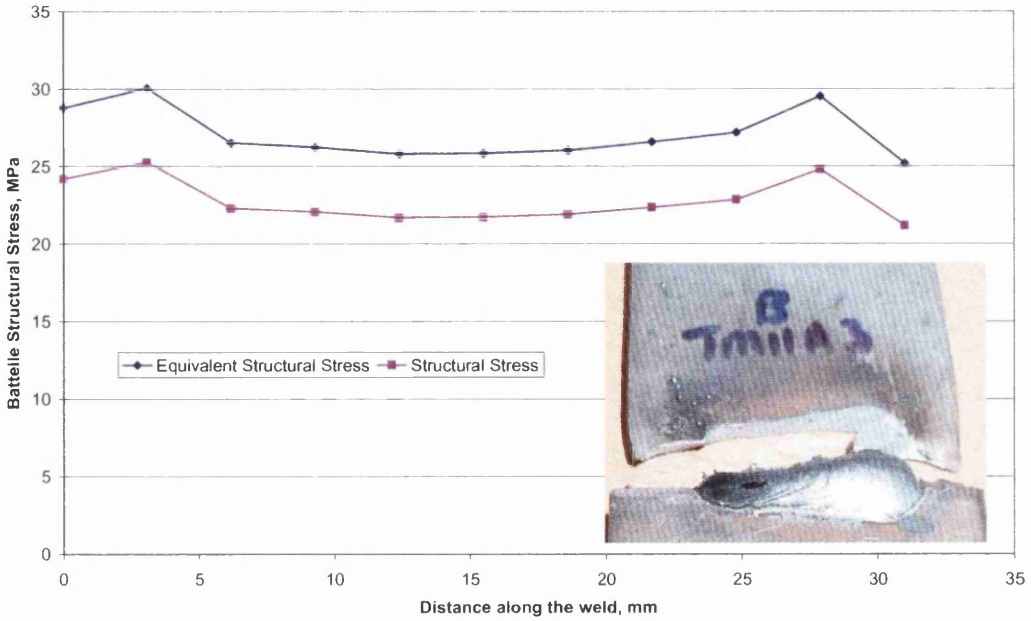

Figure 11.61: Manual Calculation of TM11A with Image of Weld

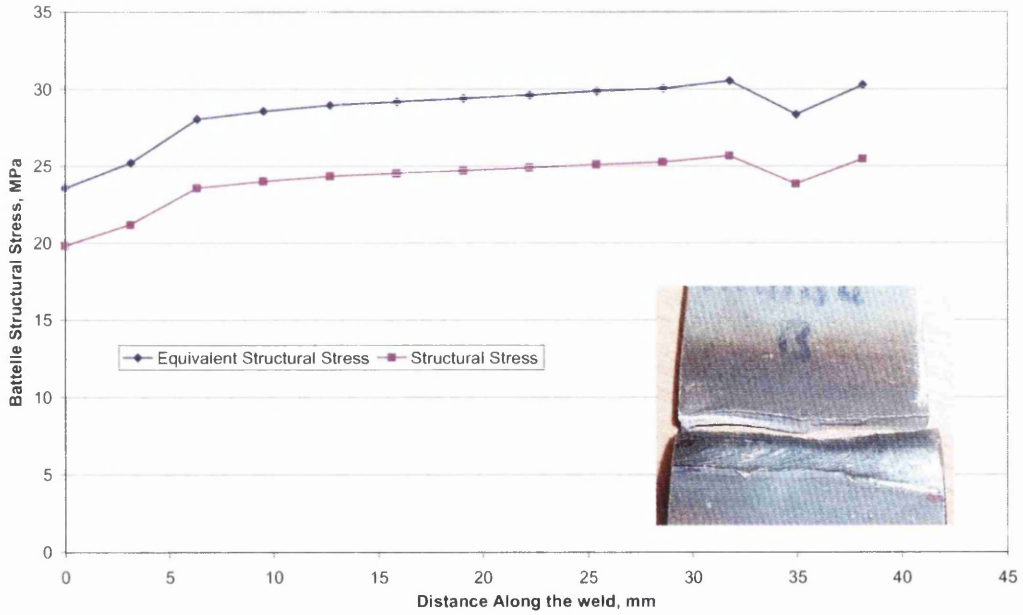

Figure 11.62: Manual Calculation of TM11B with Image of Weld

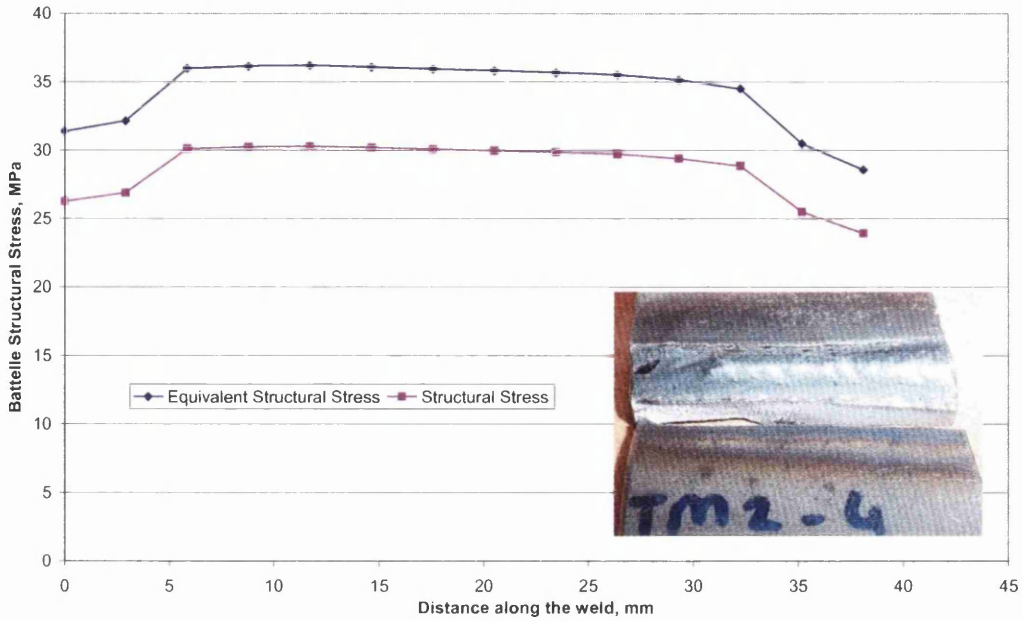

Figure 11.63: Manual Calculation of TM2 with Image of Weld

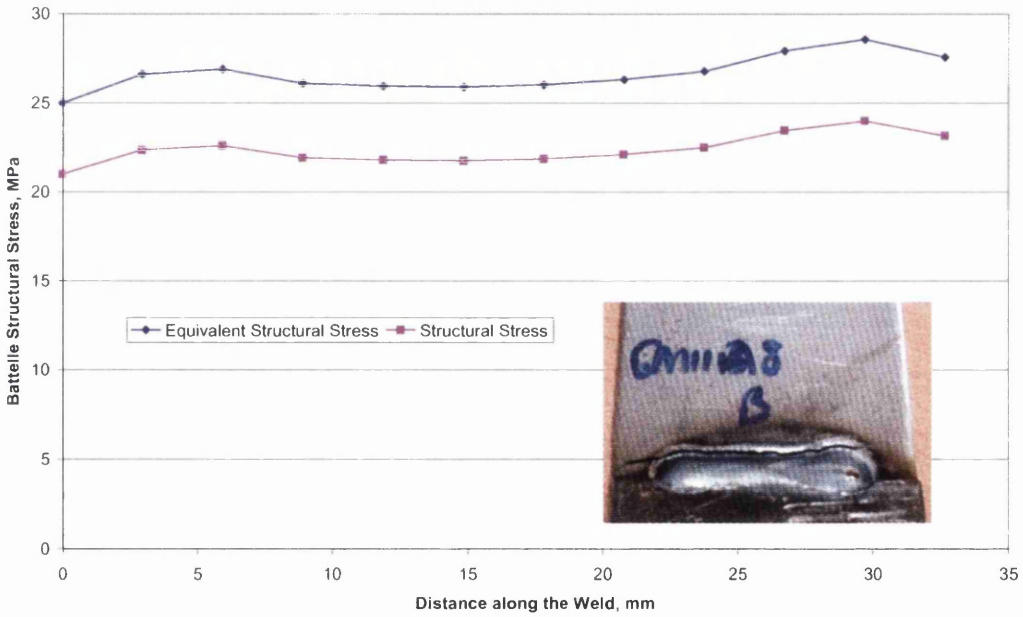

Figure 11.64: Manual Calculation of GM11A with Image of Weld

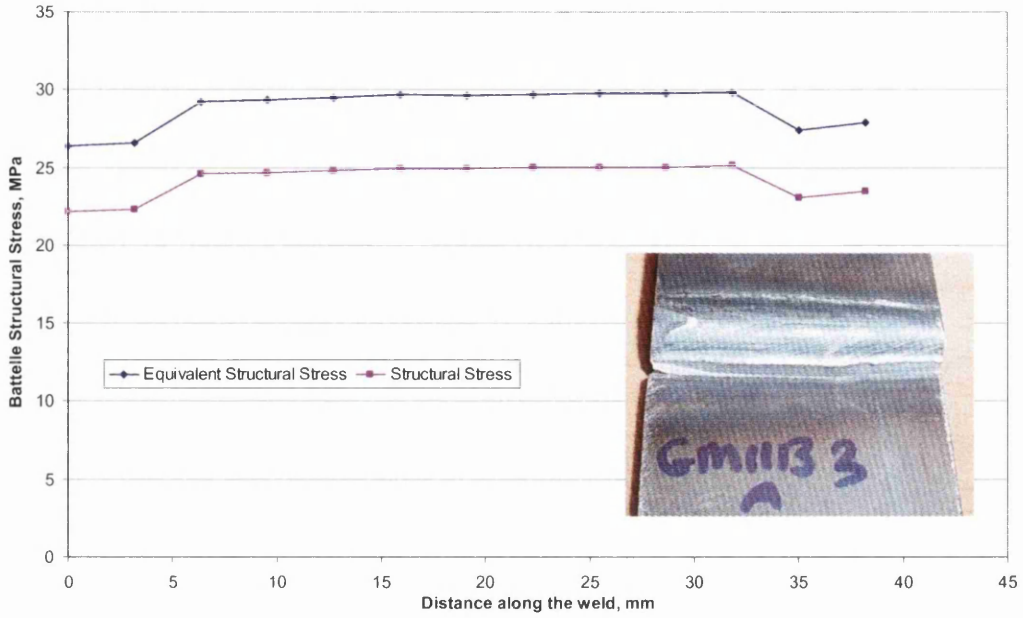

Figure 11.65: Manual Calculation of GM11B with Image of Weld

11.5.3.2 Battelle Structural Stress for Weld Throat Failures

The structural stress was calculated from the same location as the Volvo structural stress i.e. the Z1 plane of side B as shown in figure 11.66. Figures 11.67 – 11.71 show the results of the Battelle Manual calculation for the weld throat failures. For all geometries the equivalent structural stress is higher than the structural stress.

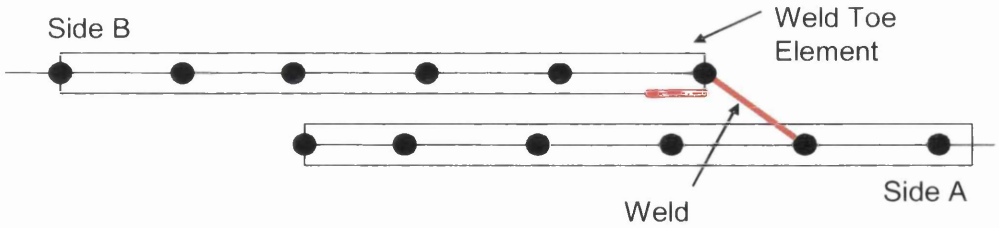

Figure 11.66: Location of Structural Stress used in Calculations

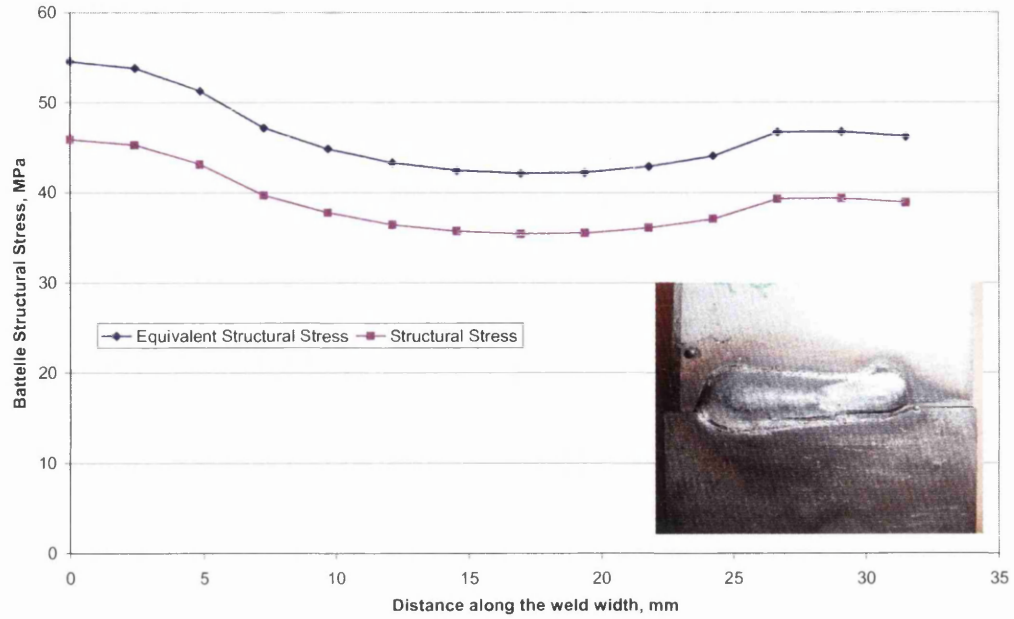

Figure 11.67: Manual Calculation of GM1 with Image of Weld

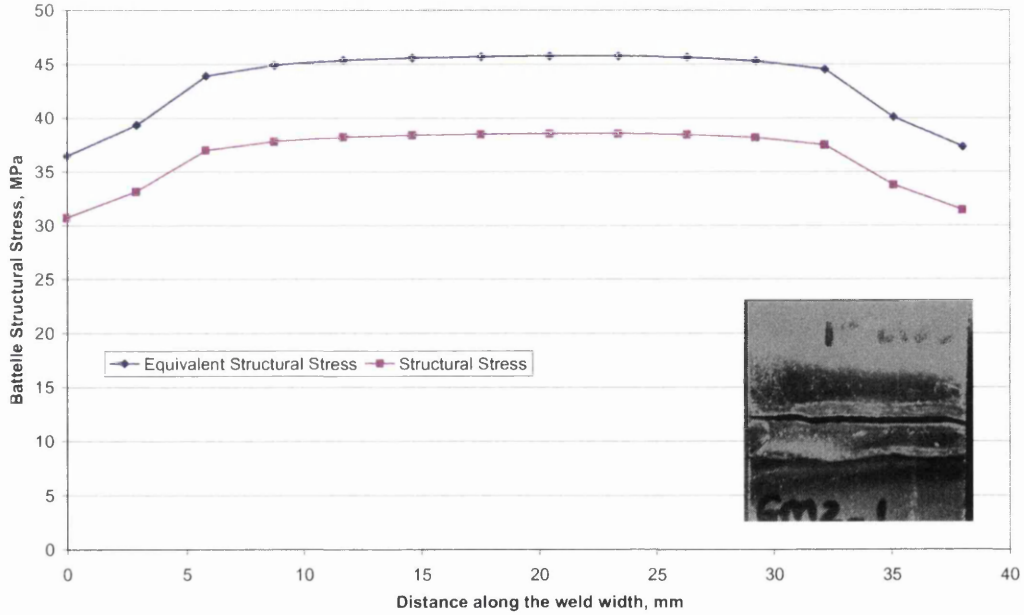

Figure 11.68: Manual Calculation of GM2 with Image of Weld

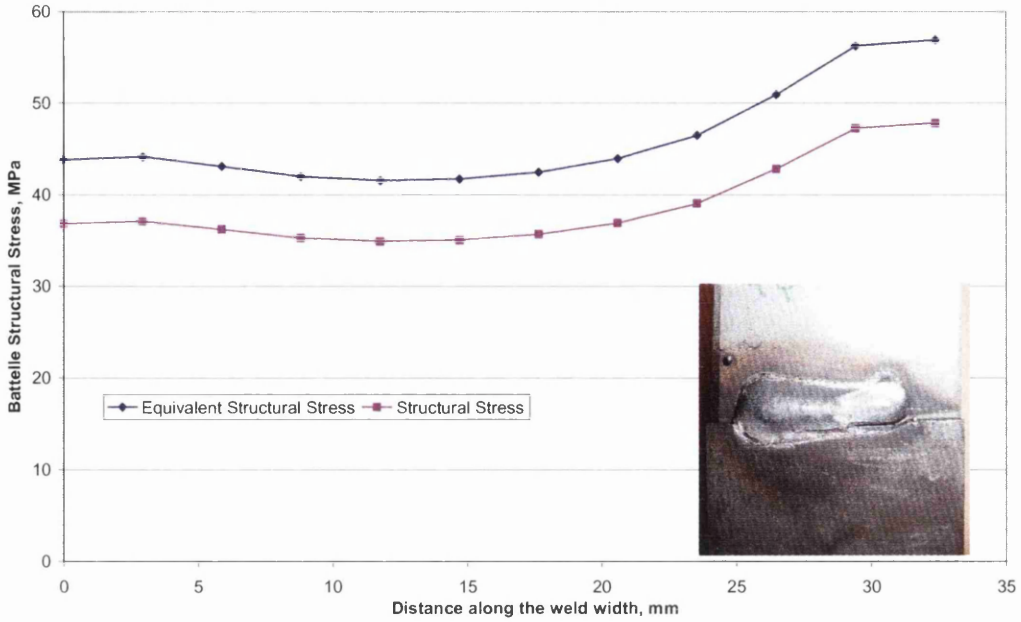

Figure 11.69: Manual Calculation of TM1 with Image of Weld

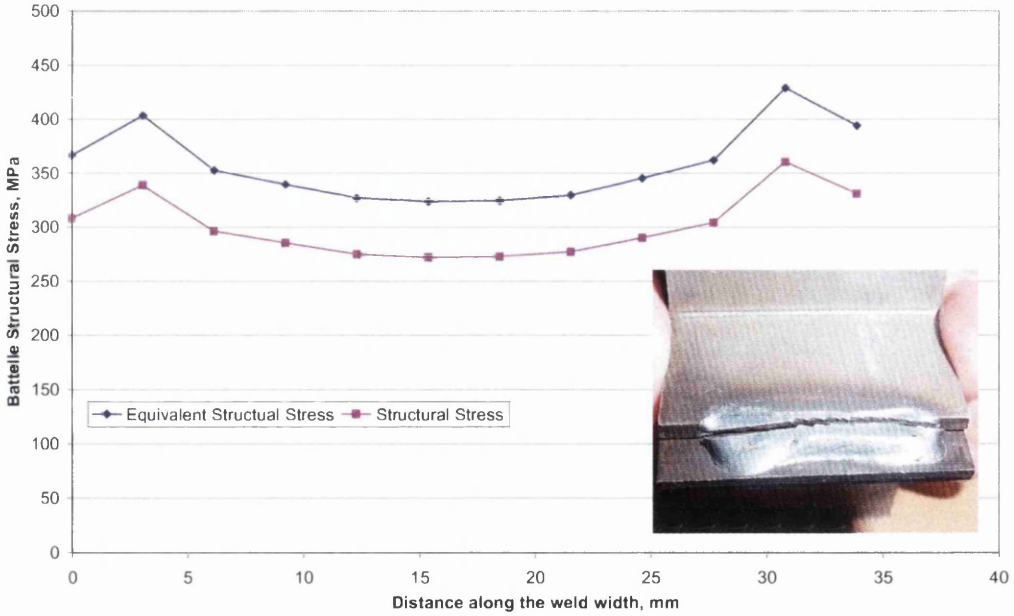

Figure 11.70: Manual Calculation of GM3 with Image of Weld

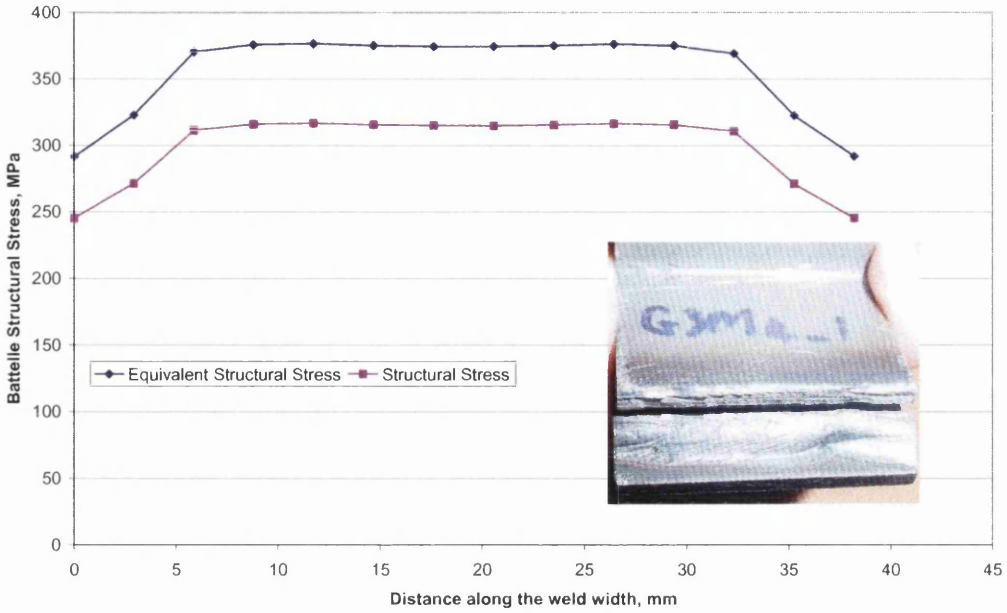

Figure 11.71: Manual Calculation of GM4 with Image of Weld

11.5.3.3 Battelle Structural Stress Manual vs. FLOW and Verity

Figures 11.72 – 11.73 show the difference in the three methods of predicting the Battelle Structural Stress. For both GM11A and GM11B, the manual and Verity results are close with FLOW marginally higher. As these results are consistent the other difference between the three methods for the other coupon geometries are shown in Appendix 6.

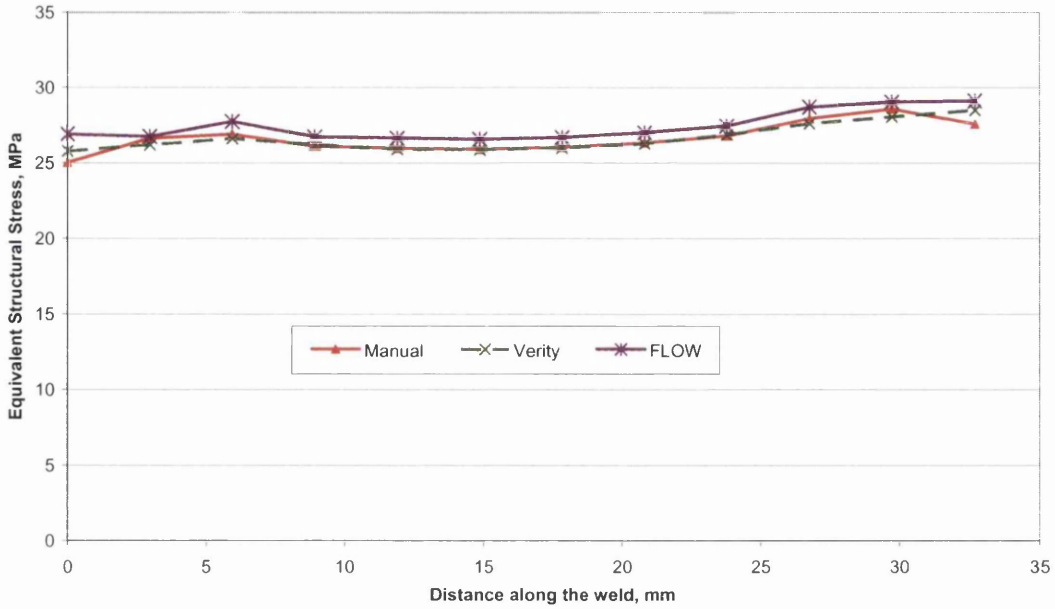

Figure 11.72: Battelle Equivalent Structural Stress Manual vs. FLOW & Verity for GM11A

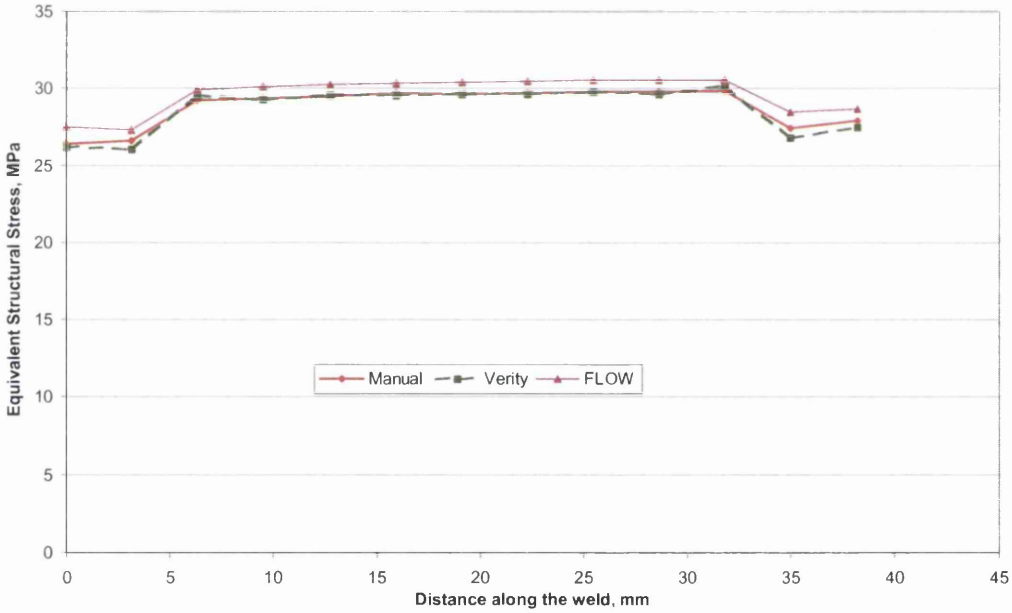

Figure 11.73: Battelle Equivalent Structural Stress Manual vs. FLOW & Verity for GM11B

Table 11.5 shows the structural stresses used to convert the load-life test data into the stress life curves.

Table 11.5: Battelle Structural Stress for a 1kN Applied Load

Coupon	Failure Locations	Equivalent Structural Stress MPa		
		Manual Centre	FLOW Centre	Verity Centre
GM11A	Weld Toe	28.553	29.035	28.058
GM11B	Weld Toe	29.840	30.497	30.204
TM11A	Weld Toe	30.062	29.688	30.006
TM11B	Weld Toe	30.516	31.034	30.866
TM2	Weld Toe	35.965	36.836	36.437
		Side B	**Side B**	**Side B**
TM1	Weld Throat	50.921	51.916	50.595
GM1	Weld Throat	51.235	52.284	50.822
GM2	Weld Throat	44.127	45.369	45.218
GM3	Weld Throat	361.684	375.238	370.489
GM4	Weld Throat	369.096	380.267	377.384

11.5.4 Structural Stress Master Curves

Using the Structural stress values shown in both Tables 11.4 and 11.5 and the load-life data in section 11.2, the conversion into Stress-Life Master Curves will be described in sections 12.4.2 and 12.4.3.

11.6 FUCA Component Fatigue Test Results

The purpose of FUCA component testing is to provide fatigue life test data for comparison with the FE predictions of the same component.

11.6.1 Failure Locations

From all the constant amplitude component tests, the majority of the components had the crack initiating from the notch at the weld start and propagating through the weld throat (Figure 11.74a) before propagating out into the parent material in the flange (Figure 11.74b). Component #12 was the only component where the crack initiated from the weld notch and propagated directly through the flange parent metal as shown in Figure 11.75. Termination for all the tests required a crack size of 40 – 50mm, this is shown in Figure 11.76.

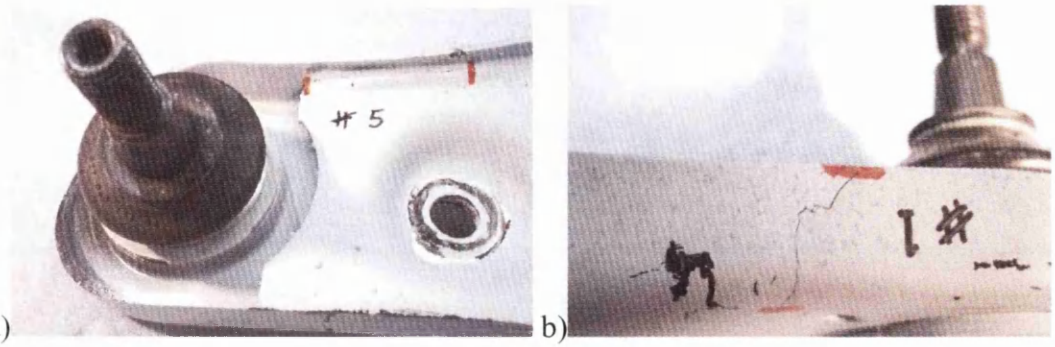

Figure 11.74: Typical Failure Locations in the FUCA a) Crack Propagation through the Weld Throat, b) Crack Propagation from the Weld Throat into the Parent Metal

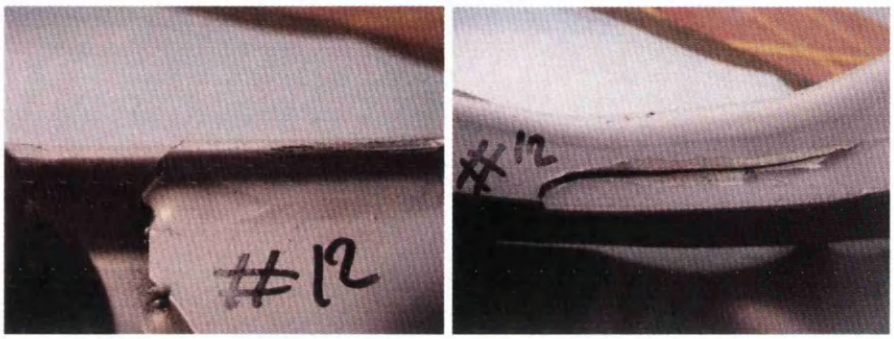

Figure 11.75: Crack Initiated at the Notch and Propagated through the Parent Material in the Flange

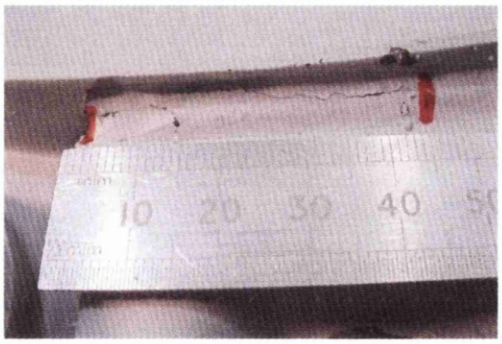

Figure 11.76: Prescribed Termination Criterion of Crack Length for Component Tests

From all the variable amplitude component tests using the SAE Bracket Load-Time History, all the components failed in a similar way to constant amplitude as shown in figure 11.77.

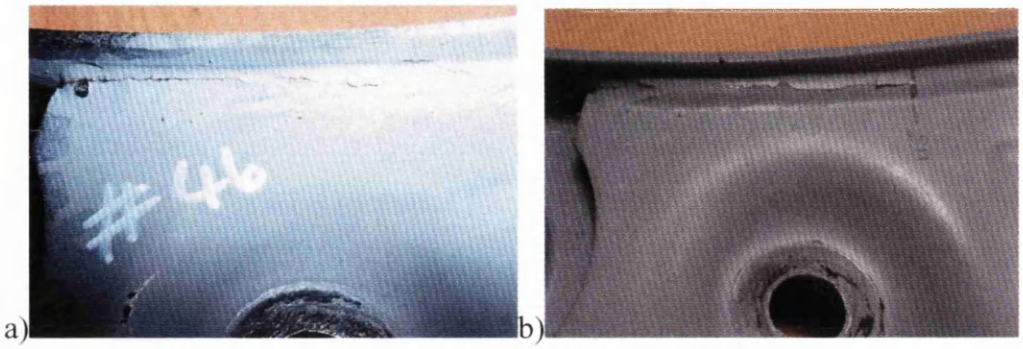

Figure 11.77: Typical Failure Locations in the FUCA for Variable Amplitude a) Block Loading, b) SAE Bracket Load-Time History

11.7.1.1 Fracture Surface Analysis

From observing the main modes of failure shown in figures 11.75 – 11.77, figure 11.78 shows how the following fracture surfaces were examined. The typical fracture surfaces for FUCA weld throat failures are shown below in figures 11.79.

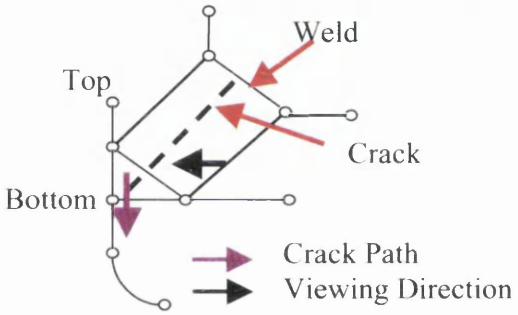

Figure 11.78: Viewing Angles for the Fracture Surface Examination

Figure 11.79 show the typical weld failure seen in the components. Fatigue initiation sites were fairly hard to identify due to damage caused during the fatigue test, and subsequent corrosion of the fracture surface due to long testing times in a non-environmentally controlled industrial laboratory. The initiation sites would be located just in from the paint layer at the root of the weld.

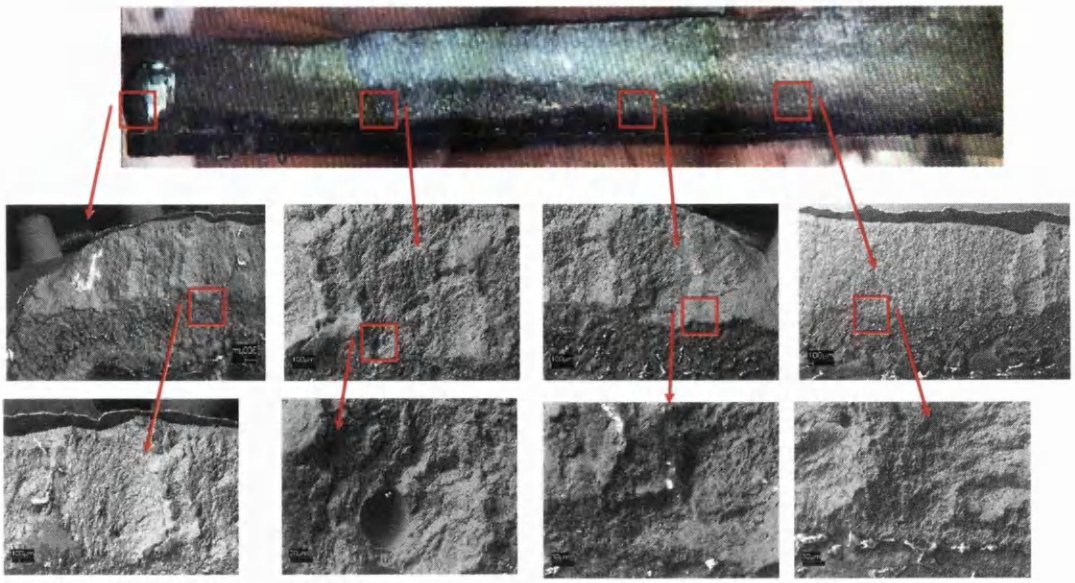

Figure 11.79: Typical FUCA Component Throat Failure

As all the other FUCA components show very similar fracture surfaces they will be found in Appendix 7.

11.6.2 Constant Amplitude FUCA Component Testing

Initial testing of a front upper control arm (FUCA) on the component rig started with constant amplitude loading of three different load levels of ±2.5kN, ±4.0kN and ±7.0kN at 2Hz, with the crack propagation measured until component failure at a crack size of 40mm. At 7kN there is some scatter in the results, whilst at both 2kN and 4kN the fatigue lives were consistent as shown in figure 11.80.

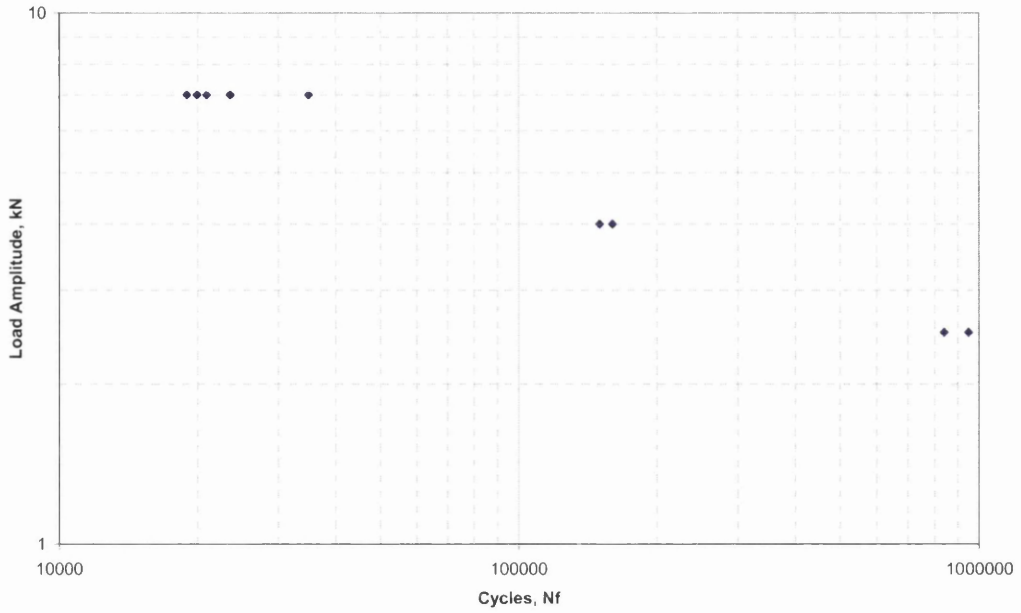

Figure 11.80: Constant Amplitude FUCA Results (Crack Length 40~50mm)

Component #12 is the only component where the crack did not propagate through the weld, but failed through the parent metal on the flange. With components #9 and #14, unfortunately the crack initiation size of 10mm was not noticed on the surface of the weld until failure. Further tests were undertaken to obtain crack initiation data and final number of cycles to failure.

The results in figure 11.81 shows that from the ten tests there is reasonable scatter between the results at each level due in part to slight differences in the placement of the weld and crack start position. It is also worth noting from figure 11.81 that, at ±2.5kN there is a much larger scatter in the life for crack initiation to 10mm (between 430,000 and 700,000 cycles).

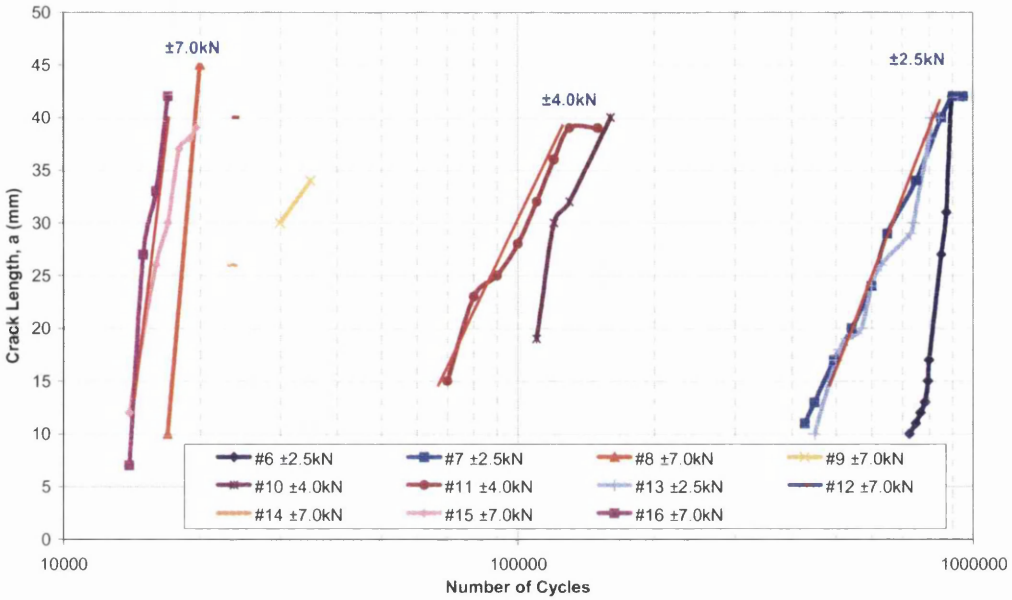

Figure 11.81: Crack Length versus Fatigue Life for FUCA

Further analysis of the data shown in figure 11.81 for variable amplitude loading conditions requires information of crack lengths to 30mm. For subsequent prediction of FUCA component, lives to crack lengths of 10mm is also required. Unfortunately for some tests this crack initiation information is not available. This is due to the crack initiating from the weld root and not visible to the eye as it has not appeared on the surface of the weld, but is still propagating through the weld. To gain this information for some crack initiation, extrapolation of the data is required.

The component fatigue test results were processed in more detail with measured component lives to specific crack sizes shown in figure 11.82 for lives at crack initiation (first visible crack length of 10mm), 20mm and 30mm.

With a high load level of ±7.0kN, the data collected was in the 10^4 cycles range and figure 11.82 shows that measured components average life to crack size of 10mm occurred at 14594 cycles. For the crack to propagate to 20mm, the life is 16362 cycles whilst for the crack to propagate from 20mm-30mm took a further 1159 cycles. The average crack growth rate da/dN is 1.172×10^{-3}mm/cycle.

With an intermediate load level of ±4.0kN, the data collected was up to 10^5 cycles range and figure 11.82 shows that measured components average life to crack size of

10mm occurred at 79999 cycles. For the crack to propagate to 20mm, the life is 94113 cycles whilst for the crack to propagate from 20mm-30mm took a further 18428 cycles. The average crack growth rate da/dN is 2.66×10^{-4} mm/cycle.

With a low load level of ±2.5kN, the data collected was up to 10^6 cycles range and figure 11.82 shows that measured components average life to crack size of 10mm occurred at 500353 cycles. For the crack to propagate to 20mm, the life reaches 651453 cycles whilst for the crack to propagate from 20mm-30mm took a further 115862 cycles. The average crack growth rate da/dN is 3.91×10^{-5}mm/cycle.

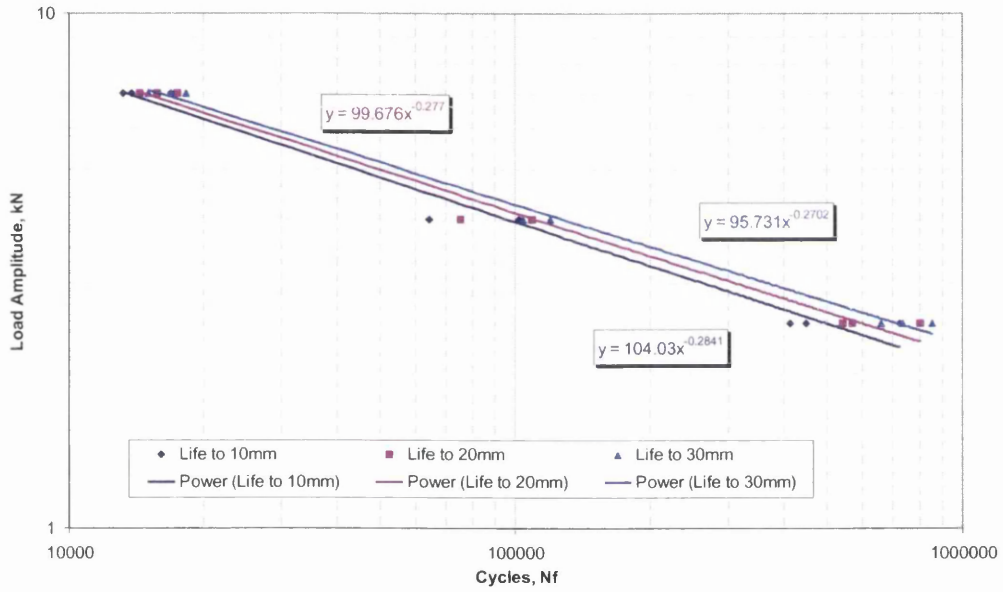

Figure 11.82: Actual Component Lives to Various Crack Lengths (R=-1)

11.6.3 Variable Amplitude Block Loading

Figure 11.83 shows the results of the two block loading levels. The graph is plotted to show the effect of the life against the range of both load levels in each of the block loading signals. This shows that the first load range of each level has the most damaging cycles.

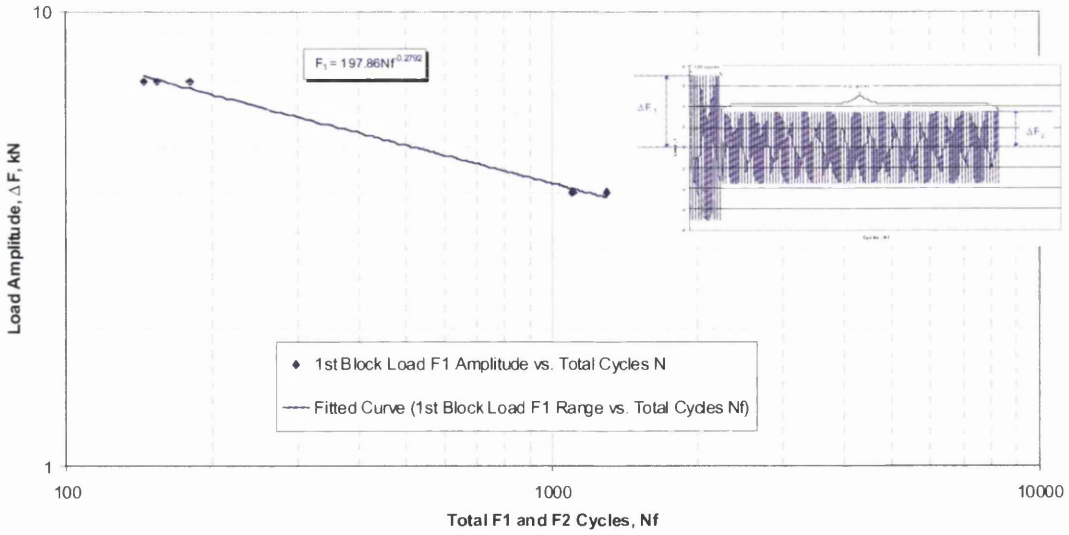

Figure 11.83: Block Loading Results for R-Ratio=-1

Table 11.6 shows the test results for all FUCA components tested at R-ratios of R=0.1 and R=-1 block loading sequences, shown in figures 10.20 – 10.22.

Table 11.6: FUCA Block Loading Results

Specimen ID	Repeats	Failure Location	R Value
#40	4000	Toe Failure	R= 0.1
#41	145.1	Toe Failure	R= -1
#42	180.1	Toe Failure	R= -1
#43	154.2	Toe Failure	R= -1
#44	1301.3	Toe Failure	R= -1
#45	1101.1	Toe Failure	R= -1
#46	1101.1	Toe Failure	R= -1

11.6.4 Variable Amplitude SAE Bracket Load-Time History

Variable amplitude results using the SAE Bracket Load – Time History are shown in figure 11.84. The majority of the tested components had results which were very consistent between 150 and 200 block repeats of the SAE Bracket signal as shown in figure 11.85. Only component numbers 26, 34, 36 and 37 were unsuccessful in failing within the 150-200 repeats range.

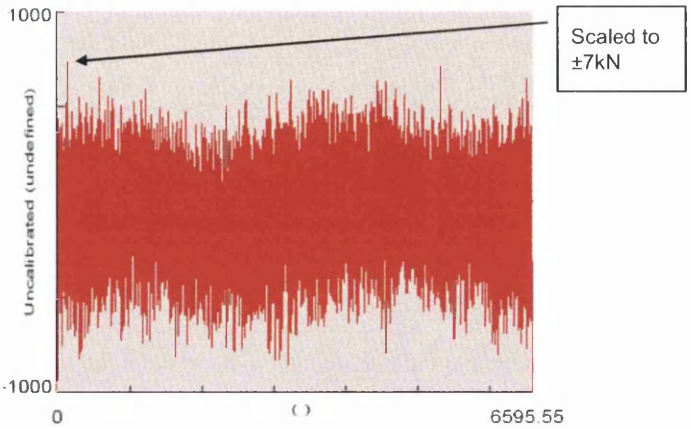

Figure 11.84: SAE Bracket Load – Time History

During testing of component number 26, there were many problems with the rig due to parts being worn out and requiring replacement. This was believed to be the main cause for the longer test life of the FUCA, as no accurate load was being applied. The short life shown for component number 34 arises from the anti-roll bar link, which applies the load to the FUCA being worn out so no accurate loading was being applied. The shorter life of component number 36 comes from the weld being imperfect and resulting in a small notch to the weld as shown in figure 11.86. Regarding the shorter life of component number 37, after investigating the weld start/stop location no defect or imperfection was noticeable in the weld and so the shorter life was just due to fatigue.

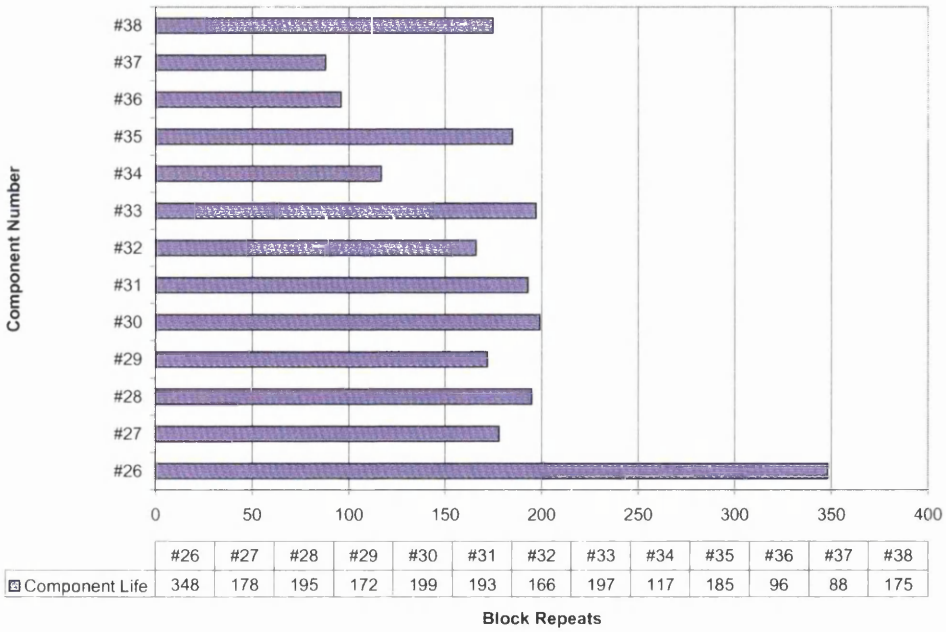

	#26	#27	#28	#29	#30	#31	#32	#33	#34	#35	#36	#37	#38
Component Life	348	178	195	172	199	193	166	197	117	185	96	88	175

Figure 11.85: Variable Amplitude Results ± 7kN

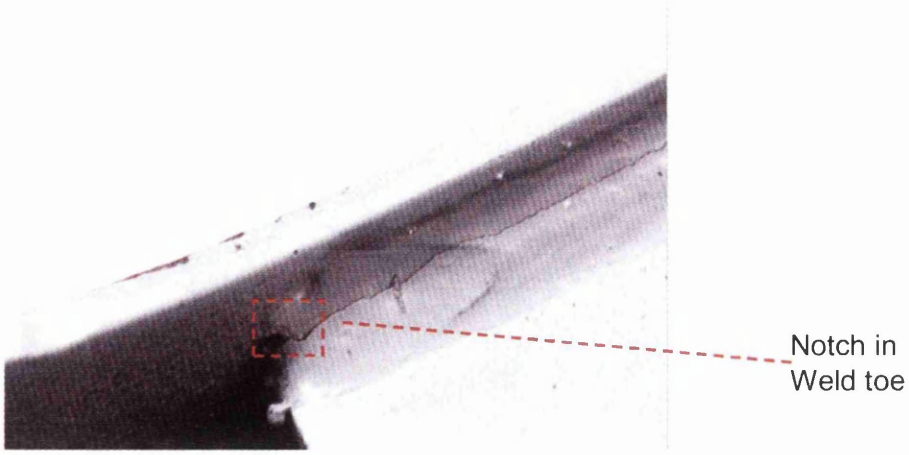

Figure 11.86: Component 36 with notched weld

11.7 FUCA Life Predictions – Constant Amplitude Loading

The ability to accurately predict the fatigue lives of actual test components is a method that will enable a large reduction in cost and decrease time to production of cars for automotive manufacturers. This will be achieved by using the S-N curves produced from the coupon fatigue test data and together with the weld root element stress to calculate the estimated fatigue lives of the FUCA component.

The models used were built as described in section 10.6.3.

Both the Volvo and Battelle methods deal with "toe failure" only, and require the structural stress to be calculated from the weld toes. This is performed by selecting the required weld lines from which the maximum structural stress will be determined.

However, the mode of failure for the FUCA component was identified as "throat failure". There is no established procedure for locating and calculating the structural stress required for fatigue analysis. Consequently, determining the throat-failure structural stress became one of the main areas of investigation and development in my current EngD research programme.

11.7.1 FUCA Model Volvo Method

All four baseline models were investigated using the peel statistical analysis curves shown in section 12.4.2 - figure 12.46, which exhibited a similar failure mode to the FUCA components – Throat Failure.

The stresses chosen on the weld line were the first 10 nodal stresses, from this the first stress and the maximum (max) stress of the first 6 elements was used to predict the life (shown in figure 11.87). Using the first and max stresses from the models and rearranging Eq.36 to obtain the estimated life in cycles of the FUCA component. Values of the constants 'a' and 'b' used were from the master weld S-N curves for 50% and 99.87% certainties of survival.

$$\sigma = aN_f^{\ b} \qquad \text{Eq.36}$$

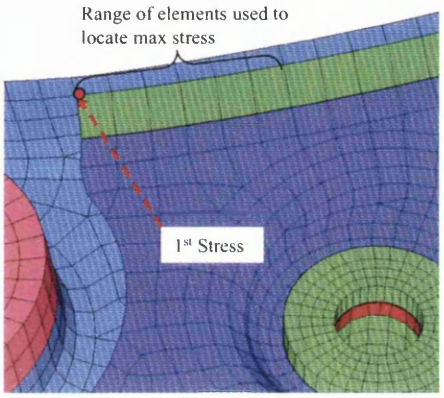

Figure 11.87: Locations of the 1st and Max Stress

For calculating the predicted life the calculated Volvo Structural Stress will use the formula generated from the peel S-N curve shown in figure 12.55. Table 11.7 shows the stress range and life values generated.

Table 11.7: Volvo Structural Stress and Life Calculations using 50% Survival $\Delta\sigma = 3034.7.Nf^{-0.2205}$

Model	Stress Location	±7kN		±4kN		±2.5kN	
		Stress Range MPa	Life	Stress Range MPa	Life	Stress Range MPa	Life
Full-Length	1st	657.84	1.03E+03	375.91	1.30E+04	234.94	1.09E+05
	Max	725.50	6.58E+02	414.57	8.33E+03	259.11	7.02E+04
Full-Length	1st	335.40	2.18E+04	191.66	2.76E+05	119.79	2.32E+06
	Max	369.22	1.41E+04	210.98	1.78E+05	131.86	1.50E+06
Cut-Length Standard	1st	750.48	5.65E+02	428.85	7.15E+03	268.03	6.02E+04
	Max	799.38	4.24E+02	456.79	5.37E+03	285.49	4.52E+04
Cut-Length Triangular	1st	417.96	8.03E+03	238.83	1.02E+05	149.27	8.56E+05
	Max	417.96	8.03E+03	238.83	1.02E+05	149.27	8.56E+05

Investigating the effects of having full-length versus cut-length welds for the 1st stress is shown in figures 11.88 – 11.89. Comparing the mean test data with the 50% certainty of survival (mean) the full-length weld accurately predicts the test data at 7kN but over predicts the life at both 4kN and 2.5kN by 100,000 and 1,000,000

cycles respectively. Whereas the cut-length weld under-predicts at 7kN and 4kN by 10,000 and 50,000 cycles respectively but accurately predicts the 2.5kN test data.

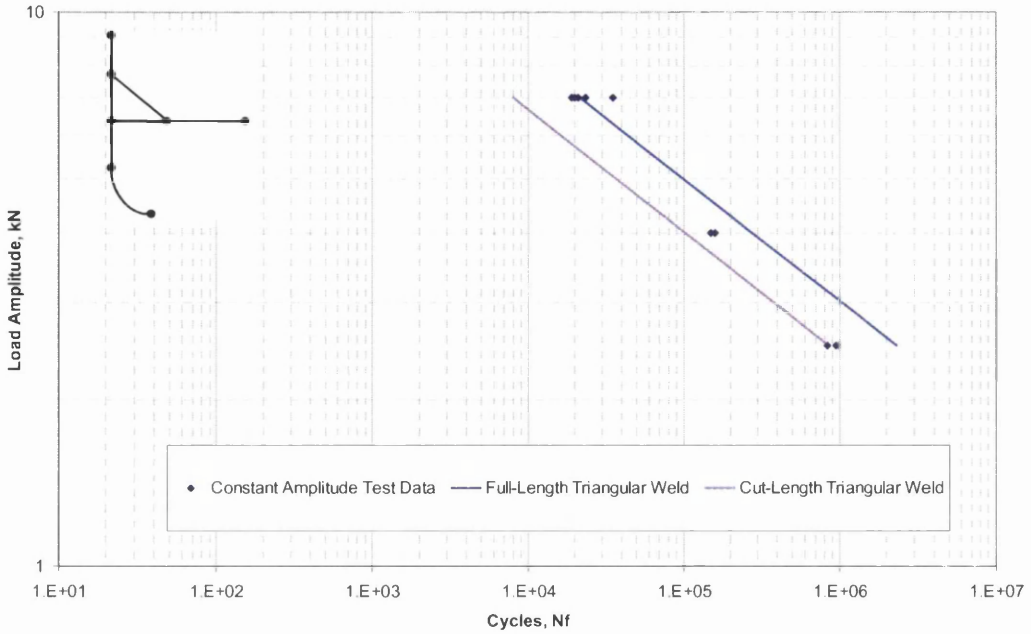

Figure 11.88: 1st Stress Full-Length vs. Cut-Length for Triangular Weld

Figure 11.89 shows that using the standard Volvo weld representation for the full-length and cut-length models under-predicts the life of the FUCA component by an order of magnitude. The full weld predicts 1000 cycles at 7kN whilst the cut-length predicts 600 cycles.

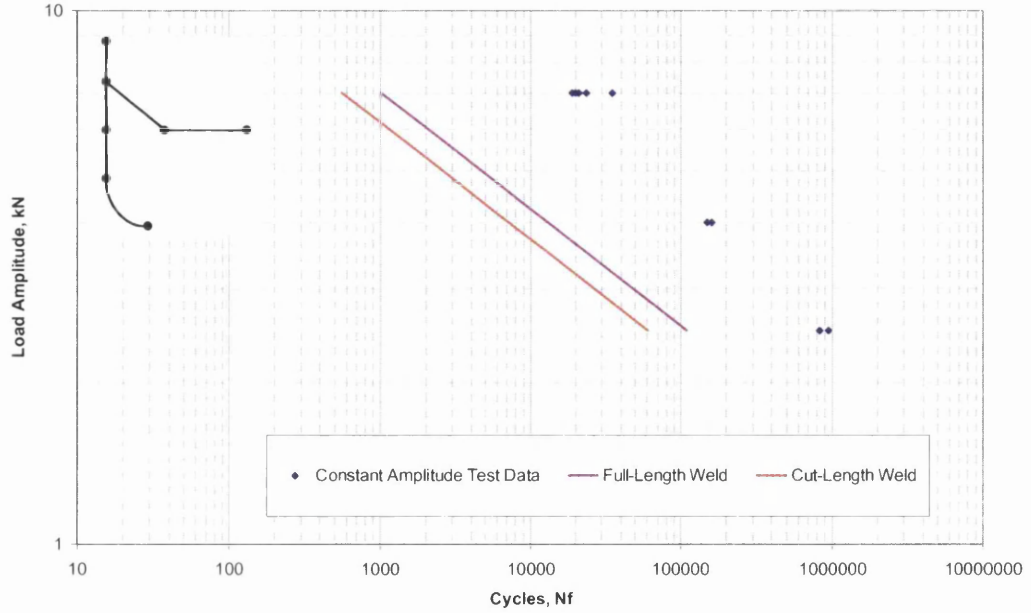

Figure 11.89: 1st Stress Full-Length vs. Cut-Length Standard Volvo Weld

Investigating the effects of the full-length versus cut-length weld triangular and the standard Volvo weld for the Max FE stress is shown in figures 11.90 - 11.91. Figure 11.90 shows that for the full-length triangular weld under-estimates the test data by 5000 cycles and over-estimates the results at 2.5kN. Whereas the cut-length triangular weld under estimates the life at both 7kN and 4kN but accurately predicts the test life at 2.5kN.

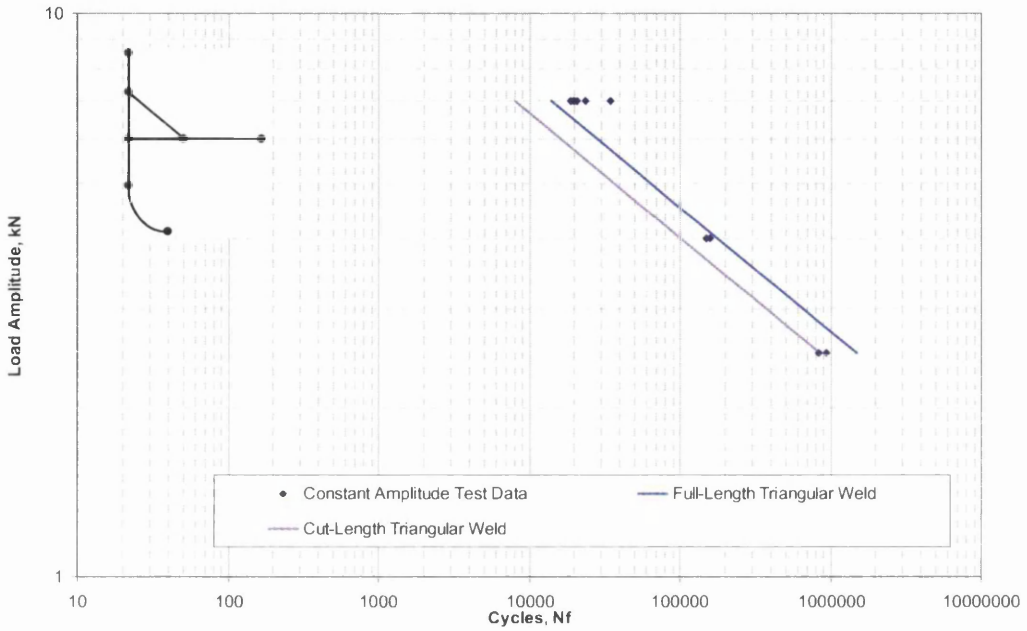

Figure 11.90: Max Stress Full-Length vs. Cut-Length Triangular Weld

Noticeable in figure 11.91 that for the standard Volvo weld representation the curves under-predict the weld fatigue lives by over a 1½ order of magnitude at 7kN, but at 2.5kN a magnitude in life is the difference between the estimated and test data life.

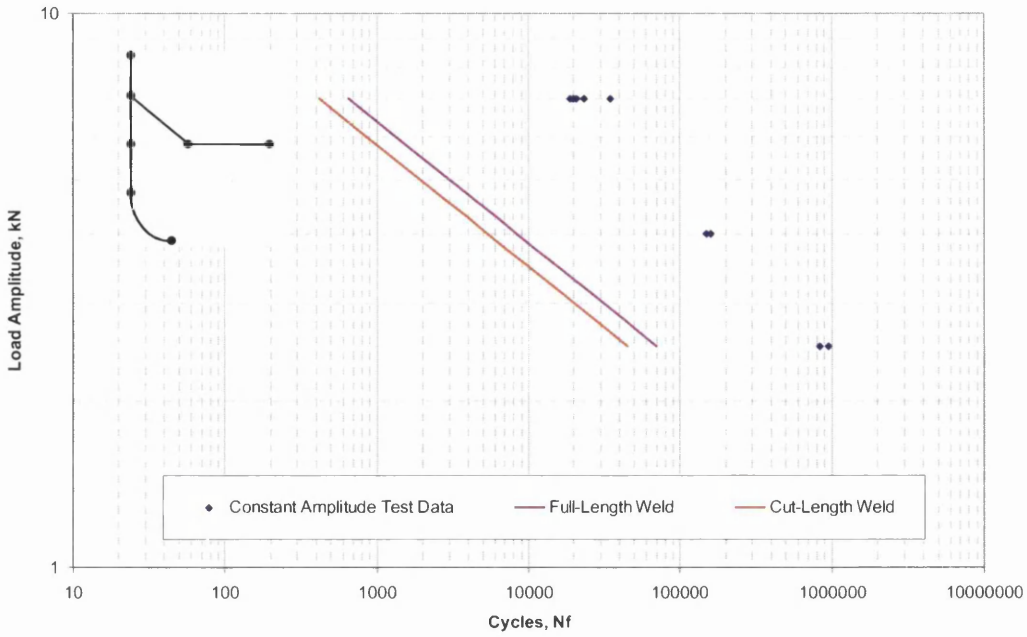

Figure 11.91: Max Stress Full-Length vs. Cut-Length Standard Volvo Weld

11.7.2 FUCA Model Battelle Method

For retrieving the FE stresses for the Battelle method the models under investigation were the full-length triangular weld and the cut-length triangular weld. For each of these models, to manually calculate the Battelle theory, the component models need to have the weld elements in a local coordinate system as shown in figure 11.92.

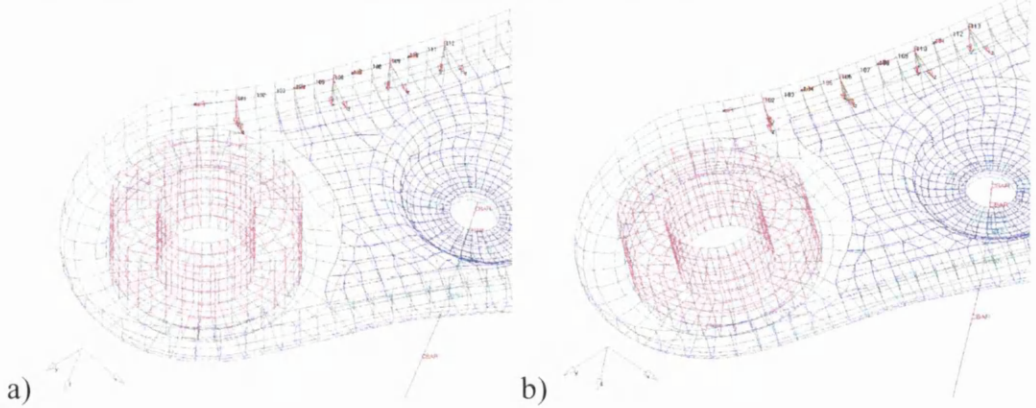

Figure 11.92: Local Coordinate Systems a) Full-Length Triangular Weld, b) Cut-Length Triangular Weld

The Battelle theory requires the correct nodal stresses from particular elements to be used for calculating the structural stress. For this method of throat failure there are two possible locations to collect the forces and moments for the weld root node: Inside the Weld Line and Weld Root Location, as shown in figure 11.93.

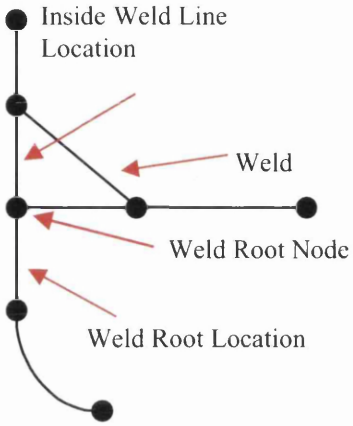

Figure 11.93: Location of Elements for Nodal Force and Moment at Weld Root

From both of these locations, the structural stress has been calculated for both the full-length triangular weld and the cut length triangular weld. The Battelle manual calculation was done using the method described in section 10.6. The local coordinate system needed to be added to the weld root location for converting global forces and moments into the local coordinate system. The local coordinate system for the weld root location is shown in figure 11.94.

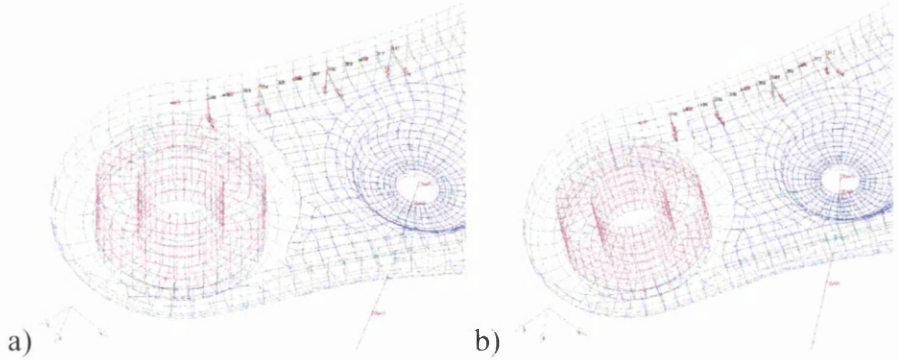

Figure 11.94: Local Coordinate System for Weld Root Location a) Full-Length Triangular Weld, b) Cut-Length Triangular Weld

Figure 11.95a and b shows the three different paths for both locations (shown in figure 11.93) used to extract the forces and moments for the full-length and cut-length triangular welds.

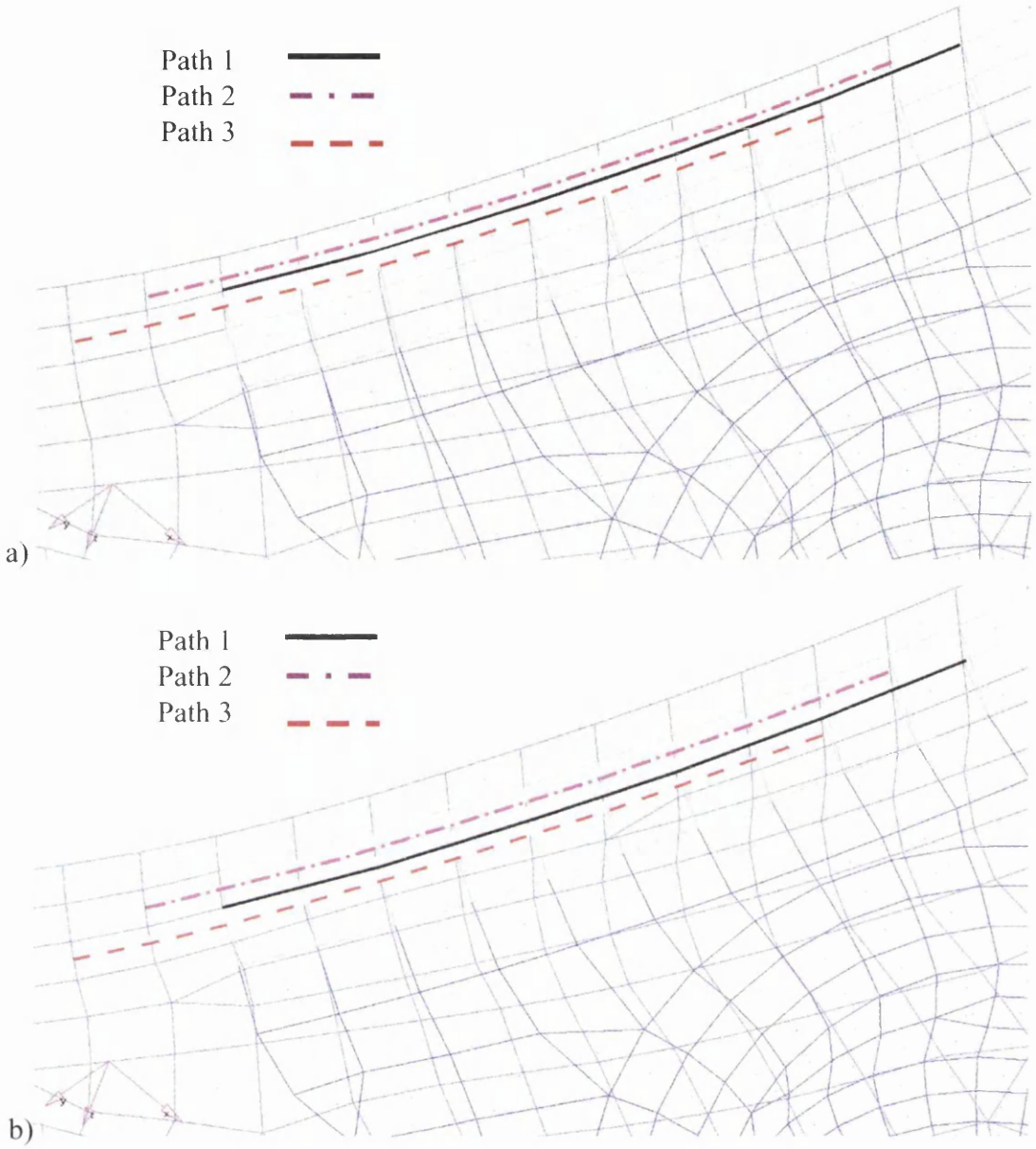

Figure 11.95: Nodal Paths used to Extract Forces and Moments for Structural Stress Calculations for a) Inside Weld Line Location, b) Weld Root Location

For calculating the predicted life the calculated Battelle Structural Stress will use the formula generated from the peel S-N curve shown in figure 12.55 in section 12.4.3.1. Table 11.8 shows the stress range and life values generated.

Table 11.8: Battelle Structural Stress and Life Calculations using 50% Survival $\Delta\sigma = 3096.1.Nf^{-0.2257}$

Model	Method	±7kN		±4kN		±2.5kN	
		Stress Range MPa	Life	Stress Range MPa	Life	Stress Range MPa	Life
Full Tri	Path 1 Inside Weld Line	197.80	1.96E+05	113.03	2.34E+06	70.64	1.88E+07
	Path 2 Inside Weld Line	54.59	5.89E+07	31.20	7.03E+08	19.50	5.64E+09
	Path 3 Inside Weld Line	65.48	2.63E+07	37.41	3.14E+08	23.38	2.52E+09
	Path 1 Weld Root	450.71	5.11E+03	257.55	6.09E+04	160.97	4.89E+05
	Path 2 Weld Root	423.77	6.71E+03	242.15	8.01E+04	151.35	6.43E+05
	Path 3 Weld Root	405.95	8.12E+03	231.97	9.69E+04	144.98	7.77E+05
Cut Tri	Path 1 Inside Weld Line	259.82	5.86E+04	148.47	7.00E+05	92.79	5.61E+06
	Path 2 Inside Weld Line	60.23	3.81E+07	34.42	4.55E+08	21.51	3.65E+09
	Path 3 Inside Weld Line	30.81	7.42E+08	17.61	8.86E+09	11.00	7.11E+10
	Path 1 Weld Root	623.59	1.21E+03	356.33	1.45E+04	222.71	1.16E+05
	Path 2 Weld Root	547.82	2.15E+03	313.04	2.57E+04	195.65	2.06E+05
	Path 3 Weld Root	536.12	2.37E+03	306.36	2.82E+04	191.47	2.27E+05

Figure 11.96 shows both inside weld line and weld root locations for the full-length and cut-length triangular weld models. Regardless of where the weld start/stop location (i.e. full-length or cut-length) is, using the nodal forces from the elements 'Inside Weld Line' over predicts the test data, thus showing that this location is not the most appropriate location. As shown in both 11.96a and b, using the Weld Root location under predicts the test results.

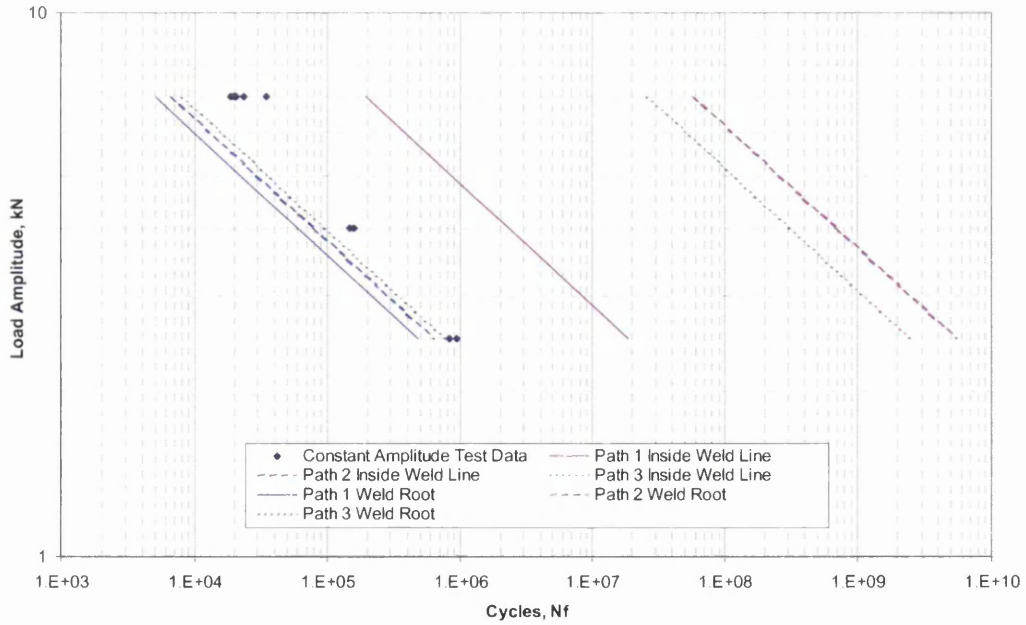

a)

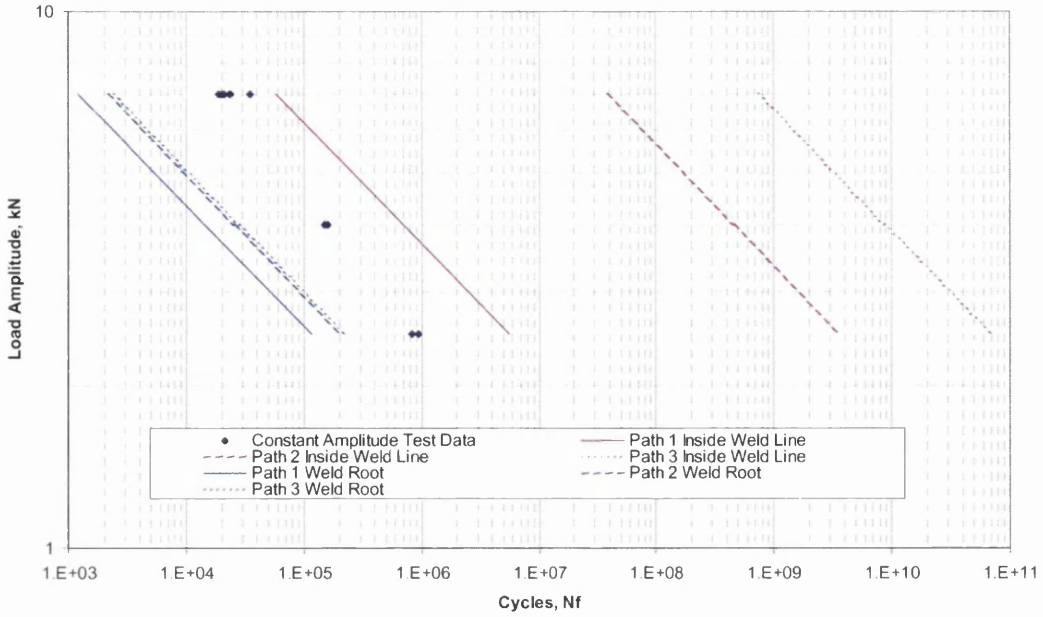

b)

Figure 11.96: Difference between Locations of Element Nodal Forces a) Full-Length Triangular Weld, b) Cut-Length Triangular Weld

Using the nodal locations from the weld root and calculating the structural stress the differences between the weld start locations full-length and cut-length is shown in figure 11.97. The difference between 'path 1' full-length and 'path 1' cut-length is clearly shown in the figure. This shows that for the full-length 'path 1' is much closer to predicting the test data than the cut-length 'path 1'.

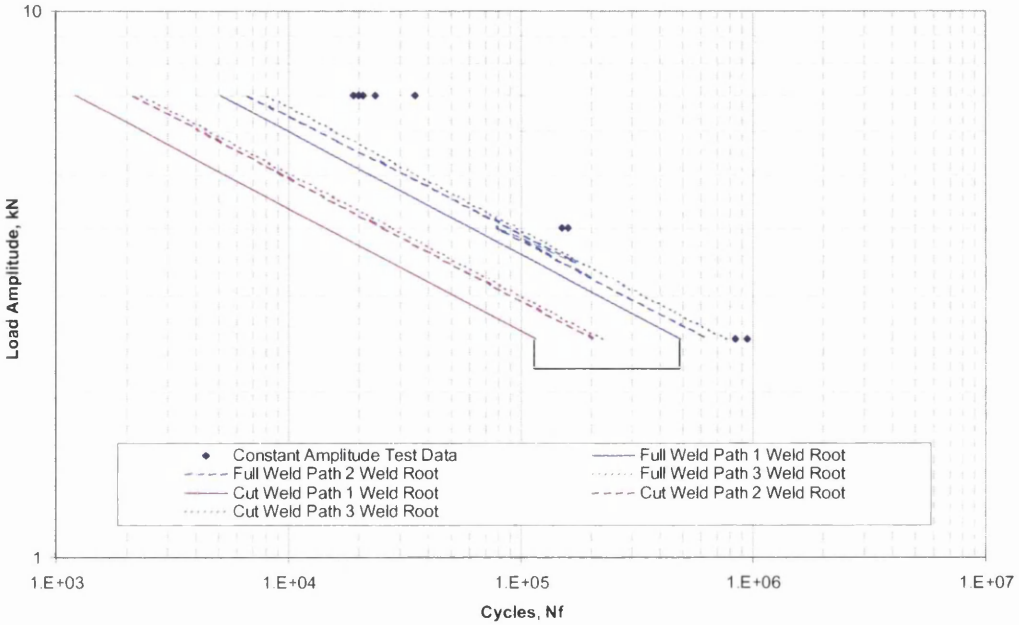

Figure 11.97: Difference between Triangular Weld Start Locations

11.8 FUCA Life Predictions – Variable Amplitude Loading

This section describes the result of using the master S-N curve for throat failure to predict FUCA test results for variable amplitude loading, using Block loading and SAE Bracket Load-Time History.

11.8.1 Variable Amplitude Block Loading

Investigating the effects of using the master S-N curve for throat failures for predicting the life of the FUCA component for the R=-1 Block Loading Signal 1 and 2 shown in figures 10.20 – 10.21. Using the stresses predicted and shown in Table 11.7 for both the full-length and cut-length models for the Volvo and Battelle Method are shown in figures 11.98 – 11.101.

Figure 11.98 shows that for the cut-length models using Volvo and Battelle methods, both under-estimate the average life of the block loading test data, when using a Miner's Damage constant D=1. For the full-length models, the Volvo method accurately predicts the test data whilst the Battelle's method under-predicts the test data. The Volvo Method incorporates mean stress correction factors, and this shows that for both full and cut-length models, they over-predict the test data.

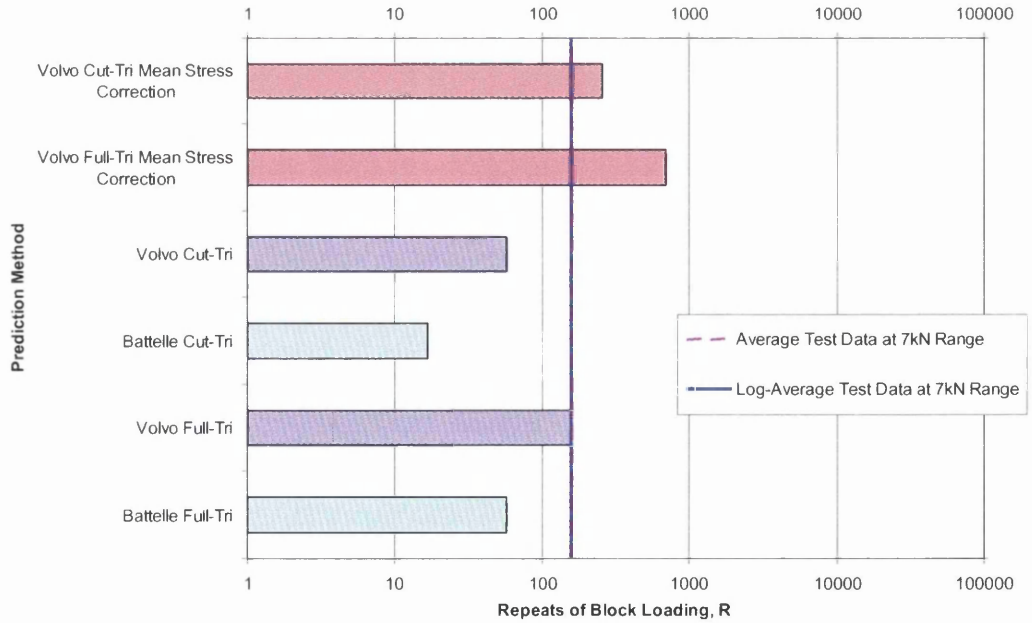

Figure 11.98: Prediction of ±7kN Block Loading Signal 1, R=-1 (D=1)

Checking the effect of changing the Miner's Damage constant to D=1.6, shown in figure 11.99, shows the number of repeats does increase for all models but the cut-

length models using Volvo and Battelle Method still under-predict the test data. The full-length model for Volvo over predicts the test data whilst the full-length model using Battelle still under-predicts the test data. Performing mean stress correction for the Volvo's Method for both models over-predicts the results.

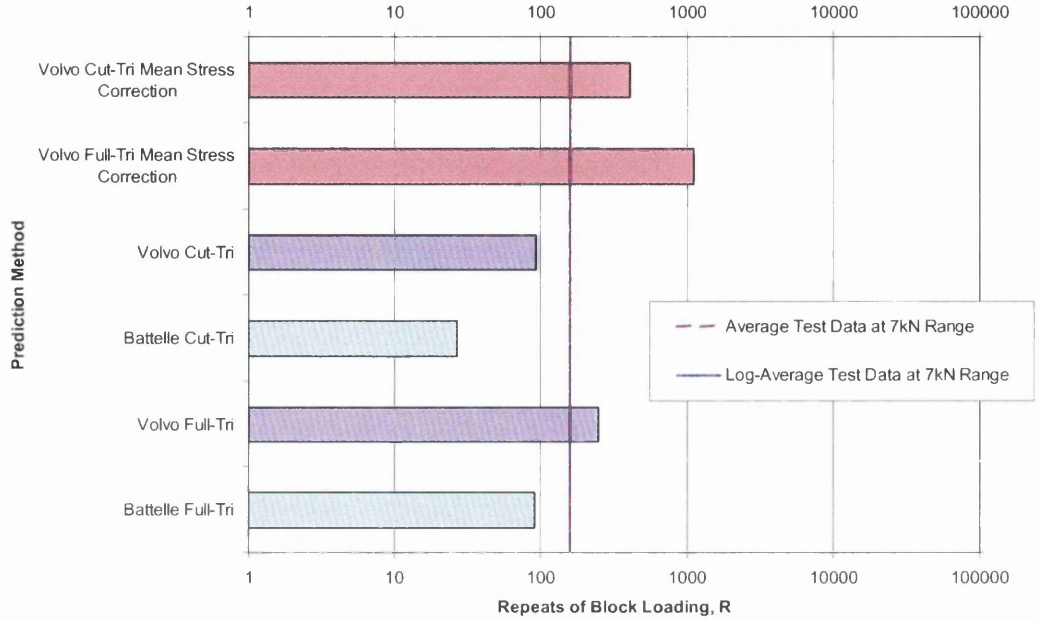

Figure 11.99: Prediction of ±7kN Block Loading Signal 1, R=-1 (D=1.6)

Figure 11.100 shows the predicted results for the Block loading signal 2 with a maximum load of 4kN. Both the cut-length models using Volvo and Battelle methods, both under-estimate the average life of the block loading test data, when using a Miner's Damage constant D=1. For the full-length models, both Volvo and Battelle method over-predicts the test data. The Volvo Method incorporates mean stress correction factors, and this shows that for both full and cut-length models, they over-predict the test data.

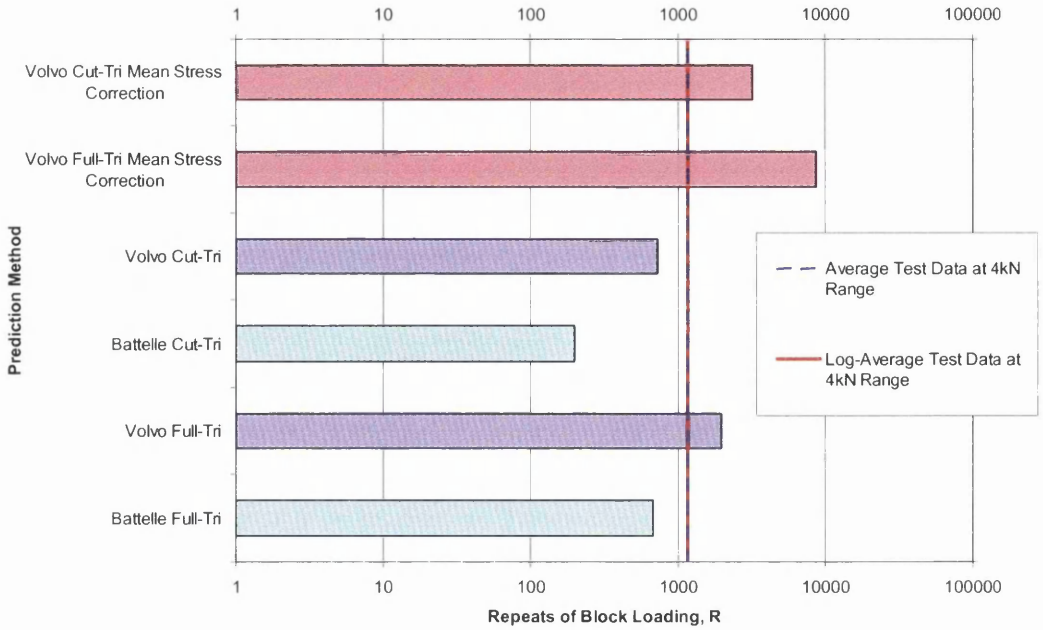

Figure 11.100: Prediction of ±4kN Block Loading Signal 2, R=-1 (D=1)

Checking the effect of changing the Miner's Damage constant to D=1.6, shown in figure 11.101, shows the number of repeats does increase for all models but the cut-length models using Volvo accurately predict the average life of the test data whilst Battelle Method still under-predict the test data. The full-length model for Volvo over-predicts the test data whilst the full-length model using Battelle still under-predicts the test data. Including mean stress correction for the Volvo Method for both models over-predicts the results.

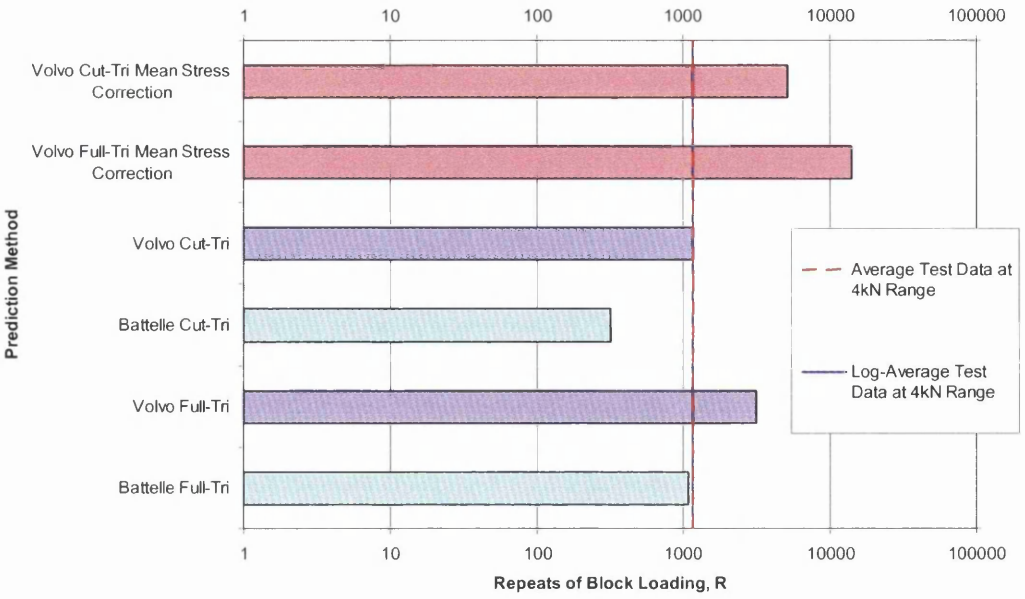

Figure 11.101: Prediction of ±4kN Block Loading Signal 2, R=-1 (D=1.6)

For the R=0.1 Block Loading signal shown in figure 10.22, the predicted FUCA life is shown in figure 11.102. Both the full-length and the cut-length models of the Volvo and Battelle Method under-predict the test data by an order of magnitude. Regardless of changing the damage constants value from D=1 to D=1.6, the results still under-predict the test data.

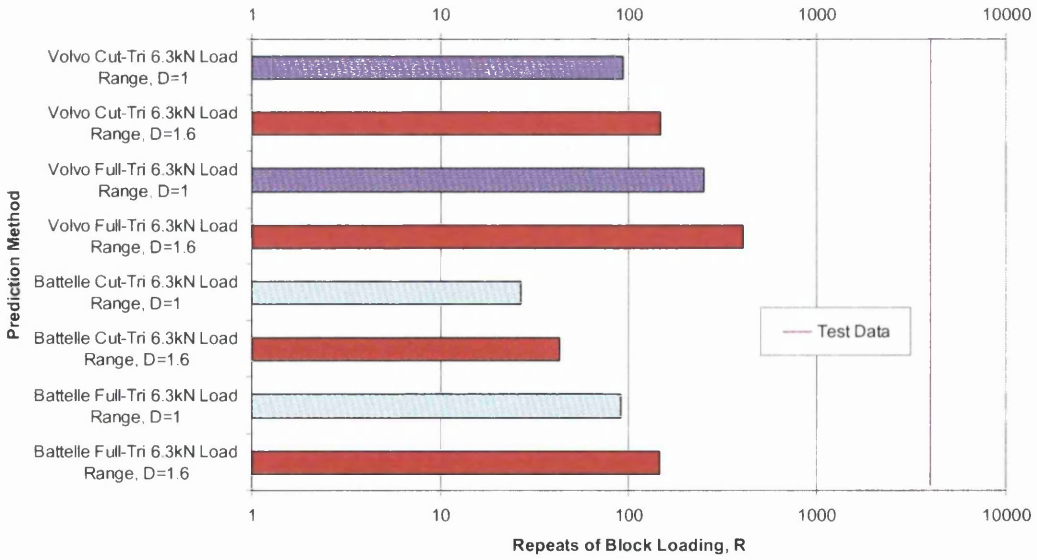

Figure 11.102: Prediction of 7kN R=0.1 Block Loading Signal

11.8.2 Variable Amplitude SAE Bracket Load-Time History

Using the master S-N curves for throat failure generated for both Volvo and Battelle's Method, the results of predicting the life of the FUCA component under SAE Bracket loading conditions is illustrated in figure 11.103. Both the full-length and cut-length models for Volvo and Battelle under-predict the average test life of the components. Incorporating the effects of mean stress for the Volvo Method in the full-length and cut-length models also under-predict the average test data.

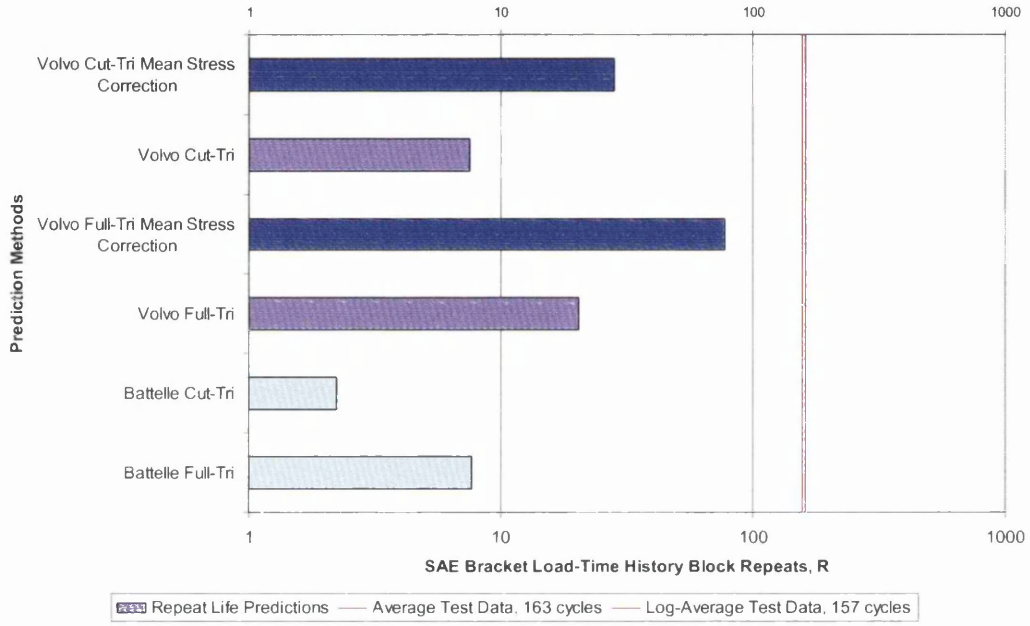

Figure 11.103: Prediction of SAE Bracket Load-Time History (D=1)

Checking the effect of changing the Miner's Damage constant to D=1.6, shown in figure 11.104, shows the number of repeats does increase for all models. Both the full-length and cut-length models for Volvo and Battelle under-predict the average test life of the components. Incorporating the effects of mean stress for the Volvo Method in the full-length and cut-length models also under-predict the average test data.

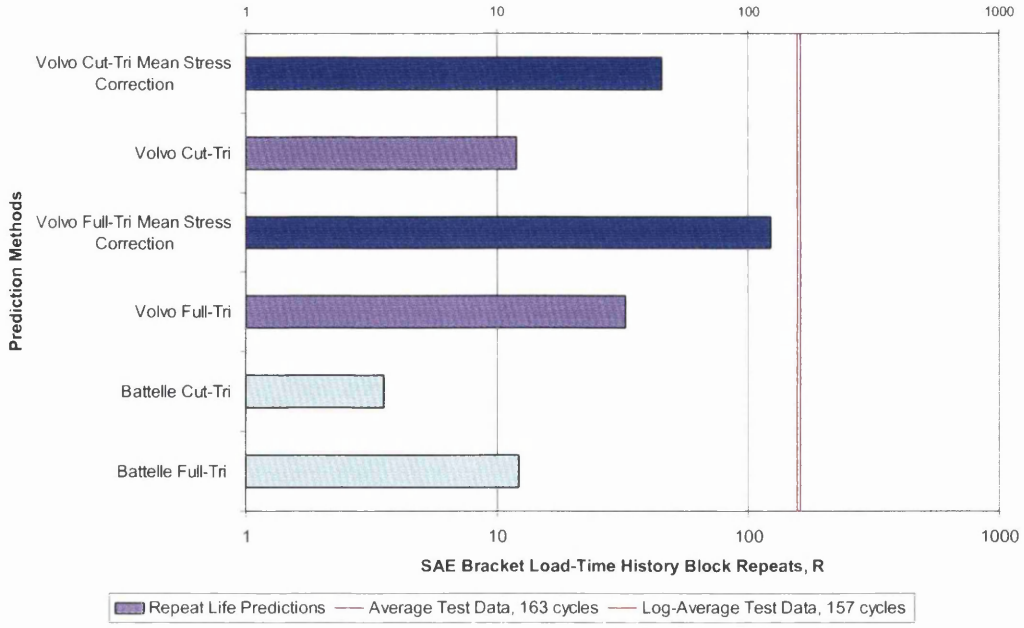

Figure 11.104: Prediction of SAE Bracket Load-Time History (D=1.6)

11.9 Results Summary

A recap of all the main results discussed in this chapter is set out in this section.

11.9.1 Coupon Testing for Data Generation

From all the results produced and analysed, these are the main conclusions:

- Test termination criteria had little effect on test results.
- There is little difference in the weld performance, on a per unit weld-line length basis, between lap-shear joints GM1 and GM2; and between the peel joints GM3 and GM4.
- Partially welded TM1, GM11A and TM11A have increased fatigue performance over the fully welded TM2, GM11B and TM11B, again on per unit weld length basis.
- T-Shaped joints performed better under axial loading (M5) than under bending and lateral loading (M8 and M6).
- Under variable amplitude block loading, high load cycles are the most damaging.
- Under variable amplitude conditions, TM11A has increased fatigue performance over GM1 and GM8.
- Mean stress affects high fatigue lives of TM11B and GM2
- The two main failure modes observed were toe and throat.
- For throat failure two modes of failure have been identified 1) root through the weld and root along the interface

11.9.2 Coupon FE Modelling

11.9.2.1 FE Modelling vs. Experimental Verification

- Using the longitudinal stresses down the centre line of the weld and ±10mm either side of the weld centre line for GM1 and GM2 show that the stresses are very close to each other. For GM11A the stresses slowly converge.
- FE stress predictions were not too sensitive to the types of elements selected.
- FE under-predictions of the stress for M11A coupon joint requires further investigation, which will be discussed in section 12.4.

11.9.2.2 Volvo and Battelle Structural Stress Results

- The highest stresses visible in the Volvo Method for both the weld throat and weld toe failures are found close to the weld start/stop.

- Using the Battelle manual calculations the effect of the weld start/stops are corrected for and the FE stress just before the weld start/stop increases.
- Equivalent Structural Stress defined in the Battelle Method is higher than Structural Stress.
- Manual and Verity Equivalent Structural Stress are very close, with FLOW calculations being marginally higher.
- The weld thickness, placement and height show no effects on the S-N curve.
- FE results for stress distributions along the coupon weld line revealed that the structural stress values were lower at the edges of those coupons having weld –toe failures. However, for those with weld throat failure, the structural stress at the edges were higher then that in the centre.

11.9.3 FUCA Component Fatigue Results

- For constant amplitude testing, failure occurred mainly through a notch in the weld start and propagating down the weld before travelling into the parent flange.
- Larger scatter occurred in ±2.5kN for crack initiation with low crack propagation rates. At ±4kN crack propagation rates were also low; this is not the case at ±7kN.
- Under variable amplitude block loading conditions, the high load cycles are the most damaging.
- Variable Amplitude SAE Bracket load-time history, the majority of the life-results fell between 150 – 200 block repeats of the signal.

11.9.4 FUCA Life Predictions

- Both Volvo and Battelle methodology is for toe failures; therefore this study has extended the methodology to incorporate throat failure. Toe Failure results prove that both methods are good for toe failure prediction.
- With three failure modes, 3 master curves exist. For each failure mode, a master curve exists regardless of joint configuration.
- For both the 1st stress (i.e. at the start of the weld) and the max stress, the current Volvo standard for weld representation under-estimates the life of the FUCA component.

- For both 1st and max stress the triangular weld shape more reasonably predicts the life of the FUCA components.
- Using the 'Inside Weld Line' location, the Battelle Structural Stress over-predicts the fatigue lives of the test data for both the full-length and cut-length welds.
- The 'Weld Root' location under-estimates slightly the fatigue lives of the component.
- Overall, the "weld root" appeared to be a much better location from which structural stress should be calculated for the weld throat failure, if Battelle Method is used.
- There is limited sensitivity in fatigue lives predicted due to the weld start locations – full and cut length welds, with the full-length weld being more sensitive than the cut-length weld.

11.9.5 FUCA Life Predictions – Variable Amplitude Loading

11.9.5.1 Variable Amplitude Block Loading

- For ±7kN Block Loading signal (R=-1), using mean stress correction over-predicts the average test data. Only full-length model using Volvo method predicts test data, Battelle method under-predicts the test data.
- For ±4kN Block Loading signal (R=-1) mean stress correction over-predicts the average test data along with the Volvo full-length model. Battelle method under-predicts the average test data.
- For Block loading signal of R=0.1 (maximum load 7kN) both the Volvo and Battelle Method along with mean stress correction under-predict the test data.
- Altering the damage constant D=1 to D=1.6 increases the number of block repeats of life.

11.9.5.2 Variable Amplitude SAE Bracket Load-Time History

- Regardless of Damage constant value D=1 or D=1.6, both Volvo and Battelle methods for both models under-predict the average test data.
- Performing mean stress correction on this random signal does increase the predicted life, but this life still under-predicts the average test data.

12. DISCUSSION

12.1 Constant Amplitude Coupon Testing for Data Generation

Figure 11.5 shows the comparison of GM1 and GM2 partially and fully welded single lap-shear coupons. The results show little difference in the weld performance, on a per unit weld-line length basis this indicates that the larger partial welds have similar crack initiator sites to the full welds. Whereas for TM1 and TM2 in figure 11.6 the increase in fatigue performance of TM1 could arise from the difference in weld failure locations of throat and toe for TM1 whilst for TM2 it is predominately at the toe.

For the double lap-shear coupons, GM11A and GM11B the effect of the full and partial welds are shown in figure 11.7. The difference in the fatigue performance has little to do with the failure location as they both fail at the weld toe but could be down to the difference in weld height. Whereas for TM11A and TM11B partial and full welded coupons as shown in figure 11.8 they both failed at the weld toes but the difference could arise from the weld quality.

Figure 11.9 shows the full and partially welded peel coupons GM3 and GM4. Both failed at the throat of the weld, although the load bearing capability of partially welded GM3 on an actual per unit weld length basis is higher than that of fully welded GM4.

Figure 12.1 shows the comparison between both suppliers TKA and GKN partially welded M1 and fully welded M2 results. For GM1, GM2 and TM1 the load-life curve shows that potentially one master curve can be used for throat failures. Whilst TM2 has a slightly lower fatigue lives for the majority of toe failures but still could potentially use the same master curve as TM1, which covers all types of failures.

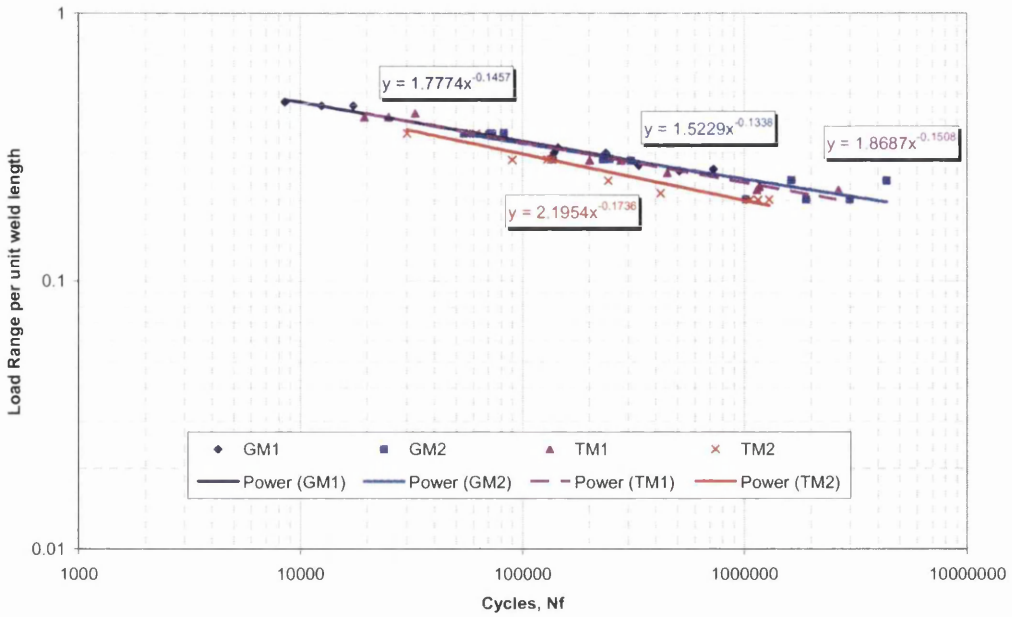

Figure 12.1: Comparison of TKA-Tallent and GKN Load-Life Data M1 and M2 Joints Results, R=0.1

Figures 12.2 – 12.3 show the results for all weld toe failures and weld throat failures respectively for both suppliers. Figure 12.2 shows reasonable load-life results for all the weld toe failures although TM2, a single lap-shear geometry, has a lower load range than all double lap-shear geometries of M11A and M11B. This is due to the double lap-shear joints being stiffer.

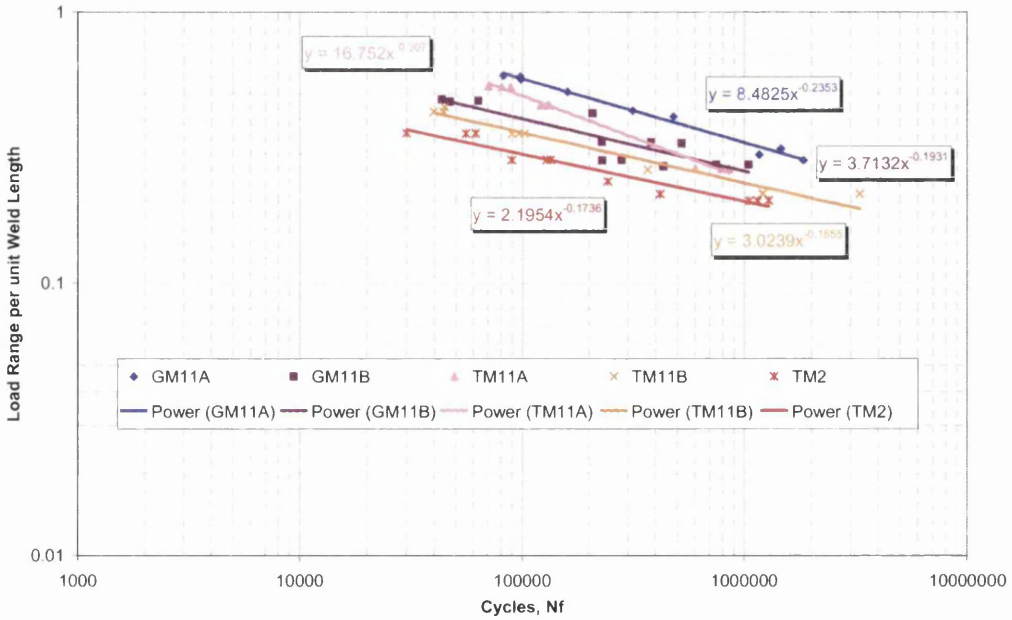

Figure 12.2: Comparison of Load-Life Data for All Weld Toe Failures, R=0.1

Figure 12.3 shows that the lap-shear joints are an order of magnitude higher in load range on a per unit weld length basis than the peel joints. All the lap-shear and peel joints have very good results on a per unit weld length basis.

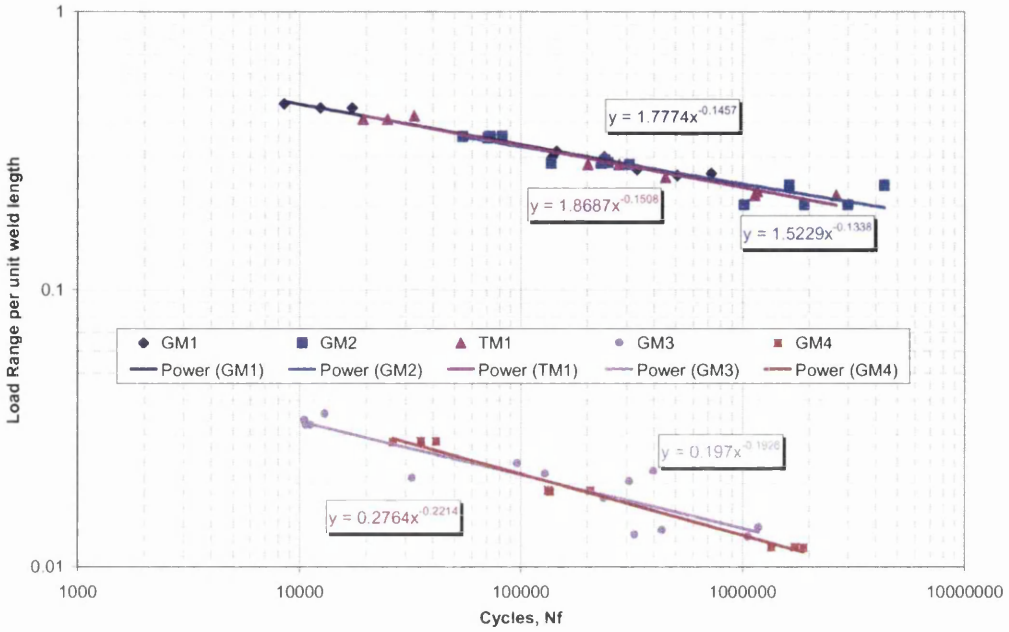

Figure 12.3: Comparison of Load-Life Data for All Weld Throat Failures, R=0.1

Figure 11.10 shows the differences between the loading conditions tensile fatigue to lateral and bending fatigue by the magnitude difference in the results for a simple T-shaped coupon. GM5 has better fatigue performance than both GM6 and GM8. GM6 and GM8 have similar fatigue lives.

12.1.1 Comparison of Single and Double Lap-Shear Welds

Figures 12.4 – 12.7 show the effect of single and double welded geometries. The effect of double the amount of welds shows a higher load bearing capability per actual weld length for GM11A when compared to the single weld GM1which is shown below in figure 12.4. This difference could arise from the differing failure modes with GM1 failing at the weld throat and GM11A fails at the weld toe, and due to a single weld being less stiff therefore more bending occurs.

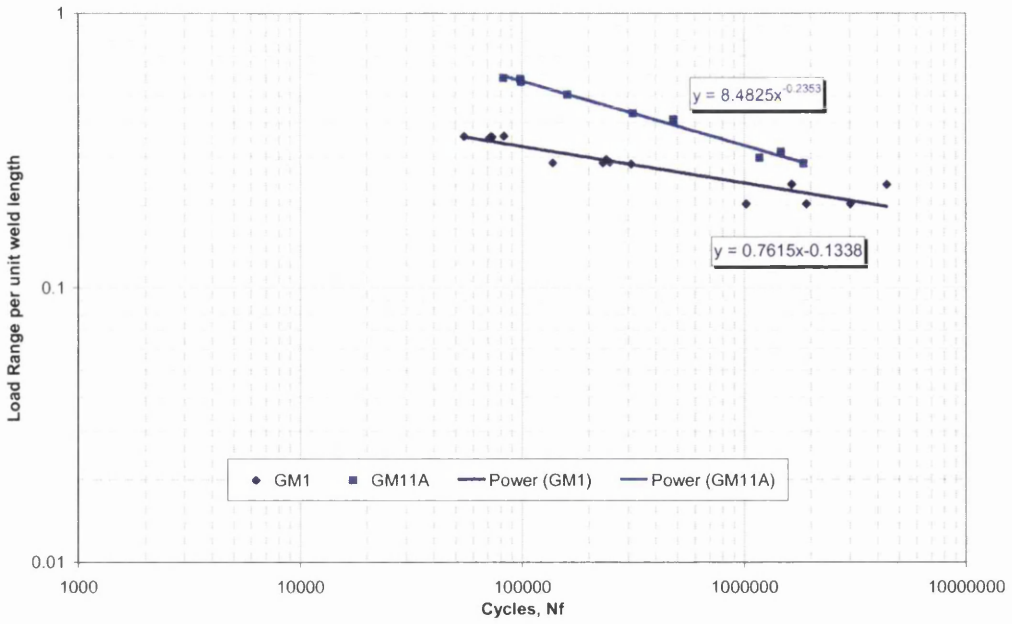

Figure 12.4: Load-Life Data for GM1 and GM11A Joints – Final Failure, R=0.1

The differences between fully welded single and double lap-shear coupons are shown in figure 12.5. The effect of a single full weld (GM2) does decrease the fatigue performance on a per weld length basis meaning that doubling the length of weld increases the fatigue performance, although the failure modes were different – GM2 fails through the weld throat and toe whilst GM11B fails at the weld toe.

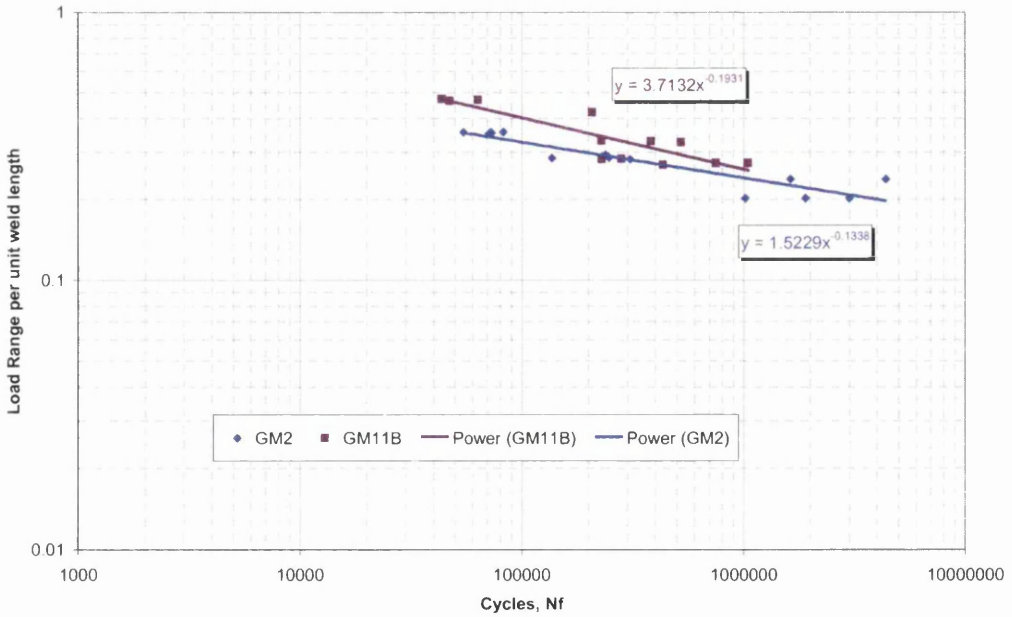

Figure 12.5: Load-Life Data for GM2 and GM11B Joints – Final Failure, R=0.1

The differences between TKA–Tallent M1 and M11A are shown in figure 12.6. TM11A has a better load bearing capability over TM1. The effect of doubling the weld length does increase the fatigue performance of the weld by increasing the load bearing capability, but it also increases the number of initiation sites for failure to occur at the weld toe.

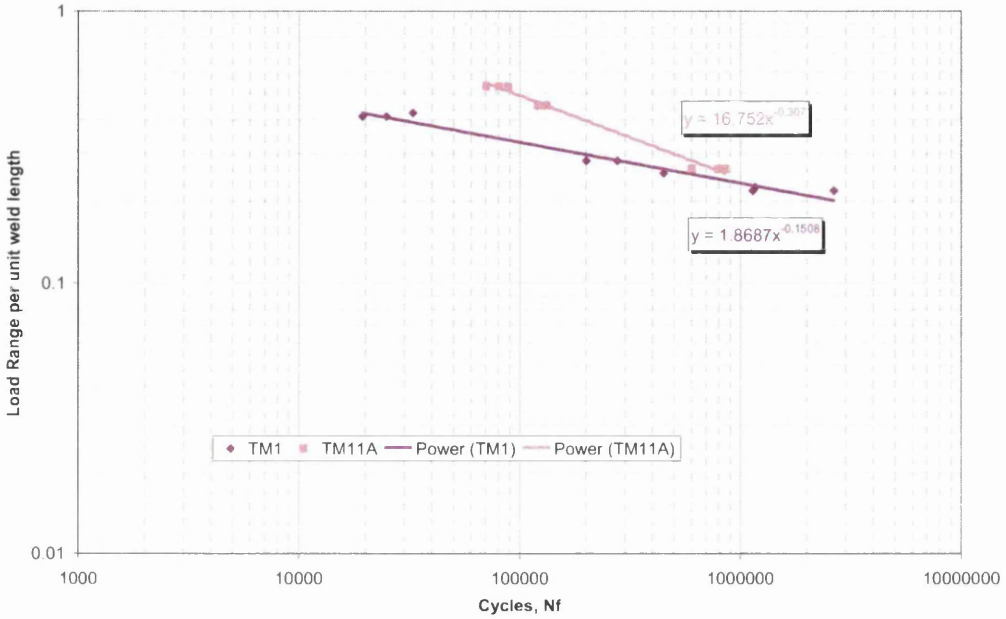

Figure 12.6: Load-Life Data for TM1 and TM11A Joints – Final Failure, R=0.1

TM11B shows improved fatigue performance on an actual per weld length basis over TM2 shown in figure 12.7. Doubling the weld length does increase the load bearing capability of the weld but increases the initiation sites available.

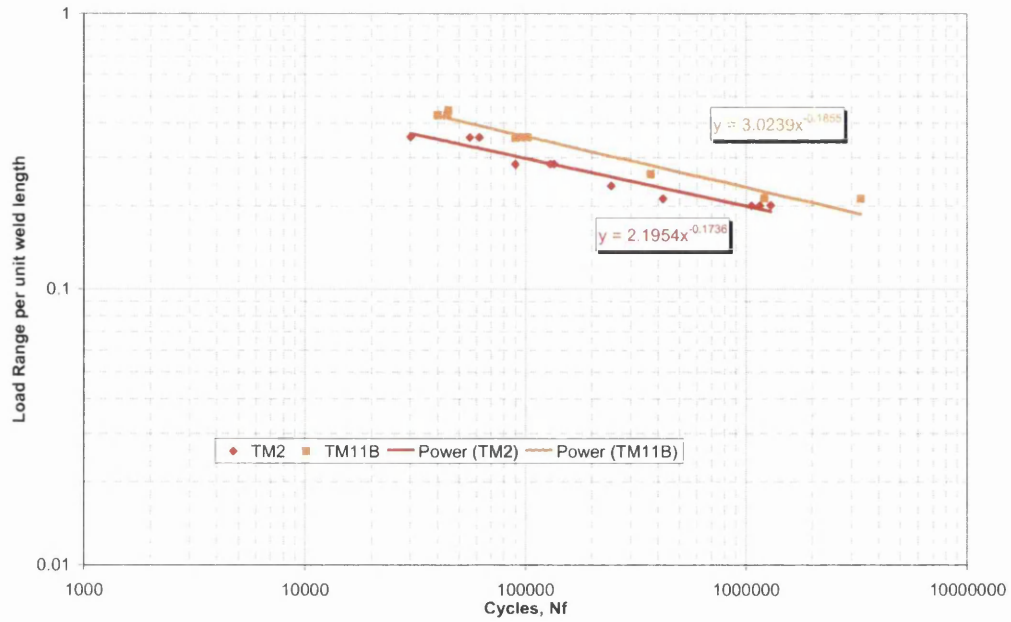

Figure 12.7: Load-Life Data for TM2 and TM11B Joints – Final Failure, R=0.1

Double welded coupons show that they are more efficient in distributing the applied load though the coupon than single welds. Doubling the weld length reduces the bending component in the single weld, which results in the failure mode change.

12.1.2 Comparison of Coupon Suppliers

Examining the fatigue test results from coupon joints fabricated by GKN and TKA-Tallent, noticeable differences were observed, as shown in figures 12.8 – 12.11. This implies that different welding processes and welders affect joint fatigue.

For single lap-shear coupons on a per unit weld length basis for both the full and partial welds, both suppliers have very similar fatigue lives and this is shown in figures 12.8 – 12.9.

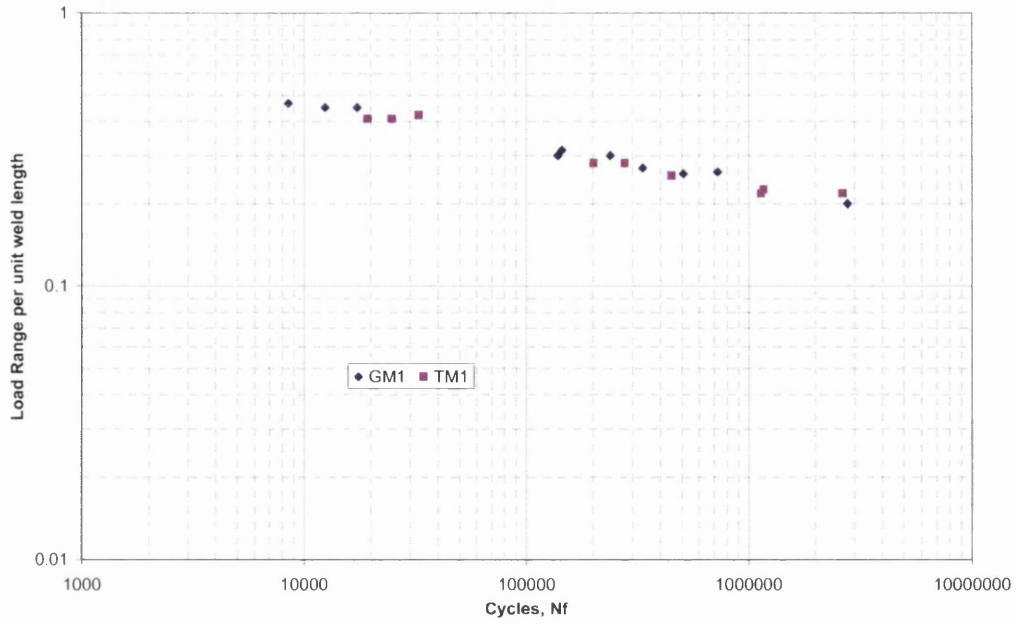

Figure 12.8: M1 Final Failure, R=0.1

TM2 has lower fatigue lives than GM2 this is shown in figure 12.9. This could be due to the different modes of failure between throat weld failures for GM2 whilst TM2 failed at the weld toe.

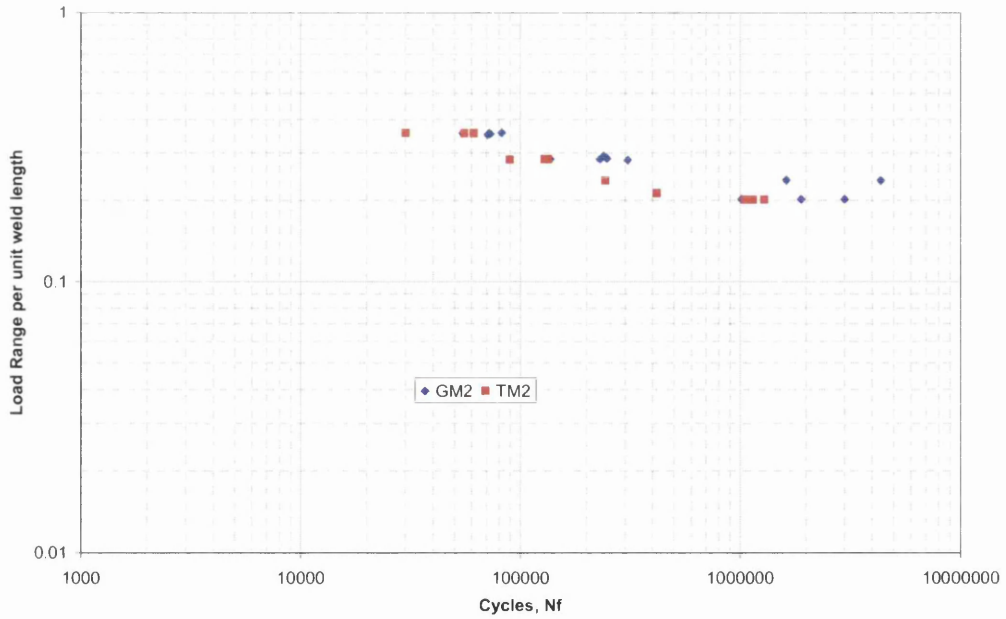

Figure 12.9: M2 Final Failure, R=0.1

For double lap-shear partially welded coupons again GKN coupons show better fatigue performance lives on a per unit weld length basis to TKA Tallent coupons, this is shown in figure 12.10.

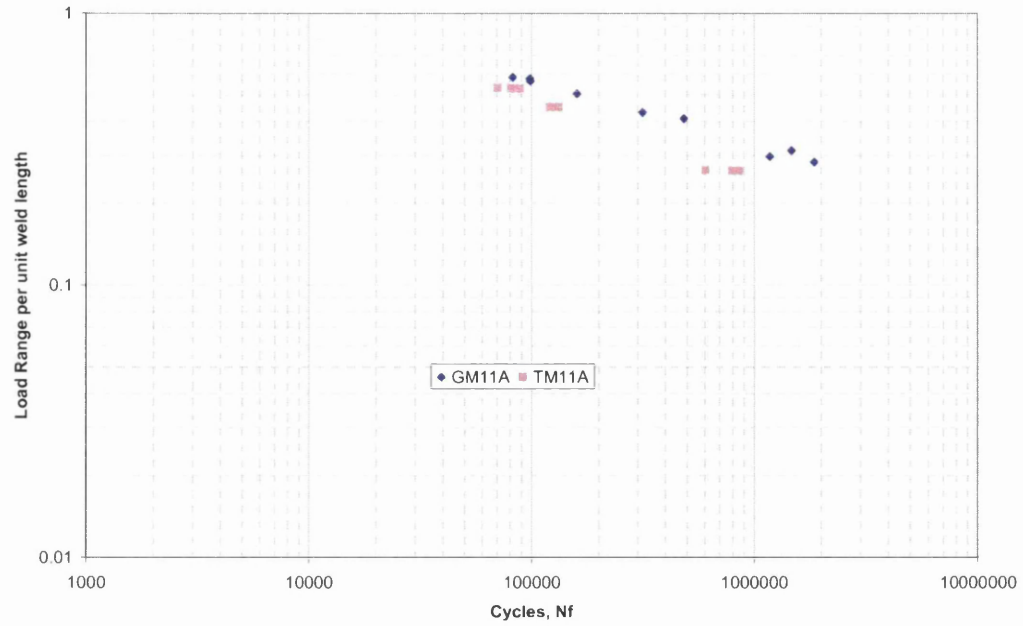

Figure 12.10: M11A Final Failure, R=0.1

For fully welded double lap-shear coupons, the differences between manufactures are not as noticeable as the partially welded coupons. Figure 12.11 shows that GM11B has better fatigue performance than TM11B. However, there is a significant overlap in scatter bands.

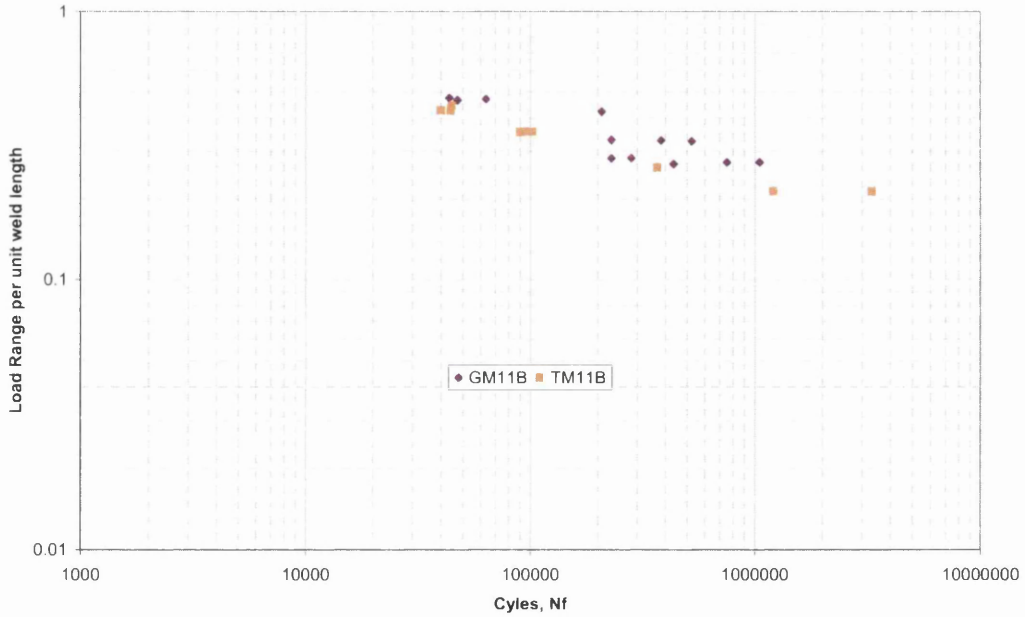

Figure 12.11: M11B Final Failure, R=0.1

Overall from the results shown in the above figures, weld fabrication does affect the fatigue lives of the coupon joints.

12.1.3 Comparison of Peel and Lap Geometries

Differences between lap and peel geometries are shown in figures 12.12 – 12.13 on a per unit weld length basis. GM1 and GM3 show similar fatigue scatter performance but the load levels are ten times higher for the same life as shown in figure 12.12.

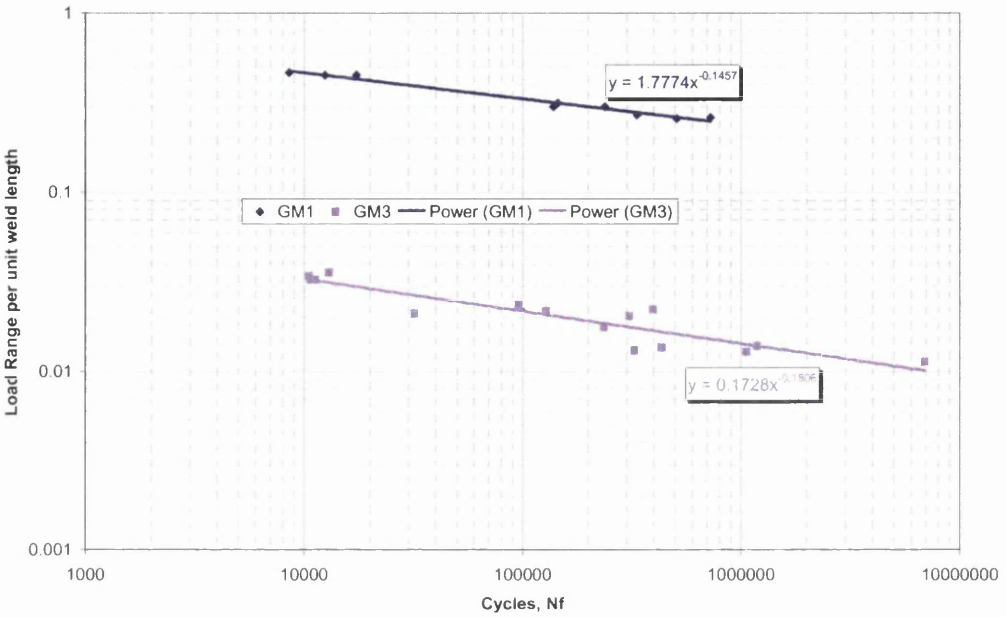

Figure 12.12: Load-Life Data for GM1 and GM3 Joints – Final Failure, R=0.1

With full welds there is a noticeable difference in the fatigue performance of lap-shear and peel coupons as shown in figure 12.13. GM2 has fatigue lives ten times higher than GM4.

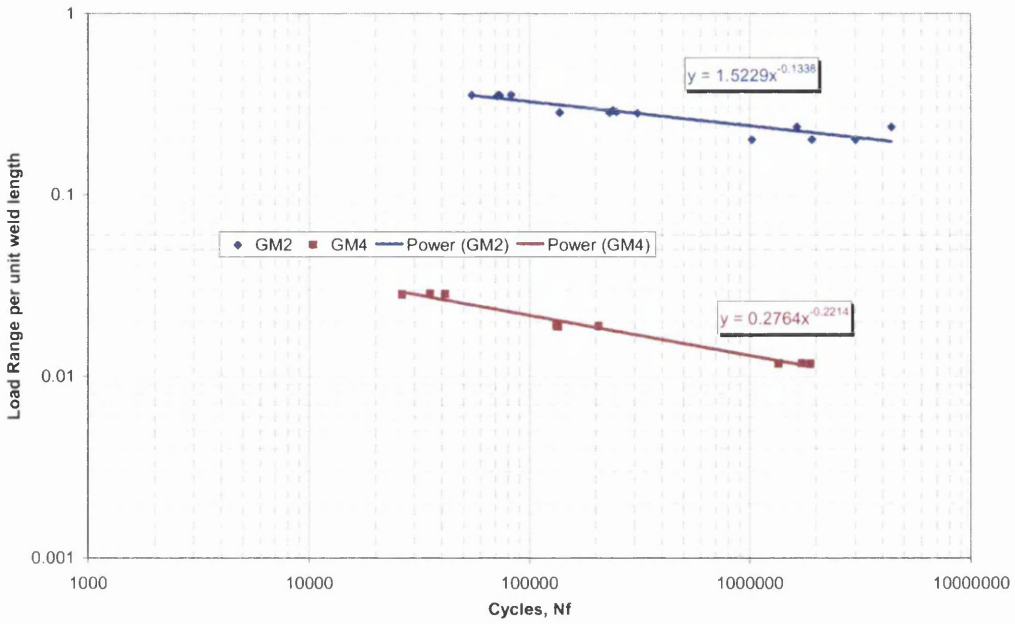

Figure 12.13: Load-Life Data for GM2 and GM4 Joints – Final Failure, R=0.1

12.1.4 Mean Stress Effects

In general most engineers tend to ignore the effects of mean stress when calculating weld fatigue for 3 reasons: 1) In comparison to load or stress range. 2) Mean stress is secondary, in the past research into the effects of mean stress on weld fatigue shows them to be relatively small as it is believed that significantly higher residual stress is found in the welds. 3) Lack of experimental data on how to correct for mean stress is available and for these reasons, mean stress effects fail to be accounted for.

In this study the effects of mean stress in weld fatigue have been investigated. Figures 11.11 and 11.12 shows that mean stress does have an effect on the fatigue lives of coupons, and therefore the effect of this stress will need to be calculated and corrected for.

Figures 11.11 – 11.12 show that for short lives (high loads) under strain-control fatigue, plastic strain will remove the mean stress effect by deformation, i.e. the residual stress is removed from the coupon. Whereas at long lives (low loads) the coupon is under stress control fatigue and under these conditions the effects of mean stress is much more important.

Figure 12.14 shows that when comparing the effects of mean stress against max load the severity of the loading is shown very clearly, unlike in figure 11.11. This shows that range as well as mean contributes to fatigue.

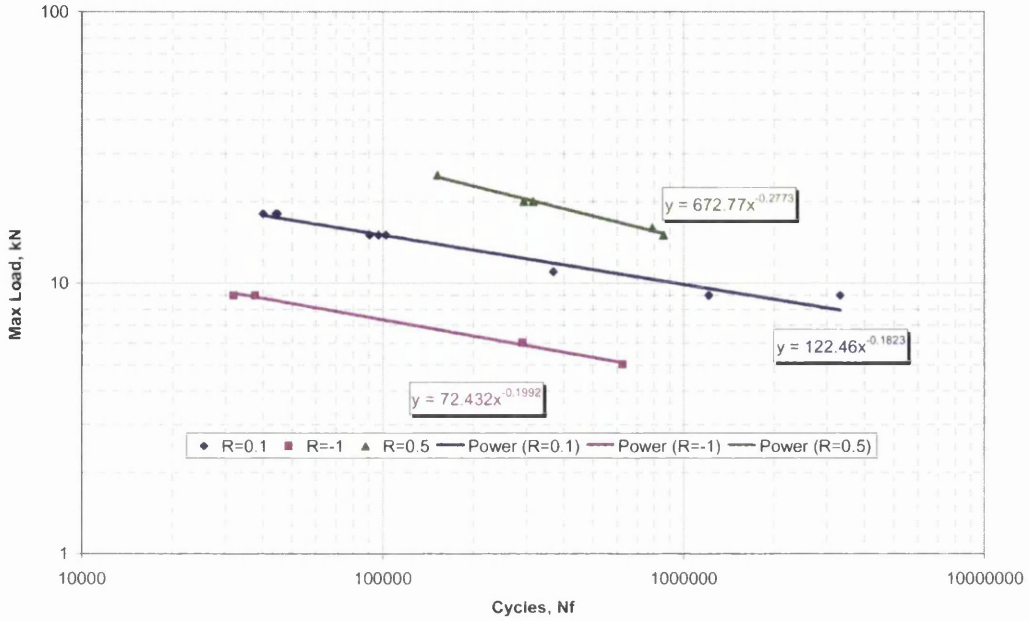

Figure 12.14: Maximum Load-Life Data for Mean Stress Effects of TM11B

12.2 Variable Amplitude Loading

12.2.1 Variable Amplitude Block Loading

Figures 12.15 – 12.16 show the comparison between the constant amplitude loading and the block loading at each of the load levels. At the first load level as shown in figure 12.15, the block loading result shows that the most damaging cycles are the first load level of each block with the lower load level of the block causing a small amount of damage.

Figure 12.15 shows the comparison of repeats of 1000 cycles for constant amplitude loading to block loading. The block loading result for the first block F1 is higher as for every block of 1000 cycles the constant amplitude has 1000 cycles at high load levels, whilst the block loading F1 is an order of magnitude higher due to only having 100 cycles of every 1000 cycles at the high load.

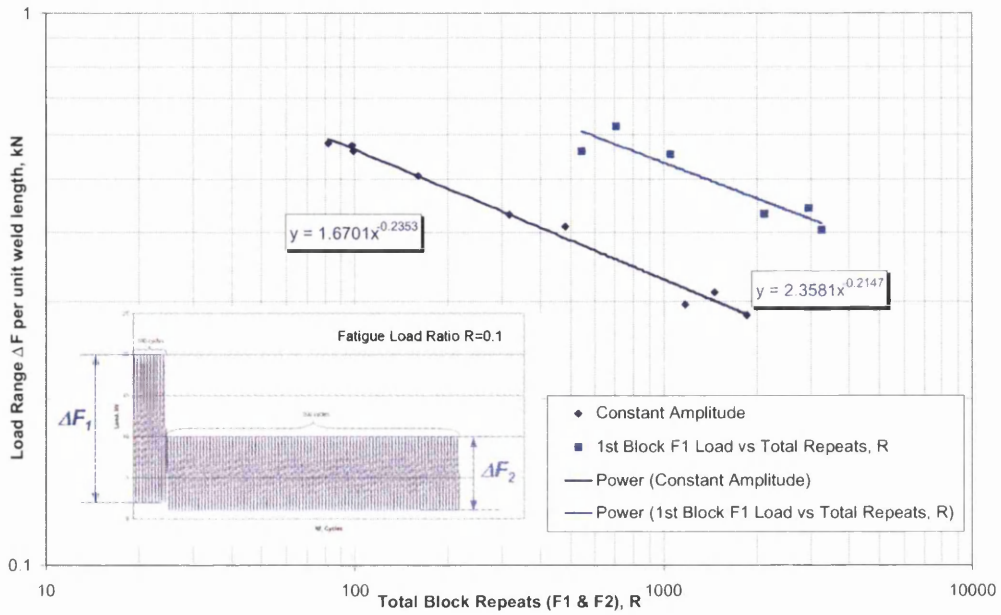

Figure 12.15: Block Loading vs. Constant Amplitude Loading at 1st Load Level, R=0.1

Figure 12.16, shows that the lower load of each block has some damaging effect, which has more effect at lower load levels.

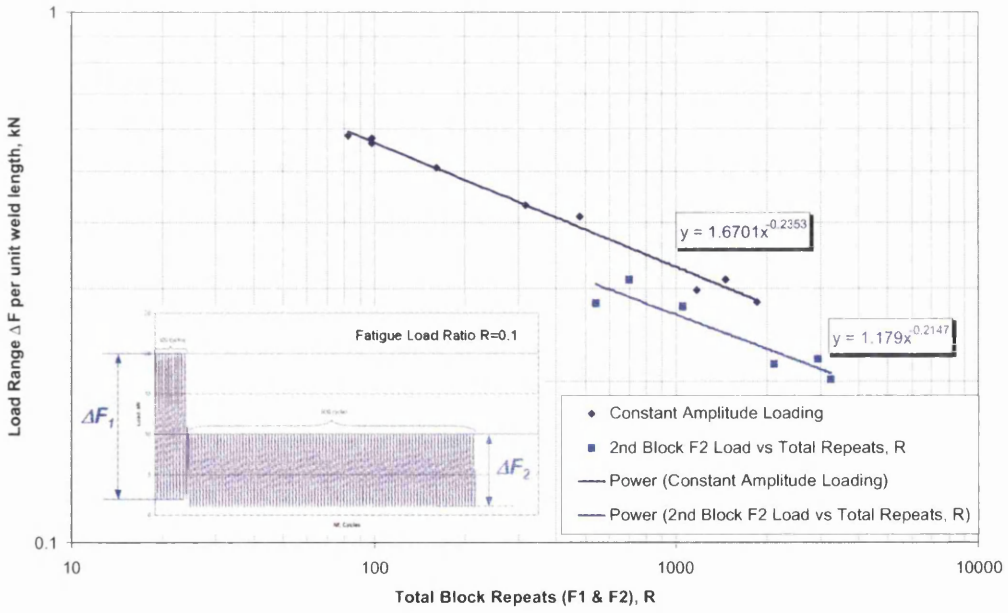

Figure 12.16: Block Loading vs. Constant Amplitude Loading at 2nd Load Level, R=0.1

In figure 12.17 using the constant amplitude results, the variable amplitude results can be predicted using Miner's Rule. Miner's Rule using a damage constant D=1 gives a good prediction of life.

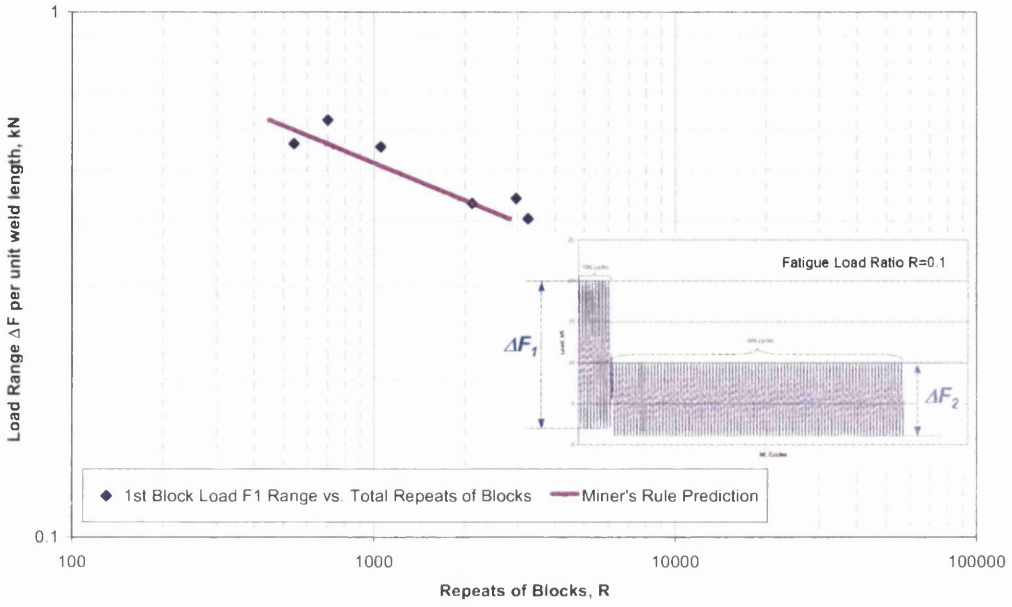

Figure 12.17: Miner's Rule

12.2.2 Variable Amplitude SAE Bracket Load-Time History

Figures 12.18 – 12.20 estimate the fatigue lives of GM1, TM11A and GM8 using the Miner's Rule analyses of figure 11.14. Figure 12.18 shows calculating the damage and estimating the fatigue life using Miner's Rule overestimates the life of GM1 regardless of using a damage constant of 1 or 0.7.

Using the Goodman mean stress correction to estimate the fatigue life with M_2 initially being 0.1, has a similar life estimation as D=0.7. Altering M_2 to 0.5 accurately predicts the variable amplitude results at high load levels, but at lower loads, it over-estimates the life. Using Miner's Rule for estimating fatigue lives of weld throat failures becomes more difficult.

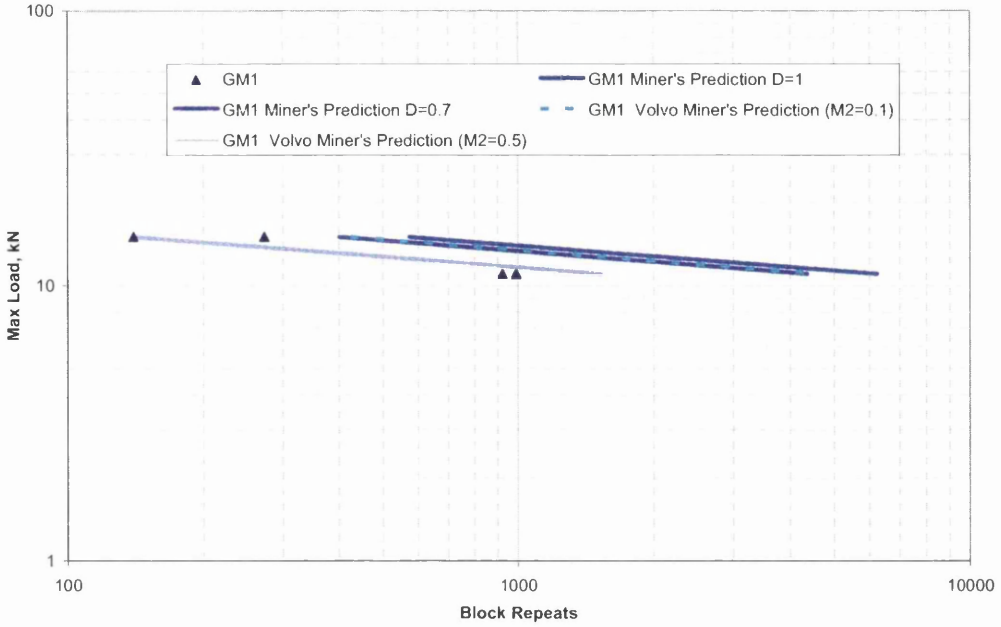

Figure 12.18: Miner's Rule for GM1

Figure 12.19 shows that for TM11A the Miner's Rule over-estimates the fatigue life of the coupon when using a damage constant D=1. Using D=0.7 and the Goodman correction method the fatigue life estimation accurately predicts the fatigue lives for weld toe failures.

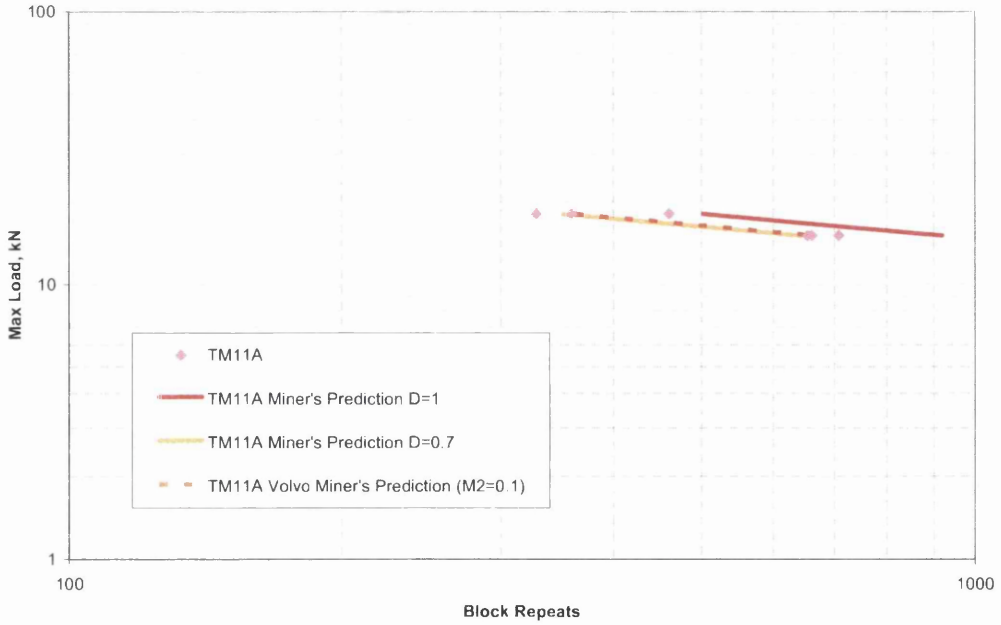

Figure 12.19: Miner's Rule for TM11A

For GM8 shown in figure 12.20, using a damage constant of D=1 and D=0.7 and Goodman correction M_2=0.1 all over-estimates the fatigue lives of the coupon.

Altering the M_2 to 0.5 accurately predicts the GM8 variable amplitude results; this shows that mean stress correction is required.

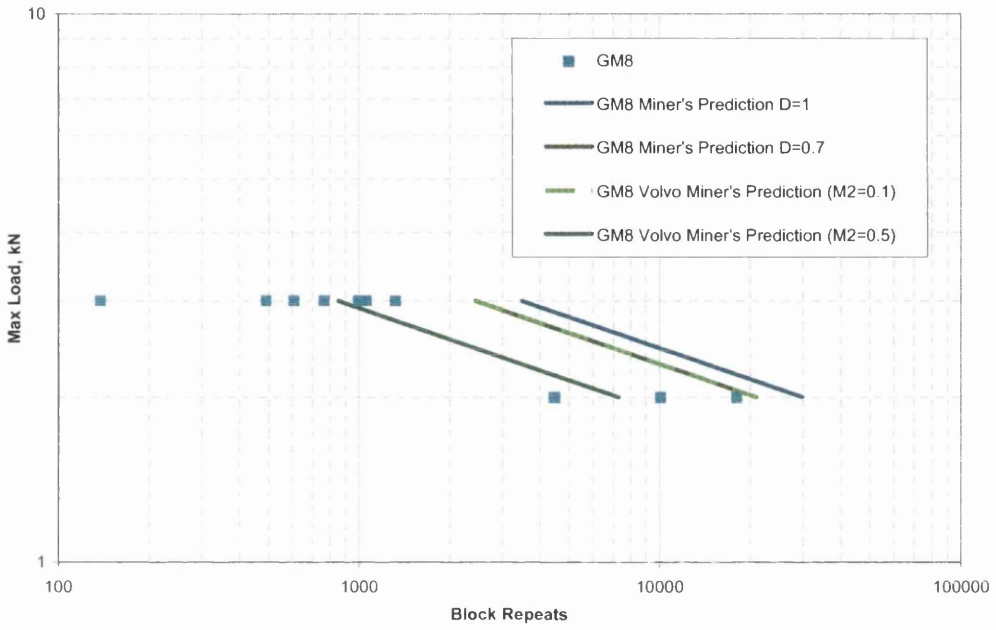

Figure 12.20: Miner's Rule for GM8

From figure 12.18 the effects from mean stress are clearly visible in the Miner's rule calculations. For analysing the variable amplitude GM1 by using the mean stress results shown in figure 11.11 and taking into account the weld length correction is shown in figure 12.21.

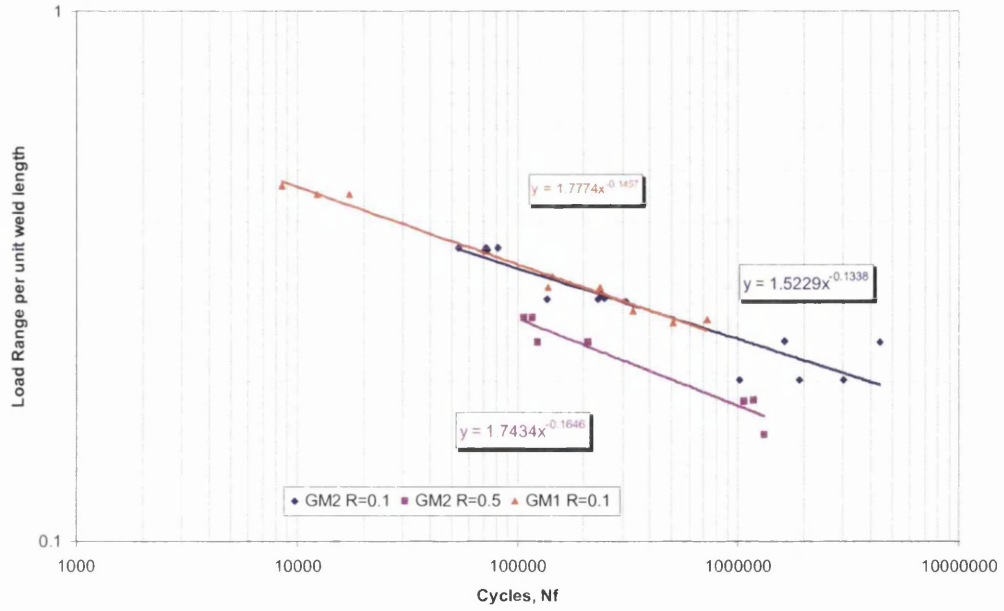

Figure 12.21: Load-Life Data for Weld Length Corrected GM1 and GM2

Noticeable from figure 12.21 is that both GM1 and GM2 at R=0.1 have very similar fatigue performance. Therefore when testing GM2 at R=0.5, GM1 will have very similar results. So correcting the GM2 R=0.5 equation of the curve with the average weld length of GM1 will be very similar to the results seen if GM1 was tested.

Figure 12.22 shows that from using figure 11.11, which has no weld length correction, Miner's rule over-predicts the life for GM1 variable amplitude loading. Using the weld length correction factor reduces the over-prediction from Miner's Rule by between 100 and 1000 cycles depending on the load.

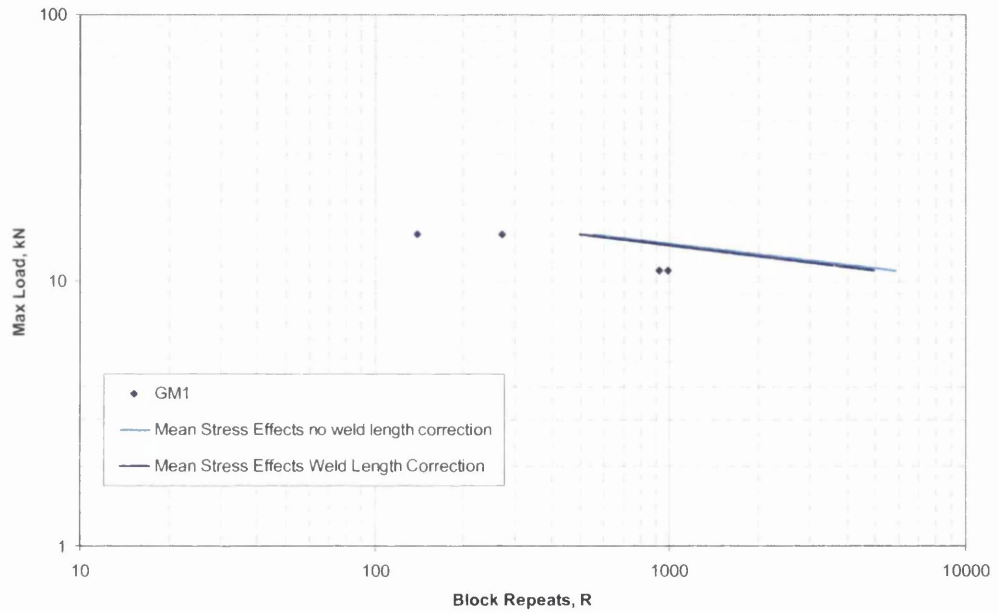

Figure 12.22: Miner's Rule for Mean Stress Correction of GM1

Using the mean stress results for TM11B shown in figure 11.12 to analyse the TM11A variable amplitude results is shown below in figure 12.23. The R-Ratio chosen was R=0.5 to analyse any of the variable amplitude signal, the mean stress effect for an R ratio higher than 0.5 is calculated as discussed in section 10.9.2.2.

The results in figure 12.23 show that correcting the load-time history for mean stress still over estimates the coupon fatigue lives. This means that when using the TM11B R=0.5 data to predict the effect of mean stress on TM11A, the difference in weld length must be accounted for.

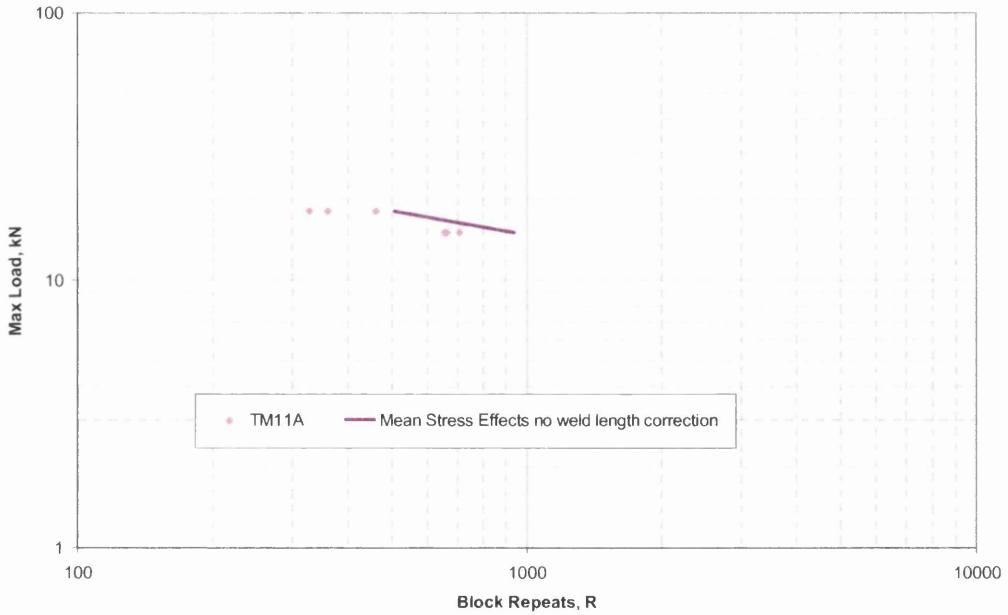

Figure 12.23: Miner's Rule for Mean Stress Correction of TM11A

Correcting for weld length for both TM11A and TM11B R=0.1 and R=0.5 test data is shown in figure 12.24.

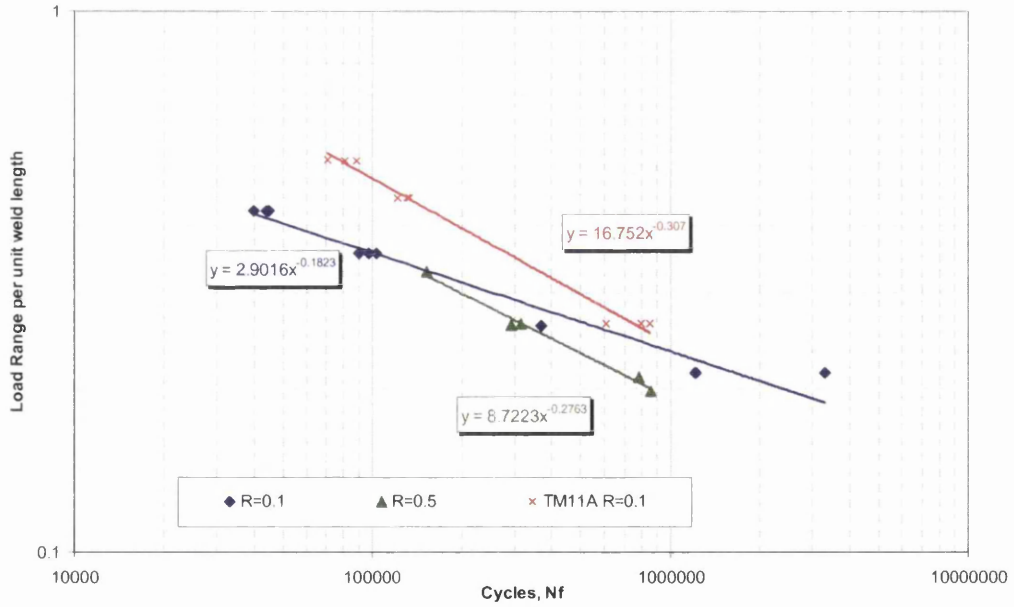

Figure 12.24: Load-Life Data for TM11A and TM11B Corrected for Weld Length

Both TM11A and TM11B R=0.1 curves have not collapsed together after correcting for the weld length, then using TM11B R=0.5 for TM11A will not be possible. Therefore the predicted TM11A R=0.5 curve must be calculated from the differences shown in TM11B. Section 10.9.3.1 describes how TM11A R=0.5 is calculated. Figure 12.25 shows the estimated TM11A R=0.5 curve.

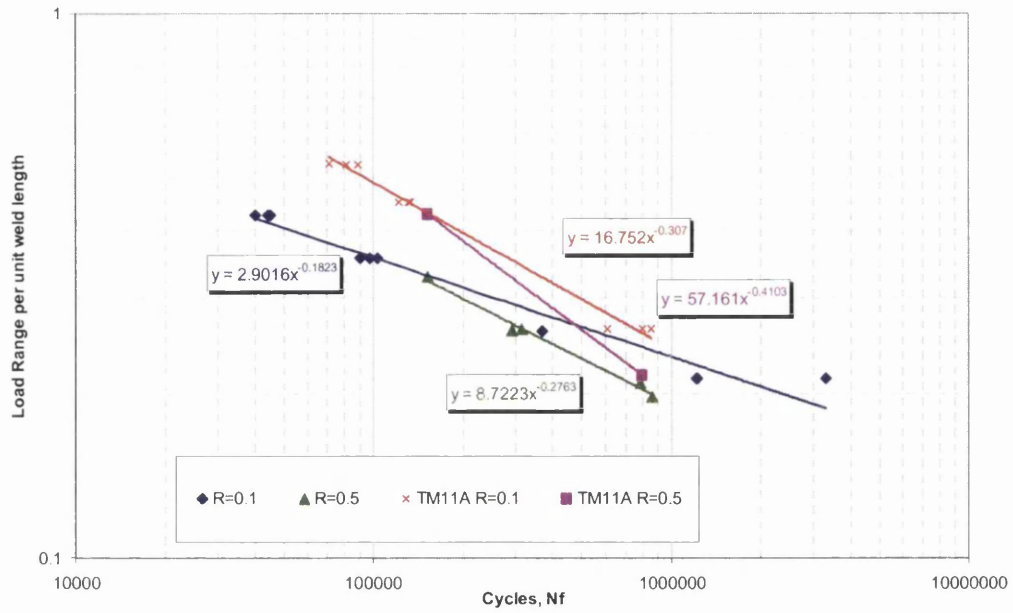

Figure 12.25: Estimated Load-Life Curve for TM11A R=0.5

From this the variable amplitude TM11A results can be reanalysed for mean stress effects. The R-Ratio chosen was R=0.5 to analyse any of the variable amplitude signal, the mean stress effect for an R ratio higher than 0.5 is calculated as discussed in section 10.9.2.2. Figure 12.26 shows the reanalysed mean stress effect with weld length correction. Weld length correction shows that the Miner's rule now more accurately predicts the TM11A variable amplitude data.

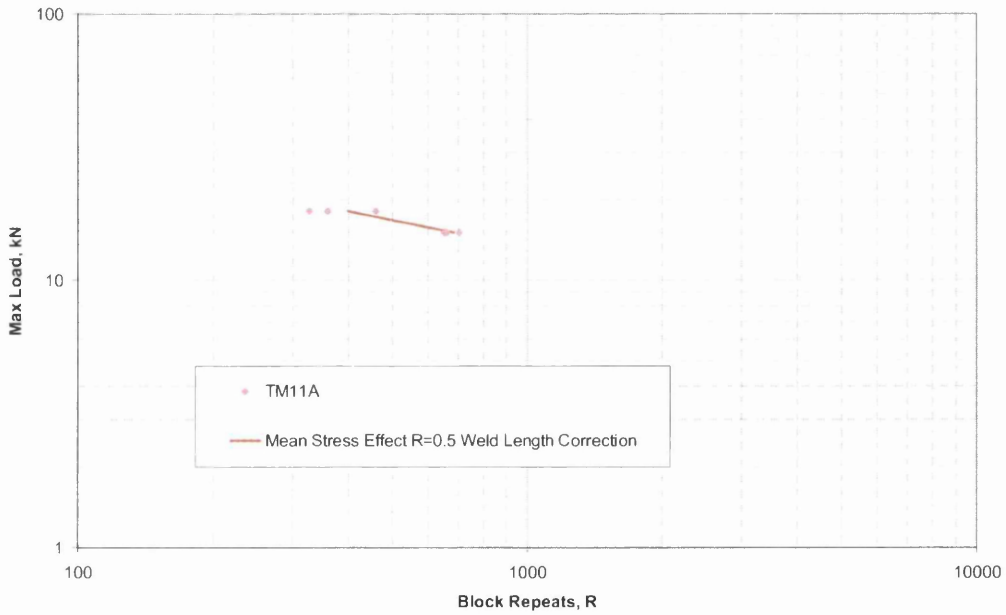

Figure 12.26: Miner's Rule for Mean Stress Correction of TM11A

12.2.2.1 Volvo Goodman Mean Stress Miner's Rule

From figures 12.18 – 12.20 the values used to calculate the Miner's Rule for mean stress was calculated based on the suggested values from Volvo's work. From the mean stress testing of TM11B and GM2 at R=0.5, and using the R=0.1 data as well, the actual M_2 values can be calculated for this work.

This was carried out on the load-life data shown in figures 12.21 and 12.24, which have been corrected for weld length differences. Calculating M_2 is described in Eq.33 in section 10.9.3.2.

Figure 12.27 shows how M_2 is affected by life. The M_2 value based on the Goodman diagram shown in section 10.9.3 is sensitive to life. At lower loads (low cycles), the slope is lower whereas at higher cycles M_2 value is much higher i.e. a steeper slope.

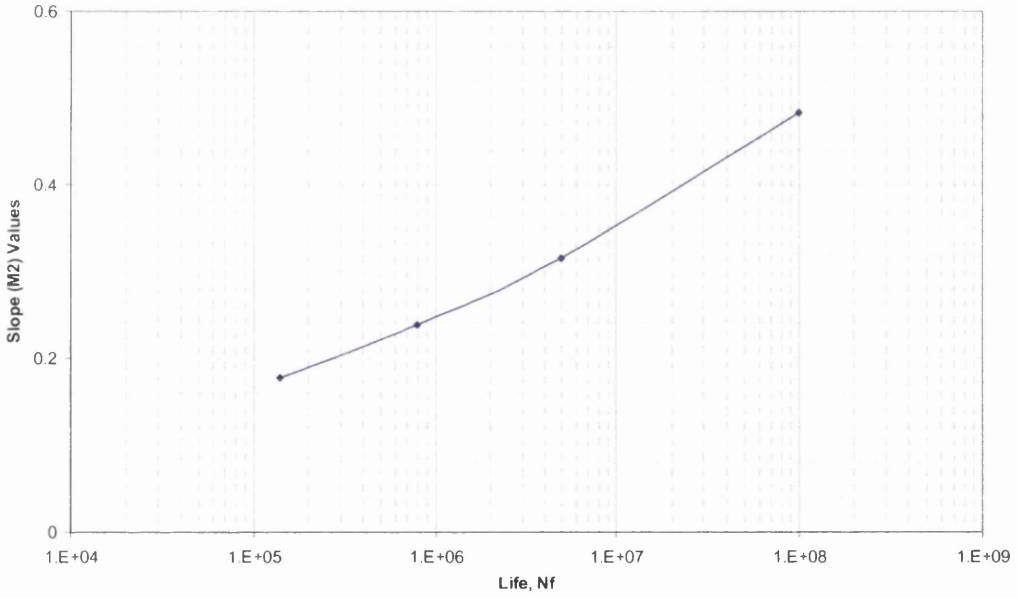

Figure 12.27: M_2 vs. Life for GM2

Figure 12.28 shows the sensitivity to life of M_2 for TM11B. At lower loads the M_2 value is lower than at higher loads.

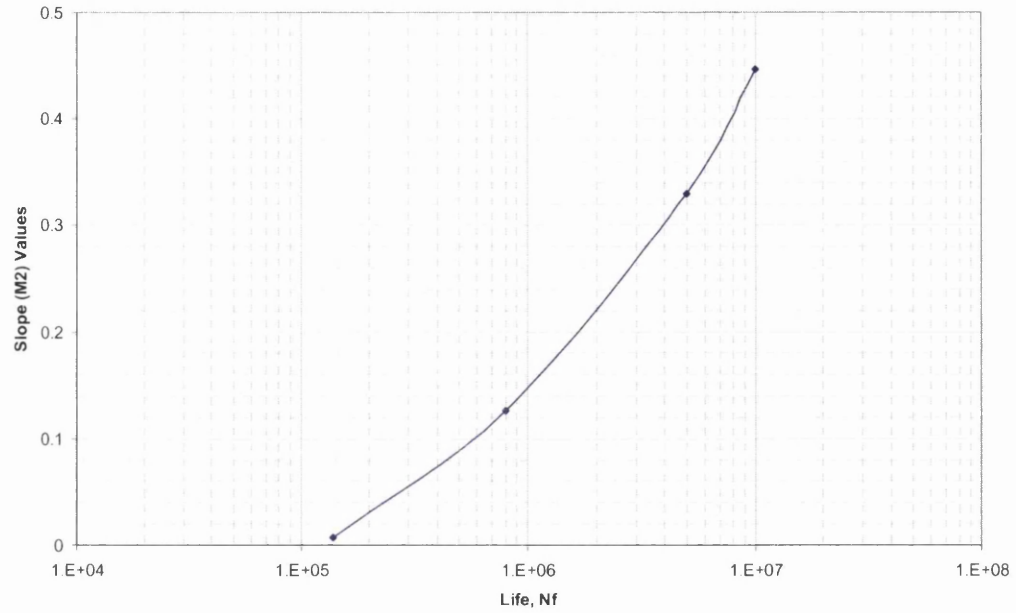

Figure 12.28: M_2 vs. Life for TM11B

From both figures 12.27 – 12.28 it is noticeable that the slope M_2 is sensitive to life. Therefore a range of M_2 values is possible for the difference between R=0.1 and R=0.5 depending on what life is selected. This is shown in figure 12.29 – 12.30 for GM2 and TM11B respectively.

Figure 12.29 shows that at low lives the slope M_2 is steep and it gradually gets steeper as the lives get longer.

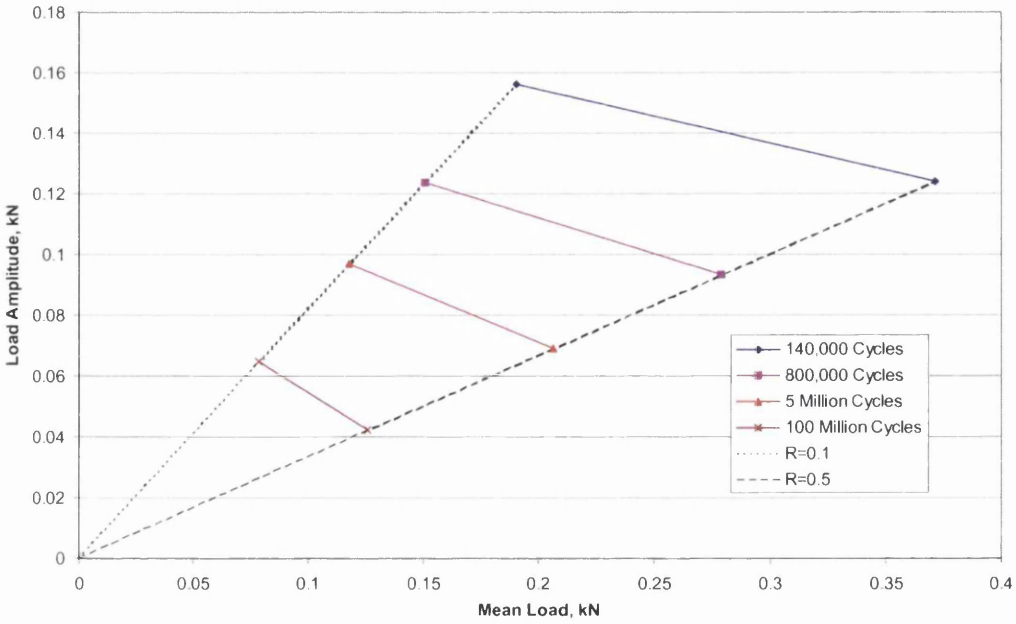

Figure 12.29: Load Amplitude vs. Load Mean for GM2

Figure 12.30 shows that at low lives, the M_2 value for the slope is virtually horizontal i.e. they are virtually the same value. At higher fatigue lives, the M_2 values (slope) become much steeper due to the effect of mean stress at higher lives.

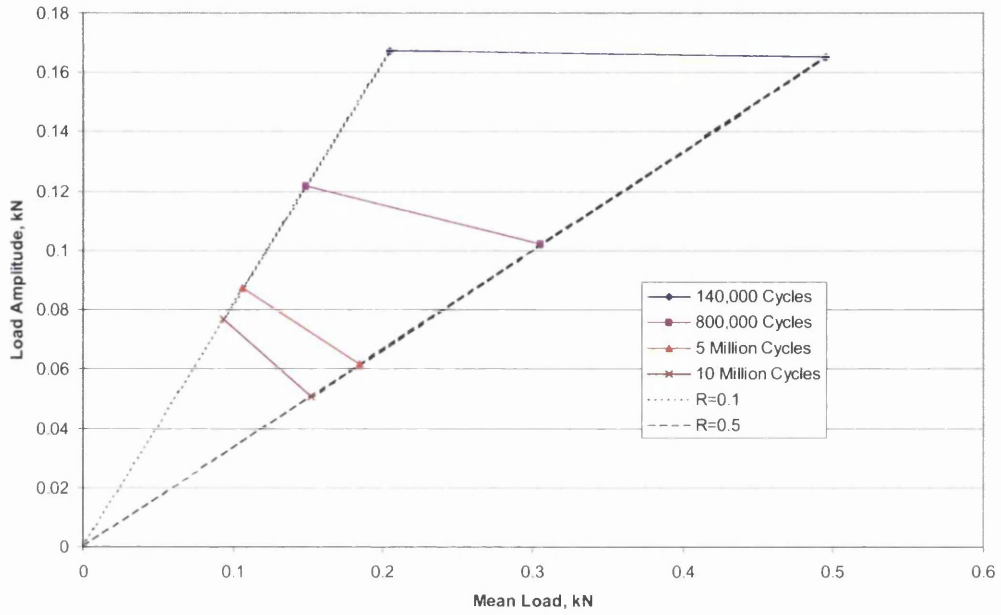

Figure 12.30: Load Amplitude vs. Load Mean for TM11B

Both figures 12.29 and 12.30 show a very similar trend to the metals Haigh diagram shown in figure 2.4. This shows that calculating the effects of mean stress is very important. Using the Goodman mean stress correction factor requires the testing for all geometries at different R-Ratios to establish the actual M_2 values for the test.

To ensure the correct mean stress correction factor for weld fatigue was used, further work is required in using the other mean stress equations such as Gerber, Morrow etc. as described in section 2.5.1.1.

12.3 Coupon Testing Failure Modes and Locations

From analysing all the coupons tested under both constant and variable amplitude loading, they all fall into the traditional categories of throat failure and toe failure. On closer inspection though there are two modes of throat failure within the coupon specimens, especially the lap-shear and peel coupon geometries fail under the vague term "throat failure".

As shown in figures 11.16 and 11.17 of the single lap-shear joints, the fatigue cracks propagate from the weld root through the interface of the sheet and the weld nugget edge. In the peel joints shown in figure 11.19, the method of throat failure also started from the weld root but propagated though the weld throat.

From this analysis there are now three main locations of failure as shown below in figure 12.31.

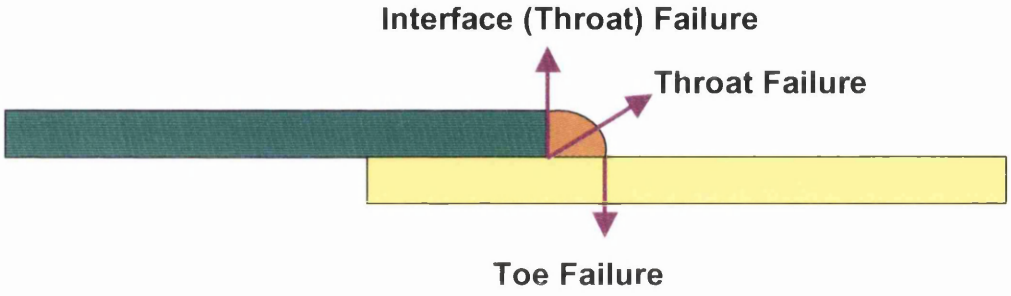

Figure 12.31: Failure Locations

- Interface Failure – failure from weld root to the weld nugget parent material sheet failure.
- Throat Failure – failure propagating from the weld root through the weld throat.
- Toe Failure – failure of the parent material sheet around the weld toe.

12.4 Coupon FE Modelling

12.4.1 FE Modelling With Experimental Verification

The purpose of such modelling-measurement comparison was to gain confidence in the coupon-joint FE models, which will be used for "structural stress" evaluations in weld fatigue analysis technique development.

12.4.1.1 Effects of Weld Representation in FE Models

Overall, it appears that little differences exist among stress results from various FE weld representations. In addition, figure 11.39, shows that the solid model predicts very similar stress results to those from the shell model. Figures 11.41 – 11.42 also indicate that no significant differences between the maximum principal stress and the stress in "y" direction σ_y stress. Therefore, in the investigations of all the factors on the predicted FE stress values, only the four-noded quadrilateral shell (Quad4) elements were used in all subsequent FE analyses.

Figure 11.40 – 11.42 show the stress distribution along three straight longitudinal paths, 10mm apart, across the coupon width at distances from the weld. M1 (figure 11.40) shows the closest correlation between the three stress distributions further from the weld. At the distance of 9mm from the weld, the weld profile acts as a stress raiser causing the 10mm left of centre line to have higher stress values recorded.

Figure 11.41 (M2) shows the same trend that further from the weld the three stress distributions are very close. At 11mm from the weld, the stress value recorded for the centre line is slightly higher than the others. This could be due to the larger size of the weld profile still influencing the stress.

Figure 11.42 (M11A) shows that the three stress distributions do not converge until the furthest possible distance from the weld. The centre stress distribution has the highest stress and the slowest to converge to similar stresses, whilst the left stress distribution converges faster due to the large size of the weld profile still influencing the stress.

12.4.1.2 FE vs. Strain Gauges

FE predictions and their comparisons with the strain-gauge results shown in figures 11.43 – 11.45 indicate that at low loads predicted and measured stress is very close, and the predicted FE stress values under-predict the actual stress. At higher loads, the FE-derived stress significantly under-predicts the measured stress by approximately 20MPa.

12.4.1.3 FE vs. Photoelasticity

The results from comparing the three methods of predicting stress in all three coupons are shown in figures 11.46 – 11.48. M1 and M2 FE stress predictions are marginally lower but they are still within the scatter of the photoelasticity results. M11A predicted results as shown in figure 11.48 produced a significant under-prediction of the coupon stress when compared to both the photoelastic and strain gauging results. This could arise from how the coupon was modelled.

To help explain the differences between the results from FE and Photoelasticity results, the effect of element size on FE stress results has been carried out. Stress

distributions from FE models of two element sizes are shown in figures 12.32 – 12.33 and, in the area of comparison, distance >10mm from the weld, both figures show similar stress distribution patterns.

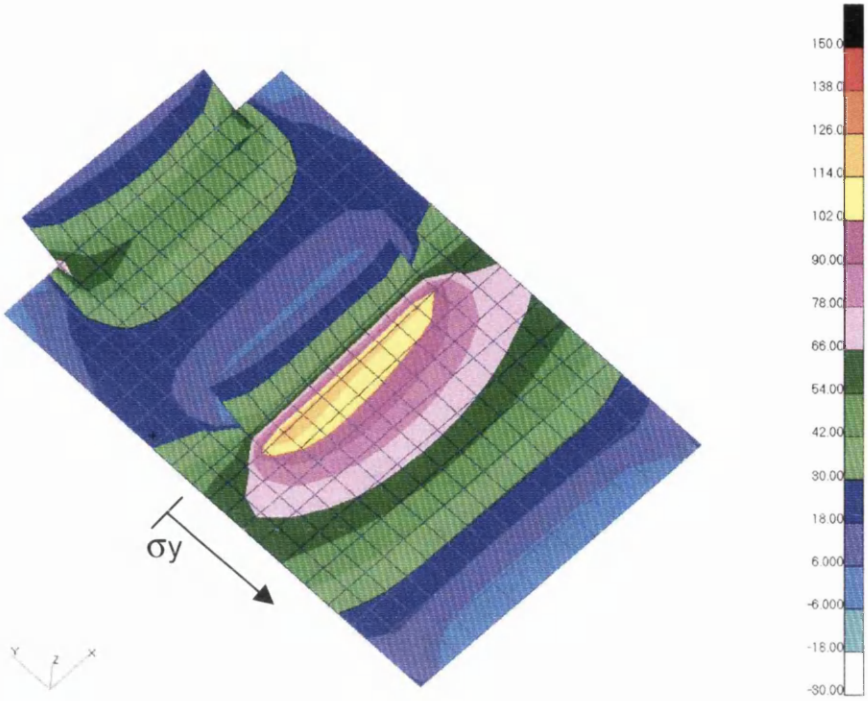

Figure 12.32: Coarse Mesh Size on M11A

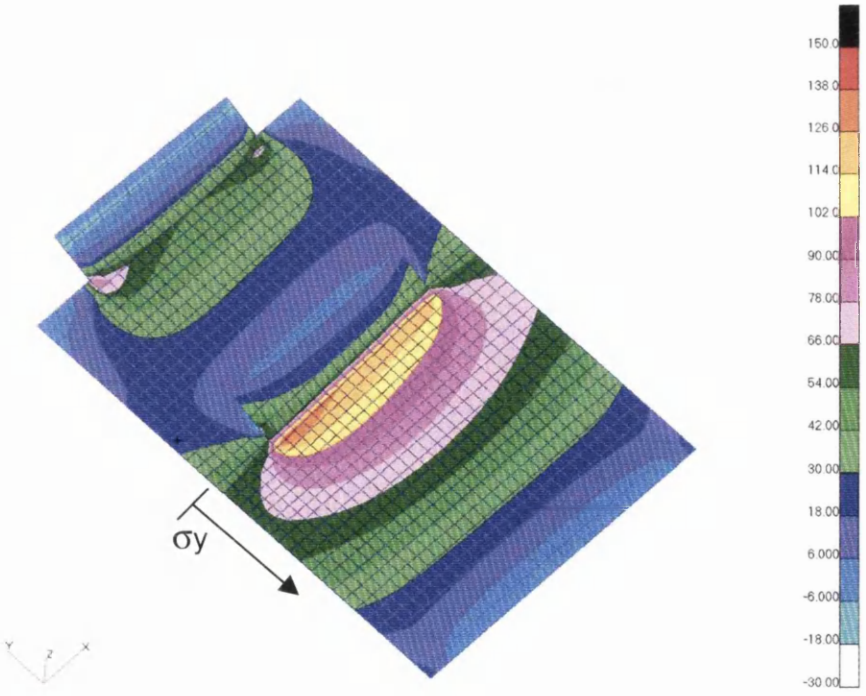

Figure 12.33: Finer Mesh Size on M11A

The effect of mesh sensitivity was also considered in this investigation to ensure that the accuracy of the predictive technique is not sensitive to the mesh size. Mesh size

of 3mm for the coarse mesh and 1.5mm for the fine mesh was used in the study. The results of the mesh sensitivity is shown in figures 12.32 – 12.33, and they indicate that there is a 10% increase in peak stress at the weld toe, as the element size gets halved indicating that the accuracy is questionable for stress in the immediate proximity of the weld.

This further supports the view that weld fatigue analysis based on FE stress results are not recommended. A different approach of weld durability assessment is needed, which will be based on "structural stress", derived post-FE from loads experienced by the weld. The stress contour maps also show that there is minimal difference in the stress in the area of interest away from the weld. Therefore, changing element size has no effect on the stress results.

The current models used to produce the results have been built with perfect alignment as shown in figure 12.34. The actual misalignment was not included in these models and this could influence the difference between the FE model predictions and the photoelastic measurements.

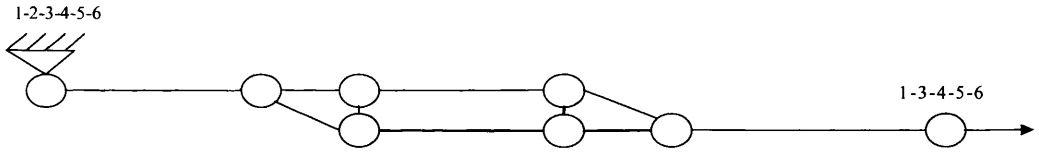

Figure 12.34: Uniform Distribution of Models

12.4.1.4 Types of Load Misalignment

Load misalignment could arise from the fatigue test machine grips being out of line and causing these effects:

- Translational shown in figure 12.35
- Rotational shown in figure 12.36
- Combination of Translation and Rotational

Out-of-straightness of the coupons, e.g. bent samples due to welding distortion, is another possible manufacturing defect that were not included in the initial FE models. The final possibility is a combination of bent coupons and misaligned grips. Together, they may cause sufficient variability in the actual stress levels in the

welded coupon joints to cause such a lack of correlation found in figure 11.48. Therefore, these effects need to be investigated.

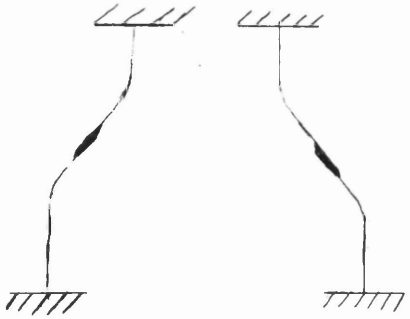

Figure 12.35: Translational Misalignment

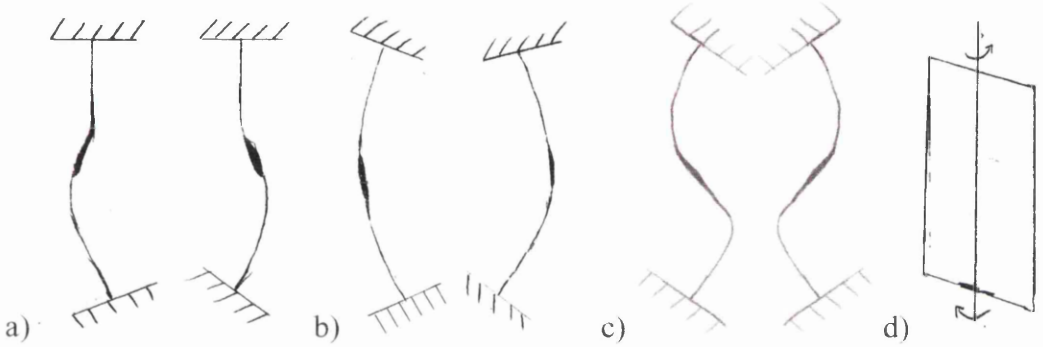

Figure 12.36: Rotational Misalignment

The effects of the misalignments are not evident by a single strain gauge or through photoelasticity measurements. However, they can be estimated from FE analyses by introducing various types and levels of load misalignments into an FE model and, then, quantifying the variations in the predicted stress distributions.

FE results of various misalignments are shown in figure 12.37. A rotational misalignment in one of the steel grips does influence the predicted stress, but it increases the stress values as the distance from the weld increases. This type of misalignment is unlikely to be the reason for the decrease in the predicted stress shown in the M11A results.

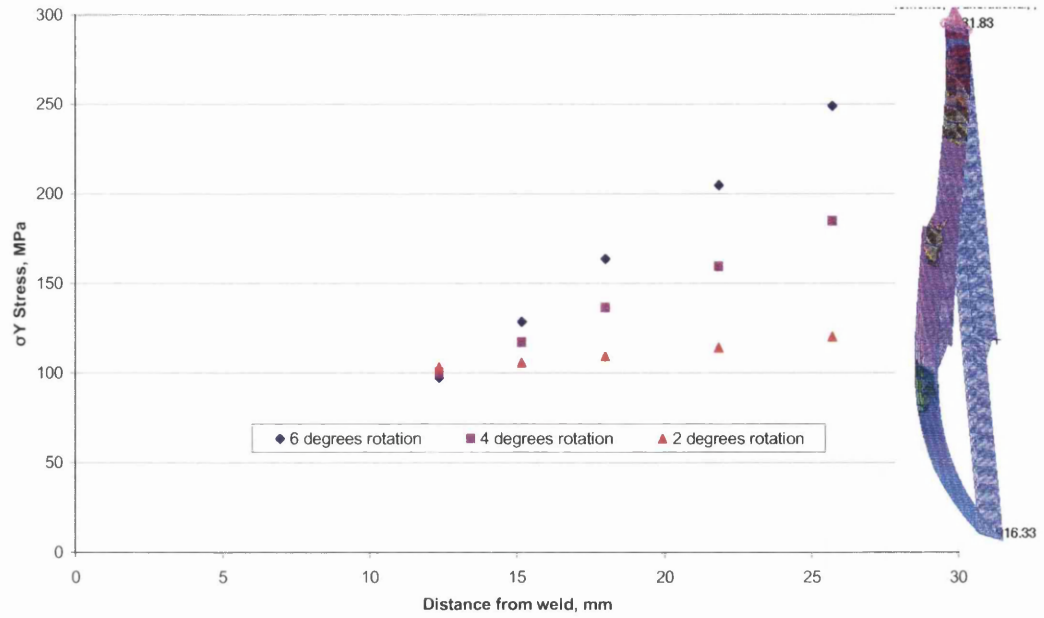

Figure 12.37: The Effects of Rotational Misalignment as Shown in Figure 12.36a

The effect of rotational misalignment in both grips is shown in figure 12.38, the results show this is the type of misalignment possibly in the coupons. Various models were built, altering the amount of rotation, which in turn increased the predicted FE stress levels significantly, which strongly suggested that this type of misalignment might have been present in the grips.

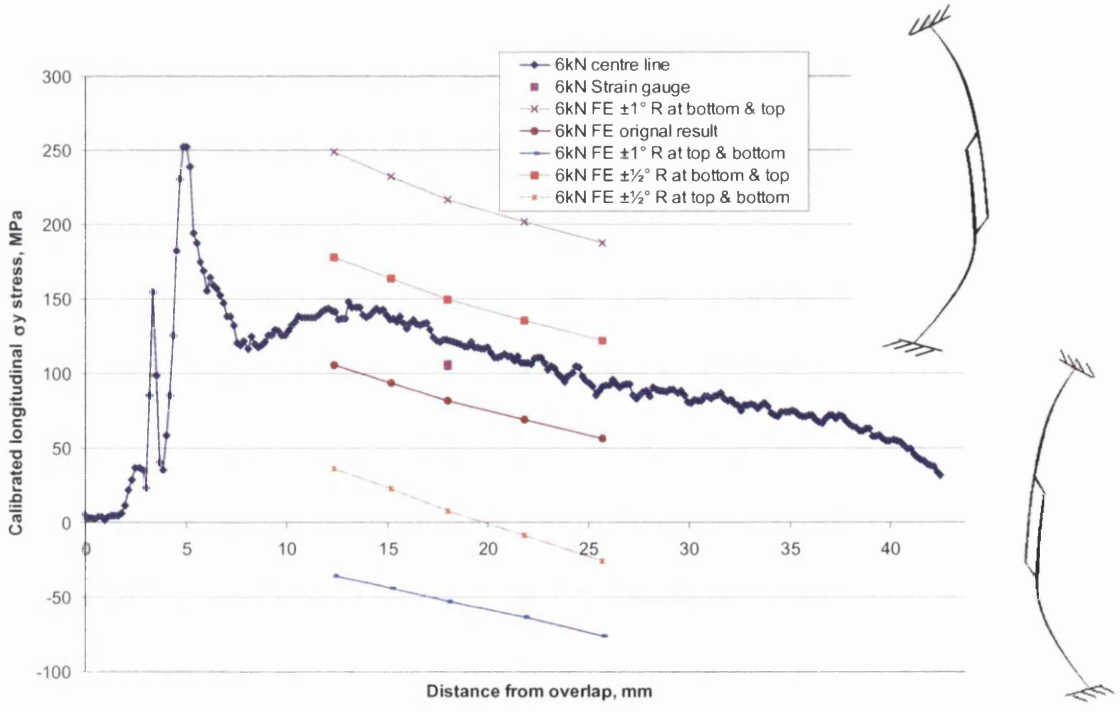

Figure 12.38: The Effects of Rotational Misalignment as Shown in Figure 12.36b

12.4.1.5 Weld Irregularities

From photographing and measuring each of the welded coupons prior to testing it is noticeable that each weld is different in location and size. The effect of this has only been partially accounted for in the basic FE models by altering the weld size across the geometry but not through moving the locations of the weld.

12.4.1.6 Photoelasticity Study Conclusions

Various methods of FE modelling a MIG/MAG seam weld in coupon test specimens have been investigated and results indicate that either increasing the shell element thickness representing the weld or having a back plate (triangular weld representation) to the weld affects little in the finite element stress values predicted. Shell-element FE models showed comparable predicted stress values to those obtained from FE analyses with the weld being represented by 3-D solid elements in the models.

Results show that predicted stress tends to under-predict strain gauged results only slightly at low load levels, but at high load levels the predicted stress is much lower.

Overall, the results show that for single-weld line lap-shear coupons (M1 and M2), the FE predicted stress is within the photoelasticity measurement scatter. For the double-weld line lap-shear coupons (M11A), the finite element results are significantly lower than the photoelasticity and strain gauge measurements.

The effects of finite element mesh sizes on the predicted FE stress were investigated, with the results indicating that the element mesh size has little effect on the prediction of the stress.

Overall the control of angular alignment is very important in testing and critical to the subsequent accuracy of the FE stress results.

12.4.2 Volvo (nCode) Structural Stress

Converting load-life curves to S-N curves is necessary to predict the fatigue life of FUCA Components. From the stresses extracted from the most damaged nodes at the weld toe (shown in Table 11.4) the stress–life curves can be produced, these are

shown in figures 12.39 and 12.41 for all weld toe failures and all weld throat failures respectively. For comparison of coupon suppliers' breakdown of all the weld toe and throat failures see Appendix 8.

Combining all the weld toe failures to produce one stress–life master curve is shown below in figure 12.39. The difference between the two suppliers is still noticeable with GKN having better fatigue lives that TKA-Tallent. Figure 12.39 shows that for TKA-Tallent joints TM11A, TM11B and TM2 there is good convergence of the results. In this case the geometry does not influence the results. When comparing the conversion of GKN GM11A and GM11B coupon joints, the stress-life curve shows reasonable convergence. Overall it is noticeable that for the entire weld toe failures one master curve could potentially be used.

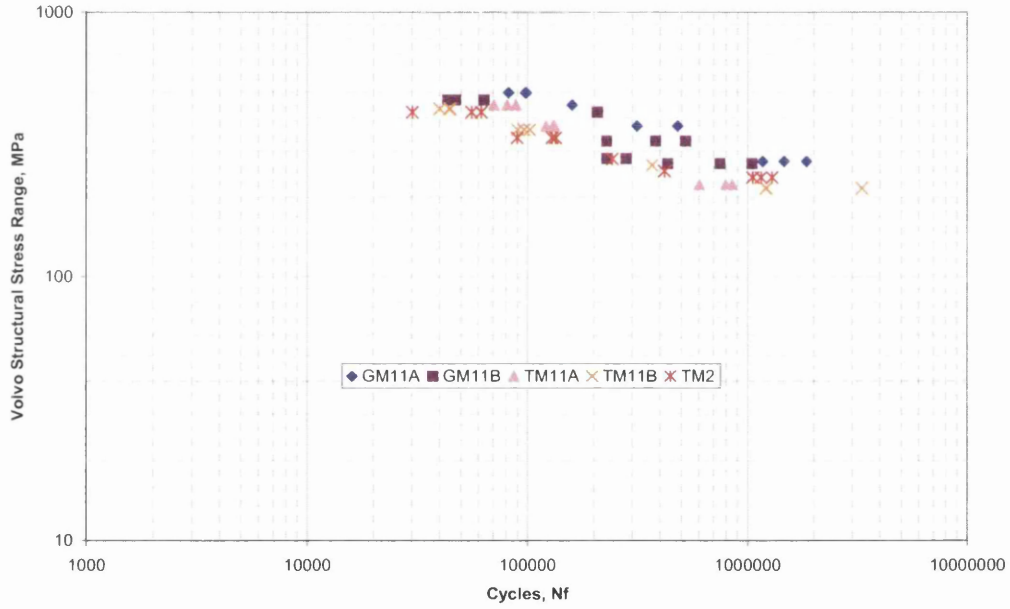

Figure 12.39: Stress–Life Master Curve Conversion for All Weld Toe Failures

Analysing the S-N curve as shown in figure 12.39 described in section 10.7.1, to understand the certainties of survival of a coupon statistical analysis occurs. Figure 12.40 shows the certainties of survival of the data at 99.87% and 0.13% of the S–N data for all the weld toe failures. Considering all weld toe failures S-N data the survival bands are subsequently much larger due to more scatter in the results.

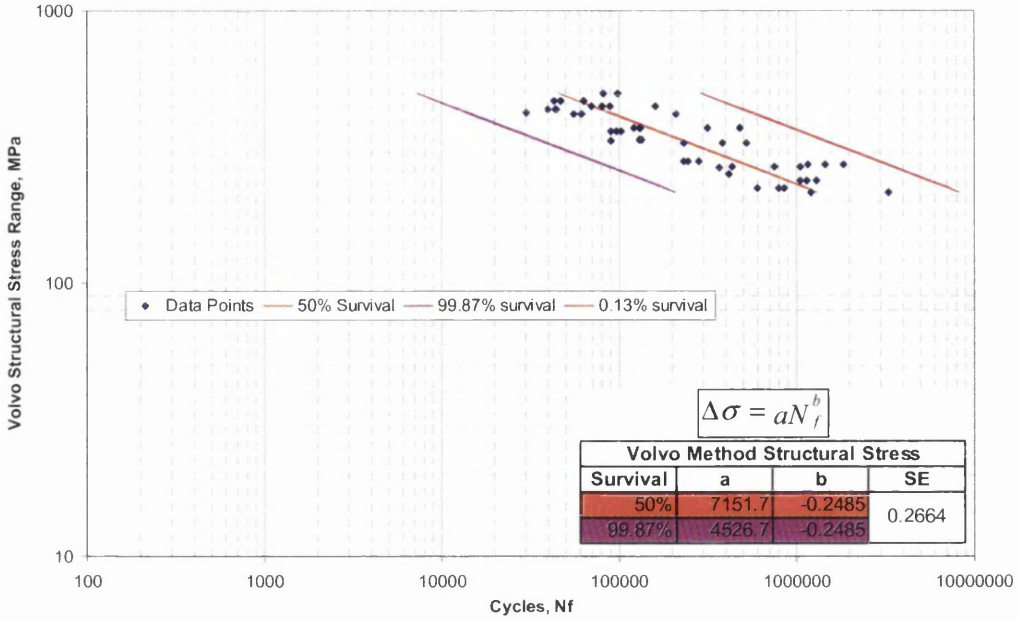

Figure 12.40: Statistical Analysis of All Weld Toe Failures

Figure 12.41 shows the Stress-Life Curve for all weld throat failures using the stress located on the underneath side of the weld toe elements above the weld on Side B as shown in figure 11.34. This graph shows that the throat failures must still be split into two S-N curves, as the predicted stress has not collapsed the peel and lap-shear results together, i.e. Throat failure vs. Interface throat failure.

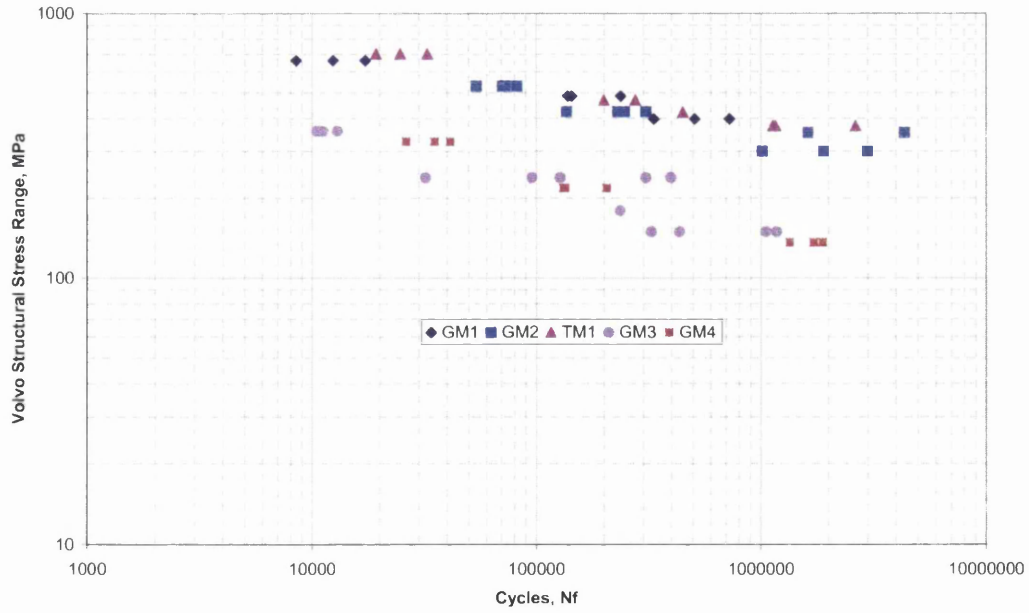

Figure 12.41: Stress–Life Master Curve Conversion for All Weld Throat Failures

Figure 12.42 shows the certainties of survival at 99.87% and 0.13% of the S–N data for all the weld throat failures. Noticeable from this graph is that the effect of the lap-shear (interface throat failure) and the peel (throat failure) S-N curves not collapsing together causes the survival bands to be very large. From this it is recommended that both the lap-shear and peel S-N curves have individual S-N curves and are not combined in all weld throat failures.

Figure 12.42 indicated the importance for the third failure mode: interface failure to be identified and separated from the throat failures and classed as a separate master S-N curve.

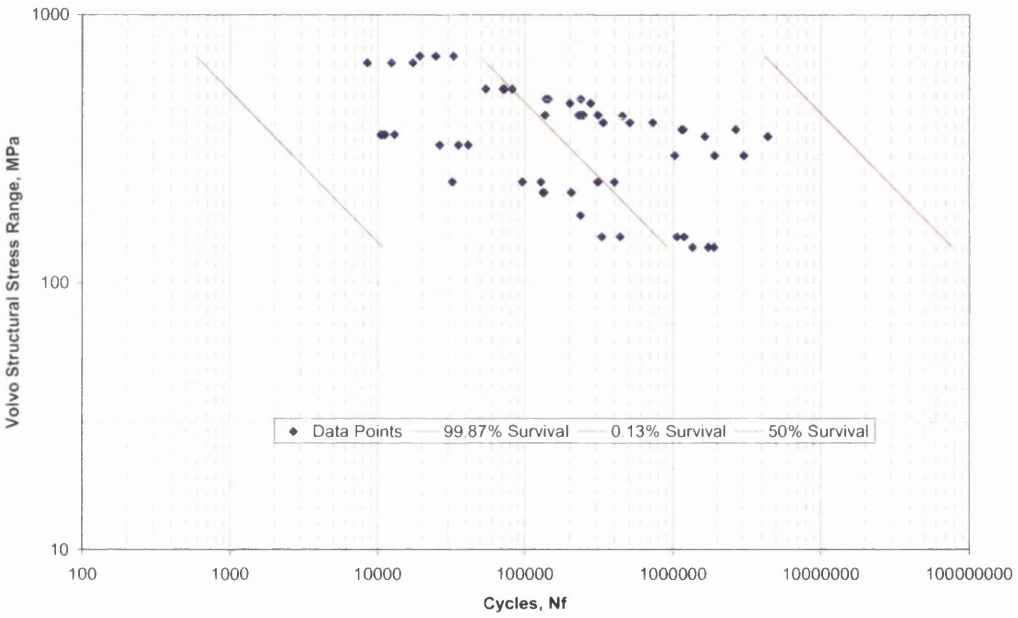

Figure 12.42: Statistical Analysis of All Weld Throat Failures

The stress–life curve for GM1, GM2 and TM1 lap-shear joints – interface failure is shown in figure 12.43. The test data for GM1, GM2 and TM1 showed very good convergence but the subsequent stress–life convergence produced reasonable convergence for interface failures. TM1 still has slightly higher fatigue lives than GM1 and GM2.

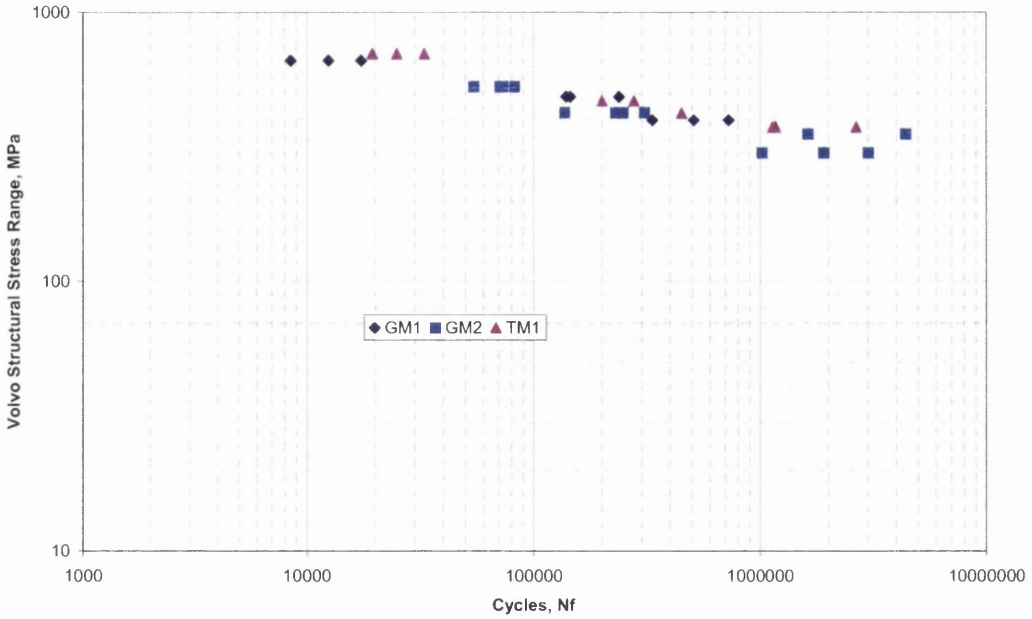

Figure 12.43: Stress–Life Master Curve Conversion for All Weld Interface Failures

Figure 12.44 shows the certainties of survival at 99.87% and 0.13% of the S–N data for all interface throat failures (GM1, GM2 and TM1). Noticeable from this graph is that by removing the peel (throat failures) S-N curve causes the survival bands to be relatively narrow.

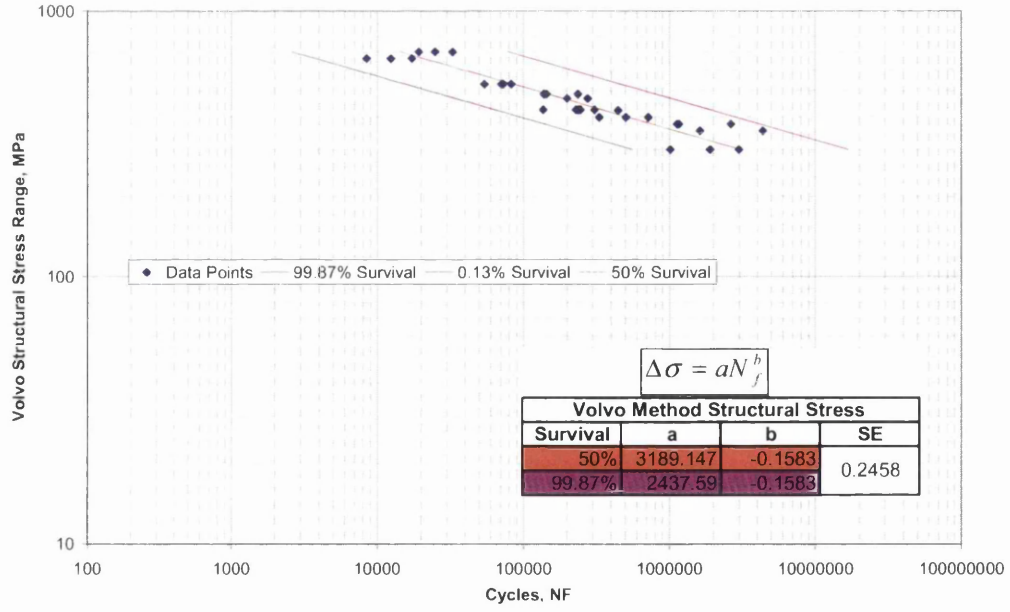

Figure 12.44: Statistical Analysis of All Weld Interface Throat Failures

The stress–life curve for the peel geometries GM3 and GM4 – throat failure, is shown below in figure 12.45. The test data for throat failures shows good

convergence, whereas when converted into a stress–life curve the results show reasonable convergence.

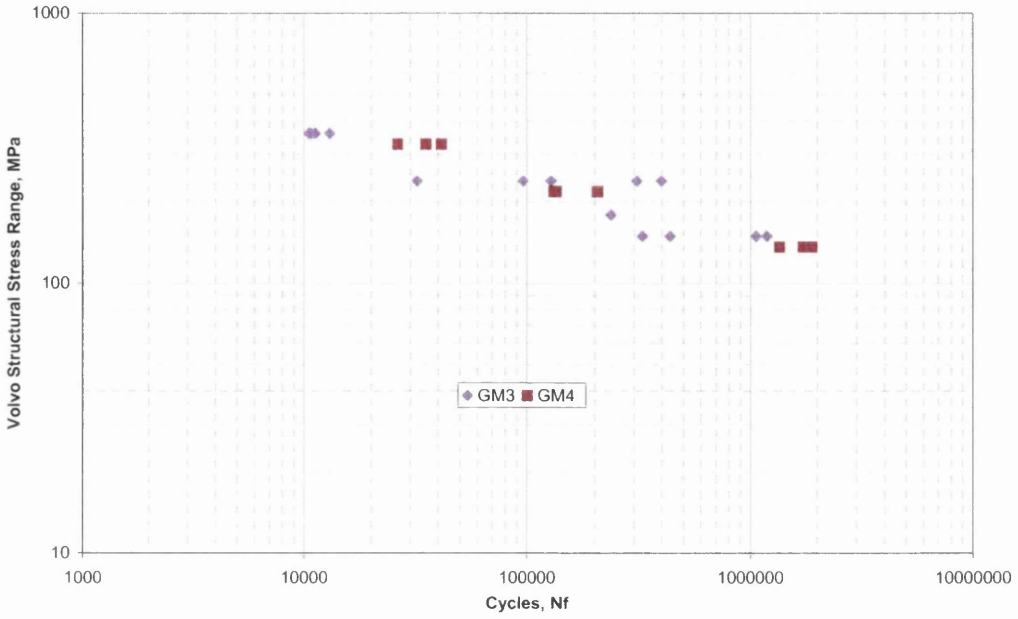

Figure 12.45: Stress–Life Master Curve Conversion for All Weld Throat Failures

Figure 12.46 shows the certainties of survival at 99.87% and 0.13% of the S–N data for all throat failures. Noticeable from this graph is that with the reasonable amount of scatter in the results, the survival bands are reasonably wide, though the survival bands bind all data points.

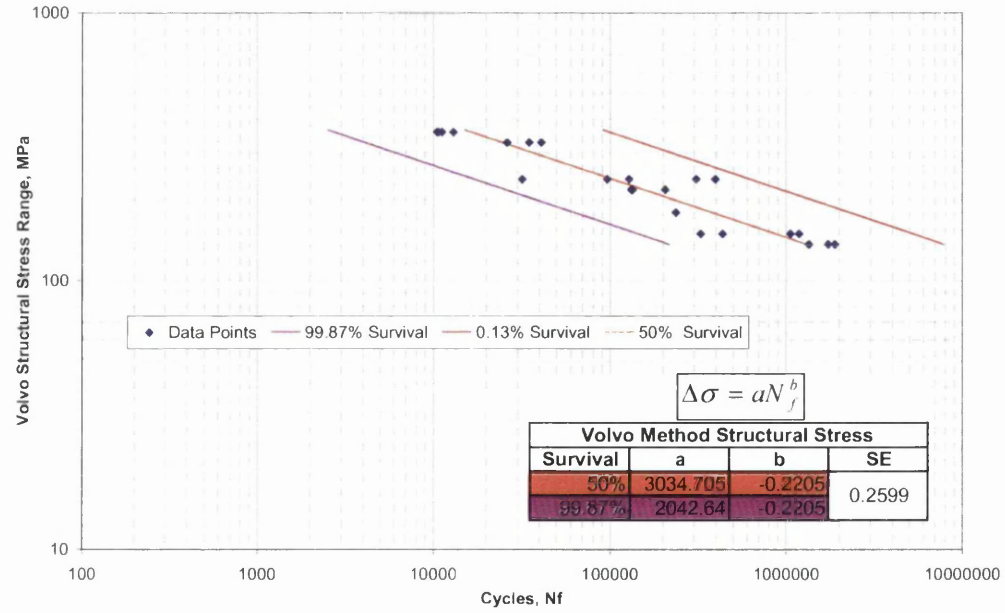

Figure 12.46: Statistical Analysis of All Weld Throat Failures

Table 12.1 shows all the master S-N curve parameters generated from this study.

Table 12.1: Volvo Master S-N Curve Parameters

$$\Delta\sigma = aN_f^b$$

Volvo Method Structural Stress				
Failure Location	**Survival**	**a**	**b**	**SE log(N_f)**
Toe Failure	50%	7151.67	-0.2485	0.2664
	99.87%	4526.7	-0.2485	
Interface Failure	50%	3189.15	-0.1583	0.2458
	99.87%	2437.59	-0.1583	
Throat Failure	50%	3034.71	-0.2205	0.2599
	99.87%	2042.64	-0.2205	

12.4.2.1 Volvo (nCode) Structural Stress – Sensitivity Study

A small sensitivity study was carried out on the TM1 results to understand if the weld location, weld height and thickness of side B affected the FE results. The extremes of geometry used came from the measured coupon specimens used in the constant amplitude testing. Table 12.2 shows the contents of the study.

Table 12.2: Sensitivity Study Contents

TM1 Sensitivity Analysis	Changes	Stress MPa
TM1 using averages	N/A	51.867
Modified weld thickness	6mm	51.92
Weld Height - High	Left:5.67, Right:10.27	52.709
Weld Height - Low	Left:7.05, Right:7.74	53.039
Weld Position - High	Left:11.56, Right:5.27	53.682
Weld Position - Low	Left:11, Right:4	52.383
Side B thickness - High	3.02mm	50.728
Side B thickness - low	2.95mm	52.581
Side A & B thickness - high	Side A:2.99, B:3.02	50.682
Side A & B thickness - low	Side A:2.94, B:2.95	52.791

Figure 12.47 shows the effect of the sensitivity study against the other throat failure lap-shear geometries GM1 and GM2. Changing the weld height and position along with the thickness has little effect on changing the predicted FE stress. Therefore using just the average coupon geometries is good enough for the collapsing of the load-life data.

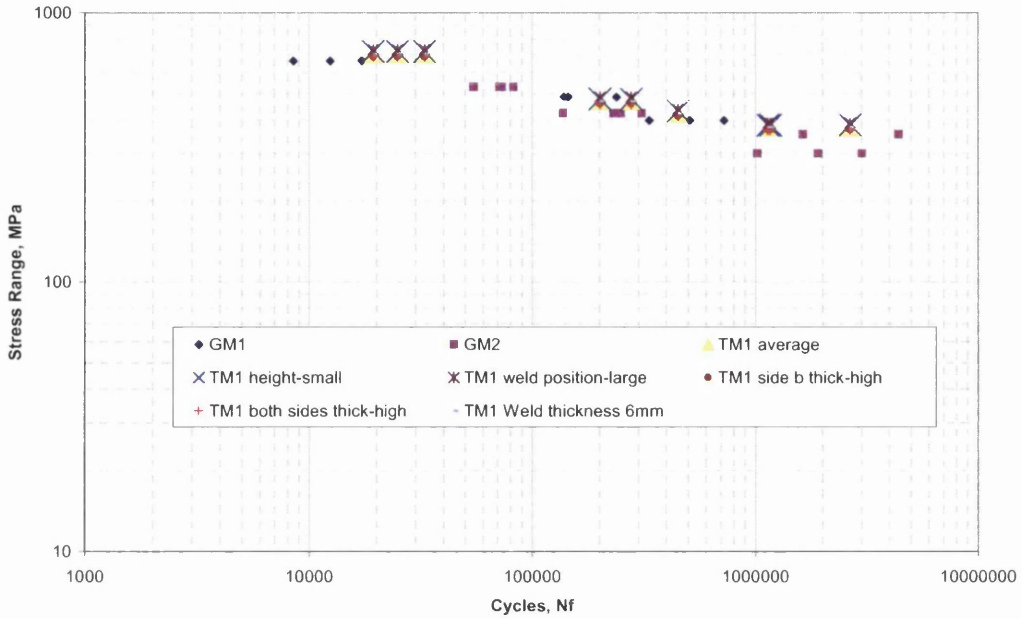

Figure 12.47: Sensitivity Study on TM1

12.4.3 Battelle Method

12.4.3.1 Battelle Structural Stress

Converting load-life curves to S-N curves using the Battelle Structural Stress Method was completed using the three different methods; Manual Calculation, FLOW and Verity. The S-N curves are used to estimate the fatigue life of FUCA Components. From the stresses extracted from the most damaged nodes at the weld toe (shown in Table 11.5) the stress–life curves can be produced for the manual method, these are shown in figures 12.48 and 12.50 for all weld toe failures and all weld throat failures respectively. For comparison of coupon suppliers' breakdown of all the weld toe and throat failures see Appendix 9.

Combining all the weld toe failures to produce one stress–life master curve is shown below in figure 12.48. The difference between the two suppliers is still noticeable with GKN having better fatigue lives that TKA-Tallent. Figure 12.48 shows that for TKA-Tallent joints TM11A, TM11B and TM2 there is good convergence of the results. In this case the geometry does not influence the results. When comparing the conversion of GKN GM11A and GM11B coupon joints, the stress-life curve shows reasonable convergence. Overall it is noticeable that for the entire weld toe failures one master curve could potentially be used.

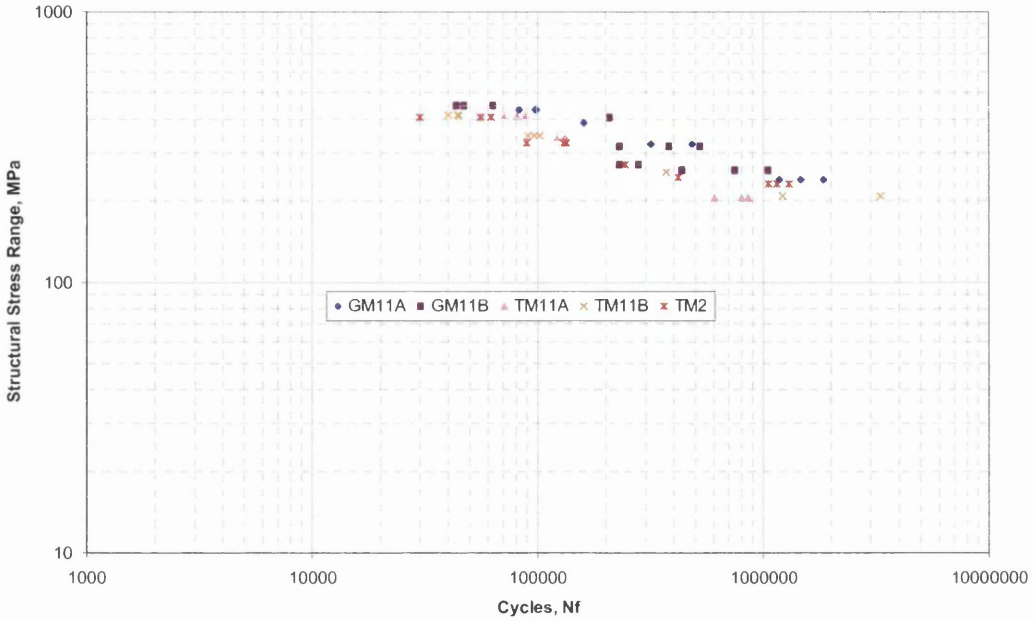

Figure 12.48: Stress–Life Master Curve Conversion for All Weld Toe Failures

Analysing the S-N curve as shown in figure 12.48 described in section 10.7.1, to understand the certainties of survival of a coupon, statistical analysis occurs. Figure 12.49 shows the certainties of survival at 99.87% and 0.13% of the S–N data for all the weld toe failures. Considering all weld toe failures S-N data the survival bands are subsequently much larger due to more scatter in the results

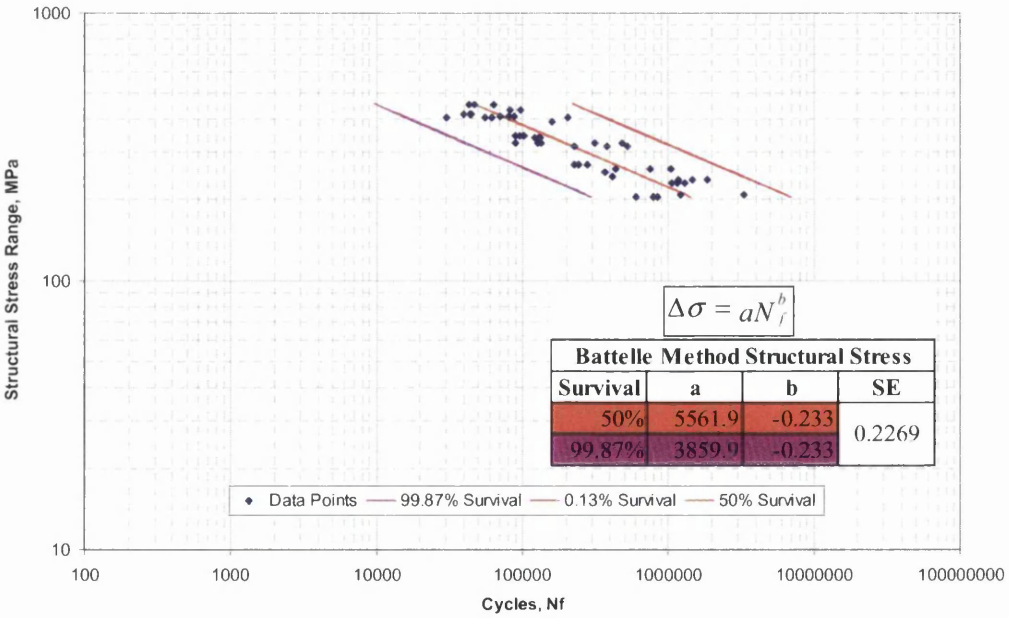

Figure 12.49: Statistical Analysis of All Weld Toe Failures

Figure 12.50 shows the Stress-Life Curve for all weld throat failures using the stress located on the underneath side of the weld toe elements above the weld on Side B as

shown in figure 11.34. This graph shows that the throat failures must still be split into two S-N curves, as the predicted stress has not collapsed the peel (throat) and lap-shear (interface) results together.

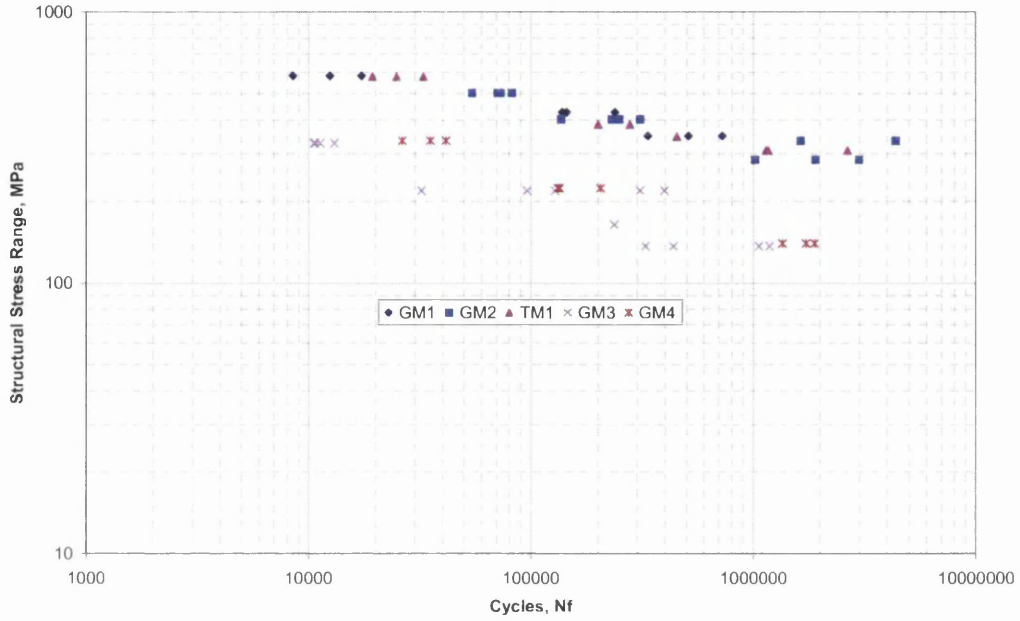

Figure 12.50: Stress–Life Master Curve Conversion for All Weld Throat Failures

Using one S-N curve to represent all weld throat failures gives very large survival bands when analysed as shown in figure 12.51, this also shows that the lap-shear geometries and the peel geometries require separate S-N curves.

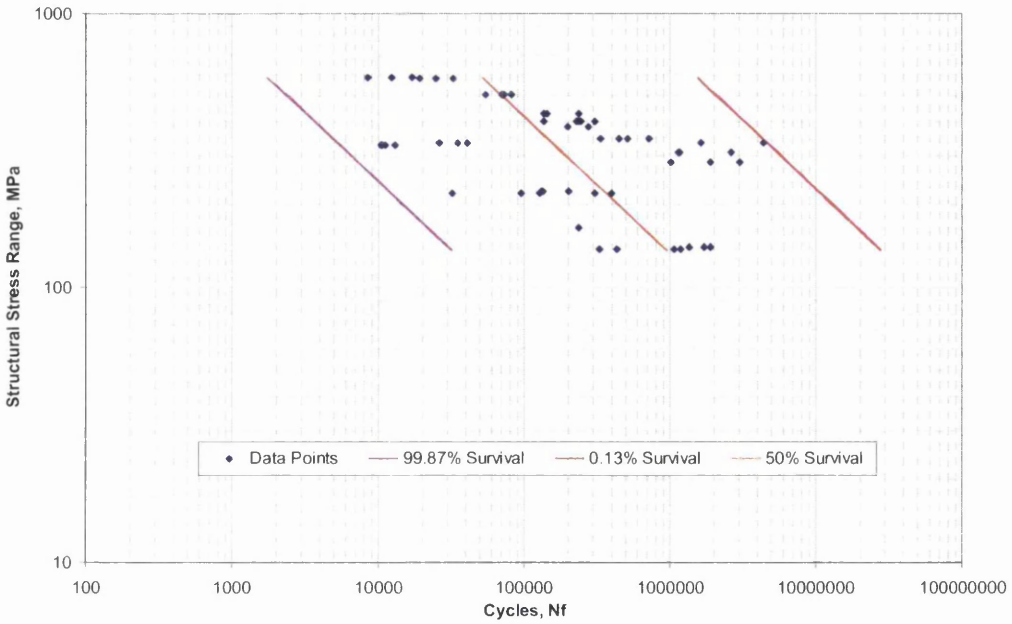

Figure 12.51: Statistical Analysis of All Weld Throat Failures

The stress–life curve for interface failures is shown in figure 12.52. The test data for interface failure showed very good convergence but the subsequent stress–life convergence produced reasonable convergence for interface failure. TM1 still has slightly higher fatigue lives than GM1 and GM2.

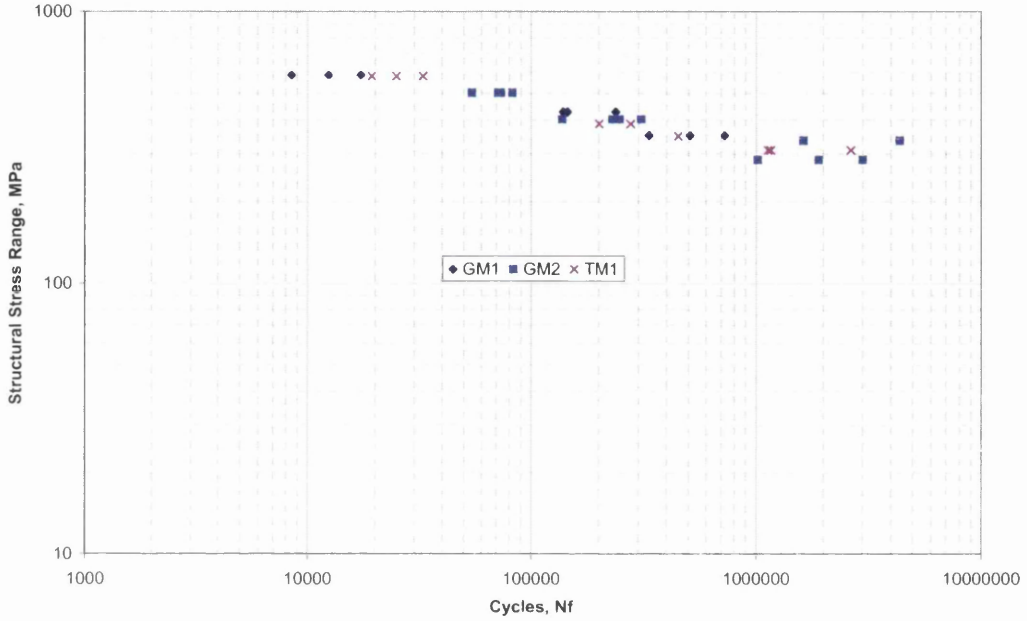

Figure 12.52: Stress–Life Master Curve Conversion for All Weld Interface Failures

Analysis of figure 12.52 is shown in figure 12.53. Removing the throat failures causes the survival bands to fit the data points much more closely with only one point just on the 0.13% survival band.

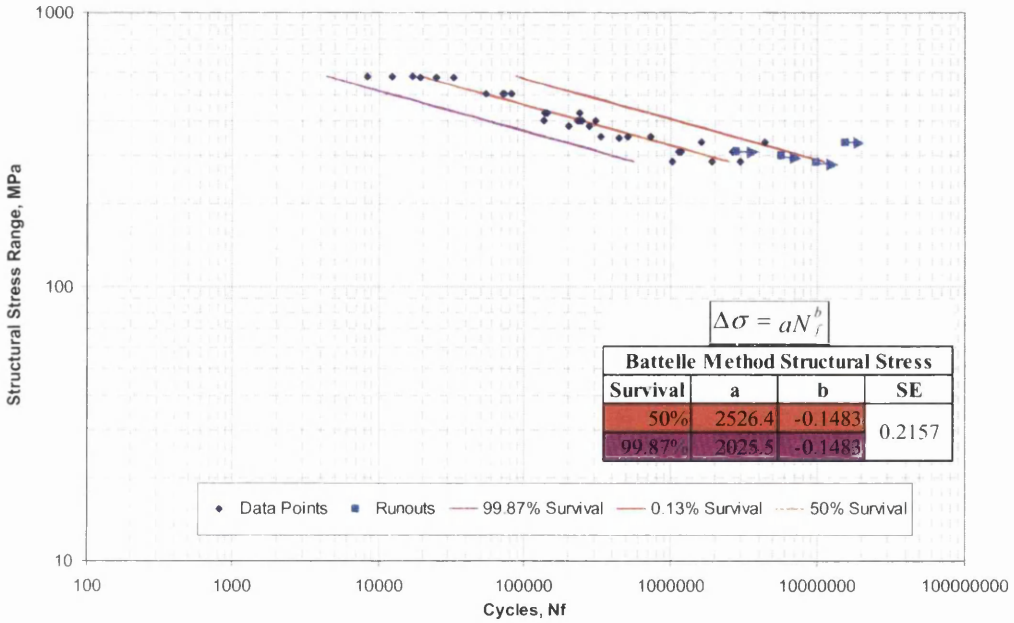

Figure 12.53: Statistical Analysis of All Weld Interface Failures

The stress–life curve for the throat failures is shown below in figure 12.54. The test data for throat failures shows good convergence, whereas when converted into a stress–life curve the results show reasonable convergence.

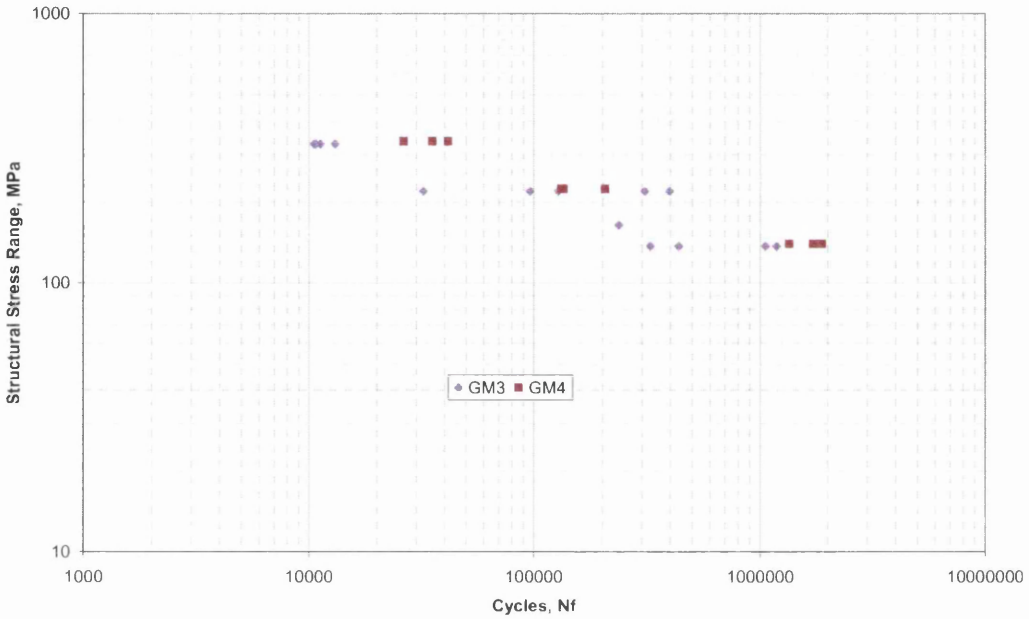

Figure 12.54: Stress–Life Master Curve Conversion for All Weld Throat Failures

Figure 12.55 shows the certainties of survival at 99.87% and 0.13% of the S–N data for all weld throat failures. Noticeable from this graph is that with the reasonable amount of scatter in the results, the survival bands to be reasonably wide, though the survival bands bind all data points.

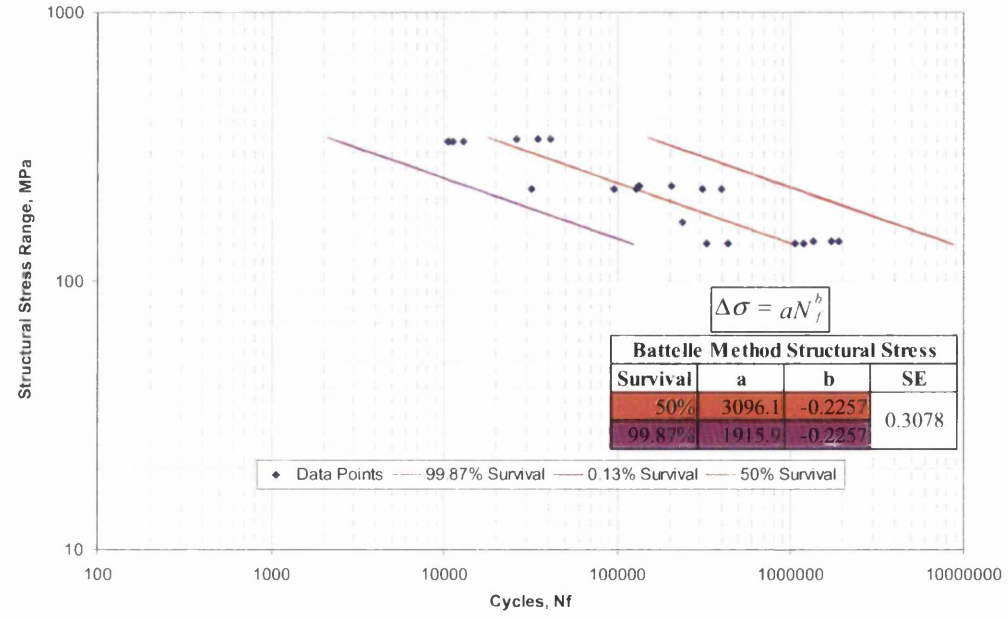

Figure 12.55: Statistical Analysis of Weld Throat Failures

For the two other methods FLOW and Verity the S-N curves are shown in Appendix 9 as they show very similar results to the manual method.

Table 12.3 shows all the parameters required for using the master S-N curves produced in this study.

Table 12.3: Battelle Structural Stress Master S-N Curve Parameters

$$\Delta\sigma = aN_f^b$$

Battelle Method Structural Stress				
Failure Location	**Survival**	**a**	**b**	**SE log(Nf)**
Toe Failure	50%	5561.9	-0.233	0.2269
	99.87%	3859.9	-0.233	
Interface Failure	50%	2526.4	-0.1483	0.2157
	99.87%	2025.5	-0.1483	
Throat Failure	50%	3096.1	-0.2257	0.3078
	99.87%	1915.9	-0.2257	

12.4.3.2 Battelle Equivalent Structural Stress

From the structural stress results in the previous section, the equivalent structural stress is calculated as described in section 10.7. These results are used to estimate the fatigue lives of the FUCA component. Figures 12.56 and 12.58 show the manual equivalent structural stress S-N curves for all weld toe failures and all weld throat failures respectively. Figure 12.56 shows that like the structural stress all the weld toe failures virtually collapse together so therefore one S-N curve is required.

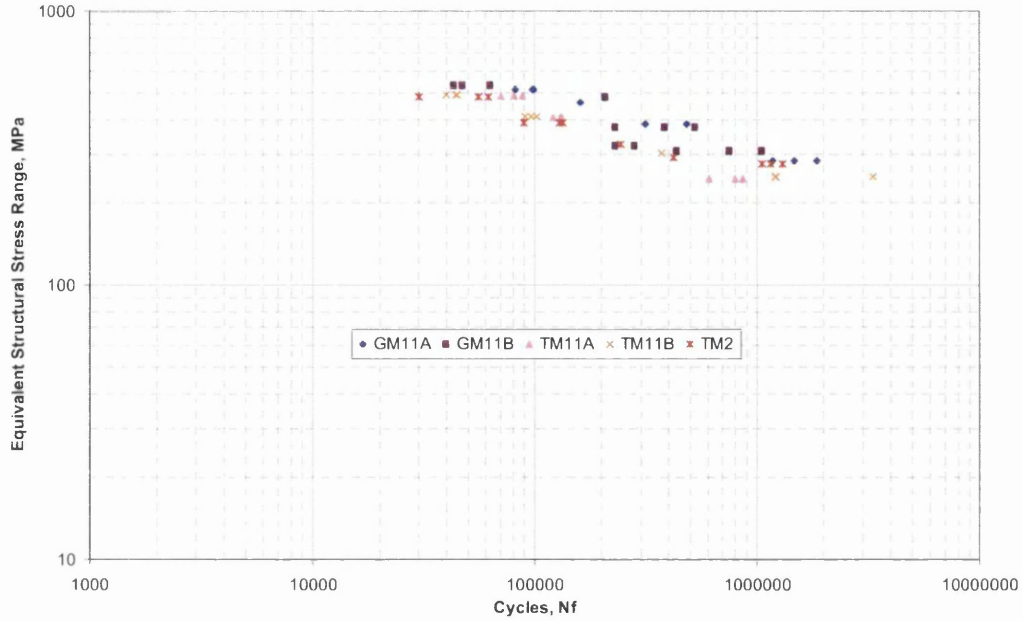

Figure 12.56: Stress–Life Master Curve Conversion for All Weld Toe Failures

Figure 12.57 analyses the S-N curve shown in figure 12.56, and it shows that the data points are well within the boundaries of the 99.87% and 0.13% survival.

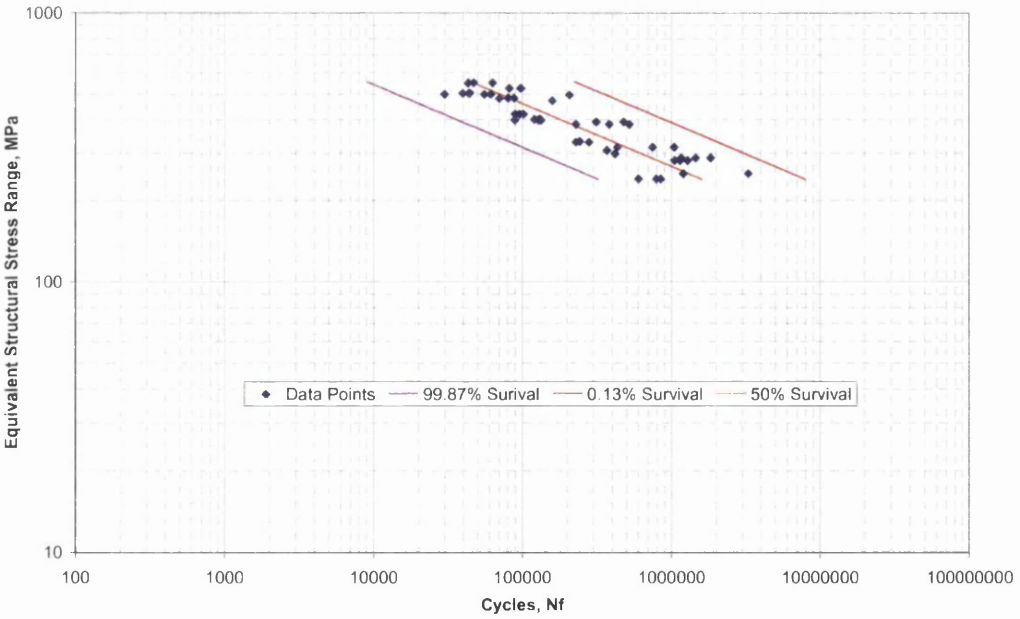

Figure 12.57: Statistical Analysis of All Weld Toe Failures

In figure 12.58 the differences between the interface and throat failures is noticeable, as they have not collapsed together at all. Therefore two separate S-N curves for weld throat failures are required.

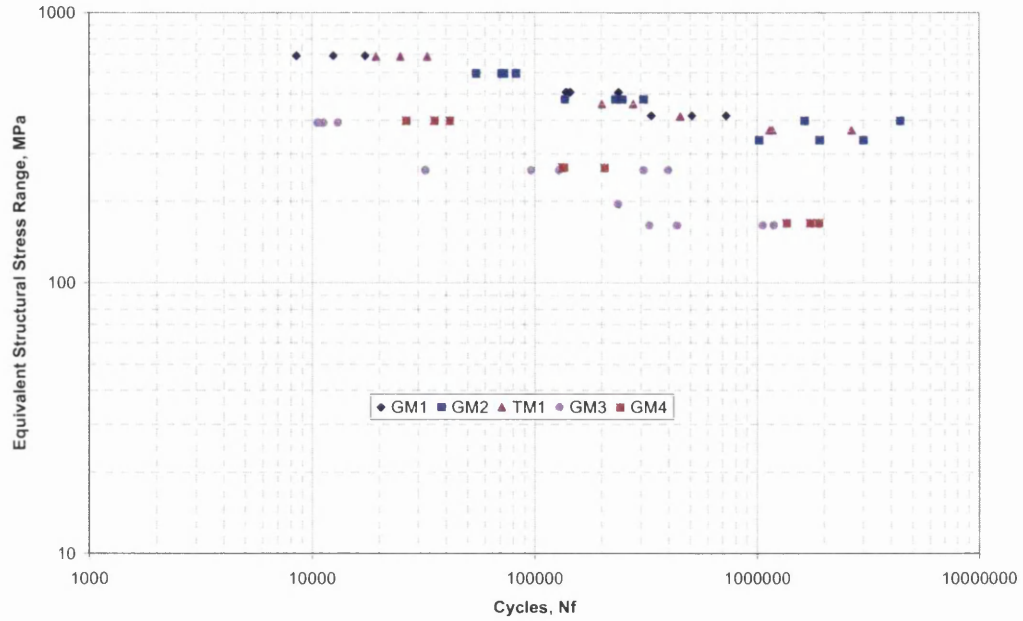

Figure 12.58: Stress–Life Master Curve Conversion for All Weld Throat Failures

From figure 12.59 the very wide survival bands for all the throat failures also shows why the lap-shear and peel geometries need separate S-N curves.

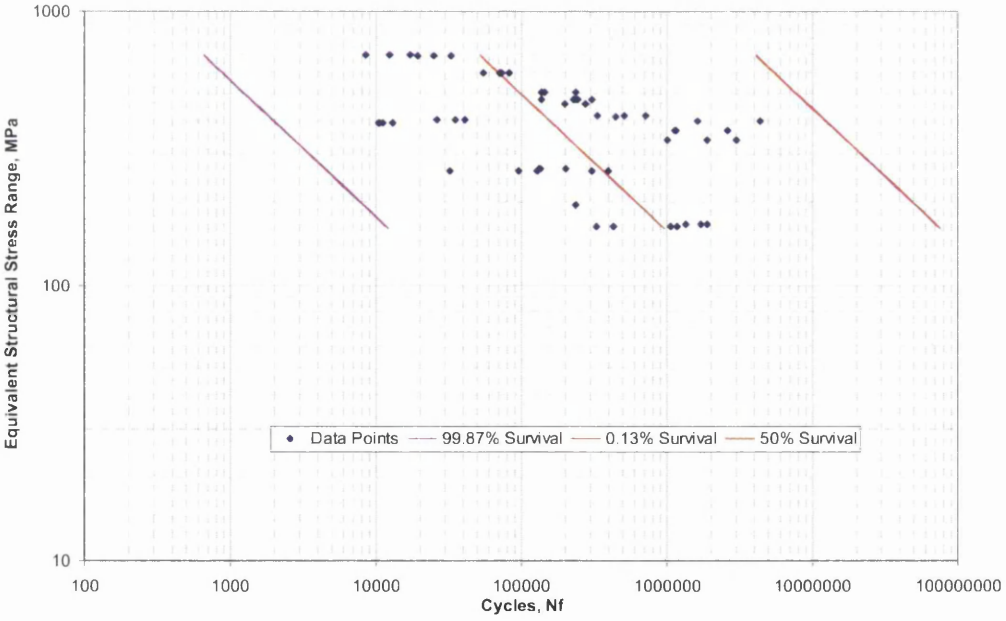

Figure 12.59: Statistical Analysis of All Weld Throat Failures

Having an S-N curve for just the interface failures is shown in figure 12.60, where the single lap-shear joints from both TKA and GKN have collapsed together, with limited scatter from the test data.

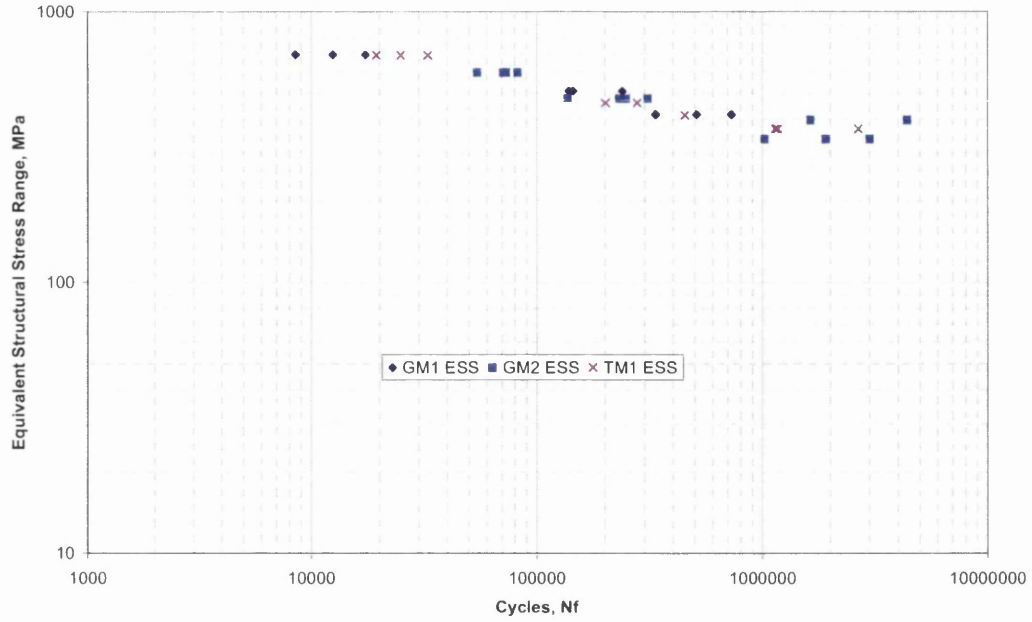

Figure 12.60: Stress–Life Master Curve Conversion for All Weld Interface Failures

Figure 12.61 shows that the 99.87% and 0.13% survival bands surround the data points closely.

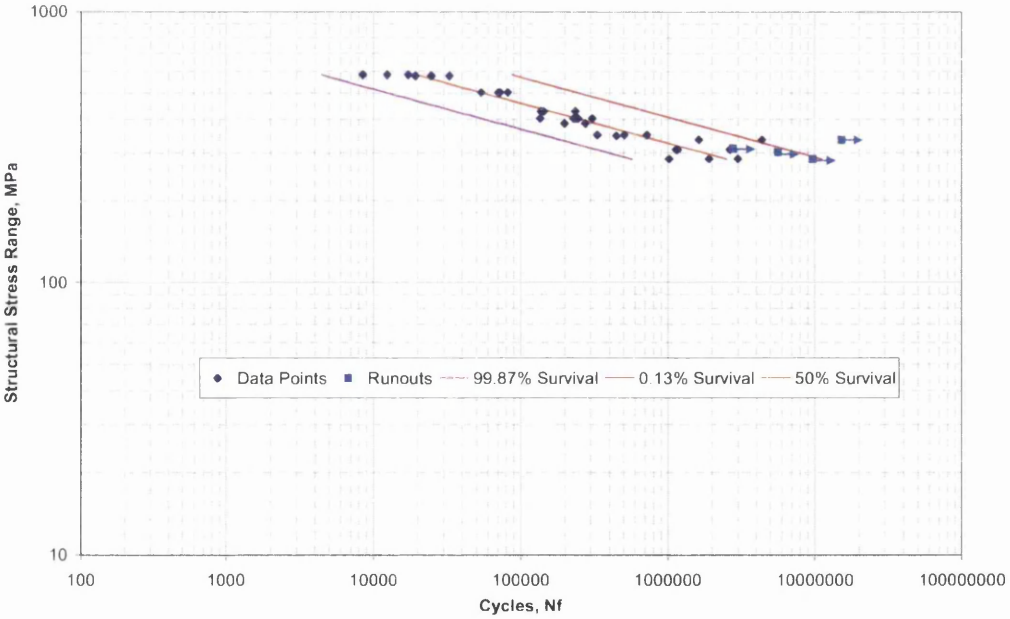

Figure 12.61: Statistical Analysis of All Weld Interface Failures

The S-N curve for the throat failures is shown in figure 12.62. This shows that there is reasonable collapsing of the load-life data for GM3 and GM4.

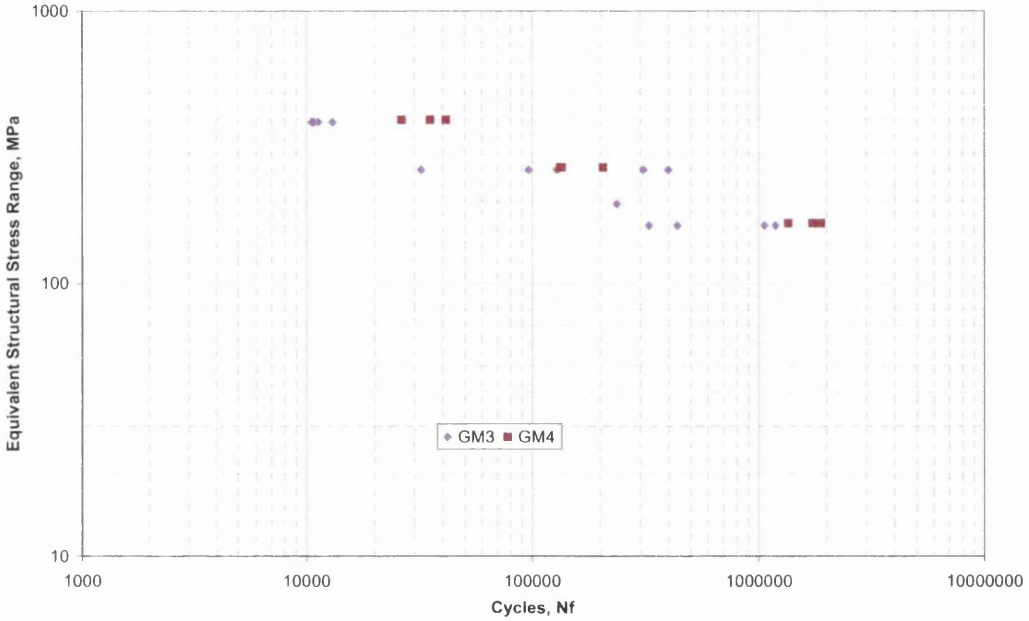

Figure 12.62: Stress–Life Master Curve Conversion for All Weld Throat Failures

Figure 12.63 analyses the throat failure S-N curve (figure 12.62) and shows that the 99.87% and 0.13% survival bands are much wider due to the scatter in the load-life results.

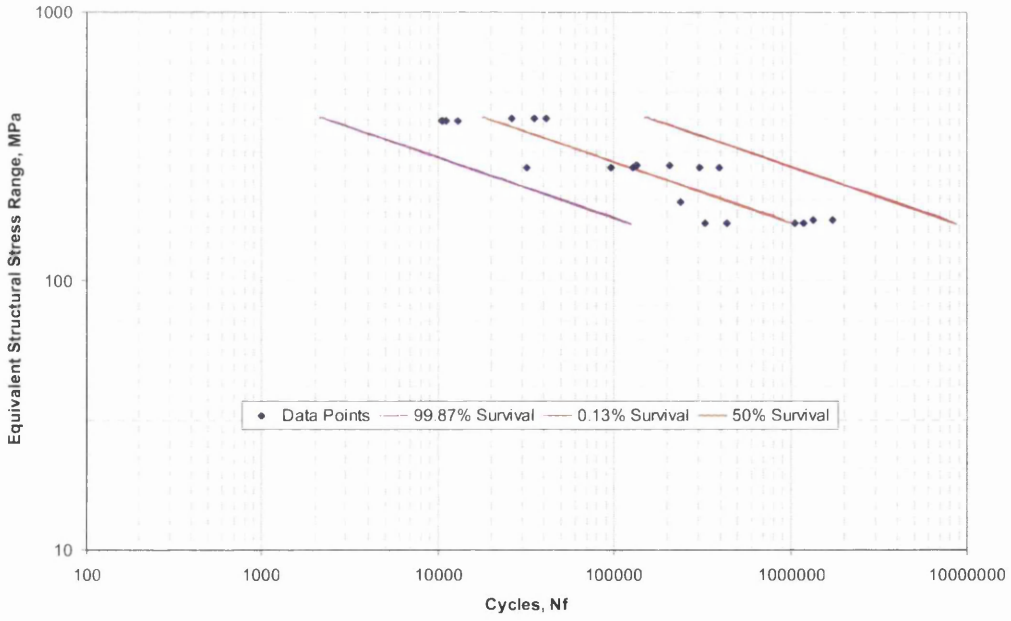

Figure 12.63: Statistical Analysis of All Weld Throat Failures

Both the FLOW and Verity Equivalent Structural Stress results are very similar to the Manual results so these will be found within Appendix 10.

Table 12.4 shows all the parameters required for using the master S-N curves produced in this study.

Table 12.4: Battelle Equivalent Structural Stress Master S-N Curve Parameters

$$\Delta\sigma = aN_f^b$$

Battelle Method Equivalent Structural Stress				
Failure Location	**Survival**	**a**	**b**	**SE log(Nf)**
Toe Failure	50%	6603.9	-0.2327	0.2262
	99.87%	4590.7	-0.2327	
Interface Failure	50%	3003.6	-0.1483	0.2150
	99.87%	2409.7	-0.1483	
Throat Failure	50%	3681.1	-0.2256	0.3072
	99.87%	2280.7	-0.2256	

12.4.3.3 Sensitivity Study on Alternative Location of FE Stress

For all the S-N curves shown in section 12.5.1 and 12.5.2 the FE stress used was located at the "centre" away from the edge of the weld to avoid the effect of the weld start/stop as shown in figure 12.64 and 12.65. For all the coupon geometries, which are fully welded the FE, stress was collected in similar locations to GM11B in 12.64. The locations for all the other coupons are shown in Appendix 11.

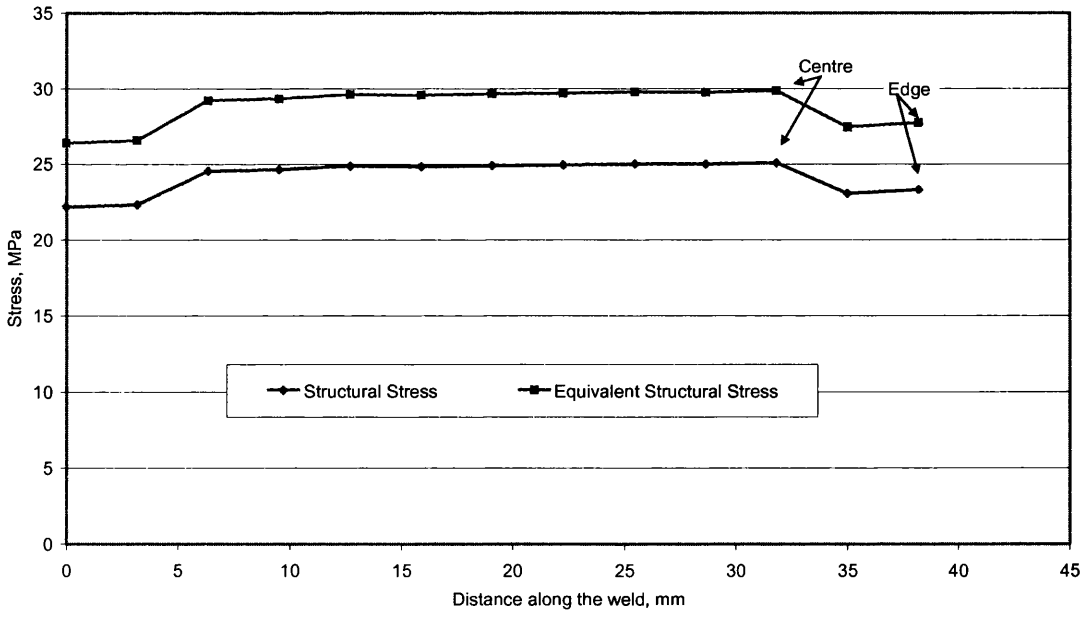

Figure 12.64: Location of FE Stresses Used for Conversion of S-N Curves of GM11B

For all partially welded coupon geometries the FE stress was collected in similar locations to GM11A in 12.65.

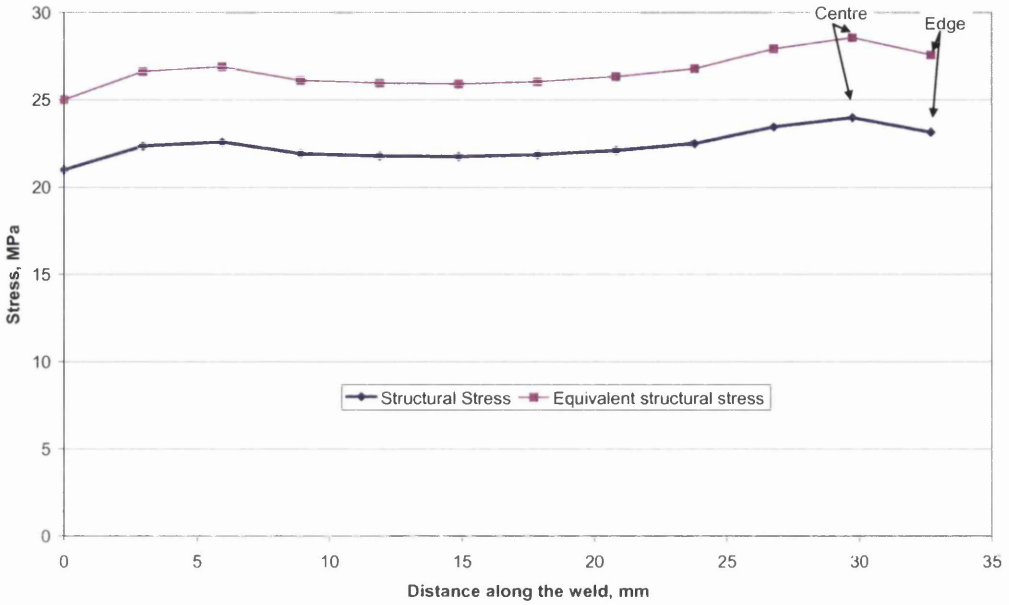

Figure 12.65: Location of FE Stresses Used for Conversion of S-N Curves of GM11A

Table 12.5 shows the comparison between the "centre" and the "edge" equivalent structural stresses. Noticeable from the table are the differences between using the centre and the edge. Coupons, which failed at the weld toe, have slightly higher "centre" equivalent structural stress than at the edge. Whereas for weld throat failures, the edge stress is much higher than the centre stress, the smoothing of the weld toes causes this.

Table 12.5: Comparison of Battelle Equivalent Structural Stress Centre vs. Edge

Coupon	Failure Locations	Equivalent Structural Stress MPa					
		Manual Centre	Manual Edge	FLOW Centre	FLOW Edge	Verity Centre	Verity Edge
GM11A	Weld Toe	28.553	27.558	29.035	29.107	28.058	28.500
GM11B	Weld Toe	29.840	27.909	30.497	28.602	30.204	27.463
TM11A	Weld Toe	30.062	28.780	29.688	29.538	30.006	29.555
TM11B	Weld Toe	30.516	30.271	31.034	30.108	30.866	29.298
TM2	Weld Toe	35.965	31.705	36.836	33.529	36.437	31.531
		Side B	**Side B**	**Side B**	**Side B**	**Side B**	**Side B**
TM1	Weld Throat	50.921	56.903	51.916	58.273	50.595	58.892
GM1	Weld Throat	51.235	54.533	52.284	55.470	50.822	56.496
GM2	Weld Throat	44.127	37.420	45.369	39.862	45.218	37.206
GM3	Weld Throat	361.684	393.800	375.238	411.468	370.489	413.931
GM4	Weld Throat	369.096	291.622	380.267	320.381	377.384	284.117

In Table 12.6 the equivalent structural stresses used to convert load-life curves to S-N curves is shown.

Table 12.6: Battelle Equivalent Structural Stress – Edge Effects Sensitivity Study

Coupon	Failure Locations	Equivalent Structural Stress MPa		
		Manual Edge	FLOW Edge	Verity Edge
GM11A	Weld Toe	27.558	29.107	28.500
GM11B	Weld Toe	27.909	28.602	27.463
TM11A	Weld Toe	28.780	29.538	29.555
TM11B	Weld Toe	30.271	30.108	29.298
TM2	Weld Toe	31.705	33.529	31.531
		SideB edge	**SideB edge**	**SideB edge**
TM1	Weld Throat	56.903	58.273	58.892
GM1	Weld Throat	54.533	55.470	56.496
GM2	Weld Throat	37.420	39.862	37.206
GM3	Weld Throat	393.800	411.468	413.931
GM4	Weld Throat	291.622	320.381	284.117

For the three Battelle Methods, using the FE stresses in Table 12.6 load-life curves were converted into S-N curves. Figures 12.66 – 12.68 show the S-N curves for the manual method. There is little effect of using the "edge stress" instead of the "centre stress" as depending on the failure mode the edge stress will either higher or lower the Equivalent Structural Stress for a given life, then completely collapse the different geometry test data to a master curve.

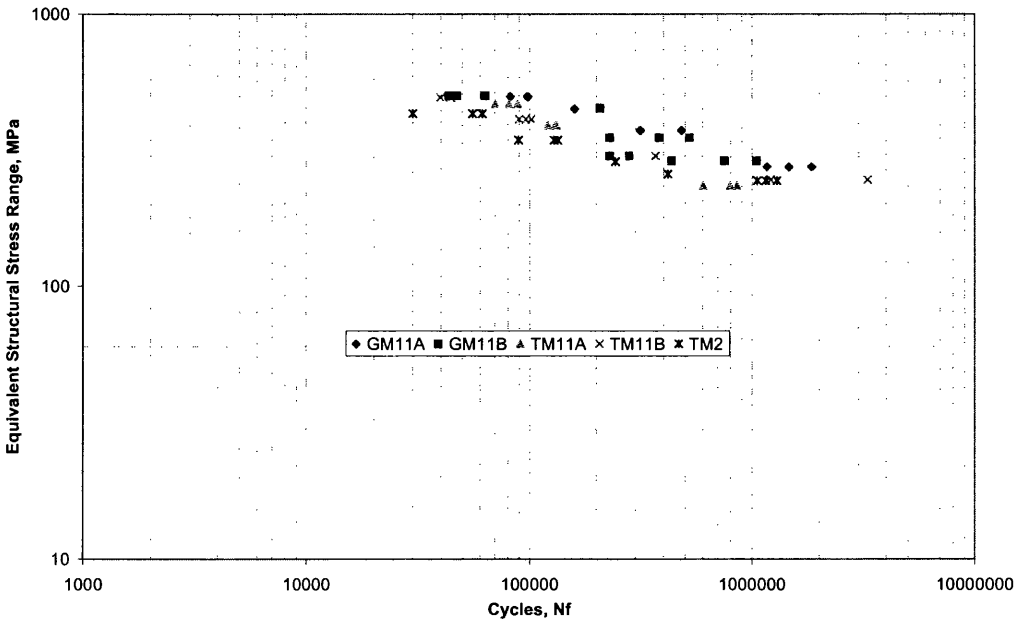

Figure 12.66: Edge Stress–Life Master Curve Conversion for All Weld Toe Failures

In figure 12.67 the effect of using the edge stress is quite clearly shown in the weld interface failures. There is limited convergence in the collapsing of the interface failure results due to the higher FE predicted stresses used to convert the results.

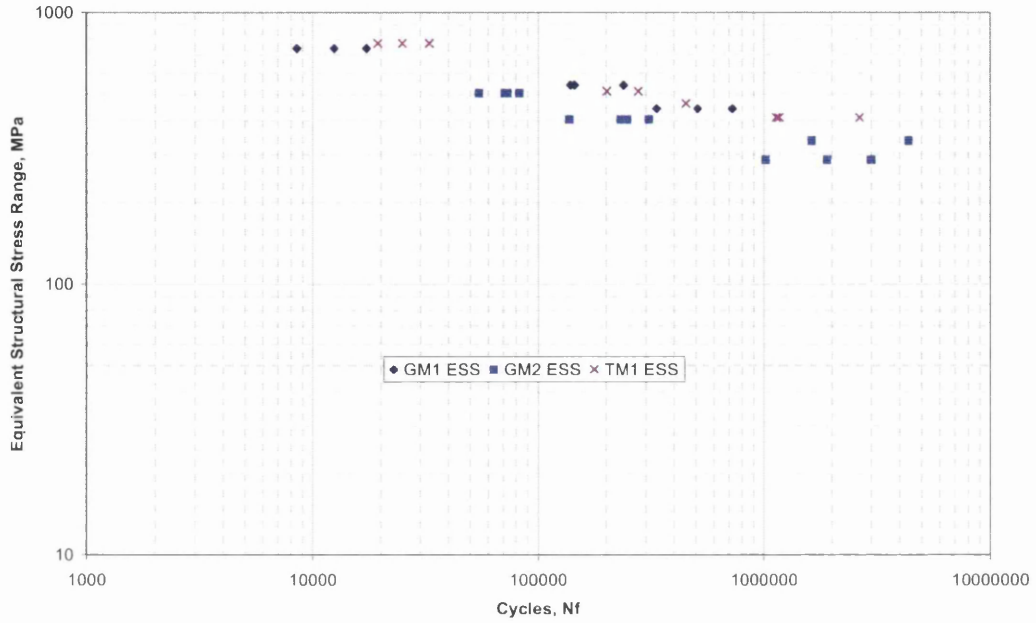

Figure 12.67: Edge Stress–Life Master Curve Conversion for Weld Interface Failures

The effect of using edge stresses for the weld throat failures is shown in figure 12.68, which shows some convergence of the test data.

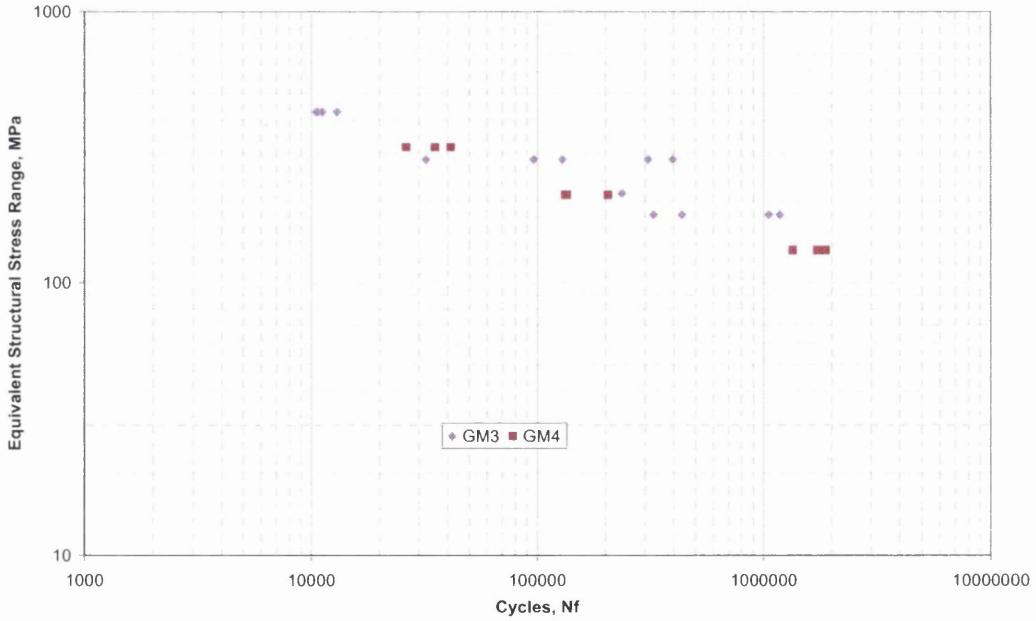

Figure 12.68: Edge Stress–Life Master Curve Conversion for Weld Throat Failures

The results of doing the sensitivity study on edge effects using both FLOW and Verity is shown in Appendix 12 as the results show similar trends with slightly higher stress values.

12.4.3.4 Comparison of Original Battelle S-N Curves with Manual, FLOW and Verity S-N Curves

The original Battelle structural stress and equivalent structural stress S-N curves (Dong 2005) generated whilst developing the Battelle theory where digitised through Sigma Scan software. These S-N curves were then compared with the Manual, FLOW and Verity S-N and shown below in figures 12.69 and 12.70 the comparison against the Manual S-N curve. The comparisons against FLOW and Verity are shown in Appendix 13, as the results are very similar.

Figure 12.69 shows that all the weld toe failures and the weld interface failure are located within the scatter of the original Battelle test data. Whilst the weld throat S-N curve at short lives is lower than the original Battelle data, at long lives it is well within the scatter of the original data.

The slope is different between the two sets of results. Overall the majority of data seems to overlap with the data converted by Battelle.

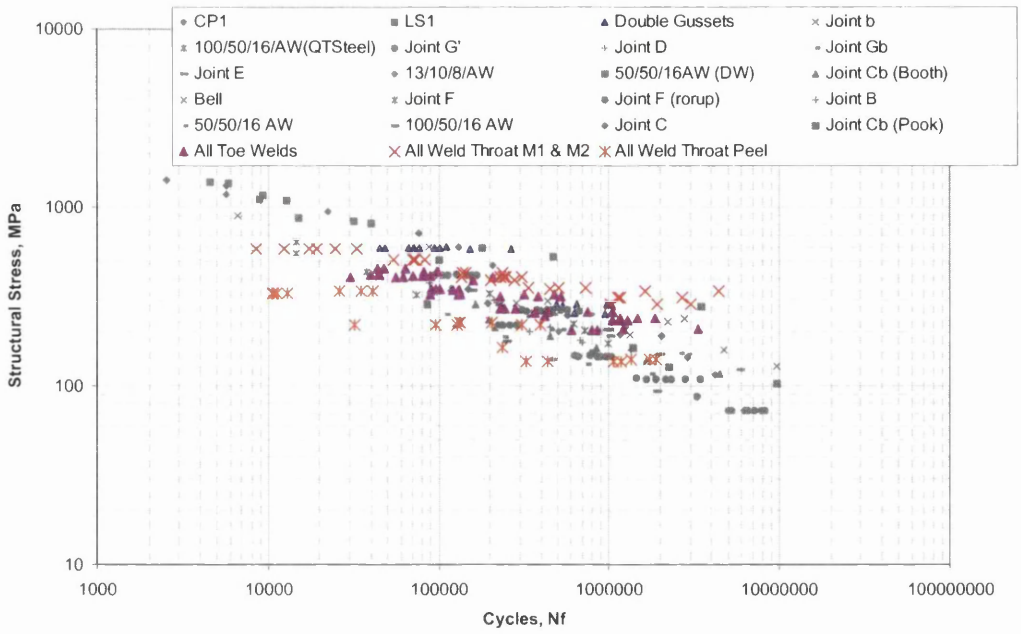

Figure 12.69: Comparison of Original Battelle Structural Stress S-N vs. Manual Structural Stress S-N Curves

The Equivalent Structural Stress is calculated using Eq.15 and described in section 10.7. The values for the factors: m and I(r) used where the ones recommended by Battelle. The thickness was the thickness used in the FE models of each coupon joint i.e. the measured thickness of the coupon.

The manual equivalent structural stress S-N curve comparison with the original Battelle S-N curves is shown in figure 12.70. From calculating the equivalent structural stress from the structural stress the graph shows that all the weld toe and interface failures have higher stress values than the original test data. The throat failure results are located within the scatter of the original Battelle data.

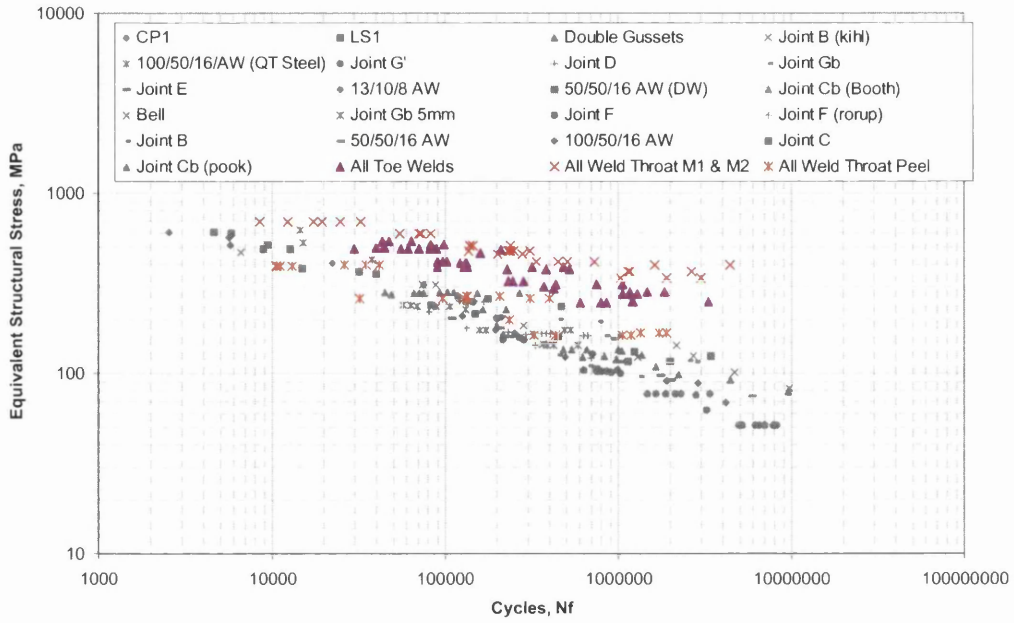

Figure 12.70: Comparison of Original Battelle Equivalent Structural Stress S-N vs. Manual Equivalent Structural Stress S-N

The differences could arise from the two factors m and I(r) values not being calculated directly from the actual test results, instead of assuming the Battelle recommended values. Further work must be carried out to see if the m value does affect the results.

Other differences could arise from the original test data used by Battelle having different geometries to the ones investigated in this project. Not to mention the fact that different test conditions and failure criterions that could have been used, which are unknown. The original Battelle tests were mainly performed on thick material approximately 10mm and this work is performed on material below 4mm in thickness. The differences also could arise from the greater flexibility within the thinner material than the thicker material used by Battelle.

Overall, to get an accurate prediction, the user is still advised to use their own coupon test fatigue data to generate the master S-N curves instead of using the Battelle curve directly, which has many unknowns.

12.5 Regression Based on Stress

Using the S-N curves generated in sections 12.4.2 and 12.4.3 for the Volvo and Battelle Methods, the regression based on stress analysis was completed as described in section 10.8.2. This method reduces the error in the stress, which enables designers to be able to estimate the endurance limit of the material or component. This regression was completed on both the Volvo and all the Battelle S-N curves generated.

12.5.1 Regression Based on Stress for the Volvo S-N Curves

Figures 12.71 – 12.73 show the regression based on stress for all weld toe failures and the interface failures and throat failures. All the analyses show that the S-N data is well within the survival bands of $\pm 3\sigma$ (99.87% and 0.13%).

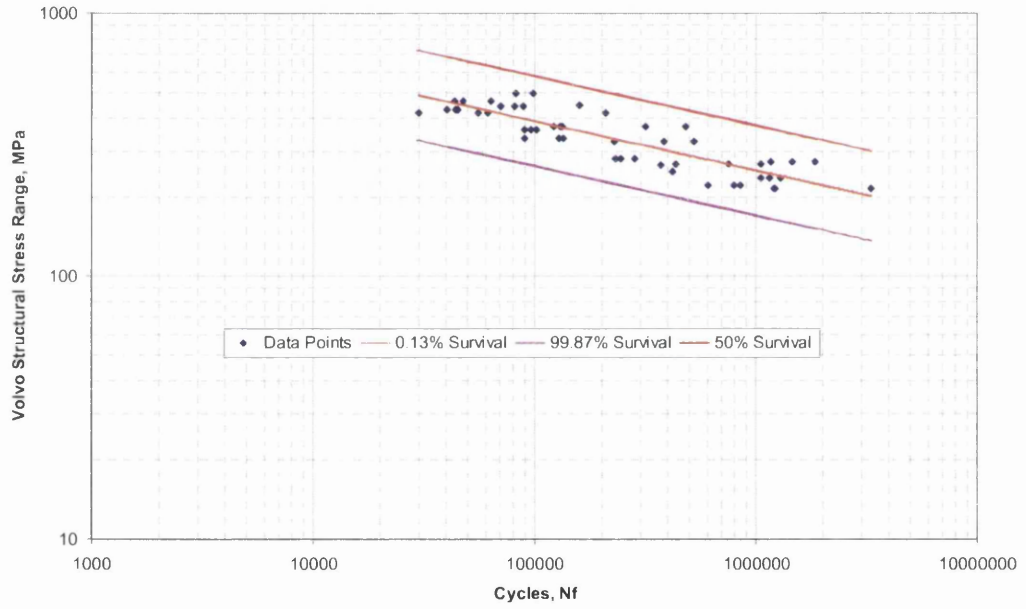

Figure 12.71: Statistical Analysis of All Weld Toe Failures

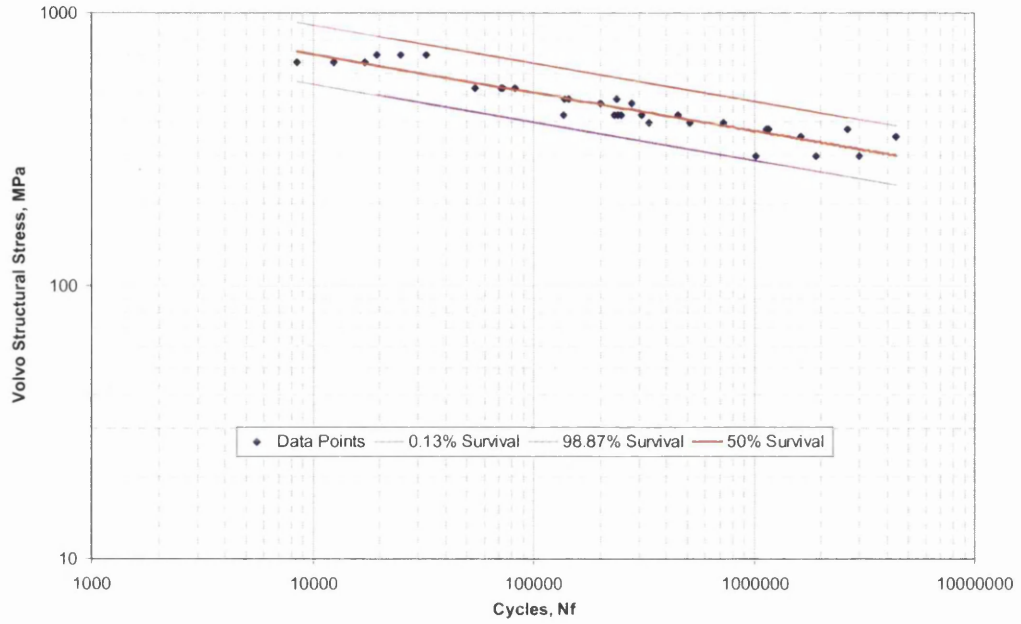

Figure 12.72: Statistical Analysis of All Weld Interface Failures

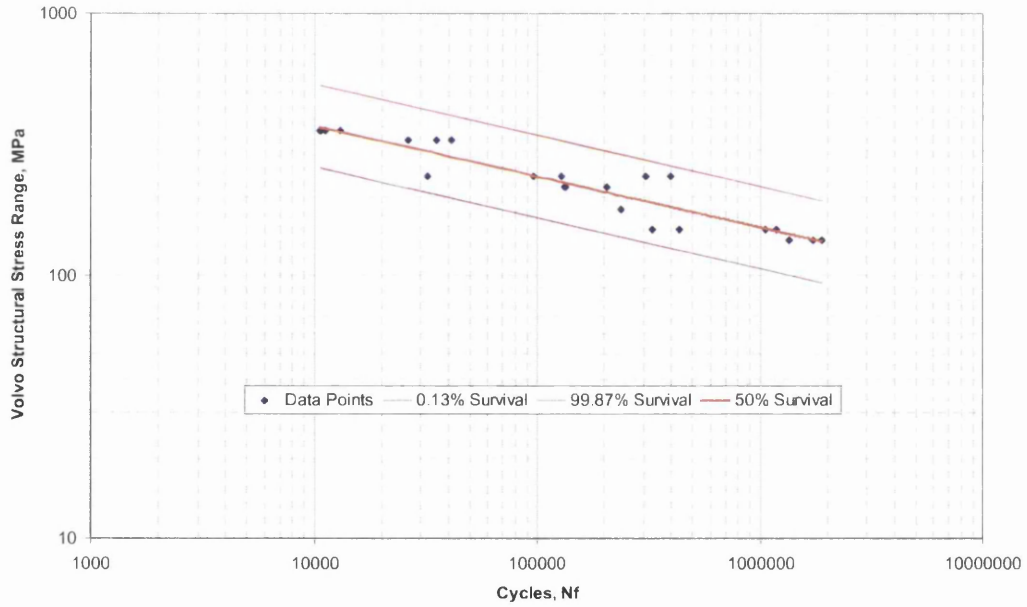

Figure 12.73: Statistical Analysis of All Weld Throat Failures

Table 12.7 shows all the parameters required for using the master S-N curves produced in this section.

Table 12.7: Volvo Structural Stress Regression Based on Stress Master S-N Curve Parameters

$$\Delta\sigma = aN_f^b$$

Volvo Method Structural Stress				
Failure Location	**Survival**	**a**	**b**	**SE log(Δσ)**
Toe Failure	50%	3384.6	-0.188	0.0570
	99.87%	2283.1	-0.188	
Interface Failure	50%	2563.50	-0.1405	0.0361
	99.87%	1998.1	-0.1405	
Throat Failure	50%	2240.70	-0.1949	0.0526
	99.87%	1557.6	-0.1949	

12.5.2 Battelle Structural Stress Regression

Analysing the S-N curves as shown in section 12.4.3 by the method described in section 10.7.2, to understand the certainties of survival of a coupon, statistical analysis occurs. For the Manual Structural Stress curves the statistical analysis is shown in figures 12.74 – 12.76. For the manual calculations weld toe and weld throat failures S-N curves fit well with the least squares regression survival bands at 99.87% and 0.13% survival. For the two other methods FLOW and Verity the statistical analysis curves are shown Appendix 14 as they show very similar results to the manual method.

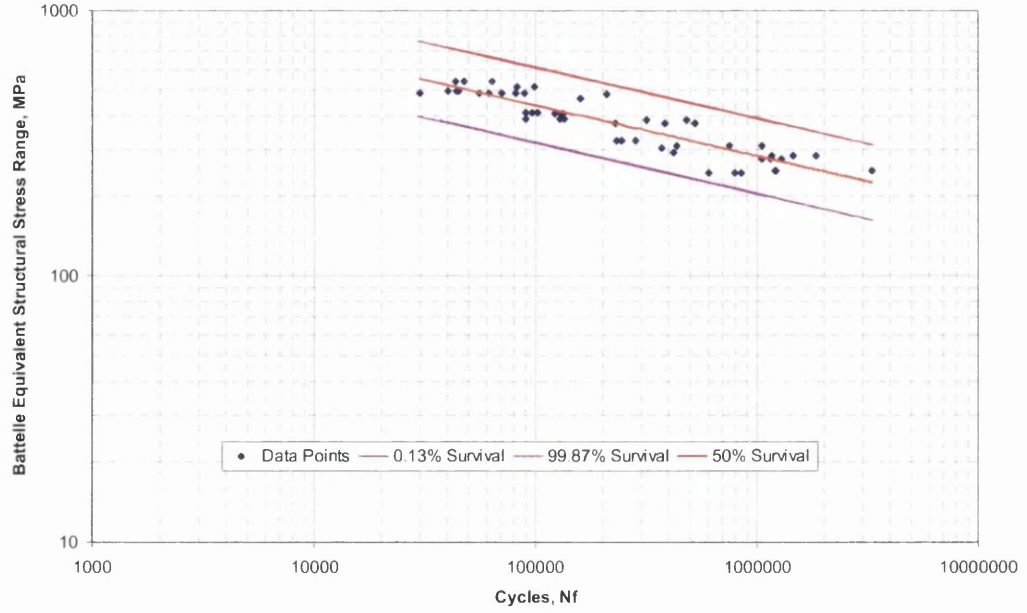

Figure 12.74: Statistical Analysis of All Weld Toe Failures

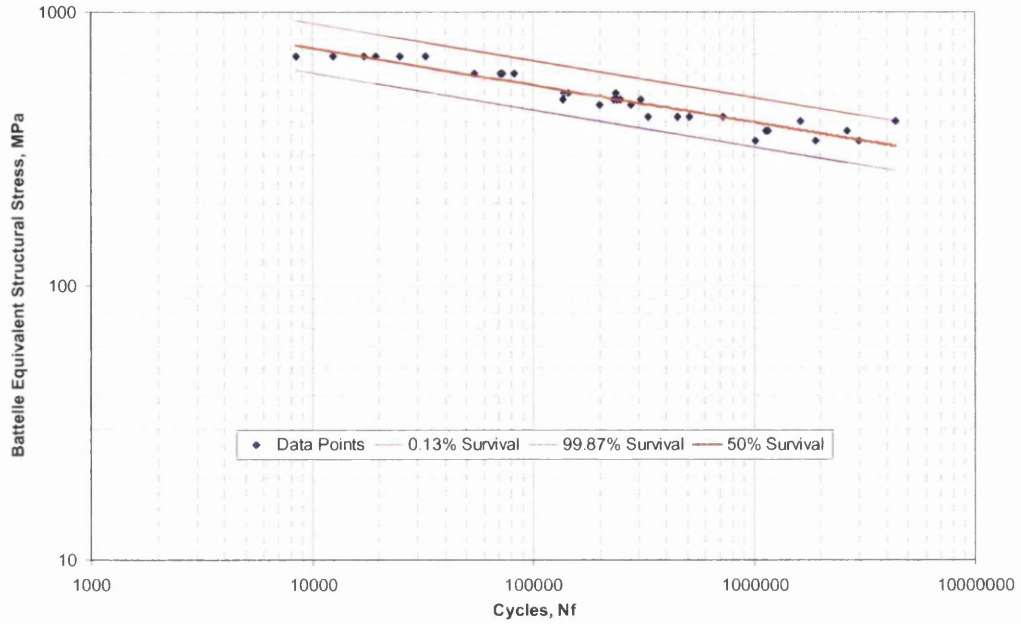

Figure 12.75: Statistical Analysis of All Weld Interface Failures

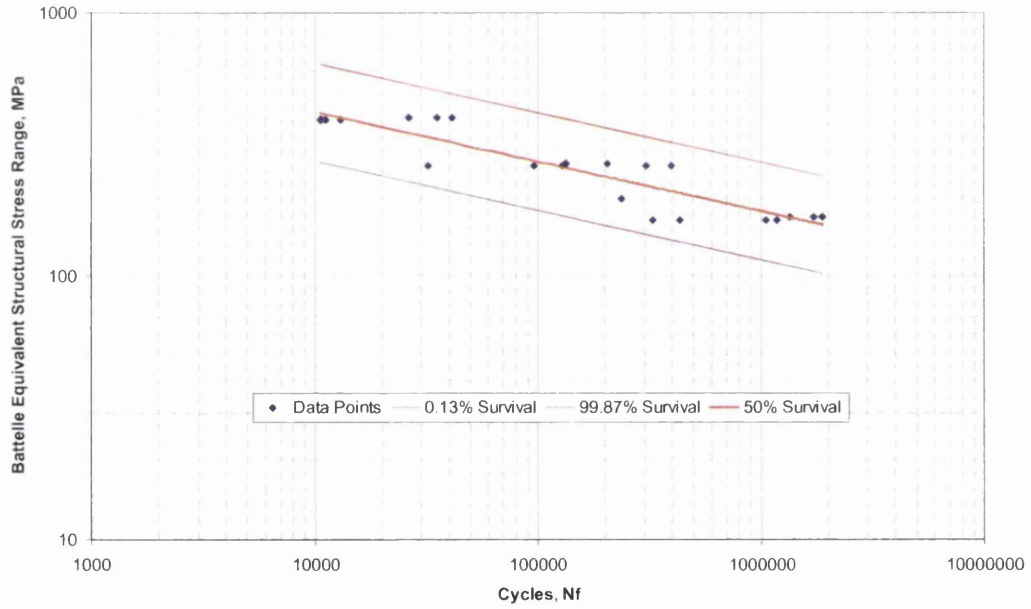

Figure 12.76: Statistical Analysis of All Weld Throat Failures

Table 12.8 shows all the parameters required for using the master S-N curves produced in this section.

Table 12.8: Battelle Structural Stress Regression Based on Stress Master S-N Curve Parameters

$$\Delta\sigma = aN_f^b$$

Battelle Method Structural Stress				
Failure Location	**Survival**	**a**	**b**	**SE log(Δσs)**
Toe Failure	50%	3342.9	-0.1918	0.0475
	99.87%	2407.9	-0.1918	
Interface Failure	50%	2158.1	-0.1355	0.0301
	99.87%	1753	-0.1355	
Throat Failure	50%	2002.9	-0.1889	0.0621
	99.87%	1304.2	-0.1889	

12.5.3 Battelle Equivalent Structural Stress

Subsequent statistical analysis occurred for the Manual, FLOW and Verity Equivalent Structural Stresses of which the Manual curves are shown in figures 12.77 – 12.79. Whilst the Flow and Verity curves which show similar trends are found in Appendix 15. Figures 12.77 – 12.79 show that the S-N curve data is well within the ±3σ survival bands.

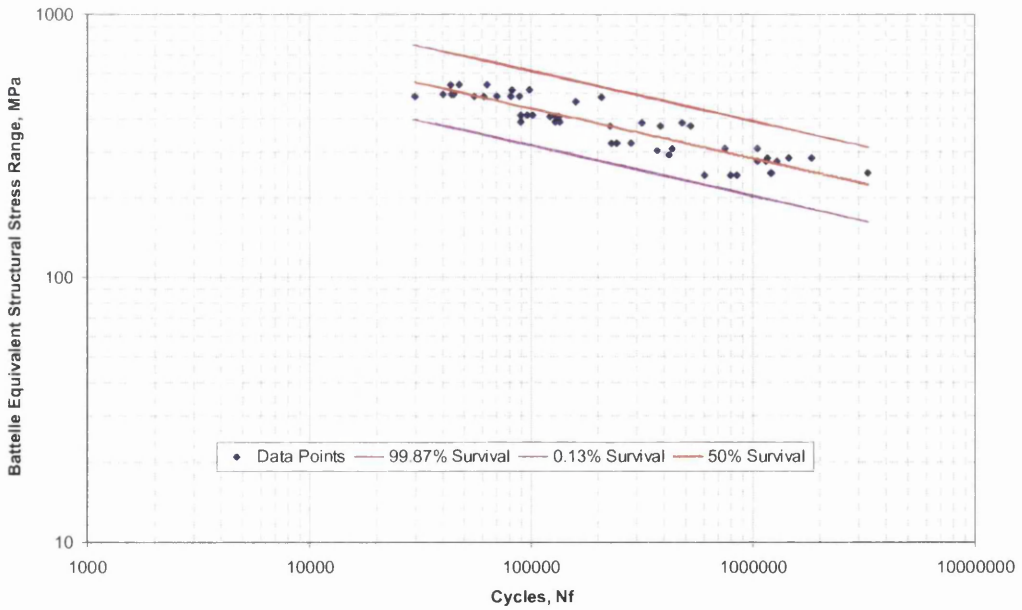

Figure 12.77: Statistical Analysis of All Weld Toe Failures

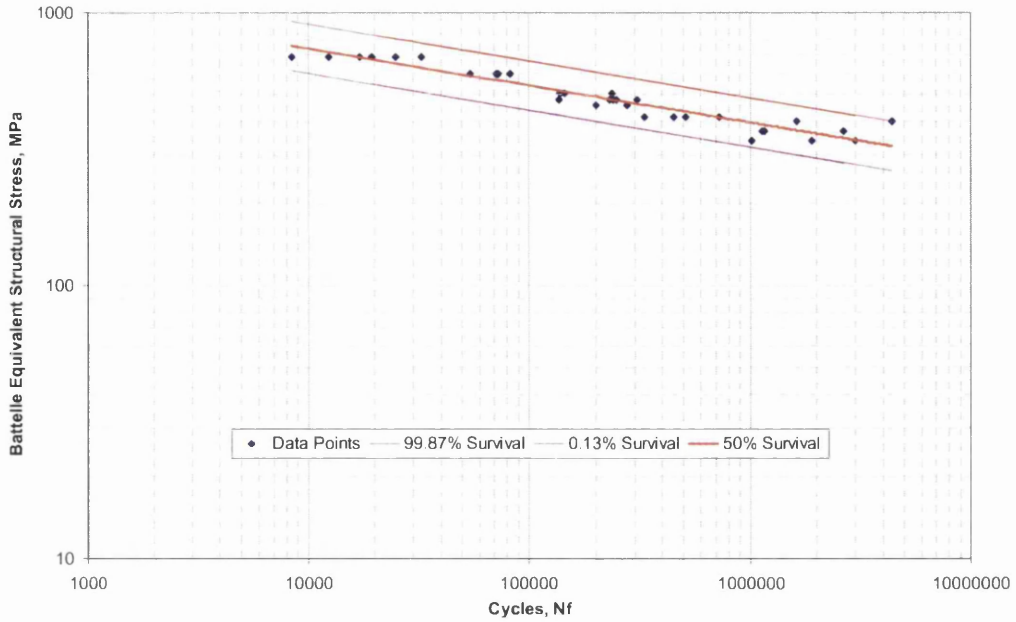

Figure 12.78: Statistical Analysis of All Weld Interface Failures

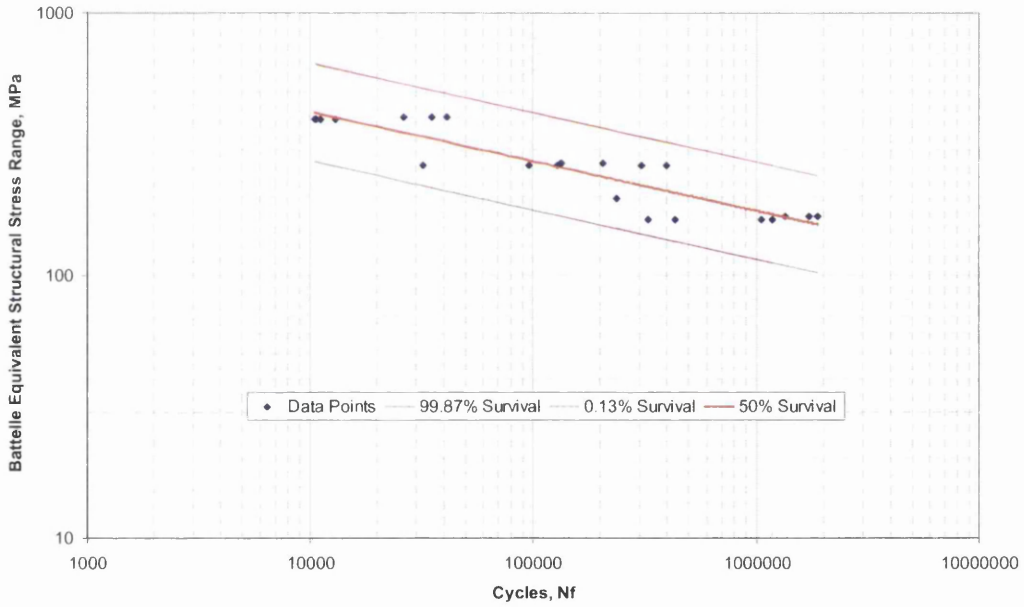

Figure 12.79: Statistical Analysis of All Weld Throat Failures

Table 12.9 shows all the parameters required for using the master S-N curves produced in this section.

Table 12.9: Battelle Equivalent Structural Stress Regression Based on Stress Master S-N Curve Parameters

$$\Delta\sigma = aN_f^b$$

Battelle Method Equivalent Structural Stress				
Failure Location	**Survival**	**a**	**b**	**SE log(ΔSs)**
Toe Failure	50%	3985.3	-0.1918	0.0473
	99.87%	2874.4	-0.1918	
Interface Failure	50%	2568.3	-0.1356	0.0300
	99.87%	2087.4	-0.1356	
Throat Failure	50%	2386.2	-0.189	0.0620
	99.87%	1555.2	-0.189	

12.6 FUCA Component

12.6.1 Failure Locations

Under constant and variable amplitude loading, the mode of failure for all the FUCA components is the same. The cracks would usually initiate at the root of the weld where it joins the flange and then propagate along the weld throat, known as "Throat Failure".

FUCA component 12 had a different mode of failure under constant amplitude loading this is due to the actual component being incorrectly blanked when manufactured, especially when compared to other tested components. Under variable amplitude SAE Bracket loading, there was found a small notch in one of the welds, which initiated cracks and therefore reduced life.

12.6.2 Constant Amplitude

Lives at 2.5kN shown in figure 11.81, shows that at low load levels, crack propagation takes up a large proportion of the life of the component with crack initiation therefore covering a large percentage of life. However the lives for crack propagation to a crack length of 35mm are very similar.

It is also worth noting from figure 11.81 that, at ±2.5kN there is a much larger scatter in the life for crack initiation to 10mm (between 430,000 and 700,000 cycles). This shows that at low load levels, crack propagation takes up an increased proportion of the life of the component with crack initiation therefore covering a small percentage

of life. However the lives for crack propagation to a crack length of 35mm are very similar.

12.6.3 Variable Amplitude Block Loading

Figure 12.80 shows the effect of the first load level in the R=-1 block loading cycle against the constant amplitude loading. This shows that the first load level of each block loading sequence is the most damaging.

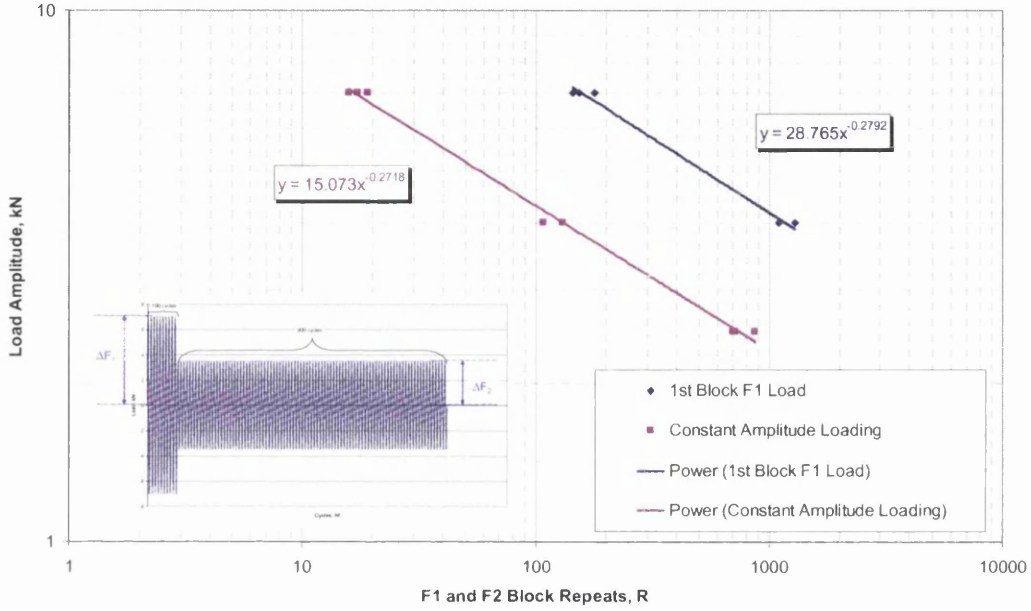

Figure 12.80: R=-1 Block Loading vs. Constant Loading at the 1st Load Level

Comparing the second load level against the constant amplitude test data is shown in figure 12.81. This shows that that the second loading level although occurs over a large number of cycles is less damaging as the results are just lower than the constant amplitude data.

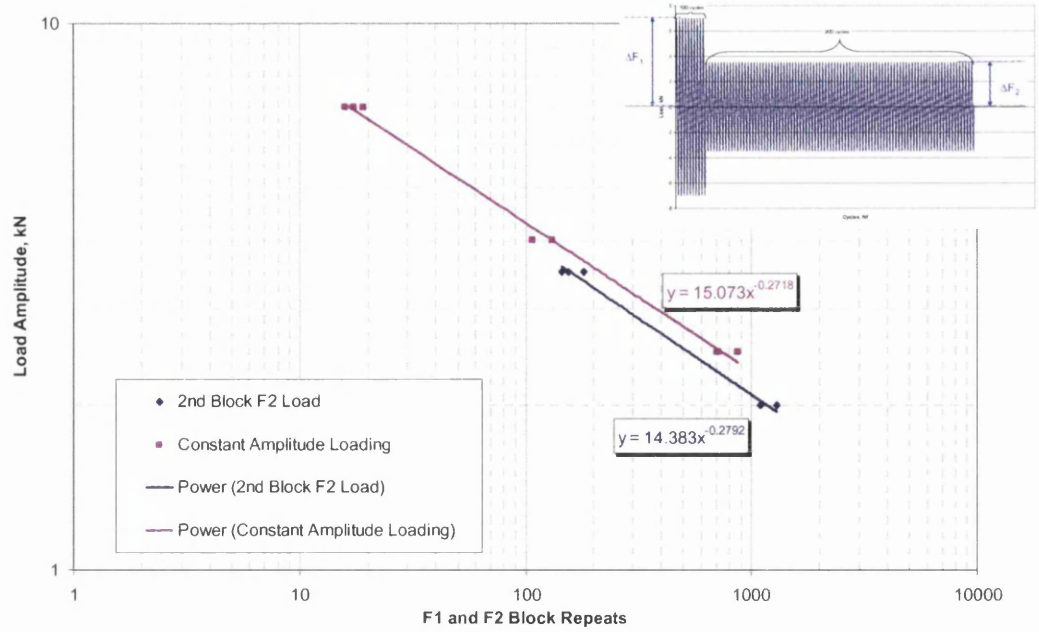

Figure 12.81: R=-1 Block Loading vs. Constant Amplitude Loading at the 2nd Load Level

Calculating the Miner's Rule from the constant amplitude data is shown in figure 12.82. Using a damage constant, D=1 under-estimates the fatigue life which is great for design purposes. The Miner's Rule Damage constant can be anywhere between 0.7 and 2.3, so for the purpose of this research, altering the Damage constant D=1.60 accurately predicts the fatigue life of the FUCA component.

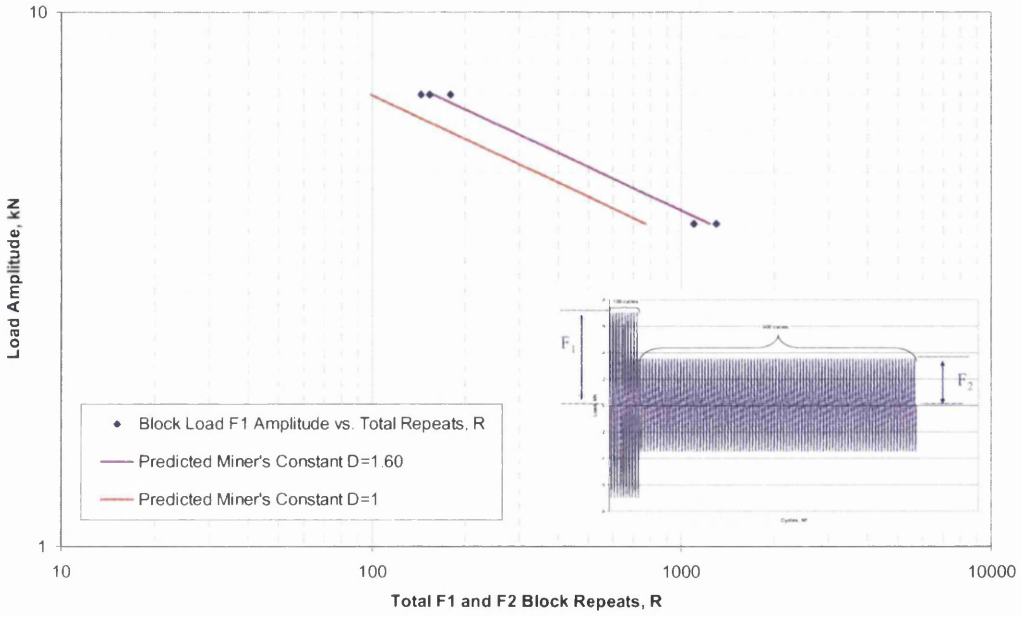

Figure 12.82: Miner's Rule for R=-1 Block Loading Sequence

Analysing the R=0.1 block loading using Miner's Rule required the load amplitude of the block loading sequence to be converted from R=0.1 to R=-1 as described in section 10.9.4.

Figure 12.83 shows that using the Miner's Rule on the converted data, a Damage constant, D=1 over-estimates the block repeats of the FUCA component. Changing the damage constant, D=1.60 also under-estimates the block repeats of the FUCA component.

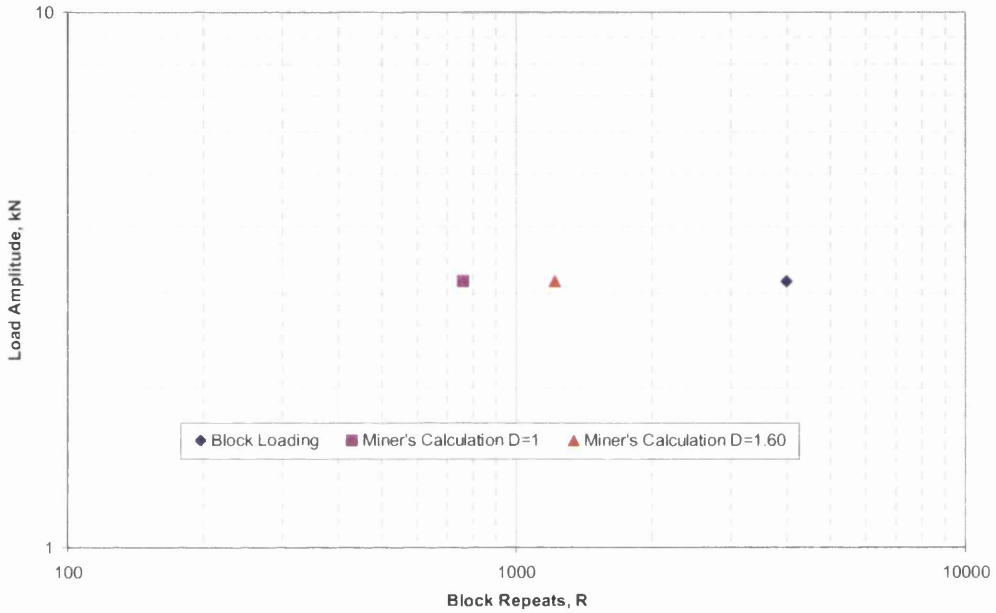

Figure 12.83: Miner's Rule for R=0.1 Block Loading Sequence

From both the under-estimations on the Miner's Rule this shows that even with converting the data back to R=-1 means that there is an alternative reason for why the FUCA component took 4000 repeats to fail.

On close inspection of the rig it was noticed that the actuator arm went out to the maximum load the load cell reading was negative and when it returned to the minimum load it was positive. This means that the whole test was being done under the compressive state.

By testing under compressive loading conditions, this would explain why the test took 4000 repeats to fail, as at 0.7kN the crack would be virtually open. Although if it were under tensile conditions, 7kN would be the most damaging as the crack is

fully open at this load. But with it being under compression no damage occurs from it.

Therefore to analyse the R=0.1 block loading results the conversion would not be using up to the R=-1 side of the Goodman diagram but the other side. This side as shown in figure 12.84 has no information available to be used therefore some assumptions must be made. For this compressive loading the R-Ratio is R=10.

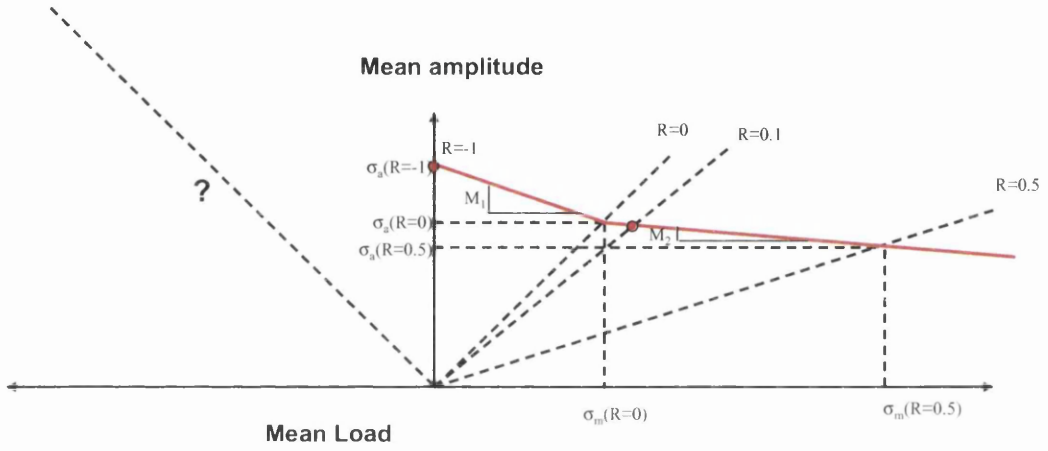

Figure 12.84: Goodman Diagram Extension

Three assumptions were made as to how to calculate the R=10 value. The subsequent Miner's Rule calculated damage is shown in Table 12.10.

Table 12.10: Miner's Rule Damage Results for the 3 Assumptions of R=10

Assumption #	Assumption Method for R=10	Estimated Constant Amplitude Life		Predicted Block Repeats
		3.535kN	1.7675kN	
1	$M_1 = M_2$	513115.1935	6572902.179	3013.738
2	$\sigma_m = -\sigma_a$	915352.514	15563330.77	5985.308
3	$M_1 = 0.25$	1214955.169	15563330.77	7315.935

One assumption that was made is that the values of M_1 and M_2 are the same and the Goodman diagram looks similar to figure 12.85. The R=10 value was calculated through changing the equation to Eq.37.

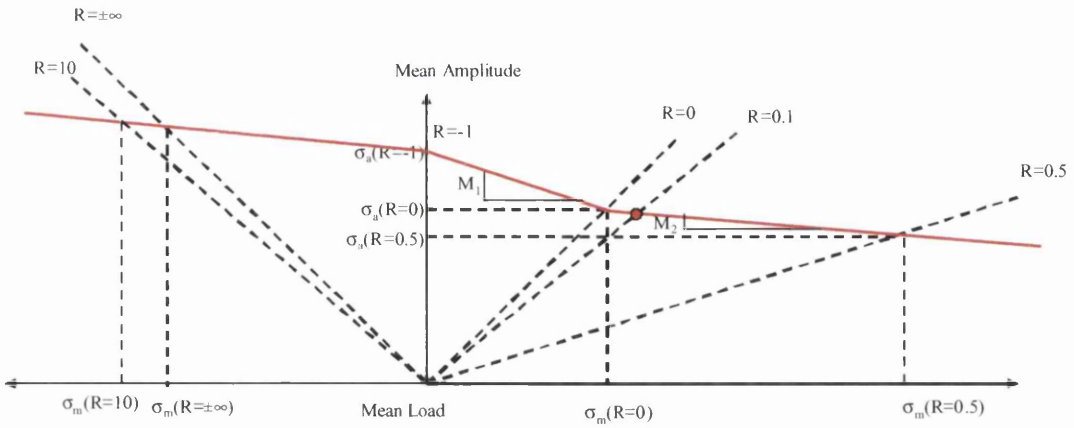

Figure 12.85: First Assumption $M_1 = M_2$ Values

$$\sigma_a^{R=-1} = (1 - M_1 \cdot (11/9)) \cdot \sigma_a \qquad \text{Eq.37}$$

The second assumption involved assuming that the mean load equalled the load amplitude i.e. $\sigma_m = -\sigma_a$ so that the Goodman Diagram for R=10 is shown in figure 12.86 with a plateau being reached at R=±∞. This is where at the maximum load applied touches 0 and everything is negative and closed, therefore no further mean stress effect occurs.

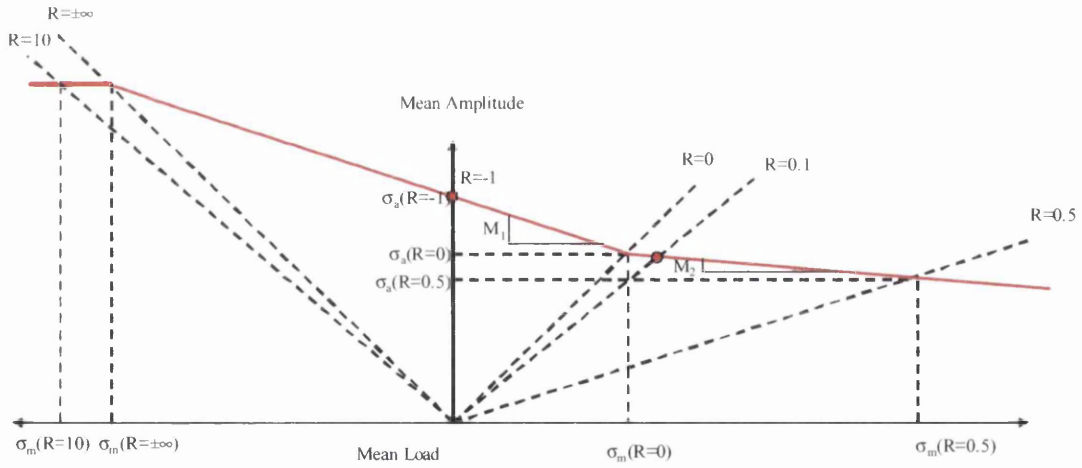

Figure 12.86: Assumption 2 Mean Load Equals Load Amplitude

The third assumption involves the M_1 value to remain the same for R=10 as it was for R=-1, i.e. M_1=0.25. The corresponding Goodman diagram is shown in figure 12.87.

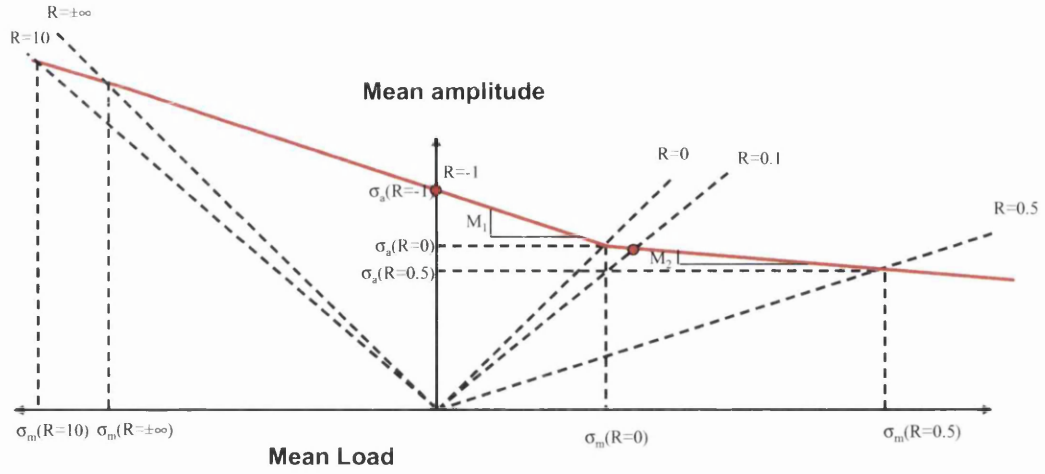

Figure 12.87: Assumption 3 M_1 Value = 0.25

Figure 12.88 shows the results of the 3 assumptions Miner's Rule for R=10. Assumption 1 under-estimates the FUCA component block repeats whilst both assumptions 2 and 3 over-estimate the block repeats.

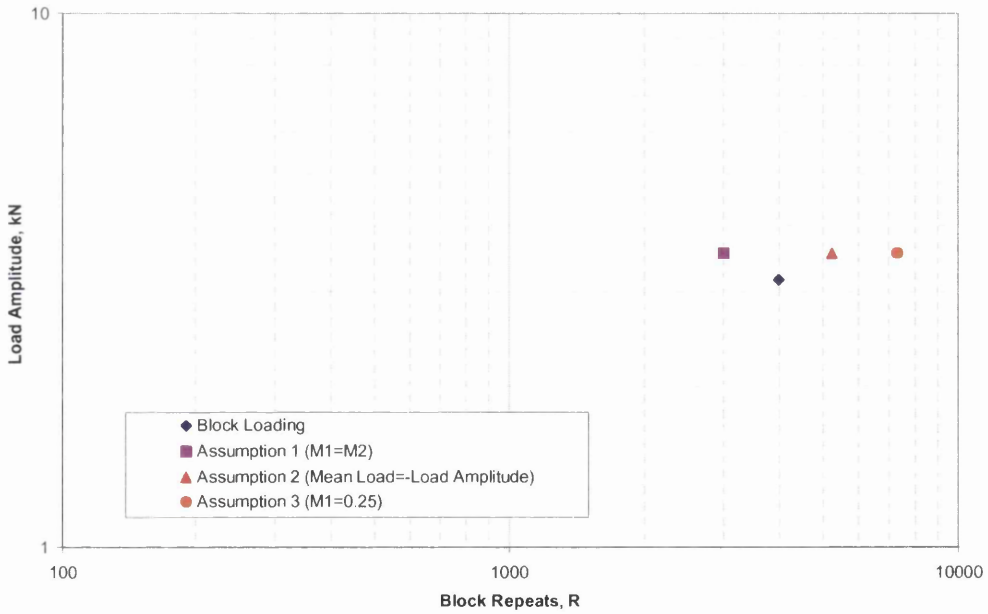

Figure 12.88: Miner's Rule for R=10

With only one test result at R=0.1 it is very difficult to establish exactly which assumption more accurately predicts the FUCA component block loading results. With a single result the approximate range of estimating the block repeats will be between assumption 1 and 2 due to the inability to determine how much scatter there will be in the fatigue results.

To more accurately predict the effect of mean stress under block loading conditions of R=0.1 will require further testing.

12.6.4 Variable Amplitude SAE Bracket Load-Time History

To analyse the variable amplitude SAE Bracket test data there are a number of methods which can be used. Figure 12.89 shows the effect of using the average life and log average life to estimate the fatigue lives, this was done by excluding component 26 which encountered several rig problems during test. The log average and average life predict the life as 157 and 162 cycles respectively. This accurately represents the majority of the test results.

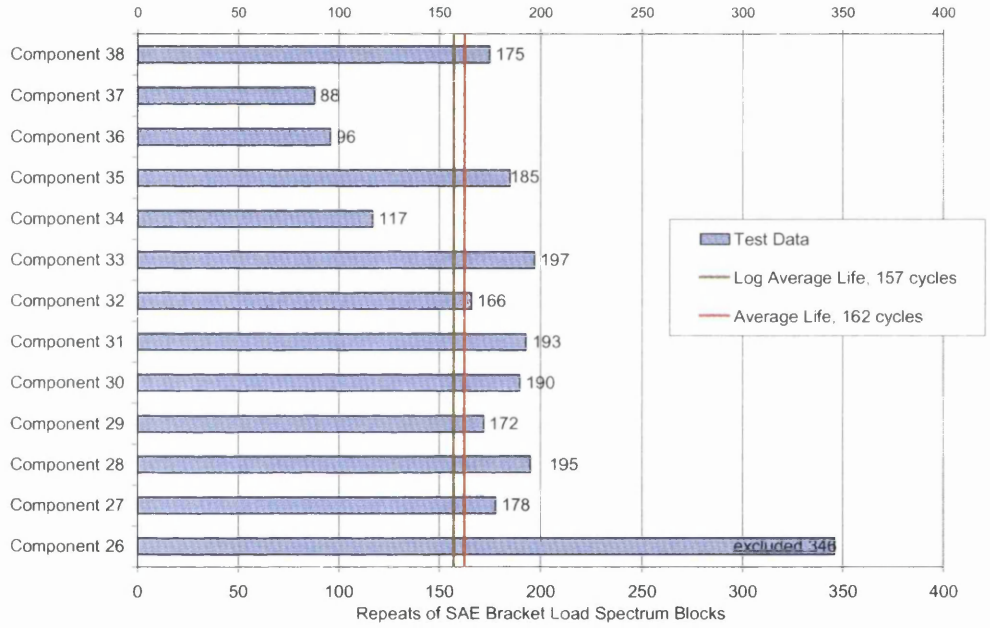

Figure 12.89: Average Life of Variable Amplitude SAE Bracket Results

Calculating Miner's Rule is shown in figure 12.90, this also bands the majority of the fatigue lives. Using the constant amplitude life to 10mm curve for the Miner's calculation accurately estimates the life to the test termination criterion. Using the constant amplitude life to 30mm curve slightly over-predicts the fatigue lives.

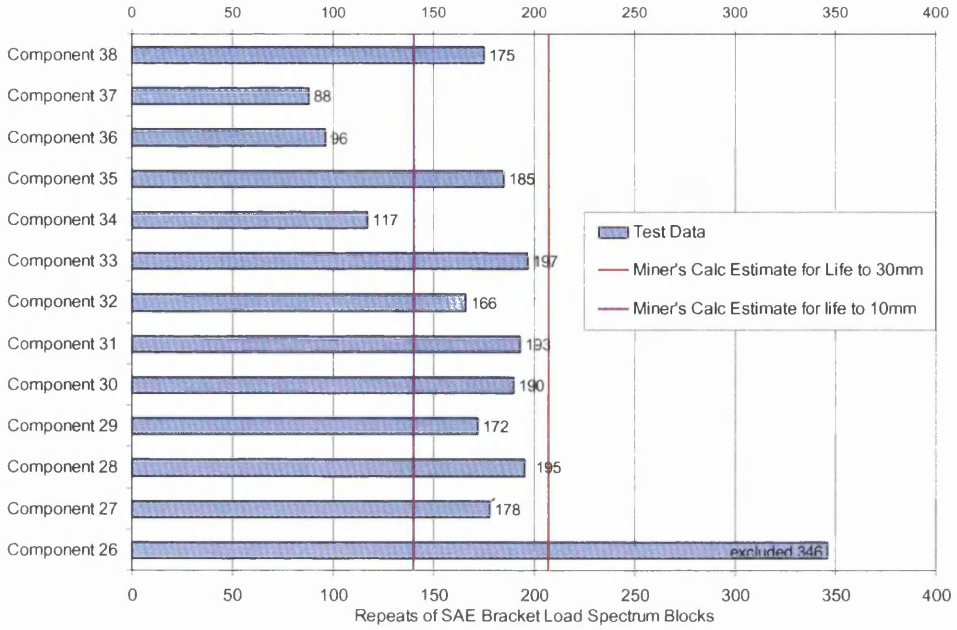

Figure 12.90: Miner's Rule

Calculating the Miner's damage using the rainflow analysis and scaling the results as described in section 10.9.2.1 is shown in figure 12.91. Both the Miner's calc estimate and calc Miner's damage D=1 predict very similar results as they both use D=1 to calculate the estimated life. Changing the damage constant D=0.7 for life to 10mm more accurately predicts the results as it covers the shorter fatigue lives from one test. Using D=0.7 to a life of 30mm also under-estimates the majority of the final failures of the test components which is good as the test termination criterion was 40 – 50mm crack length.

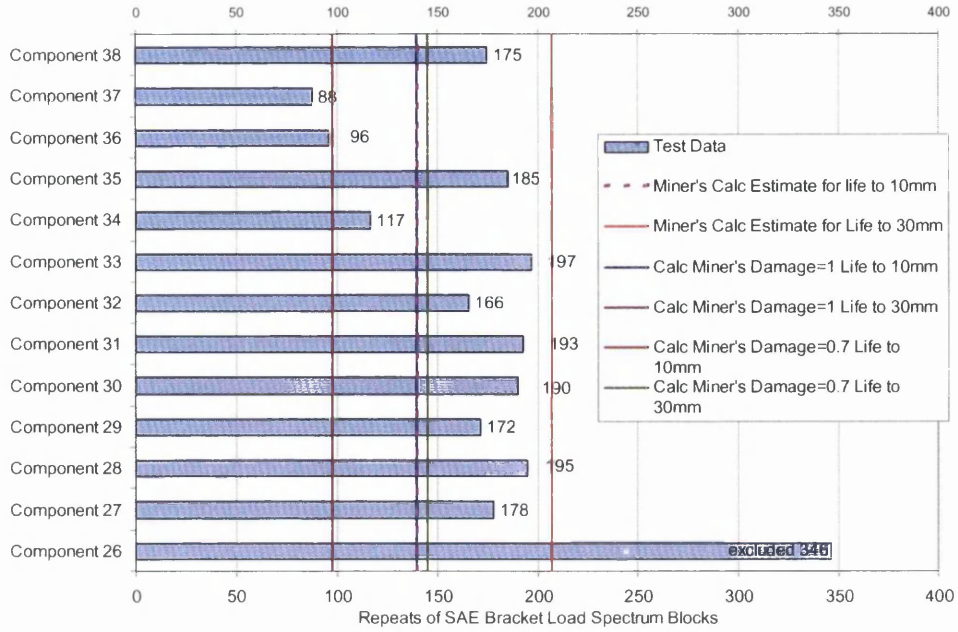

Figure 12.91: Miner's Rule Manually Calculated

12.6.5 FUCA Life Predictions

For both the Volvo and Battelle methods, the models have been produced with a variation in the weld start/stop location, which represents the difference between the actual tested FUCA components, which had smaller weld start/stop differences.

Both the Volvo and Battelle Methods are well-established for generating stresses and fatigue lives at the weld toe but they have no method for dealing with weld throat failures. The FUCA component failed through the weld throat and so this part of the research has been to identify the correct locations for the FE stress used to calculate estimated fatigue lives.

12.6.5.1 Volvo Method

From the figures 11.88 – 11.91 the results clearly show that when comparing the full-length and cut-length standard Volvo weld representation that they do not model the stress in the weld properly. They produce a high stress value, which in turn lowers the predicted fatigue lives. The full-length and cut-length triangular weld representation more closely estimates the fatigue lives of the FUCA components. From this investigation it is clear that the standard Volvo weld requires modification to incorporate the back panel as this better represents the stiffness of the weld nugget.

The Volvo methodology incorporated into MSC.Fatigue was based on generating fatigue lives of thick materials and therefore the standard weld representation shown in figure 10.39 was developed as in thick material the weld does not penetrate the parent sheet material as shown in figure 12.92a. Whereas this research was carried out on HSLA with a material thickness ~3mm which is deemed thin material and therefore the weld will penetrate the parent sheet material as shown in figure 12.92b. This is why the standard Volvo weld representation is not rigid enough to estimate the fatigue lives.

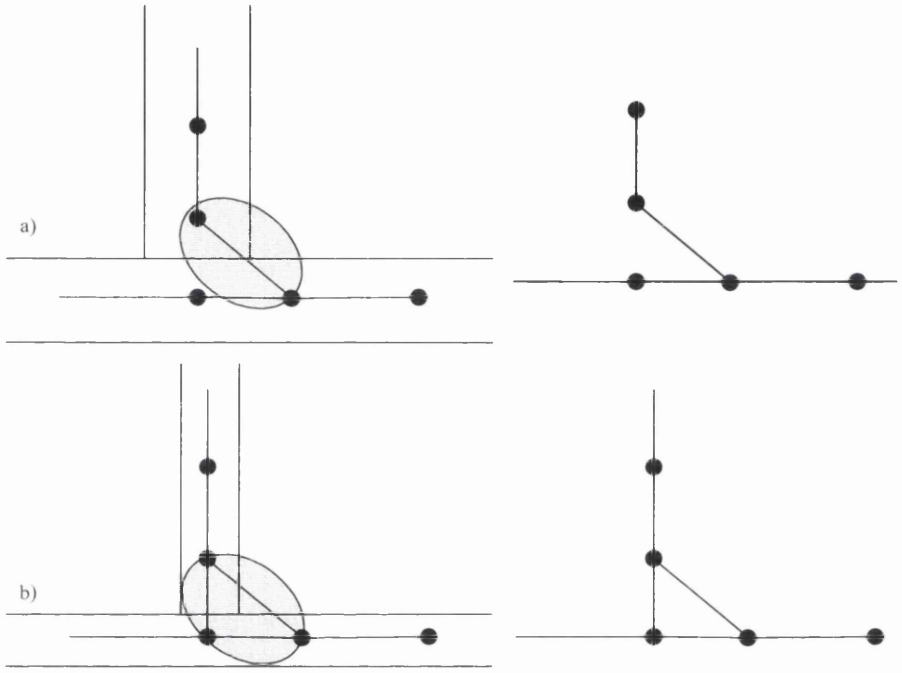

Figure 12.92: Schematic Diagram of a) Thick Material Welded Joint Used to Generate Original MSC.Fatigue Program, b) Thin Material Welded Joint Used in this Research

The position of the weld in the FE model has little effect on the fatigue lives and this is shown in the full and cut length in the triangular welds (figure 11.88). The FUCA test data is well within the range of the full-length and cut-length estimate fatigue lives.

12.6.5.2 Battelle Method

From figure 11.96 the location of the elements used to collect the nodal force from is critical in determining the predicted fatigue lives of the FUCA component. Using the elements from inside the weld line as the weld root over estimates fatigue lives of the

FUCA components shown in figure 11.93. Using the elements underneath the weld root node as the weld root under estimates the fatigue lives.

The different paths used to calculate the Battelle Structural Stress was a necessity as the definition of the weld line in the FUCA component is difficult. For coupons the weld line has a definite start/stop location (i.e. the edge of the coupons), whilst in the components it is unclear how to define a weld line that is welded to a longer piece of material.

Path 1 was the weld line itself and Paths 2 and 3 were the weld line incorporating elements of the component flange. Using Path 1 for both the full-length and the cut-length triangular welded models under-estimates the fatigue lives as it a has a very high stress which is the outcome of just using the last element of the weld and not averaging the forces and moments between two elements.

Whilst Path 2 and 3 much more closely predict the fatigue lives, with Path 3 having the nodal forces and elements averaged over more of the component flange, which in turn lowers the structural stress and increases fatigue lives. This indicates that with paths 2 and 3 the elements surrounding the weld provide structural support and load sharing capabilities. This therefore more accurately represents the stiffness of the welded component, which is observed through fatigue testing.

The position of the weld start/stop shown in figure 11.97 shows that the estimated fatigue lives are sensitive to the weld start/stop location. Showing that for as close an estimate to the actual lives, the FE model requires the weld to cover the plate to produce a stiffer model. Whereas removing one element to represent the weld start location of some of the actual FUCA components causes the model to have a reduced stiffness and therefore have a higher stress so reducing the fatigue lives.

Accurate representation of the weld starting point is critical to achieve reasonable representation of fatigue lives.

12.7 FUCA Life Predictions – Variable Amplitude Loading

12.7.1 Variable Amplitude Block Loading

From figures 11.98 – 11.99, it is noticeable that with a triangular weld representation used for both Volvo and Battelle Methods, modelling the weld start/stop location has some effect on the predicted number of repeats of the block loading signal for the 1st load level (shown in figure 10.20). For Battelle full and cut-length and Volvo cut-length models with two values of the Miner's Damage constant, the predicted number of block repeats of signal 1 is much less than the average and log-average test data.

The full-length model under Volvo's Method accurately predicts the average test life at D=1, and over-predicts life when D=1.6. A similar trend is noticeable in figures 11.100 – 11.101.

This under-prediction could arise from the fact the test was done at an R-ratio of R=-1, whilst the master S-N curve for throat failure, which was used to predict the lives, was generated through coupon fatigue tests with an R-ratio of R=0.1.

As shown in figures 11.98 – 11.101 when mean stress correction factors are applied to the Volvo method, the under-predictions become over-predictions for both models. Battelle's Method currently has no mean stress correction, therefore, the difference in R-Ratio between master curve and test cannot be overcome.

To accurately predict variable amplitude life of any component, it is necessary for the coupon fatigue test work to cover different R-ratios before converting into a master S-N curve. Longer levels of life prediction would have been possible if an R=-1 master S-N curve was available.

Also this under-prediction could arise from the fact that typical FE prediction is based on life to a "small crack" e.g. 10mm. Whereas the life used was to 40 – 50mm for the FUCA component test, instead of life to a small crack. In components, when a crack propagates, the applied load is being redistributed along many different redundant load paths, so an error was introduced due to the load pattern change.

In other words, since there is only one (a single) load path in the coupon joints for the master S-N data generation, the initiation and propagation of cracks in the coupons resulted in an increase in the crack growth driving force. This accelerated crack growth rate, resulted in little differences in fatigue lives to cracks of 10mm or 30-40mm, and to final failure even. In the case of the FUCA component, on the other hand, the redundant load paths caused a reduction in the crack driving force as the crack lengths increased, and in turn a slow-down in the crack growth rate. This resulted in a larger difference in the lives to cracks of 10mm and 40~50mm.

Changing Damage constant values from between D = 1 – 1.6 cannot be used to explain the fatigue life under-predictions noticed as other factors such as residual stress are different for different components. Therefore from this work keeping a D=1 is recommended.

Figure 11.102 shows that when comparing the FUCA component test at R=0.1 to the master S-N curve for throat failure generated at R=0.1, no mean stress correction was required. The predicted life is much lower than that of the test data because the prediction is based on life to a small crack in a coupon whilst in the component, life to a small crack would be much lower. Therefore, with the load redistributed to life at 30mm there is much more under-prediction in repeats of block life.

12.7.2 Variable Amplitude SAE Bracket Load-Time History

Figures 11.103 – 11.104 show that, for the Battelle method regardless of the damage constant and the model weld start/stop location, the predicted block repeats of the signal is over an order of magnitude less than the log-average test data. Whereas for the Volvo method changing the Damage constant to D=1.6 both models are with an order of magnitude difference of the log-average test data. Using D=1 the full-length model is within an order of magnitude whilst the cut-length model is over an order of magnitude less than the test data.

Mean stress correction on both models for the Volvo method increased the predicted life by a factor of 3.75, which is a very good trend even though the values still under-predict the log-average test repeats.

Tables 12.11 – 12.12 show the ratios of predicted life compared to actual lives for different Damage constant values. For the fully random load-time history, it is noticeable that the full-length model has a higher stress than the cut-length model. Therefore accurate weld start position must be modeled to get more accurate predictions.

Table 12.11: Comparing Predicted Life to Average Test Data for Each Method at D=1

Prediction Method at D=1	Predicted Life Repeats	Test Data	Ratio Predicted vs. Actual
Battelle Full-Tri	7.64	163	0.047
Battelle Cut-Tri	2.23	163	0.014
Volvo Full-Tri	20.35	163	0.125
Volvo Full-Tri Mean Stress Correction	77.15	163	0.473
Volvo Cut-Tri	7.5	163	0.046
Volvo Cut-Tri Mean Stress Correction	28.15	163	0.173
Battelle Constant Amplitude	8120	23705.17	0.343
Volvo Constant Amplitude	8029.32	23705.17	0.339

Table 12.12: Comparing Predicted Life to Average Test Data for Each Method at D=1.6

Prediction Method at D=1.6	Predicted Life Repeats	Test Data	Ratio Predicted vs. Actual
Battelle Full-Tri	12.22	163	0.075
Battelle Cut-Tri	3.56	163	0.022
Volvo Full-Tri	32.56	163	0.200
Volvo Full-Tri Mean Stress Correction	123.44	163	0.757
Volvo Cut-Tri	12	163	0.074
Volvo Cut-Tri Mean Stress Correction	45.5	163	0.279
Battelle Constant Amplitude	8120	23705.17	0.343
Volvo Constant Amplitude	8029.32	23705.17	0.339

From these two tables it is noticeable that more errors were introduced from the simple counting method and from the Miner's Calculation.

Overall, the Battelle Method for variable amplitude loading does require an algorithm to correct for the effects of mean stress. The current mean stress correction factor within the Volvo method also needs further work to establish an improved best correction method for the mean stress effects.

13. INDUSTRIAL APPLICATIONS

The current EngD research has identified that, for any weld there are a number of possible failure modes and locations:

- Toe Failure – 2 locations
- Throat Failure
    - Interface
    - Throat Failure

To analyse components without knowing the failure modes to start with will require all possible failure modes to be checked. This chapter will illustrate this process.

13.1 Volvo Method

For the Volvo Method, the location of stresses to be collected from for the various modes of failure are shown in figure 13.1, the locations are:

- Toe Failure – Positions 1 and 2
- Throat Failure – Position 3
- Interface Failure – Position 3

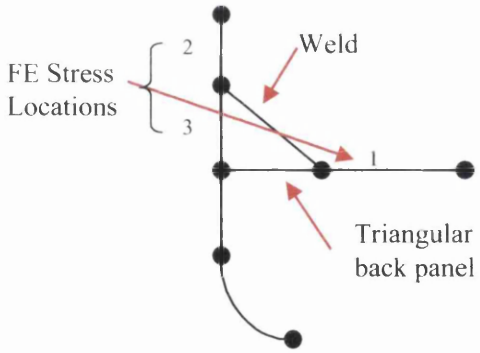

Figure 13.1: Location of FE Stresses for Various Modes of Failure

Full-length and cut-length triangular weld models used are shown in figure 11.41b and 11.42b. For each model and the various modes of failure the 1st and max stress was collated, as described in section 11.7.1 and figure 11.87. Figures 13.2 – 13.3 show the predicted fatigue lives for the various modes of failure for the full-length and cut-length models.

For the full-length model, as shown in figure 13.2, the mode of failure with the lowest values of both the 1st and max stress is the throat failure mode. The throat failure 1st and max stress reasonably predicts the test components fatigue lives.

Throat failure has the lowest stress and is therefore the most likely mode of failure. Noticeable from the figure is that the majority of the toe failure's stress and the interface failure stress is much higher than the throat failure so the range of predicted fatigue lives is much greater.

Based on calculated "structural stress" life prediction toe failure position 2 is the most likely failure mode. However, the throat failure stress is not much higher than toe failure position 2, and because of the scatter associated with fatigue, both failure modes are likely. However the predictions are too close to distinguish the predicted mode of failure. From the test the failure mode observed was throat failure but it could be possible that toe failure could occur as well.

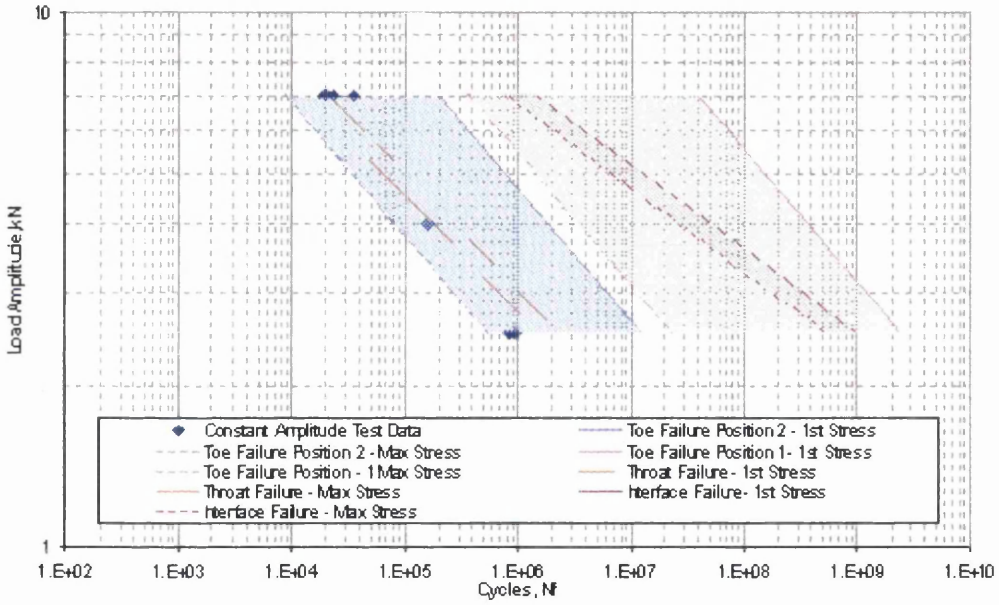

Figure 13.2: Full-Length Triangular Weld Predicted Fatigue Lives for All Possible Modes of Failure

Figure 13.3 shows the effect of altering the weld start position by an element on the predicted fatigue lives for all modes of failure for the cut-length model. For the majority of the failure modes, the 1st and max stress results are exactly the same for the cut model so no fatigue life range is shown. Clearly noticeable from the figure is that again the throat failure has the lowest stress and lowest fatigue life predictions to all the other modes of failure.

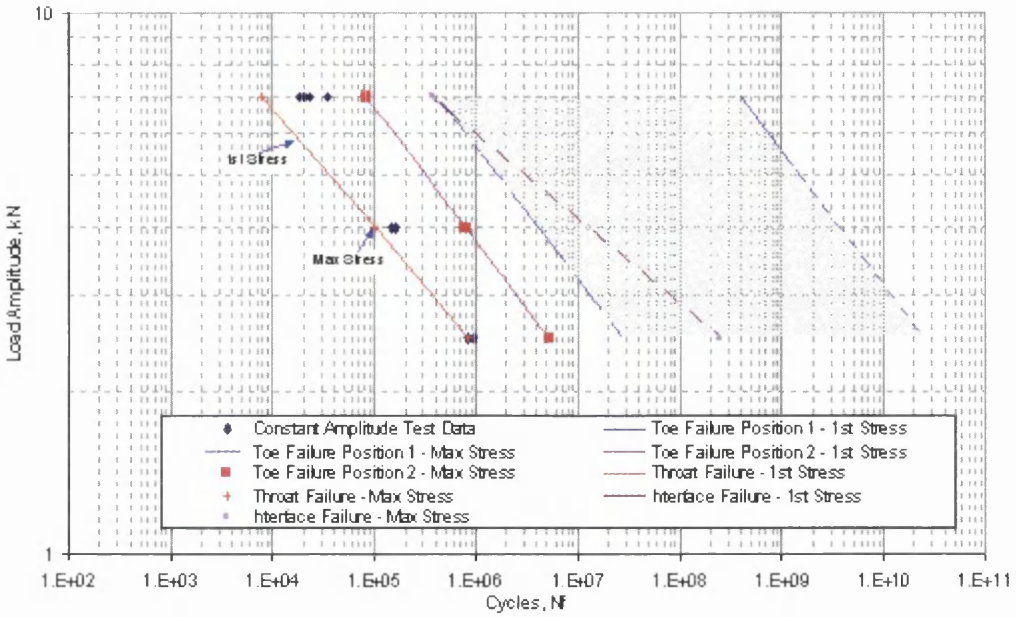

Figure 13.3: Cut-Length Triangular Weld Predicted Fatigue Lives for All Possible Modes of Failure

From this study, further work has been identified and is required to distinguish the locations of the FE stress used for the throat and interface failure modes, as currently they use the same location.

13.1.1 Assessment of the Volvo Method

In this EngD study, the FE-package MSC.Nastran has been used for fatigue life predictions of welded joints. For weld toe failures, the MSC.Fatigue module is automated to predict stresses and the fatigue lives at both weld toe positions.

The limitation of this package is that for weld throat and interface failures, there is no automated method of predicting the stress in the correct locations. For this the fringe results around the weld had to be manually interrogated to collate the predicted stress, and fatigue lives were manually calculated. This is time-consuming method, which needs automating within MSC.Fatigue module for ease of use.

13.2 Battelle Method

For the Battelle Method the location of stresses to be collected from for the various modes of failure are shown in figure 13.4, the locations are:

- Toe Failure – Positions 1 and 2

- Throat Failure – Position 4
- Interface Failure – Position 3

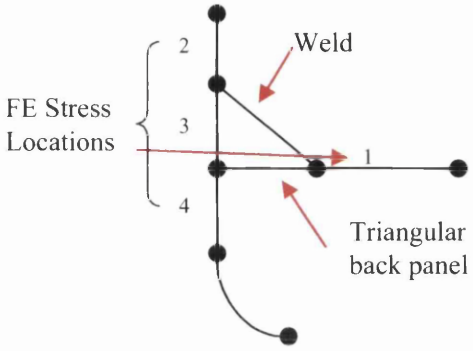

Figure 13.4: Location of FE Stresses for Various Modes of Failure

Full-length and cut-length triangular weld models used are shown in figure 11.41b and 11.42b. For each model the structural stress was calculated as described in section 10.7. Figures 13.5 – 13.6 show the predicted fatigue lives for the various modes of failure for the full-length and cut-length models.

Figure 13.5 shows that for the full-length model, the throat failure mode likewise has the lowest stress for a given life and therefore in this case will be the predicted mode of failure. Both locations of the toe failure and the interface failure have much higher stresses and over predict the test data by several magnitudes of life.

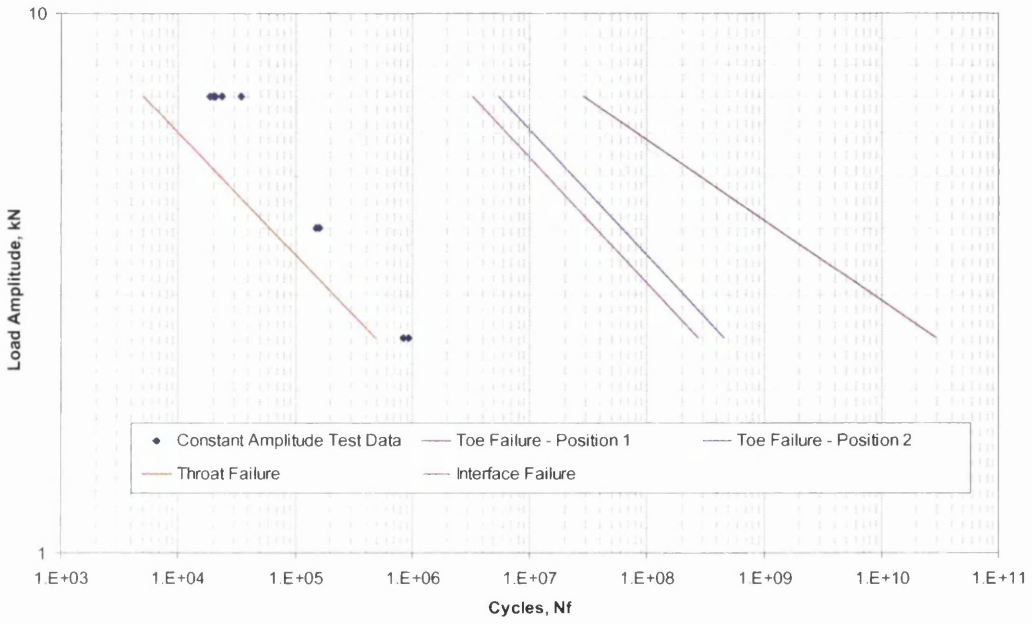

Figure 13.5: Full-Length Triangular Weld Predicted Fatigue Lives for All Possible Modes of Failure

Figure 13.6 shows the affect of the weld start location on the predicted fatigue lives of the FUCA component. It is clearly shown in the figure that the main predicted failure is at the weld throat for this component as this mode of failure has the lowest fatigue life. Checking the toe failure and the interface failure positions shows that they over predict the failures of the test data by several magnitudes of life.

The throat failure of the cut-length model has lower life than the full-length model showing that the predicted fatigue lives are sensitive to the weld start location.

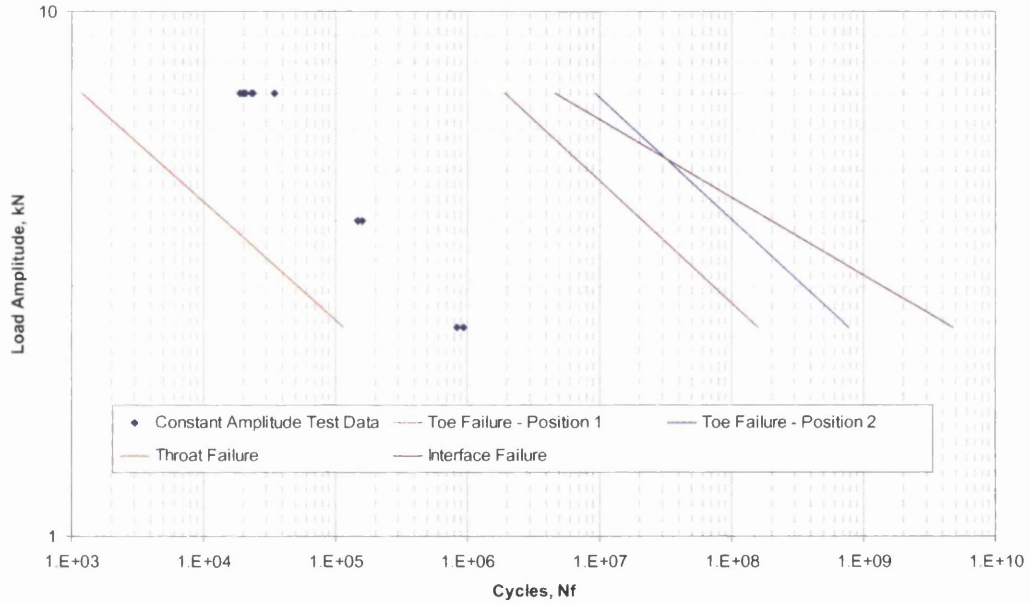

Figure 13.6: Cut-Length Triangular Weld Predicted Fatigue Lives for All Possible Modes of Failure

13.2.1 Assessment of the Battelle Method

In this EngD study, the Battelle methodology was incorporated into two CAE techniques FLOW and FE-Safe Verity. This is an improved technique to MSC.Fatigue as, the Battelle method is automated for predicting stresses and the fatigue lives at both weld toe failures and weld throat failures.

The Battelle methodology was derived for weld toe failure with the correct S-N curve used, the techniques should predict for weld throat failures - but this is were the technique needs improvement.

For weld throat failures, there are two methods of crack propagation from the weld root, identified during this study must be separated. The original methodology generalises throat and interface failure as "throat failure". Therefore the 3rd failure mode - Interface failure must be accounted for.

The result tables should therefore clearly state which mode of failure is predicted along with the fatigue lives.

13.3 Summary

To summarise all my EngD work described so far I propose the following procedures for predicting weld fatigue lives using both Volvo and Battelle methods. These procedures provide significant enhancements to the existing methods, which are limited to fatigue life predictions of weld toe failures only.

MSC.Nastran has been the main FE software code used throughout the present research. Therefore some of the steps may be specific to MSC.Nastran. However equivalent functions may be found in other FE codes.

13.3.1 Analysis Procedure Based on the Volvo Method

I. Prepare and Analyse the FE Model

- Select the component or region of an automotive chassis structure to be analysed.
- Build FE Model using shell elements, with a recommended element size of 3~6mm.
- Weld Representation – Use triangular arrangement to represent welds with shell thickness the same as rest of component.
- Create a copy of the model – one for toe failure, the other for throat and interface failure.
- Ensure the element normals are in the correct direction for the subsequent FE analysis shown in figure 13.7.

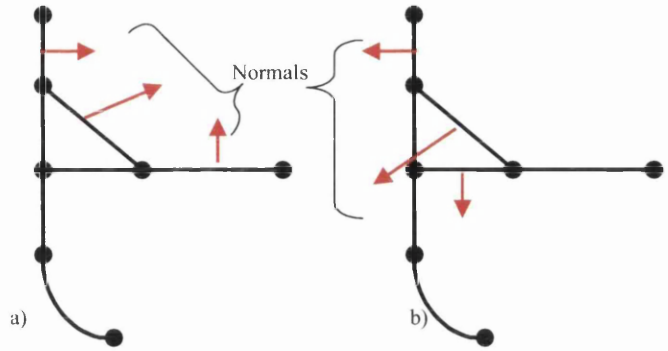

Figure 13.7: Normal Directions for a) Toe Failure, b) Throat and Interface Failures

- **Optional** - Renumber nodes along the weld line to easily identify them during the FE result extrapolation phase.
- Apply load and boundary conditions representative of test or actual in-service conditions.
- Select relevant FE result outputs, e.g.: stresses, strains and grid point balance forces (GPFORCE) to be written out when running MSC.Nastran.
- Edit FEmodel_input file (.bdf or .dat) to ensure the "cubic" stress extrapolation option is selected instead of the bi-linear extrapolation "bilin" - e.g.: STRESS(PLOT,SORT1,REAL,VONMISES,CUBIC)=ALL
- Perform linear elastic FE analysis.

II. Extract FE Results in Preparation for Fatigue Analysis

- Check all possible weld locations as shown in figure 13.8:

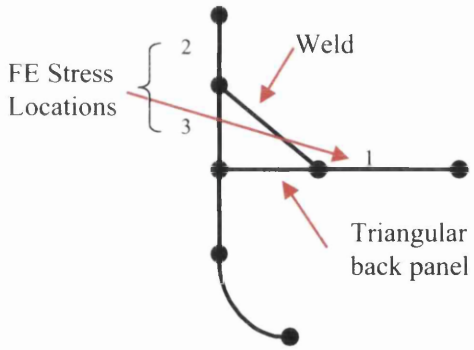

Figure 13.8: Location of FE Stresses for Various Modes of Failure

- **Toe Failure:**
  - For toe failure, select all weld toes elements and nodes (MSC.Fatigue has a software module available to do this).
  - Ensure that the shell Maximum Principal 2D in-plane stress is used.
  - Extract the weld toe stress – maximum principal 2D stress from both surfaces of the element (Z_1 and Z_2) as described in figure 11.35.
- **Throat and Interface Failure:**
  - For throat and Interface failure, remove the toe weld elements to ensure the FE stress is not averaged over those elements.
  - Ensure that the shell maximum principal 2D in-plane stress is used.
  - Extract the weld throat or interface maximum principal 2D stress from both surfaces of the element (Z_1 and Z_2) as described in figure 11.35.

III. Perform Fatigue Analysis For All Failure Modes and Locations

- Scale and or offset the extracted FE Stress to represent the load-time history.
- Superposition the stress if required for multiple load-time histories.
- Establish the effective stress range and mean values from Rainflow counting.
- Calculate the damage, based on the weld S-N curve for the same weld failure mode. Perform mean stress correction as appropriate.
- Sum up the total damage using Miner's Rule.
- Establish the fatigue lives $N = \frac{1}{\Sigma D_i}$.
- Or if component or system has been fatigue tested, for all methods calculate the predicted life from the data generation S-N curves for the respective modes of failure.

IV. Review Fatigue Analysis Results

- The lowest life is the predicted failure location. With the lowest life showing the predicted mode, location and life of failure.

13.3.2 Analysis Procedure Based on the Battelle Method

I. Prepare and Analyse the FE Model

- Select the component or region of automotive chassis structure to be analysed.
- Build FE Model using shell elements with a recommended element size of 3~6mm.
- Weld Representation - Use triangular arrangement to represent welds with shell thickness the same as rest of component.
- Define the force direction as parallel to the weld line.
- **Optional** - Renumber nodes along the weld line to easily identify them during the FE result extrapolation phase.
- Create on selected nodes for each potential failure locations a local coordinate system in the correct orientation for the Battelle Structural Stress Calculation.
- **Optional** - Renumber coordinate system along the weld line to easily identify them during the FE result extrapolation phase.
- Apply load and boundary conditions representative of test or actual in-service conditions.
- Select relevant FE result outputs, e.g.: stresses, strains and grid point balance forces (GPFORCE) to be written out when running MSC.Nastran.
- Perform linear elastic FE analysis.
- **Optional** - Edit FEmodel_input.bdf (or .dat) file to ensure:
    - GPFORCE(punch)=all or for specific data set GPFORCE(Punch)=1
    - To write out for renumber nodes set 1 = node start,thru,node end
- From FEmodel_input.dat file write out the relevant local coordinate system details for each node of the local coordinate system.
- If necessary, calculate the vector cross products for converting force from global to local coordinate system.

II. Extract FE Results in Preparation for Fatigue Analysis

- Check all possible weld locations as shown in figure 13.9:

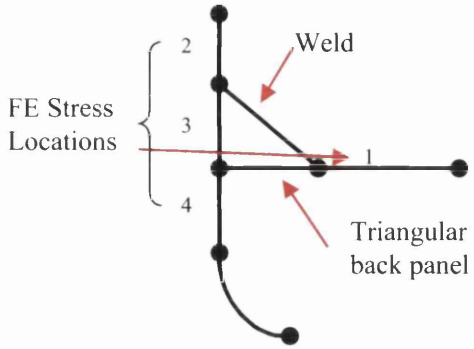

Figure 13.9: Location of FE Stresses for Various Modes of Failure

- For toe failure, throat and interface failures select the relevant positions.
- From the Nastran FE results (punch) file, read out the respective force and moments for the nodes for the correct elements.
- Transfer these global positions into a local coordinate system.
- Convert the nodal forces and moments into distributed forces and moments along element edges (weld lines)
- Calculate the Battelle Structural Stress.

III. Perform Fatigue Analysis

- Scale and or offset the calculated Battelle Structural Stress to represent the load-time history.
- Superposition the stress, if required, for multiple load-time histories.
- Establish the effective stress range from Rainflow counting.
- Calculate the damage, based on the weld master structural S-N curve for the same weld failure mode.
- Sum up the total damage using Miner's Rule.
- Establish the fatigue lives $N = \frac{1}{\Sigma D_i}$.
- Or if component or system has been fatigue tested, for all methods calculate the predicted life from the data generation S-N curves for the respective modes of failure.

IV. Review Fatigue Analysis

- The lowest life is the predicted failure location. With the lowest life showing the predicted mode, location and life of failure.

14. CONCLUSIONS

14.1 Coupon Testing for Data Generation

From all the results produced and analysed, these are the main conclusions:

- Test termination criteria had little effect on test results, for coupon joints.
- There is little difference in the weld performance, on a per unit weld-line length basis for lap-shear joints GM1 and GM2 and the peel joints GM3 and GM4.
- Partially welded single lap and double lap-shear joints performed marginally better than the fully weld joints.
- Full and partially welded coupon test data for the single lap-shear joints from both suppliers could potentially use the same master curve.
- Partially welded and fully welded peel joints show very good correlation with some crossover between high and low loads.
- Double-weld lap-shear joints appear to have better fatigue lives than the single lap-shear welds.
- Single lap-shear joints for both suppliers have similar fatigue lives.
- GKN double lap-shear joints have better fatigue lives than TKA, indicating that welding settings and weld quality do affect fatigue performance.
- Lap-shear joints performed significantly better than the peel joints.
- T-Shaped joints performed better under axial loading than under bending and lateral loading.
- Mean stress does affect fatigue lives especially at long lives for TM11B and GM2.
- High load cycles are the most damaging cycles in block loading.
- Under variable amplitude conditions, double lap-shear welds are more efficient than single welds.
- Under variable amplitude conditions, lap-shear welds perform better than T-shaped joints.
- At present, R=0.1 curve was used for R-ratios less than 0.5 and R=0.5 was used for R-ratios greater than 0.5, which under-estimates the life of TM11A. Further test work required to improve the predictions.

14.2 Failure Locations

- **Three locations of failure defined – toe failure, Interface (throat) failure and Throat failure all seen in the coupons joints tested.**

14.3 Coupons FE Modelling

14.3.1 FE Modelling with Experimental Verification

- The results indicate that increasing the thickness of the weld, or having a back plate (tri) affects the finite element stress predicted. Shell models showed better predicted stress values than solid models.
- Results show that predicted stress would slightly under-predict strain gauged results at low load levels but at high load levels the predicted stress is significantly lower.
- Compiling all the results it shows that for single lap-shear coupons the predicted stress is within the photoelasticity scatter. Whilst for the double lap-shear, the finite element results are very conservative in predictions.
- The effects of finite element mesh sizes on the predicted FE stress were investigated, with the results indicating that the element mesh size has little effect on the prediction of the stress in simple joints.
- Overall the control of angular alignment is very important in testing and critical to the subsequent analysis of the results.

14.3.2 Volvo Structural Stress

- Data for all weld toe failures can result in a single master structural stress S-N curve. However the data for peel and lap-shear coupon joints were grouped based on their failure modes, i.e. throat and interface failures. A master structural stress S-N curve do exist for each mode.

14.3.3 Battelle Structural Stress Results

- Using the manual calculations the effect of the weld start/stops are not corrected for and the FE stress just before the weld start/stop increases. Using the Battelle programme the weld start/stops did get corrected but the predicted FE stress prior to the start/stop is still high.
- Manual calculations are very similar to the Verity software structural stress with FLOW having slightly higher predicted stress results.

14.4 Weld Fatigue Performance Master Curves

- For weld toe failure, the existing analysis programmes can readily predict the fatigue lives, whereas for weld throat failures, the predictive methodologies especially the "structural stress" calculation had to be researched.
- The weld toe failures of TKA–Tallent show very good master curve conversion, whilst GKN weld toe failures, show reasonable master curve conversion due to the scatter in the results.
- For the weld throat failures, the stress was located above the weld on the top plate and using the Z1 side of the shell elements to get reasonable master curve conversion. For the peel throat failures the stress was located behind the weld on the base plate and Z2 surface was used. Reasonable master curve convergence was achieved.
- The regression based on life method for statistical analysis is much more conservative than the regression based on stress method of analysis, as it has much wider scatter bands. The Endurance limit method of regression based on stress analysis produced scatter bands that did not bind the data, by changing to the regression based on life, all the data was bound by the survival curves.
- **Overall, for both Volvo and Battelle approaches, structural stress-life (S-N) curves for welds are dependent on failure modes. For each failure mode, however, a master S-N curve does exist and relatively independent of joint geometry.**

14.5 FUCA Component Fatigue Test Results

- Generally one mode of failure for the FUCA components was identified, i.e. weld throat failure.
- Large scatter occurred in ±2.5kN for crack initiation with low crack propagation rates. At ±4kN crack propagation rates were also slow; this is not the case at ±7kN.
- Under variable amplitude block loading conditions the high load cycles are the most damaging.
- Using a damage constant for the block loading sequence R=-1, D=1 under-estimates the fatigue life which is great for design purposes, D=1.60 accurately predicts the fatigue life of the FUCA component.

- For block loading sequence R=0.1, both D=1 and D=1.6 under-estimates fatigue life, which does not explain why FUCA at R=0.1 failed after 4000 repeats.
- Using the Goodman diagram to calculate Miner's Rule R=10, gives 3 assumptions. 1st assumption under predicts life with assumption 2 and 3 over predicting life, showing mean stress does have an effect of predicting fatigue life.
- Using average life and log(average life) predicts the fatigue lives of the FUCA component under variable amplitude SAE Bracket Load-time history.
- Using 10mm constant amplitude load-life curve for Miner's Rule predictions, predicts fatigue lives of FUCA whilst using the 30mm constant amplitude load-life curve, over-estimates the fatigue life.
- Calculating the Miner's Rule from Rainflow counting predicts the same life at 10mm. Using D=0.7 to 10mm crack more accurately predicts the results due to its lower life estimation. Whilst using D=0.7 to 30mm crack under estimates the majority of the final failure, which is good as test termination was at 40-50mm crack.

14.5.1 FUCA Life Predictions

One of the main achievements of the current EngD research is the extension of the existing Volvo and Battelle methods to allow life prediction of fatigue failure from weld throat and interface.

14.5.1.1 Volvo Method

- For both the 1st stress and the maximum stress, the current Volvo standard for weld representation under-estimates the life of the FUCA component.
- For both 1st and maximum stress the triangular weld shape more reasonably predicts the life of the FUCA components.
- Volvo original definition of the weld representation is not stiff enough for the thin sheet material under test so therefore requires a back panel forming a triangular weld for thin material.
- Weld start/stop location has little effect on the predicted fatigue lives using the Volvo method.

14.5.1.2 Battelle Method

- Using the 'Inside Weld Line' location the Battelle Structural Stress over-predicts the fatigue lives of the test data for both the full-length and cut-length welds.
- The 'Weld Root' location under-estimates the fatigue lives of the test data and therefore the correct location for the FE stress pick up for weld throat failures.
- There is limited sensitivity in fatigue lives predicted due to the weld start locations – full and cut length welds with the full-length weld being more sensitive than the cut-length weld.
- Using paths 2 and 3, which incorporate the elements surrounding the weld into the Structural stress calculation, has lower stress and more closely predict fatigue lives. This is due to the surrounding elements providing structural support and load sharing capabilities. Therefore, more accurately represents the stiffness of the welded component, which is observed through fatigue testing.
- Weld start/stop location is critical in this as a full-length weld ensures the weld is much stiffer and more accurately predicts fatigue lives. Therefore accurate representation of the weld starting point is critical to achieve reasonable representation of fatigue lives.

14.5.2 FUCA Life Predictions Variable Amplitude Loading

14.5.2.1 Variable Amplitude Block Loading

- Mean stress correction of R=-1 block loading signal over-predicts the average test data regardless of the damage constant value.
- Volvo method under-predicts the cut-length model accurately predicts the full-length model.
- Battelle method for both models under-predicts the average test data.
- Both methods require accurate weld start location to be modelled to predict accurate results.
- For Block loading signal of R=0.1 (maximum load 7kN) both the Volvo and Battelle Method along with mean stress correction under-predict the test data.
- Changing Damage constant values from between D = 1 – 1.6 cannot be used to explain the fatigue life under-predictions noticed as other factors such as

residual stress are different for different components. Therefore from this work keeping a D=1 is recommended.

- To accurately predict variable amplitude life of any component, it is necessary for the coupon fatigue test work to cover different R-ratios before converting into a master S-N curve. Longer levels of life prediction would have been possible if R=-1 master S-N curve was available.

14.5.2.2 Variable Amplitude SAE Bracket Load-Time History

- Regardless of Damage constant value D=1 or D=1.6, both Volvo and Battelle methods for both models under-predict the average test data.
- Mean stress correction on both models for the Volvo method, show an increase predicted life by a factor of 3.75, which is a very good trend even though the values still under-predict the log-average test repeats.
- Overall, the Battelle Method for variable amplitude loading does require an algorithm to correct for the effects of mean stress.
- The current mean stress correction factor within the Volvo method also needs further work to establish an improved best correction method for the mean stress effects.
- **The mean stress effect must be accounted for and incorporated into CAE fatigue life predictions.**

14.6 Industrial Applications

- From all this analysis, two methods of predicting weld fatigue failure in components or regions of assemblies for the Volvo and Battelle methods have been proposed.

15. FURTHER WORK

From this work, it is evident that there are certain factors which need to be further investigated. Especially, these include the effects of mean stress on all coupon geometries and subsequent mean stress correction, which will enable better CAE weld analysis that weld durability requires. The effect of mean stress on the component fatigue lives needs further analysis, as this will improve understanding of weld durability.

T-shaped coupons were tested under constant and variable conditions mainly for understanding mean stress correction. FE analysis of this more complex joint and its loading arrangements would be a useful intermediate step to the FUCA component test. This would enable the correct stresses to be located and better understanding of the fatigue lives.

The method of analysing the FE model for the peel joints has shown that the actual mode of failure is not the relatively easy sheet failure but more the throat failure of the weld. The location of the FE stress obtained needs further investigation. This will aid the FE techniques used to be modified to become more useable for weld throat failures.

While calculating the Battelle structural stress manually the issue arising from the weld start/end stress calculations needs to be resolved. Further investigations are also necessary to understand the equivalent structural stress algorithm to better manually calculate the FE stress.

To accurately predict variable amplitude life of any component, it is necessary for the coupon fatigue test work to cover different R-ratios before converting into a master S-N curve.

Overall, the Battelle Method for variable amplitude loading does require an algorithm to correct for the effects of mean stress. The current mean stress correction factor within the Volvo method also needs further work to establish an improved best correction method for the mean stress effects.

16. REFERENCES

Abdalla, A. J., C. d. M. Neto, et al. (2001). Optimization of the Mechanical Properties of Low-Carbon Steels by Formation of a Multiphase Microstructure. International Mobility Technology Conference and Exhibit, Sao Paulo, Brazil, Society of Automotive Engineers.

Arnold, K. (2001). A Procedure for Statistical Analysis of Fatigue (S-N) Data. C. I. Report. Coventry, Corus Automotive.

ASTME (1995). Standard Definitions of Fatigue, Annual Book of Standards.

Bannantine, J. A., J. J. Comer, et al. (1990). Fundamentals of Metal Fatigue Analysis. Englewood Cliffs, New Jersey, Prentice Hall.

Becker, W. T. and R. J. Shipley, Eds. (2002). Failure Analysis and Prevention. ASM Handbook Volume 11. Ohio, USA, ASM International.

Berger, C., K.-G. Eulitz, et al. (2002). "Betriebsfestigkeit in Germany — An Overview." International Journal of Fatigue **24**(60): 603-712.

Boyce, B. R., G. C. Calvert, et al. (2003). Real-Time Photoelastic Stress Analysis - A New Dynamic Photoelastic Method for Non-Destructive Testing. 3rd International Conference on Emerging Technologies in NDT, Thessaloniki, Greece, The British Institute of Non-Destructive Testing.

Brandon, D. and W. D. Kaplan (1997). Joining Processes An Introduction. Chichester, John Wiley and Sons.

Brenner, C. E., B. Unger, et al. (1998). Fatigue Assessment of Welding Seams and Spot Joints Based on FEA. SAE 2000 World Congress, Detroit, Michigan, USA, Society of Automotive Engineers, Inc. Warrendale, Pennsylvania, USA.

BSI (BS 5400:Part 10:1980). Code of Practice for Fatigue of Steel Structures.

BSI (BS 7608:1993). Code of Practice for Fatigue Design and Assessment of Steel Structures.

Cazaud, R. (1953). Fatigue of Metals. London, Chapman & Hall Ltd.

Clough, A. (2003). Vehicle Structures - Past, Present and Future, Corus Automotive Engineering.

Cole, G. S. and A. M. Sherman (1994). Lightweight Materials for Automotive Applications. International Metallographic Society Symposium on "Microstructural Characterisation of Lightweight Materials for Transportation", Montreal.

Cui, W. (2002). "A State of the Art Review on Fatigue Life Prediction Methods for Metal Structures." Journal Marine Science and Technology: 43-56.

Dieter, G. E. (2001). Mechanical Metallurgy. Singapore, McGraw-Hill.

Dong, P. (2001). "A Structural Stress Definition and Numerical Implementation for Fatigue Analysis of Welded Joints." International Journal of Fatigue **23**(10): 865-876.

Dong, P. (2005). Verity™ Structural Stress Method for Fatigue Evaluation of Welded Structures - An Introductory Training Course, Centre for Welded Structures Research, Battelle Memorial Institute.

Dong, P. (2005). Verity™ Structural Stress Method for Fatigue Evaluation of Welded Structures - An Introductory Training Course, Center for Welded Structures Research, Battelle Memorial Institute.

Dong, P., J. K. Hong, et al. (2003). "Stress and Stress Intensities at Notches, 'Anomalous Crack Growth' revisited." International Journal of Fatigue **25**: 811-825.

Dowling, N. E. (1987). A Review of Fatigue Life Prediction Methods. Passenger Car Meeting and Exposition, Dearborn, Michigan, Society of Automotive Engineers.

Dowling, N. E. (1993). Mechanical Behaviour of Materials: Engineering Methods for Deformation. Fracture and Fatigue. Englewood Cliffs, New Jersey, Prentice-Hall, INC.

Ellwood, R. and C. Lewis (1999). Maximising the Fatigue Durability of Down-gauged High Strength Steel Structures. Compass '99 - Component Optimisation from Materials Properties and Simulation Software, IRC, University of Wales, Swansea, UK, EMAS Publishing.

Evans, P. J., L. K. Crawford, et al. (1997). "High Strength C-Mn Steels for Automotive Applications." Iron and Steelmaking **24**(5): 361-367.

Ewalds, H. L. and R. J. H. Wanhill (1996). Fracture Mechanics. London, Arnold.

Fermér, M. and H. Svensson (2001). "Industrial Experiences of FE-based Fatigue Life Predictions of Welded Automotive Structures." Fatigue & Fracture of Engineering Materials & Structures **24**: 489-500.

Fine, M. E. and Y.-W. Chung "Fatigue in Metals." 63-72.

Fricke, W. (2003). "Fatigue Analysis of Welded Joints: State of Development." Marine Strucutres **16**: 185-200.

Gao, Y., D. Chucas, et al. (2001). Review of CAE Fatigue Analysis Techniques for Spot-Welded High-Strength Steel Automotive Structures. SAE 2001 World Congress, Detroit, Michigan, USA.

Haight, B. (2003). Living in a Materials World: Advanced Technologies are Opening Doors for New Materials - Product: Materials- Materials in Automotive Industry - Industry Overview. Automotive Industries.

Hartmann, G., U. Heidtnamm, et al. (1997). High Strength Steel Sheet for Autobody Design. Advanced Body Concept & Development, IBEC.

Higdon, A., E. H. Ohlsen, et al. (1985). 4th Ed Mechanics of Materials. New York, John Wiley & Sons.

Hughes, R. L. (1995). Lightweight Automotive Design: The Ultralight Steel Auto Body. IBEC '95 - Body Design and Engineering.

Johnson, K. C. and A. E. Mascarin (2002). New Materials Technologies in the Automotive Industry: A Review of Successes and Failure. Technical Report. Warrendale, USA, Society of Automotive Engineers.

Kihl, D. P. and S. Sarkani (1999). "Mean Stress Effects in Fatigue of Welded Steel Joints." Probabilistic Engineering Mechanics **14**: 97-104.

Klesnil, M. and P. Lukáš (1967). "Fatigue Softening and Hardening of Annealed Low Carbon Steel." Journal of The Iron and Steel Institute: 746-749.

Kou, S. (2003). "Solidification and Liquidation Cracking Issues in Welding." Journal Of Materials Joining **55**(6): 37-43.

Kyuba, H. and P. Dong (1993). Equilibrium -Equivalent Structural Stress Approach to Fatigue Analysis of a Tubular Joint, International Institute of Welding.

Lewis, C. (1996). "Fatigue Performance of Fusion Welded Automotive High Strength Steels." Welding & Metal Fabrication **64**(7): 275-278.

LMS, I. (1999-2000). "Fatigue Analysis of Seam Welds."

Maddox, S. J. (1991). Fatigue Strength of Welded Structures, Abington Publishing.

Manson, S. S. (1953). Behaviour of Materials Under Thermal Stress. Heat Transfer Symposium, University of Michigan, Engineering Research Institute.

Mansour, A. E., P. H. Wirsching, et al. (1995). Probability - Based Ship Design: Implementation of Design Guidelines. Washington D.C., NTIS.

Matsuishi, M. and T. Endo (1968). Fundamentals of Metals Subjected to Varying Stress. Japan Society of Mechanical Engineers, Fukuoka, Japan.

Millington, D. (1973). TIG Dressing to Improve Fatigue Properties in Welded High-Strength Steels, The Welding Institute.

Moan, T. and S. Berge (1997). Fatigue and Fracture. Committee III.2, Proceedings of the 13th International Ship and Offshore Structures Congress, Norwegian University of Science and Technology, Trondheim, Norway, International Welding Institute.

MSC, F. (1999). MSC. Fatigue Users Guide, MSC. Software Corporation.

Neard, J. (2004). Cars are Becoming Real Lightweights. Driving Today.

Newsletter, A. (1999). What's the Fastest Growing Lightweight Material in Auto Industry? AISI. **3**.

Nieme, E. (2001). Structural Stress Approach to Fatigue Analysis of Welded Components, Designers Guide, International Institute of Welding.

Pekkari, B. Environmental Concerns are Driving the Development of Welding Processes and Applications. Götenburg, ESAB AB.

Plaskitt, R. J. and C. J. Musiol (2002). Developing a Durable Product. Agricultural Equipment Technology Conference, Kansas City, Missouri, ASAE.

Pope, J. A. (1959). Metal Fatigue. London, William Clowes & Sons Ltd.

Potukutchi, R., H. Agrawal, et al. (2004). Fatigue Analysis of Steel MIG Welds in Automotive Structures. 2004 SAE World Congress, Detroit, Michigan, Society of Automotive Engineers.

Poutianinen, I., P. Tanskanen, et al. (2004). "Finite Element Methods for Structural Hot Spot Stress Determination - A Comparison of Procedures." International Journal of Fatigue **26**: 1147-1157.

Power, E. M. (1978). Cycle Counting Methods and the Development of Block Load Fatigue Programmes. Automotive Engineering Congress and Exposition, Detroit, Michigan, Society of Automotive Engineers, Inc.

Radaj (1987). Hot Spot Stress Concept for Spot-Welded Joints, International Institute of Welding.

Ritchie, R. O. (1999). "Mechanism of Fatigue - Crack Propagation in Ductile and Brittle Solids." International Journal of Fracture **100**: 55-83.

Shaw, J. R. and B. K. Zuidema (2001). New High Strength Steels Help Automakers Reach Future Goals for Safety, Affordability, Fuel Efficiency and Environmental Responsibility. Warrendale USA, Society of Automotive Engineers.

Sperle, J.-O., Trogen, H. (1989). "Influence of Yield Ratio on the Fatigue Strength of Steel Sheet." Scandinavian Journal of Metallurgy **18**: 147-154.

Suban, M. and J. Tušek (2001). "Dependence of Melting Rate in MIG/MAG Welding on the Type of Shielding Gas Used." Journal of Materials Processing Technology **119**: 185-192.

The MSC Institute of Technology (1995). Durability and Fatigue Life Estimation Using MSC/PATRAN FATIGUE. California, USA.

Tomita, K., Shiozaki, T. , Urabe, T. and Yoshitake, A., (2000). Development of 780MPa Grade High Strength Hot Rolled Steel Sheet. FISITA World Automotive Congress, Seoul, Korea.

TWI (1999). TWI World Centre for Materials Joining Technology. Job Knowledge For Welders, The Welding Institute: Chapters 41-48.

ULSAB-AVC (2001). Body Structure Materials, ULSAB-AVC Consortium.

Unger, B., H. Dannbauer, et al. (2003). Virtual Fatigue Optimisation of Automotive Structures. Fatigue 2003, "Fatigue & Durability Assessment of Materials, Components & Structures", Cambridge, The Engineering Integrity Society.

Wallentowitz, P. H., J. Leyers, et al. (2003). Materials for Future Automotive Body Structures. Business Briefing: Global Automotive Manufacturing & Technology.

Wards "Automotive Year book."

Wikipedia, C. (2006). Strain Gauges, Wikipedia, the Free Encyclopaedia. http://en.wikipedia.org/wiki/Strain_gauge

15. APPENDIX

15.1 Appendix 1 Testing

15.1.1 Coupon Testing

Coupon geometries used in this study:

GM1; Partially Welded Lap-Shear Coupon Fabricated by GKN

GM2: Fully Welded Lap-Shear Coupon Fabricated by GKN

GM3: Partially Welded Peel Coupon Fabricated by GKN

GM4; Fully Welded Peel Coupon Fabricated by GKN

GM5, 6, 8: T-Shaped Coupon Fabricated by GKN

GM11A: Partially Welded Lap-Shear Coupon Fabricated by GKN

GM11B: Fully Welded Double Lap-Shear Coupon Fabricated by GKN

TM1: Partially Welded Lap-Shear Coupon Fabricated by TKA

TM2: Fully Welded Lap-Shear Coupon Fabricated by TKA

TM11A: Partially Welded Lap-Shear Coupon Fabricated by TKA

TM11B: Fully Welded Double Lap-Shear Coupon Fabricated by TKA

Table A10.2.1: Coupon Testing Loading

Coupon Geometry	Loading History	R-Ratio	Load Levels kN
GM1	Constant Amplitude	0.1	9, 11, 15
GM2			8.5, 12, 15
GM2		0.5	7, 10
GM11A		0.1	11, 15, 20
GM11B			11.5, 14, 20
GM3			0.5, 0.8, 1.2
GM4			0.5, 0.8, 1.2
GM5			18, 30, 36
GM6			2, 3
GM8			2, 3
TM1			8, 10, 15
TM2			8.5, 12, 15
TM11A			9, 15, 18
TM11B			9, 15, 18
TM11B		0.5	7.5, 10, 12.5
TM11B		-1	5, 9
GM11A	Variable Amplitude Block Loading		20 &10, 15 & 7.5
GM1	Variable Amplitude SAE Bracket		11, 15
TM11A			15, 18
GM8			2, 3

15.1.2 Component Testing

Table A10.3.1: FUCA Component Testing Loading Schedule

Loading Regime	Freq	Applied Load kN
Constant Amplitude	2Hz	± 7
		± 4
		± 2.5
Variable Amplitude Block Loading		± 7, ± 3.5
		± 4, ± 2
Variable Amplitude SAE Bracket		± 7

15.2 Appendix 2 Battelle Manual Calculation

1. Edit the model.bdf file at the GP Force line to GPFORCE(PUNCH)=ALL

2. Rerun Nastran

3. Open Patran model view weld toe area and note the Weld toe Element and node numbers

4. Input into Excel spreadsheet with element and node numbers going from left to right

5. Locate in the model.bdf file the GRID Points section and find correct nodes

6. Input the Node x, y and z locations into excel

7. Find weld toe element edge lengths along the weld line by either using Patran function or excel formula $\sqrt{(x-x_1)^2(y-y_1)^2(z-z_1)^2}$

8. If weld toe elements are not horizontal to the Global Co-ordinate system the angle from global to local must be calculated using the first and last elements x and y co-ordinates

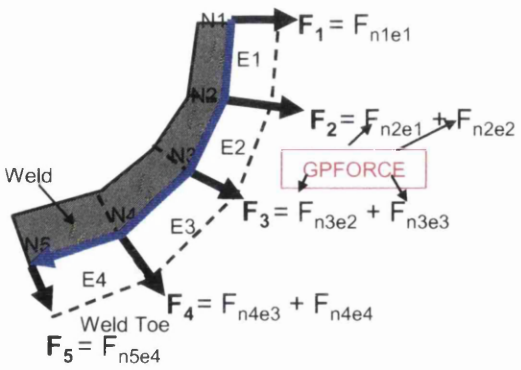

$$\theta = \arctan\left(\frac{YNode_{ni} - YNode_n}{XNode_{ni} - XNode_n}\right)$$

9. Opening the Nastran punch file (model.pch) find the required node numbers and read off for each element the force and moment lines and tabulate them in excel.

10. Create columns of Total forces and moments in x and y for each node

11. Calculate the total forces and moments in x and y to local co-ordinate system
12. Create a highlighted area in excel for the matrix n*n.

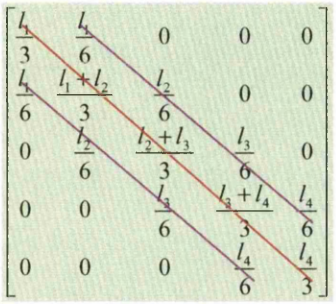

13. Fill the matrix initially with 0
14. For the diagonals tabulate $\frac{l_n}{6}$ and $\frac{(l_n + l_{n+1})}{3}$
15. Down the main diagonal enter $\frac{l_n}{3}$ copy, select diagonal cells and paste values in
16. Either side of main diagonal enter $\frac{l_n}{6}$ values, copy, select diagonal cells and paste values in
17. Create another highlighted area in excel for the matrix n*n for inverse matrix
18. Select all the cells, F2 to select first cell, input MInverse select the first matrix as the array
19. Calculate the edge distributed loads and moments in the local coordinate system $Fy' = Fx\sin\theta - Fy\cos\theta$, $Mx = -Mx\cos\theta - My\sin\theta$
20. Calculate Structural Stress $= \sigma_s = \frac{f_{y'}}{t} - \frac{6m_{x'}}{t^2}$,

Calculate the Equivalent Structural Stress = $\Delta S_s = \frac{\Delta\sigma_s}{t^{-0.2222} * 1.07}$

15.3 Appendix 3 Test Termination Criterion Results

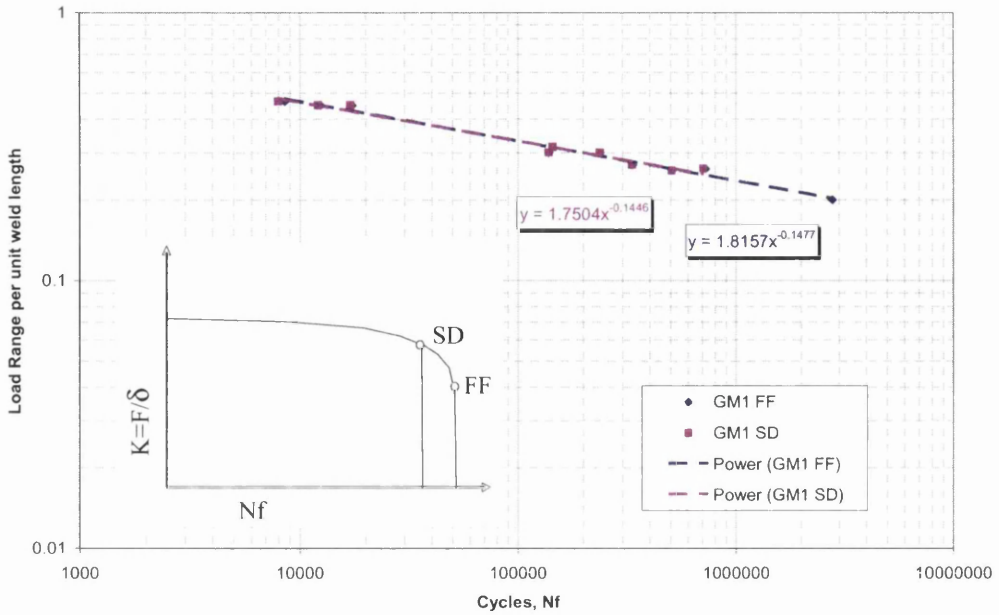

Figure A11.1.1: GKN Fabricated M1 (GM1) Coupon Joint Final Failure and 10% Stiffness Drop

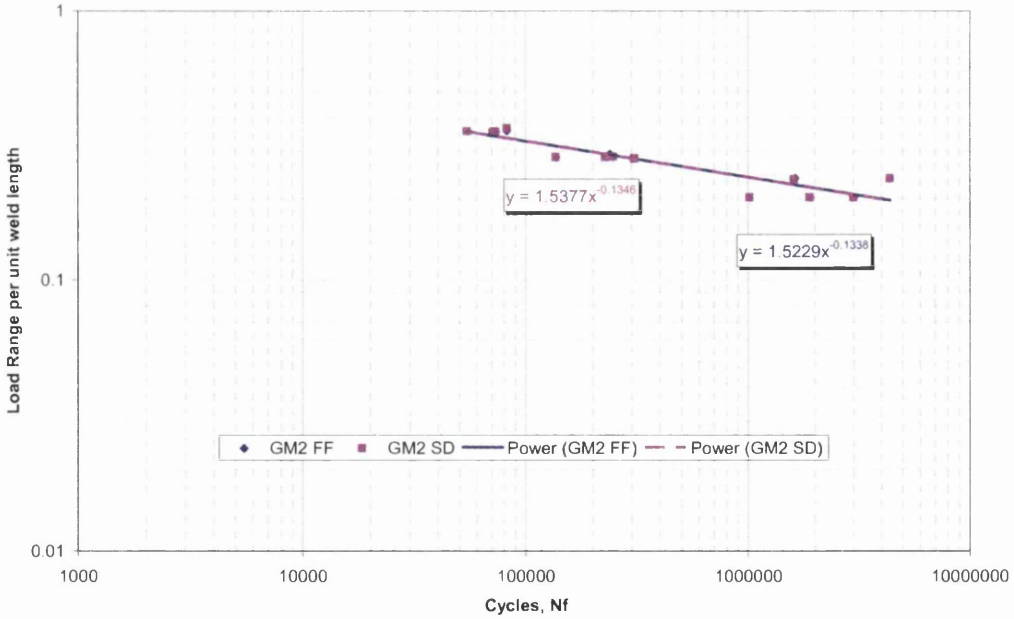

Figure A11.1.2: GKN Fabricated M2 (GM2) Coupon Joint Final Failure and 10% Stiffness Drop

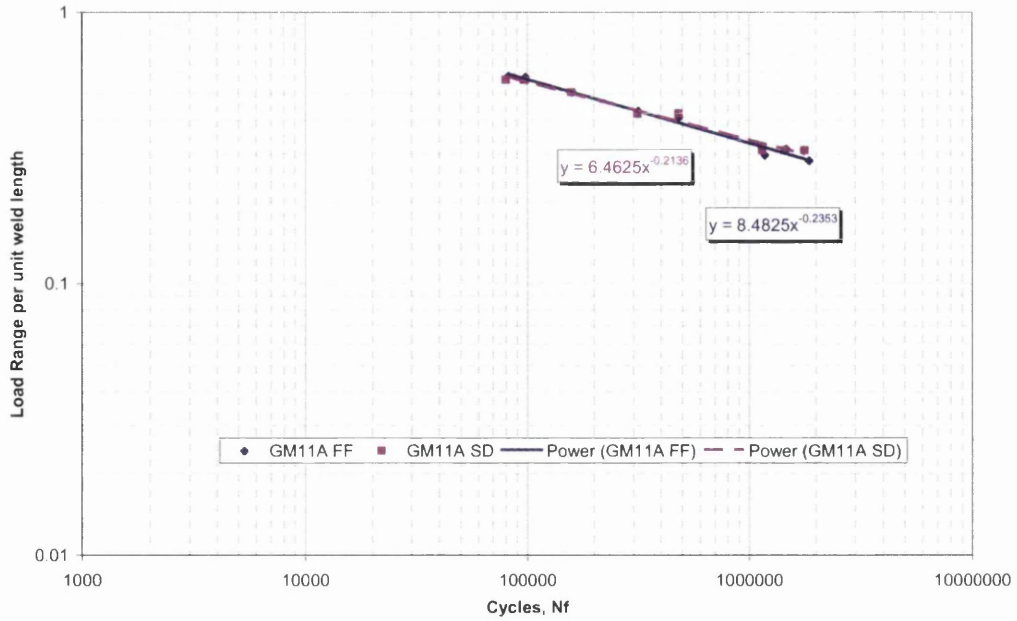

Figure A11.1.3: GKN Fabricated M11A (GM11A) Coupon Joint Final Failure and 10% Stiffness Drop

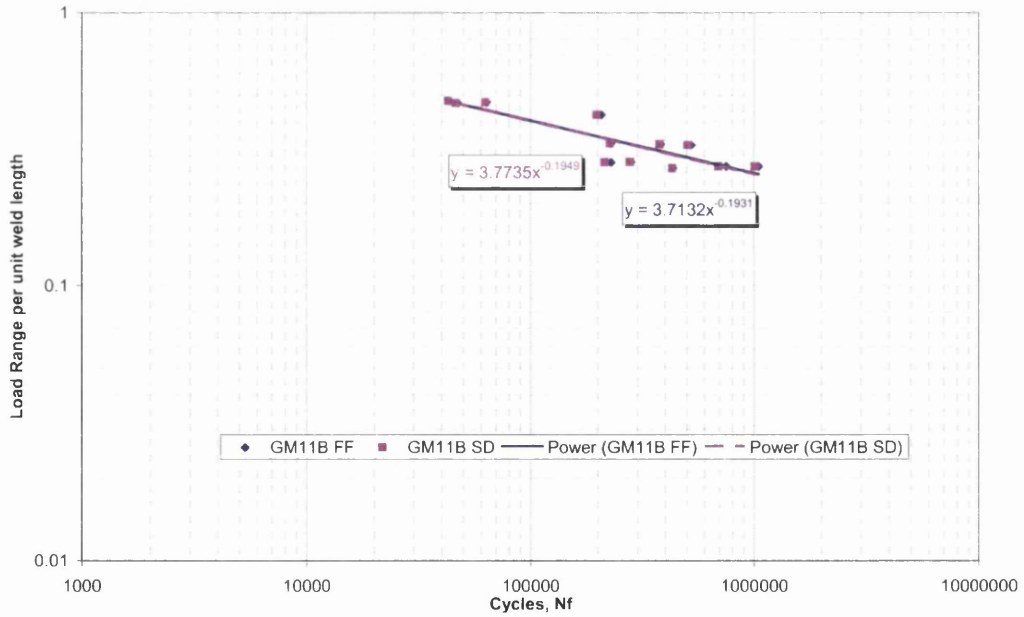

Figure A11.1.4: GKN Fabricated M11B (GM11B) Coupon Joint Final Failure and 10% Stiffness Drop

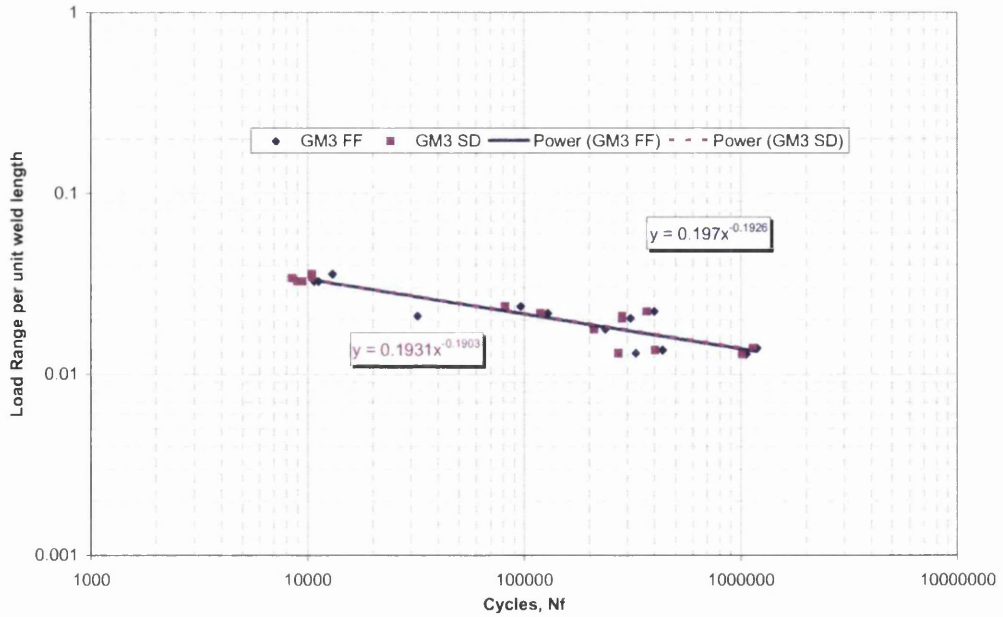

Figure A11.1.5: GKN Fabricated M3 (GM3) Coupon Joint Final Failure and 10% Stiffness Drop

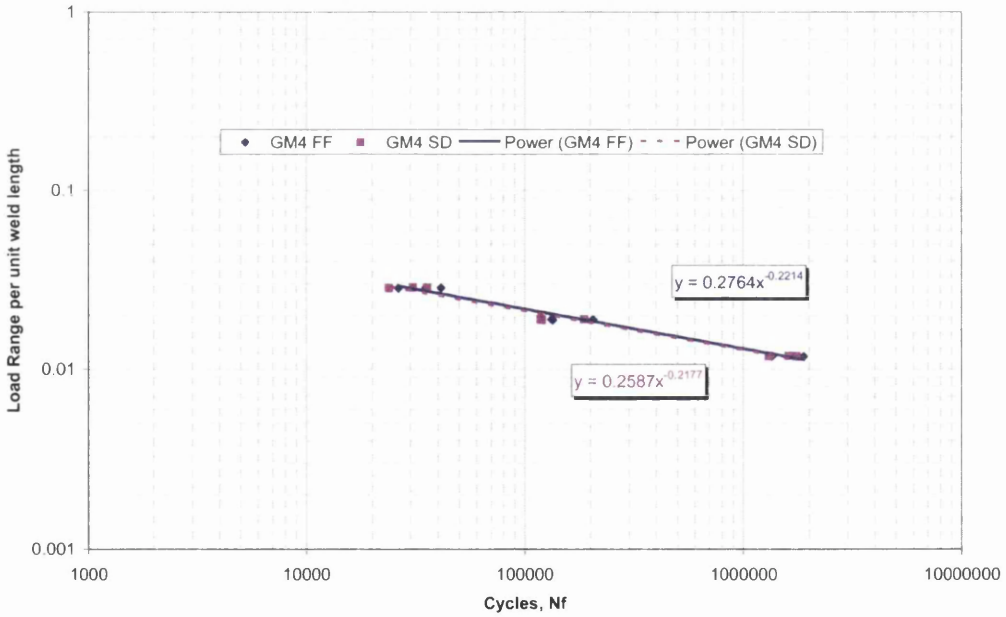

Figure A11.1.6: GKN Fabricated M4 (GM4) Coupon Joint Final Failure and 10% Stiffness Drop

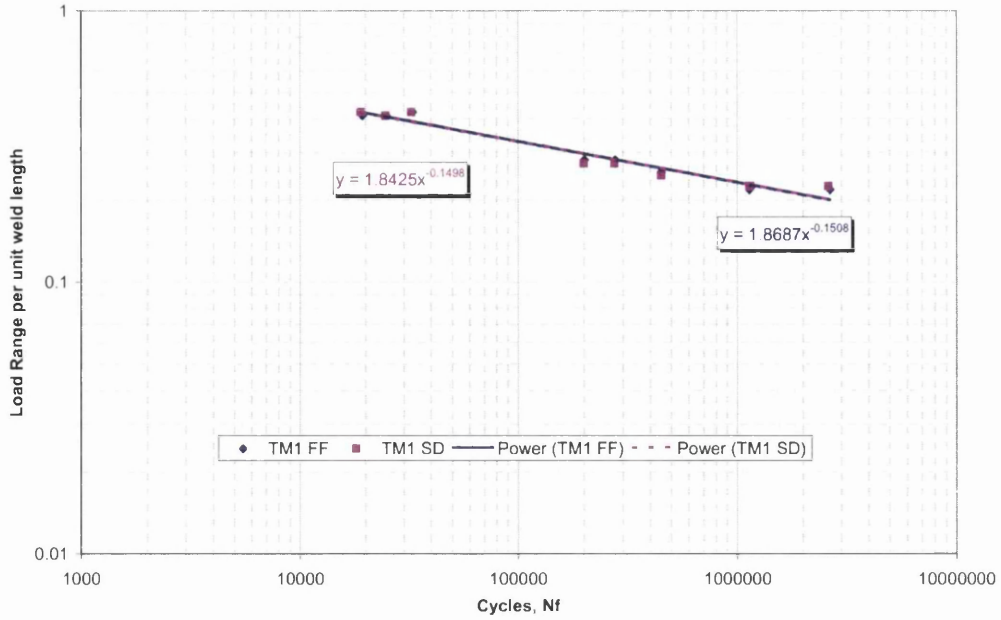

Figure A11.1.7: TKA Fabricated M1 (TM1) Coupon Joint Final Failure and 10% Stiffness Drop

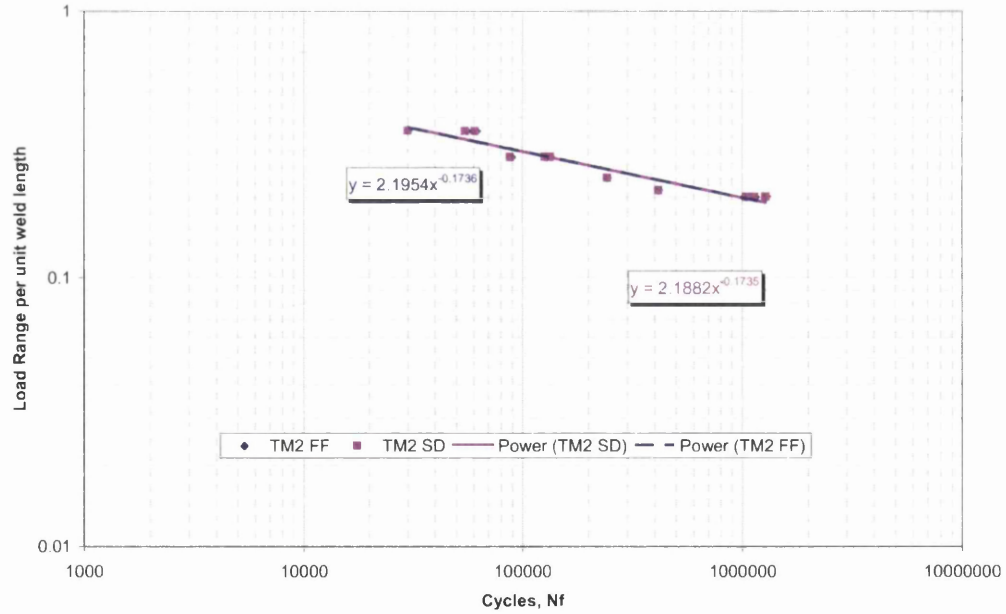

Figure A11.1.8: TKA Fabricated M2 (TM2) Coupon Joint Final Failure and 10% Stiffness Drop

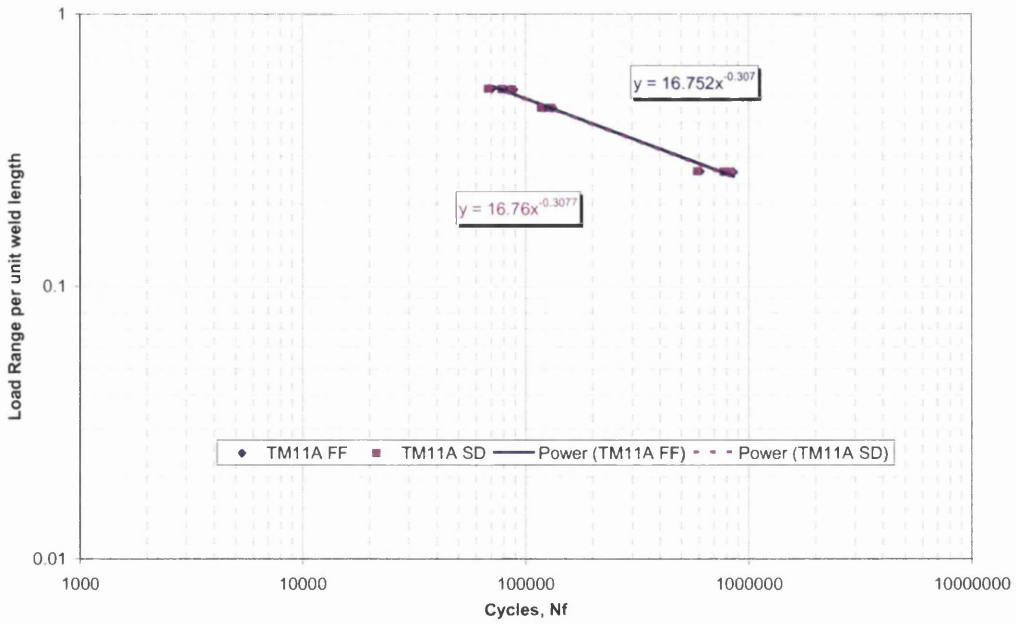

Figure A11.1.9: TKA Fabricated M11A (TM11A) Coupon Joint Final Failure and 10% Stiffness Drop

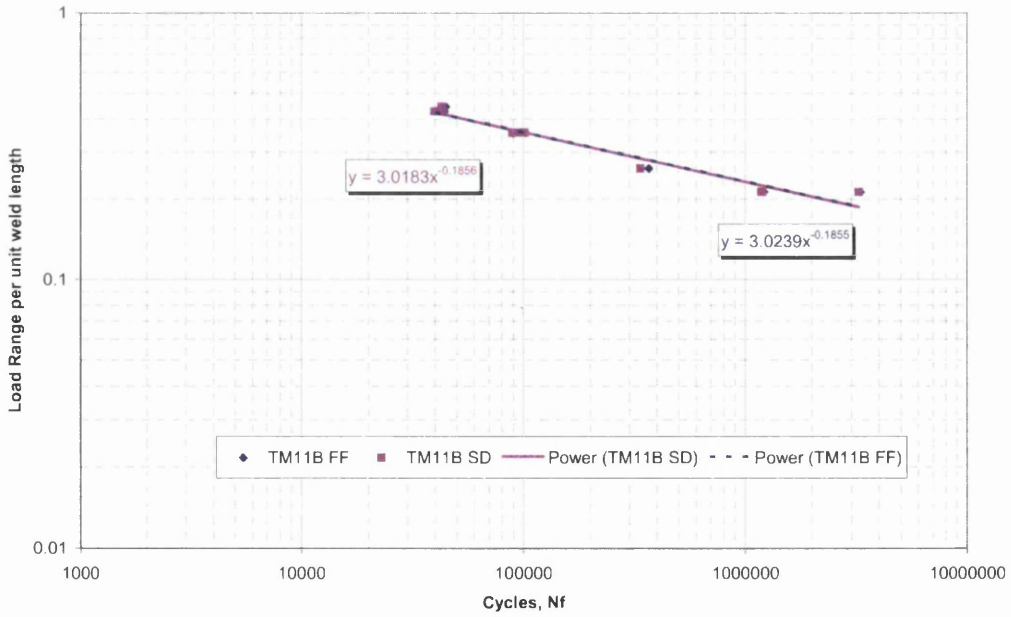

Figure A11.1.10: TKA Fabricated M11B (TM11B) Coupon Joint Final Failure and 10% Stiffness Drop

15.4 Appendix 4 Original Coupon Test Data Final Failure Results

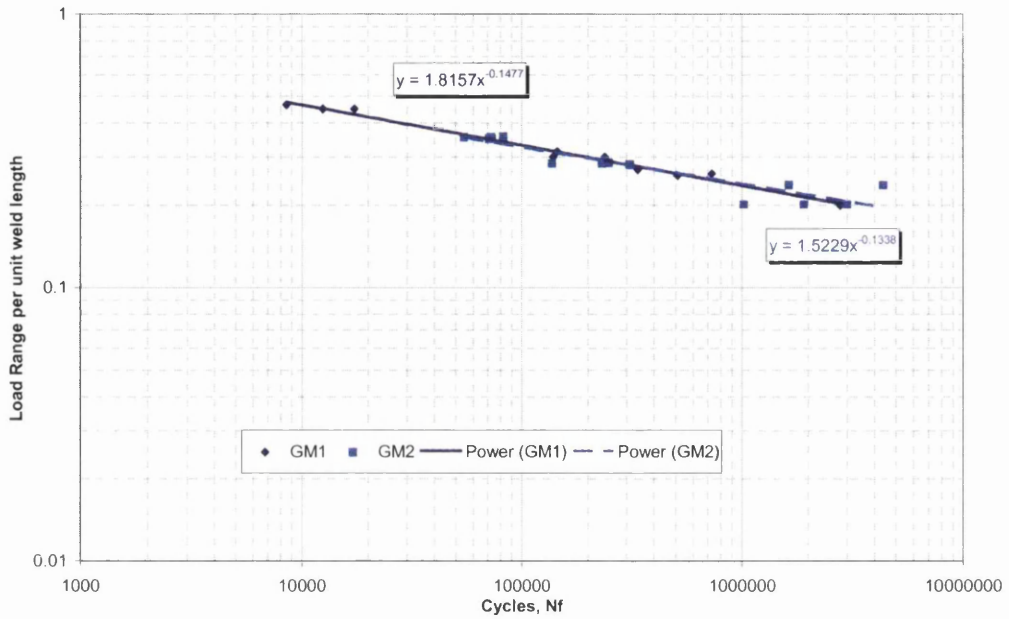

Figure A11.1.11: GM1 and GM2 Final Failure

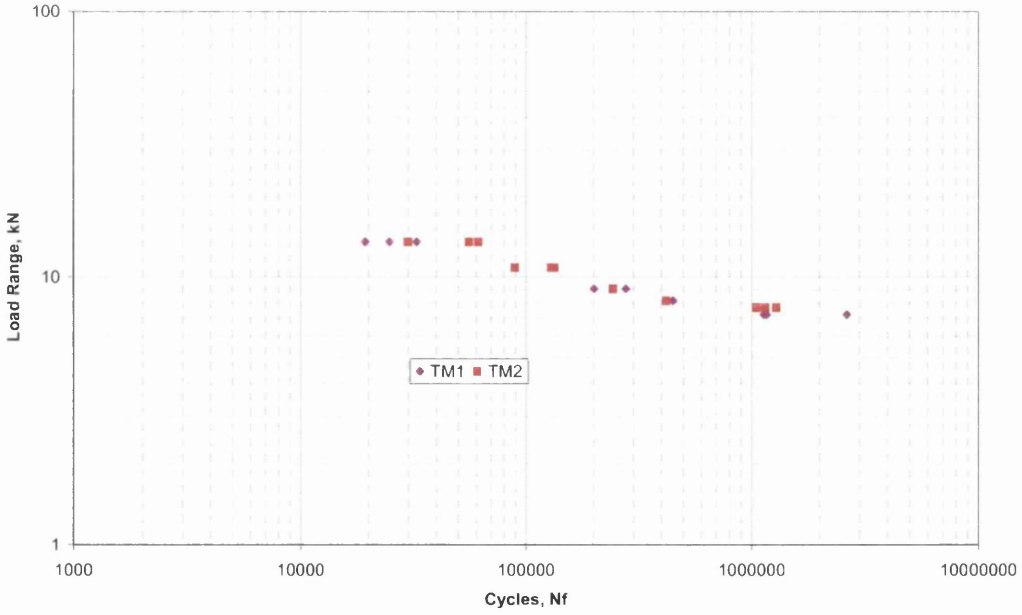

Figure A11.1.12: TM1 and TM2 Final Failure

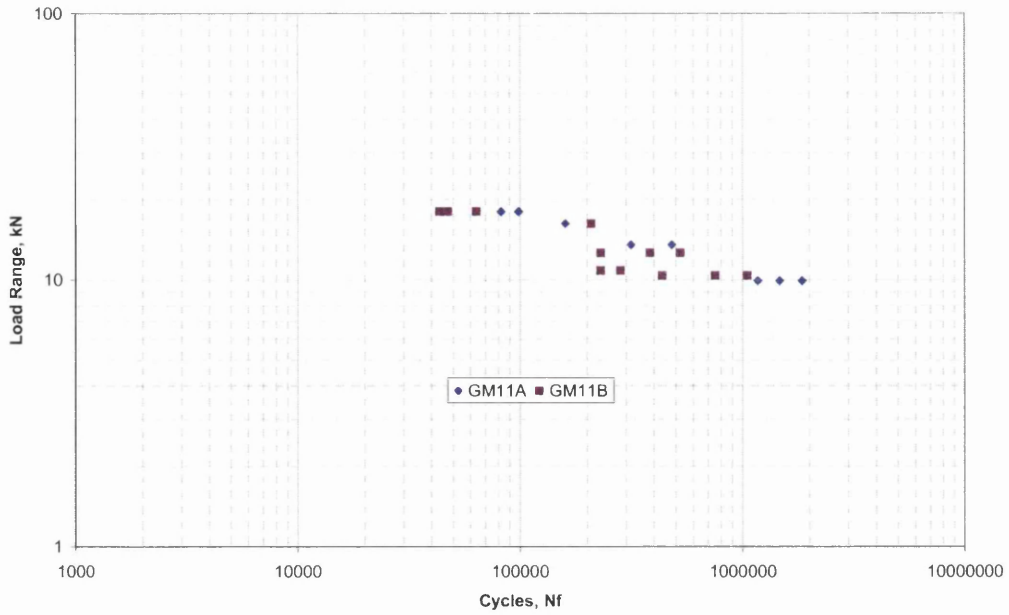

Figure A11.1.13: GM11A and GM11B Final Failure

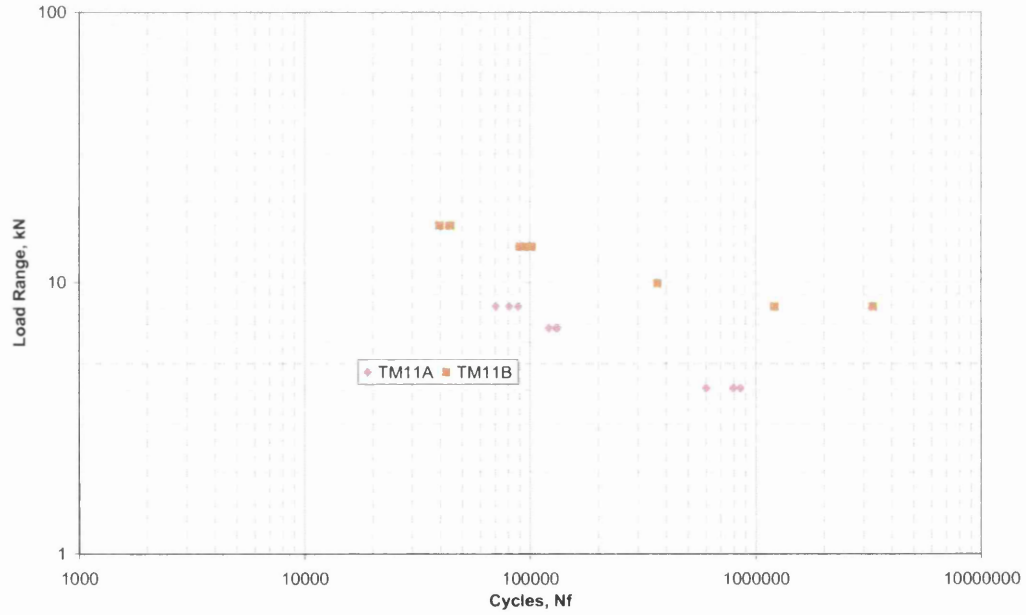

Figure A11.1.14: TM11A and TM11B Final Failure

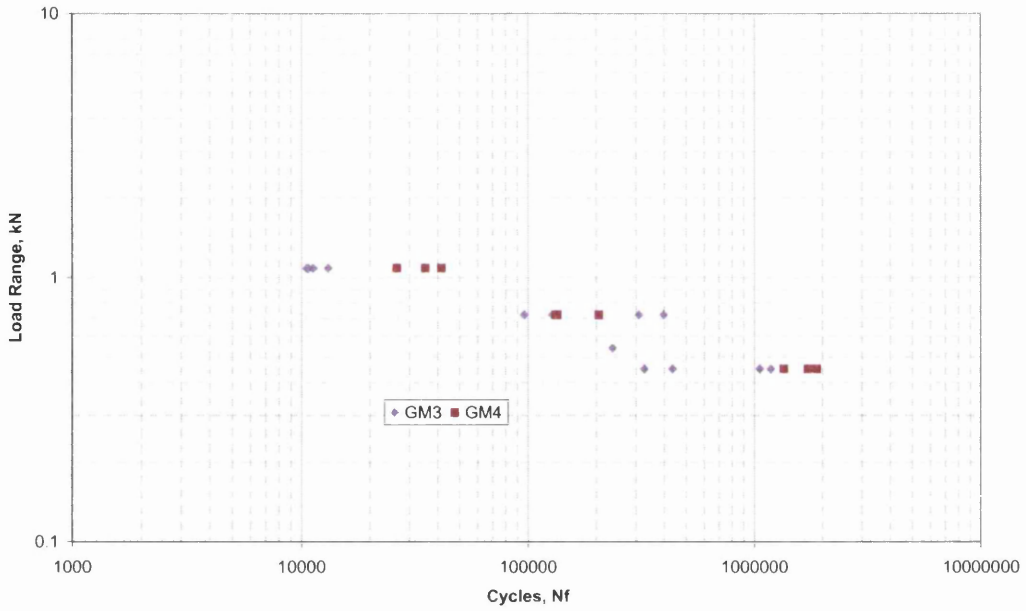

Figure A11.1.15: GM3 and GM4 Final Failure

15.5 Appendix 5 Coupon Fracture Surface Analysis

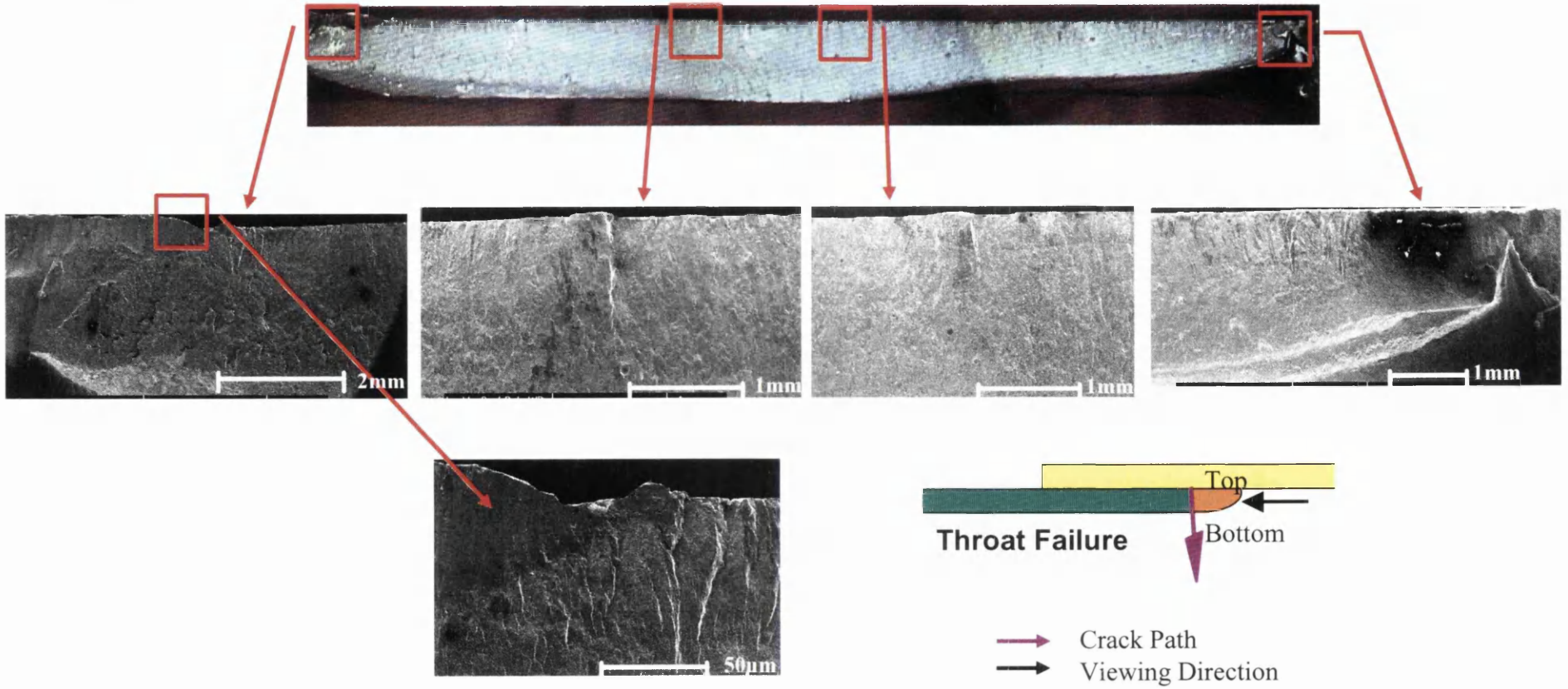

Figure A11.4.1: Typical Fracture Surface for GM1 Weld Throat Failure – Sheet View

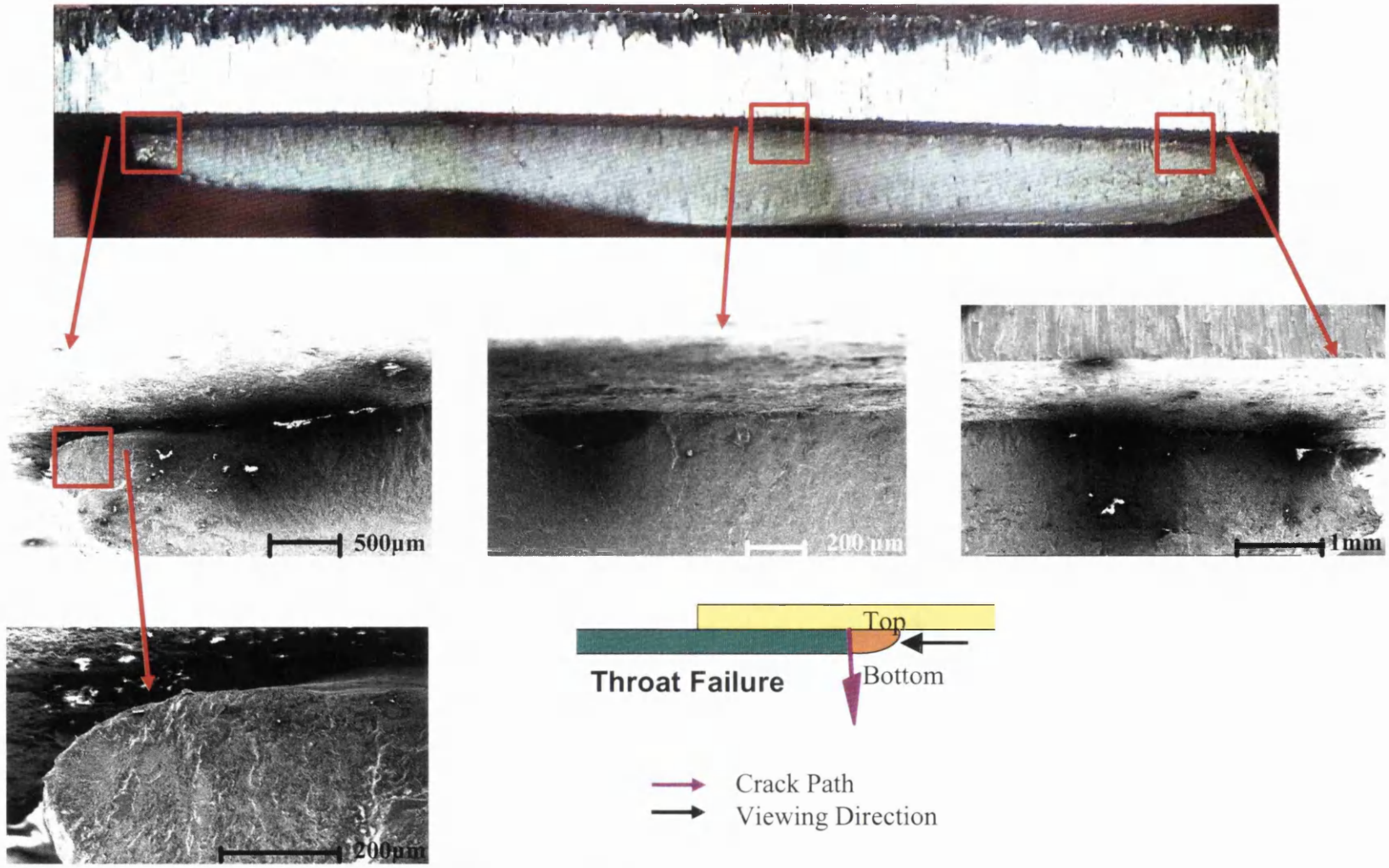

Figure A11.4.2: Typical Fracture Surface for GM1 Weld Throat Failure – Weld View

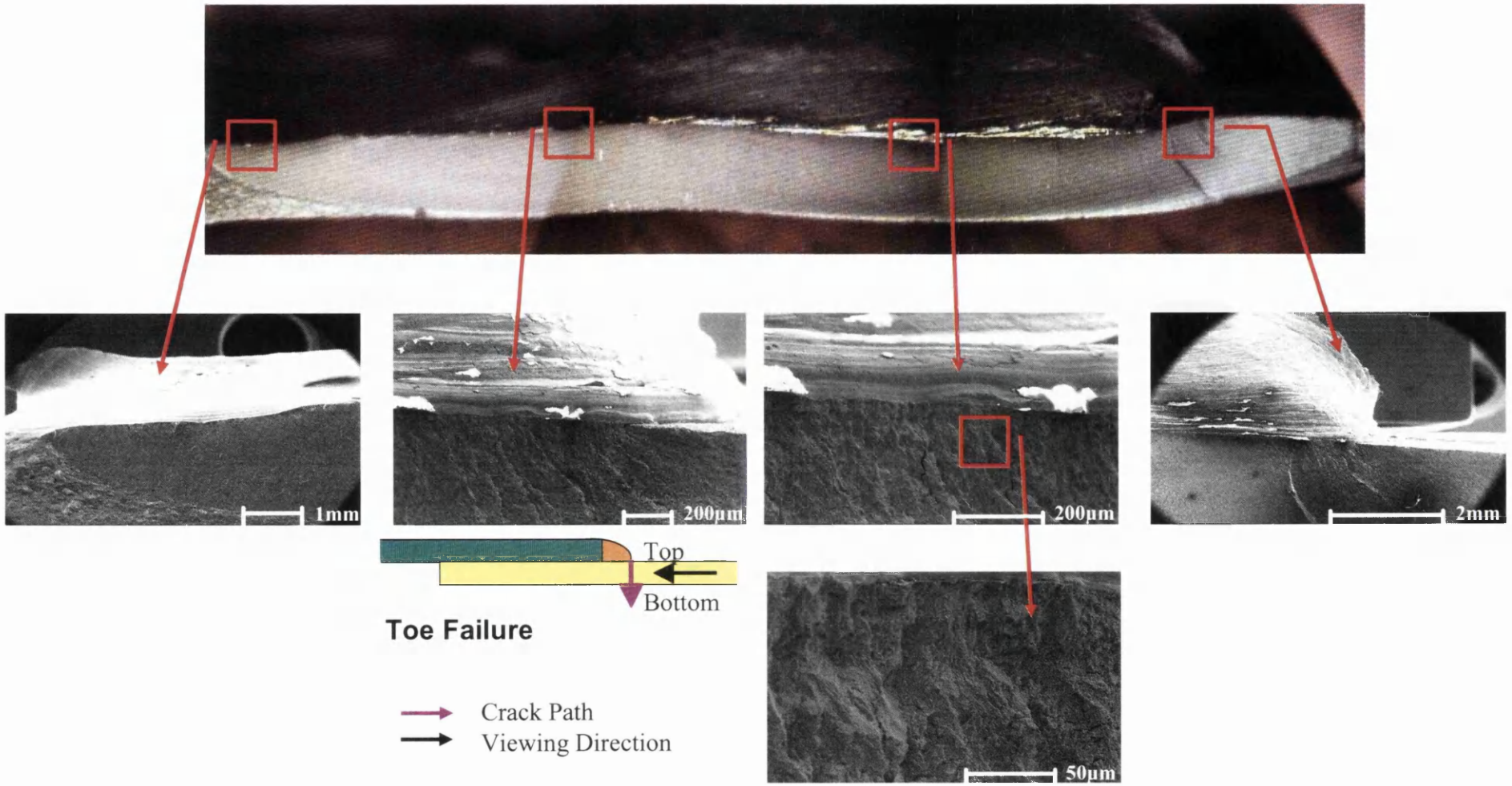

Figure A11.4.3: Typical Fracture Surface for TM1 Weld Toe Failure – Weld View

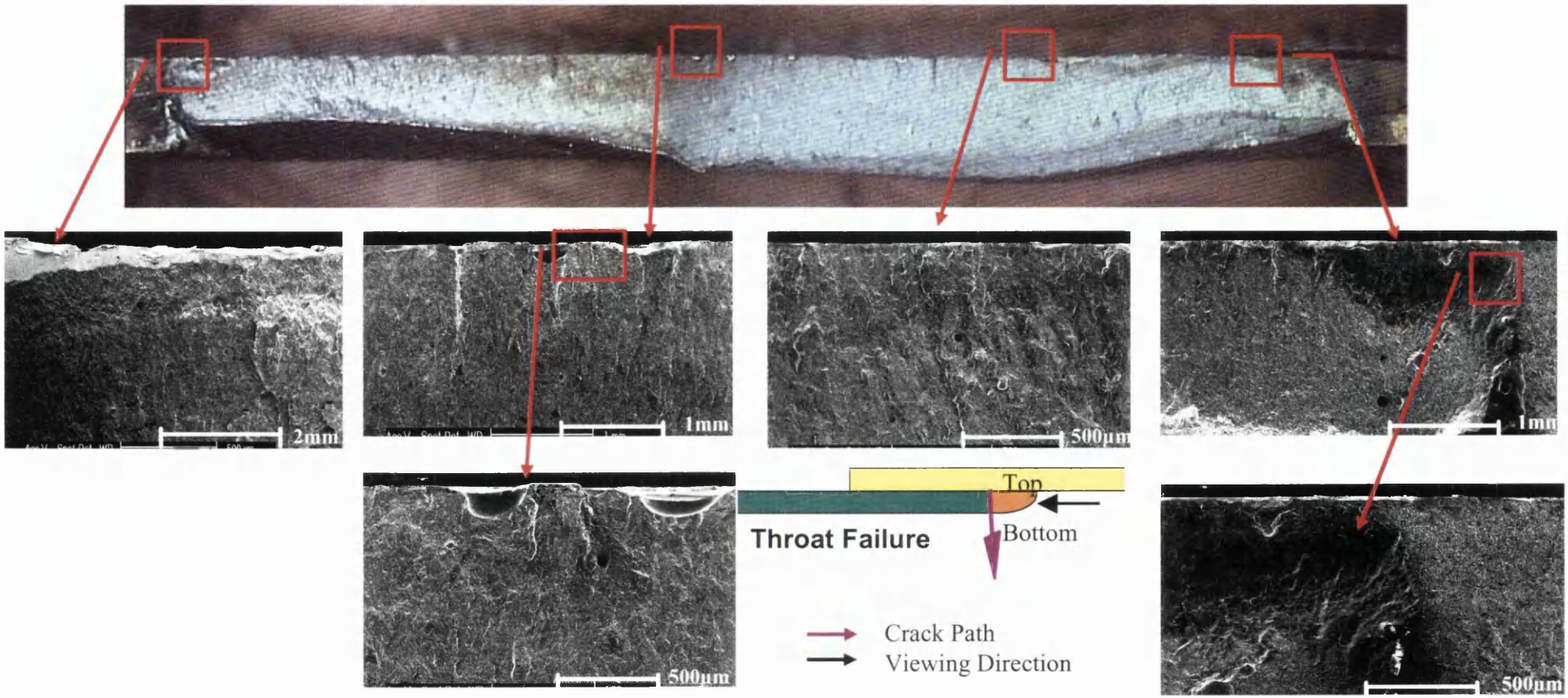

Figure A11.4.4: Typical Fracture Surface for TM1 Weld Throat Failure – Sheet View

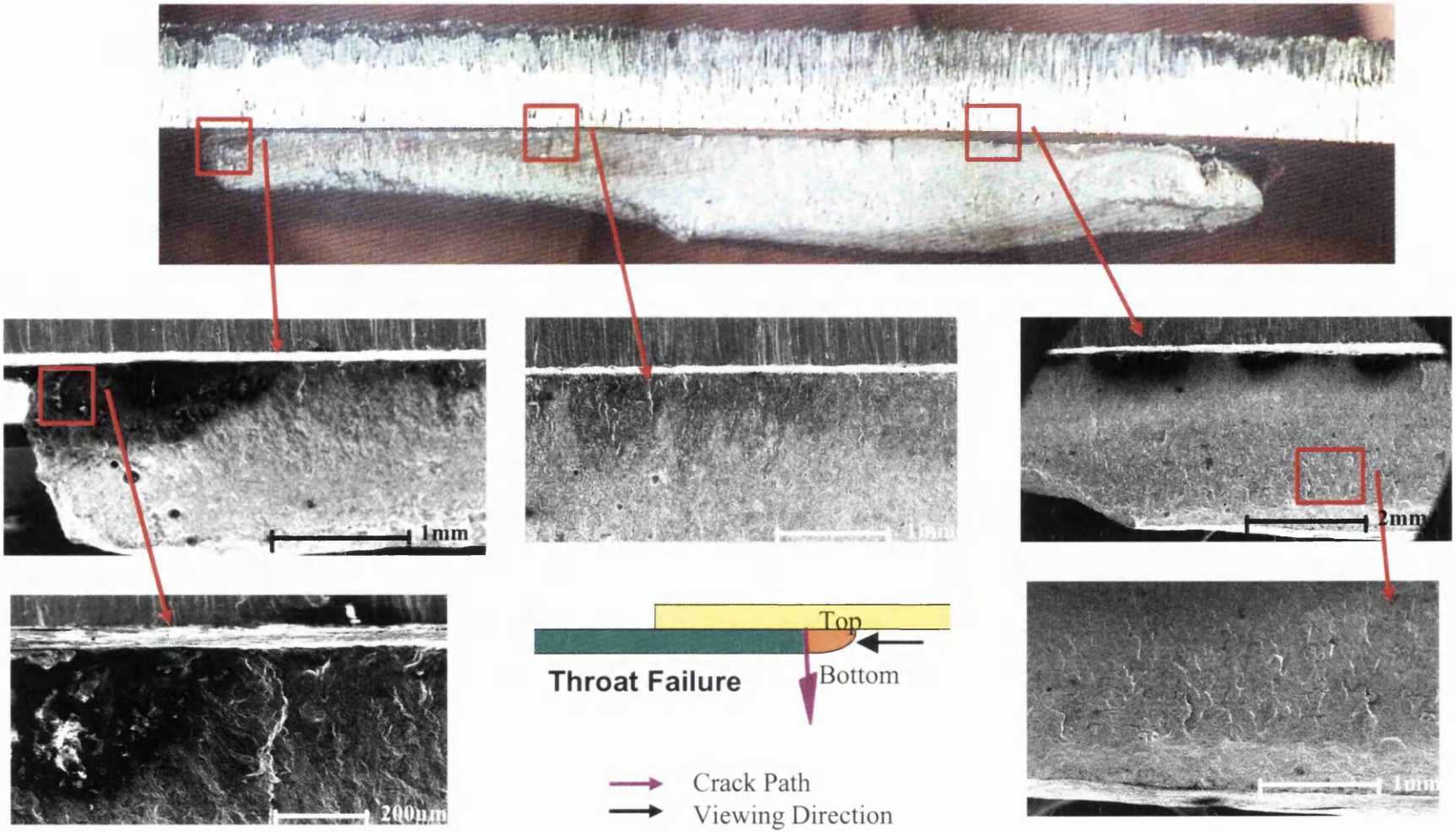

Figure A11.4.5: Typical Fracture Surface for TM1 Weld Throat Failure – Weld View

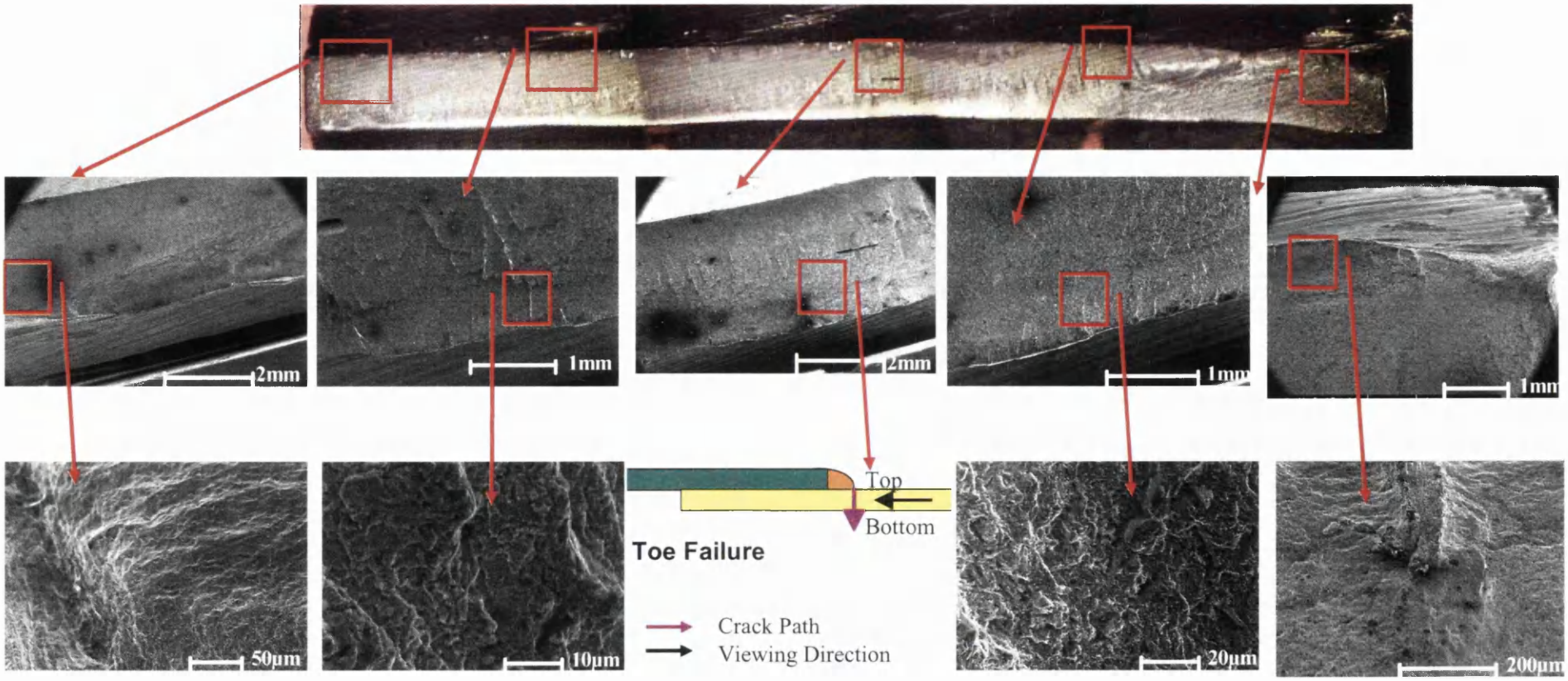

Figure A11.4.6: Typical Fracture Surface for GM2 Weld Toe Failure – Weld View

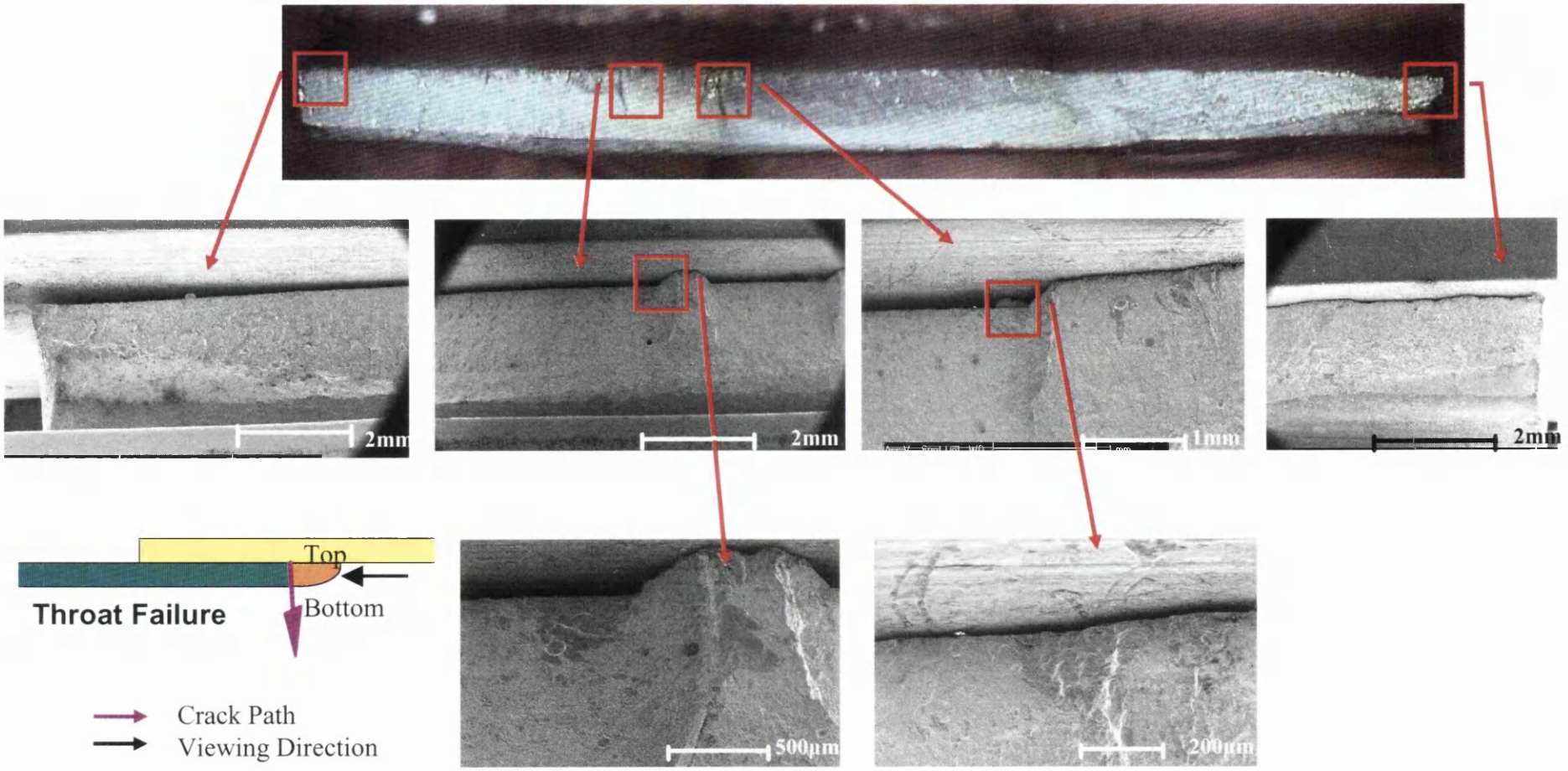

Figure A11.4.7: Typical Fracture Surface for GM2 Weld Throat Failure – Sheet View

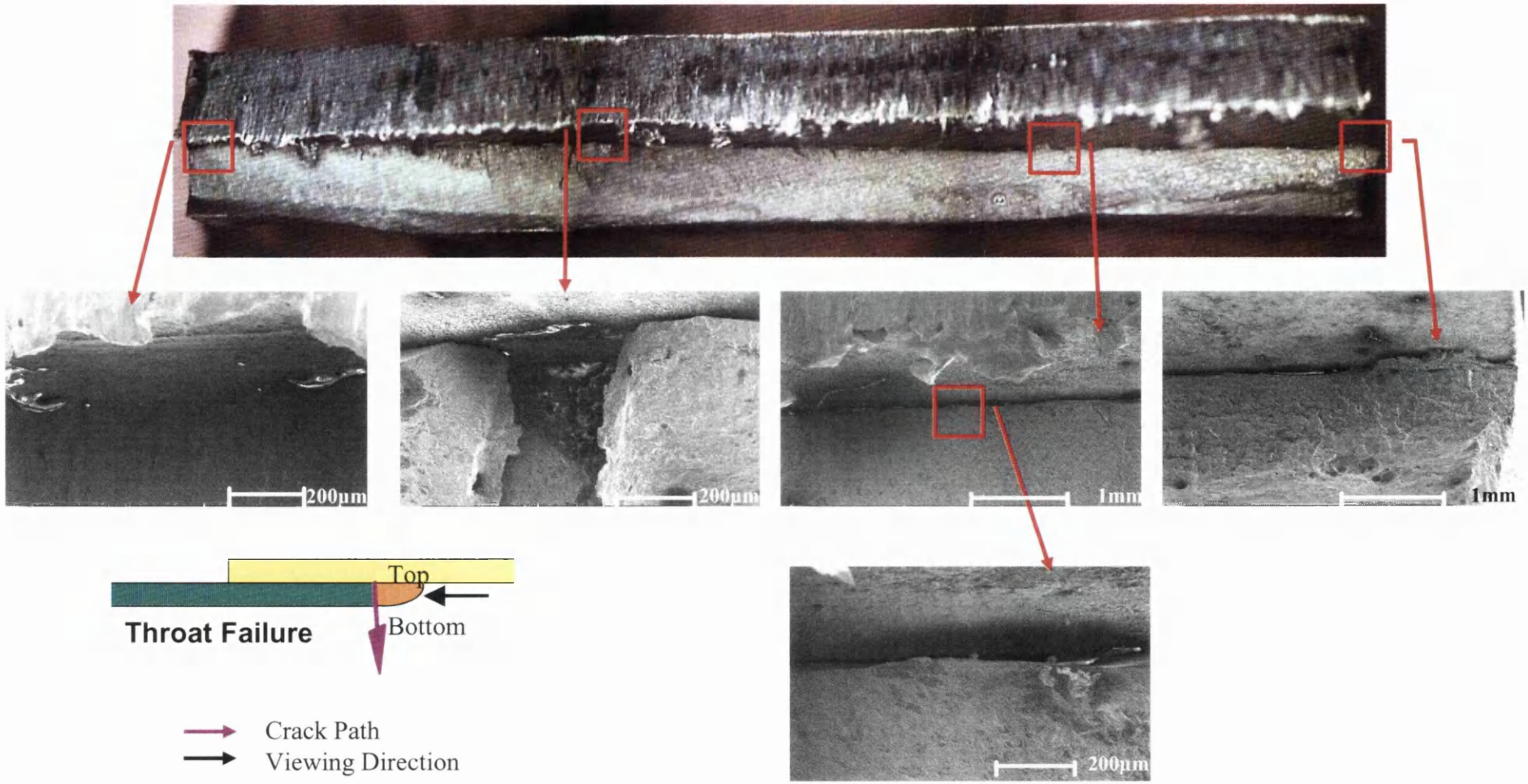

Figure A11.4.7: Typical Fracture Surface for GM2 Weld Throat Failure – Weld View

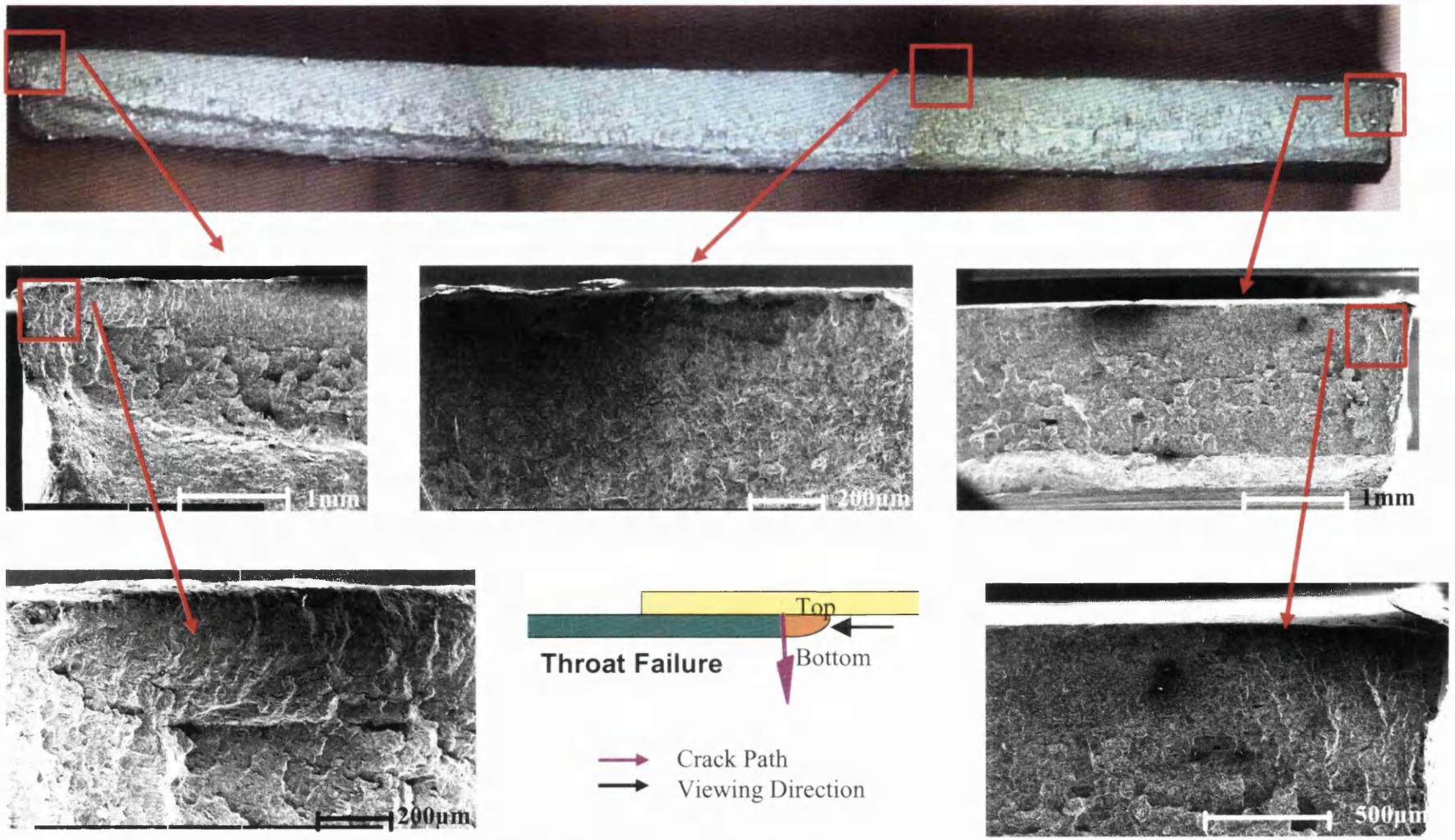

Figure A11.4.8: Typical Fracture Surface for TM2 Weld Throat Failure – Sheet View

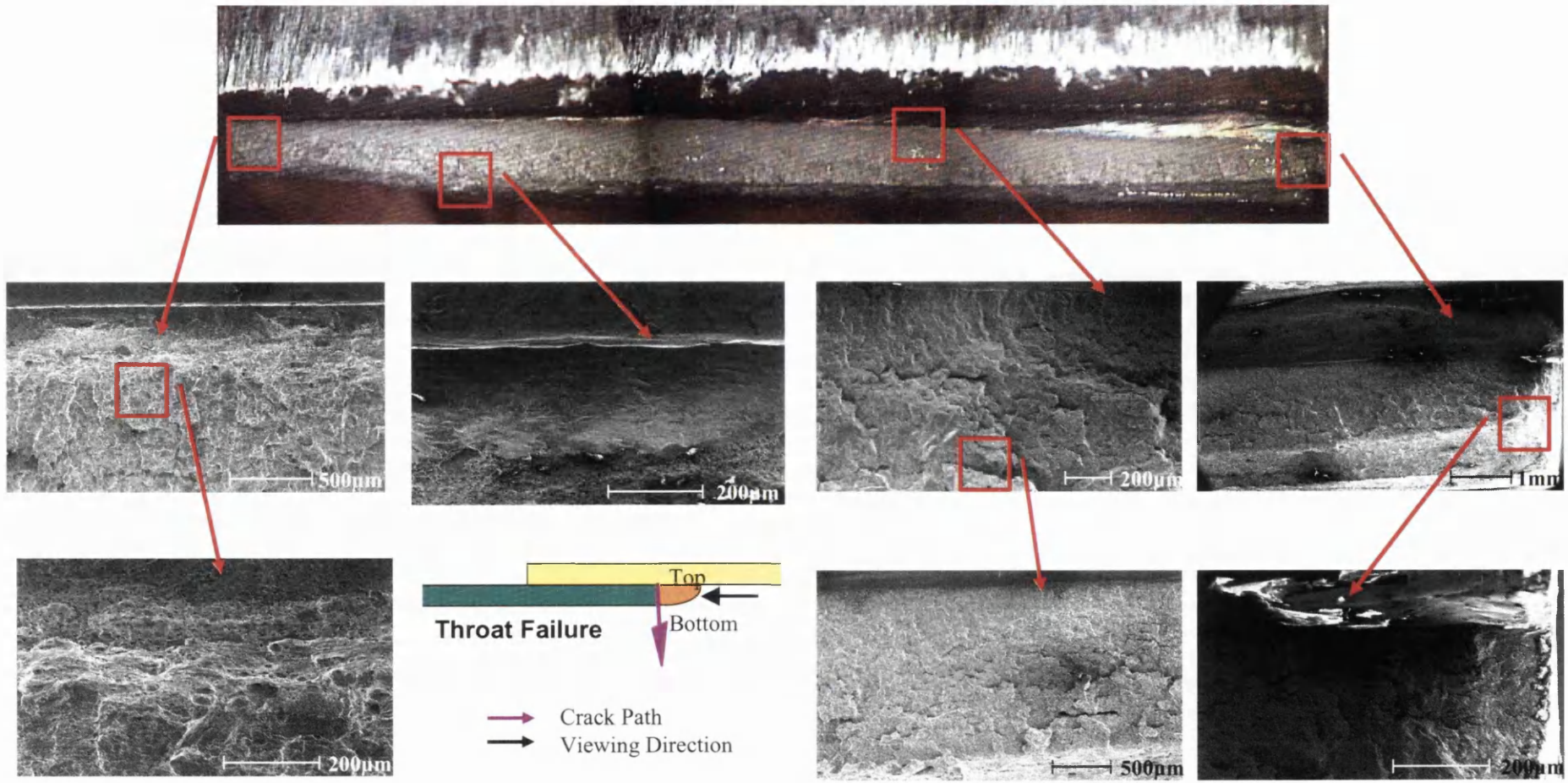

Figure A11.4.9: Typical Fracture Surface for TM2 Weld Throat Failure – Weld View

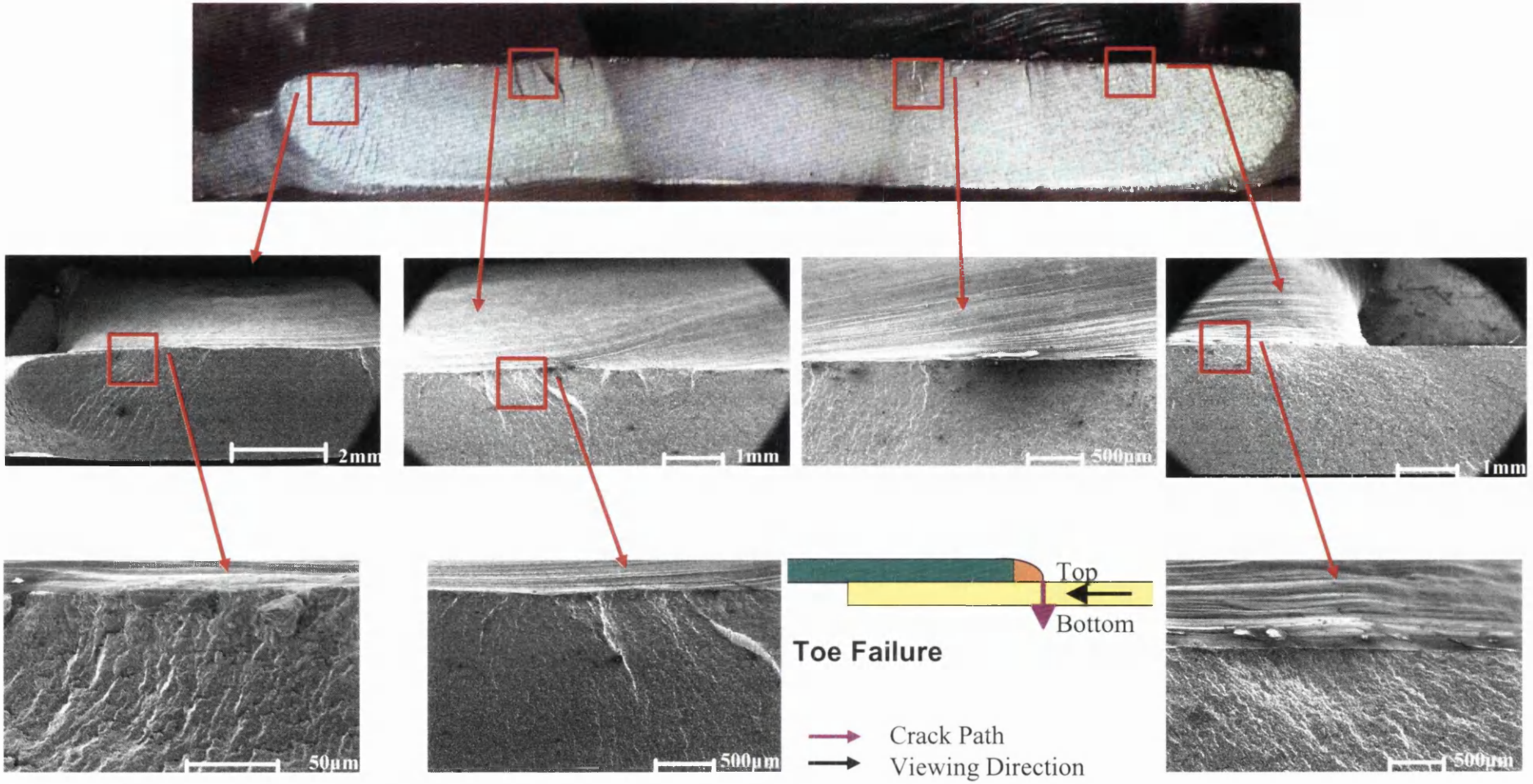

Figure A11.4.10: Typical Fracture Surface for GM11A Weld Toe Failure – Weld View

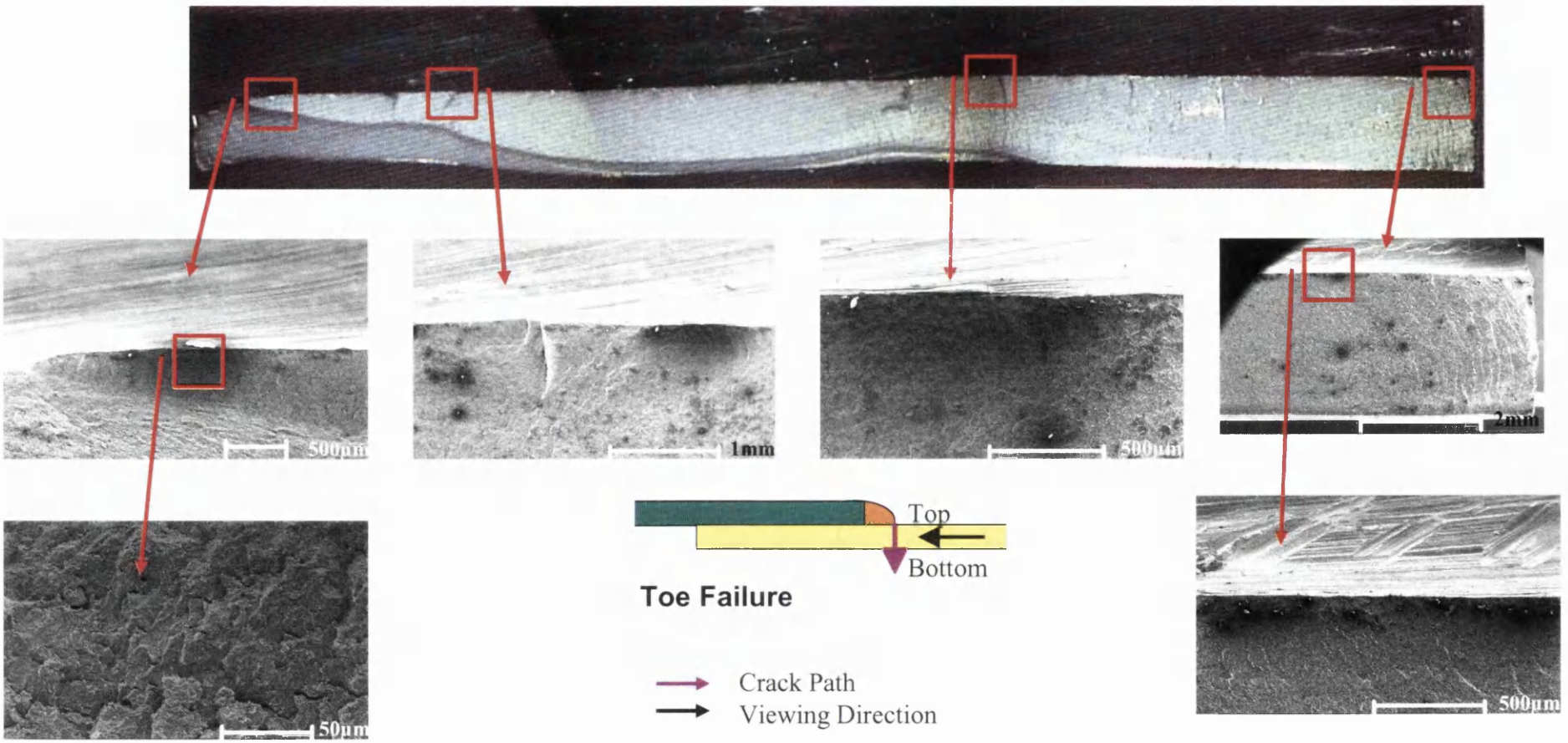

Figure A11.4.11: Typical Fracture Surface for GM11B Weld Toe Failure – Weld View

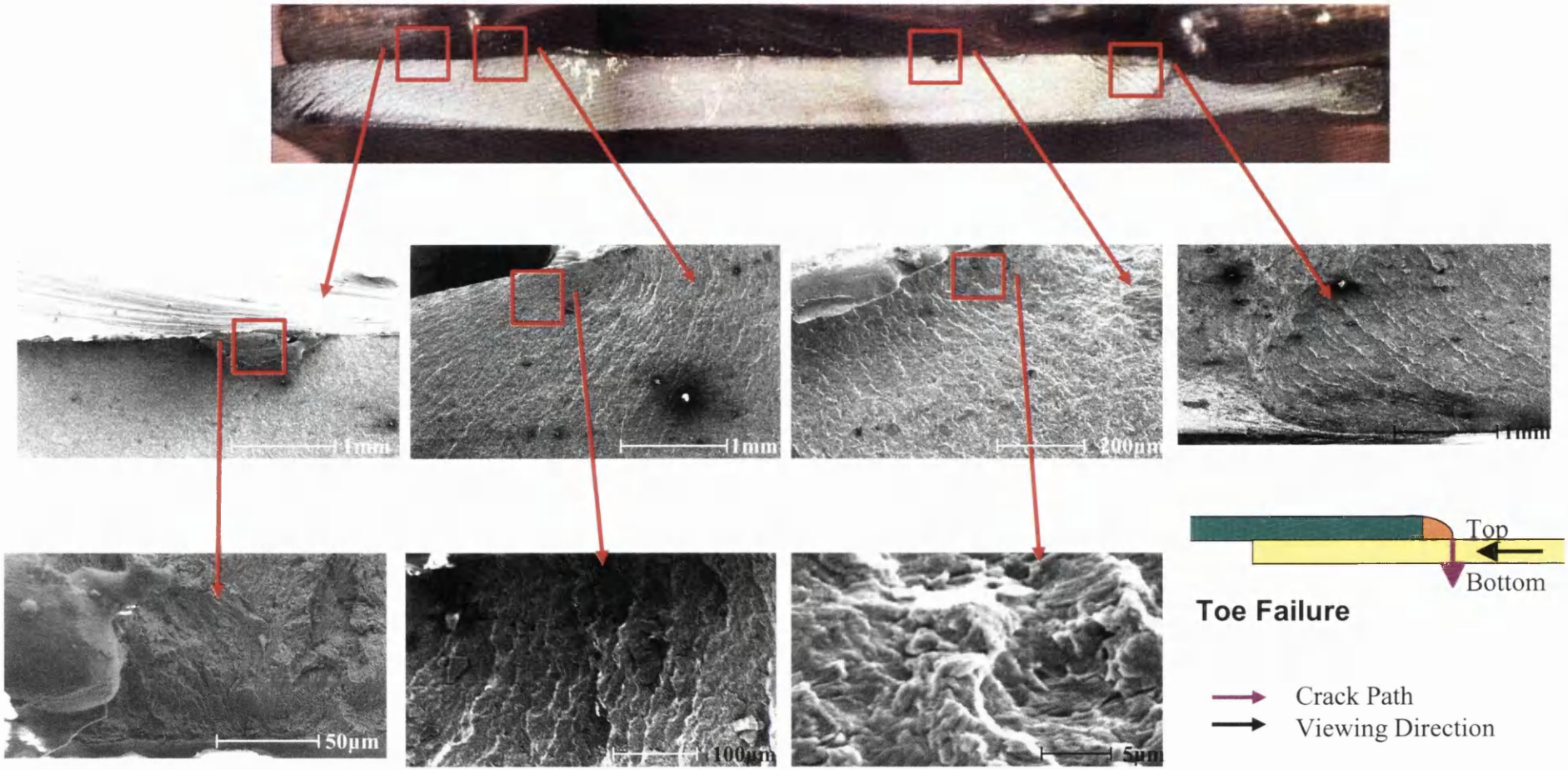

Figure A11.4.12: Typical Fracture Surface for TM11A Weld Toe Failure – Weld View

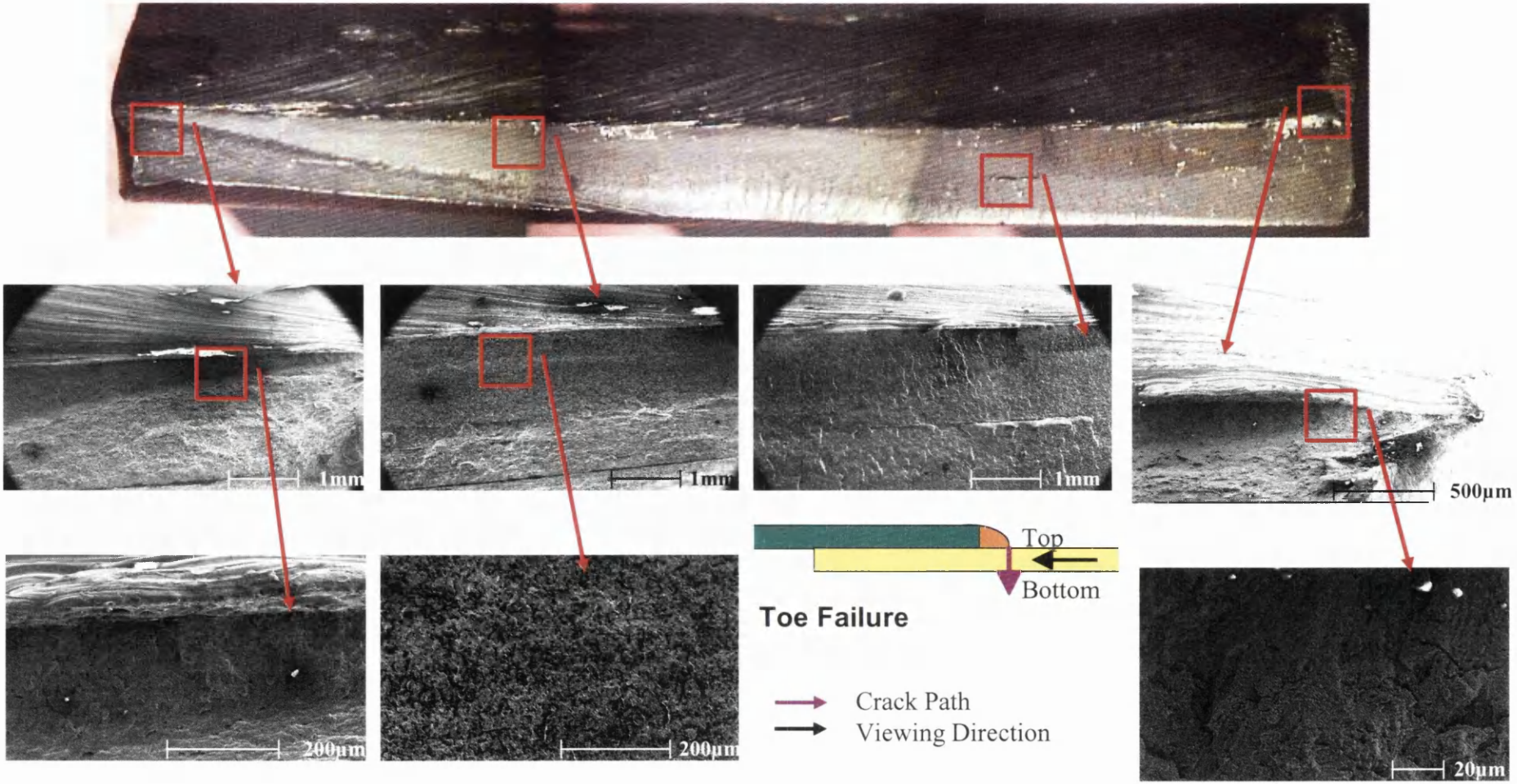

Figure A11.4.13: Typical Fracture Surface for TM11B Weld Toe Failure – Weld View

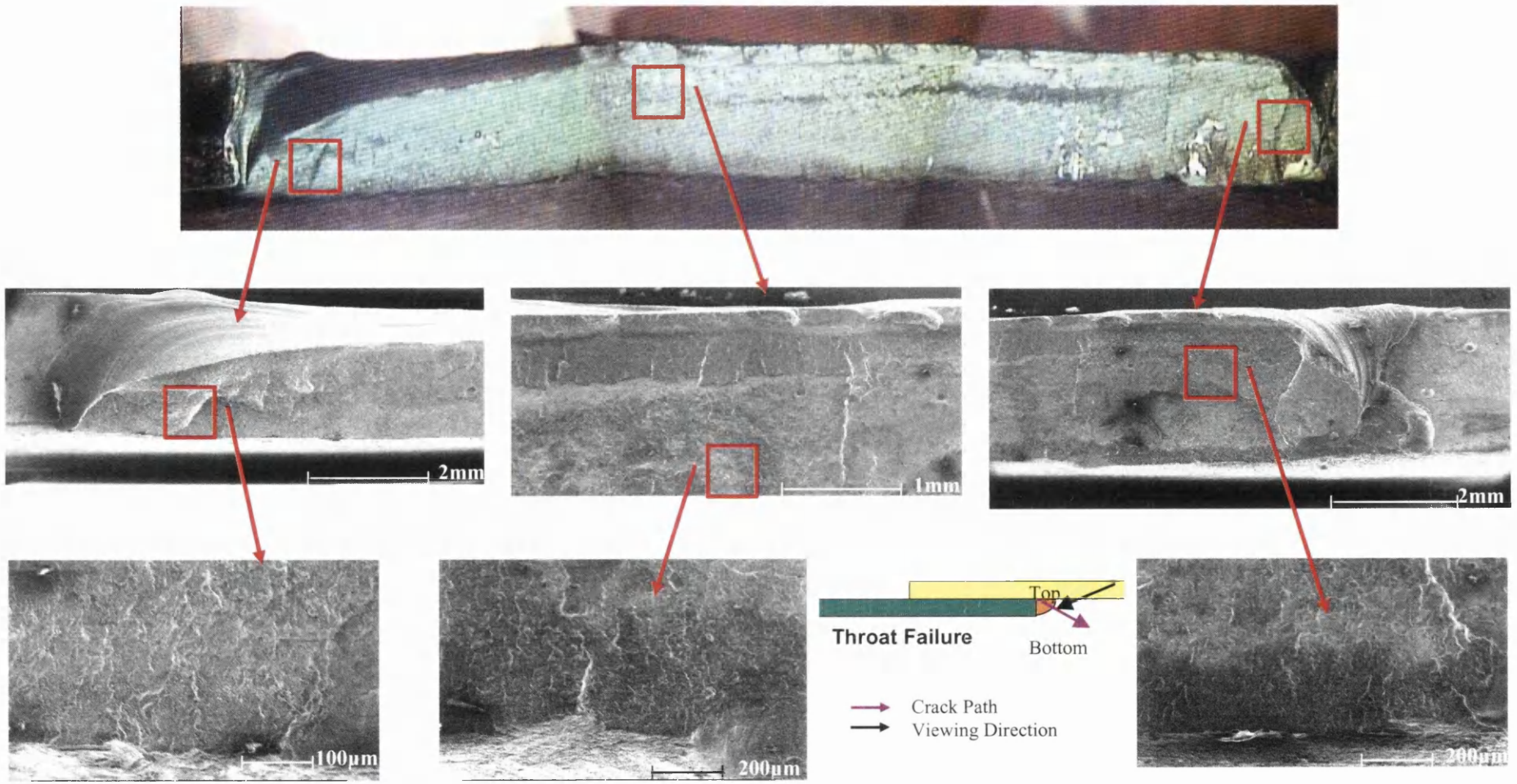

Figure A11.4.14: Typical Fracture Surface for GM3 Weld Throat Failure – Sheet View

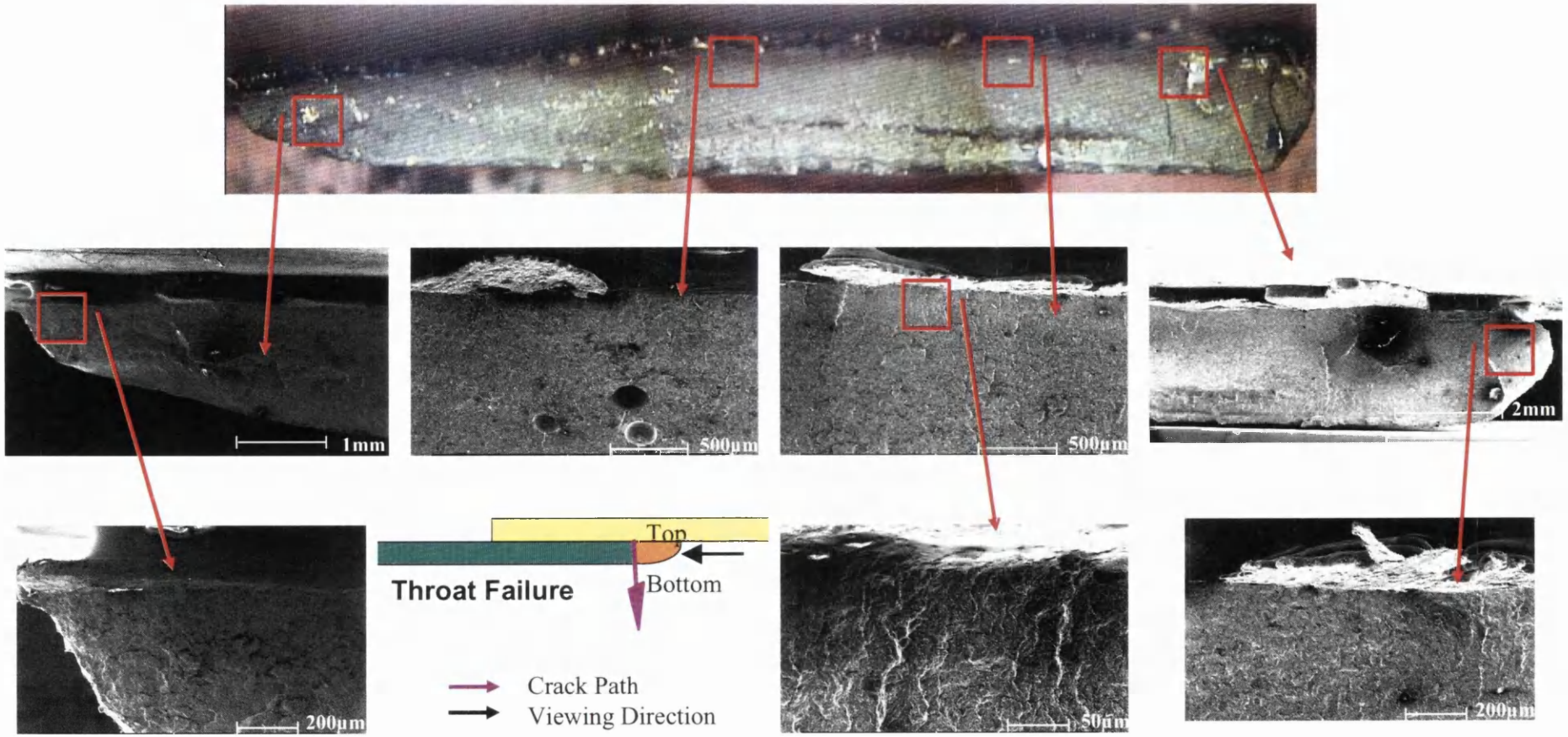

Figure A11.4.15: Typical Fracture Surface for GM3 Weld Throat Failure – Weld View

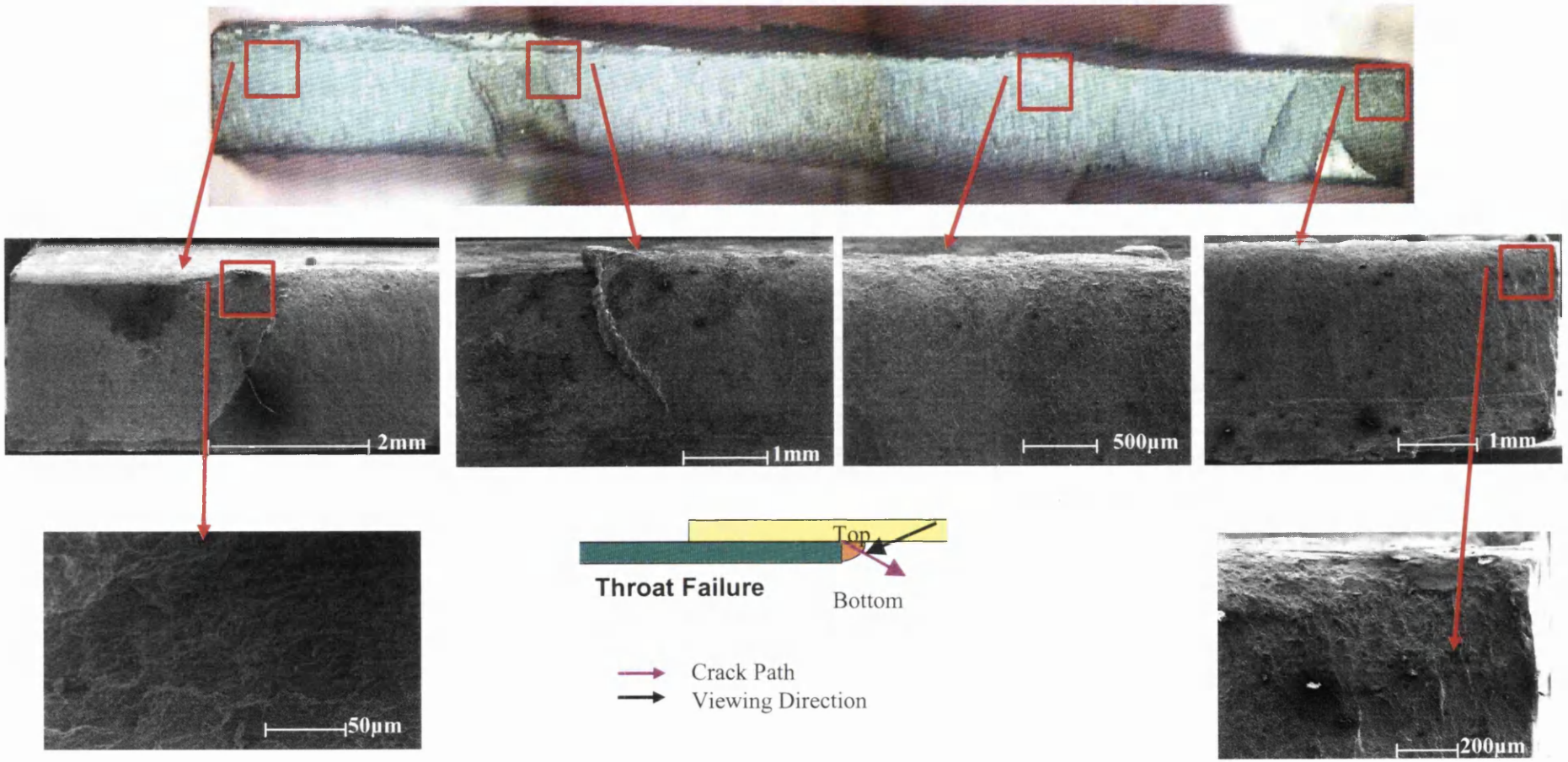

Figure A11.4.16: Typical Fracture Surface for GM4 Weld Throat Failure – Sheet View

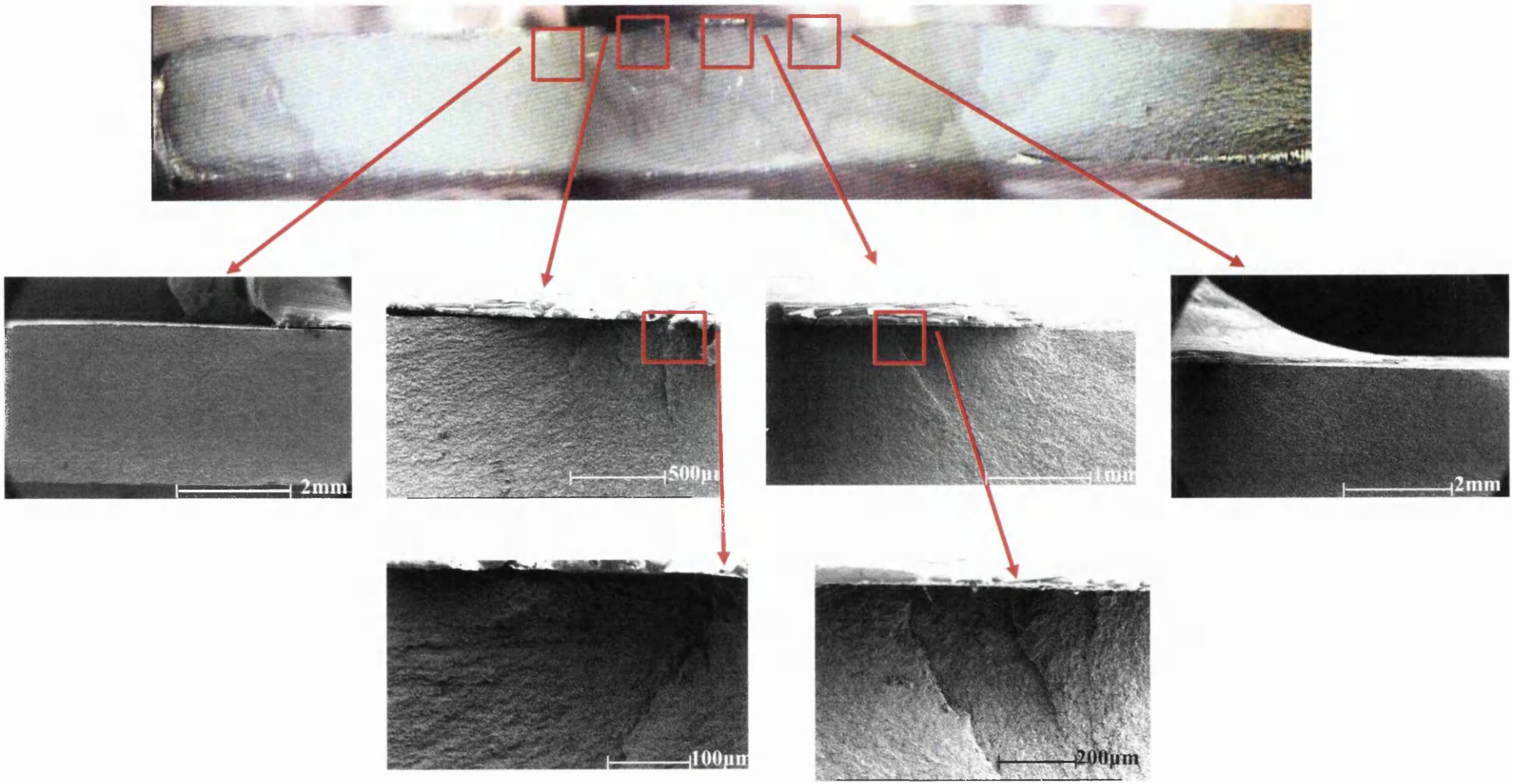

Figure A11.4.17: Typical Fracture Surface for GM5 Weld Throat Failure – Weld View

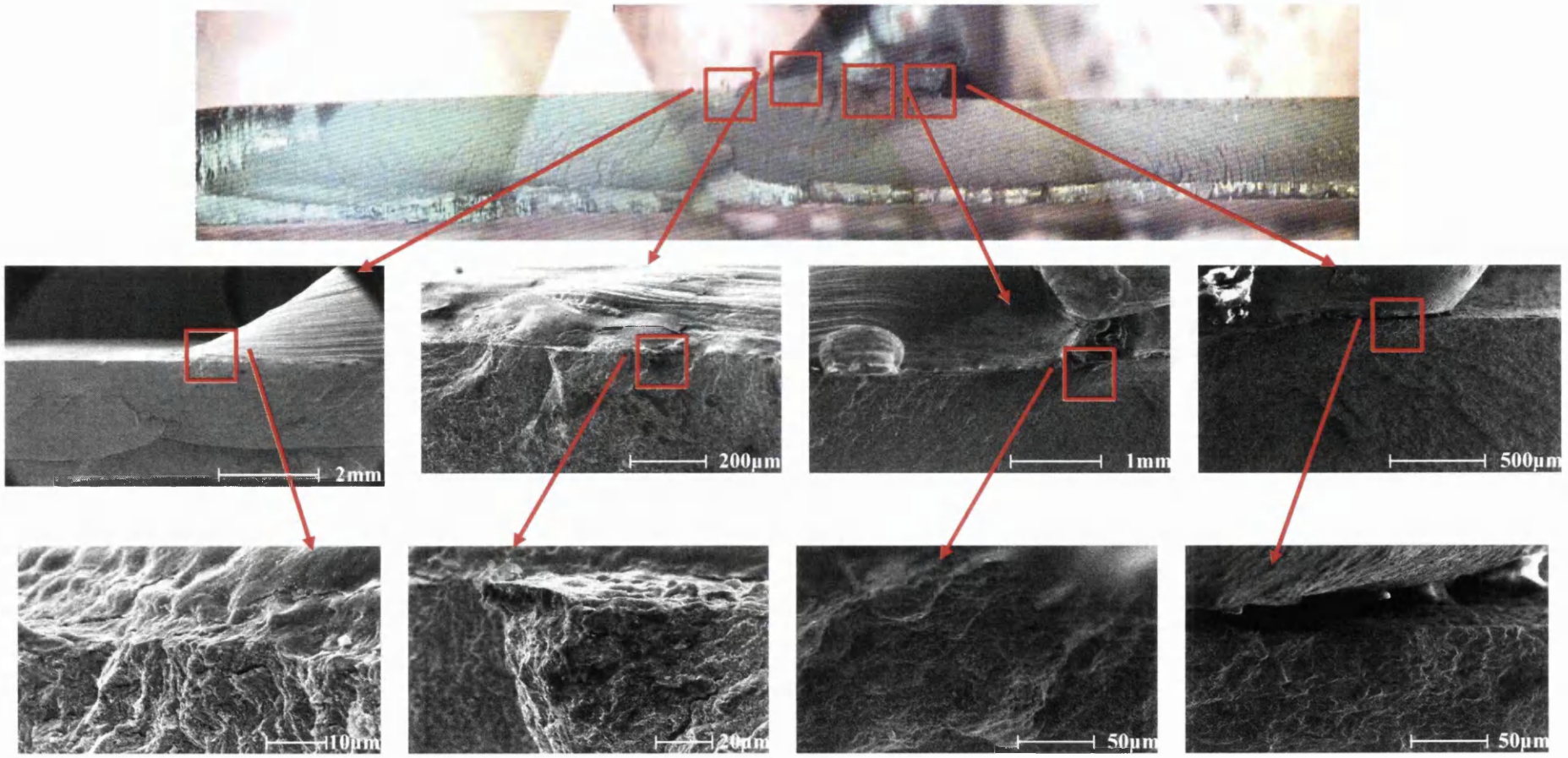

Figure A11.4.18: Typical Fracture Surface for GM6 Weld Throat Failure – Weld View

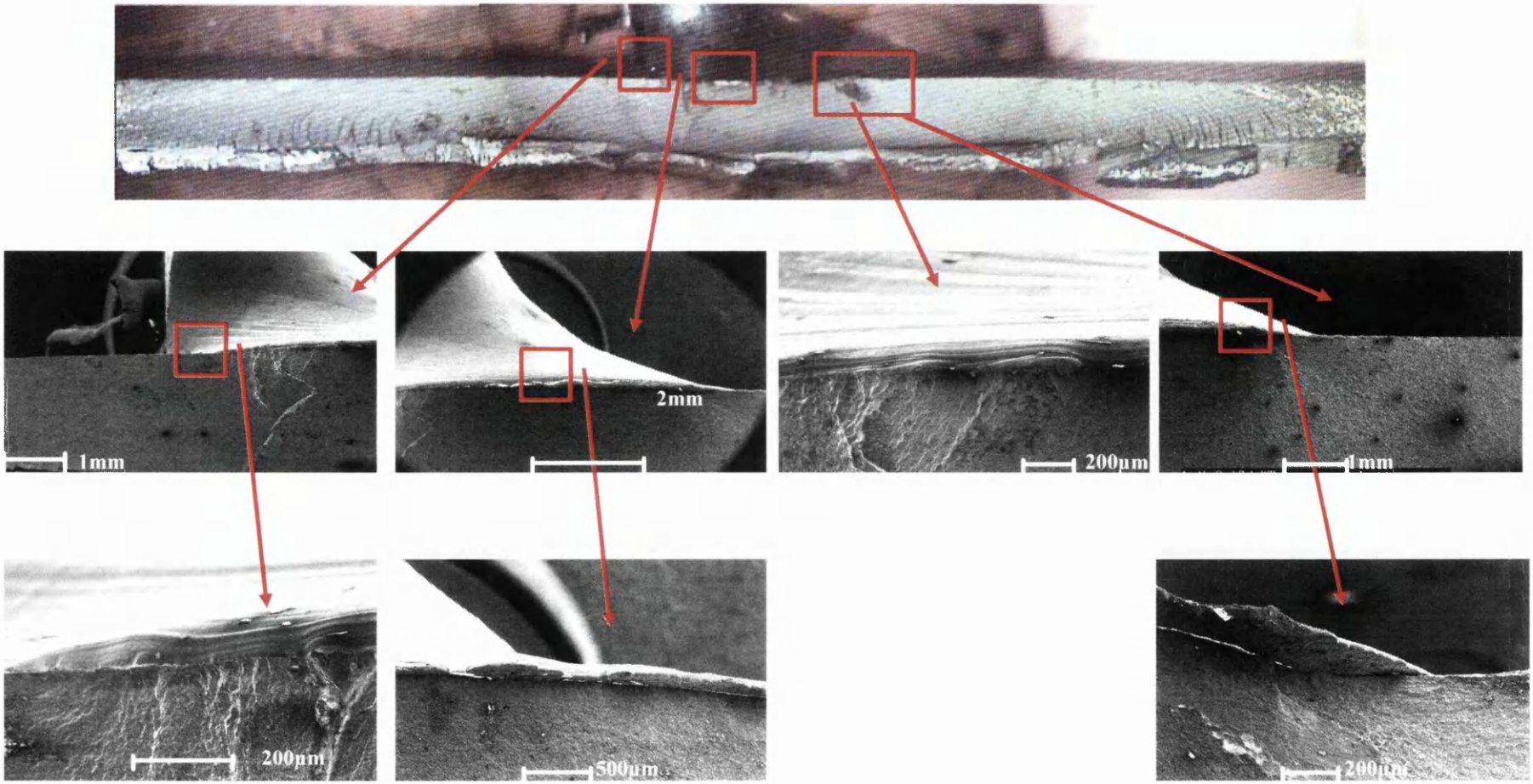

Figure A11.4.19: Typical Fracture Surface for GM8 Weld Throat Failure – Weld View

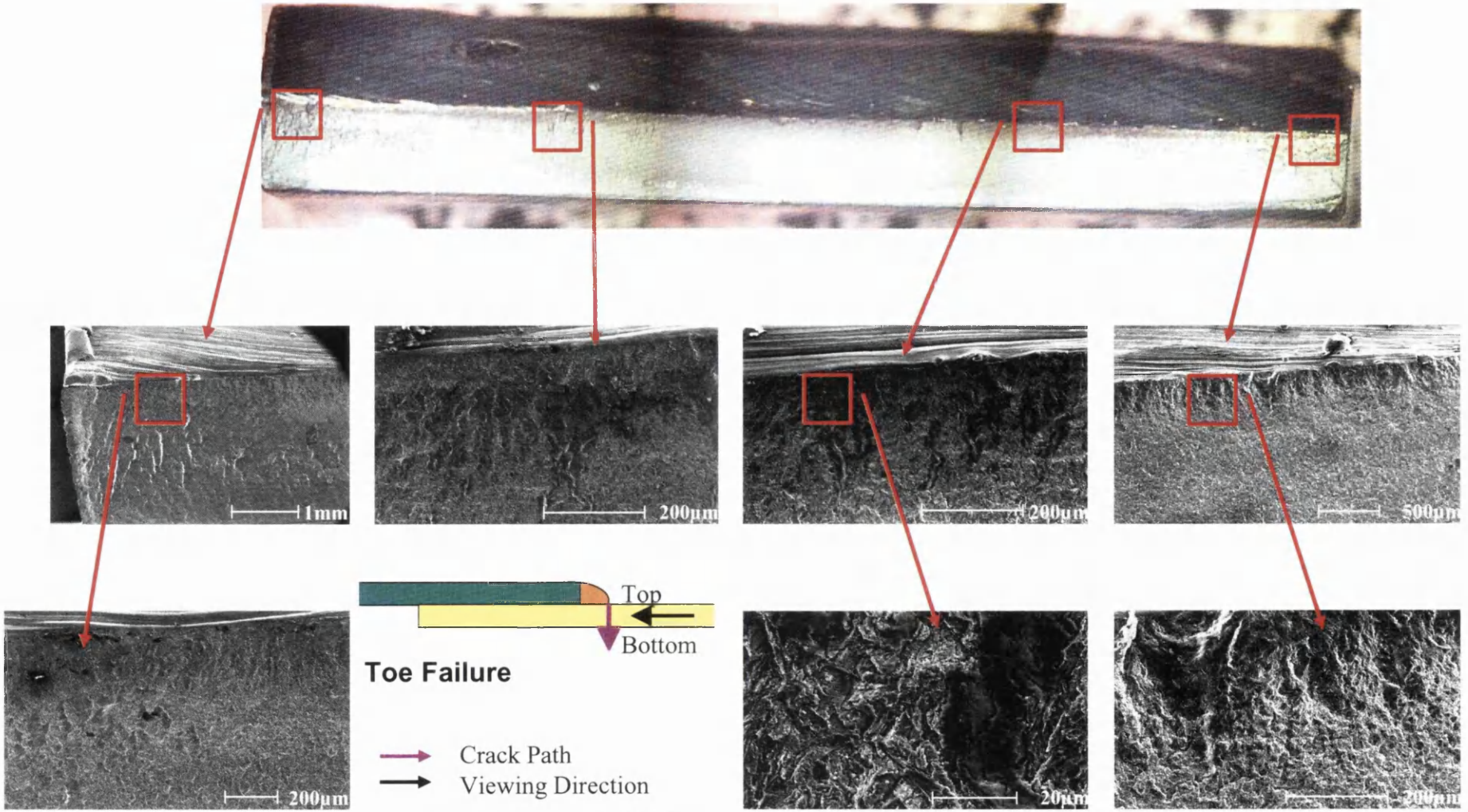

Figure A11.4.20: Typical Fracture Surface for R-Ratio R=0.5 TM11B Weld Toe Failure – Weld View

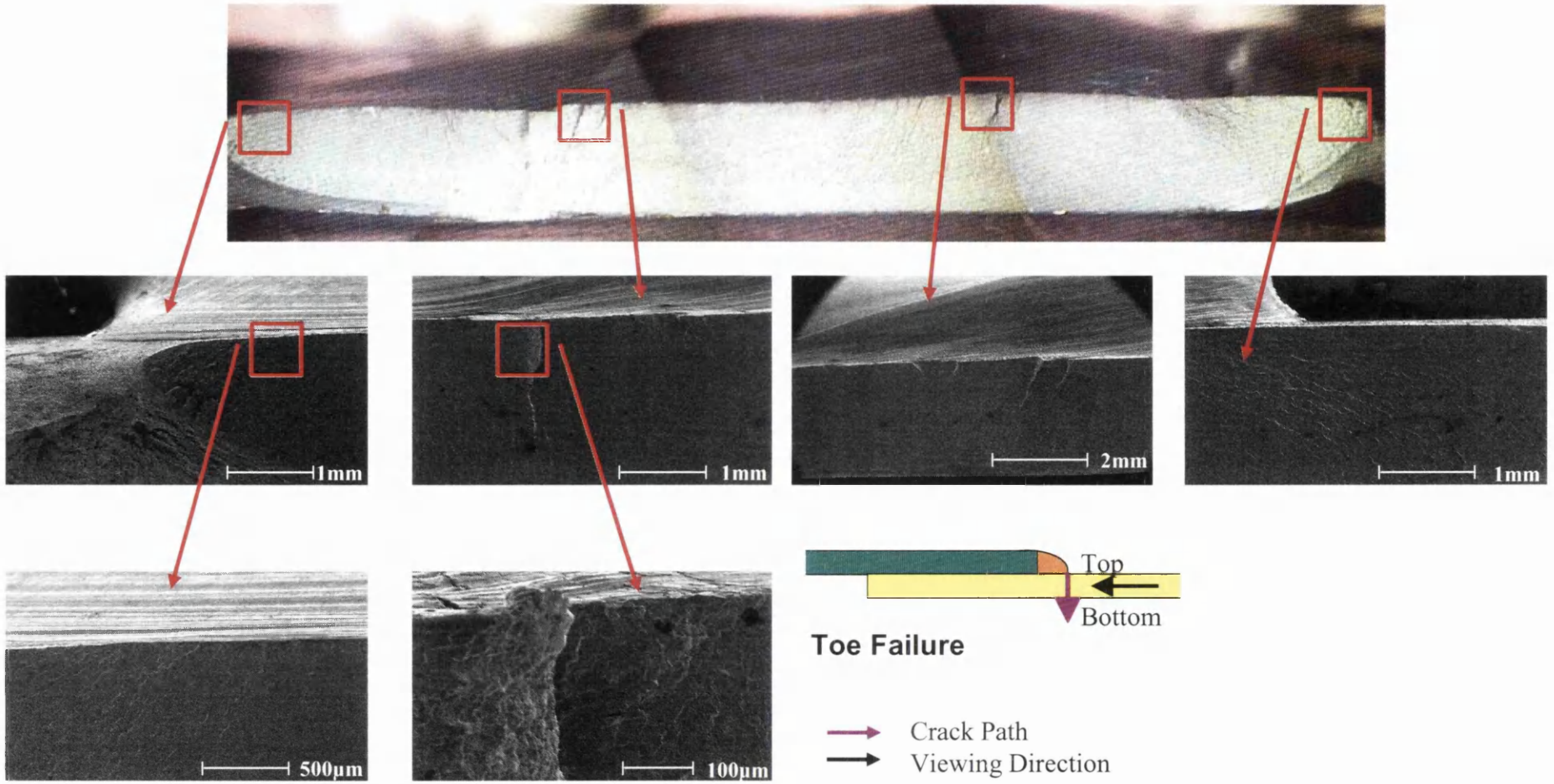

Figure A11.4.21: Typical Fracture Surface for Variable Amplitude Block Loading GM11A Weld Toe Failure – Weld View

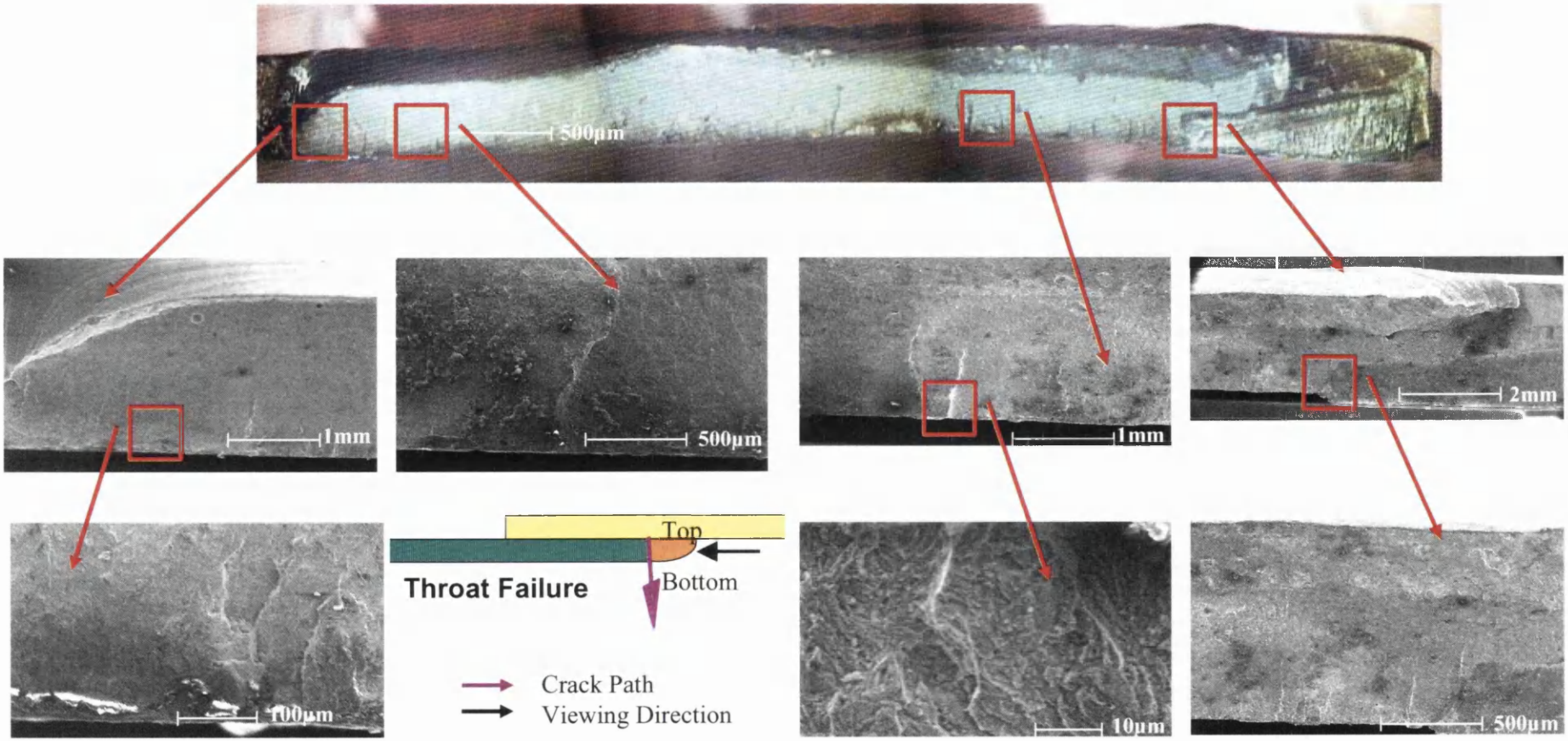

Figure A11.4.22: Typical Fracture Surface for Variable Amplitude SAE Bracket Load-Time History GM1 Weld Throat Failure – Sheet View

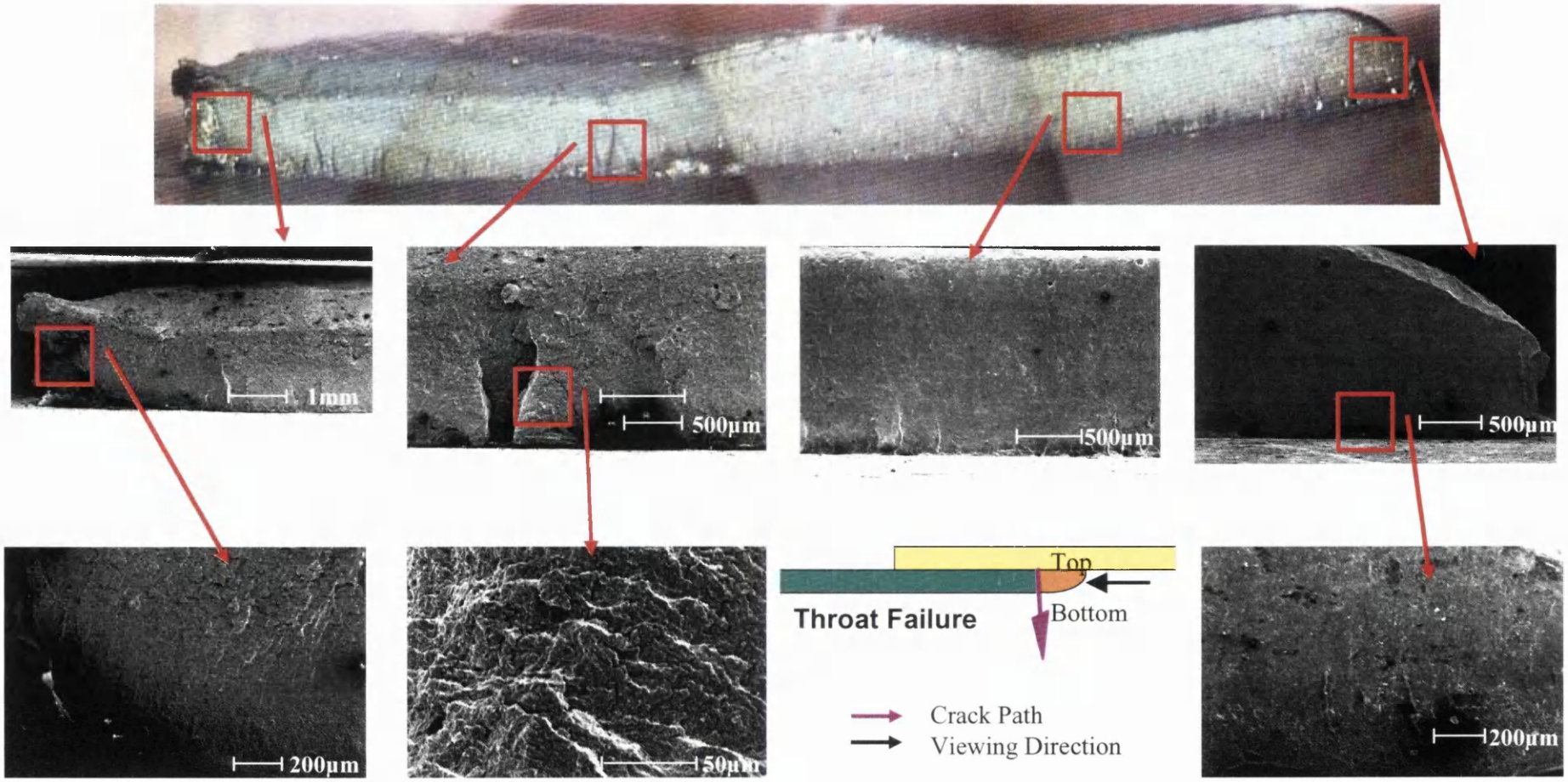

Figure A11.4.23: Typical Fracture Surface for Variable Amplitude SAE Bracket Load-Time History GM1 Weld Throat Failure – Weld View

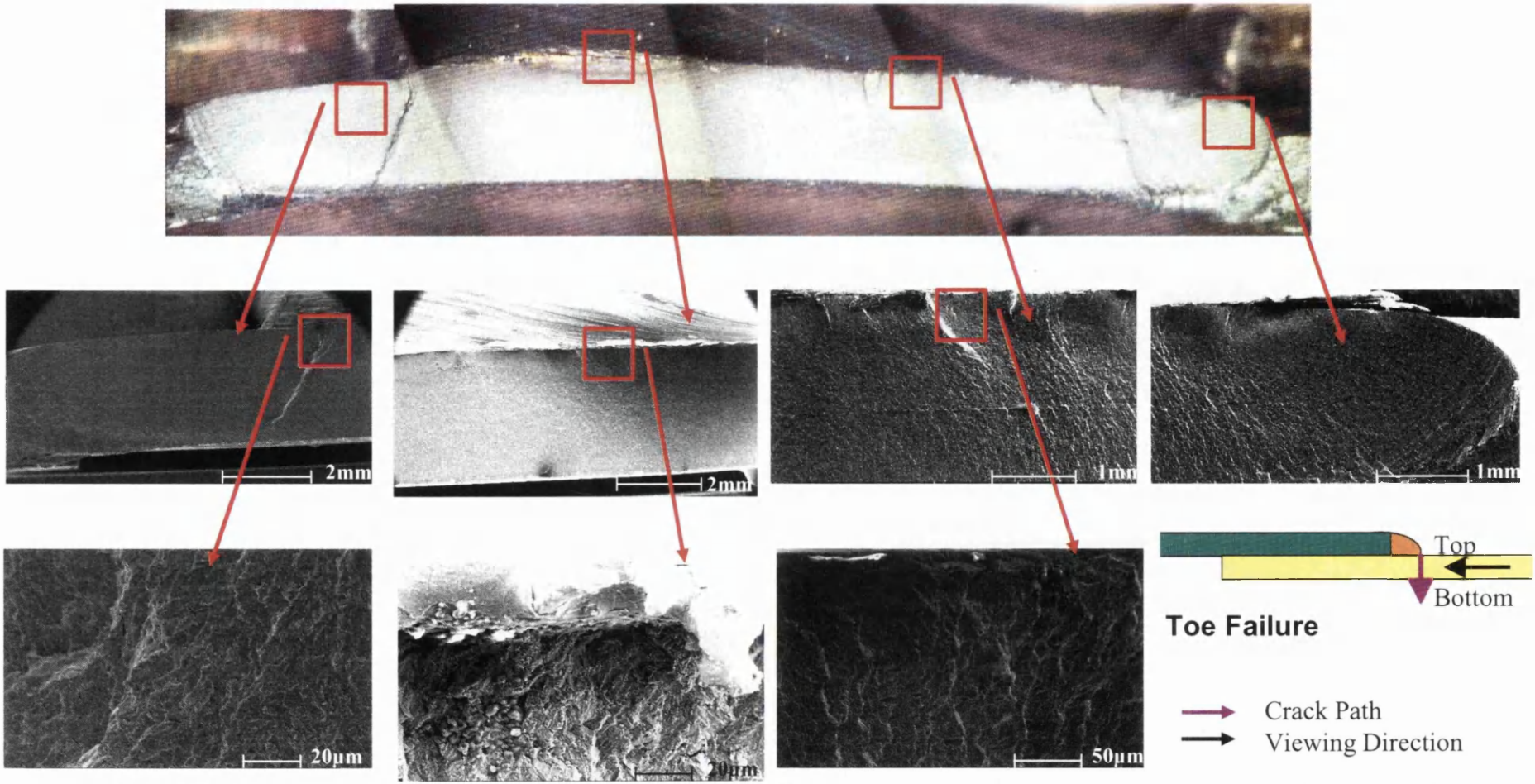

Figure A11.4.24: Typical Fracture Surface for Variable Amplitude SAE Bracket Load-Time History TM11A Weld Toe Failure – Weld View

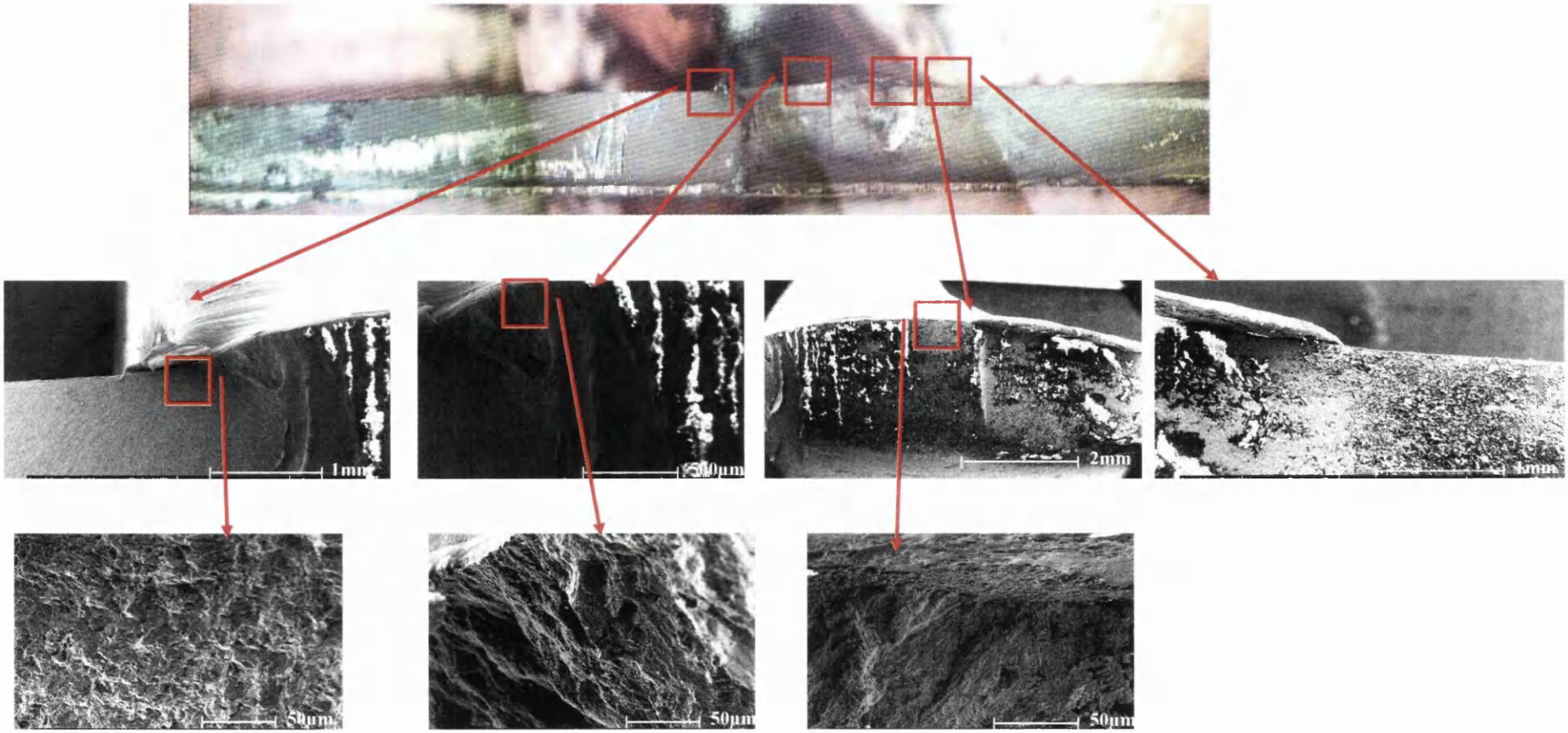

Figure A11.4.25: Typical Fracture Surface for Variable Amplitude SAE Bracket Load-Time History GM8 Weld Throat Failure – Weld View

15.6 Appendix 6 Battelle Structural Stress Manual Calculations vs. FLOW and Verity

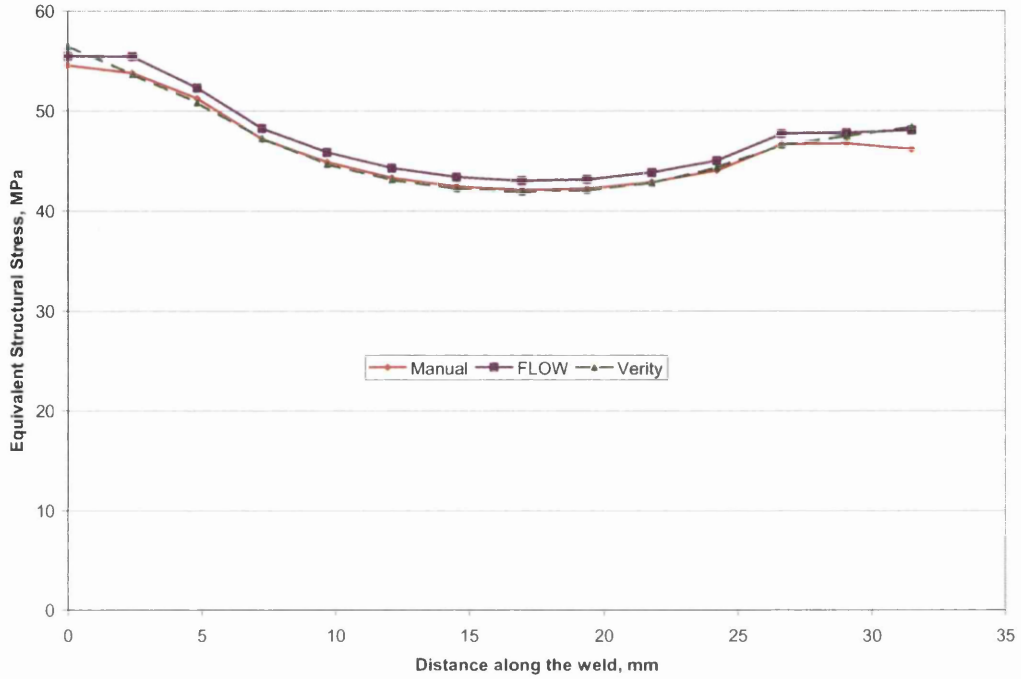

Figure A11.7.1: Battelle Structural Stress Manual vs. FLOW & Verity for GM1

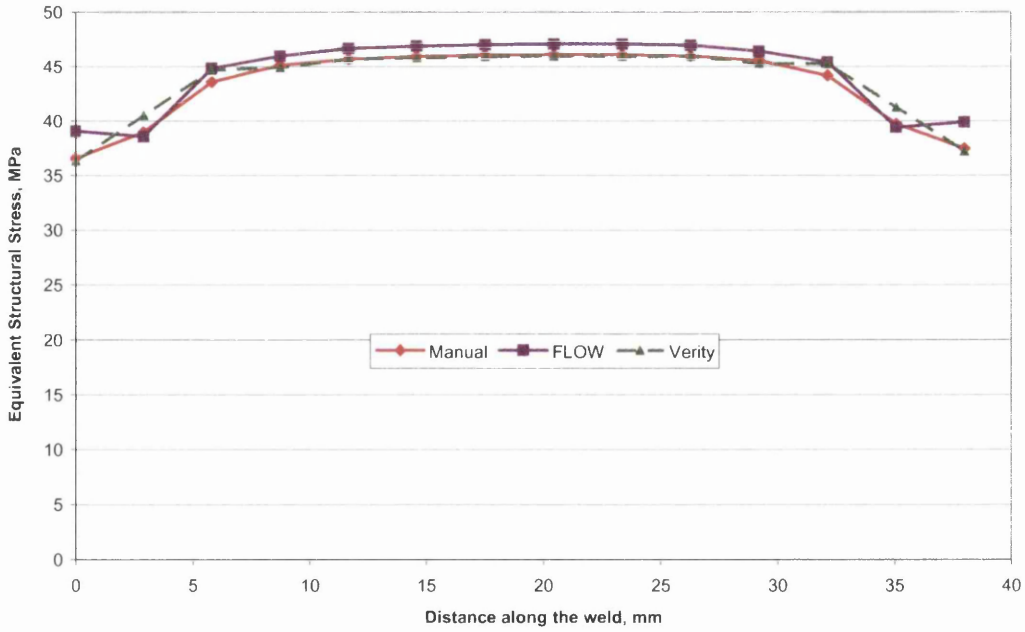

Figure A11.7.2: Battelle Structural Stress Manual vs. FLOW & Verity for GM2

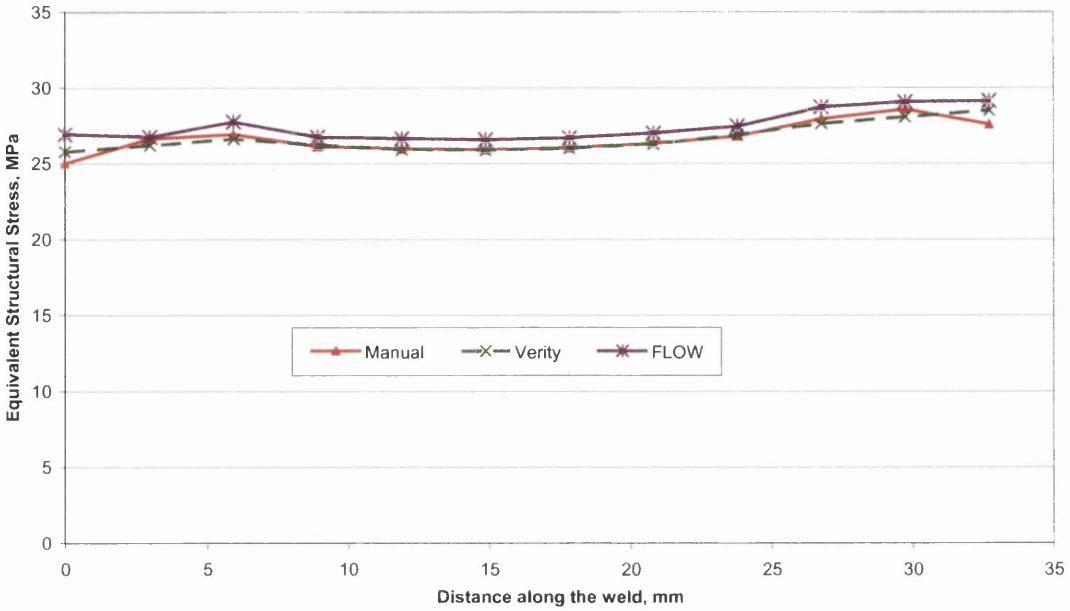

Figure A11.7.3: Battelle Structural Stress Manual vs. FLOW & Verity for GM11A

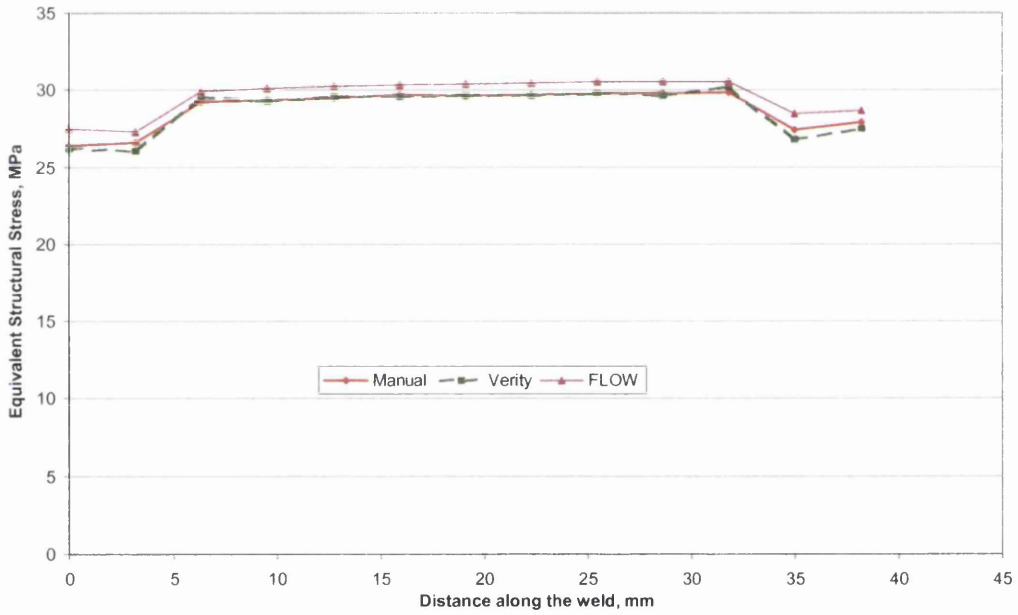

Figure A11.7.4: Battelle Structural Stress Manual vs. FLOW & Verity for GM11B

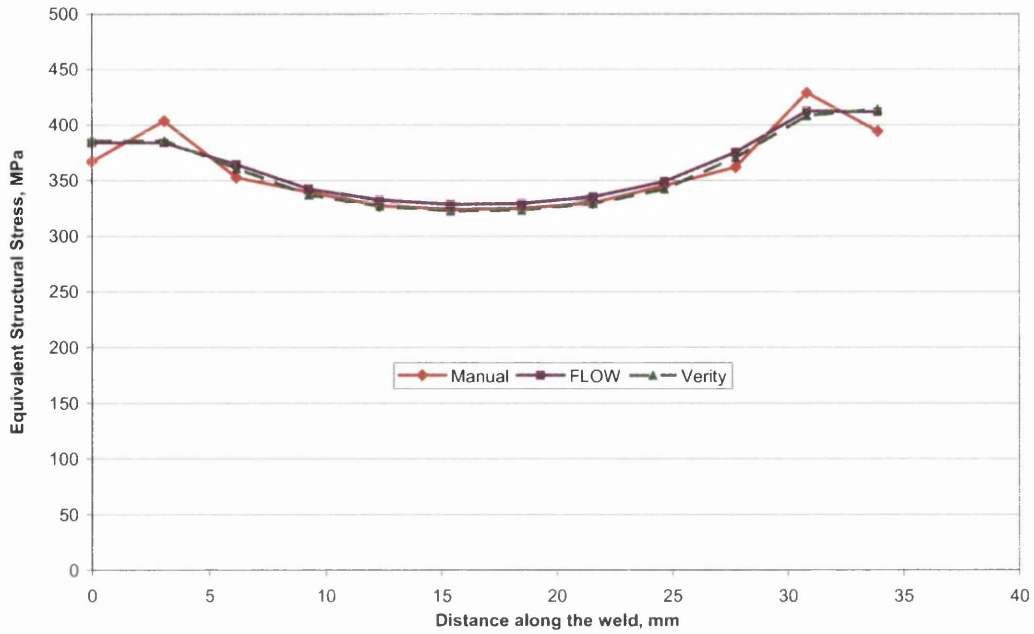

Figure A11.7.5: Battelle Structural Stress Manual vs. FLOW & Verity for GM3

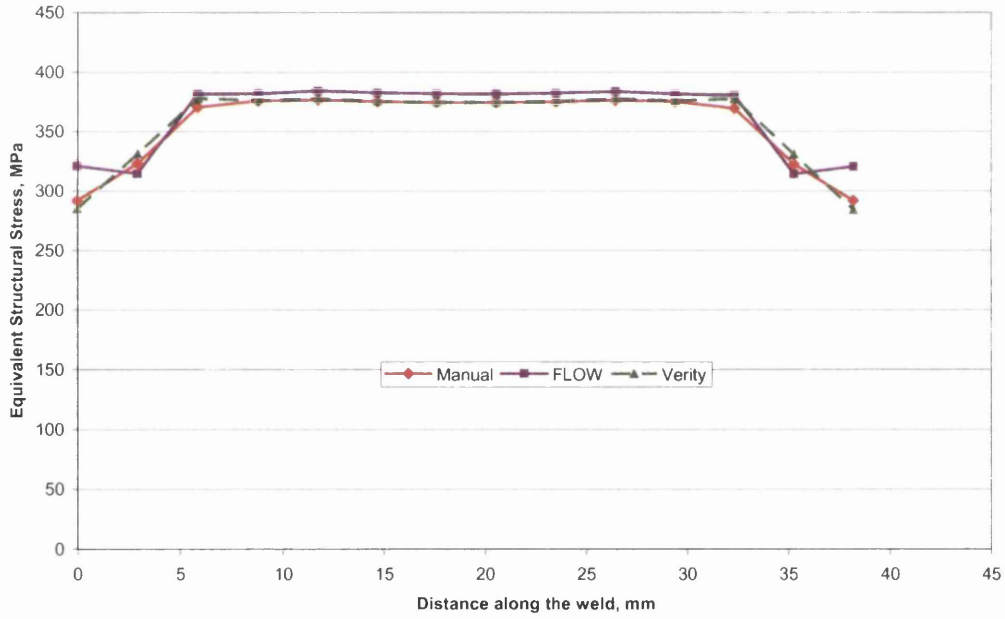

Figure A11.7.6: Battelle Structural Stress Manual vs. FLOW & Verity for GM4

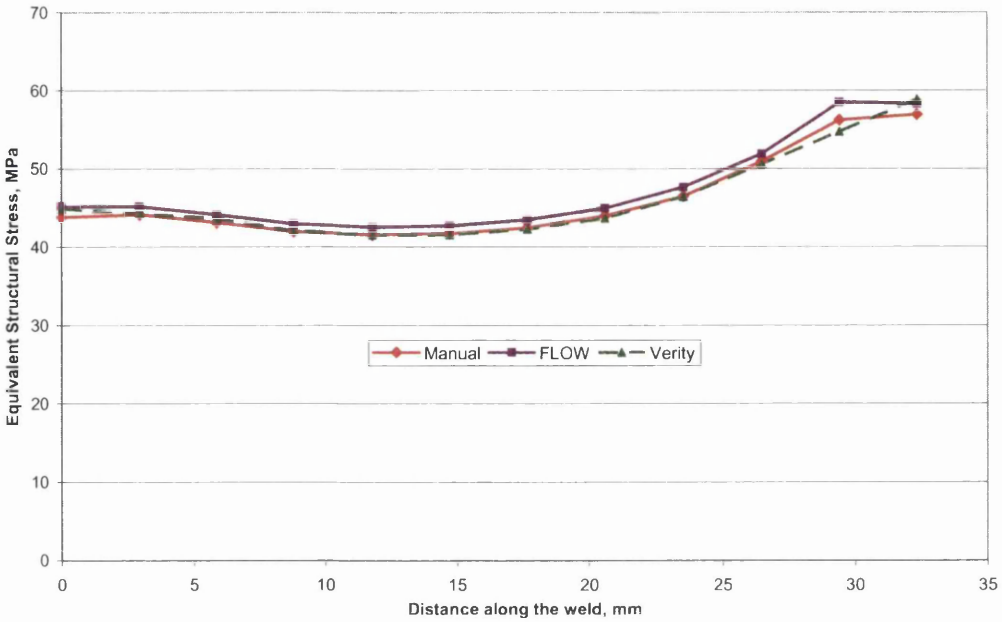

Figure A11.7.7: Battelle Structural Stress Manual vs. FLOW & Verity for TM1

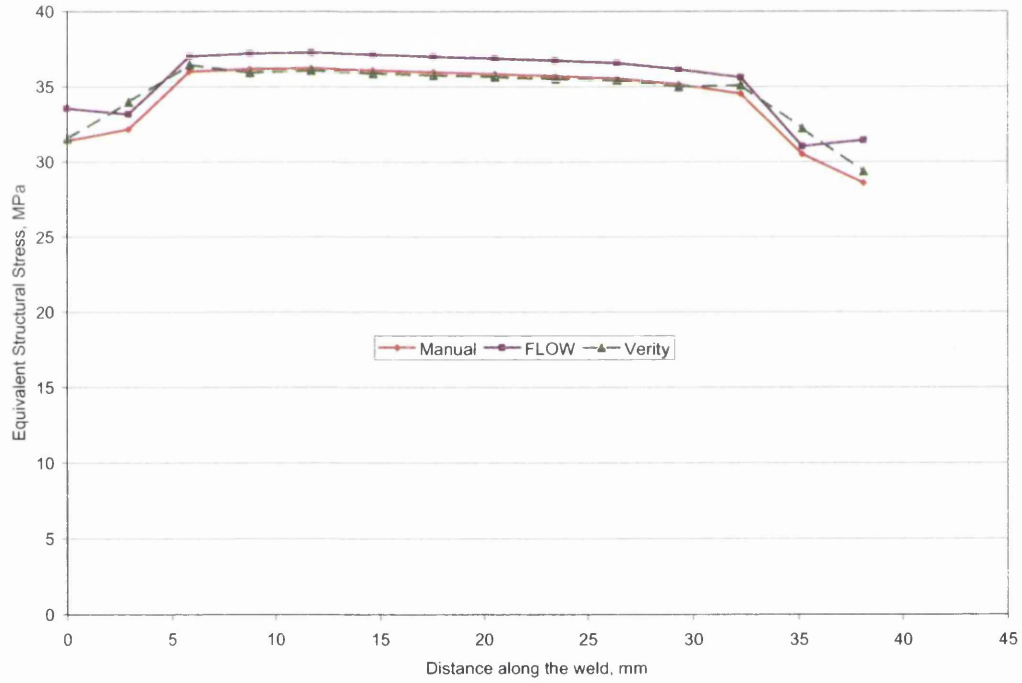

Figure A11.7.8: Battelle Structural Stress Manual vs. FLOW & Verity for TM2

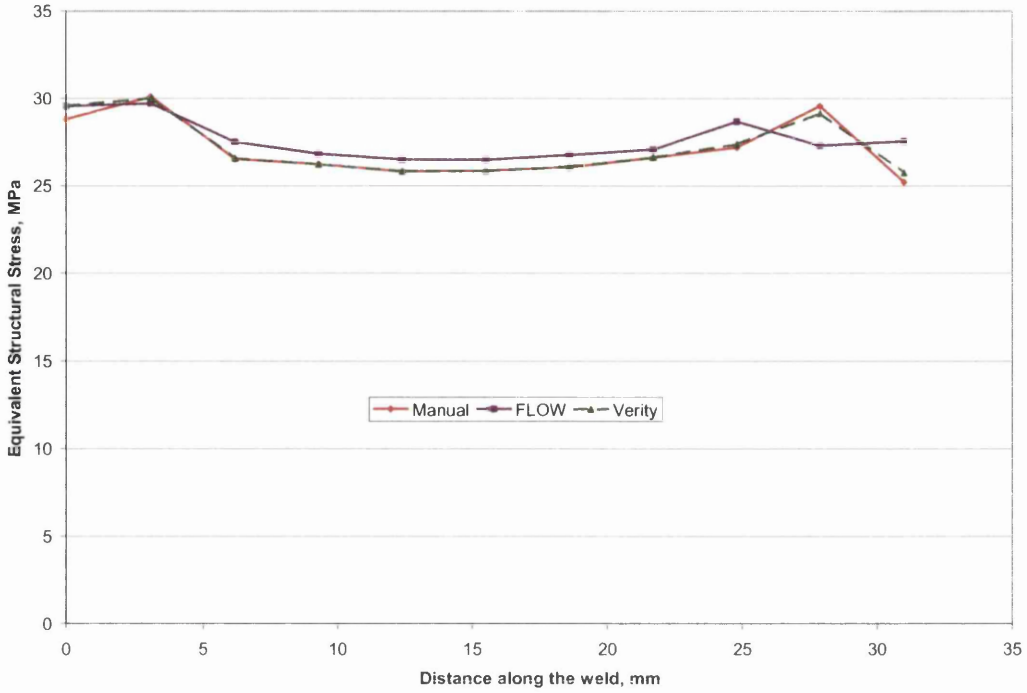

Figure A11.7.9: Battelle Structural Stress Manual vs. FLOW & Verity for TM11A

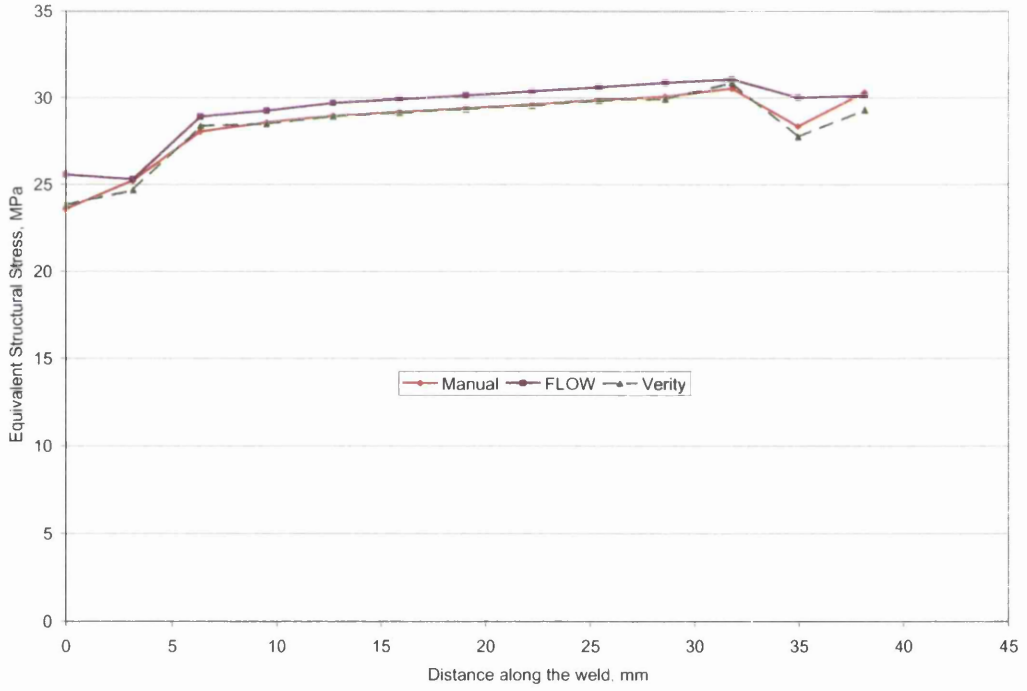

Figure A11.7.10: Battelle Structural Stress Manual vs. FLOW & Verity for TM11B

15.7 Appendix 7 FUCA Component Fracture Surface Analysis

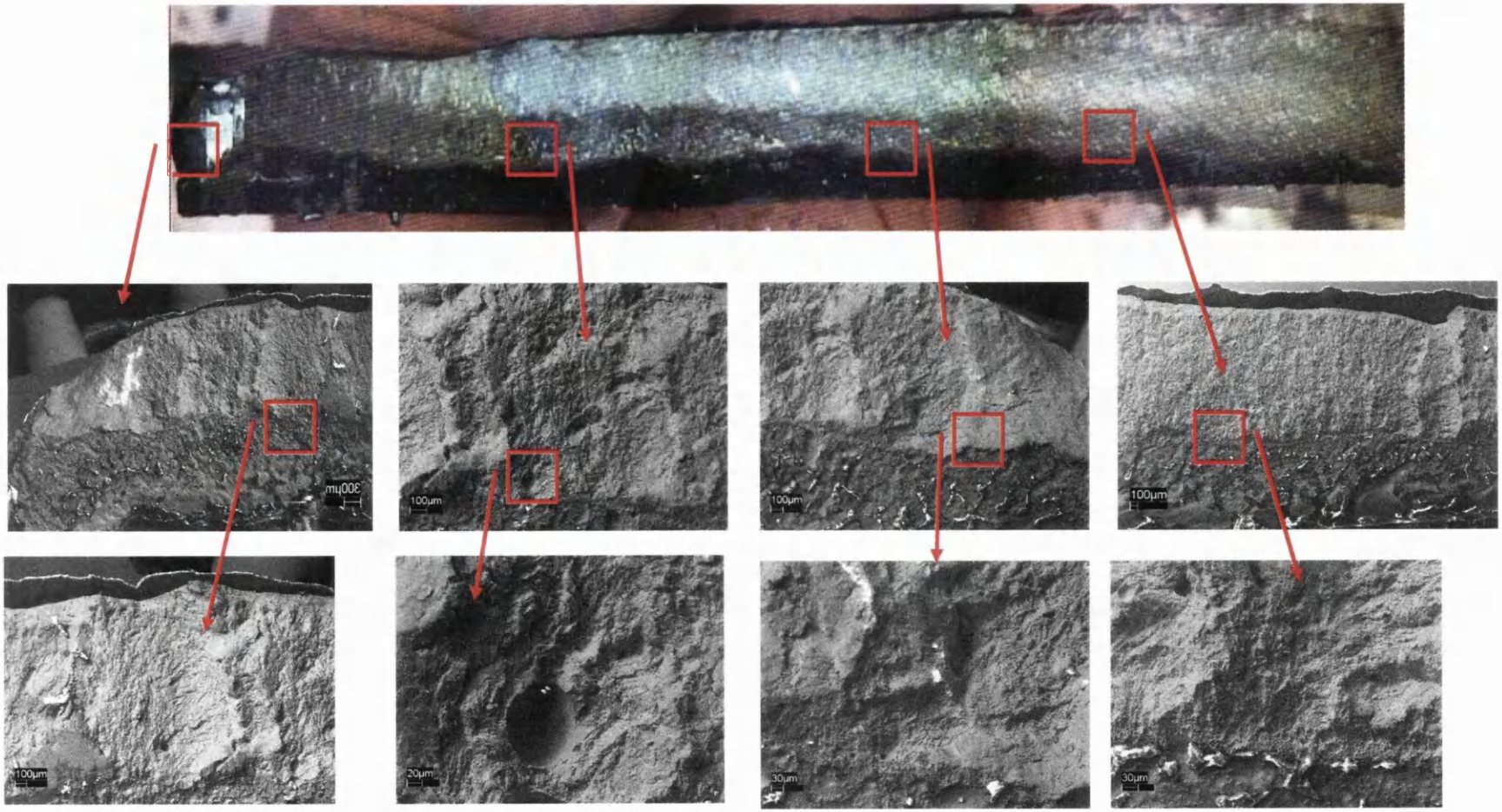

Figure A11.7.1: Component #11 – Weld View

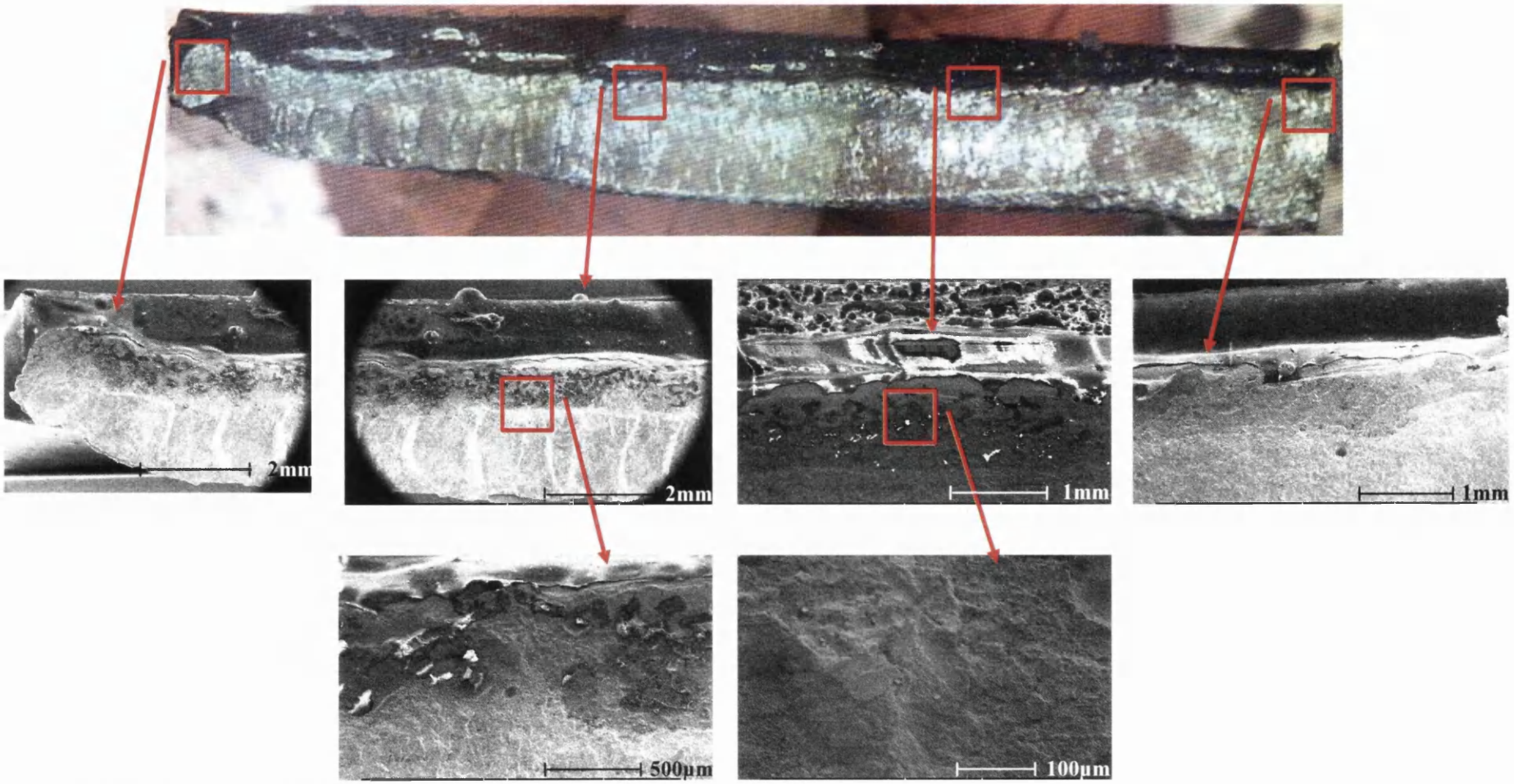

Figure A11.7.2: Component # 26 – Weld View

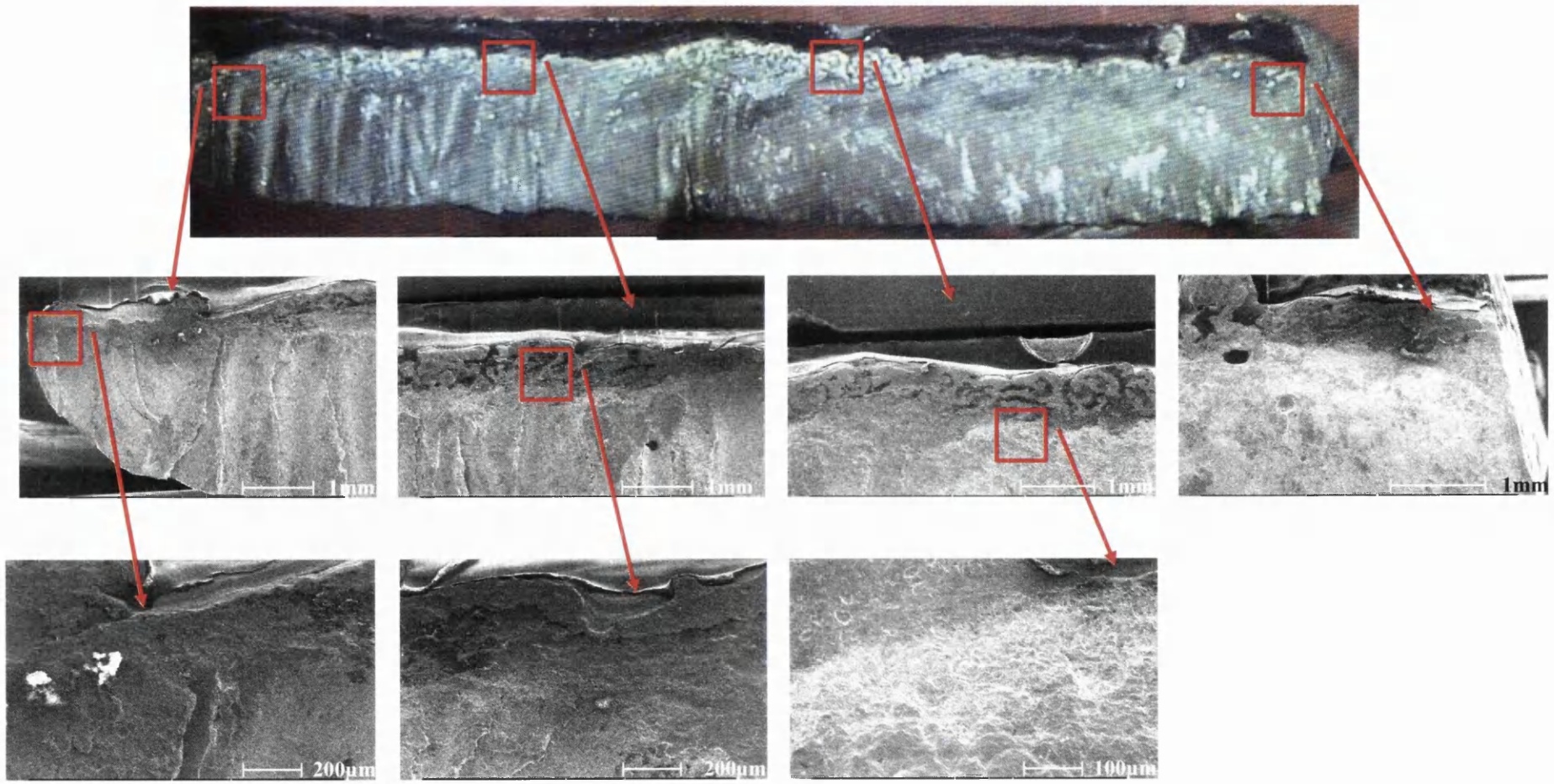

Figure A11.7.3: Component # 40 – Weld View

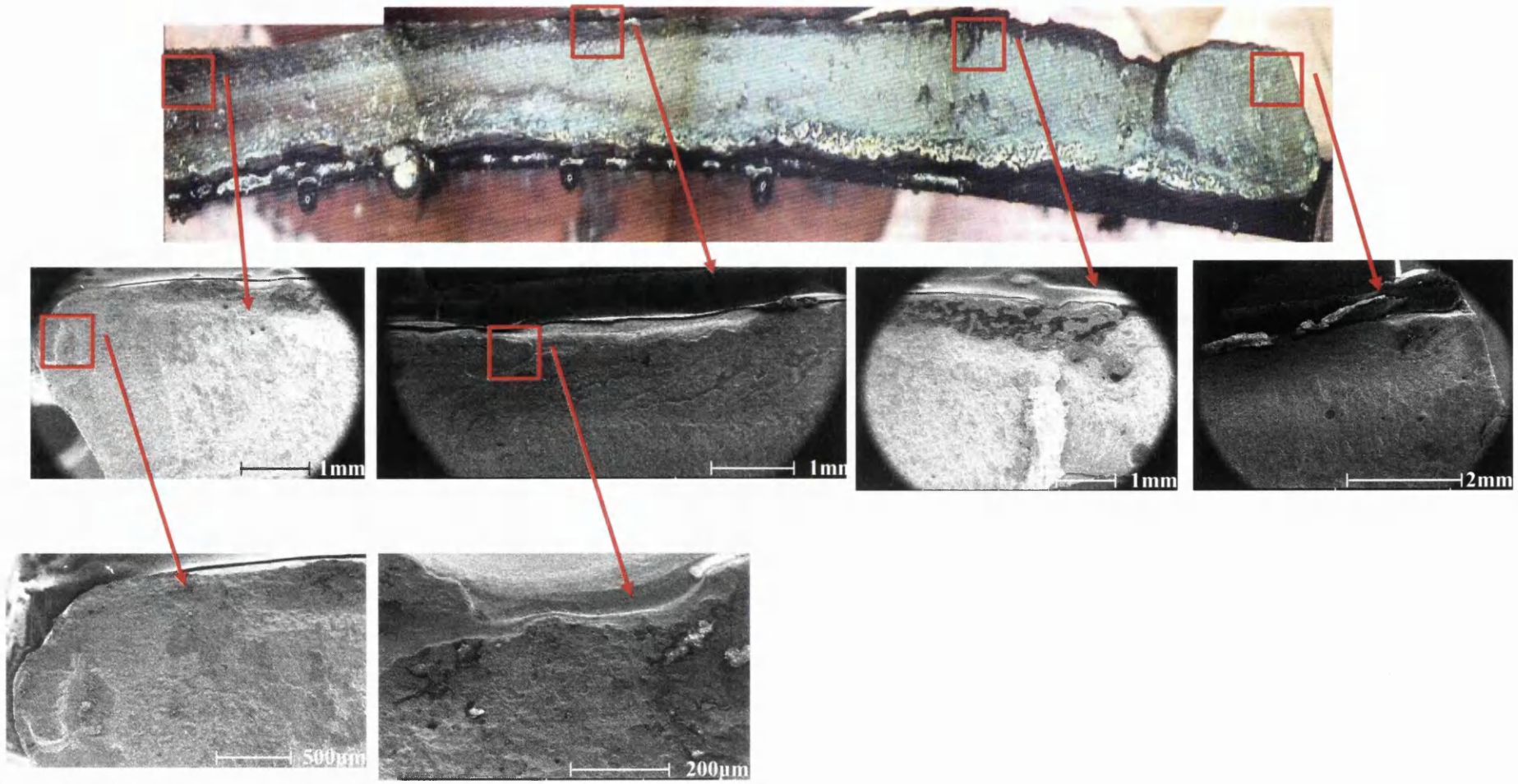

Figure A11.7.4: Component # 41 – Weld View

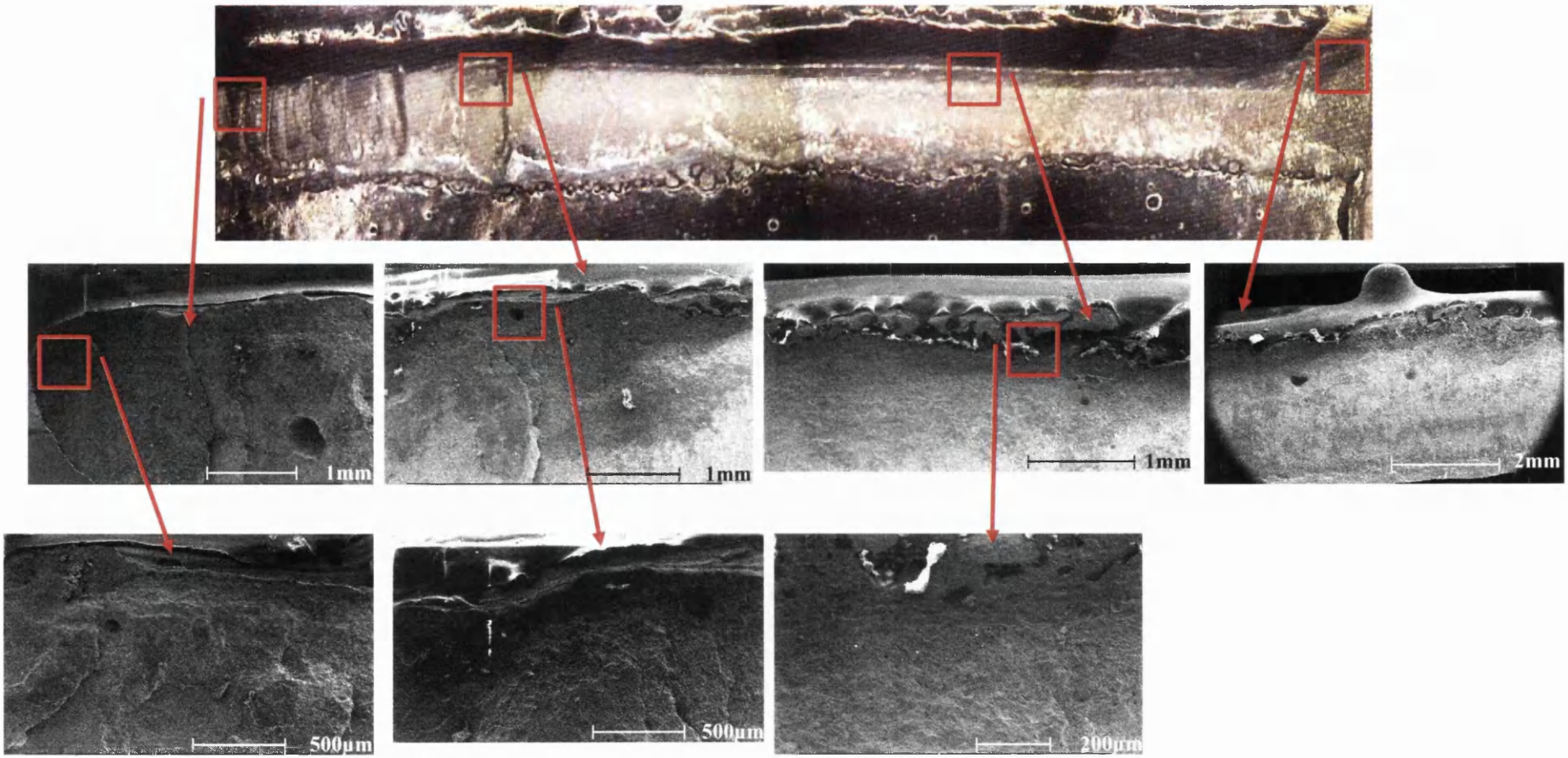

Figure A11.7.5: Component # 45 – Weld View

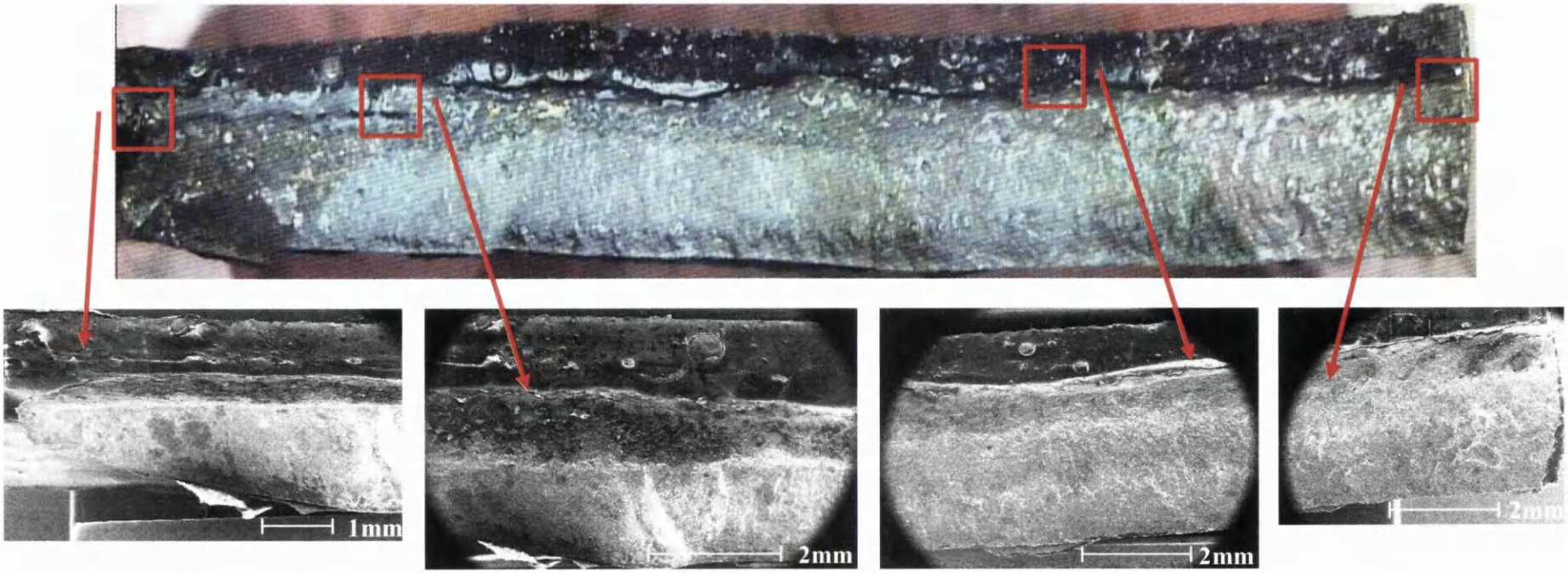

Figure A11.7.6: Component # 8 – Weld View

15.8 Appendix 8 Volvo Structural Stress S-N Curves

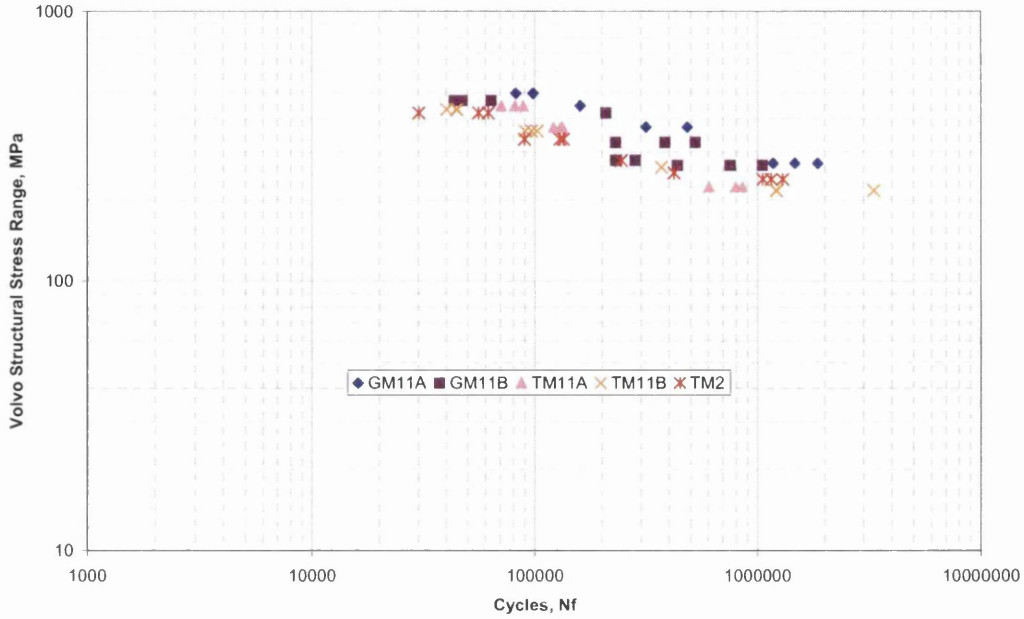

Figure A12.5.1: Stress–Life Master Curve Conversion for All Weld Toe Failures

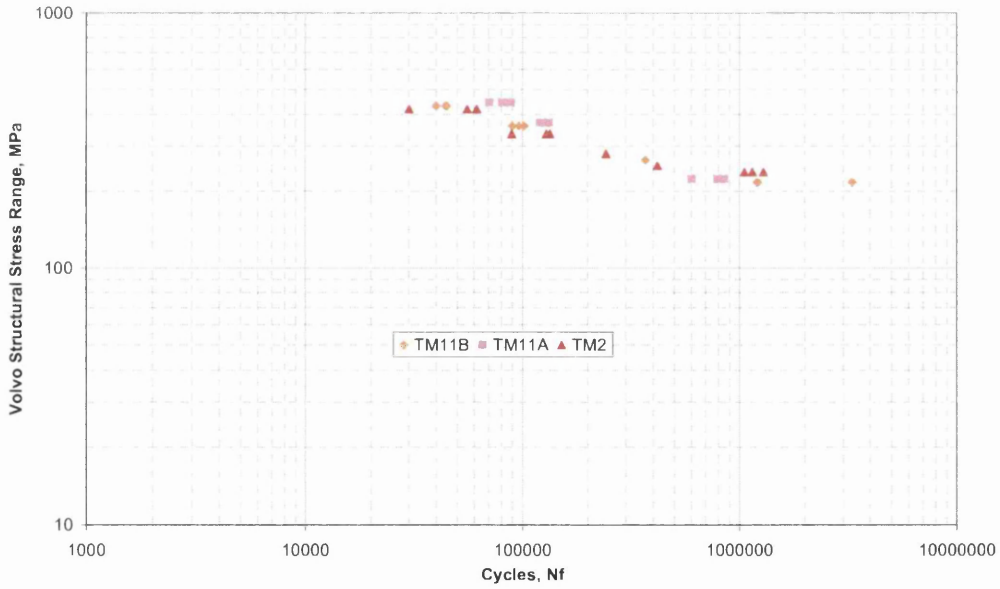

Figure A12.5.2: Stress–Life Master Curve Conversion for TKA Weld Toe Failure

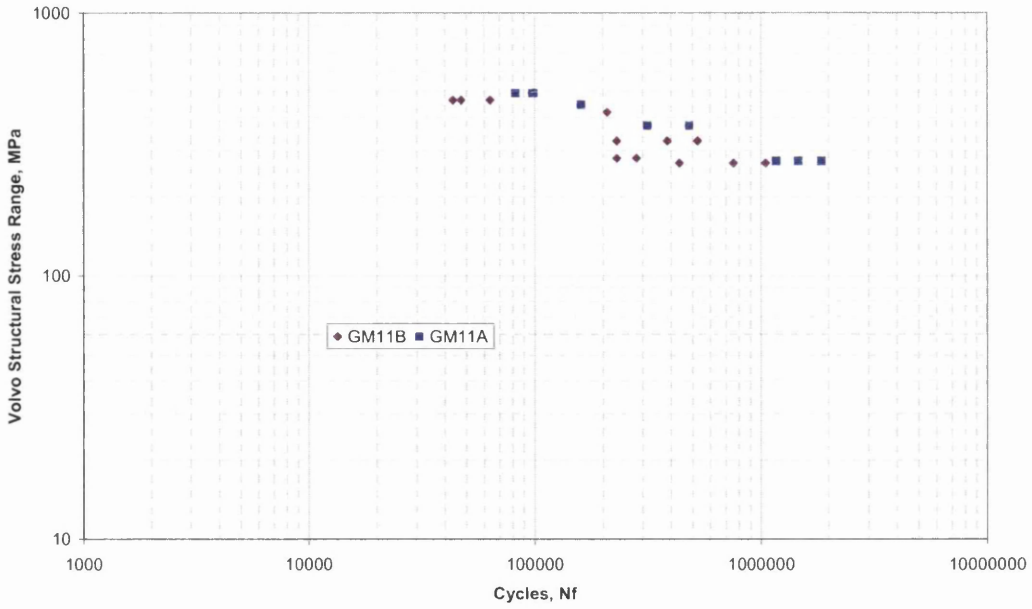

Figure A12.5.3: Stress–Life Master Curve Conversion for GKN Weld Toe Failure

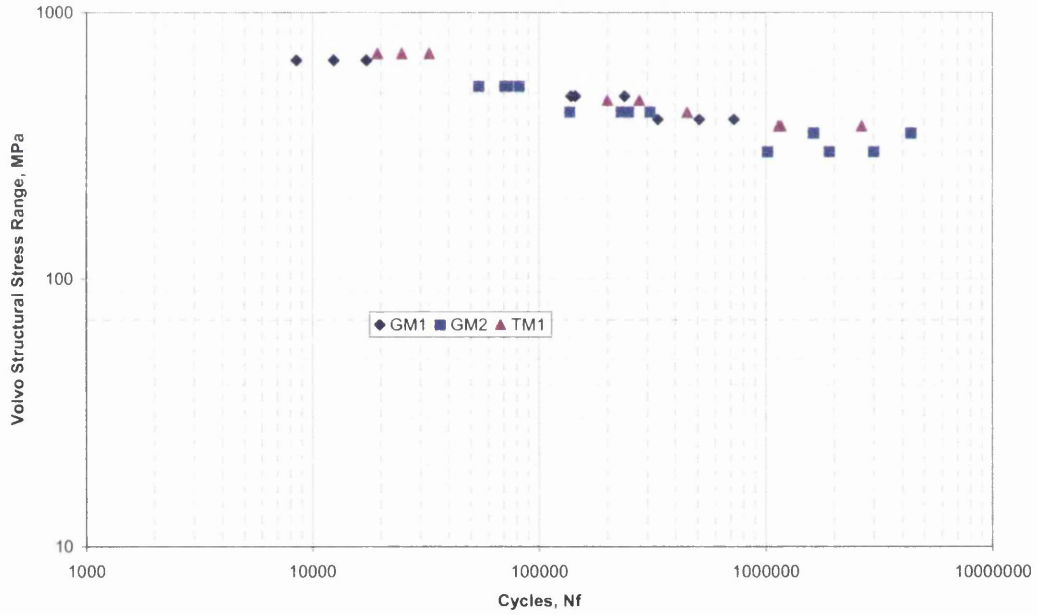

Figure A12.5.4: Stress–Life Master Curve Conversion for Weld Interface Failure

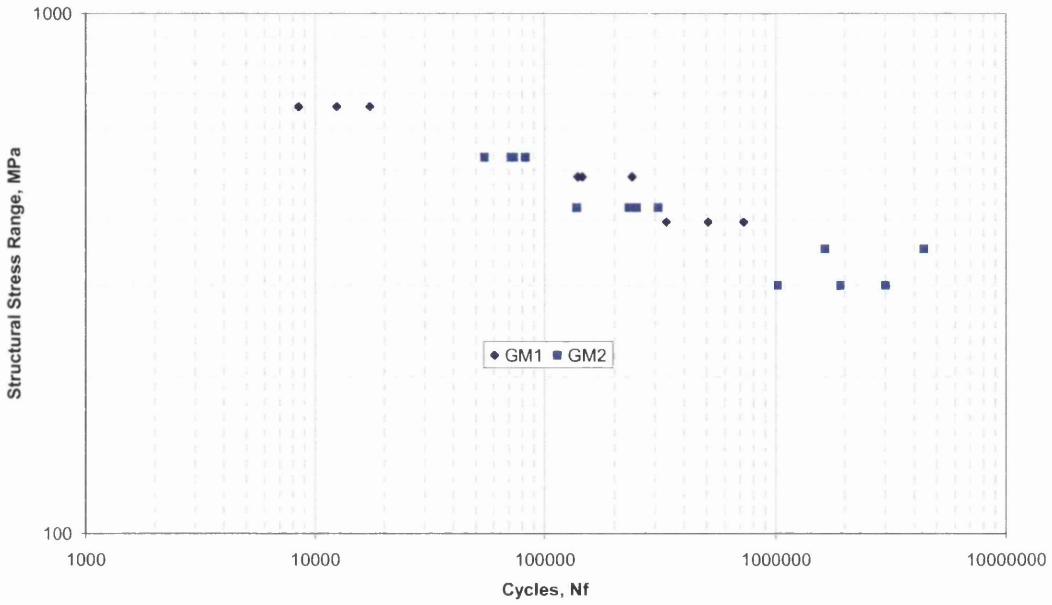

Figure A12.5.5: Stress–Life Master Curve Conversion for GKN Interface Weld Failure

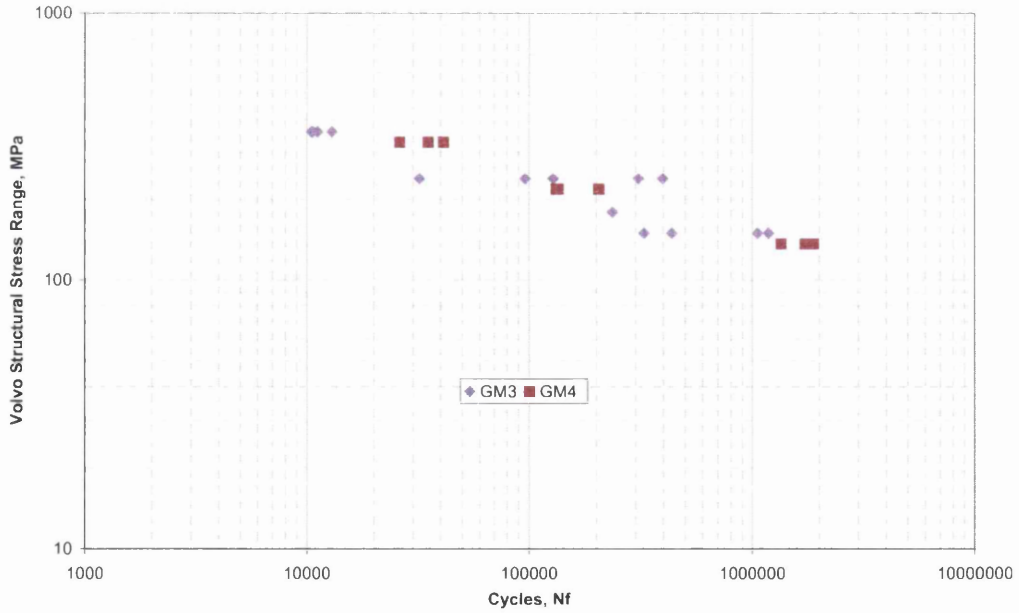

Figure A12.5.6: Stress–Life Master Curve Conversion for GKN Weld Throat Failure

Table A12.5.1: Volvo Master S-N Curve Parameters

$$\Delta\sigma = aN_f^b$$

Volvo Method Structural Stress				
Failure Location	**Survival**	**a**	**b**	**SE log(N_f)**
Toe Failure	50%	7151.67	-0.2485	0.2664
	99.87%	4526.7	-0.2485	
Interface Failure	50%	3189.15	-0.1583	0.2458
	99.87%	2437.59	-0.1583	
Throat Failure	50%	3034.71	-0.2205	0.2599
	99.87%	2042.64	-0.2205	

15.9 Appendix 9 Battelle Structural Stress S-N Curves

15.9.1 Manual Structural Stress

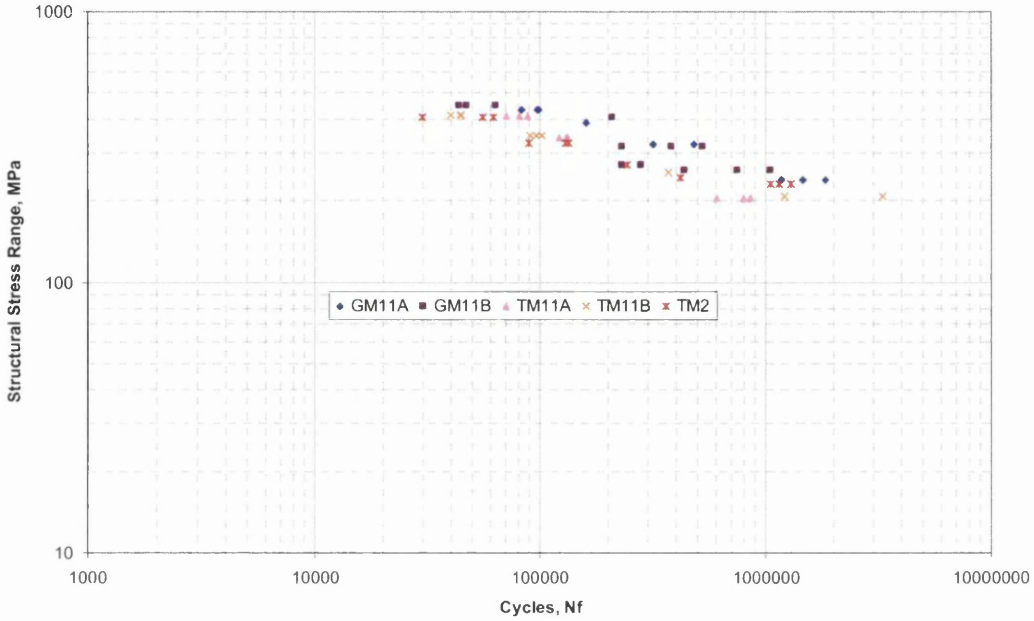

Figure A12.6.1: Stress–Life Master Curve Conversion for All Weld Toe Failures

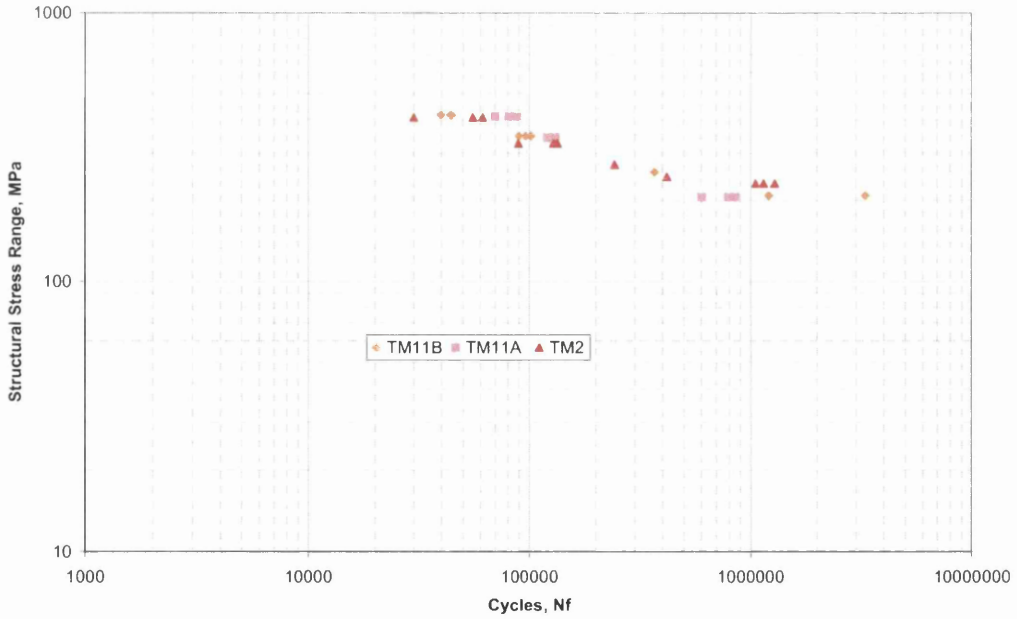

Figure A12.6.2: Stress–Life Master Curve Conversion for TKA Weld Toe Failure

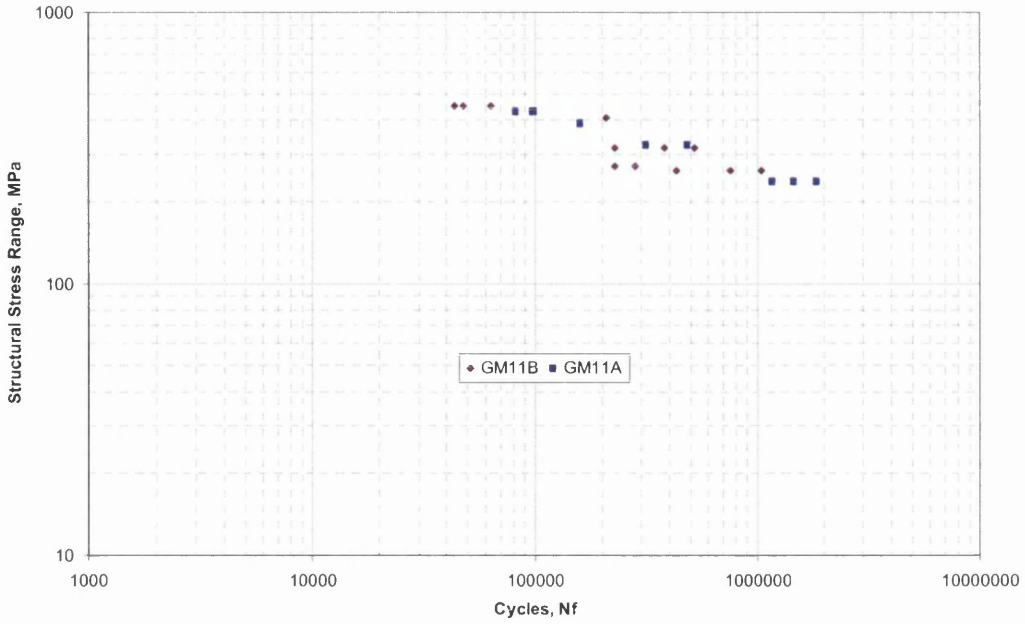

Figure A12.6.3: Stress–Life Master Curve Conversion for GKN Weld Toe Failure

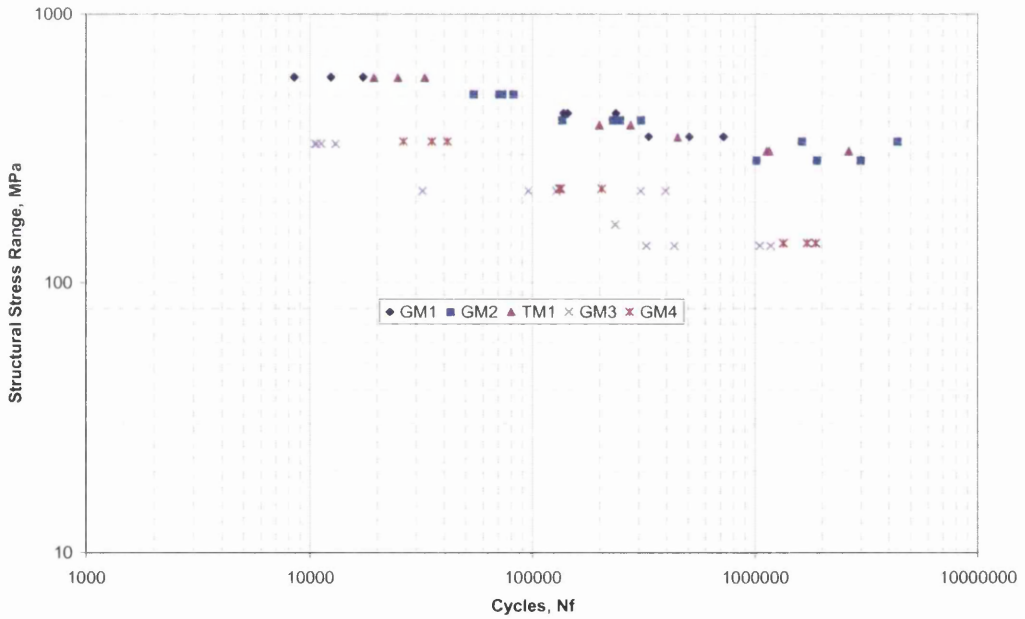

Figure A12.6.4: Stress–Life Master Curve Conversion for All Weld Throat Failures

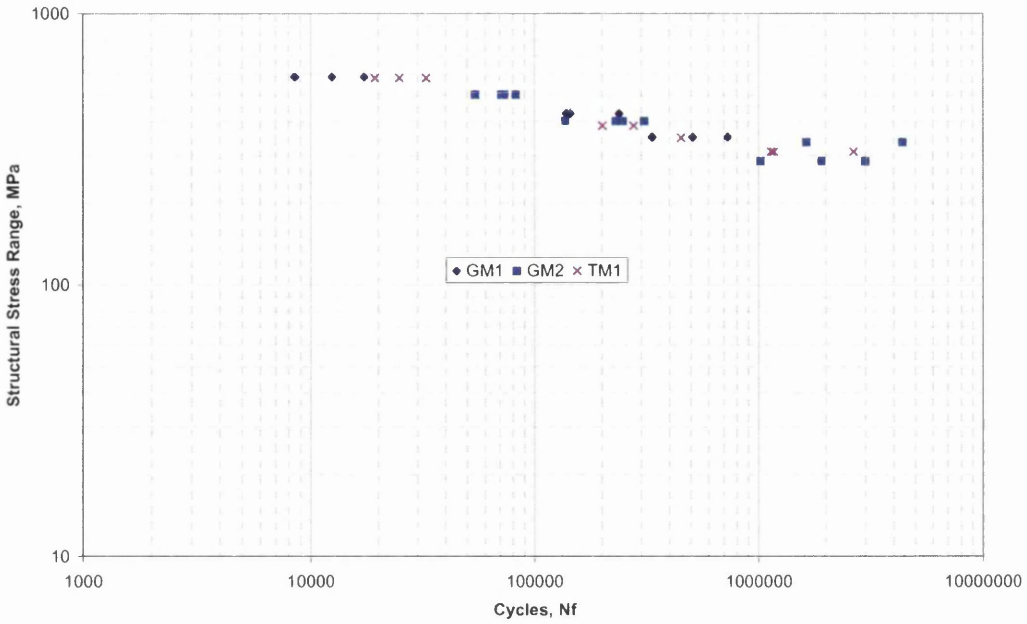

Figure A12.6.5: Stress–Life Master Curve Conversion for All Weld Interface Failures

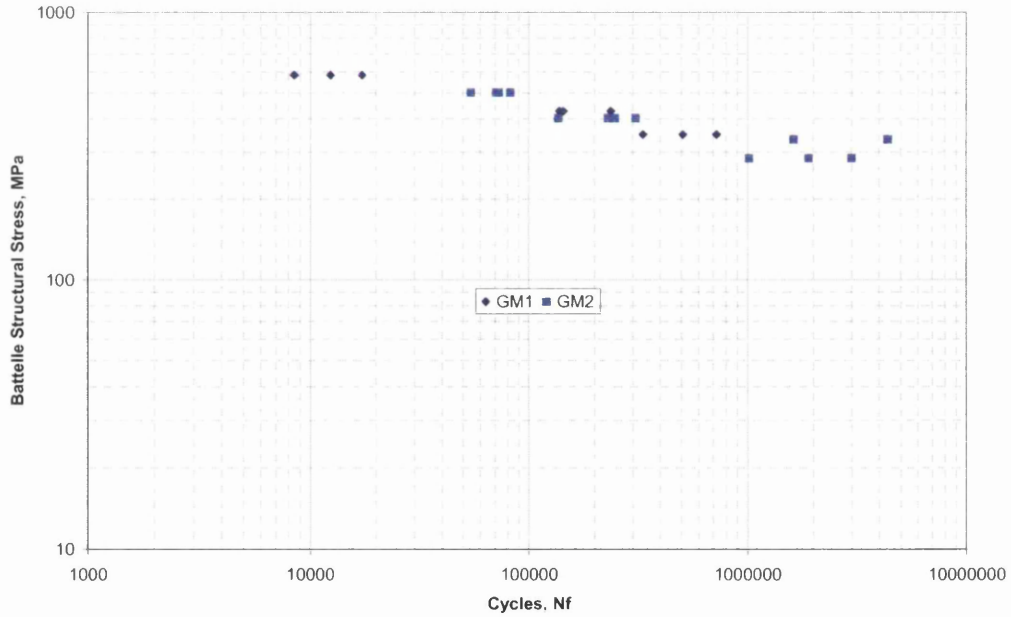

Figure A12.6.6: Stress–Life Master Curve Conversion for GKN Interface Weld Failures

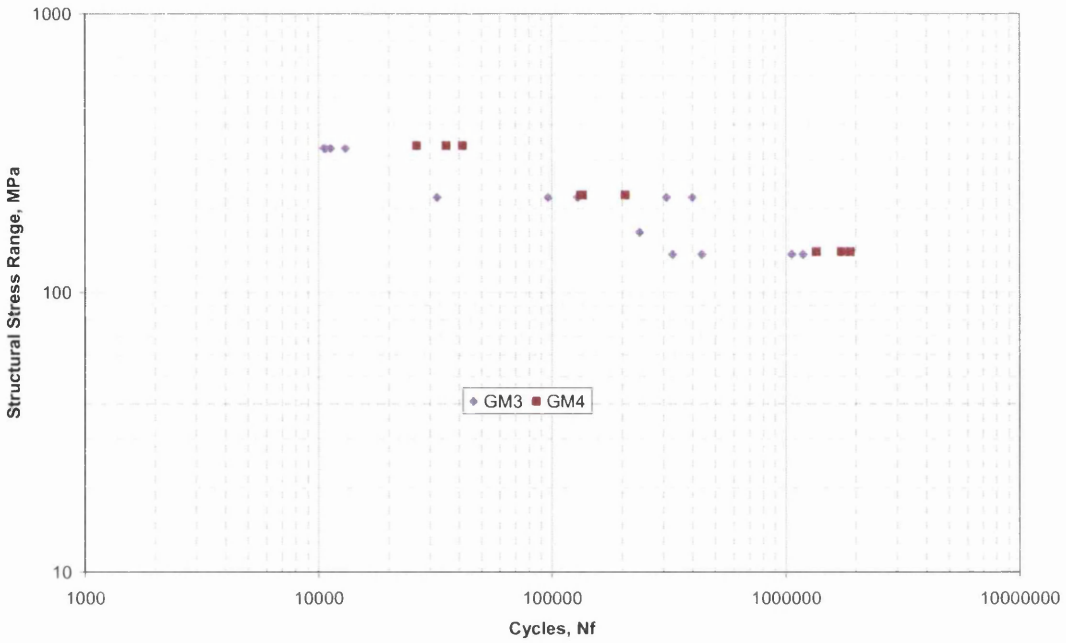

Figure A12.6.7: Stress–Life Master Curve Conversion for All Weld Throat Failures

Table A12.6.1: Battelle Manual Structural Stress Master S-N Curve Parameters

$$\Delta\sigma = aN_f^b$$

Battelle Method Structural Stress				
Failure Location	**Survival**	**a**	**b**	**SE log(Nf)**
Toe Failure	50%	5561.9	-0.233	0.2269
	99.87%	3859.9	-0.233	
Interface Failure	50%	2526.4	-0.1483	0.2157
	99.87%	2025.5	-0.1483	
Throat Failure	50%	3096.1	-0.2257	0.3078
	99.87%	1915.9	-0.2257	

15.9.2 FLOW Structural Stress

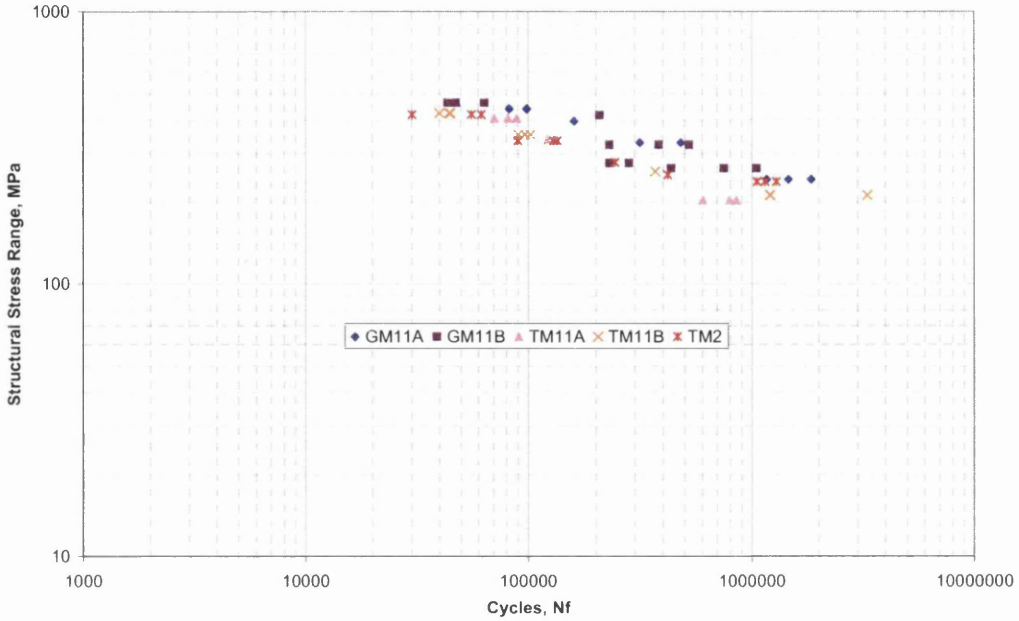

Figure A12.6.8: Stress-Life Master Curve Conversion for All Weld Toe Failures

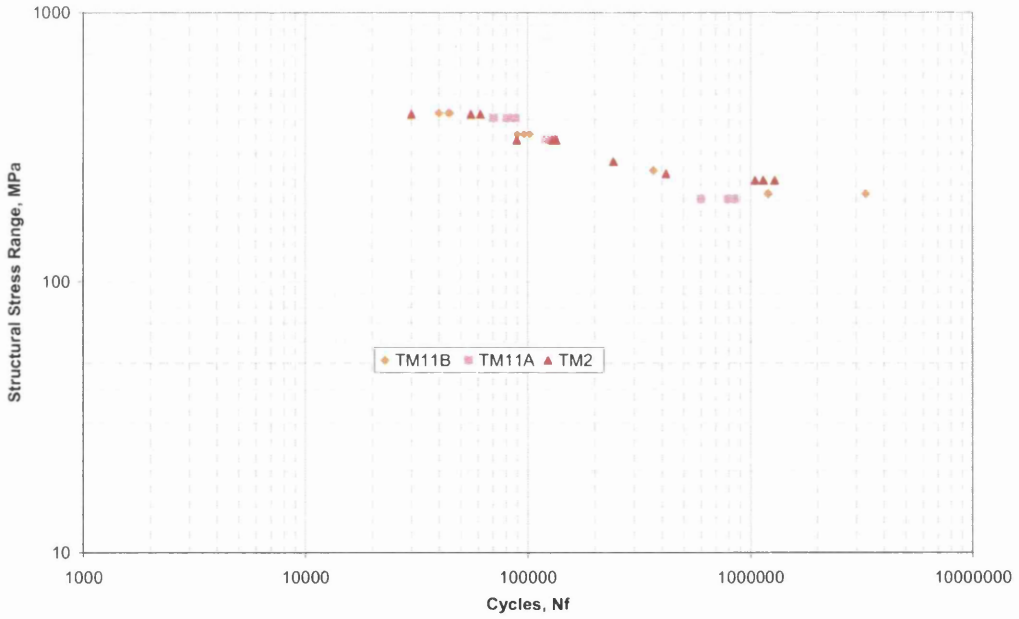

Figure A12.6.9: Stress–Life Master Curve Conversion for TKA Weld Toe Failures

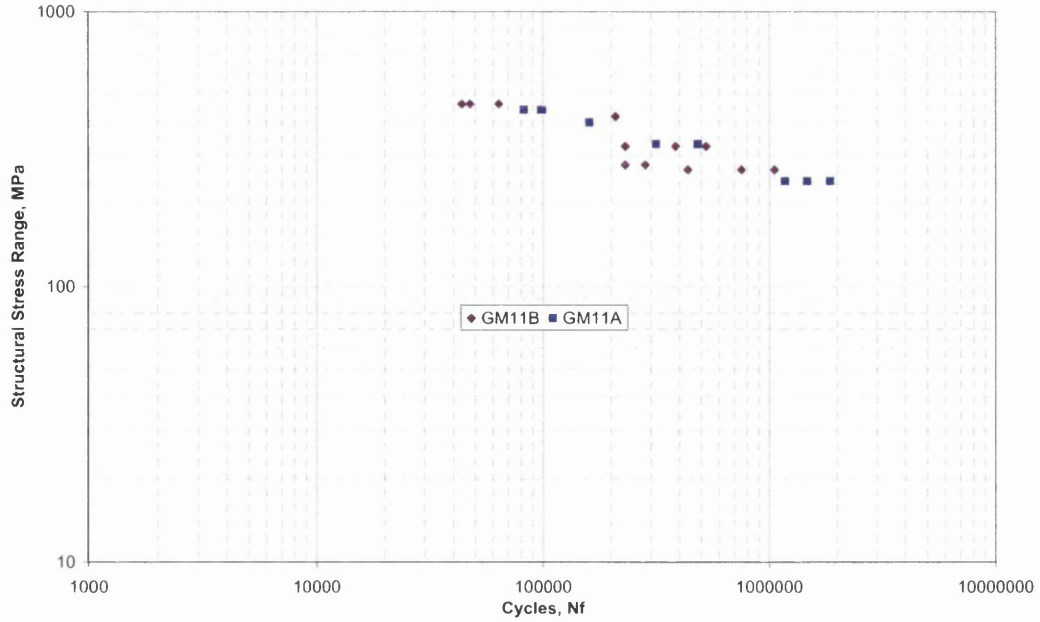

Figure A12.6.10: Stress–Life Master Curve Conversion for GKN Weld Toe Failures

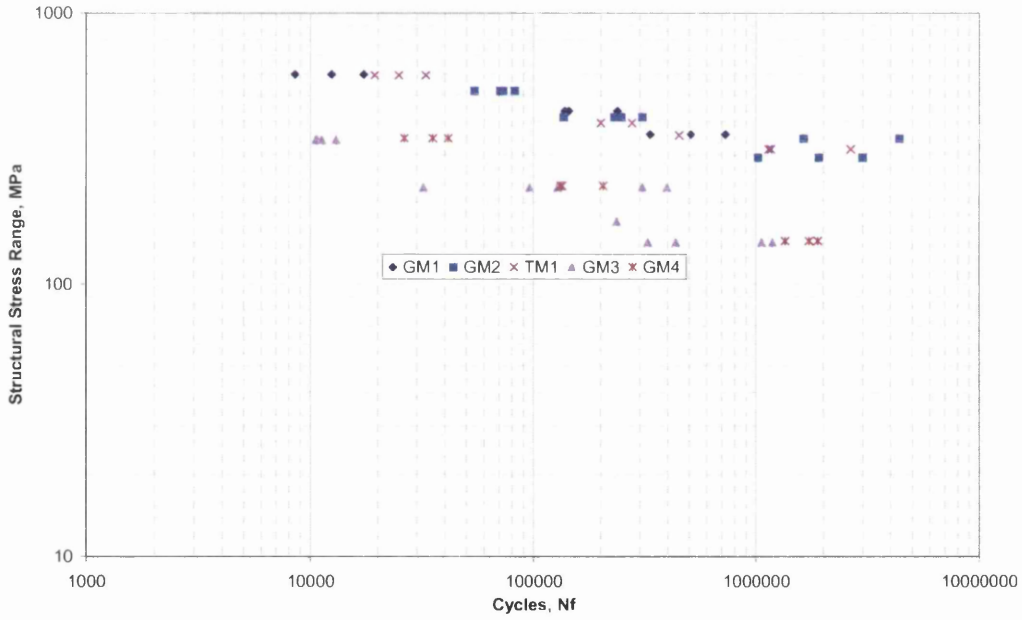

Figure A12.6.11: Stress–Life Master Curve Conversion for All Weld Throat Failures

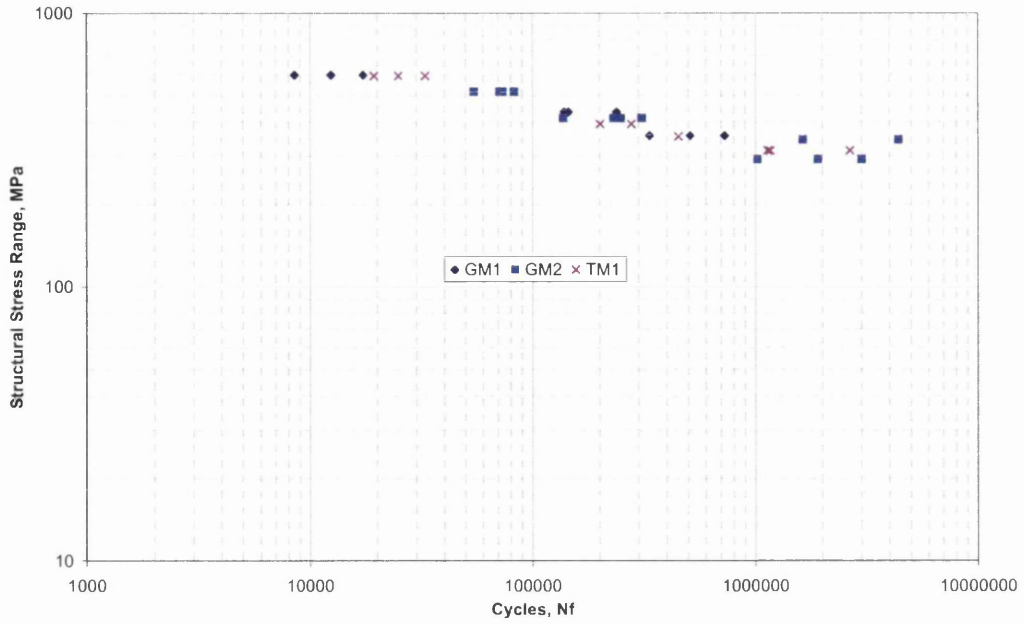

Figure A12.6.12: Stress–Life Master Curve Conversion for All Weld Interface Failures

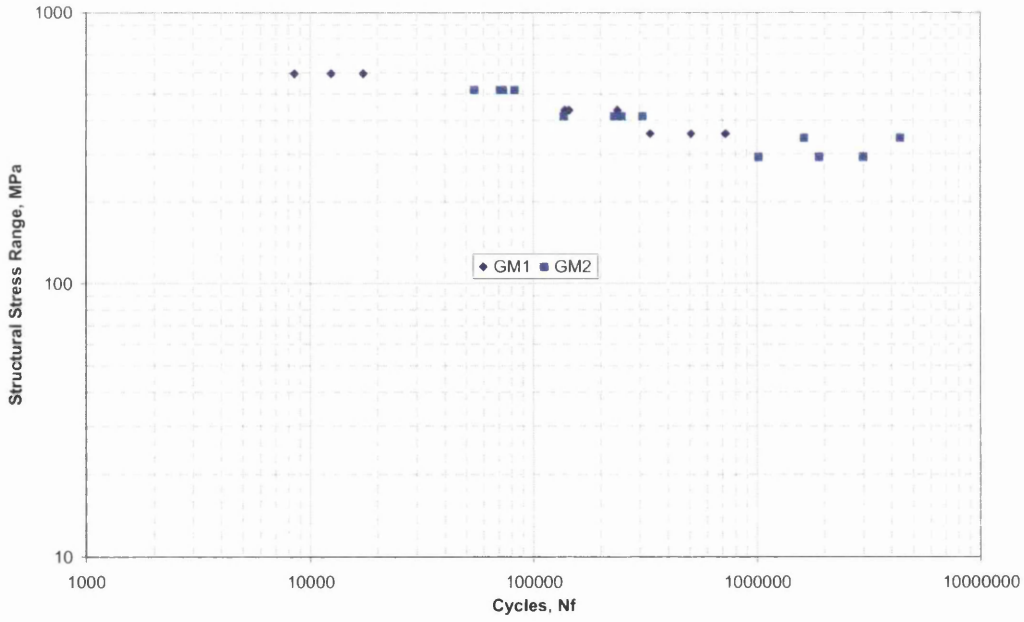

Figure A12.6.13: Stress–Life Master Curve Conversion for GKN Weld Interface Failures

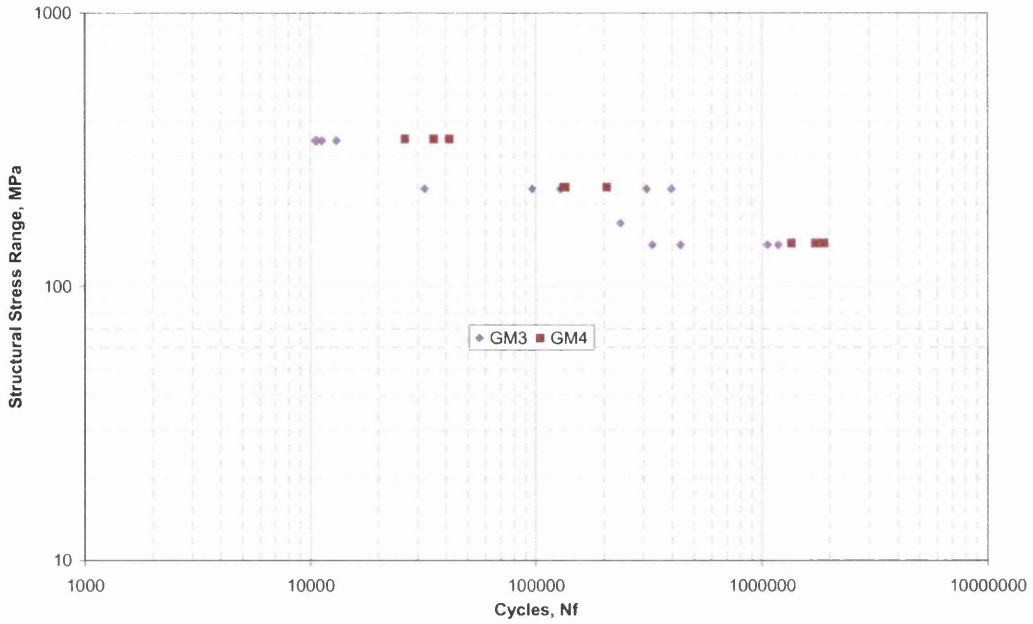

Figure A12.6.14: Stress–Life Master Curve Conversion for All Weld Throat Failures

Table A12.6.2: Battelle FLOW Structural Stress Master S-N Curve Parameters

$$\Delta\sigma = aN_f^b$$

Battelle Method Structural Stress				
Failure Location	**Survival**	**a**	**b**	**SE log(Nf)**
Toe Failure	50%	5763.9	-0.2347	0.2316
	99.87%	3959.4	-0.2347	
Interface Failure	50%	2583.3	-0.1482	0.2194
	99.87%	2063.6	-0.1482	
Throat Failure	50%	3178.4	-0.2257	0.3040
	99.87%	1981.6	-0.225	

15.9.3 Verity Structural Stress

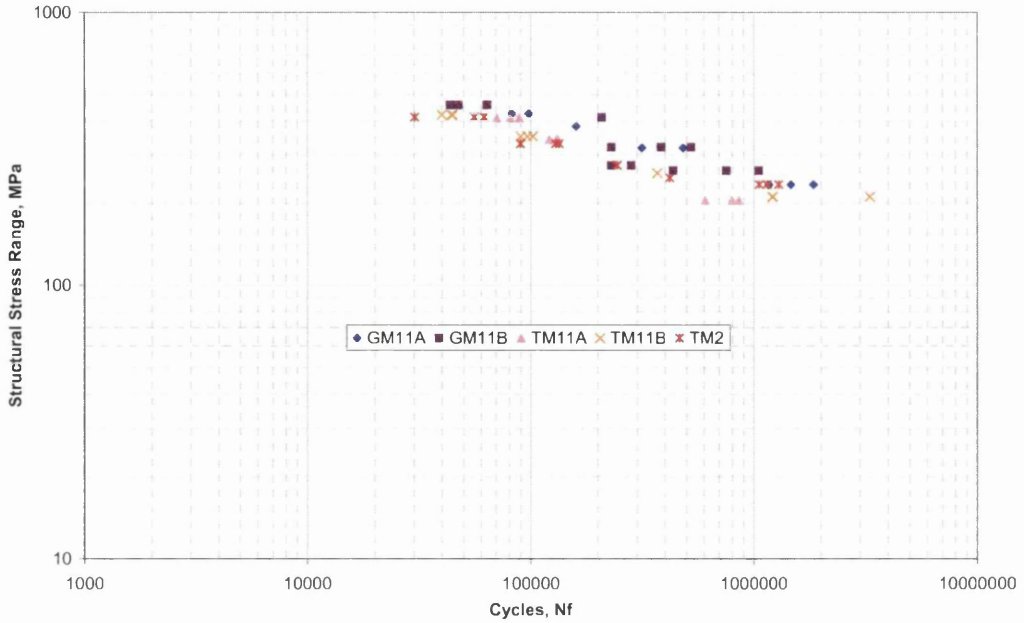

Figure A12.6.15: Stress-Life Master Curve Conversion for All Weld Toe Failures

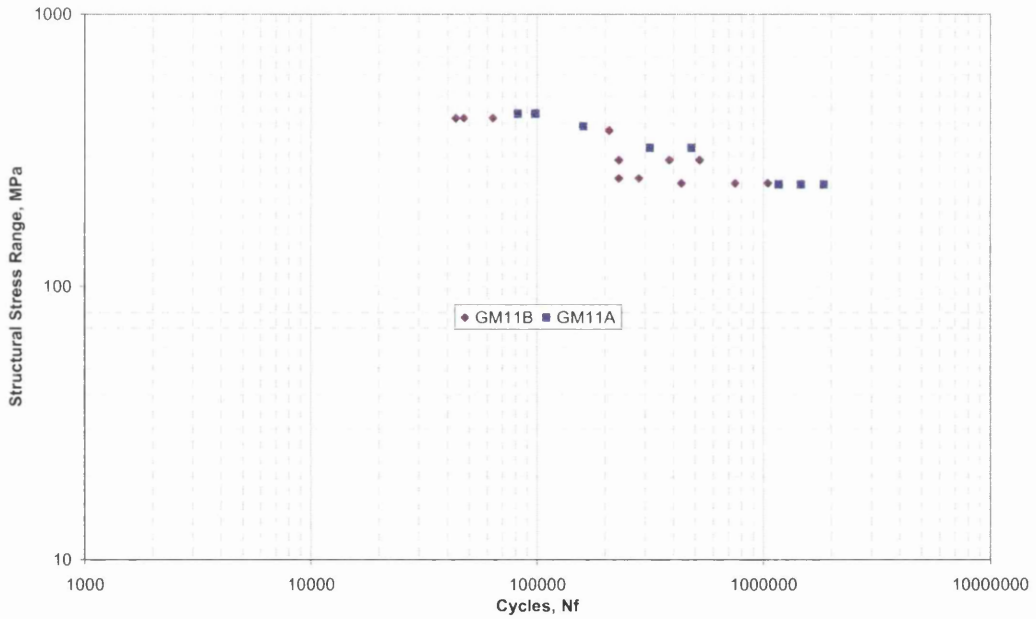

Figure A12.6.16: Stress-Life Master Curve Conversion for GKN Weld Toe Failures

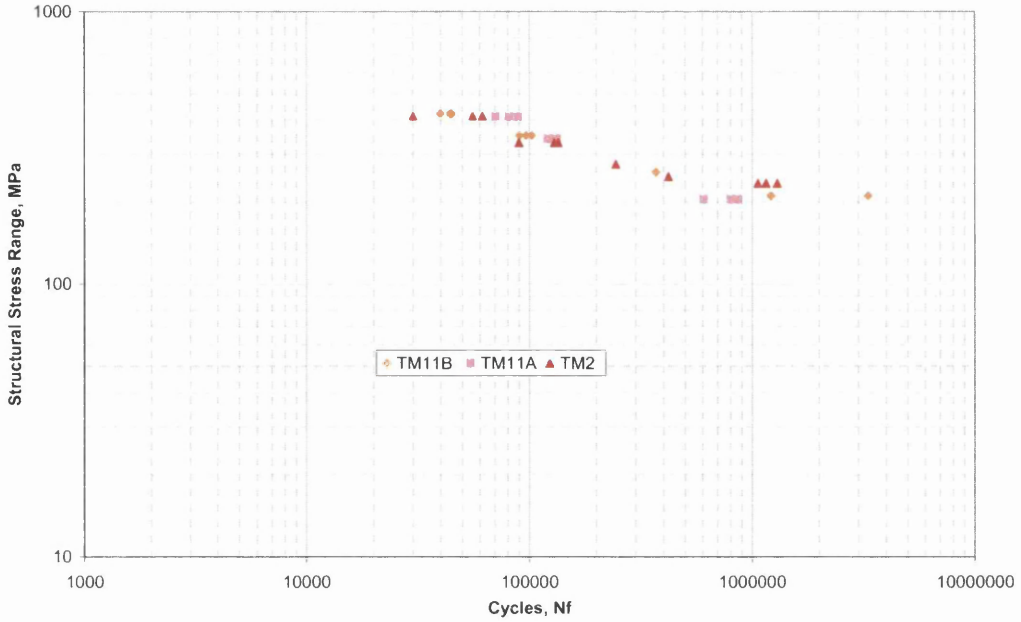

Figure A12.6.17: Stress-Life Master Curve Conversion for TKA Weld Toe Failures

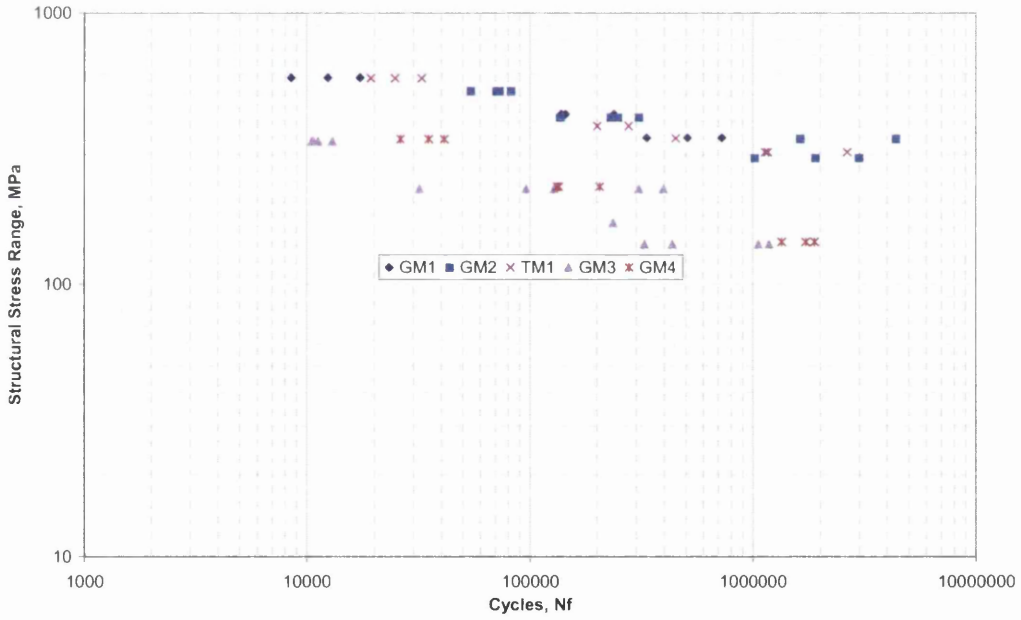

Figure A12.6.18: Stress-Life Master Curve Conversion for All Weld Throat Failures

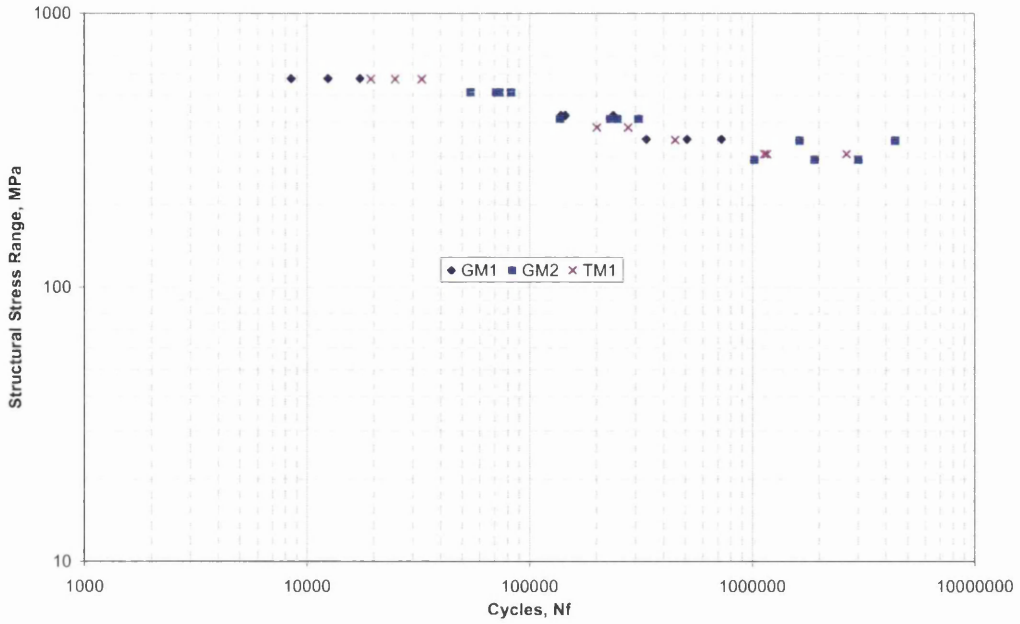

Figure A12.6.19: Stress-Life Master Curve Conversion for All Weld Interface Failures

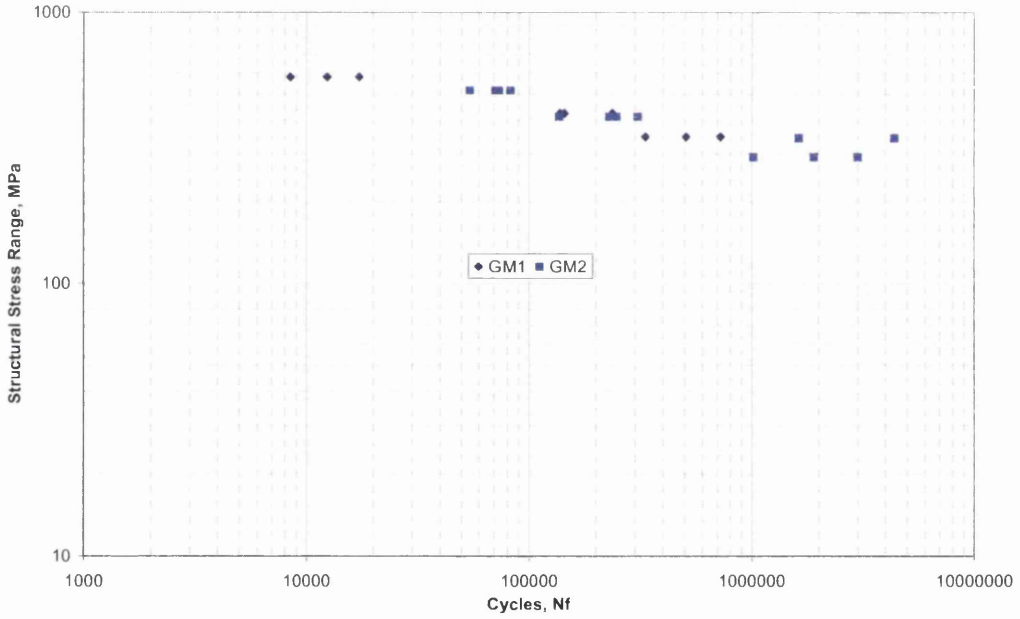

Figure A12.6.20: Stress-Life Master Curve Conversion for GKN Weld Interface Failures

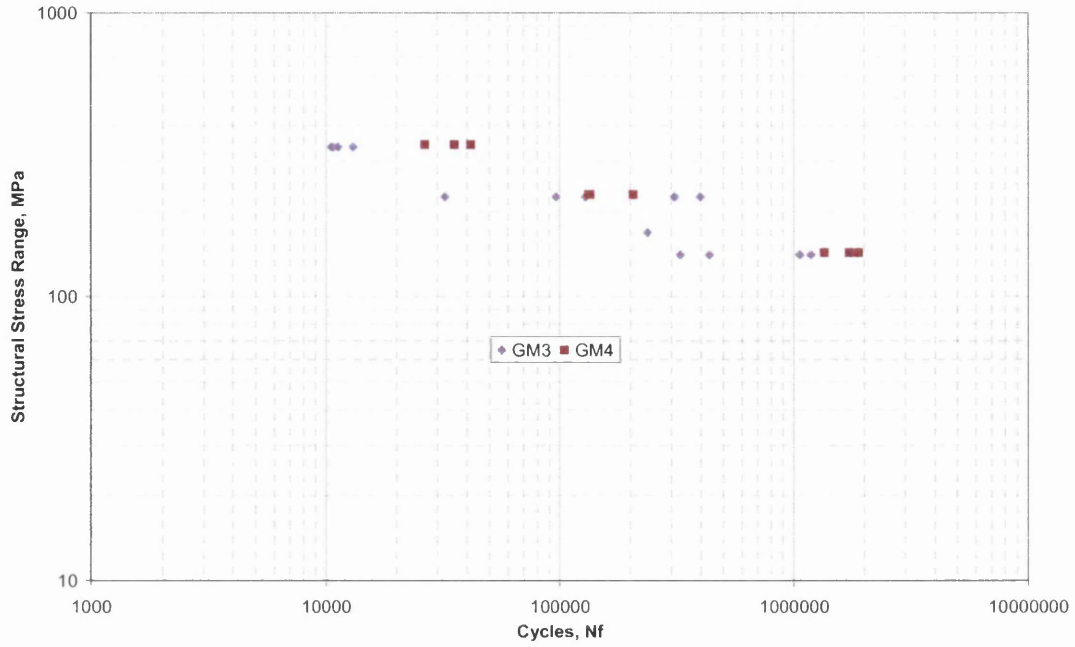

Figure A12.6.21: Stress-Life Master Curve Conversion for All Weld Throat Failures

Table A12.6.3: Battelle Verity Structural Stress Master S-N Curve Parameters

$$\Delta\sigma = aN_f^b$$

Battelle Method Structural Stress				
Failure Location	**Survival**	**a**	**b**	**SE log(Nf)**
Toe Failure	50%	5437.8	-0.2308	0.2186
	99.87%	3837.3	-0.2308	
Interface Failure	50%	2545	-0.1483	0.2344
	99.87%	2001.7	-0.1483	
Throat Failure	50%	3162.5	-0.2255	0.3068
	99.87%	1960.9	-0.2255	

15.10 Appendix 10 Battelle Equivalent Structural Stress

15.10.1 Manual Equivalent Structural Stress

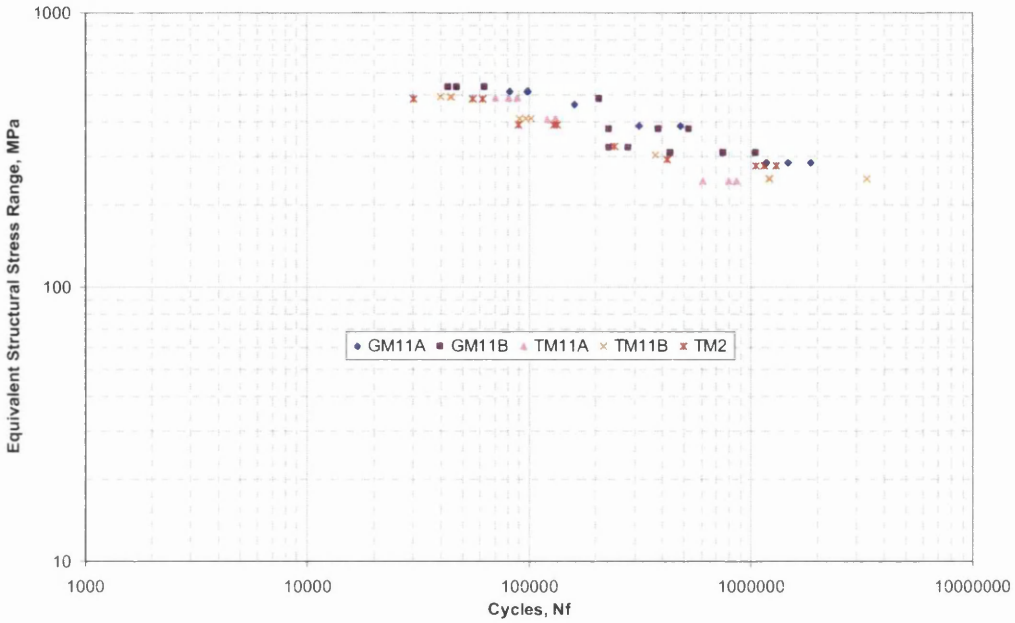

Figure A12.6.22: Stress-Life Master Curve Conversion of All Weld Toe Failures

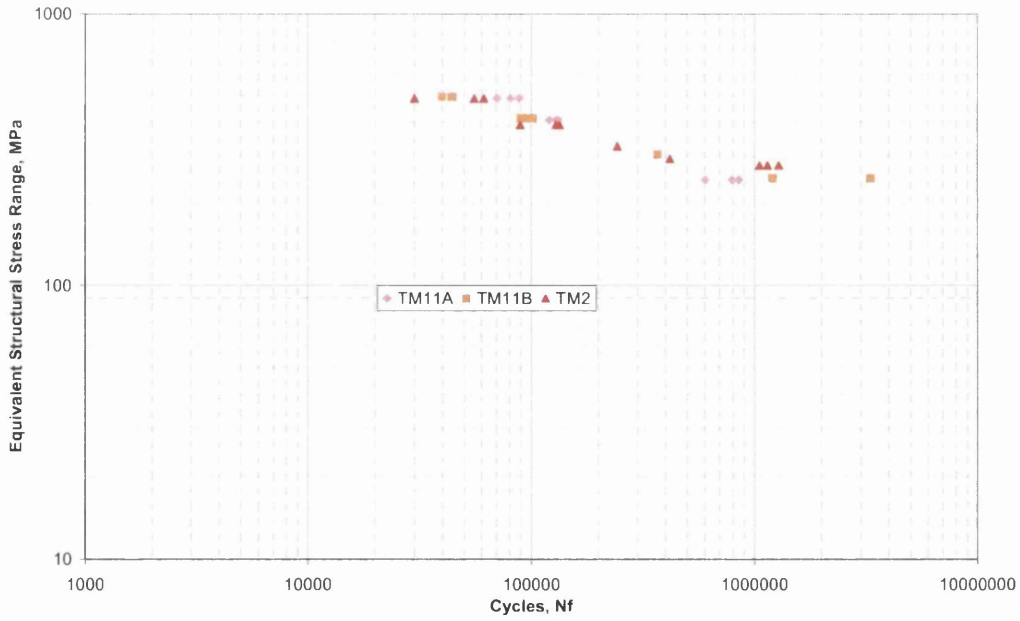

Figure A12.6.23: Stress-Life Master Curve Conversion of TKA Weld Toe Failures

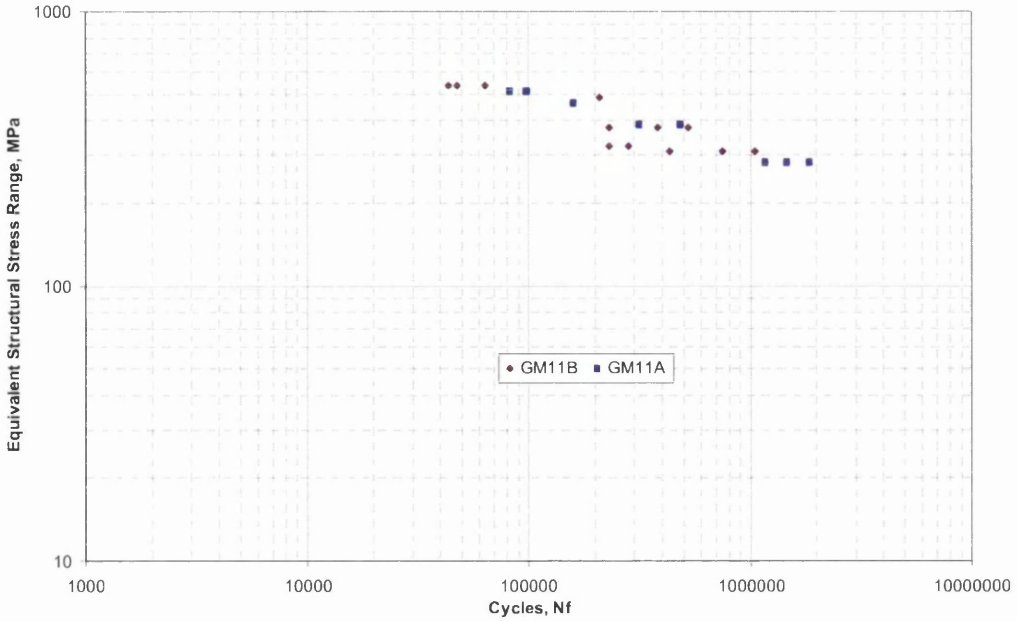

Figure A12.6.24: Stress-Life Master Curve Conversion of GKN Weld Toe Failures

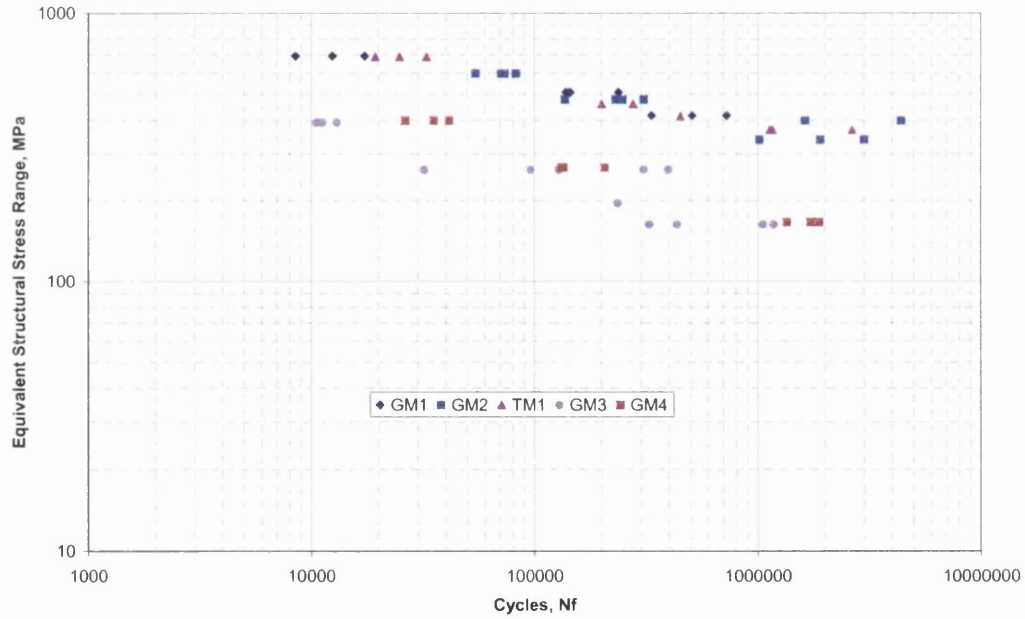

Figure A12.6.25: Stress-Life Master Curve Conversion of All Weld Throat Failures

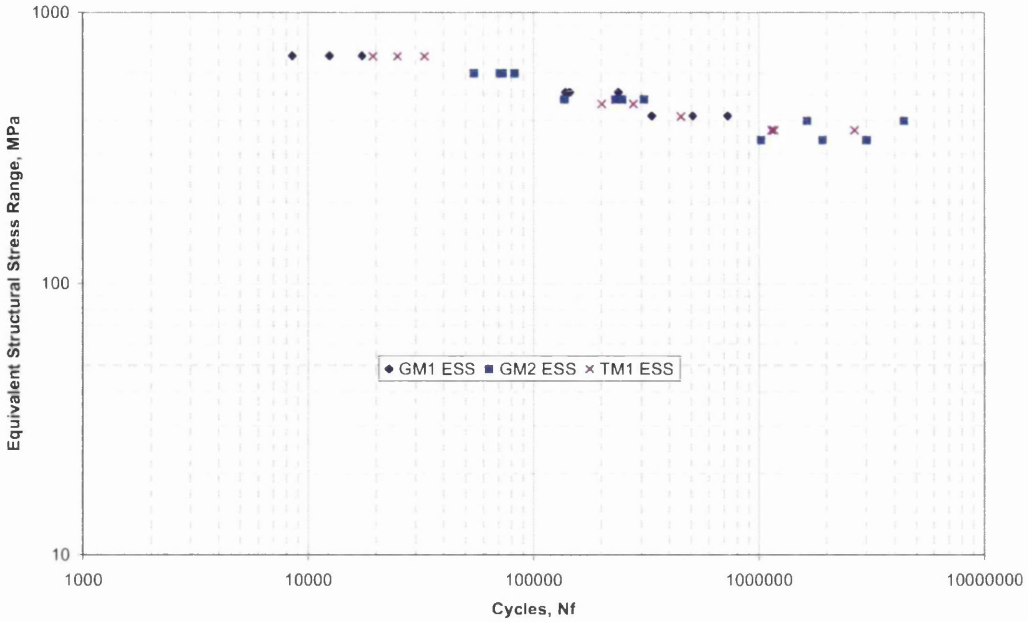

Figure A12.6.26: Stress-Life Master Curve Conversion of All Weld Interface Failures

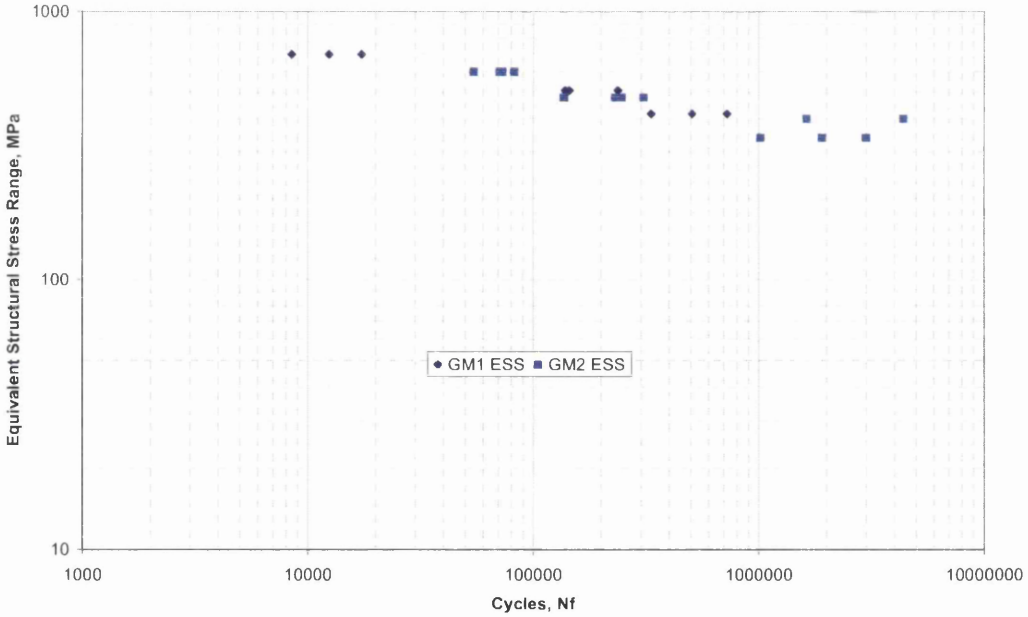

Figure A12.6.27: Stress-Life Master Curve Conversion of GKN Weld Interface Failures

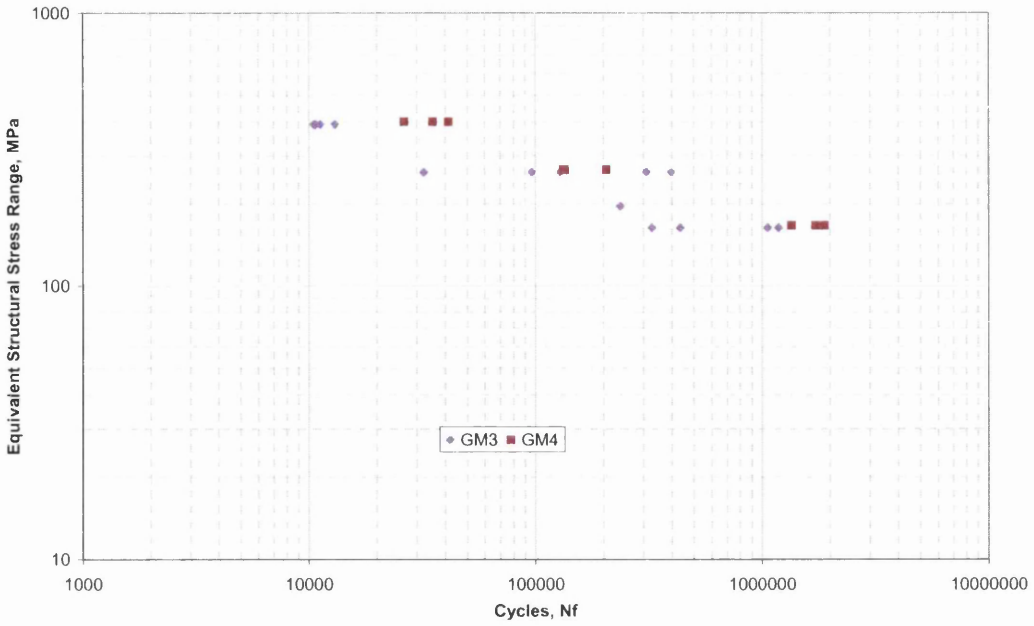

Figure A12.6.28: Stress-Life Master Curve Conversion of All Weld Throat Failures

Table A12.6.4: Battelle Manual Equivalent Structural Stress Master S-N Curve Parameters

$$\Delta\sigma = aN_f^b$$

Battelle Method Equivalent Structural Stress				
Failure Location	**Survival**	**a**	**b**	**SE log(Nf)**
Toe Failure	50%	6603.9	-0.2327	0.2262
	99.87%	4590.7	-0.2327	
Interface Failure	50%	3003.6	-0.1483	0.2150
	99.87%	2409.7	-0.1483	
Throat Failure	50%	3681.1	-0.2256	0.3072
	99.87%	2280.7	-0.2256	

15.10.2 FLOW Equivalent Structural Stress

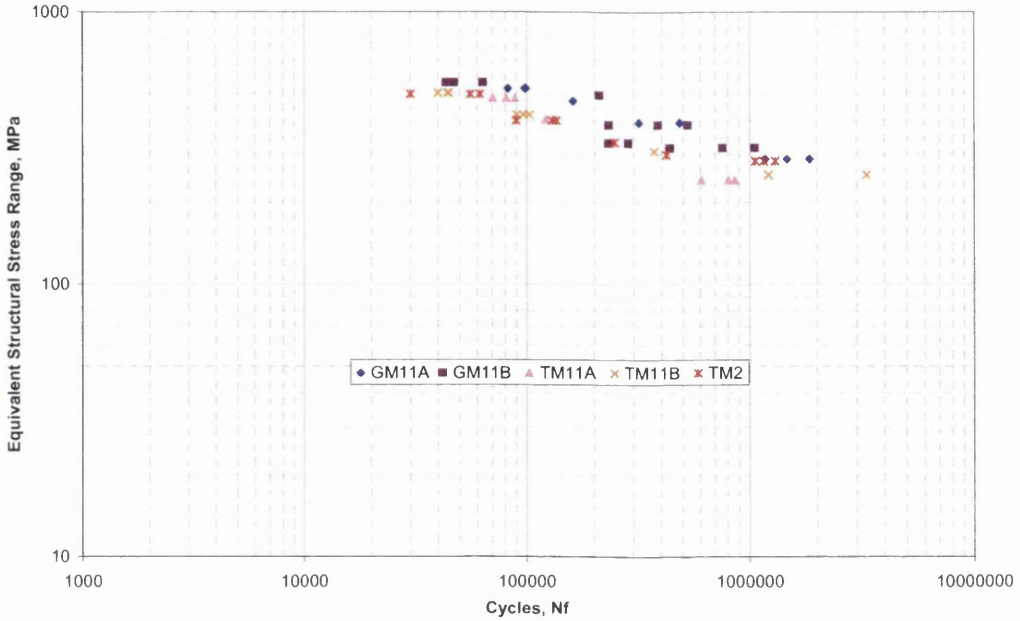

Figure A12.6.29: Stress-Life Master Curve Conversion of All Weld Toe Failures

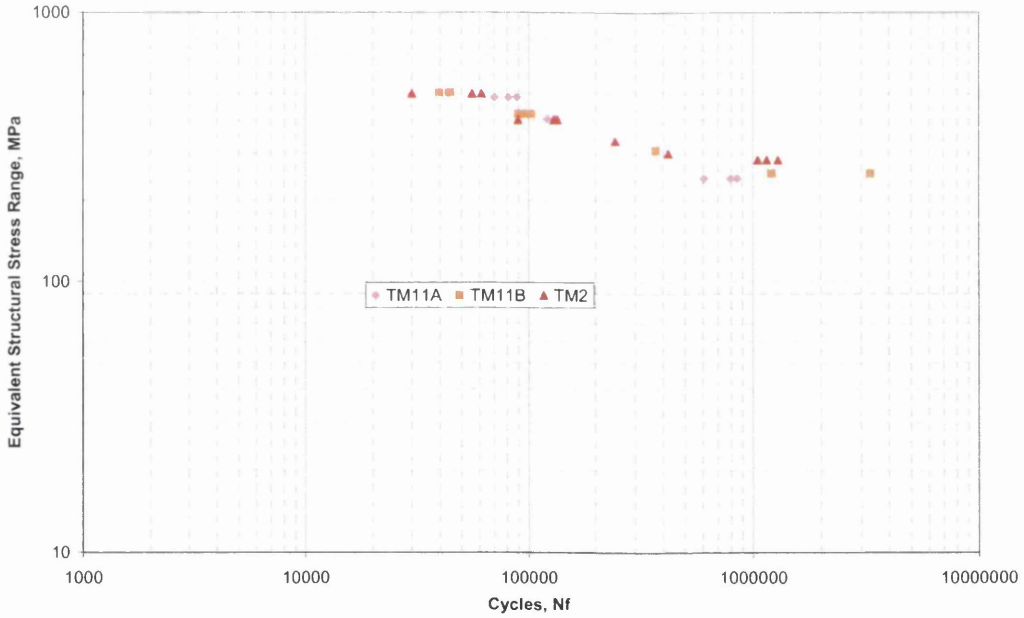

Figure A12.6.30: Stress-Life Master Curve Conversion of TKA Weld Toe Failures

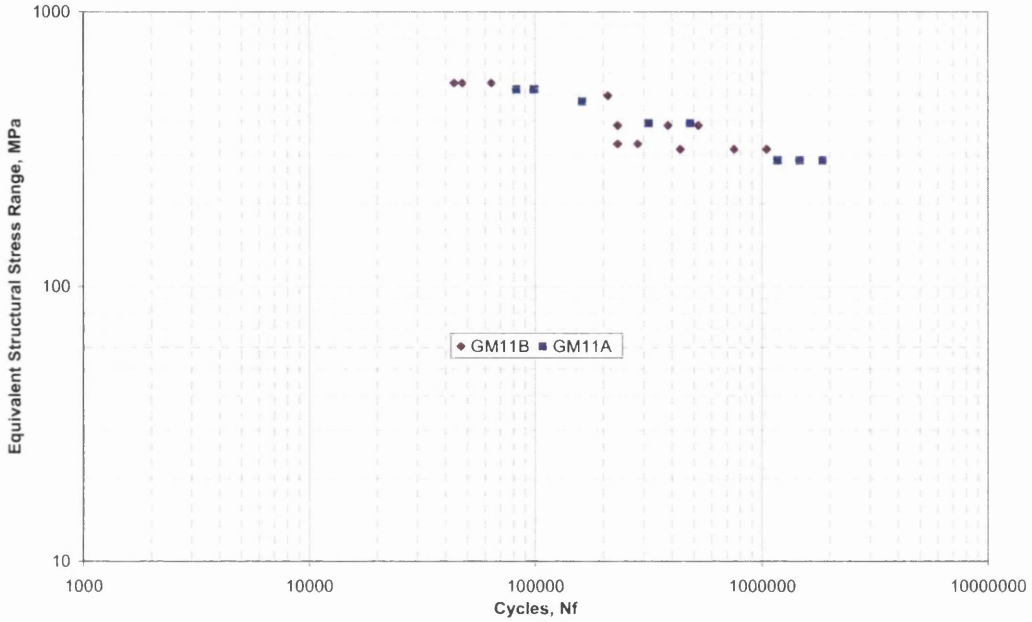

Figure A12.6.31: Stress-Life Master Curve Conversion of GKN Weld Toe Failures

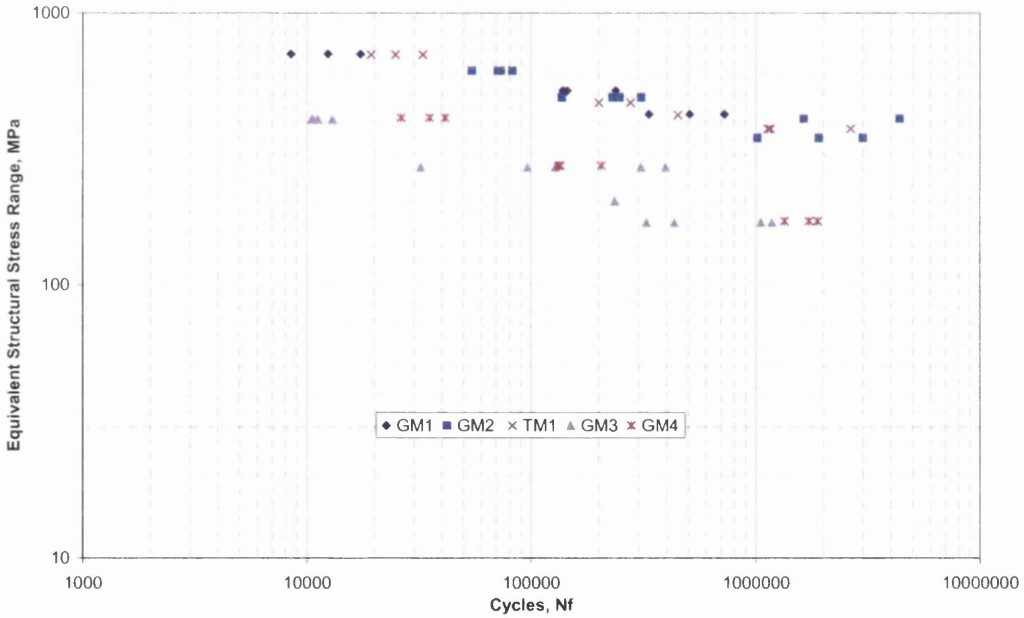

Figure A12.6.32: Stress-Life Master Curve Conversion of All Weld Throat Failures

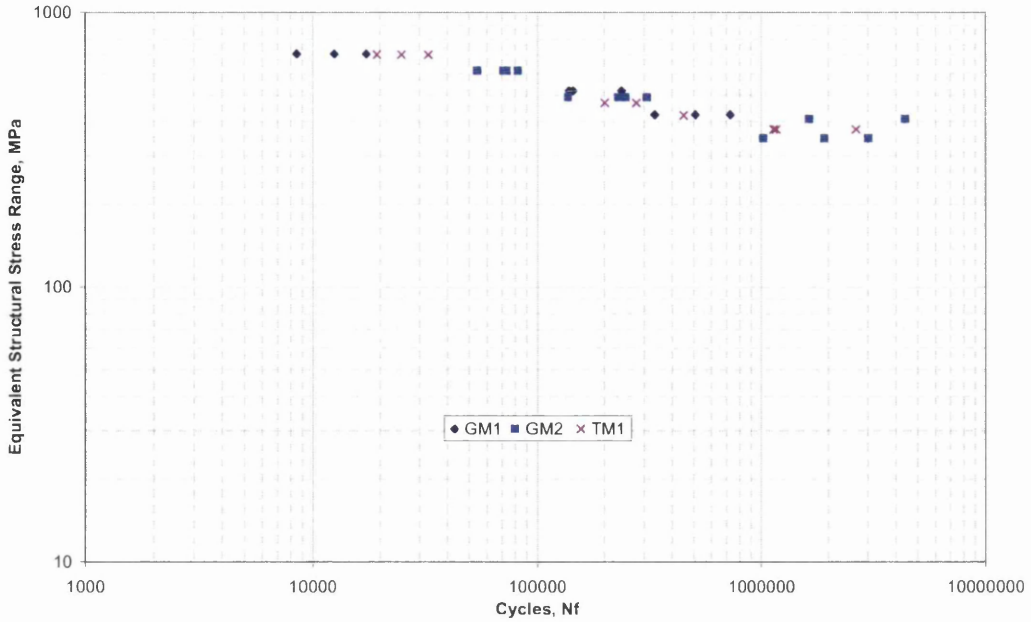

Figure A12.6.33: Stress-Life Master Curve Conversion of All Weld Interface Failures

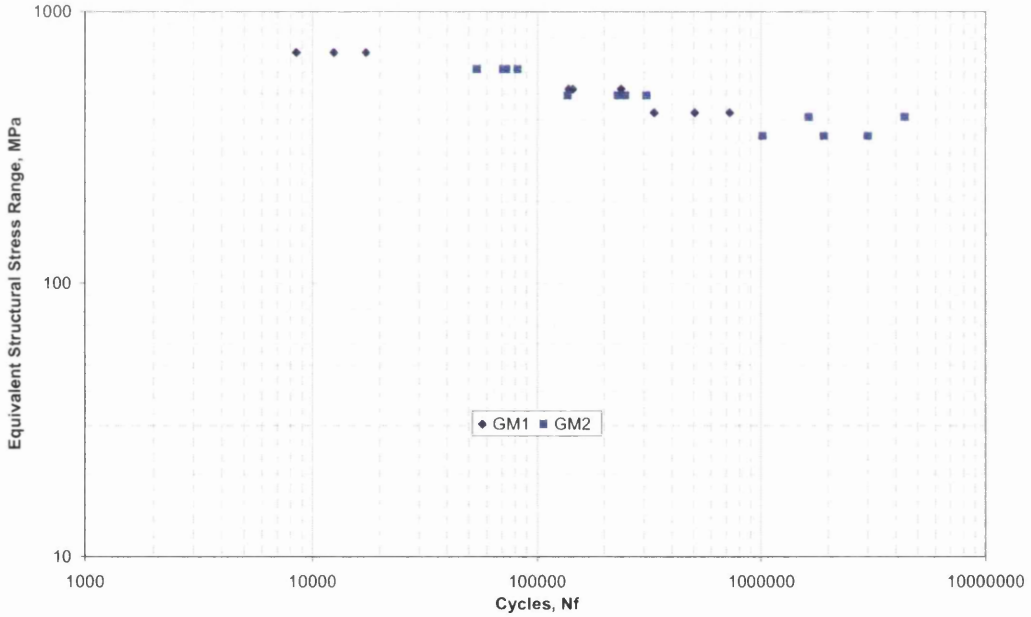

Figure A12.6.34: Stress-Life Master Curve Conversion of GKN Weld Interface Failures

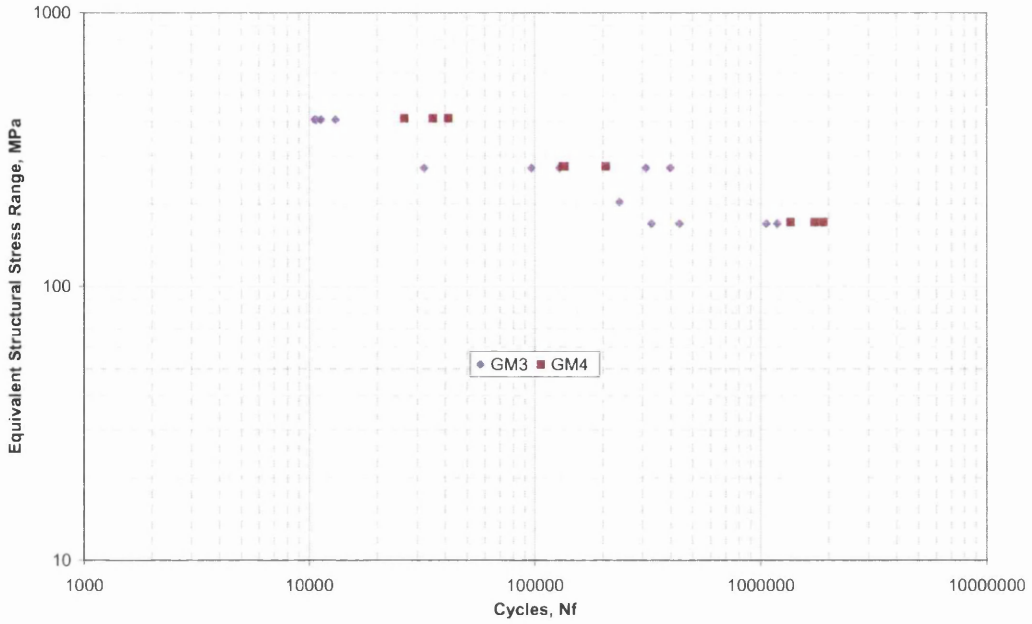

Figure A12.6.35: Stress-Life Master Curve Conversion of All Weld Throat Failures

Table A12.6.5: Battelle FLOW Equivalent Structural Stress Master S-N Curve Parameters

$$\Delta\sigma = aN_f^b$$

Battelle Method Equivalent Structural Stress				
Failure Location	**Survival**	**a**	**b**	**SE log(Nf)**
Toe Failure	50%	6865.6	-0.2347	0.2318
	99.87%	4714.8	-0.2347	
Interface Failure	50%	3070.4	-0.1482	0.2185
	99.87%	2454.9	-0.1482	
Throat Failure	50%	3779.3	-0.2249	0.3034
	99.87%	2359	-0.2249	

15.10.3 Verity Equivalent Structural Stress

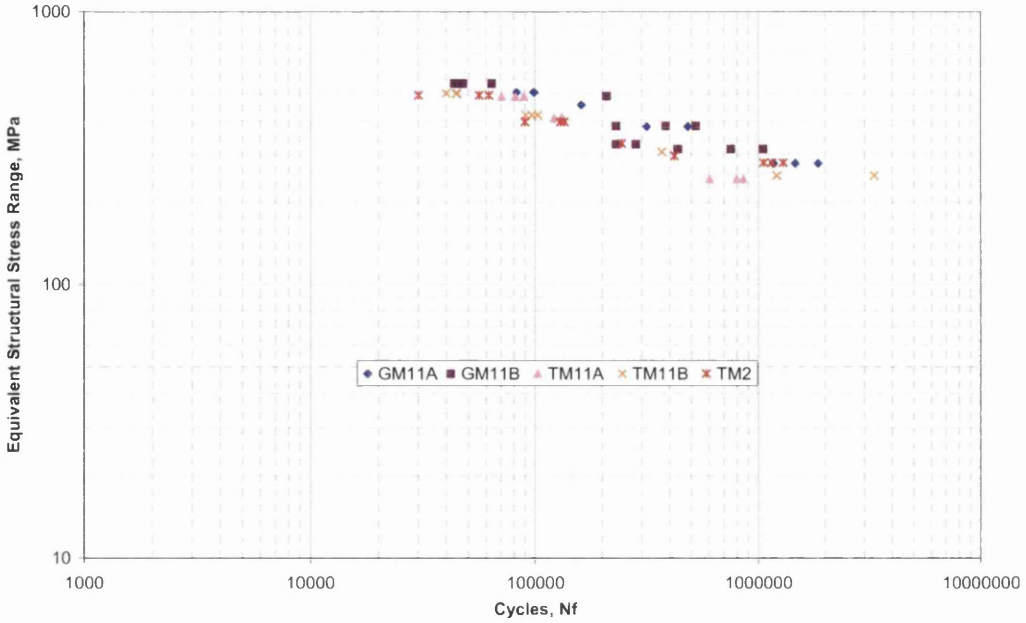

Figure A12.6.36: Stress-Life Master Curve Conversion of All Weld Toe Failures

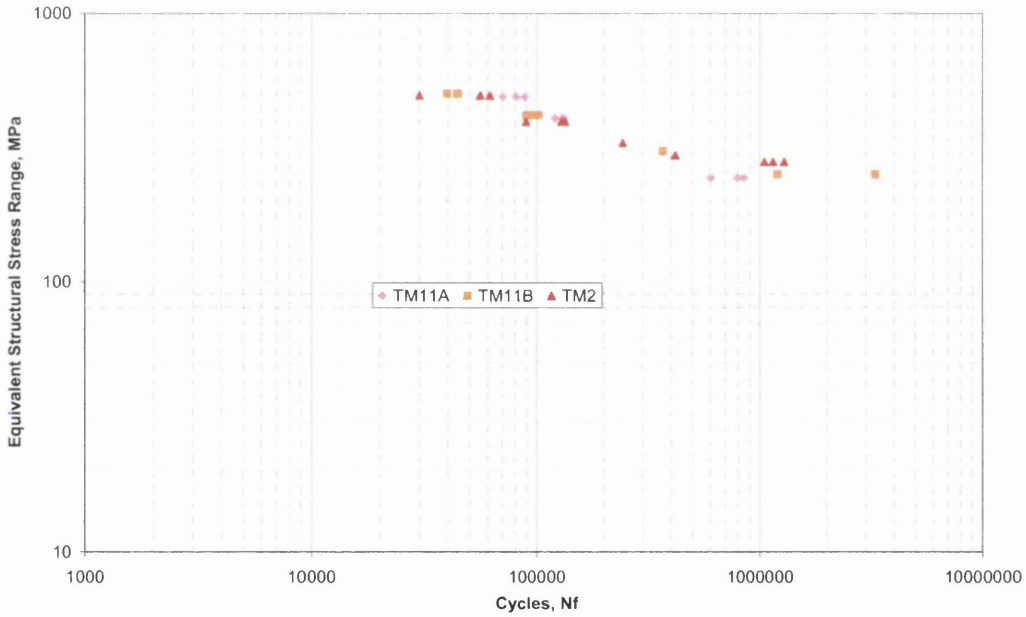

Figure A12.6.37: Stress-Life Master Curve Conversion of TKA Weld Toe Failures

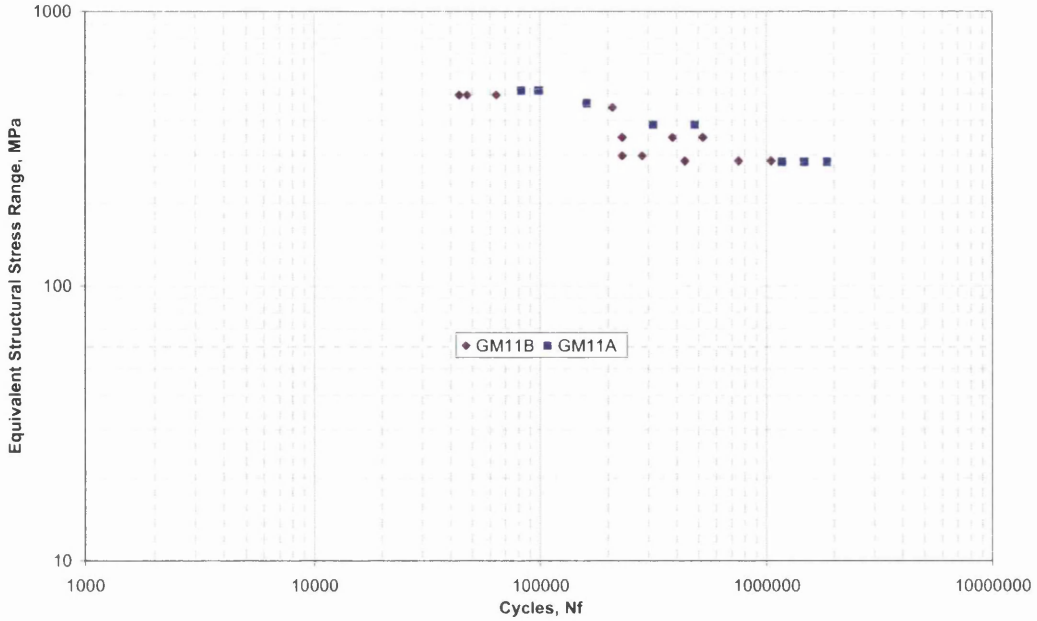

Figure A12.6.38: Stress-Life Master Curve Conversion of GKN Weld Toe Failures

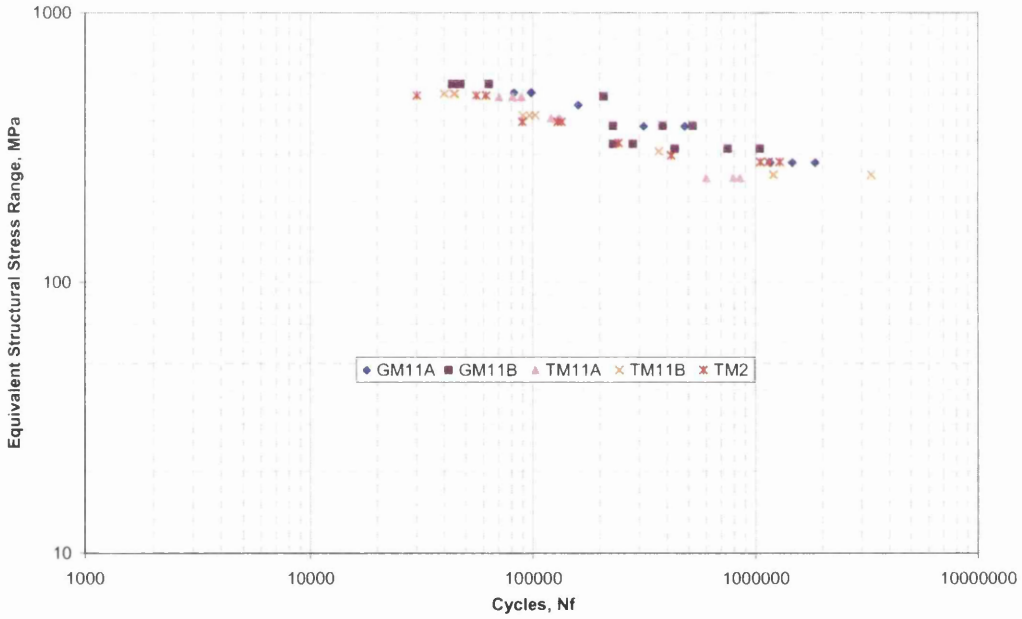

Figure A12.6.39: Stress-Life Master Curve Conversion of All Weld Throat Failures

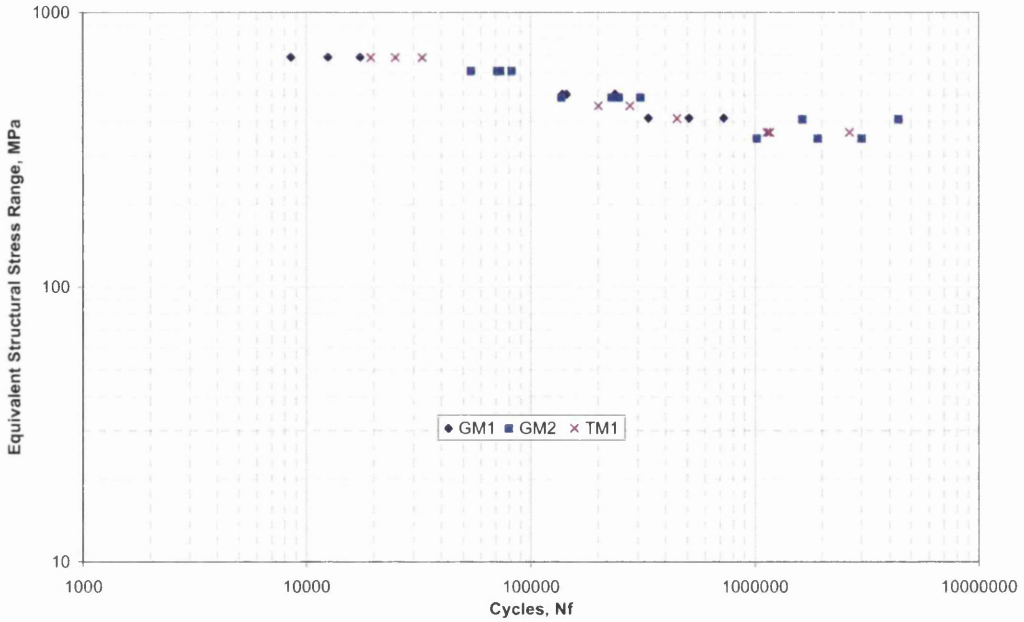

Figure A12.6.40: Stress-Life Master Curve Conversion of All Weld Interface Failures

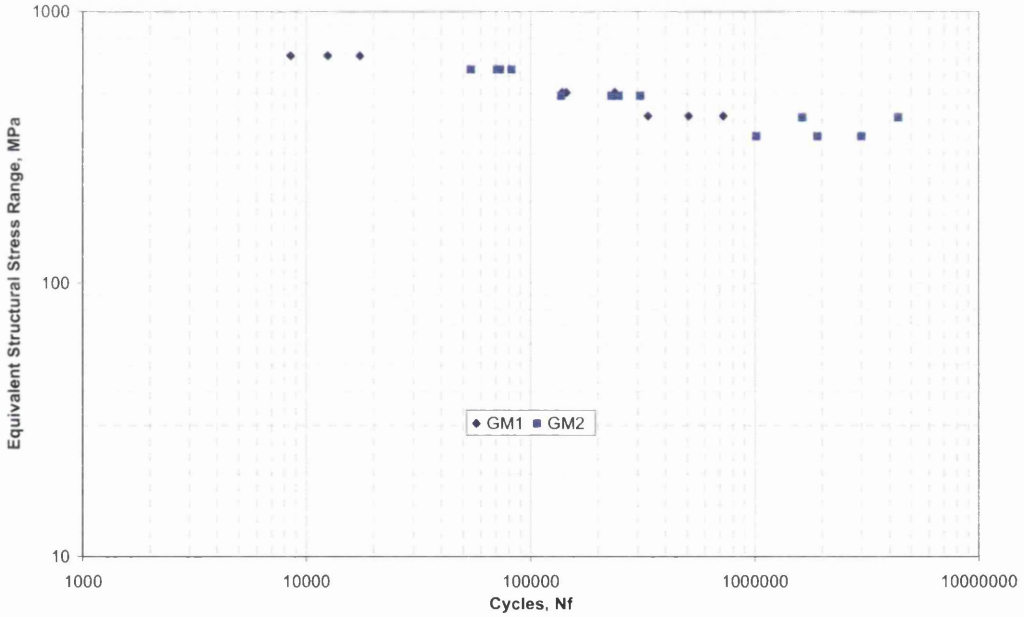

Figure A12.6.41: Stress-Life Master Curve Conversion of GKN Weld Interface Failures

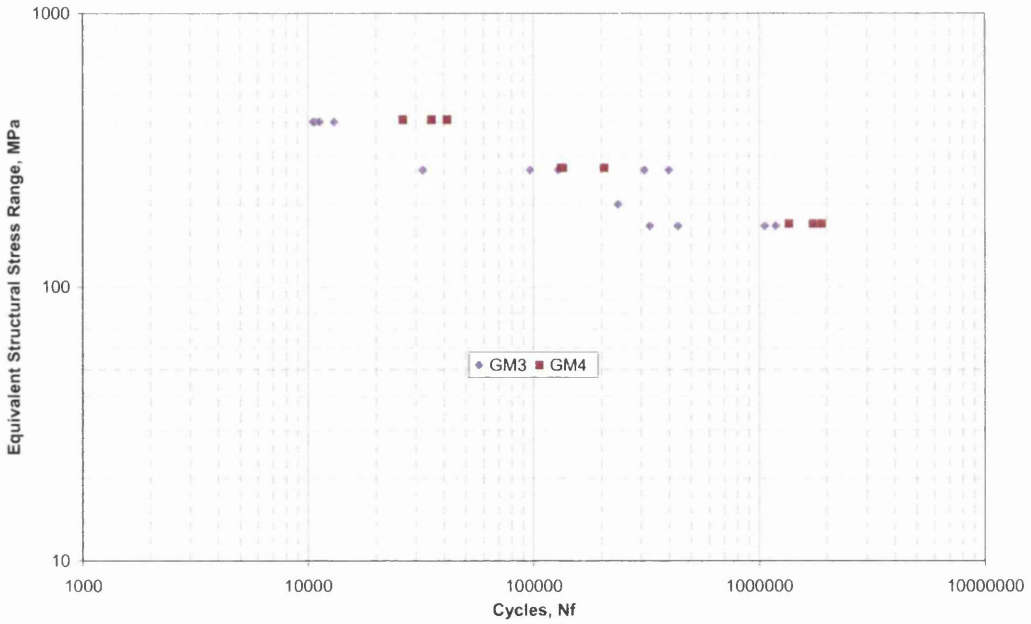

Figure A12.6.42: Stress-Life Master Curve Conversion of All Weld Throat Failures

Table A12.6.6: Battelle Verity Equivalent Structural Stress Master S-N Curve Parameters

$$\Delta\sigma = aN_f^b$$

Battelle Method Equivalent Structural Stress				
Failure Location	**Survival**	**a**	**b**	**SE log(Nf)**
Toe Failure	50%	6459.4	-0.2306	0.2179
	99.87%	4565.2	-0.2306	
Interface Failure	50%	3022.4	-0.1483	0.2331
	99.87%	2380.5	-0.1483	
Throat Failure	50%	3790.1	-0.2262	0.3090
	99.87%	2338.7	-0.2262	

15.11 Appendix 11 Battelle FE Stress Location – Edge Effects

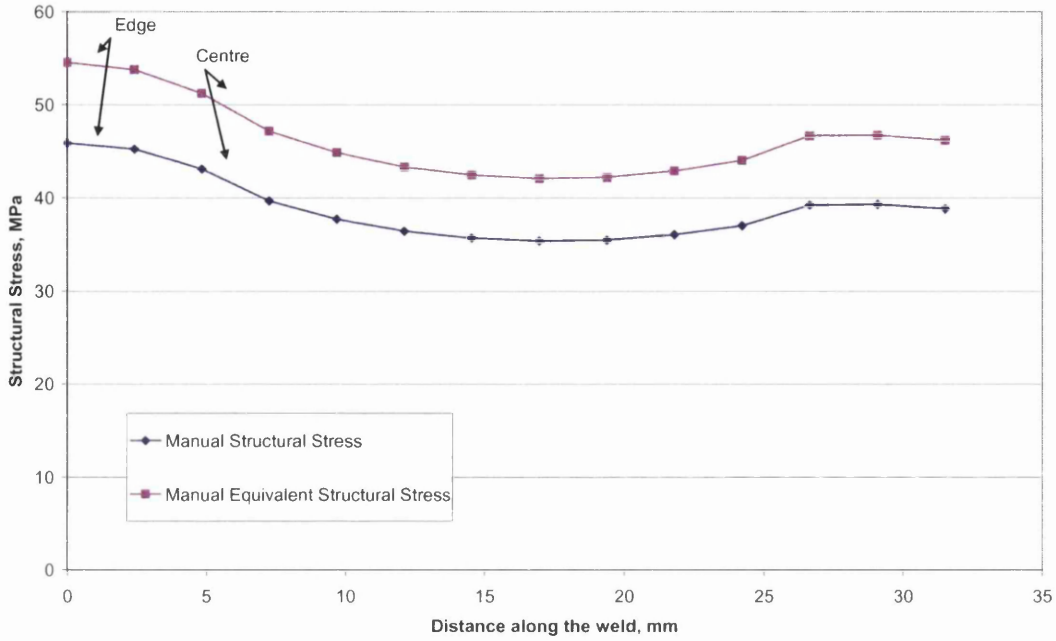

Figure A12.6.43: Location of FE Stresses Used for Conversion of S-N Curves of GM1

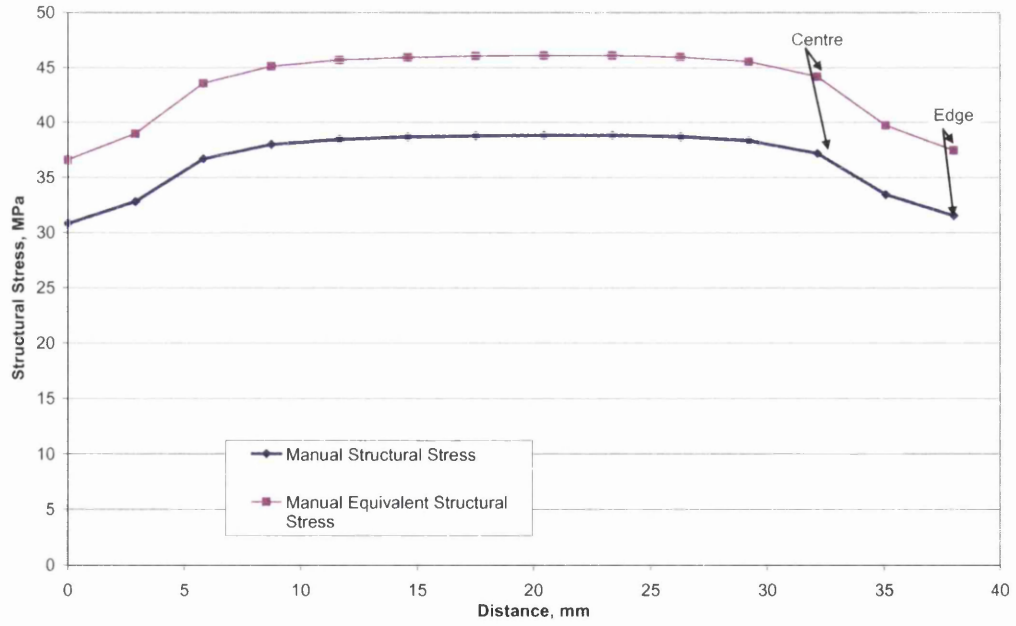

Figure A12.6.44: Location of FE Stresses Used for Conversion of S-N Curves of GM2

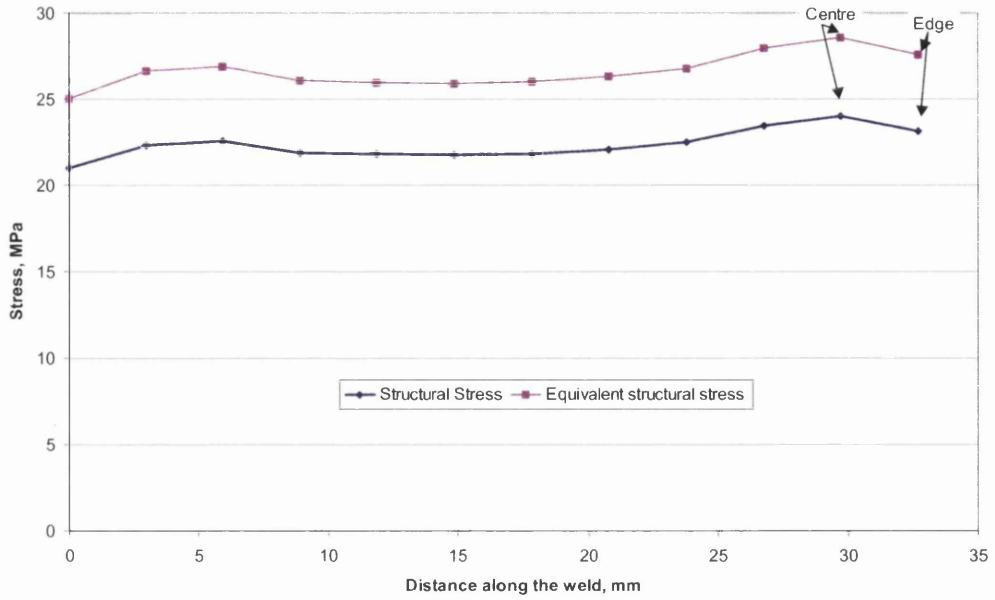

Figure A12.6.45: Location of FE Stresses Used for Conversion of S-N Curves of GM11A

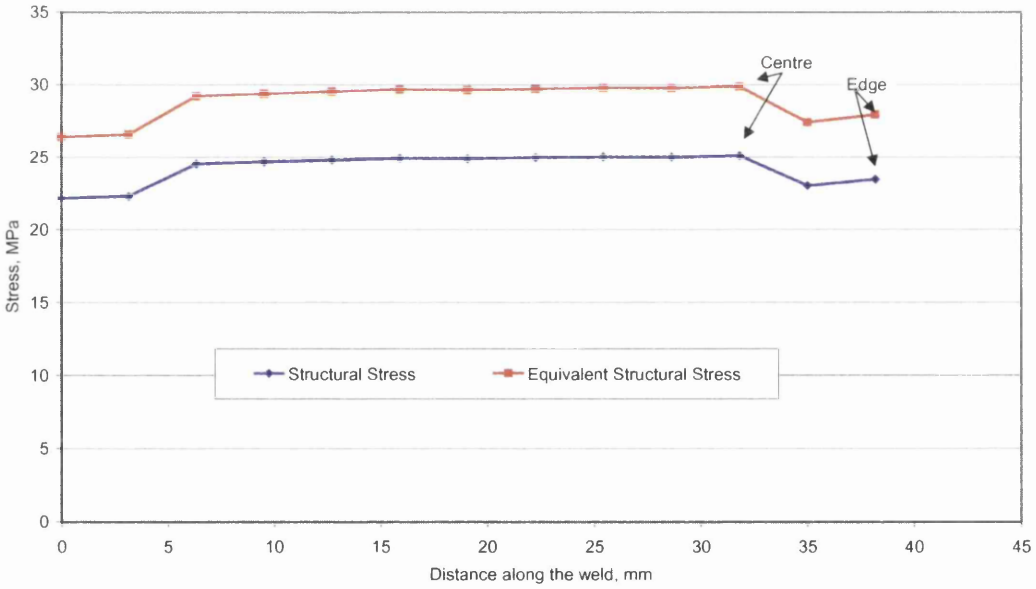

Figure A12.6.46: Location of FE Stresses Used for Conversion of S-N Curves of GM11B

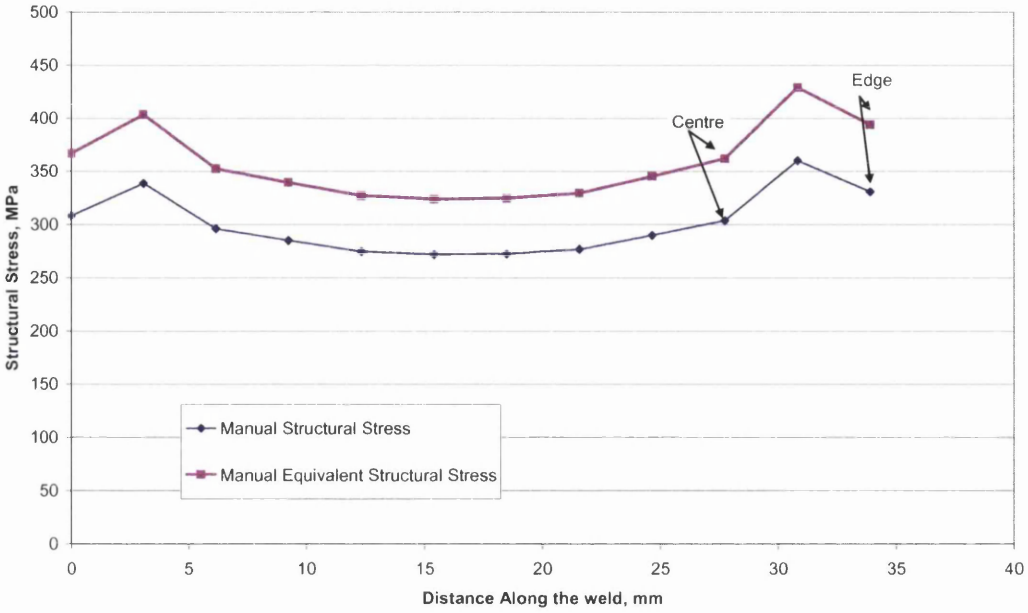

Figure A12.6.47: Location of FE Stresses Used for Conversion of S-N Curves of GM3

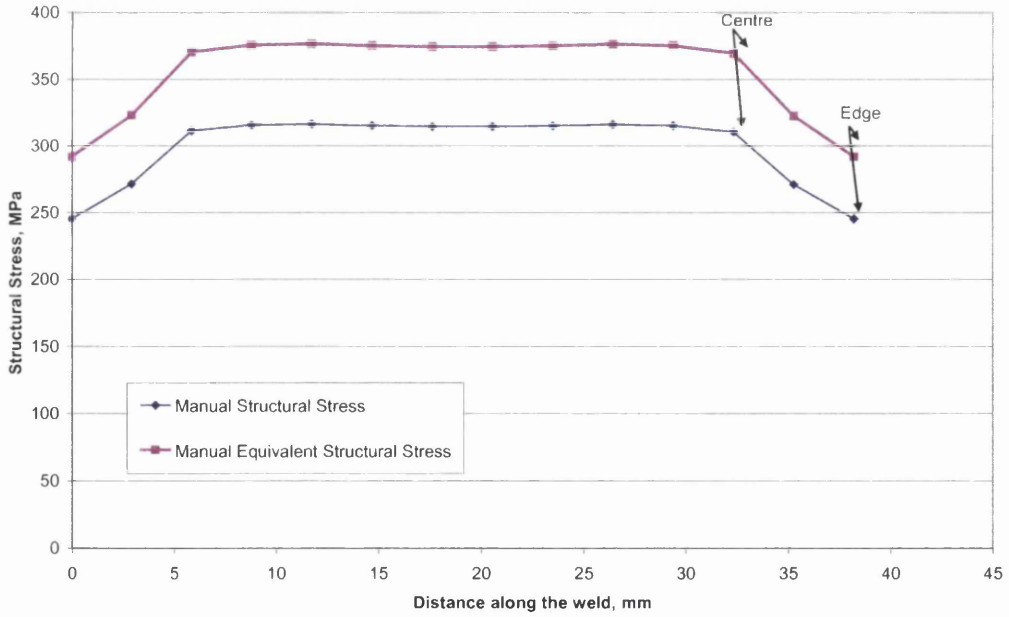

Figure A12.6.48: Location of FE Stresses Used for Conversion of S-N Curves of GM4

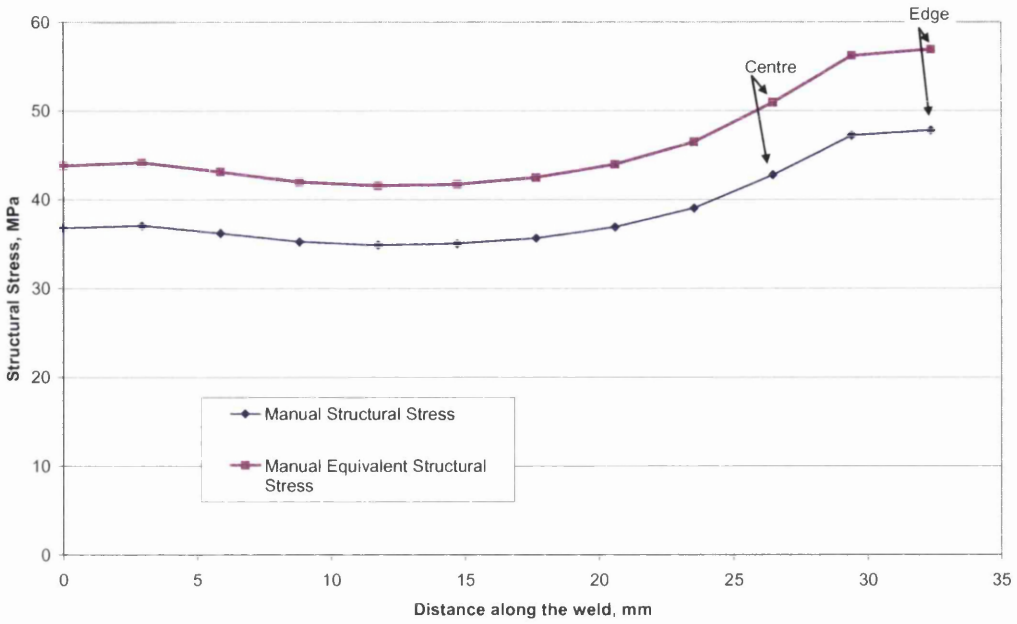

Figure A12.6.49: Location of FE Stresses Used for Conversion of S-N Curves of TM1

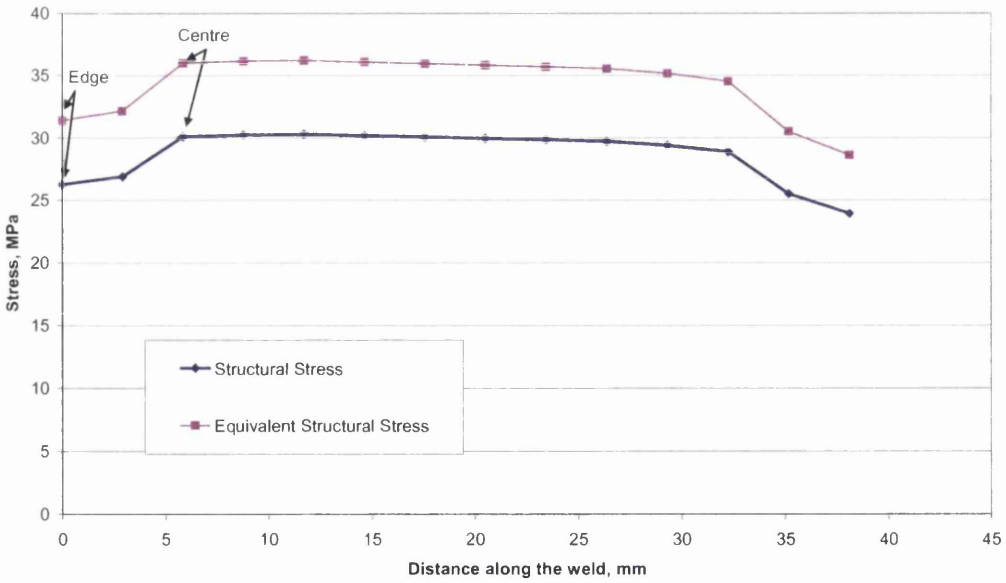

Figure A12.6.50: Location of FE Stresses Used for Conversion of S-N Curves of TM2

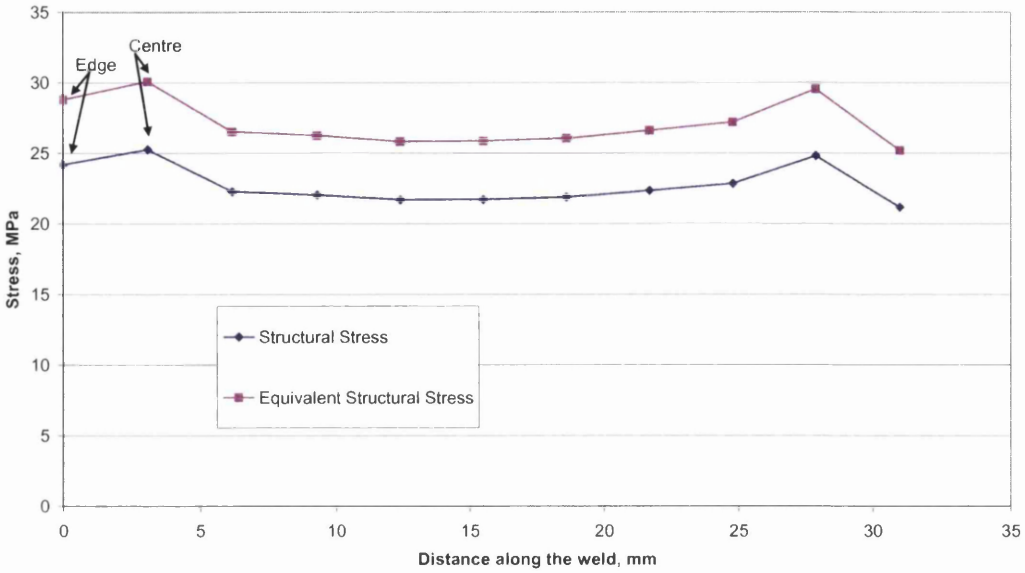

Figure A12.6.51: Location of FE Stresses Used for Conversion of S-N Curves of TM11A

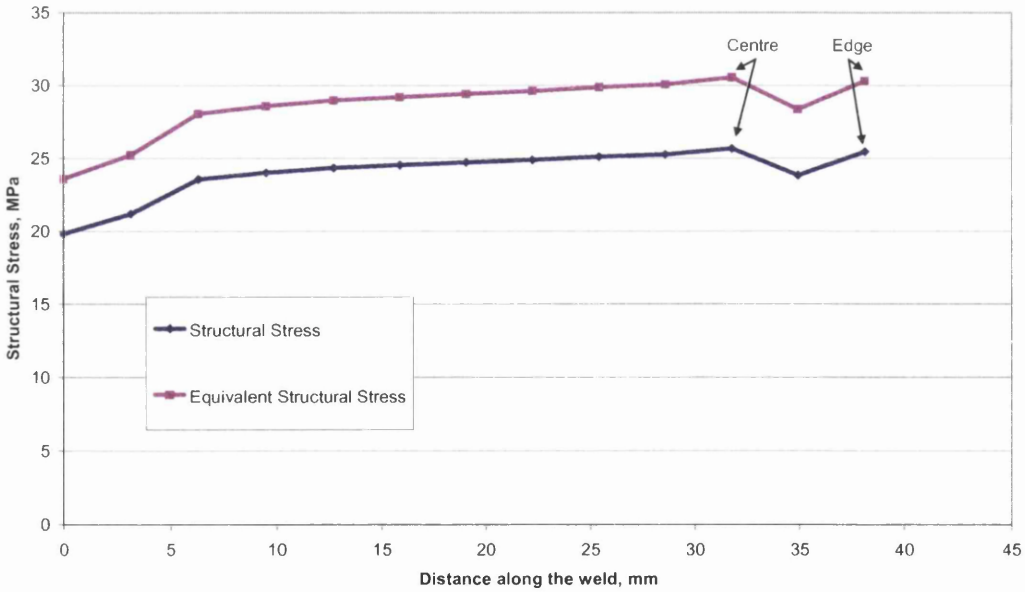

Figure A12.6.52: Location of FE Stresses Used for Conversion of S-N Curves of TM11B

15.12 Appendix 11 Battelle Sensitivity Study – Edge Effects

15.12.1 Manual Equivalent Structural Stress

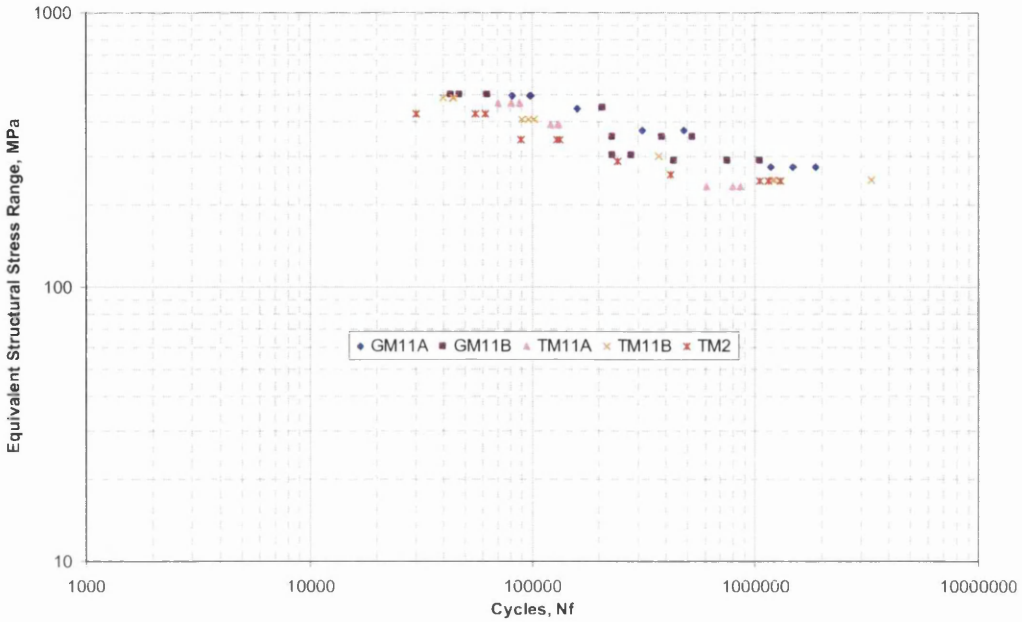

Figure A12.6.53: Stress–Life Master Curve Conversion for All Weld Toe Failures

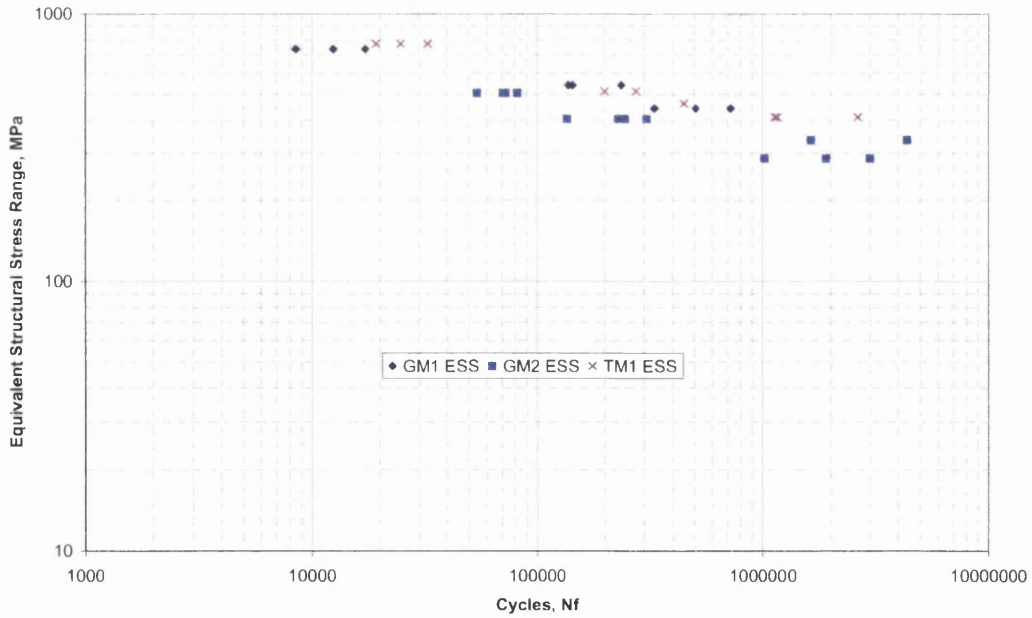

Figure A12.6.54: Stress–Life Master Curve Conversion for All Weld Interface Failures

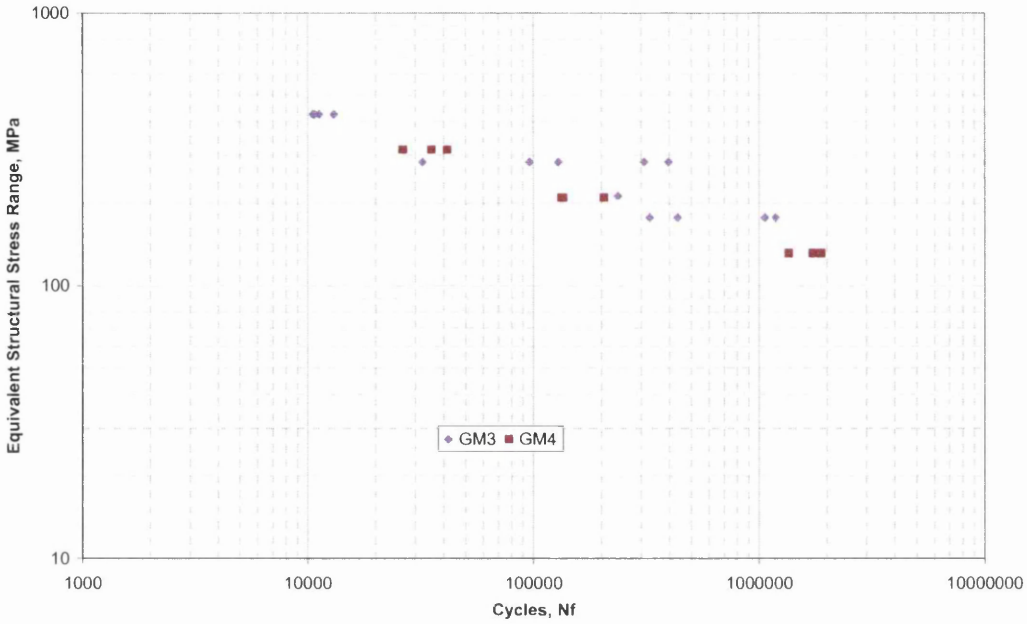

Figure A12.6.55: Stress–Life Master Curve Conversion for All Weld Throat Failures

15.12.2 FLOW Equivalent Structural Stress

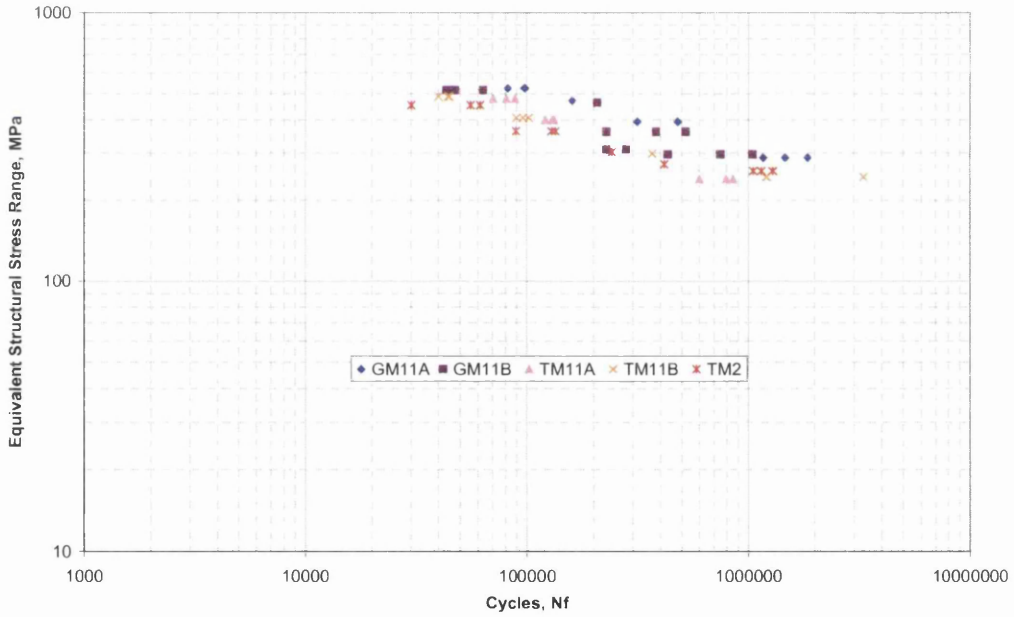

Figure A12.6.56: Stress–Life Master Curve Conversion for All Weld Toe Failures

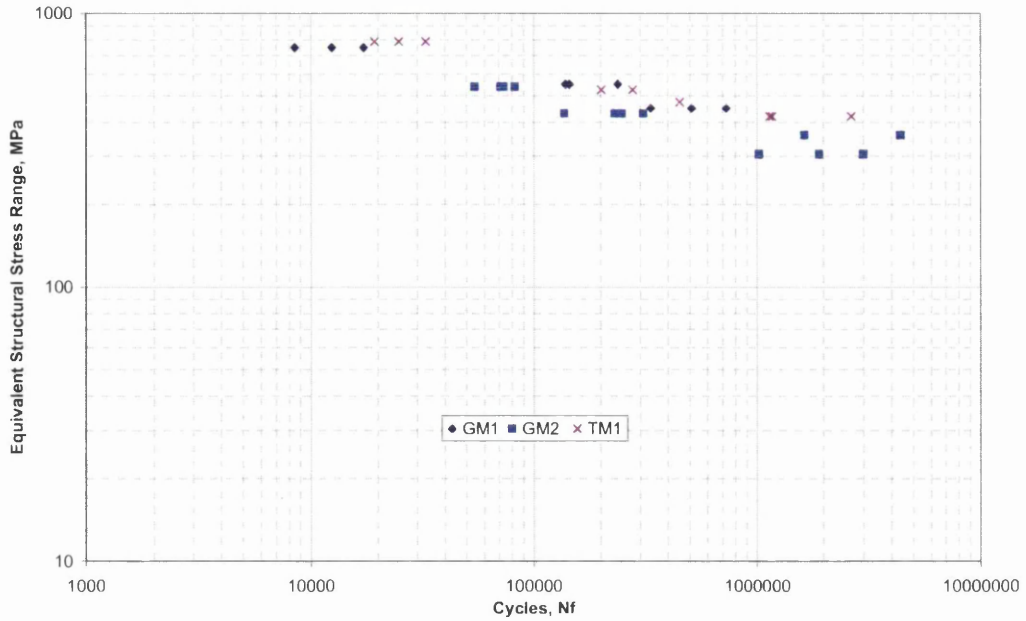

Figure A12.6.57: Stress–Life Master Curve Conversion for All Weld Interface Failures

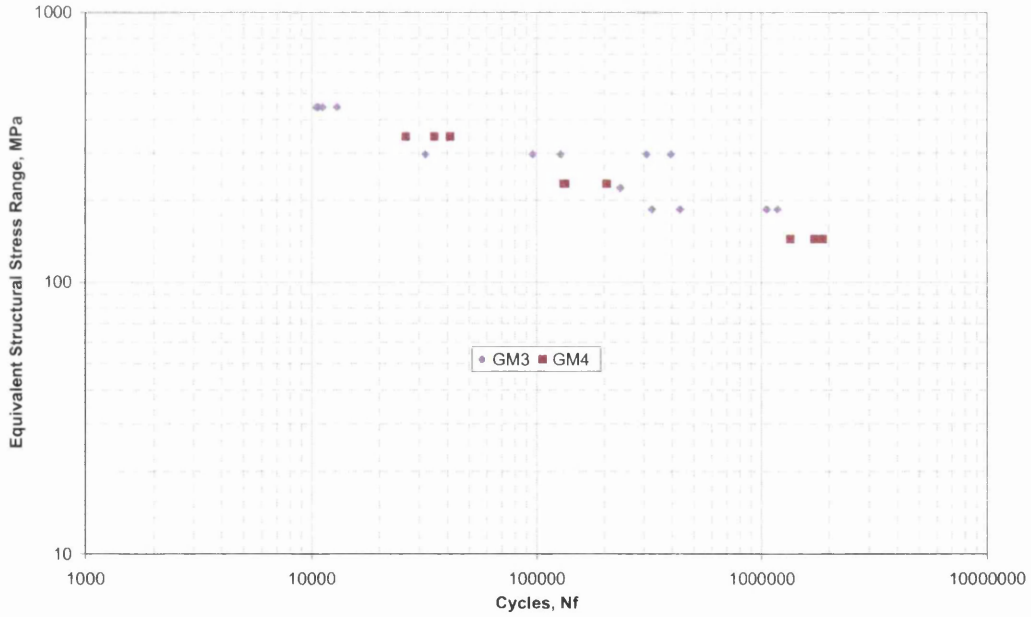

Figure A12.6.58: Stress–Life Master Curve Conversion for All Weld Throat Failures

15.12.3 Verity Equivalent Structural Stress

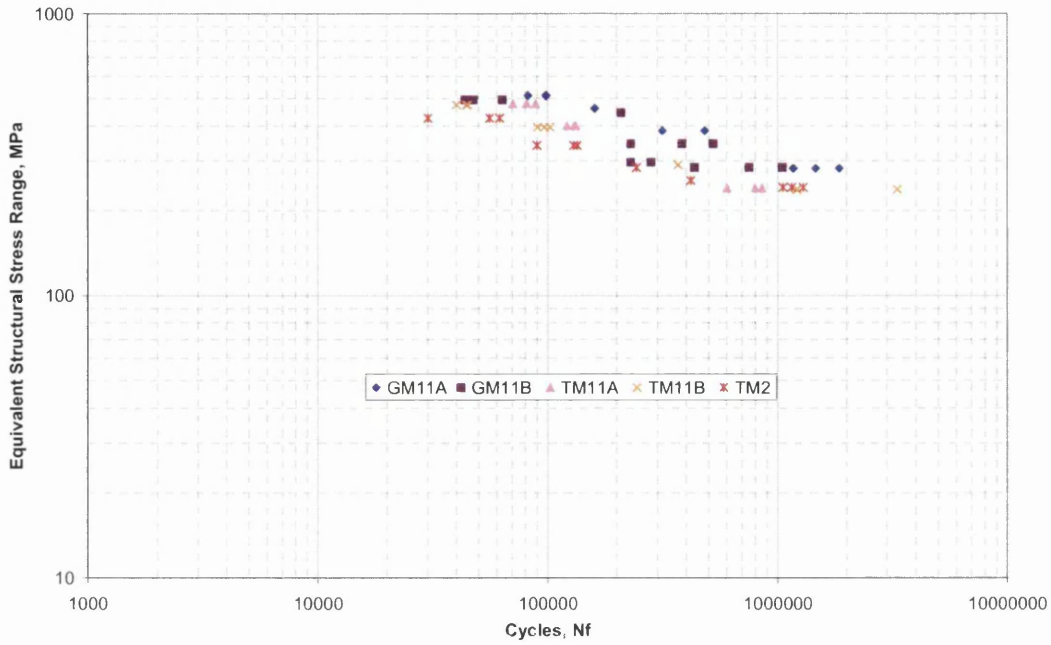

Figure A12.6.59: Stress–Life Master Curve Conversion for All Weld Toe Failures

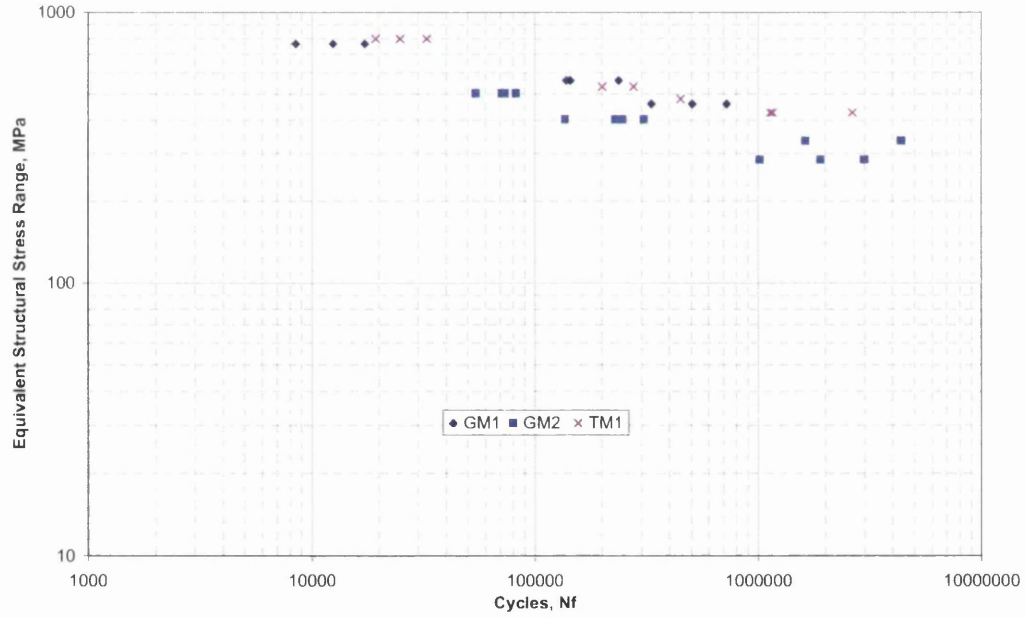

Figure A12.6.60: Stress–Life Master Curve Conversion for All Weld Interface Failures

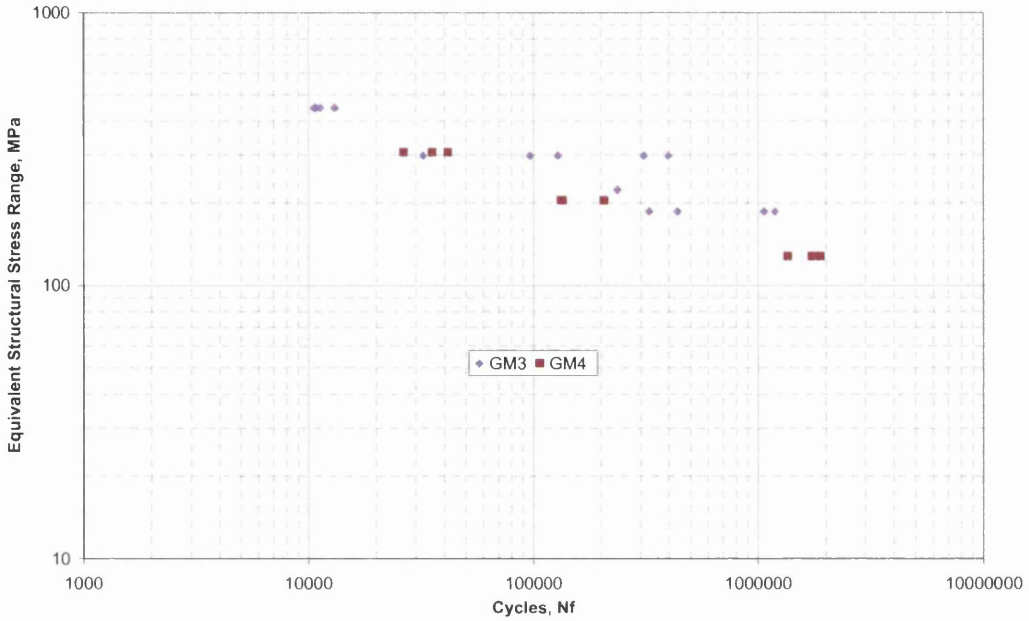

Figure A12.6.61: Stress–Life Master Curve Conversion for All Weld Throat Failures

15.13 Appendix 13 Comparison of Original Battelle Curves Vs. Manual, FLOW and Verity

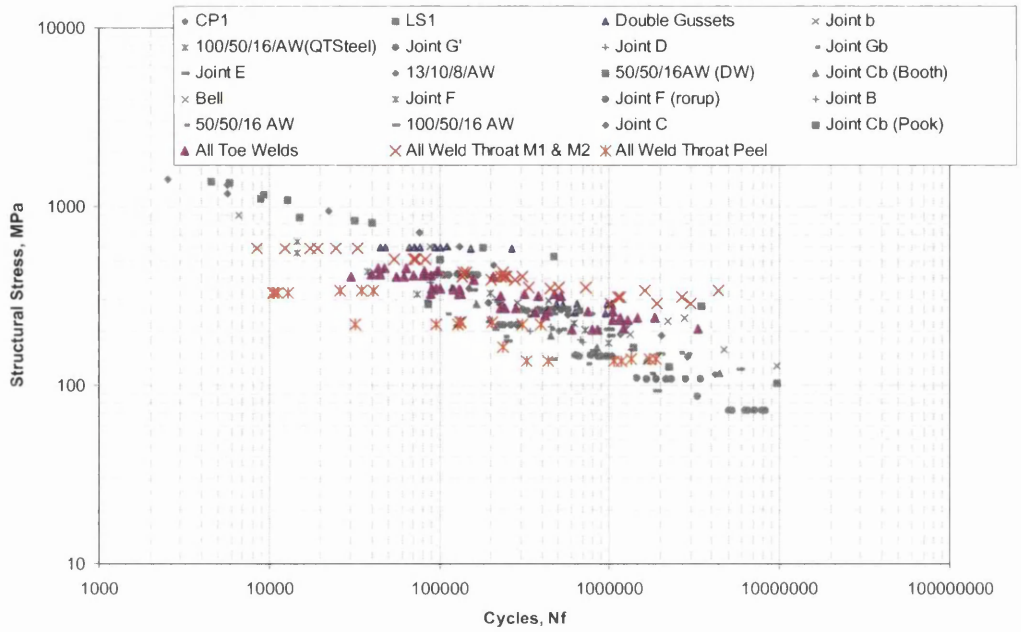

Figure A12.6.62: Comparison of Original Battelle Structural Stress S-N vs. Manual Structural Stress S-N

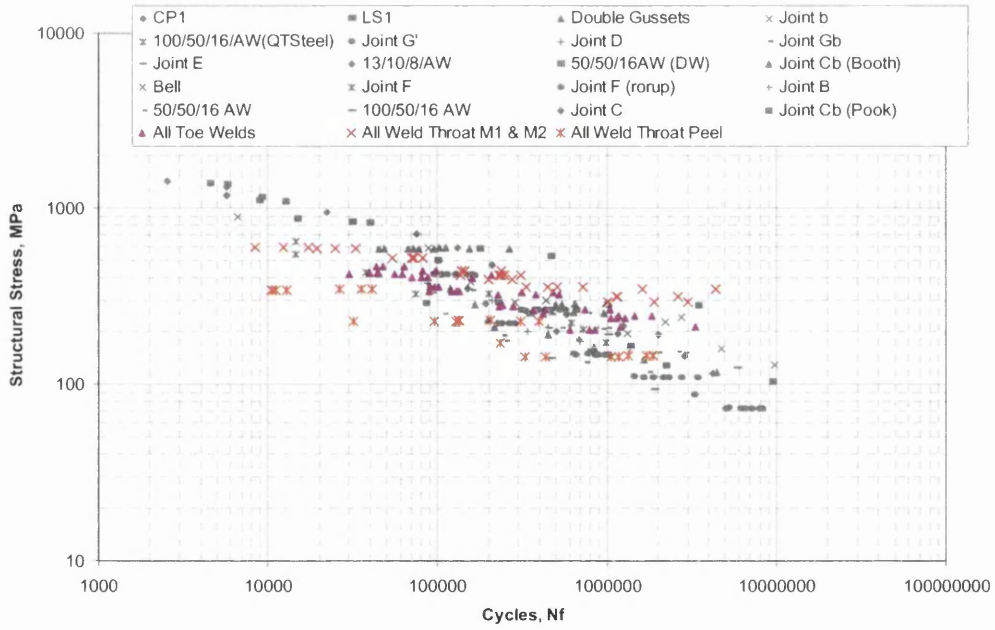

Figure A12.6.63: Comparison of Original Battelle Structural Stress S-N vs. FLOW Structural Stress S-N

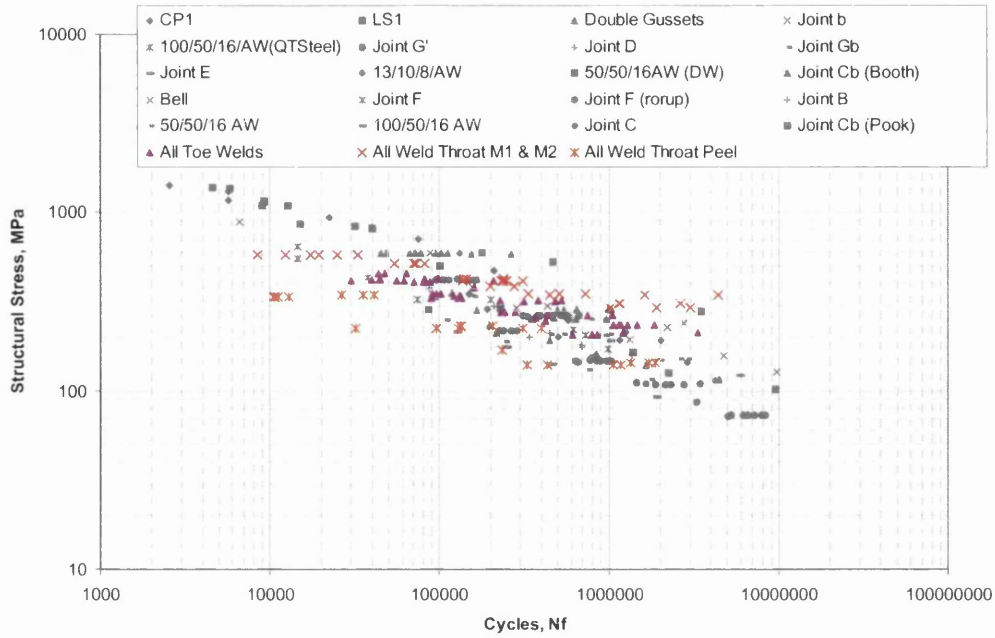

Figure A12.6.63: Comparison of Original Battelle Structural Stress S-N vs. Verity Structural Stress S-N

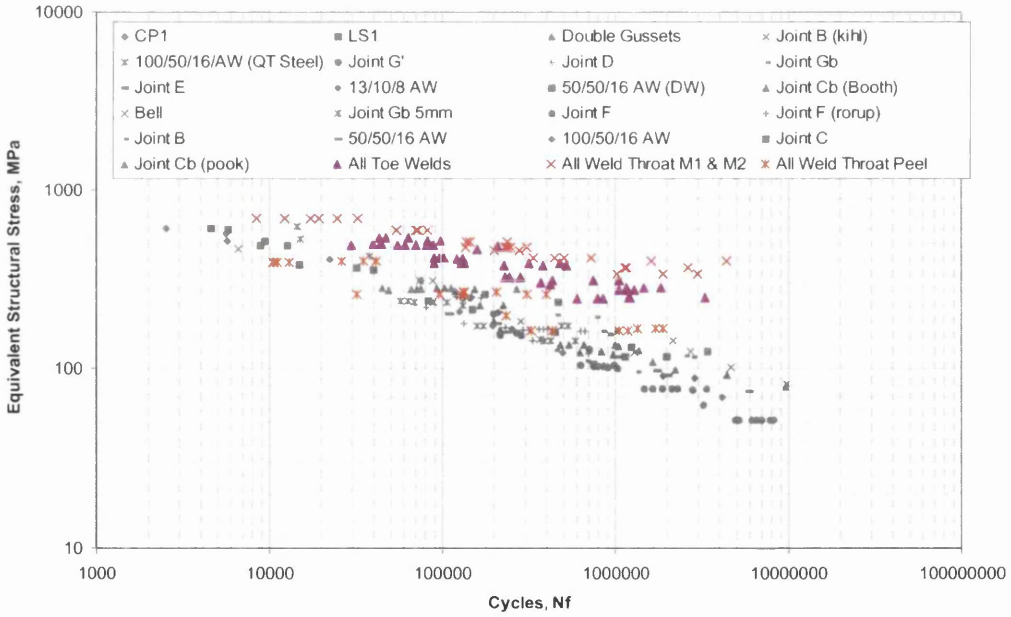

Figure A12.6.64: Comparison of Original Battelle Equivalent Structural Stress S-N vs. Manual Equivalent Structural Stress S-N

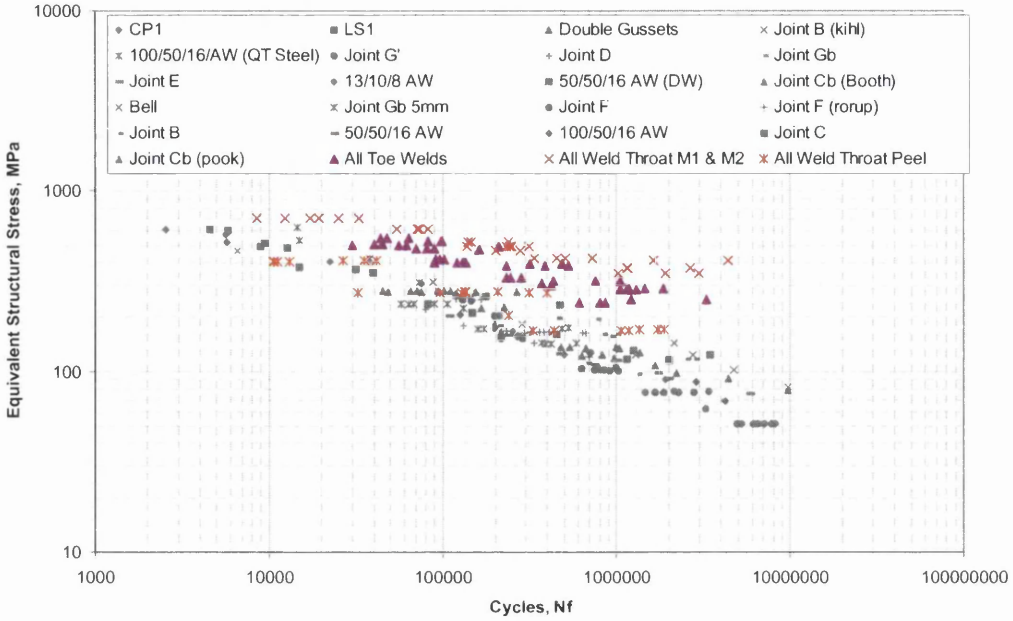

Figure A12.6.65: Comparison of Original Battelle Equivalent Structural Stress S-N vs. FLOW Equivalent Structural Stress S-N

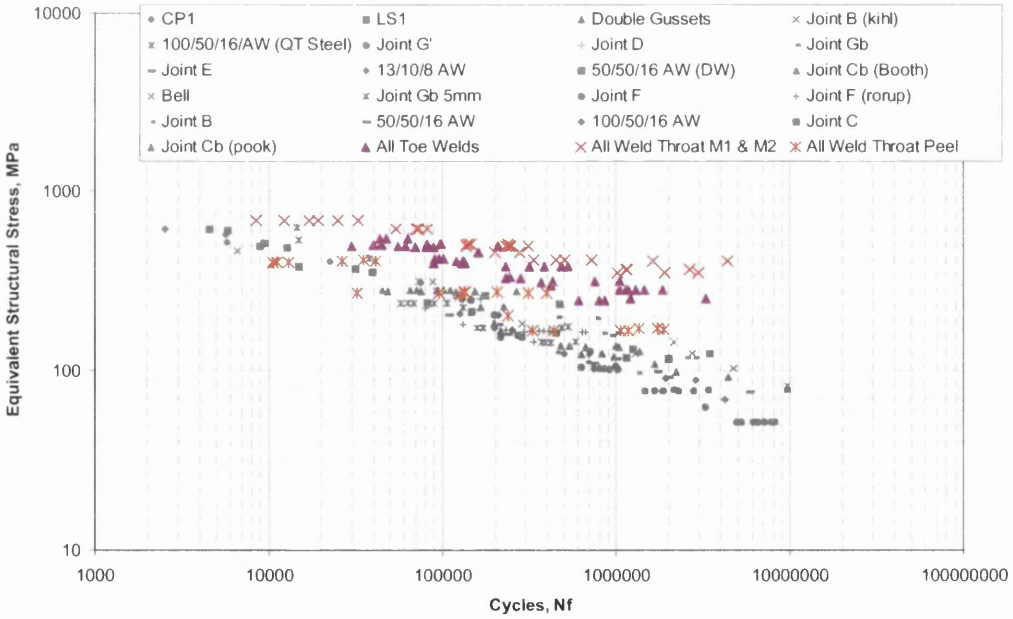

Figure A12.6.66: Comparison of Original Battelle Equivalent Structural Stress S-N vs. Verity Equivalent Structural Stress S-N

15.14 Appendix 14 Regression Based on Stress for Battelle Structural Stress Method

15.14.1 Manual Regression

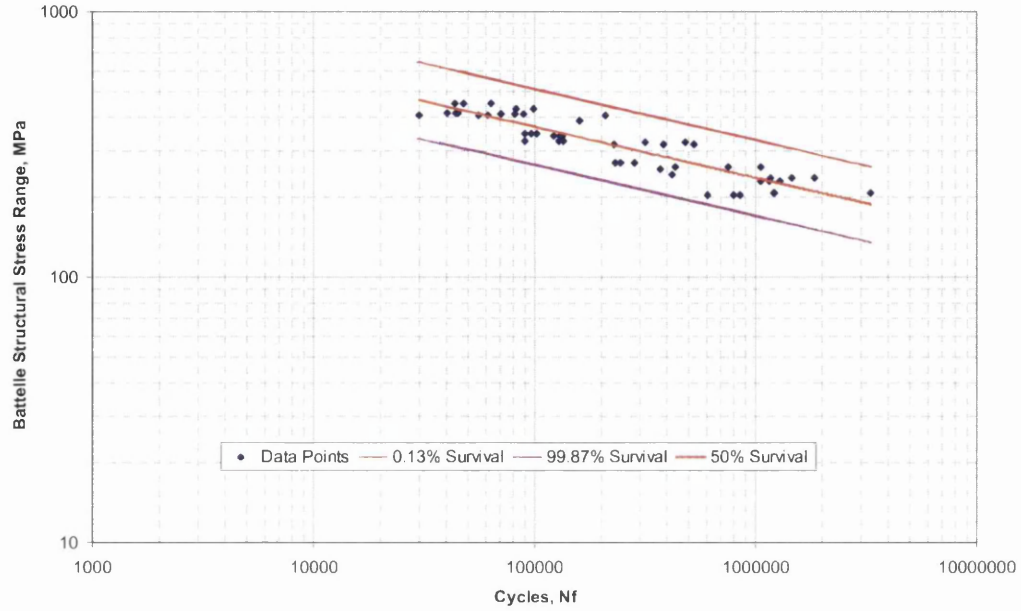

Figure A12.7.1: Statistical Analysis of All Weld Toe Failures

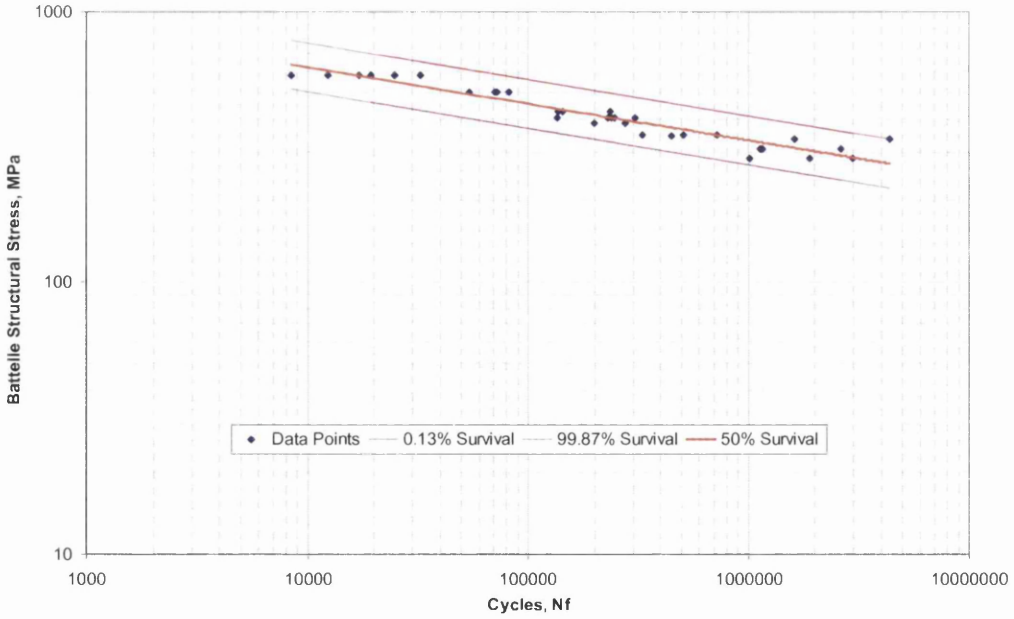

Figure A12.7.2: Statistical Analysis of All Weld Interface Failures

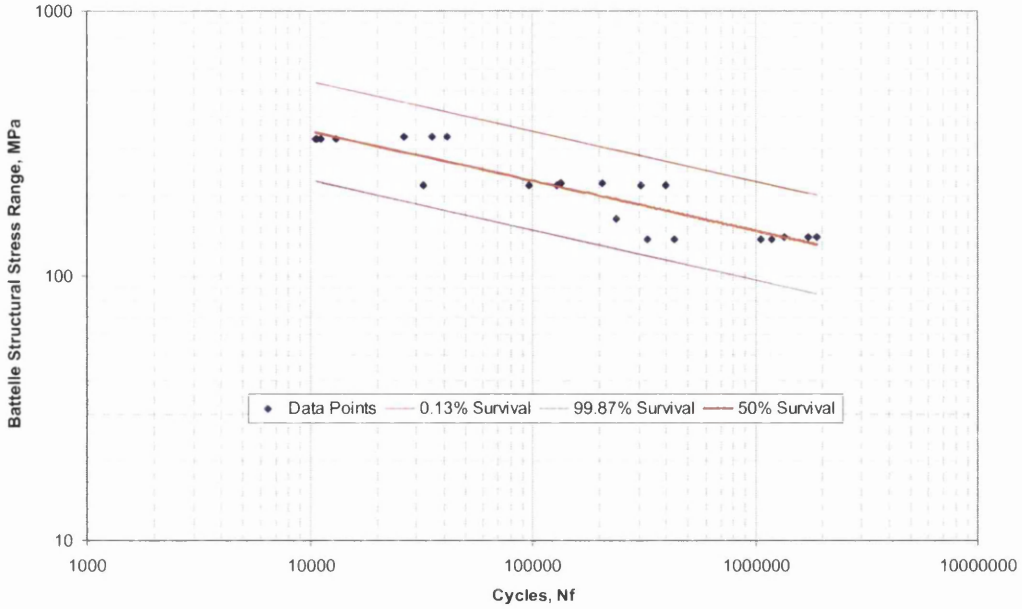

Figure A12.7.3: Statistical Analysis of All Weld Throat Failures

Table A12.7.1: Battelle Manual Structural Stress Regression Based on Stress Master S-N Curve Parameters

$$\Delta\sigma = aN_f^b$$

Battelle Method Structural Stress				
Failure Location	**Survival**	**a**	**b**	**SE log(Δσs)**
Toe Failure	50%	3342.9	-0.1918	0.0475
	99.87%	2407.9	-0.1918	
Interface Failure	50%	2158.1	-0.1355	0.0301
	99.87%	1753	-0.1355	
Throat Failure	50%	2002.9	-0.1889	0.0621
	99.87%	1304.2	-0.1889	

15.14.2 FLOW Regression

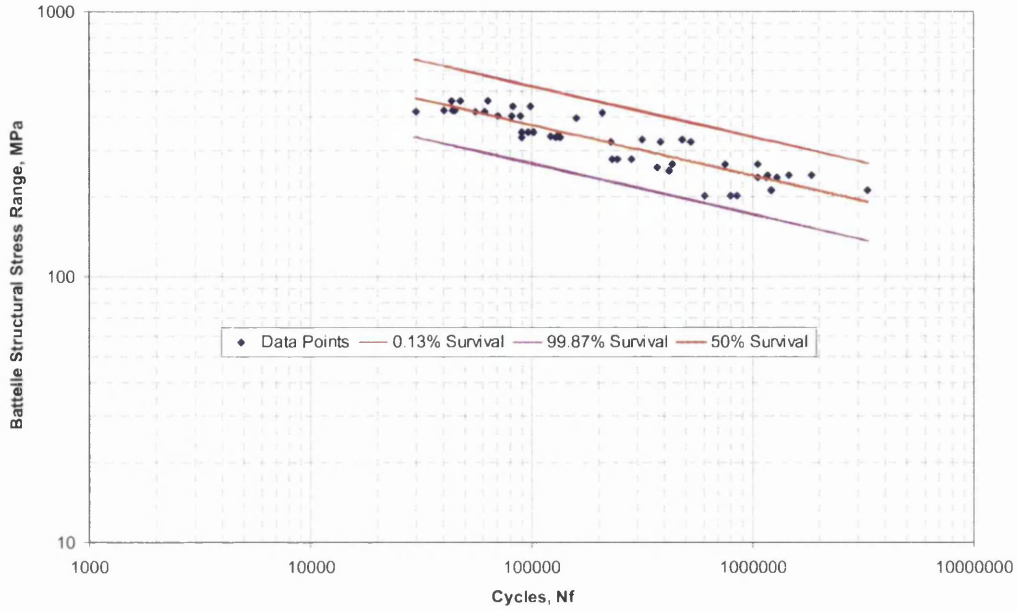

Figure A12.7.4: Statistical Analysis of All Weld Toe Failures

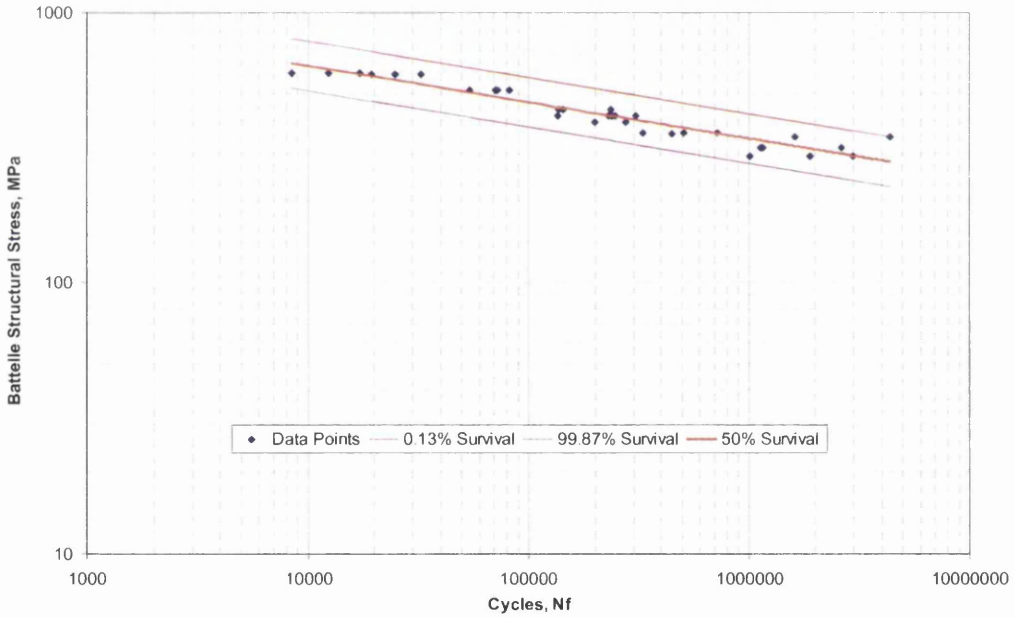

Figure A12.7.5: Statistical Analysis of All Interface Failures

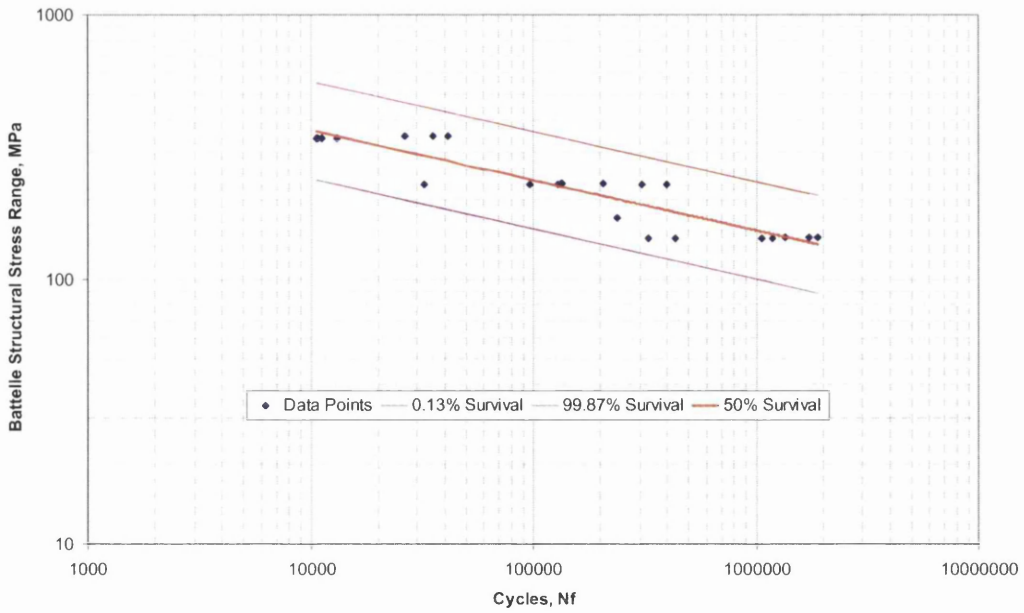

Figure A12.7.6: Statistical Analysis of All Weld Throat Failures

Table A12.7.2: Battelle FLOW Structural Stress Regression Based on Stress Master S-N Curve Parameters

$$\Delta\sigma = aN_f^b$$

Battelle Method Structural Stress				
Failure Location	**Survival**	**a**	**b**	**SE log(Δσs)**
Toe Failure	50%	3378.6	-0.1914	0.0486
	99.87%	2415.1	-0.1914	
Interface Failure	50%	2195	-0.135	0.0305
	99.87%	1777.5	-0.135	
Throat Failure	50%	2081.4	-0.1893	0.0613
	99.87%	1362.9	-0.1893	

15.14.3 Verity Regression

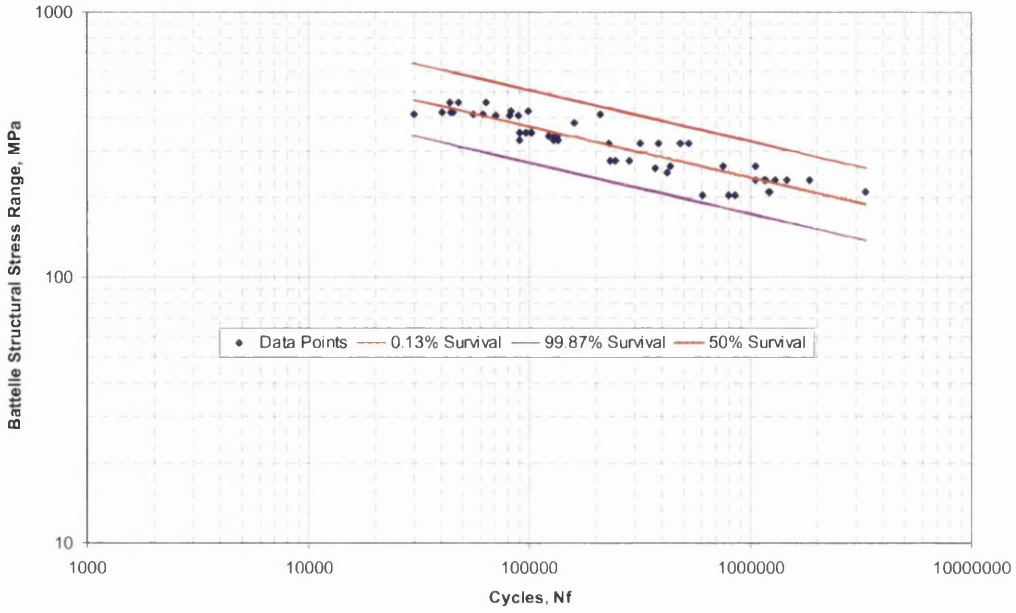

Figure A12.7.7: Statistical Analysis of All Weld Toe Failures

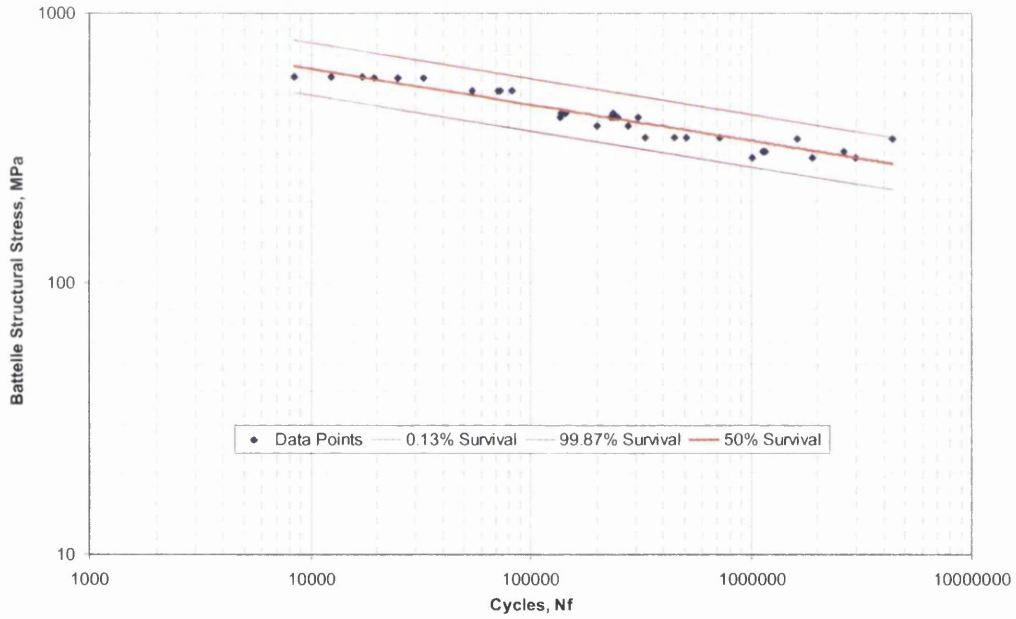

Figure A12.7.8: Statistical Analysis of All Interface Failures

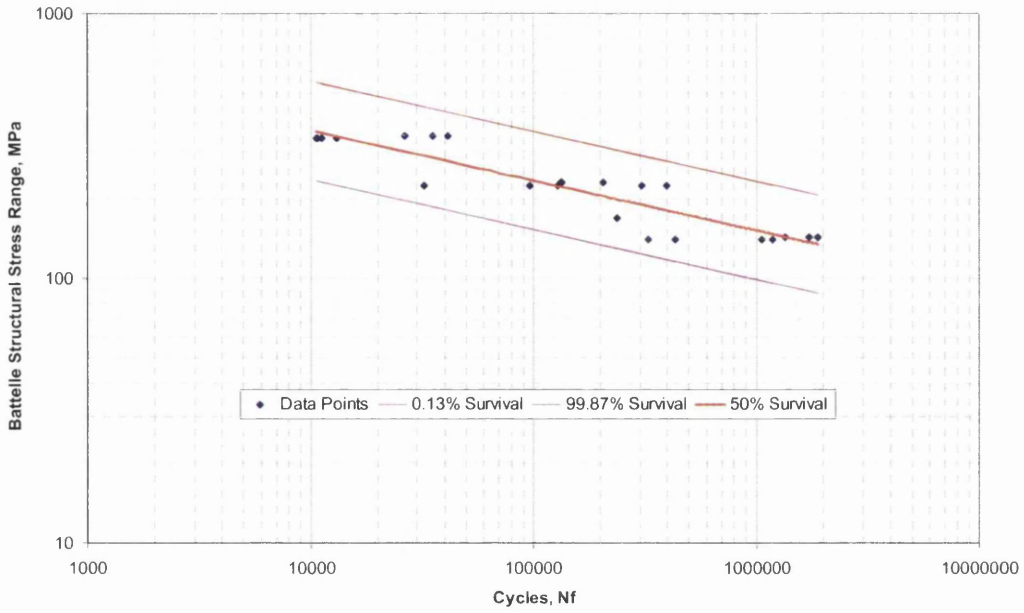

Figure A12.7.9 Statistical Analysis of All Weld Throat Failures

Table A12.7.3: Battelle Verity Structural Stress Regression Based on Stress Master S-N Curve Parameters

$$\Delta\sigma = aN_f^b$$

Battelle Method Structural Stress				
Failure Location	**Survival**	**a**	**b**	**SE log(Δσs)**
Toe Failure	50%	3405.3	-0.1929	0.0457
	99.87%	2483.9	-0.1929	
Interface Failure	50%	2112.9	-0.1332	0.0324
	99.87%	1688.9	-0.1332	
Throat Failure	50%	2052.6	-0.189	0.0619
	99.87%	1338.5	-0.189	

15.15 Appendix 15 Regression Based on Life for Battelle Method Equivalent Structural Stress

15.15.1 Manual regression

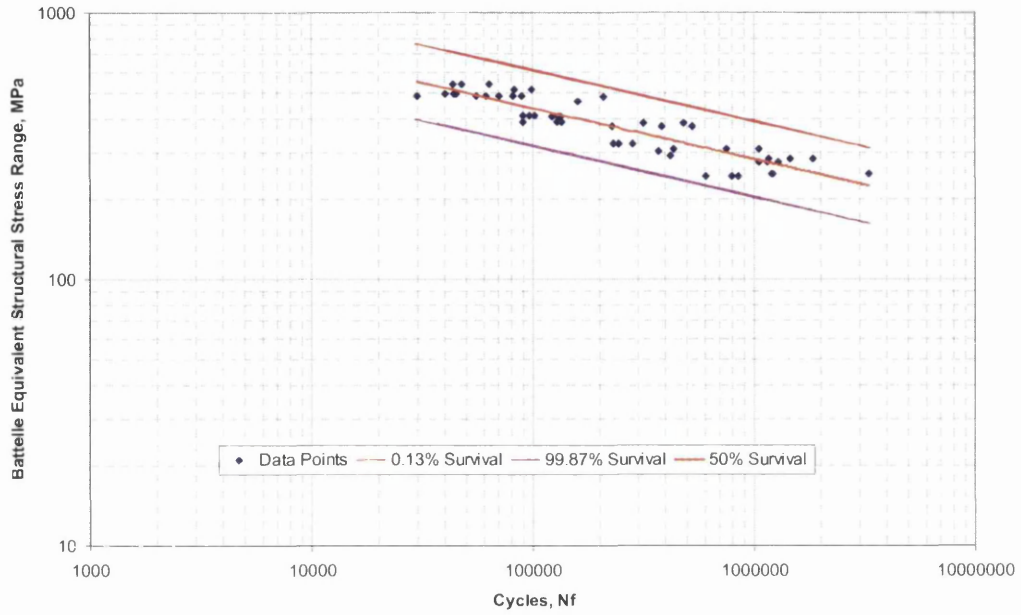

Figure A12.7.10: Statistical Analysis of All Weld Toe Failures

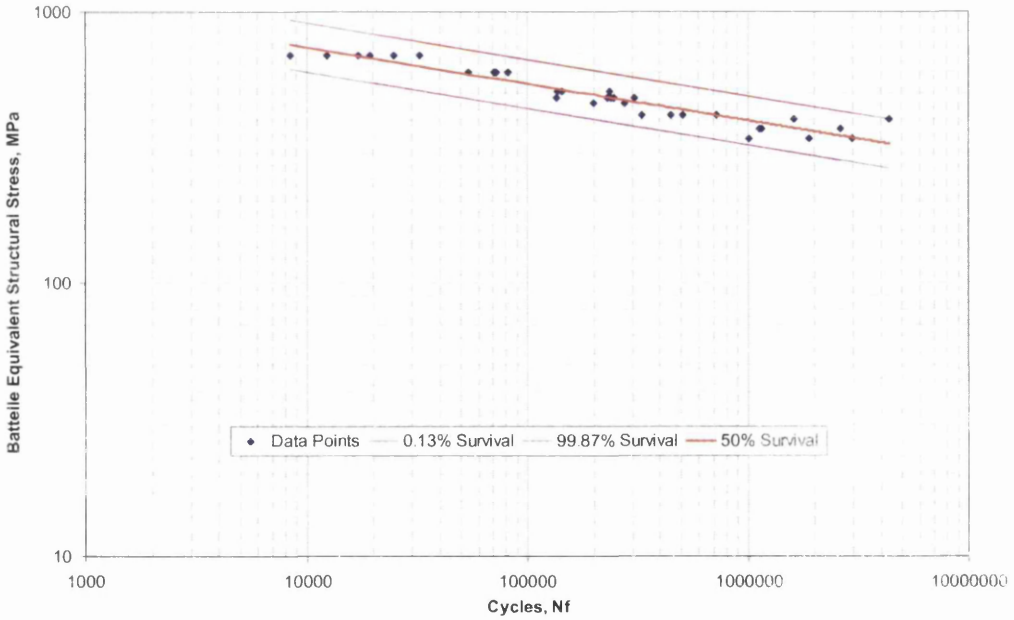

Figure A12.7.11: Statistical Analysis of All Weld Interface Failures

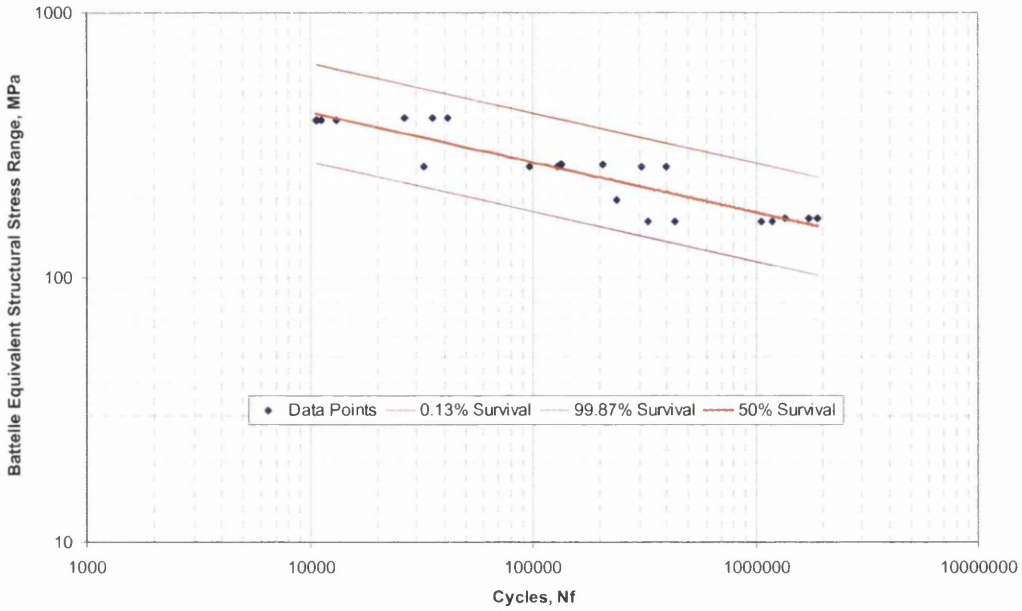

Figure A12.7.12: Statistical Analysis of All Weld Throat Failures

Table A12.7.4: Battelle Manual Equivalent Structural Stress Regression Based on Stress Master S-N Curve Parameters

$$\Delta\sigma = aN_f^b$$

Battelle Method Equivalent Structural Stress				
Failure Location	**Survival**	**a**	**b**	**SE log(ΔSs)**
Toe Failure	50%	3985.3	-0.1918	0.0473
	99.87%	2874.4	-0.1918	
Interface Failure	50%	2568.3	-0.1356	0.0300
	99.87%	2087.4	-0.1356	
Throat Failure	50%	2386.2	-0.189	0.0620
	99.87%	1555.2	-0.189	

15.15.2 FLOW Regression

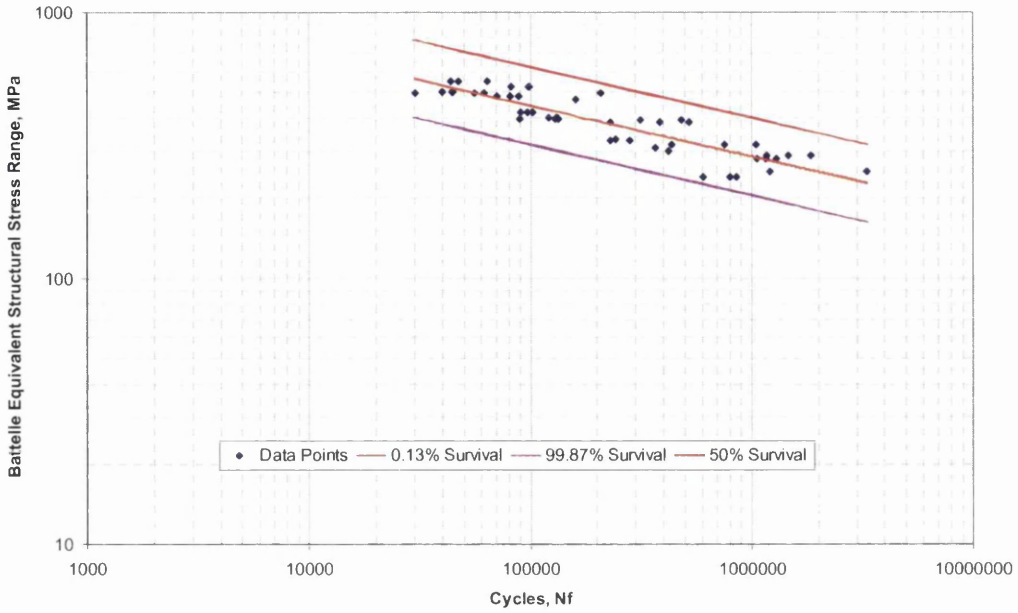

Figure A12.7.13: Statistical Analysis of All Weld Toe Failures

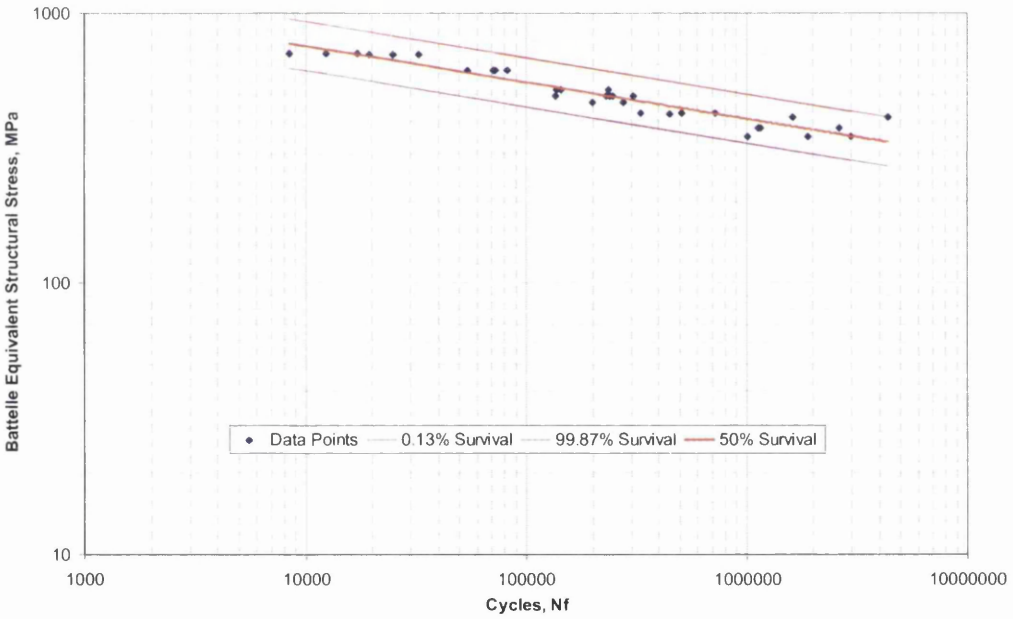

Figure A12.7.14: Statistical Analysis of All Weld Interface Failures

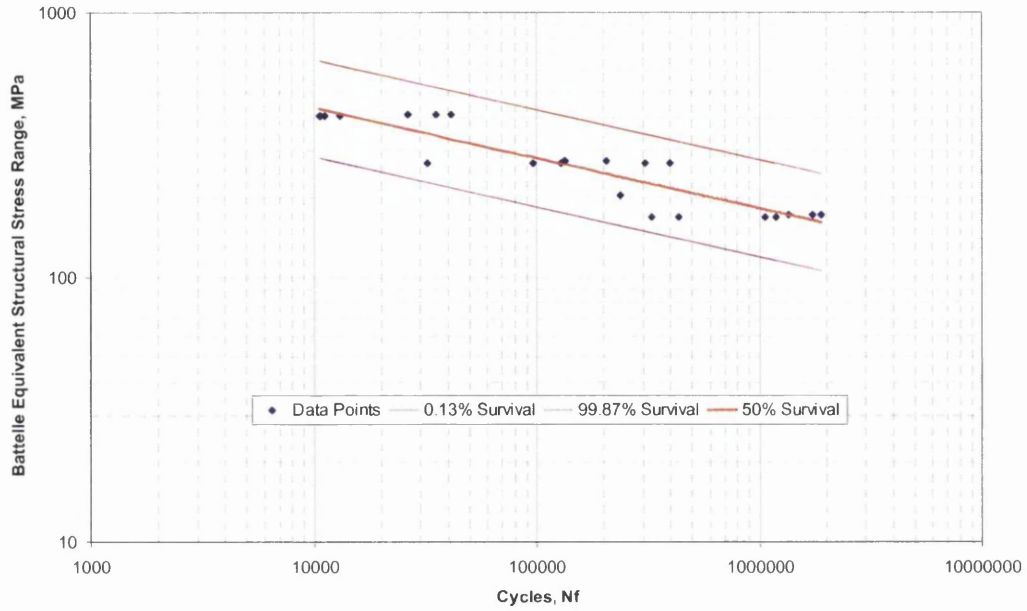

Figure A12.7.15: Statistical Analysis of All Weld Throat Failures

Table A12.7.5: Battelle FLOW Equivalent Structural Stress Regression Based on Stress Master S-N Curve Parameters

$$\Delta\sigma = aN_f^b$$

Battelle Method Equivalent Structural Stress				
Failure Location	**Survival**	**a**	**b**	**SE log(ΔSs)**
Toe Failure	50%	4021.2	-0.1914	0.0486
	99.87%	2873.7	-0.1914	
Interface Failure	50%	2612.2	-0.135	0.0304
	99.87%	2117	-0.135	
Throat Failure	50%	2479.7	-0.1894	0.0612
	99.87%	1625.2	-0.1894	

15.15.3 Verity Regression

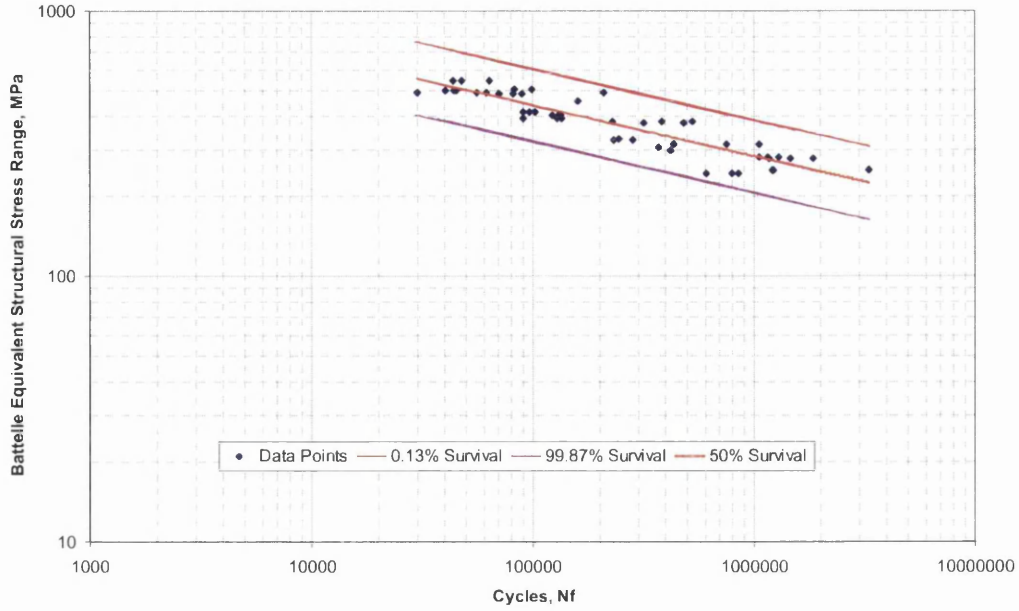

Figure A12.7.16: Statistical Analysis of All Weld Toe Failures

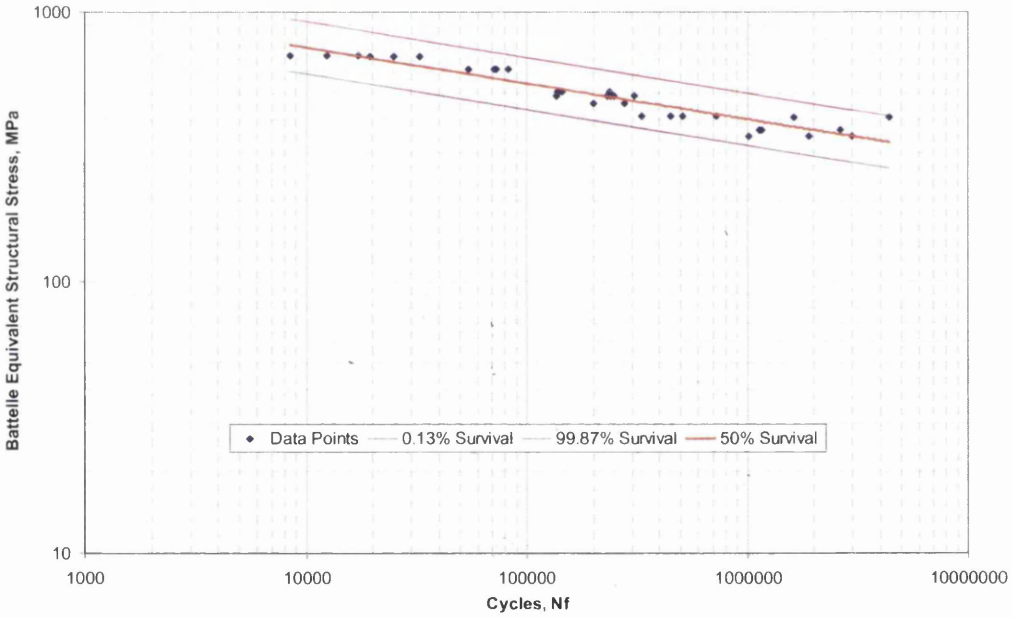

Figure A12.7.17: Statistical Analysis of All Weld Interface Failures

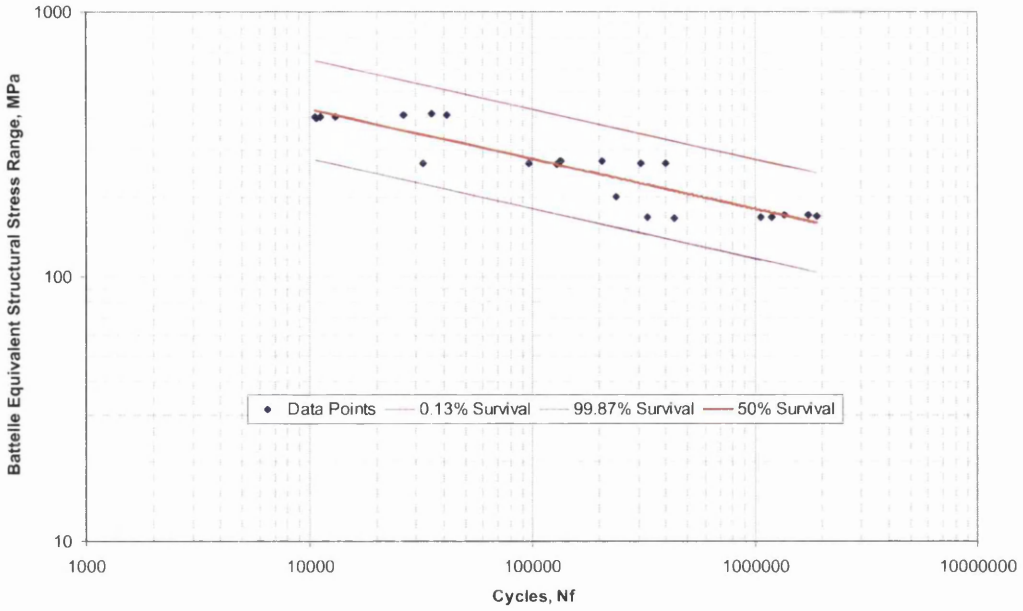

Figure A12.7.18: Statistical Analysis of All Weld Throat Failures

Table A12.7.6: Battelle Verity Equivalent Structural Stress Regression Based on Stress Master S-N Curve Parameters

$$\Delta\sigma = aN_f^b$$

Battelle Method Equivalent Structural Stress				
Failure Location	**Survival**	**a**	**b**	**SE log(ΔSs)**
Toe Failure	50%	4059.7	-0.193	0.0455
	99.87%	2964.7	-0.193	
Interface Failure	50%	2514.4	-0.1333	0.0323
	99.87%	2012.2	-0.1333	
Throat Failure	50%	2441.6	-0.1891	0.0624
	99.87%	1586.3	-0.1891	